NASA/CP—2004-213205/VOL2

Strategic Research to Enable NASA's Exploration Missions Conference and Workshop

Poster Session

August 2004

The NASA STI Program Office . . . in Profile

Since its founding, NASA has been dedicated to the advancement of aeronautics and space science. The NASA Scientific and Technical Information (STI) Program Office plays a key part in helping NASA maintain this important role.

The NASA STI Program Office is operated by Langley Research Center, the Lead Center for NASA's scientific and technical information. The NASA STI Program Office provides access to the NASA STI Database, the largest collection of aeronautical and space science STI in the world. The Program Office is also NASA's institutional mechanism for disseminating the results of its research and development activities. These results are published by NASA in the NASA STI Report Series, which includes the following report types:

- TECHNICAL PUBLICATION. Reports of completed research or a major significant phase of research that present the results of NASA programs and include extensive data or theoretical analysis. Includes compilations of significant scientific and technical data and information deemed to be of continuing reference value. NASA's counterpart of peer-reviewed formal professional papers but has less stringent limitations on manuscript length and extent of graphic presentations.

- TECHNICAL MEMORANDUM. Scientific and technical findings that are preliminary or of specialized interest, e.g., quick release reports, working papers, and bibliographies that contain minimal annotation. Does not contain extensive analysis.

- CONTRACTOR REPORT. Scientific and technical findings by NASA-sponsored contractors and grantees.

- CONFERENCE PUBLICATION. Collected papers from scientific and technical conferences, symposia, seminars, or other meetings sponsored or cosponsored by NASA.

- SPECIAL PUBLICATION. Scientific, technical, or historical information from NASA programs, projects, and missions, often concerned with subjects having substantial public interest.

- TECHNICAL TRANSLATION. English-language translations of foreign scientific and technical material pertinent to NASA's mission.

Specialized services that complement the STI Program Office's diverse offerings include creating custom thesauri, building customized databases, organizing and publishing research results . . . even providing videos.

For more information about the NASA STI Program Office, see the following:

- Access the NASA STI Program Home Page at ***http://www.sti.nasa.gov***

- E-mail your question via the Internet to help@sti.nasa.gov

- Fax your question to the NASA Access Help Desk at 301–621–0134

- Telephone the NASA Access Help Desk at 301–621–0390

- Write to:
  NASA Access Help Desk
  NASA Center for AeroSpace Information
  7121 Standard Drive
  Hanover, MD 21076

NASA/CP—2004-213205/VOL2

Strategic Research to Enable NASA's Exploration Missions Conference and Workshop

Poster Session

Proceedings of a conference held at and sponsored by
the NASA Office of Biological and Physical Research
and hosted by NASA Glenn Research Center and
the National Center for Microgravity Research on Fluids and Combustion
Cleveland, Ohio, June 22–23, 2004

National Aeronautics and
Space Administration

Glenn Research Center

August 2004

Acknowledgments

This conference was sponsored by the NASA Office of Biological and Physical Research (OBPR).

Available from

NASA Center for Aerospace Information
7121 Standard Drive
Hanover, MD 21076

National Technical Information Service
5285 Port Royal Road
Springfield, VA 22100

Available electronically at http://gltrs.grc.nasa.gov

Table of Contents
Poster Session

Abbud-Madrid, Angel; McKinnon, J. Thomas; Delplanque, Jean-Pierre; Kailasanath, Kazhikathra; Gokoglu, Suleyman; and Wu, Ming-Shin
SPACECRAFT FIRE SUPPRESSION: TESTING AND EVALUATION 1

Agrawal, Ajay K.; and Parthasarathy, Ramkumar N.
BUOYANCY EFFECTS ON FLOW STRUCTURE AND INSTABILITY OF LOW-DENSITY GAS JETS 12

Avedisian, C.T.; Chandra, S.; and Mostaghimi, J.
THE FLUID MECHANICS OF LIQUID JET IMPINGEMENT: THE HYDRAULIC JUMP IN MICROGRAVITY 21

Banerjee, H.; Blackshear, M.; Mahaffey, K.; Knight. C.; Khan, A.A.; and Delucas, L.
EFFECT OF MICROGRAVITY ON MAMMALIAN LYMPHOCYTES 24

Bar-Ilan, A.; Putzeys, O.; Rein, G.; and Fernandez-Pello, A.C.
TRANSITION FROM FORWARD SMOLDERING TO FLAMING IN SMALL POLYURETHANE FOAM SAMPLES 29

Bergroth, M.; Solomon, T.; Gebremichael, Y.; Keys, A.S.; Vogel, M.; Solomon, M.J.; and Glotzer, S.C.
SPATIALLY HETEROGENEOUS DYNAMICS AND THE EARLY STAGES OF CRYSTAL NUCLEATION AND GROWTH IN METASTABLE LIQUIDS AND COLLOIDS 30

Bhattacharjee, Subrata; Paolini, Chris; Wakai, Kazunori; and Takahashi, Shuhei
FLAMMABILITY MAP FOR MICROGRAVITY FLAME SPREAD 32

Bhunia, Avijit; Chandrasekaran, Sriram; and Chen, Chung-Lung
LIQUID MICRO-JET IMPINGEMENT COOLING OF A POWER CONVERSION MODULE 34

Buckley, Steven G.; Rangwala, Ali S.; and Torero, Jose L.
MODELING AND ANALYSIS OF CO-CURRENT FLAME SPREAD APPLIED TO THE UPWARD BURNING OF PMMA 36

Cavanagh, Jane M.; Torvi, David A.; Gabriel, Kamiel S.; and Ruff, Gary A.
TESTS OF FLAMMABILITY OF COTTON FABRICS AND EXPECTED SKIN BURNS IN MICROGRAVITY 38

Colver, Gerald M.; Greene, Nate; and Xu, Hua
EPS (ELECTRIC PARTICULATE SUSPENSION) MICROGRAVITY TECHNOLOGY PROVIDES NASA WITH NEW TOOLS 52

Colwell, Joshua E.; Horányi, Mihály; Robertson, Scott; Sture, Stein; Batiste, Susan; and Sternovsky, Zoltan
LUNAR SURFACE ENVIRONMENT LABORATORY 54

Dreyer, Michael E.; Rosendahl, Uwe; and Ohlhoff, Antje
CRITICAL VELOCITIES IN OPEN CAPILLARY CHANNEL FLOWS (CCF) 70

Dryer, F.L.; Kroenlein, K.G.; Kazakov, A.; Williams, F.A. and Nayagam, V.
ISOLATED LIQUID DROPLET COMBUSTION: INHIBITION AND EXTINCTION STUDIES 85

Ettema, R.; Marshall, J.S.; and McAlister, G.
WIND-DRIVEN RIVULET BREAK-OFF IN CONDITIONS RANGING FROM 0G TO 1G 95

Faghri, M.; and Charmchi, M.
MELTING AND SOLIDIFICATION IN A RECTANGULAR CAVITY UNDER ELECTROMAGNETICALLY SIMULATED LOW GRAVITY 97

Fernandez-Pello, A.C.; Bar-Ilan, A.; Putzeys, O.M.; Rein, G.; and Urban, D.L.
TRANSITION FROM FORWARD SMOLDERING TO FLAMING IN SMALL POLYURETHANE FOAM SAMPLES 98

Gillis, Keith A.; Shinder, Iosif I.; and Moldover, Michael R.
PROGRESS ON ACOUSTIC MEASUREMENTS OF THE BULK VISCOSITY OF NEAR-CRITICAL XENON (BVX) 100

Glushko, V.
STUDYING BIOLOGICAL RHYTHMS OF PERSON'S SKIN-GALVANIC REACTION AND DYNAMICS OF LIGHT TRANSMISSION BY ISOMERIC SUBSTANCE IN SPACE FLIGHT CONDITIONS 114

Goree, John
ELECTROSTATIC RELEASE OF FINE PARTICLES ADHERED TO SURFACES ON THE MOON OR MARS 116

Hamins, A.; Bundy, M.; Oh, C.B.; Park, J.; and Puri, I.K.
SUPPRESSION OF LOW STRAIN RATE NONPREMIXED FLAMES BY AN AGENT 117

Hermanson, J.C.; Johari, H.; Ghaem-Maghami, E.; Stocker, D.P.; and Hegde, U.G.
BUOYANCY EFFECTS IN STRONGLY-PULSED, TURBULENT DIFFUSION FLAMES 128

Hirsch, David
FLAMMABILITY CONFIGURATION ANALYSIS FOR SPACECRAFT APPLICATIONS 139

Ishii, Mamoru; Sun, Xiaodong; and Vasavada, Shilp
TWO-FLUID MODEL AND INTERFACIAL AREA TRANSPORT IN MICROGRAVITY CONDITION 146

Jenkins, James T.; Pasini, José Miguel; and Valance, Alexandre
AEOLIAN SAND TRANSPORT WITH COLLISIONAL SUSPENSION 158

Jun, Yonggun; Zhang, Jie; and Wu, Xiao-Lun
TWO DIMENSIONAL TURBULENCE IN PRESENCE OF POLYMER 163

Kashiwagi, Takashi; Nakamura, Yuji; Olson, Sandra L.; and Mell, William
TRANSITION FROM IGNITION TO FLAME GROWTH UNDER EXTERNAL RADIATION IN THREE DIMENSIONS (TIGER-3D) 164

Kazakov, A.; Kroenlein, K.G.; Dryer, F.L.; Williams, F.A.; and Nayagam, V.
ISOLATED LIQUID DROPLET COMBUSTION: INHIBITION AND EXTINCTION STUDIES 175

Khusid, Boris; and Acrivos, Andreas
ELECTRIC-FIELD-DRIVEN PHENOMENA FOR MANIPULATING PARTICLES IN MICRO-DEVICES 177

Kim, Chang-Soo
MICROSENSOR TECHNOLOGIES FOR PLANT GROWTH SYSTEM MONITORING 188

Kizito, John P.; Vander Wal, Randy L.; Berger, Gordon; and Tryggvason, Gretar
SPRAY COOLING PROCESSES FOR SPACE APPLICATIONS 198

Koepp, R.A.; Parthasarathy, R.N.; and Gollahalli, S.R.
EFFECTS OF GRAVITY ON BUBBLE FORMATION IN AN ANNULAR JET 206

Kopacka, Wesley M.; Hollingsworth, Andrew D.; Russel, William B.; and Chaikin, Paul M.
A STUDY OF COLLOIDAL CRYSTALLIZATION 216

Kuhlman, John; Gray, Donald D.; Glaspell, Shannon; Kreitzer, Paul; Battleson, Charlie; Lechliter, Michelle; Campanelli, Michael; Fredrick, Nicholas; Sunderlin, Christopher; and Williams, Brianne
POSITIONING OF SIMULATED VAPOR BUBBLES IN MICROGRAVITY BY THE KELVIN FORCE 219

Lastochkin, Dmitri; Wang, Ping; and Chang, Hsueh-Chia
AC ELECTROKINETIC JETS AND SPRAYS FOR SPACE APPLICATIONS 235

Lebedev, Nikolai; Trammell, Scott A.; and Spano, Anthony
PHOTOREGULATED ELECTRON TRANSFER AT BIO-INORGANIC INTERFACES 236

Lee, C. Ted, Jr.
MIMICKING MICROGRAVITY IN BIO- AND NANO-COLLOIDAL SYSTEMS USING SUPERCRITICAL CARBON DIOXIDE 250

Lin, Yiqiang; Lei, Zhiheng; Farouk, Bakhtier; and Oran, Elaine S.
THERMOACOUSTIC CONVECTION AND TRANSPORT IN GASES AND NEAR-CRITICAL FLUIDS UNDER NORMAL AND MICRO-GRAVITY CONDITIONS 260

Lipa, J.
FLUID PHYSICS AND TRANSPORT PHENOMENA IN A SIMULATED REDUCED GRAVITY ENVIRONMENT 262

Martineau, R.; Piccini, M.; and Towe, B.
A CONTINUOUS MICROCULTURE DEVICE FOR MONITORING THE EFFECTS OF SPACE ENVIRONMENTS ON LIVING SYSTEMS 278

Mikofski, M.A.; Blevins, L.G.; Williams, T.C.; and Shaddix, C.R.
EFFECT OF VARIED AIR FLOW ON FLAME STRUCTURE OF LAMINAR INVERSE DIFFUSION FLAMES 280

Mohraz, Ali; and Solomon, Michael J.
LIGHT SCATTERING AND DIRECT VISUALIZATION STUDIES OF ANISOMETRIC COLLOIDAL AGGREGATES AND GELS 282

Nakagawa, Masami
CHARACTERIZING MECHANICAL PROPERTIES OF SIMULANT SOILS USING WAVE VELOCITY TECHNIQUE 283

Nave, Jean-Christophe; and Banerjee, Sanjoy
DIRECT NUMERICAL SIMULATION OF GAS-LIQUID SYSTEMS IN VARIABLE GRAVITY ENVIRONMENTS 284

Olson, S.L.; Beeson, H.D.; Haas, J.P.; and Baas, J.S.
A NEW TEST METHOD FOR MATERIAL FLAMMABILITY ASSESSMENT IN MICROGRAVITY AND EXTRATERRESTRIAL ENVIRONMENTS 286

Olson, S.L.
MOST PROBABLE FIRE SCENARIOS IN SPACECRAFT AND EXTRATERRESTRIAL HABITATS - WHY NASA'S CURRENT TEST 1 MIGHT NOT ALWAYS BE CONSERVATIVE 296

Ozen, Ozgur
INTERFACIAL INSTABILITIES DURING EVAPORATION 306

Panzarella, Charles
MICROFLUIDIC BIOCHIP DESIGN 307

Pillai, Dilip; Rosenbaum, David S.; Liszka, Kathy J.; York, David W.; Mackin, Michael A.; and Lichter, Michael J.
DETECTION AND PREVENTION OF CARDIAC ARRHYTHMIAS DURING SPACE FLIGHT 309

Popova, Natalya
THE EFFECT OF GRAVITY MODULATION ON FILTRATIONAL CONVECTION IN A HORIZONTAL LAYER 311

Potember, Richard S.
MINIATURE TIME OF FLIGHT MASS SPECTROMETER 322

Puri, Ishwar K.; Aggarwal, Suresh K.; Lock, Andrew J.; and Hegde, Uday
PARTIALLY PREMIXED FLAME (PPF) RESEARCH FOR FIRE SAFETY 324

Qiao, L.; Kim, C.H.; and Faeth, G.M.
EFFECTS OF CHEMICALLY-PASSIVE SUPPRESSANTS ON LAMINAR PREMIXED HYDROGEN/AIR FLAMES 335

Ramé, Enrique
DYNAMIC WETTING OF ROOM TEMPERATURE POLYMER MELTS: DEVIATIONS FROM NEWTONIAN BEHAVIOR 337

Rangwala, Ali S.; Buckley, Steven G.; and Torero, Jose L.
UNDERSTANDING MATERIAL PROPERTY IMPACTS ON CO-CURRENT FLAME SPREAD: IMPROVING UNDERSTANDING CRUCIAL FOR FIRE SAFETY 338

Revankar, Shripad T.; and Kong, Xiangcheng
STUDY OF CO-CURRENT AND COUNTER-CURRENT GAS-LIQUID TWO-PHASE FLOW THROUGH PACKED BED IN MICROGRAVITY 349

Rich, D.B.; Lautenberger, C.W.; Yuan, Z.; and Fernandez-Pello, A.C.
EFFECTS OF HEAT FLUX, OXYGEN CONCENTRATION AND GLASS FIBER VOLUME FRACTION ON PYROLYSATE MASS FLUX FROM COMPOSITE SOLIDS 351

Roby, Richard; Zhang, Wei; Gaines, Glenn; Olenick, Stephen; Klassen, Michael; and Torero, Jose L.
THE INTEGRATION OF A SMOKE DETECTOR MODEL WITH LARGE EDDY SIMULATION FIRE MODELING FOR PREDICTING SMOKE DETECTOR ACTIVATION IN MICROGRAVITY 352

Roushan, Pedram; and Wu, Xiao-Lun
STUDY OF THE VON-KÁRMÁN VORTEX STREET CLOSE TO ONSET OF SHEDDING 354

Ruff, Gary A.; Hicks, Michael; and Pettegrew, Richard
EVALUATION OF CO_2, N_2 AND HE AS FIRE SUPPRESSION AGENTS IN MICROGRAVITY 355

Sankaran, Subramanian; and Allen, Jeffrey S.
VISUALIZATION OF ELECTRIC FIELD EFFECTS ON NUCLEATE AND FILM BOILING 364

Shafirovich, Evgeny; and Varma, Arvind
NICKEL-COATED ALUMINUM PARTICLES: A PROMISING FUEL FOR MARS MISSIONS 366

Sharp, M. Keith
COMPUTER MODELING OF CARDIOVASCULAR RESPONSES TO GRAVITY 377

Shaw, Benjamin D.
BI-COMPONENT DROPLET COMBUSTION IN REDUCED GRAVITY 387

Shaw, Benjamin D.
REDUCED GRAVITY STUDIES OF SORET TRANSPORT EFFECTS IN LIQUID FUEL COMBUSTION 398

Son, Youngjin; Ronney, Paul D., and Gokoglu, Suleyman
COMPARISON OF CARBON DIOXIDE AND HELIUM AS FIRE EXTINGUISHING AGENTS FOR SPACECRAFT 409

Sorensen, C.M.; Kim, W.; Fry, D.; and Chakrabarti, A.
AGGREGATES AND SUPERAGGREGATES OF SOOT WITH FOUR DISTINCT FRACTAL MORPHOLOGIES 419

Steen, Paul H.; Bhandar, Anand; Vogel, Michael J.; and Hirsa, Amir H.
DYNAMICS AND STABILITY OF CAPILLARY SURFACES: LIQUID SWITCHES AT SMALL SCALES 434

Takahashi, Fumiaki; Linteris, Gregory T.; and Katta, Viswanath R.
FIRE SUPPRESSION IN LOW GRAVITY USING A CUP BURNER 448

Teclemariam, Nerayo P.; Muller, Susan J.; Beck, Victor A.; and Shaqfeh, Eric S.G.
A BIOSENSOR FOR SINGLE-MOLECULE DNA SEQUENCING 451

Thiessen, David B.; and Marston, Philip L.
SUPPORTED CAPILLARY PIPES 453

Thomas, Aaron
OSCILLATORY FLOWS AS A MEANS OF SEPARATION OF CONTAMINANTS FROM AIR 457

Tolmachoff, Erik; and Kezirian, Michael T.
REDUCING FUEL SLOSH IN SPACECRAFT PROPULSION SYSTEMS 470

Uguz, A. Kerem; and Narayanan, R.
COMPARISON OF THE STABILITY OF AN ELLIPTICAL LIQUID BRIDGE WITH A COMPANION CIRCULAR LIQUID BRIDGE 471

Unuvar, C.; Fredrick, D.; Anselmi-Tamburini, U.; Manerbino, A.; Guigne, J.Y.; Munir, Z.A.; and Shaw, B.D.
ELECTRIC CURRENT ACTIVATED COMBUSTION SYNTHESIS AND CHEMICAL OVENS UNDER TERRESTRIAL AND REDUCED GRAVITY CONDITIONS 472

Vander Wal, Randy L.; Kizito, John P.; Tryggvason, Gretar; Berger, Gordon M.; and Mozes, Steven D.
DROPLET-SURFACE IMPINGEMENT DYNAMICS FOR INTELLIGENT SPRAY DESIGN 483

Veretennikov, Igor; and Glazier, James A.
CONVECTIVE INSTABILITIES IN LIQUID FOAMS 485

Walton, Krista S.; and LeVan, M. Douglas
SEPARATION OF CARBON MONOXIDE AND CARBON DIOXIDE FOR MARS ISRU 500

Wei, Wei; Thiessen, David B.; and Marston, Philip L.
ENHANCED DAMPING FOR CAPILLARY BRIDGE OSCILLATION USING VELOCITY FEEDBACK 503

Zhang, Jie; Jun, Yonggun; and Wu, X.L.
THE STUDY OF TOPOLOGICAL STRUCTURE DISTRIBUTIONS IN STRATIFIED SOAP FILM CONVECTIONS 509

SPACECRAFT FIRE SUPPRESSION: TESTING & EVALUATION

Angel Abbud-Madrid, J. Thomas McKinnon, and Jean-Pierre Delplanque
Center for Commercial Applications of Combustion in Space
Colorado School of Mines
Golden, CO 80401
Phone: (303) 384-2300 E-mail: aabbudma@mines.edu

Kazhikathra Kailasanath
Center for Reactive Flow & Dynamical Systems
Naval Research Laboratory
Washington, DC 20375

Suleyman Gokoglu and Ming-Shin Wu
NASA Glenn Research Center
Cleveland, OH 44135

The objective of this project is the testing and evaluation of the effectiveness of a variety of fire suppressants and fire-response techniques that will be used in the next generation of spacecraft (Crew Exploration Vehicle, CEV) and planetary habitats. From the many lessons learned in the last 40 years of space travel, there is common agreement in the spacecraft fire-safety community that a new fire suppression system will be needed for the various types of fire threats anticipated in new space vehicles and habitats. To date, there is no single fire extinguishing system that can address all possible fire situations in a spacecraft in an effective, reliable, clean, and safe way. The testing conducted under this investigation will not only validate the various numerical models that are currently being developed, but it will provide new design standards on fire suppression that can then be applied to the next generation of spacecraft extinguishment systems.

The test program will provide validation of scaling methods by conducting small, medium, and large scale fires. A variety of suppression methods will be tested, such as water-mist, carbon dioxide, and nitrogen with single and multiple injection points and direct or distributed agent deployment. These injection methods cover the current ISS fire suppression method of a portable hand-held fire extinguisher spraying through a port in a rack and also next-generation spacecraft units that may have a multi-point suppression delivery system built into the design. Consideration will be given to the need of a crew to clean-up the agent and recharge the extinguishers in flight in a long-duration mission.

The fire suppression methods mentioned above will be used to extinguish several fire scenarios that have been identified as the most relevant to spaceflight, such as overheated wires, cable bundles, and circuit boards, as well as burning cloth and paper. As it has been shown in our previous work, the threat of these scenarios is not only the fire itself but also the smoke generated from flight-rated materials and wiring insulation that can be extremely toxic. Further testing will be conducted in which obstructions and ventilation will be added to represent actual spacecraft conditions (e.g., a series of cards in a card rack). The transport of the suppressant agent at various locations in the enclosure will be measured. The system will also test the effectiveness of fire suppressants in fighting low (28 VDC) and high (120 VDC) voltage

electrical fires. Tests will be conducted at the lowest gravity level possible in NASA's Reduced-Gravity Aircraft, as well as at Lunar (0.16 *g*) and Martian (0.38 *g*) levels. The Fire Suppression Testing Facility (FSTF) that will be built and used for this investigation may in the future serve as a prototype for the development of a Fire Suppression Insert that may use the Combustion Integrated Rack onboard the ISS to conduct long-duration μg tests. This insert will be capable of providing a demonstration of a fire-suppression system prototype under spaceflight conditions, raising the technology readiness level of the project to a prototype demonstration level (TRL 6). This prototype may help in the design of the fire extinguisher to be used in the first manned flight of the Crew Exploration Vehicle planned for 2014.

The main deliverable of this project will be the evaluation and practical demonstration of the most effective fire extinguishing and fire response strategy that will efficiently put out a fire inside an equipment rack and in any spacecraft module or planetary habitat with a minimum amount of suppressant agent and toxic byproducts, and with easy cleanup and recovery after the fire event is over. The experimental study will include testing under various gravity levels (normal, microgravity, Lunar, and Martian conditions) and under the worst-case fire scenarios and environments (pressure, ventilation, power, materials, and surrounding fluids) anticipated in future spacecraft and planetary habitats considered under the new NASA Vision for Exploration Agenda.

SPACECRAFT FIRE SUPPRESSION: TESTING AND EVALUATION

Angel Abbud-Madrid
J. Thomas McKinnon
Jean-Pierre Delplanque

Center for Commercial Applications of Combustion in Space/Colorado School of Mines

Kazhikathra Kailasanath

Naval Research Laboratory

Suleyman Gokoglu
Ming-Shin Wu

NASA Glenn Research Center




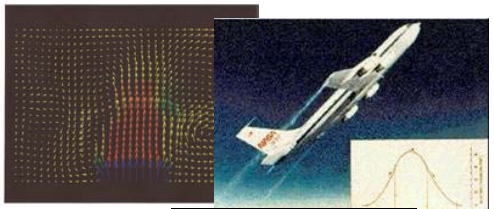

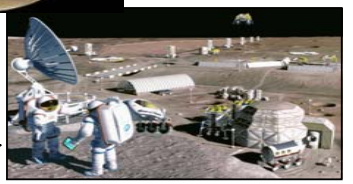


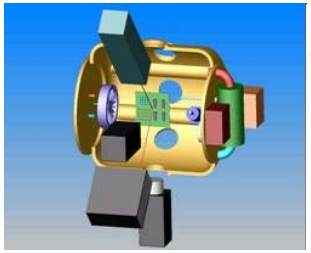
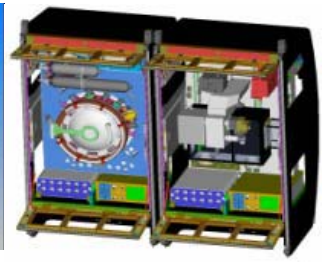

CCACS
CENTER FOR COMMERCIAL APPLICATIONS OF COMBUSTION IN SPACE

OBJECTIVE

- **TESTING AND EVALUATION OF THE EFFECTIVENESS OF:**
  - FIRE SUPPRESANTS
  - FIRE RESPONSE TECHNIQUES

- **FOR NEXT GENERATION OF:**
  - SPACECRAFT
  - PLANETARY HABITATS

CCACS
CENTER FOR COMMERCIAL APPLICATIONS OF COMBUSTION IN SPACE

FIRE SUPPRESSION PROCESS

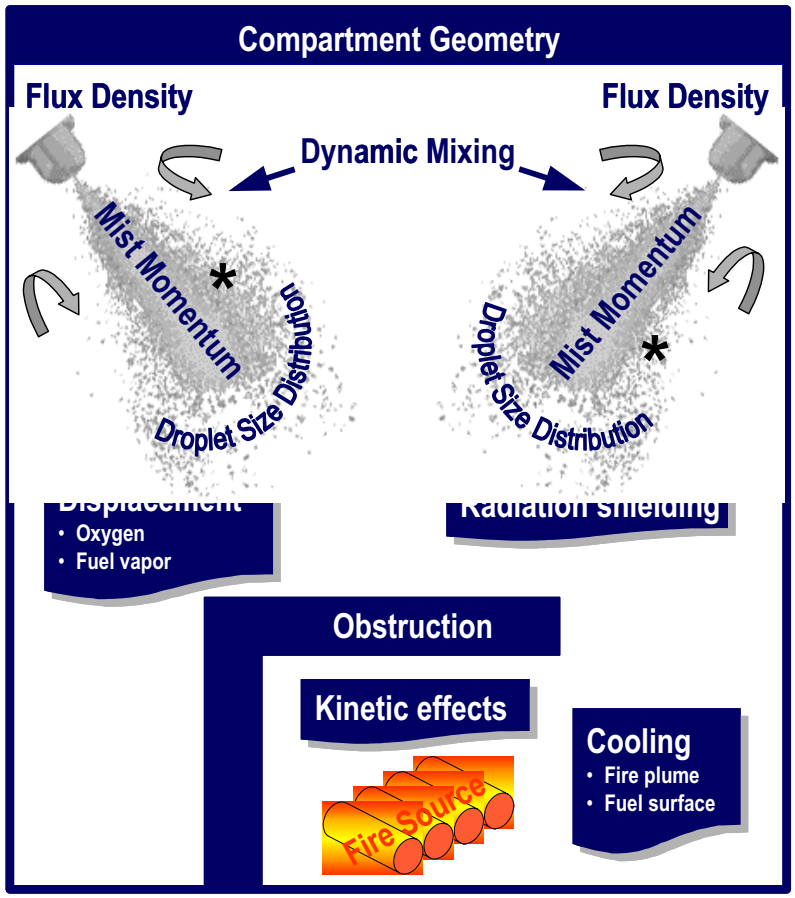

Drawing after Liu and Kim (2000)

SUPPRESSION MECHANISMS:

- **Thermal**
  - Cooling by sensible and latent heats
- **Physical**
  - Oxygen depletion
  - Cooling surfaces
  - Reduction in radiative transfer of energy
- **Chemical**
  - Enhance radical recombination

FACTORS AFFECTING PERFORMANCE:

- Suppressant flux density and momentum
- Mixing
- Obstructions
- Gravity

* Suppressant can be water mist or any other gaseous agent

CCACS
CENTER FOR COMMERCIAL APPLICATIONS OF COMBUSTION IN SPACE

CHALLENGES

- Conduct evaluation and practical demonstration of:
  - Most effective fire suppression and response strategy
  - Fire suppression under spacecraft conditions
  - Use of minimum amount of suppressant agent
  - Generation of minimum amount of toxic byproducts
  - Easy agent clean up and prompt recovery
  - Worst-case scenarios and environments (pressure, ventilation, power, materials, surrounding fluids)
  - Effect of gravity (micro, partial, and normal *g*)

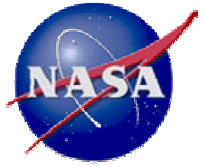

C C A C S

CENTER FOR COMMERCIAL APPLICATIONS OF COMBUSTION IN SPACE

NUMERICAL APPROACH

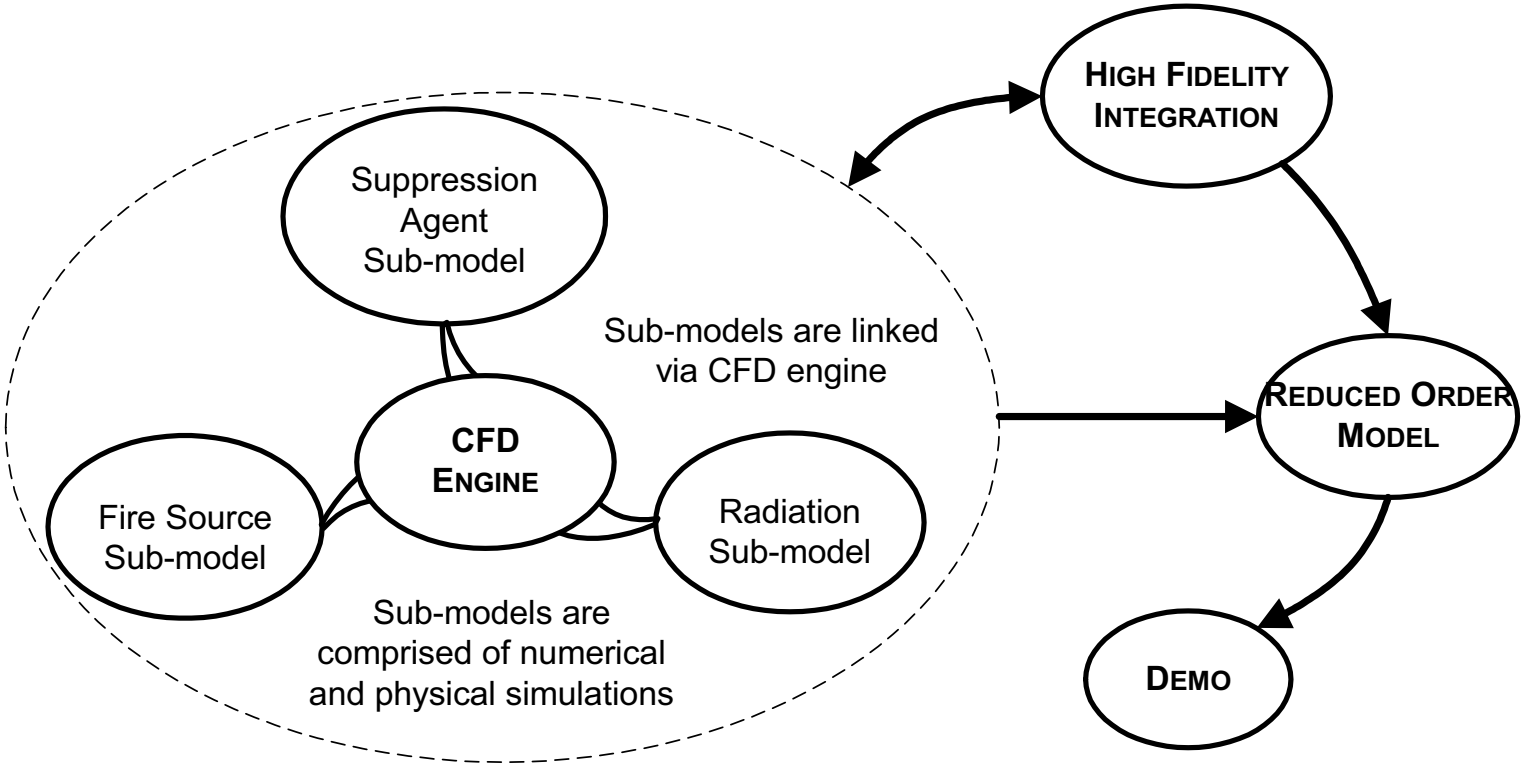

NUMERICAL APPROACH (II)

- Small and large-scale experiments to verify and validate numerical submodels and final reduced-order model

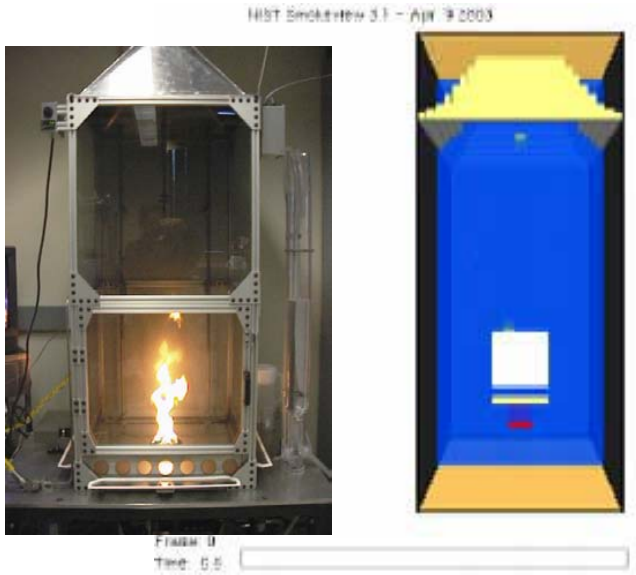

COMPONENTS OF MODEL

- Fire source (chemical kinetics)
- Fluid dynamics
- Suppressant agents (water mist, CO_2, N_2)
- Radiation
- Normal and partial gravity

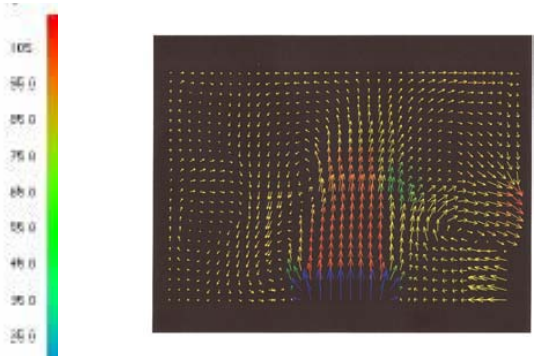

NUMERICAL STUDY DELIVERABLE

Software code for help in the design of spacecraft fire suppression systems

CCACS
CENTER FOR COMMERCIAL APPLICATIONS OF COMBUSTION IN SPACE

EXPERIMENTAL APPROACH

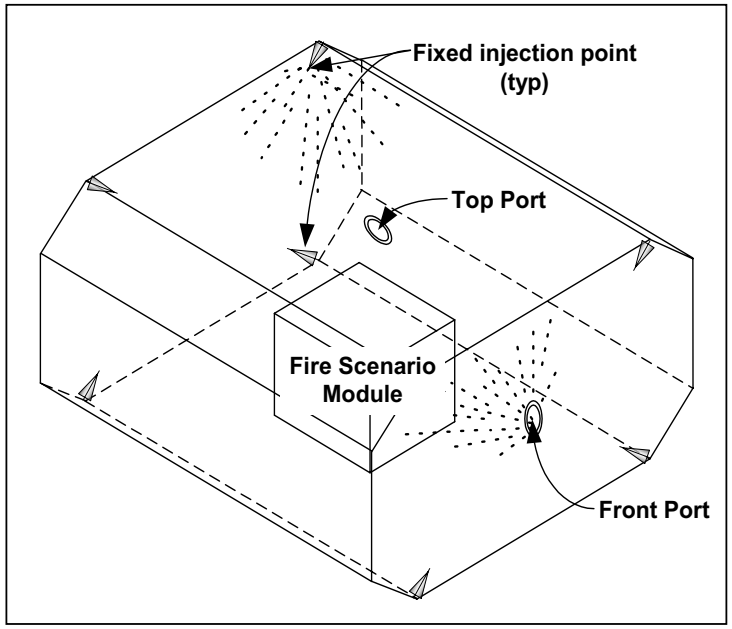

I. FIRE SCENARIOS

- Single Cable
- Cable bundle
- Circuit board
- Cloth and paper

II. SUPPRESSION AGENTS

- Water mist
- Carbon dioxide (CO_2)
- Nitrogen (N_2)
- Dual-fluid

III. SUPPRESSION METHODS

- No agent (baseline)
- Single injection port
- Multiple injection ports (dispersion)

IV. EXPERIMENTAL CONFIGURATIONS

- Forced ventilation
- Obstructions
- Applied Voltage (24 VDC and 120 VDC)
- Micro, partial, and normal gravity

V. MEASUREMENTS

- Temperature
- Gas analysis
- Suppressant transport
- Fire extinction

PARTIAL GRAVITY TESTING

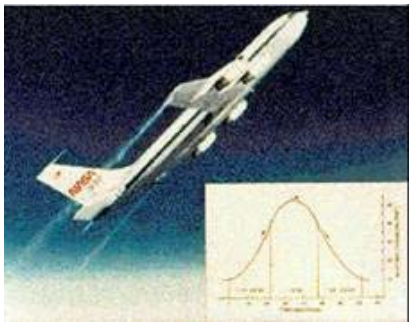

CURRENT TESTING:
KC-135 Parabolic flights
(0.01, 0.16, 0.38 *g*)

FUTURE PLANS:
Microgravity tests on
ISS (10^{-6} *g*)

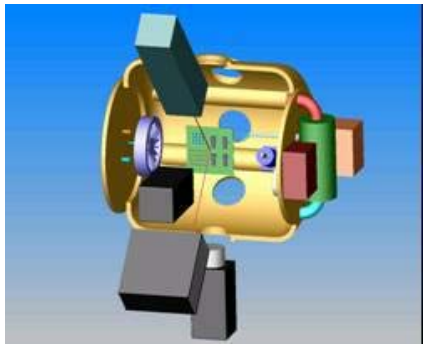

Fire Suppression Insert

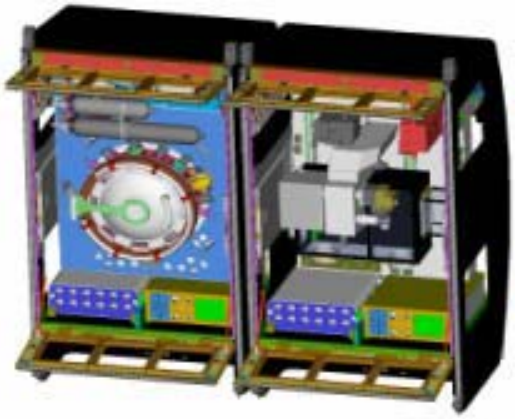

Combustion Integrated Rack (CIR)

RESEARCH POTENTIAL

- Current Low-Gravity Testing Facility could be used as prototype for a Fire Suppression Insert in the Combustion Integrated Rack (CIR) onboard the ISS
- Testing under long durations of μg could provide a demonstration of a fire-suppression system prototype under spaceflight conditions (Technology Readiness Level, TRL 6)

CONTRIBUTION TO NASA'S EXPLORATION MISSION

DELIVERABLE

- Evaluation and practical demonstration of the most effective fire extinguishing system to put out a fire inside an equipment rack, spacecraft module, or planetary habitat

EVALUATION TOOLS

- Numerical modeling
- Ground testing (normal gravity)
- Validation of scaling methods
- Partial-gravity testing
- Human Factors Engineering
- Risk analysis assessment

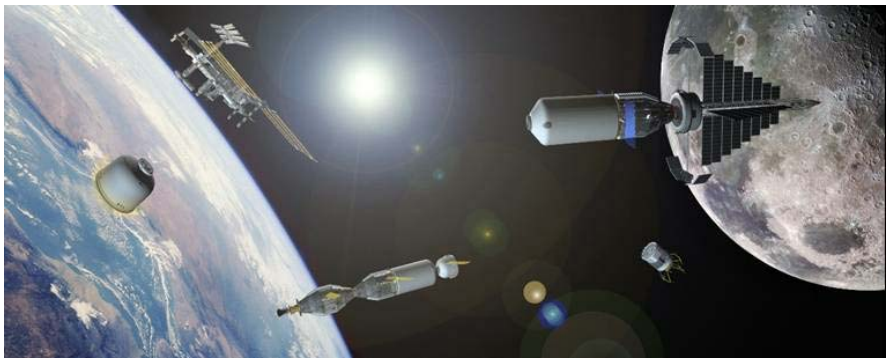

TIMETABLE

- Fire-suppression system prototype ready by 2008 for use in the design of fire extinguisher for Crew Exploration Vehicle (1st Manned Mission: 2014)

CCACS
CENTER FOR COMMERCIAL APPLICATIONS OF COMBUSTION IN SPACE

BUOYANCY EFFECTS ON FLOW STRUCTURE AND INSTABILITY OF LOW-DENSITY GAS JETS

Ajay K. Agrawal and Ramkumar N. Parthasarathy
School of Aerospace and Mechanical Engineering
University of Oklahoma
Norman, Oklahoma 73019

OBJECTIVES

- To study the scalar flow structure of self-excited buoyant helium jets discharged vertically into air and identify the shape, structure, and evolutionary path of the entrainment region in Earth gravity.
- To investigate buoyancy effects on the flow structure by subjecting the self-excited helium jet to micro gravity (free-fall) in buoyant to momentum-dominated regime.
- To perform computational simulations to obtain simultaneous visualization of the concentration and flow fields.
- To perform linear temporal and spatio-temporal stability analyses in variable density jets discarding the parallel flow assumption and considering buoyancy effects.

Rainbow schlieren images during an oscillation cycle in Earthgravity Re = 147, Ri = 6.0, d = 32mm.

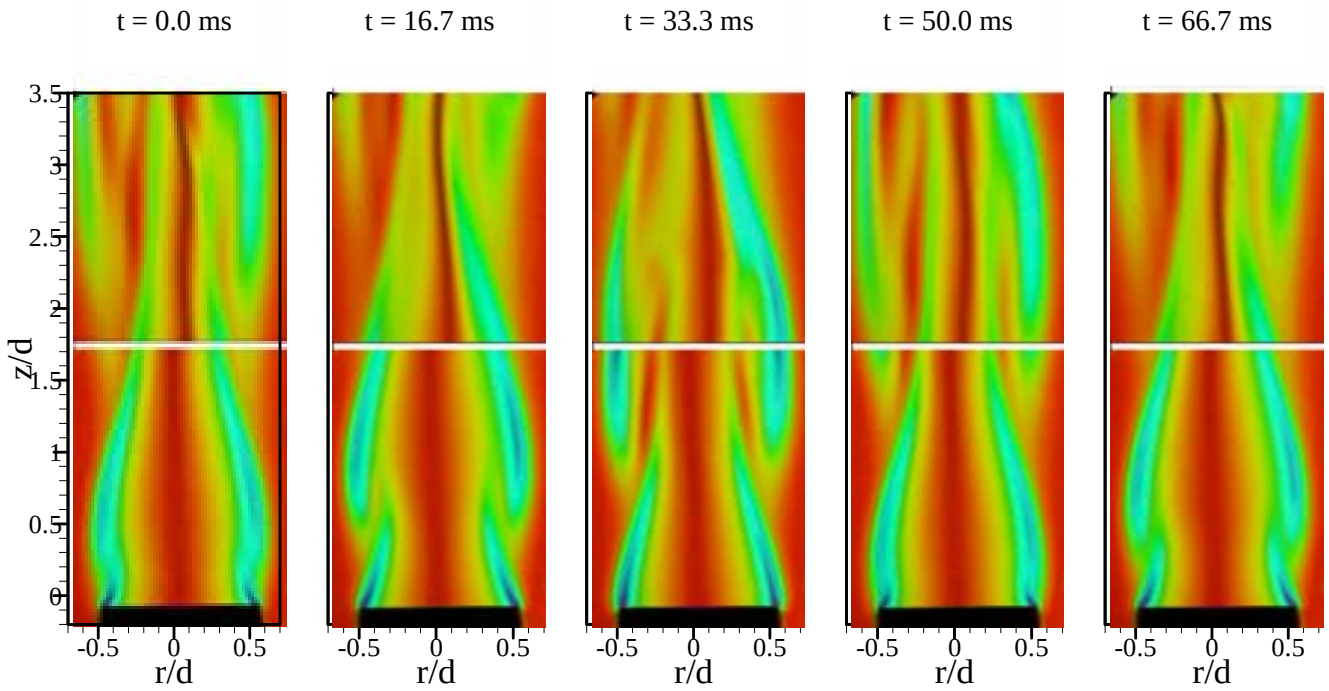

Computed contours of helium mole percentage during an oscillation cycle for Re = 147, Ri = 6.0, d = 32mm.

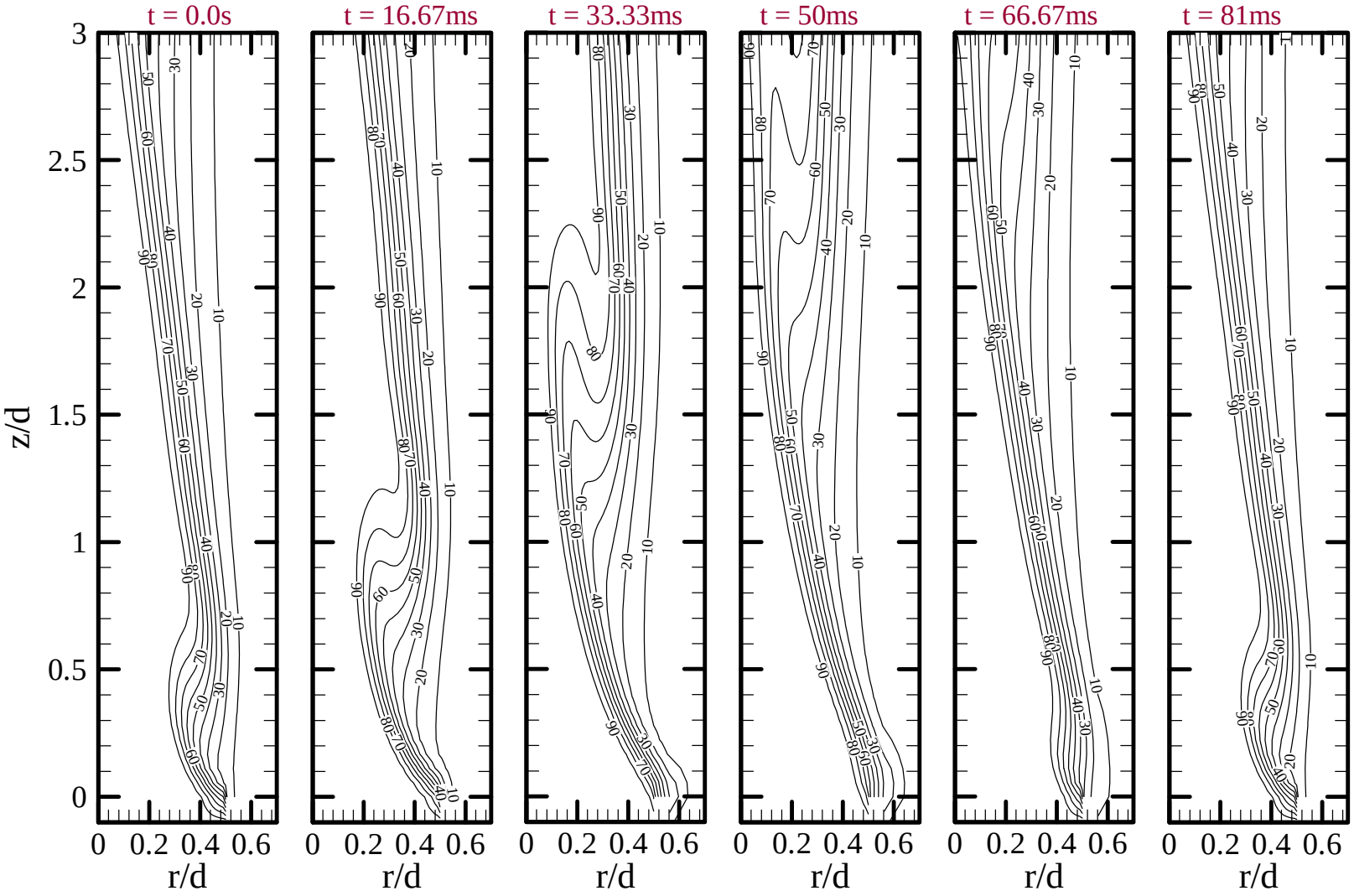

Temporal evolution of helium concentration during change from Earthgravity to micro gravity.

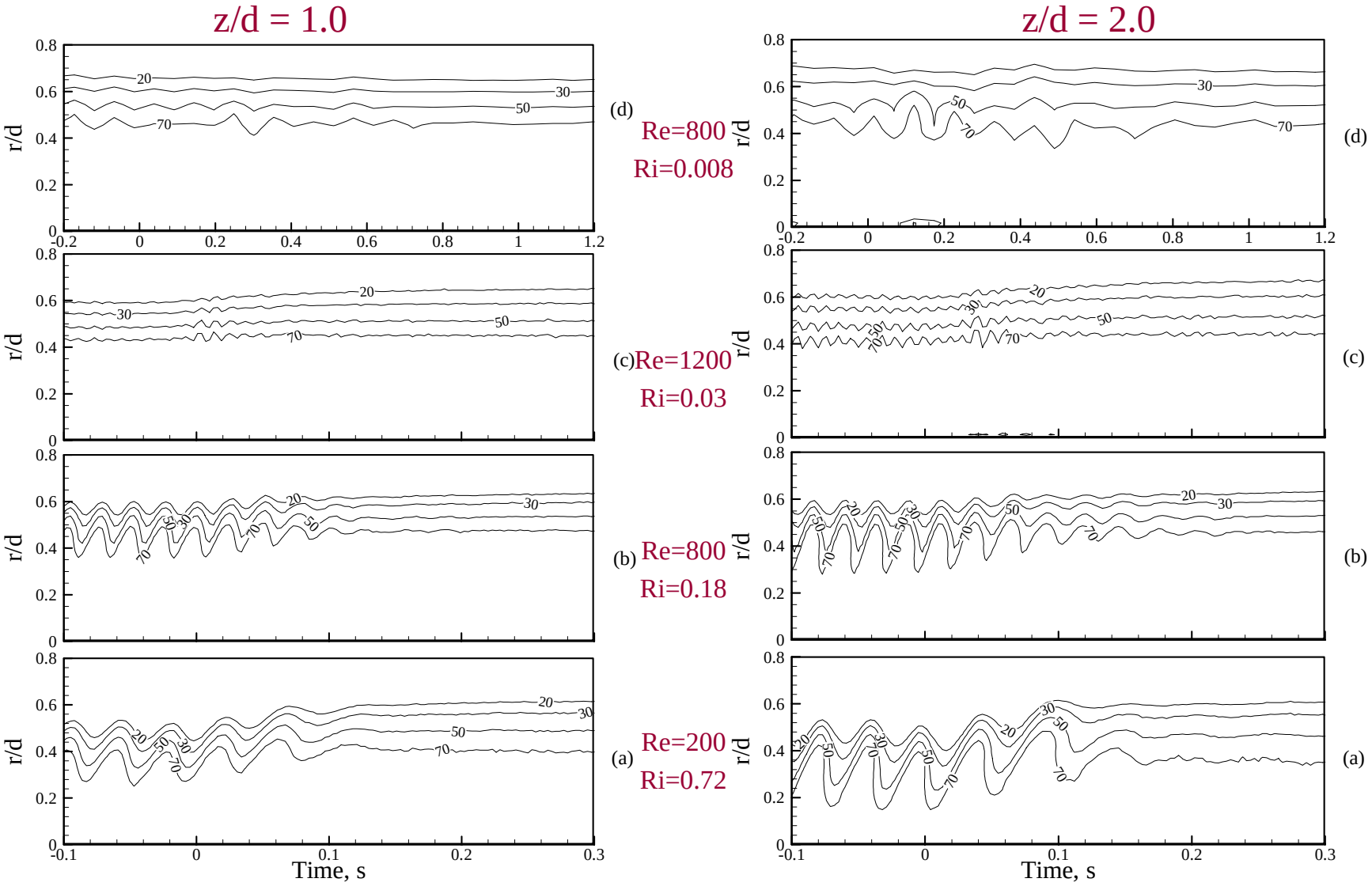

Power spectra of angular deflection data in Earth gravity (left) and microgravity (right) for d = 10.5mm.

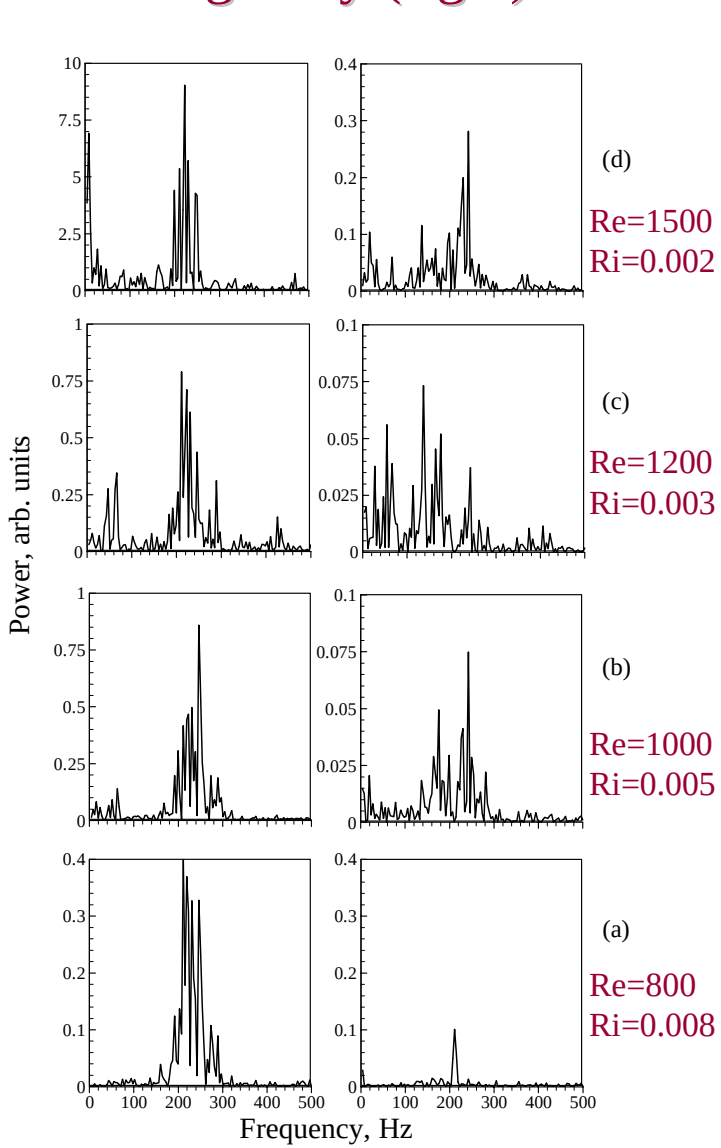

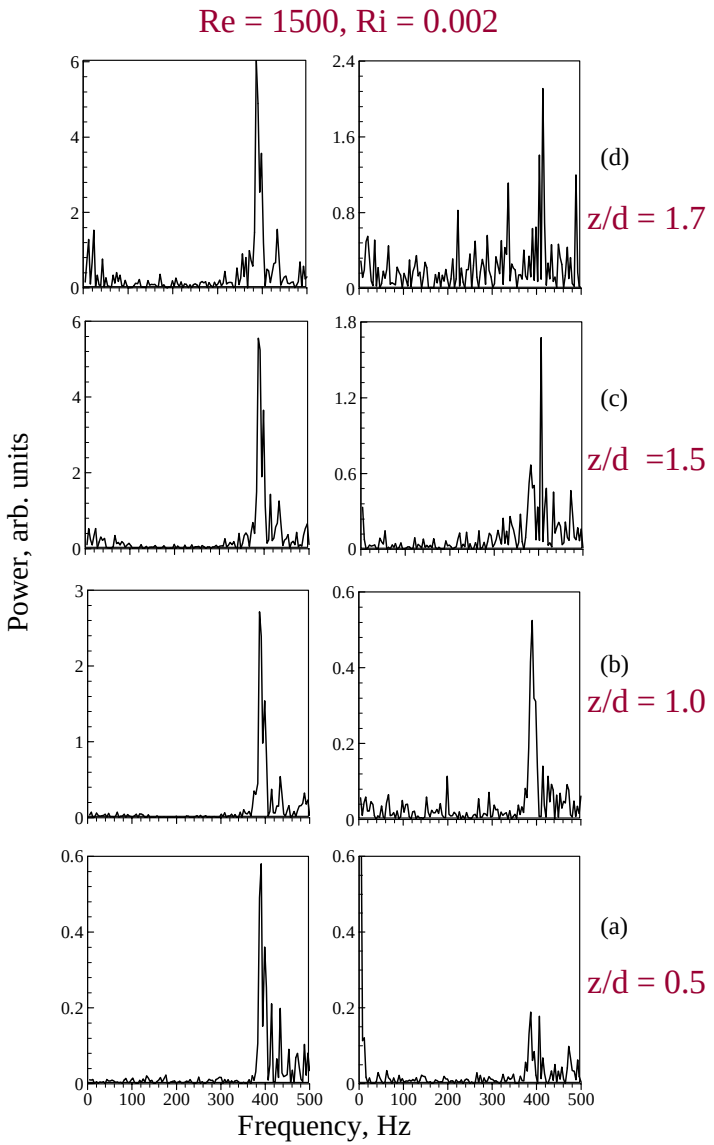

Stability Theory

- Normal mode disturbances.

$$q' = \hat{q}(r)\, e^{i\left[(k_r + ik_i)z - (\Omega_r + i\Omega_i)t\right]}$$

- Non-parallel flow assumption.

$$\left(\frac{\partial \bar{u}}{\partial z}, \frac{\partial \bar{\rho}}{\partial z} \neq 0\right)$$

- Conservation Equations

$$\frac{\partial \tilde{\rho}}{\partial t} + \frac{\partial(\tilde{\rho}\tilde{u})}{\partial \tilde{z}} + \frac{1}{\tilde{r}}\frac{\partial(\tilde{r}\tilde{\rho}\tilde{v})}{\partial \tilde{r}} + \frac{1}{\tilde{r}}\frac{\partial(\tilde{\rho}\tilde{w})}{\partial \phi} = 0$$

$$\tilde{\rho}\left[\frac{\partial \vec{v}}{\partial t} + \vec{v} \bullet \nabla \vec{v}\right] = -\nabla p + g(\rho_\infty - \tilde{\rho})\delta_{i1} + \nabla \bullet (\mu \nabla \vec{u})$$

$$\tilde{\rho}\left[\frac{\partial Y_j}{\partial t} + \vec{v} \bullet \nabla Y_j\right] = \nabla \bullet \left[\tilde{\rho} D_b \nabla Y_j\right]$$

- Mean velocity and density profiles.
- Eigenvalue problem.
- Disturbance Equation

$$-\frac{\bar{\rho}}{C_1}\frac{d^2\hat{p}}{d\tilde{r}^2} + \frac{i\tilde{k}}{C_7}\left(-C_3 + \frac{C_2}{C_6}\frac{\partial \bar{\rho}}{\partial \tilde{z}}\right)\hat{p} + \left(-\frac{1}{C_1}\left[\frac{\bar{\rho}}{\tilde{r}} + \frac{\partial \bar{\rho}}{\partial \tilde{r}}\right] + \frac{1}{C_1}\frac{C_2}{C_6}\frac{\partial \bar{\rho}}{\partial \tilde{r}} + \frac{\bar{\rho}}{{C_1}^2}\frac{\partial C_1}{\partial \tilde{r}} + \frac{C_8}{C_1 C_7}\left[C_3 - \frac{C_2}{C_6}\frac{\partial \bar{\rho}}{\partial \tilde{z}}\right]\right)\frac{d\hat{p}}{d\tilde{r}} = 0$$

$$C_1 = i\bar{\rho}\left(\tilde{k}\bar{u} - \tilde{\Omega}\right) \qquad C_5 = \bar{u}\frac{\partial \bar{u}}{\partial \tilde{z}} + g$$

$$C_2 = \frac{C_1}{\bar{\rho}} + \frac{\partial \bar{u}}{\partial \tilde{z}} \qquad C_6 = \frac{C_1}{\bar{\rho}}$$

$$C_3 = i\bar{\rho}\tilde{k} + \frac{\partial \bar{\rho}}{\partial \tilde{z}} \qquad C_7 = C_4 - \frac{C_5}{C_6}\bar{\rho}\frac{\partial \bar{\rho}}{\partial \tilde{z}}$$

$$C_4 = C_1 + \bar{\rho}\frac{\partial \bar{u}}{\partial \tilde{z}} \qquad C_8 = \bar{\rho}\frac{\partial \bar{u}}{\partial \tilde{r}} - \frac{C_5}{C_6}\frac{\partial \bar{\rho}}{\partial \tilde{r}}$$

Variation of absolute temporal growth rate Ω_i^0 with Ri for S = 0.14 at z/d=1.0 and 2.67.

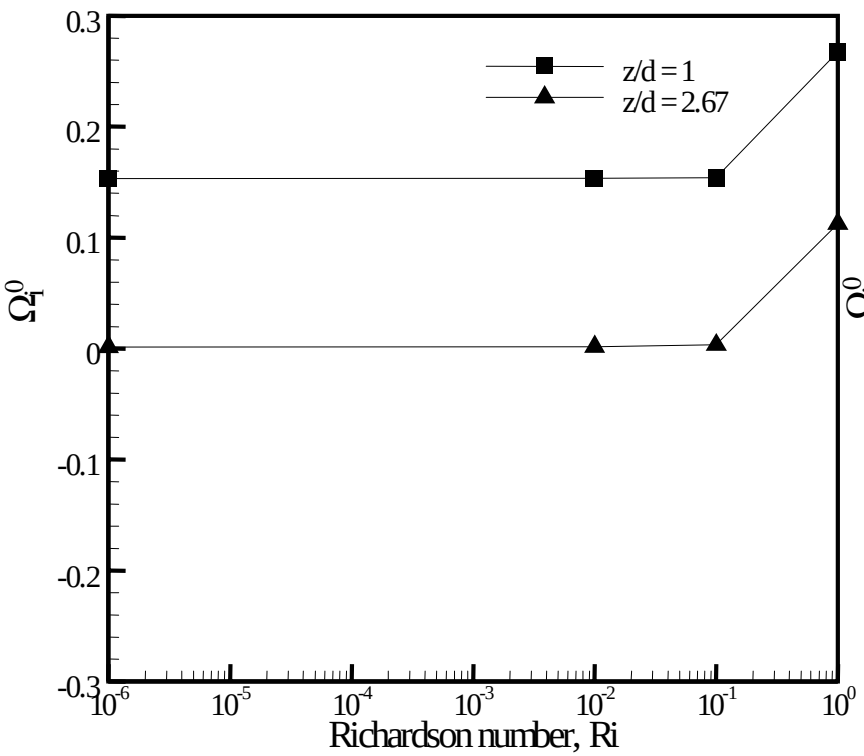

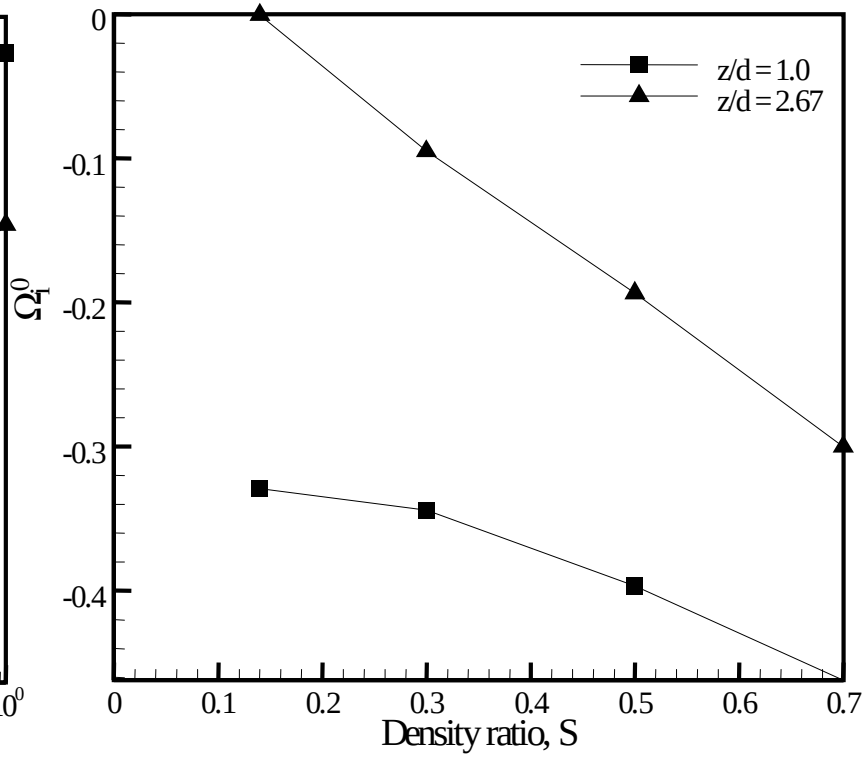

CONCLUSIONS

- Quantitative rainbow schlieren deflectometry (RSD) was successfully applied to study the scalar structure of self-excited buoyant helium jets discharged vertically in air.
- The measurements in self-excited momentum-dominated helium jets in Earth gravity and microgravity provided direct physical evidence of buoyancy effects on oscillation instability and jet flow structure.
- Temporal and spatio-temporal stability analyses were performed in low-density jets using non-parallel flow assumption. Absolute instability was observed for all cases with finite Ri ($\sim 10^{-6}$). In the absence of buoyancy forces (at Ri = 0.0), the previously existing absolute instability disappeared at all locations establishing buoyancy as the primary instability mechanism in self-excited low-density jets.

The Fluid Mechanics of Liquid Jet Impingement: the hydraulic jump in microgravity

C. T. Avedisian[1], S. Chandra[2] and J. Mostaghimi[2]
[1]Cornell University
[2]University of Toronto

Introduction

Liquid jet impingement is an important process for thermal management to dissipate very high heat fluxes [1] and for coating solid surfaces with a liquid (e.g., applying thin films on paper to produce a high-gloss finish). Rapid cooling is achieved by taking advantage of the high liquid velocity in the thin film flowing away from the stagnation point. If a hydraulic jump forms (figure 1a for a circular hydraulic jump) the physical extent of cooling, or uniformity of a film coating, degrades because the film thickness increases substantially downstream of the jump. The discovery of steady noncircular jump shapes in normal gravity experimentation ([2-4]; figure 1b illustrates an example at G=1 for polygonal jumps) shows unusual patterns in the flow near to the jump boundary and downstream of it (figure 1c [3] which shows fluid ejection at the corners) that are poorly understood, yet which could hold some promise for heat transfer.

This project is the first phase of an anticipated two-part effort to understand the mechanisms of heat transfer from impinging liquid jets at reduced gravity. The first part focuses on the fluid mechanics of isothermal flows and the conditions under which hydraulic jumps form. An emphasis is on the formation of noncircular jumps and the conditions and flow patterns associated with them at reduced gravity. As we have just begun the research in 2004, we describe briefly some of the objectives and methods we will pursue during the first phase.

Objectives

The overall objectives of this phase are to examine the fluid dynamics of hydraulic jumps of various shapes at normal and reduced gravity. The following aspects will be addressed: response time of the fluid to changes in the jump position due to a sudden reduction of gravity; flow conditions that polygonal jumps will form; stability of polygonal jumps in microgravity; change (if any) of jump shape after the transition to $G<<1$ (where $G=g/g_o$ and $g_o=9.8 m/s^2$); effect of a sudden change from G=1 to $G<<1$ on the curvature of the free surface across a polygonal jump; downstream flow pattern and possible jetting in the corners of polygonal jumps. The work includes a combination of experiment, direct numerical simulation (DNS) and theoretical modeling.

Noncircular jumps have thus far been observed for flows in which a toroidal vortex exists just behind the jump (schematically illustrated in figure 2a). The vortex shows the presence of a tangential velocity component in the roller which can distort the circular symmetry and lead to steady jumps of noncircular shape. Thus far, polygonal jumps have been observed at G=1 for ethylene glycol (which has a viscosity about ten times larger than water) while water tends to produce circular jumps.

Gravity's influence on the jump will be investigated experimentally by determining how a hydraulic jump (of whatever shape) responds to a sudden change to low gravity. For circular jumps the transition zone across a hydraulic jump is much more gradual in microgravity than normal gravity and the jump radius is larger. Figure 2b [5] shows how a circular hydraulic jump transitions from normal to microgravity. The increase in jump radius (r_j) as gravity is lowered (figure 2c) is a consequence of the Froude number increasing from G=1 to $G<<1$. There are no companion observations for noncircular jumps.

Plan of Research

The DNS portion of the research will be carried out to predict the jump shape, radial position of the jump, the flow pattern downstream of the jump, and the evolution of these quantities due to a sudden transition of the flow from G=1 to G<<1. The computations will be carried out using a 3-D Eulerian structured grid. Free surface and shape deformations will be tracked using the volume-of-fluid (VOF) algorithm [6]. The grid will be fixed so that mesh variations have to be analyzed to ensure that gradients are accurately captured and with a reasonable computational time.

We did some preliminary coding assuming G=1 for a 8m/s water jet created by a 0.45mm diameter tube (Reynolds number of 227) impinging onto a dry surface (in the experiments the target surface will be submerged to a controlled depth so that the downstream fluid height is known). Since the surface was initially dry in this simulation, a hydraulic jump does not form. The DNS was started when the jet just touched the surface and the subsequent evolution of the spreading liquid along the surface was tracked. We chose a fixed 3D grid of 768,000 points (160x160x30) structured in a rectangular fashion. This appeared like a sufficiently dense grid to give a useful result. Figure 3 is a computed snapshot of the flow 0.7ms after the jet contacted the solid surface. The simulation shows details of the liquid film break-up into droplets at the rim. A jump does not form since, as noted previously, the plate was initially dry.

The DNS will be coded for a submerged plate to match the experiments. A tangential velocity component will be assumed for the rim of the jet just as it contacts the surface. Growth/decay of the velocity should determine the jump stability, for example producing a circular jump if the tangential component decays. This general approach of perturbing the velocity has been effective for simulating instabilities in liquid droplet impingement [7,8].

For the experiments, a flow loop will be constructed for a drop tower. The general experimental methodology will be to first establish a jump at G=1 - either circular or noncircular – and to use digital photography to record the jump shape, position and flow pattern as G is suddenly reduced. This situation should be suitable for drop towers with their limited experimental run time, in that prior work [5] showed that steady (circular) jumps are created within 400ms of transitioning from normal to microgravity within drop towers. The output of the experimental phase will be photographs from which physical dimensions of the impingement process will be extracted. These include the jump shape and physical size. The data will be compared with the output of the DNS.

References

1. Liu, X. and Lienhard, J.H. 1993a J. Heat Transf. 115, 472.
2. Ellegaard, C., Hanse, A.E., Haaning, A, Hansen, K., Marcussen, A., Bohr, T., Hansen, J.L. and Watanabe, S. 1999 Nonlinearity 12, 1-7.
3. Ellegaard, C., Hansen, A.E., Haaning, A. and Bohr, T. 1996 Physicq Scripta, T67, 105.
4. Ellegaard, C., Hanse, A.E., Haaning, A, Hansen, K., Marcussen, A., Bohr, T., Hansen, J.L. and Watanabe, S. 1998 Nature, 392, 767.
5. Avedisian, C.T. and Zhao, Z. 2000 Proc. R. Soc. Lond. A, 456, 2127-2151.
6. Hirt, C.W. and B. D. Nichols 1981 Journal of Computational Physics 39, 201-225
7. Bussmann, M., J. Mostaghimi and S. Chandra 1999 Physics of Fluids 11, 1406-1417.
8. Bussmann, M, S. Chandra and J. Mostaghimi 2000 Physics of Fluids 12, 3121-3132.

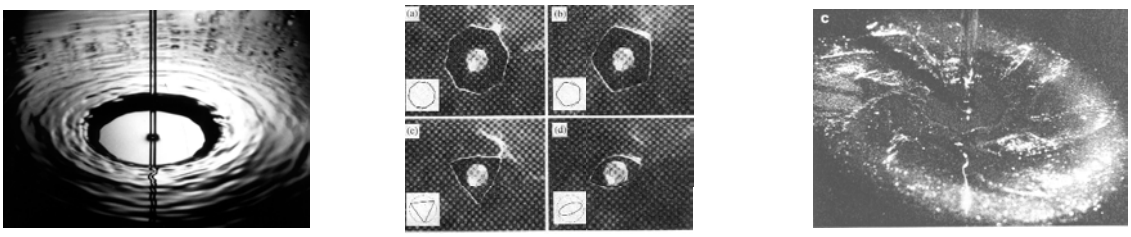

a) b) c)

Figure 1: a) circular hydraulic jump for water; b) polygonal jumps for ethylene glycol [2]; c) downstream flow pattern for a 6-sided polygon [3].

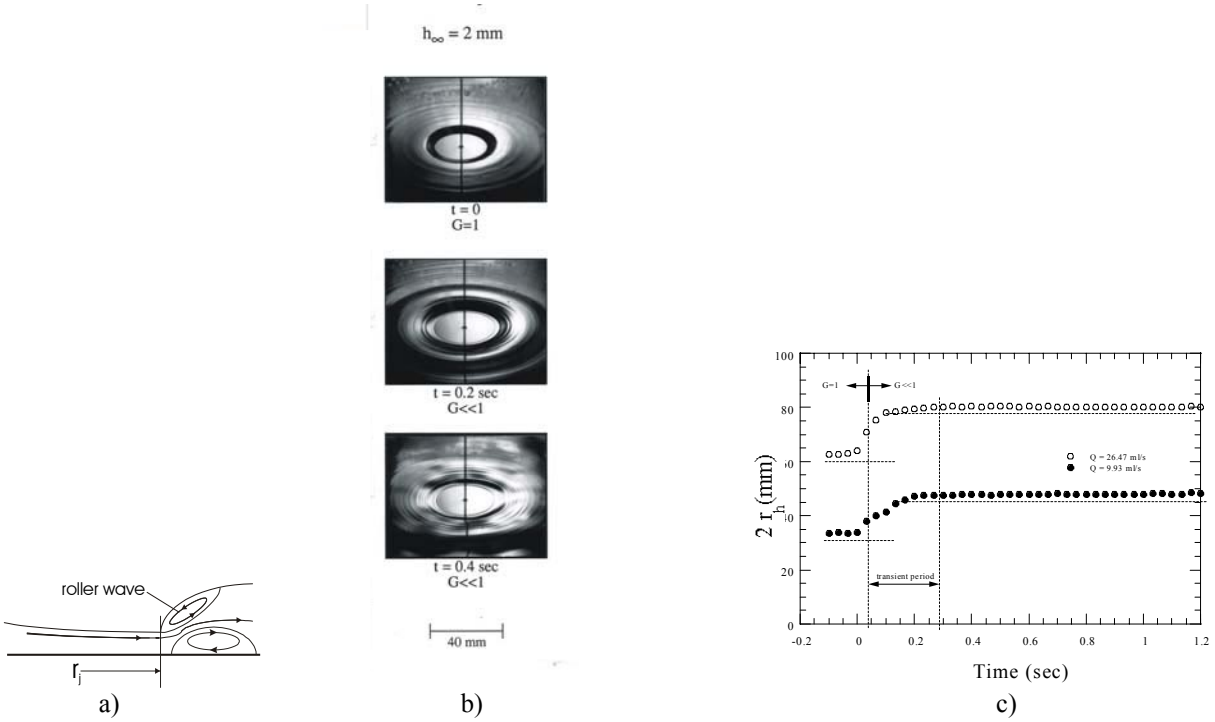

a) b) c)

Figure 2: a) hydraulic jump showing surface rollers; b) water jump during transition from normal (G=1) to microgravity (G<<1); c) measurements of the circular jump radius during transition from normal to microgravity.

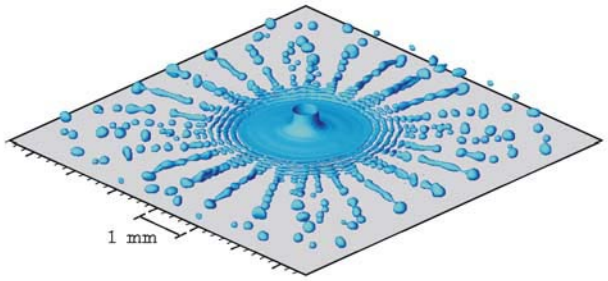

Figure 3: Simulation of the impact of a 0.45 mm diameter water jet with a velocity of 8 m/s on a flat surface 0.70ms after the jet contacts the surface. For the imposed boundary conditions, the liquid film becomes unstable and breaks up into droplets and a hydraulic jump does not form.

EFFECT OF MICROGRAVITY ON MAMMALIAN LYMPHOCYTES

H. Banerjee, M. Blackshear, K. Mahaffey, A.A. Khan
Department of Biology
Elizabethcity State University
Elizabethcity, NC 27909

L. Delucas
CBSE, University of Alabama at Birmingham
Birmingham, AL 35294

ABSTRACT

The effect of microgravity on mammalian system is an important and interesting topic for scientific investigation, since NASA's objective is to send manned flights to planets like Mars and eventual human colonization. The Astronauts will be exposed to microgravity environment for a long duration of time during these flights. Our objective of research is to conduct in vitro studies for the effect of microgravity on mammalian immune system and nervous system. We did our preliminary investigations by exposing mammalian lymphocytes and astrocyte cells to a microgravity simulator cell bioreactor designed by NASA and manufactured at Synthecon, Inc. (USA).Our initial results showed no significant change in cytokine expression in these cells up to a time period of 120 hours exposure. Our future experiments will involve exposure for a longer period of time.

INTRODUCTION

During space flight the function of the immune system changes significantly. Several papers reported that postflight the number and the proportion of circulating lymphocytes in astronauts are modified (Uchakin et al 2002), the in vitro mitogen induced T cell activation is depressed (Cogoli et al. 2002 Konstantinova et al. 1993) and there are detectable differences in cytokine production. Lymphocytes as well (Chapes et al. 1992). One of the possible modifying forces is the microgravity condition itself. Our aim was to analyze mechanisms responsible for changing lymphocyte functions in low gravity environment. For terrestrial simulation of microgravity we used a Rotary Cell Culture System (RCCS) developed by NASA.

In these experiments we exposed mouse B Lymphocyte cells and human Astrocytoma cells to microgravity conditions and then analyzed the cells for cytokine expression. We exposed the cells to different time periods, however, our initial results failed to show any significant changes in cytokine expression under microgravity conditions.

MATERIALS AND METHODS

Mouse B Lymphocyte cells and Human Astrocytoma cells were purchased from ATCC, VA, USA and cultured in L-15 medium at 37 °C in a cell culture incubator. Cells were exposed to microgravity conditions in a Rotary Cell Culture System (RCCS) developed by NASA for 24 hours, 48 hours and 72 hours with proper control. After exposure cells were collected, lysed by antigen lysis buffer and cytokine expression (TGF-beta1 and IL-6) was determined by standard ELISA technique according to manufacturers instructions.

RESULTS

No significant changes in any cytokine expression tested was found during that particular exposure period in any of the cell lines tested.

DISCUSSION

Several attempts have been made to investigate the effects of microgravity on the growth and function of animal cells. Cellular activation of immune T lymphocytes is greatly affected by microgravity. On the other hand, little is known about the effects of microgravity on B lymphocytes. Thus, we attempted to study the effect of microgravity simulation on mouse B lymphocytes.

Our current experiment did not show any significant change in cytokine expression in microgravity exposed immune cells. We look forward to do experiments with longer exposure time, since astronauts are exposed to microgravity conditions for months and years. Also for shorter time periods of exposure, we did not see any significant change in Human brain cells like Astrocytes on the specific cytokine expression that were tested. Several researchers have reported alteration of the immune system due to microgravity conditions (Uchakin et al 2002).

However, we did not notice any significant change in cytokine expression in any of our experiments done for shorter intervals of time i.e., 24 hours, 48 hours, and 72 and 120 hours.

ACKNOWLEDGEMENT

This research is supported by NIH-EARDA Grant, NASA/ONR grant NAG5-1254 and NSF-EPSCOR University of Alabama subcontract# DTD42501.We are very grateful to Mr. James Harrington of NASA for his continuous support.

BIBLIOGRAPHY

1) Meloni MA, Galleri G, Carta S, Negri R, Costanzo G, De Sanctis V, Cogoli A, Pippia P. Preliminary study of gene expression levels in human T-cells exposed to cosmic radiations. J Gravity Physiology. 2002 Jul;9(1):P291–2.
2) Chaps SK, Sims SJ, Forman AD, Bateman TA, Zimmerman RJ. Effects of space flight and IGF-1 on immune function. Adv Space Res. 1999;23(12):1955-64.
3) Cogoli A. From cell biology to biotechnology in space. Korean J Biol Sci. 2000 Sep;4(3):195-200.
4) Konstantinova NA, Matveeva NA, Sirko IV, Firsov NN. The influence of cryoglobulins on the temperature-dependent erythrocyte backscattering nephelometry. Clin Hemorheol Microcirc. 2004;30(1):25-32.
5) Uchakin PN, Tobin BW, Morukov BV, Larina IV, Cubbage ML. Type 1 vs. type 2 cytokine secretion in vitro and its regulation by hydrocortisone in humans subjected to 120-day anti-orthostatic bed-rest regime. J Gravity Physiology. 2002 Dec;9(2):71–82.

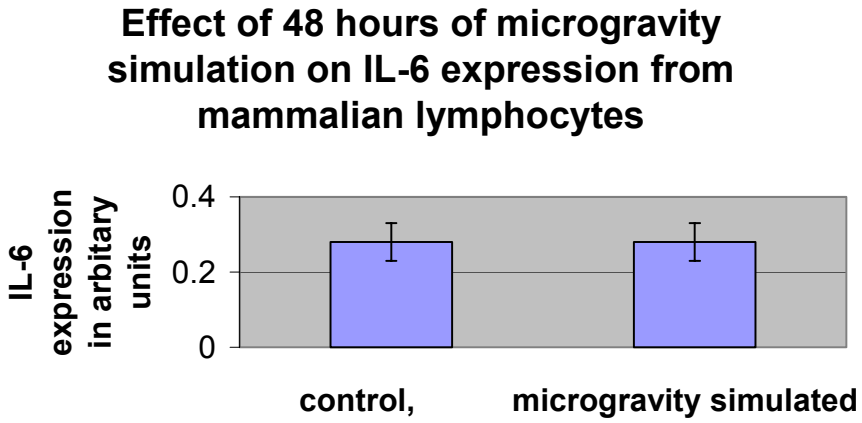

Figure 1

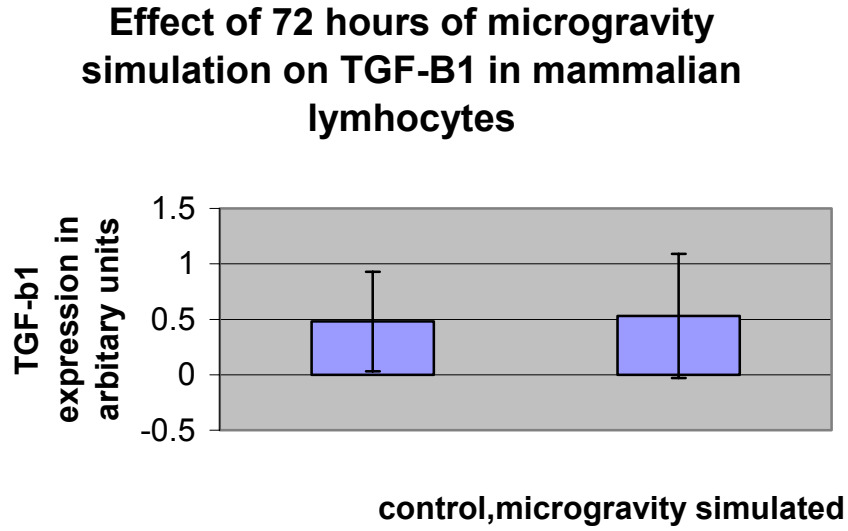

Figure 2

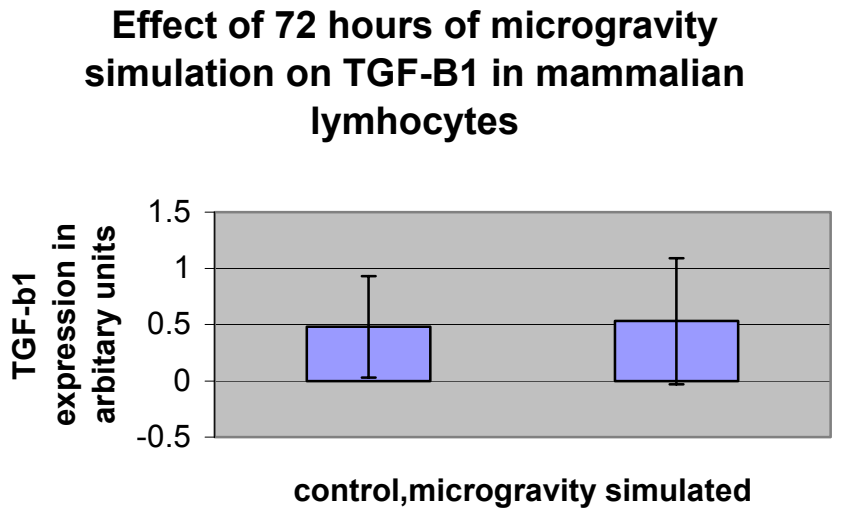

Figure 3

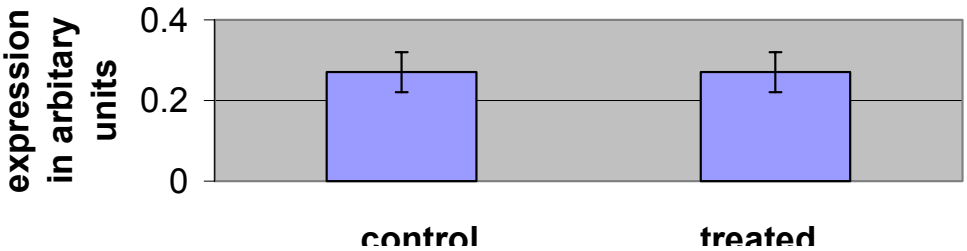

Figure 4

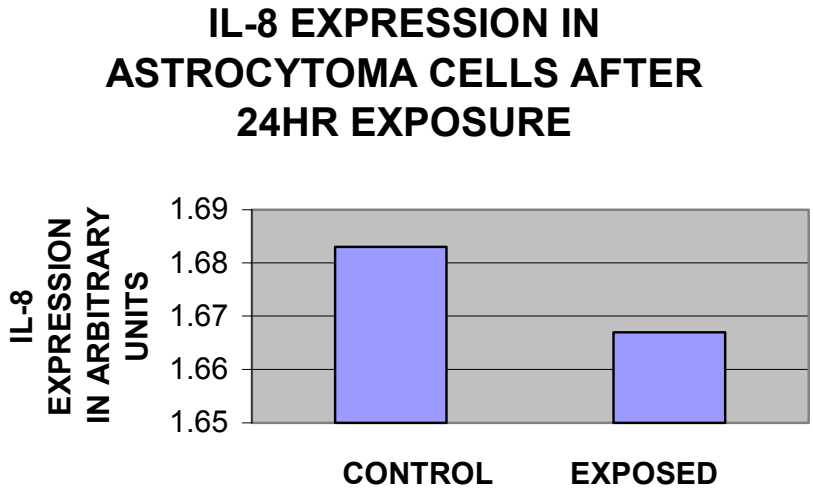

Figure 5

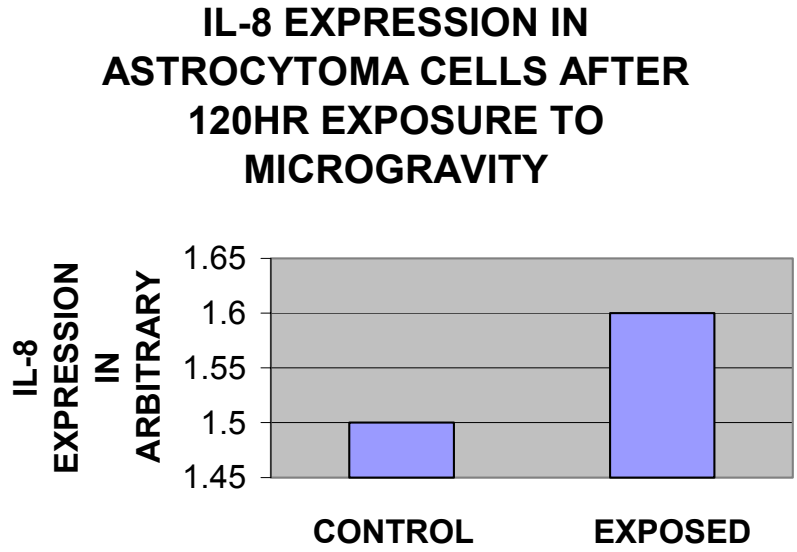

Figure 6

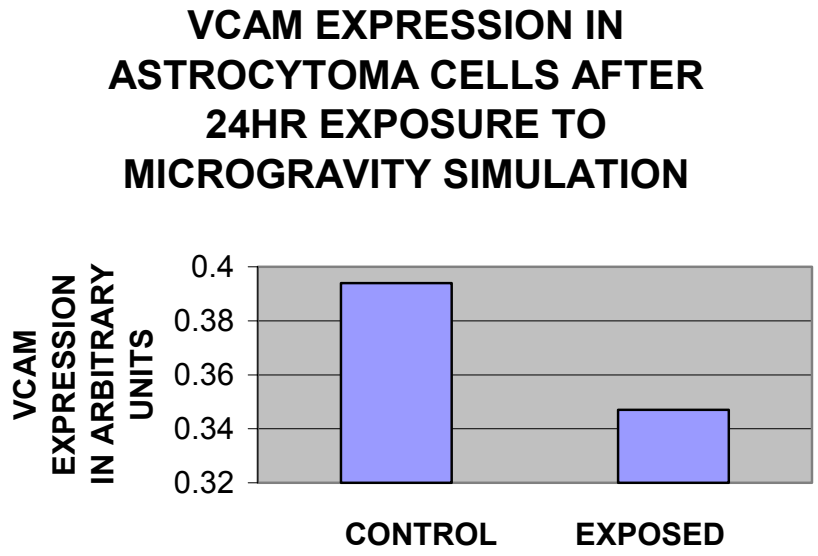

Figure 7

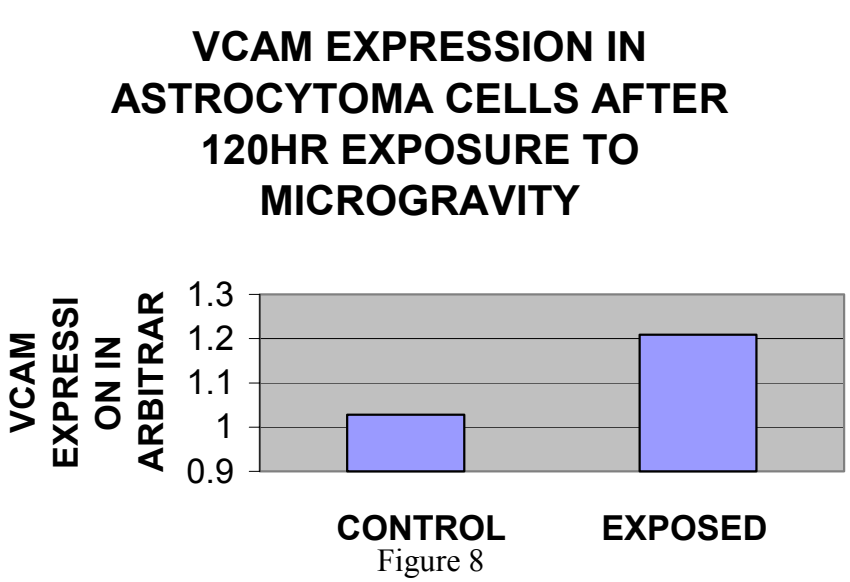

Figure 8

TRANSITION FROM FORWARD SMOLDERING TO FLAMING IN SMALL POLYURETHANE FOAM SAMPLES

A. Bar-Ilan, O. Putzeys, G. Rein, and A.C. Fernandez-Pello

Experimental observations are presented of the effect of the flow velocity and oxygen concentration, and of a thermal radiant flux, on the transition from smoldering to flaming in forward smoldering of small samples of polyurethane foam with a gas/solid interface. The experiments are part of a project studying the transition from smolder to flaming under conditions encountered in spacecraft facilities, i.e., microgravity, low velocity variable oxygen concentration flows. Because the microgravity experiments are planned for the International Space Station, the foam samples had to be limited in size for safety and launch mass reasons. The feasible sample size is too small for smolder to self propagate because of heat losses to the surrounding environment. Thus, the smolder propagation and the transition to flaming had to be assisted by reducing the heat losses to the surroundings and increasing the oxygen concentration. The experiments are conducted with small parallelepiped samples vertically placed in a wind tunnel. Three of the sample lateral-sides are maintained at elevated temperature and the fourth side is exposed to an upward flow and to a radiant flux. It is found that decreasing the flow velocity and increasing its oxygen concentration, and/or increasing the radiant flux enhances the transition to flaming, and reduces the delay time to transition. Limiting external ambient conditions for the transition to flaming are reported for the present experimental set-up. The results show that smolder propagation and the transition to flaming can occur in relatively small fuel samples if the external conditions are appropriate. The results also indicate that transition to flaming occurs in the char left behind by the smolder reaction, and it has the characteristics of a gas-phase ignition induced by the smolder reaction, which acts as the source of both gaseous fuel and heat.

SPATIALLY HETEROGENEOUS DYNAMICS AND THE EARLY STAGES OF CRYSTAL NUCLEATION AND GROWTH IN METASTABLE LIQUIDS AND COLLOIDS

M. Bergroth, T. Solomon, Y. Gebremichael, A.S. Keys, M. Vogel, M.J. Solomon and S.C. Glotzer
Department of Chemical Engineering, University of Michigan, Ann Arbor, MI 48109-2136

ABSTRACT

Controlling the behavior of metastable liquids leading to solidification is essential to controlling the ultimate properties and behavior of these liquids and the materials made from them. Although a great deal is known about the behavior of bulk crystals and glasses, considerably less is known about the atomistic scale processes that control either vitrification or the earliest stages of nucleation and growth of the crystal phase. This situation is due largely to the difficulty in directly visualizing small and critical nuclei in metastable liquids and the local processes that inhibit their formation and promote the formation of macroscopic amorphous materials like bulk metallic glasses.

We are carrying out research pertinent to the earliest stages of nucleation and growth of crystals in metastable liquids via a coordinated simulation-experimental program. One aspect of our studies is concerned with mapping the local dynamics in a computer model of a homogeneous metastable liquid, relating the spatial heterogeneity of the dynamics to aspects of the local liquid structure, and in turn relating features of both the local dynamics and structure to nucleation processes. In the so-called Dzugutov liquid, crystallization is temporarily suppressed by introducing frustration through the interaction potential, rather than through size polydispersity as is typically done in colloids. Through comparison of the simulation results with confocal laser scanning microscopy (CLSM) experiments on colloids of varying degrees of polydispersity, we are ascertaining the role of SHD in nucleation and the effects of polydispersity and interactions on the suppression of crystallization. We expect that our work will provide new insight into controlling solidification processes in materials, with strategic relevance for both high-strength structural materials such as bulk metallic glass and for advanced food technologies for long-term storage and preservation.

In this poster, we show that particle motion in simulated supercooled, metastable liquids is highly coordinated and that particles move primarily along one-dimensional, string-like paths[1,2]. We further show the tendency for particles in the metastable liquid to form clusters in which the particles are arranged in icosahedra, and we show how strings emanate from and wrap around these clusters[3]. We show that particle motion is dynamically facilitated, supporting recent theoretical predictions[3]. We further show how the degree of facilitation and cooperative particle motion increases with the degree of undercooling[3]. Finally, we present preliminary results on the early stages of nucleation in the deeply supercooled liquid.

Experimentally, we study analogous properties in colloidal suspensions by direct visualization with CLSM. The colloidal model system is composed of monodisperse, sterically stabilized silica colloids of diameter approximately 1 micron dispersed in a density and refractive

index matched solvent mixture. The initially amorphous, high volume fraction suspensions exhibit glass-like dynamics. By means of CLSM, we observe the three-dimensional ordering of suspensions under quiescent conditions and as they are subjected to oscillatory shear flow. Qualitatively, we find that shear flow induces nucleation and growth of colloidal crystals in the initially amorphous suspensions. The pair correlation function and local bond orientation parameters are extracted from the CLSM image volumes by means of quantitative image processing. The strain rate and amplitude dependence of these measures of local ordering are quantified.

PI: Sharon C. Glotzer, Department of Chemical Engineering, University of Michigan, 3406 G.G. Brown Bldg., 2300 Hayward Street, Ann Arbot, MI 48109-2136. Email: sglotzer@umich.edu. Fax: 734.764.0459. Phone: 734.615.6296.

[1] Y. Gebremichael, M. Vogel and S.C. Glotzer, "Formation of transient clusters on nanoscopic length scales in a simulated one-component liquid," Mol. Simulation **30**(5), 281-287 (2004).

[2] Y. Gebremichael, M. Vogel and S.C. Glotzer, "Particle dynamics and the development of string-like motion in a mono-atomic, supercooled liquid," J. Chem. Phys., **120** (9): 4415-4427 (2004).

[3] M. Bergroth, Y. Gebremichael, A.S. Keys, M. Vogel and S.C. Glotzer, manuscript in preparation.

FLAMMABILITY MAP FOR MICROGRAVITY FLAME SPREAD

SUBRATA BHATTACHARJEE
CHRIS PAOLINI
San Diego State University, San Diego, California, subrata@thermo.sdsu.edu

KAZUNORI WAKAI and **SHUHEI TAKAHASHI**
Gifu University, Gifu, Japan

Recently[1], a simplified theory has been advanced to predict radiative extinction in a quiescent environment. It has been shown that steady flame spread over a fuel with a thickness greater than a critical thickness is impossible in a microgravity environment, irrespective of any ambient or fuel parameters. Building upon this result, we have extended this analysis[2] to a general case of microgravity flame spread at low opposing velocity over fuels of any thickness - thermally thin or thick. Spread rate expressions, similar to de Ris formulas[3] have been developed by including surface radiation as a representative loss mechanismin the surface energy balance, which are:

$$\textbf{Thin Limit: } \eta_{f,\text{thin}} \sim \frac{1-\eta_g}{2} + \frac{1}{2}\sqrt{\left(1+\eta_g\right)^2 - 4\Re_0} \tag{1}$$

$$\textbf{Thick Limit: } \eta_{f,\text{thick}} \sim \frac{F^2}{\Omega^2}\eta_g\left(1-\frac{\Re_0}{\eta_g}\right)^2 \tag{2}$$

$$\text{where, } \eta_g \equiv \frac{V_g}{V_{f,\text{ thermal, thin}}},\ \eta_f \equiv \frac{V_f}{V_{f,\text{ thermal, thin}}} \text{ , and } \Omega \equiv \sqrt{\frac{\lambda_s \rho_s c_s}{\lambda_g \rho_g c_g}} \tag{3}$$

$$\text{and , } \Re_0 \equiv \frac{1}{F^2}\frac{\rho_s c_s}{\rho_g c_g}\frac{\varepsilon\sigma\tau}{\lambda_g}\left(\frac{T_v^4 - T_\infty^4}{T_v - T_\infty}\right) \text{ and } \Omega \equiv \sqrt{\frac{\lambda_s \rho_s c_s}{\lambda_g \rho_g c_g}} \tag{4}$$

For small value of the radiation parameter $\Re_0$ or for large value of opposing flow velocity η_g de Ris expressions are recovered. In fact in the thermal regime, where radiation can be neglected, the thin and thick limit expressions can be combined.

$$\eta_{f,\text{thermal}} \sim \max\left(1, \frac{F^2}{\Omega^2}\eta_g\right) \tag{5}$$

The thermally thick solution is applicable when $\frac{F^2}{\Omega^2}\eta_g \geq 1$; therefore, the criterion for a fuel to be considered thermally thick in the thermal regime can be written as

$$\eta_g \geq \frac{\Omega^2}{F^2};\ \text{or},\ \tau \geq \tau_{\text{cr},1};\ \text{where},\ \tau_{\text{cr},1} = \frac{\lambda_s}{\rho_g c_g V_g F}; \tag{6}$$

Equations (1) and (2) have been found to reproduce experimental trends remarkably well for both thin PMMA[4] and thin cellulosic fuels[5]. for the flame spread rates in a microgravity environment. The formulas above can also be used for determining when a steady flame is impossible in a microgravity environment. By setting η_f to zero, conditions for flame extinguishment can be obtained.

References:

[1] Bhattacharjee, S., Takahashi, S., and Wakai, K., Comb. Flame, Vol. 132, pp. 523-532, (2003).
[2] Bhattacharjee, S., Ayala, R., Takahashi, S., and Wakai, K., Proceedings of the Combustion Institute, Vol. 30, (2004).
[3] de Ris, J.N., Proceedings of the Combustion Institute, 12:241 (1969)
[4] Takahashi, S., Wakai, K., and Bhattacharjee, S., Proceedings of the Combustion Institute, Vol. 29, (2002).
[5] Olson, S.L., Kashiwagi, T., Fujita, O, Kikuchi, M., and Ito, K., Comb. Flame, Vol. 125, pp. 852-864, (2001).

LIQUID MICRO-JET IMPINGEMENT COOLING OF A POWER CONVERSION MODULE

Avijit Bhunia[1, 2], Sriram Chandrasekaran[1] and Chung-Lung Chen[1]
[1] Rockwell Scientific Company, 1049 Camino Dos Rios, Thousand Oaks, CA 91360
[2] Corresponding Author, Tel: (805) – 373 – 4348, e-mail: abhunia@rwsc.com

The Power Management and Distribution (PMAD) system for NASA's long duration HEDS program is envisioned to distribute up to megawatt levels of electric power. The future military directed energy, surveillance and communication missions also demand electric power of similar magnitude with sophisticated power conditioning systems. As a result the power dissipation is projected to grow multifold in coming years, e.g., ~200W/cm^2 for silicon devices and >1000W/cm^2 for wide bandgap semiconductor (silicon carbide, gallium nitride) devices. With traditional heat spreading and air-cooling techniques, the thermal management system will be bulky, if not insufficient. In this article we demonstrate that liquid impingement and subsequent phase change, has the potential to make thermal management compact, and thus reduce weight and launch costs.

We present liquid (DI water) micro-jet array impingement cooling of a commercial power module (Figure 1a). The silicon devices (six IGBTs and Diodes) are placed on a packaging and isolation layer (DBC), which in turn is mounted on a base plate. At a switching frequency of 22KHz, the module converts DC input power to 3-phase AC output to drive a 50HP motor (Figure 1b). We implement base plate level micro-jet (D_j = 200μm) impingement targeted at the heater footprint location (Figure 1c). The jet impingement cooling chamber and the overall closed loop system are shown in Figure 2a and b respectively.

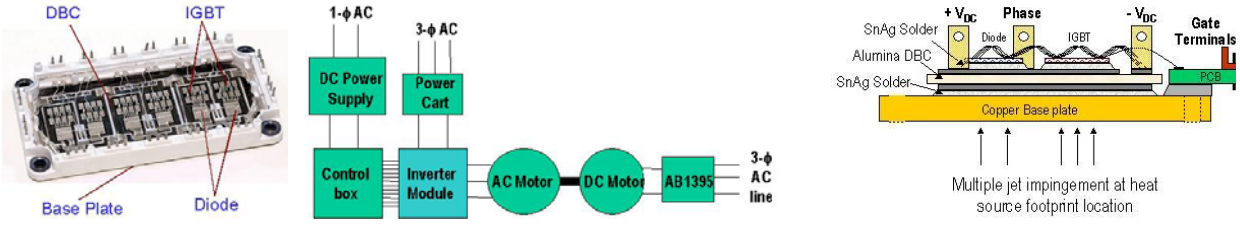

(a) (b) (c)

Figure 1: (a) 1200V-150A Power module from EUPEC (BSM100GD120DN2), (b) Schematic of the inverter module driving a 3-phase motor, (c) Schematic of the devices, packaging layers and base plate level liquid micro-jet array impingement.

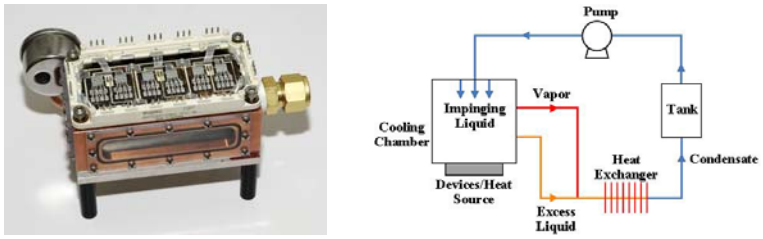

Figure 2: (a) Power module and liquid impingement cooling chamber. (b) Schematic of closed loop cooling system.

The high heat transfer coefficient associated with impingement and the simple orifice design lead to a cooling chamber conformal to the module. The resulting high volumetric power density (P_{VD} = heat

dissipated/cooling chamber volume) and the convenience of placing the heat exchanger at any desired remote location make the overall thermal management scheme compact.

Figure 3 shows a performance comparison of liquid micro-jet impingement, cold plate and air-cooling. The input power for cooling (to fan for air-cooling and to pump for liquid impingement and cold plate) is held constant at ~40W. The module operates at ~95% efficiency. Temperatures are measured at the base plate (T_{bp}) underneath each device. Figure 3a suggests that at module input power P_{in} = 13KW, liquid impingement lowers the maximum T_{bp} by 32°C compared to air-cooling (2X reduction) and by 18°C compared to cold plate (1.6X reduction). Figure 3b shows that at P_{in} = 13KW, the non-uniformity between T_{bp} values is reduced from 6°C in air-cooling to 4°C in cold-plate to <1°C for impingement cooling. From a system standpoint better the uniformity, higher is the module reliability. The diverging trend of the curves suggests that the payoff will be significantly more at higher power.

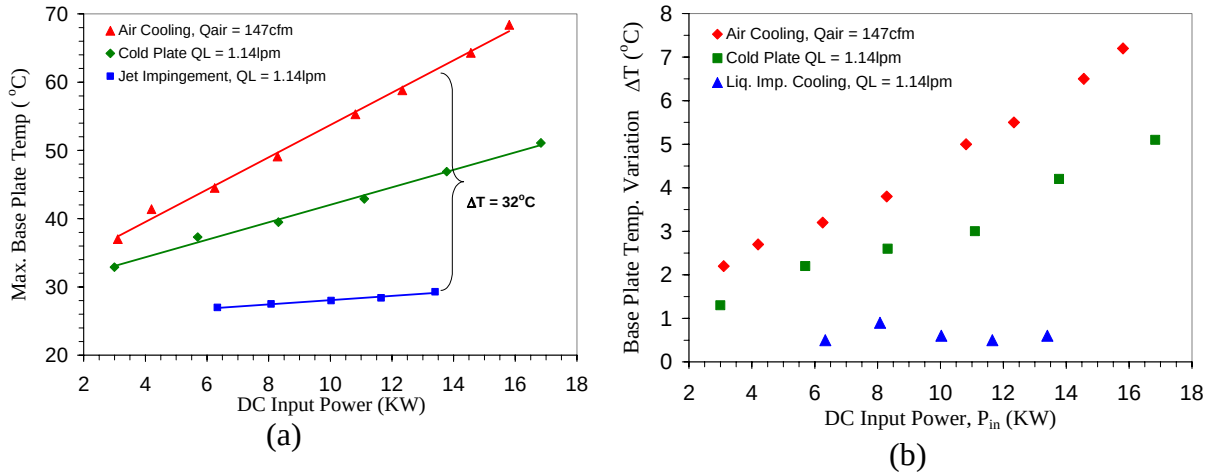

Figure 3: Comparison of performance between various cooling techniques. (a) Maximum base plate temperature, (b) Non-uniformity in base plate temperature.

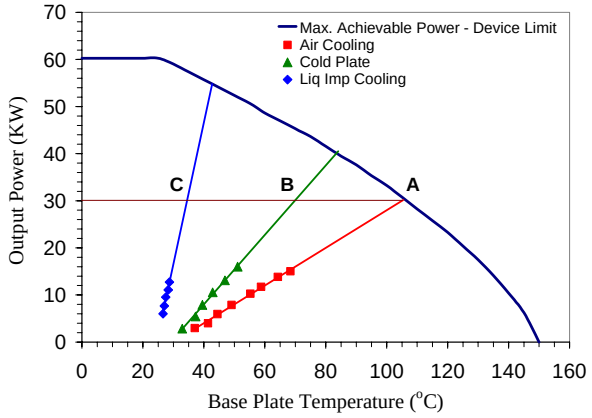

Figure 4: Comparison of cooling performance with reference to device limit.

Further comparison of the cooling techniques in light of the current carrying capability limit of the device (maximum achievable power from the module) is shown in Figure 4. With liquid impingement cooling, the module can deliver a maximum output power (P_{out}) of 55KW, compared to 40KW for cold-plate and 30KW for air-cooling. The corresponding P_{DV} values are 6.4, 6.7 and 1.2MW/m^3 respectively. P_{DV} for jet impingement cooling can be improved further by reducing the cooling chamber volume. Furthermore, at P_{out} = 30KW, T_{bp} and thus T_j can be reduced ~70°C compared to air-cooling (Points A-C) and ~35°C compared to cold plate (Points B-C).

The present results show that the liquid micro-jet impingement cooling far outperforms the conventional techniques. It is suitable for compact thermal management in space-based systems, especially with wide bandgap devices (such as silicon carbide) having dissipation densities >1000W/cm^2.

MODELING AND ANALYSIS OF CO-CURRENT FLAME SPREAD APPLIED TO THE UPWARD BURNING OF PMMA

Steven G. Buckley*, Ali S. Rangwala
Department of Mechanical and Aerospace Engineering, University of California, San Diego
9500 Gilman Drive, MS 0411; La Jolla, CA 92093-0411
buckley@ucsd.edu; 858-534-5681 / 858-534-5354 (F)

Jose L. Torero
School of Engineering and Electronics, University of Edinburgh, Scotland, United Kingdom

NASA uses tests involving upward flame spread as a flammability criterion to evaluate materials that could be potentially used in manned spacecraft. However, such tests remain an ON/OFF criterion, and no real translation of the ground based results to a micro-gravity environment has been proposed so far. The traditional 2-D solution proposed in 1956 by Emmons with extensions by Kodson, Williams and Buman (1968), Pagni and Shih (1978), and Annamalai and Sibulkin (1979) provides a baseline model for the Upward Flame Spread Test. Within this framework, measurements of the flame stand-off distance could be compared to predicted values obtained through this theory and used to establish a mass transfer number (B). The mass transfer number could then be used as a flammability criterion.

Recent experiments in upward burning flame spread over PMMA have shown the importance of lateral entrainment in the dynamics of the flame evolution, challenging the validity of 2-D boundary layer assumptions used to obtain the analytical solution. In this work we have tested the application of the classical 2-D model with an experimental setup modeled after the Upward Flame Spread Test. Analysis of video images allowed the extraction of the stand-off distance of the flame as a function of time, and an effective mass transfer number B is determined from these stand-off distances. When B is plotted as a function of streamwise distance x normalized by the pyrolysis length x_p, as in Figure 1, the data should collapse to a single curve. The failure of the data to collapse indicates the insufficiency of the classical model to fully describe this flow.

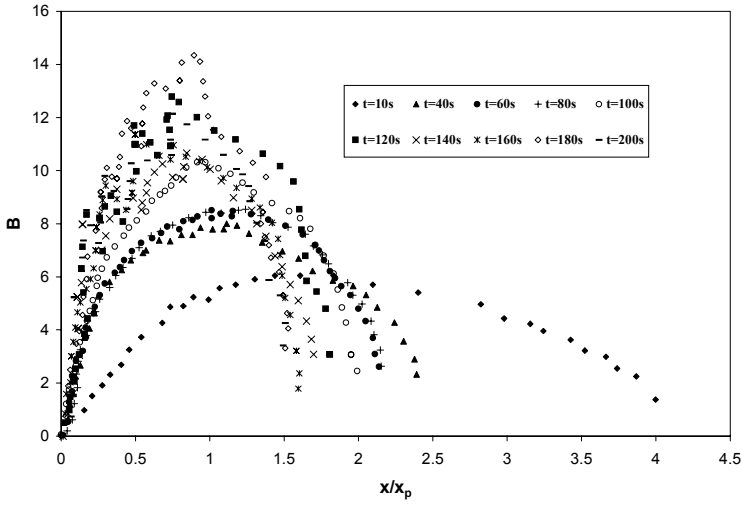

Figure 1: Evolution of empirical B number with time, from classical theory applied to experiments.

Experiments applied particle image velocimetry to ascertain the magnitude of lateral (side) entrainment suspected of diminishing the applicability of the 2-D analytical solution. Measurements of lateral entrainment were compared to 3-D predictions from the Fire Dynamic Simulator (FDS) code developed by NIST, as described by McGratten et

al. (2001). The simulations of upward-burning flame spread in several configurations showed good agreement with the experimentally measured the lateral entrainment. The results of these and further experiments are compared with measured experimental data for flame length and pyrolysis length. The agreement between experiments and the FDS model suggests that FDS could be used to obtain the stand-off distance and to extract the B number for solid fuels. Such application would allow the determination of a flammability criterion from the normal gravity tests and suggests possible extrapolation of these results to micro-gravity through the ability of the numerical code to remove the gravity term.

Beyond the observed agreement of FDS and experimental results, it is vital to validate the fundamental assumption of the proportionality of mass burning rate and shear stress inherent in traditional analytical solutions. Central to the approach of Emmons is the assumption that $\dot{m}'' \propto \partial u/\partial y$ in the 2-D flow, which propagates through later analytical solutions referenced above, but the validity of this has never been directly tested in this flame configuration. Testing of this assumption provides evidence of whether the insufficiency of the two-dimensional boundary layer solution is due to an inadequacy in the modeling approach, or merely to the need for an accounting of mass and/or heat transfer in the third dimension. Using the large eddy simulation model in FDS we provide data (Figure 2) to indicate that, while the two-dimensional boundary layer approach does not agree with experimental values, at steady state and in the plane of symmetry the assumption $\dot{m}'' \propto \partial u/\partial y$ holds, and hence the boundary condition imposed by Emmons appears to be valid. The verification of this assumption, in concert with the agreement of the numerical results and experimental data, allows us to conclude that predictions the stand-off distance using the FDS code are consistent with models incorporating a B-number type boundary condition, and thus it should be valid to extract a B number from such model outputs.

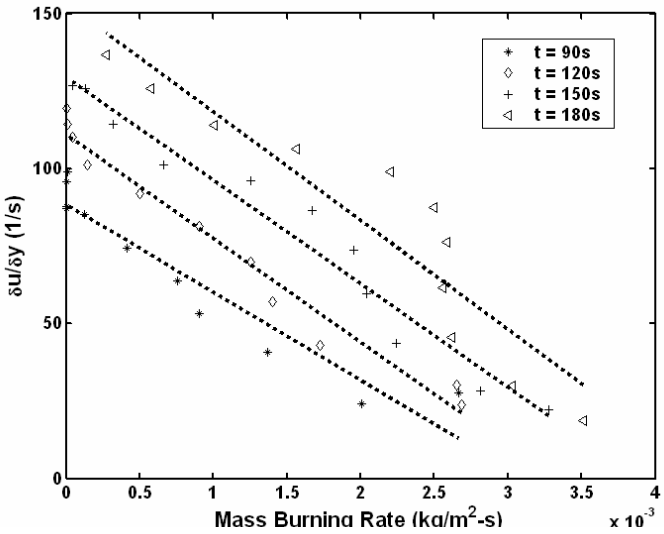

Figure 2: Proportionality of mass burning rate and strain rate du/dy predicted by FDS.

REFERENCES

H. Emmons, Z. angew. Math. Mech. 36 (1-2) (1956) 60-71.

F.J. Kosdon, F.A. Williams and C. Buman, Proc. Combust. Inst. 12 (1969) 253-264.

P.J. Pagni and T.M. Shih, Proc. Combust. Inst. 16 (1978) 1329-1343.

K. Annamalai and M. Sibulkin, Combust. Sci. Tech. 19 (1979) 167-183.

K.B. McGrattan, H.R. Baum, R.G. Rehm, A. Hamins, G.P. Forney and J.E. Floyd, Fire Dynamics Simulator - Technical Reference Guide (Version 2) National Institute of Standards and Technology (2001)

TESTS OF FLAMMABILITY OF COTTON FABRICS AND EXPECTED SKIN BURNS IN MICROGRAVITY

Jane M. Cavanagh, David A. Torvi,[1] and Kamiel S. Gabriel
Department of Mechanical Engineering
University of Saskatchewan
Saskatoon, SK

Gary A. Ruff
NASA Glenn Research Center
Cleveland, OH

During a shuttle launch and other portions of space flight, astronauts wear specialized flame resistant clothing. However during most of their missions on board the Space Shuttle or International Space Station, astronauts wear ordinary clothing, such as cotton shirts and pants. As the behaviour of flames is considerably different in microgravity than under earth's gravity, fabrics are expected to burn in a different fashion in microgravity than when tested on earth. There is interest in determining how this change in burning behaviour may affect times to second and third degree burn of human skin, and how the results of standard fabric flammability tests conducted under earth's gravity correlate with the expected fire behaviour of textiles in microgravity.

A new experimental apparatus was developed to fit into the Spacecraft Fire Safety Facility (SFSF), which is used on NASA's KC-135 low gravity aircraft. The new apparatus was designed to be similar to the apparatus used in standard vertical flammability tests of fabrics. However, rather than using a laboratory burner, the apparatus uses a hot wire system to ignite 200 mm high by 80 mm wide fabric specimens. Fabric temperatures are measured using thermocouples and/or an infrared imaging system, while flame spread rates are measured using real time observations or video. Heat flux gauges are placed between 7 and 13 mm away from the fabric specimen, so that heat fluxes from the burning fabric to the skin can be estimated, along with predicted times required to produce skin burns.

In November of 2003, this new apparatus was used on the KC-135 aircraft to test cotton and cotton/polyester blend fabric specimens in microgravity. These materials were also been tested using the same apparatus in 1-g, and using a standard vertical flammability test that utilizes a flame. In this presentation, the design of the test apparatus will be briefly described. Examples of results from the KC-135 tests will be provided, including heat fluxes and skin burn predictions. These results will be compared with results from 1-g tests using the same apparatus and a standard fabric flammability test apparatus. Recommendations for future microgravity fabric flammability tests will also be discussed.

[1] Corresponding Author: Phone (306) 966-5493, Fax (306) 966-5427,
Email: David.Torvi@usask.ca

TESTS OF FLAMMABILITY OF COTTON FABRICS AND EXPECTED SKIN BURNS IN MICROGRAVITY

Jane M. Cavanagh, David A. Torvi[1] and Kamiel S. Gabriel
Department of Mechanical Engineering, University of Saskatchewan, Saskatoon, SK
Gary A. Ruff
NASA Glenn Research Center, Cleveland, OH

Introduction

During a shuttle launch and other portions of space flight, astronauts wear specialized flame resistant clothing. However during most of their missions on board the Space Shuttle or International Space Station, astronauts wear ordinary clothing, such as cotton shirts and pants. As the behaviour of flames is considerably different in microgravity than under earth's gravity, fabrics are expected to burn in a different fashion in microgravity than when tested on earth. There is also interest in determining how this change in burning behaviour may affect human skin burn injury, and how the results of standard fabric flammability tests conducted under earth's gravity correlate with the expected fire behaviour of textiles in microgravity.

This paper briefly describes a new apparatus that was developed to measure the flammability of fabrics in microgravity, as well as under earth's gravity. This apparatus also measures heat fluxes from burning fabrics and estimates the burn damage that may occur if fabrics do ignite. Examples of test results obtained for cotton and cotton-polyester blend fabrics are provided. Suggested future work is also briefly discussed.

Experimental Apparatus

A new experimental apparatus was developed to fit into the Spacecraft Fire Safety Facility (SFSF), which is used on NASA's KC-135 low gravity aircraft (Figure 1). This apparatus was designed to be similar to that used in a standard vertical fabric flammability test. However, rather than using a laboratory burner, a hot wire system is used to ignite 200 mm high by 80 mm wide fabric specimens. Fabric temperatures are measured using thermocouples and/or an infrared imaging system, while flame spread rates are measured using real time observations or video. Heat flux gauges are placed between 7 and 13 mm away from the fabric specimen, to measure heat fluxes from the burning fabric. Two copper disk calorimeters (CD1 and CD2 in Figure 1) are used, along with two thin film heat flux gauges (SS1 and SS2). The latter gauges are also known as skin simulant sensors, as they have a combination of thermal properties that is similar to human skin. Measured heat fluxes can then be used to predict the times required to produce second and third degree skin burns. Further details on the experimental apparatus can be found in References [1] and [2].

[1] Corresponding Author: Phone (306) 966-5493, Fax (306) 966-5427,
Email: David.Torvi@usask.ca

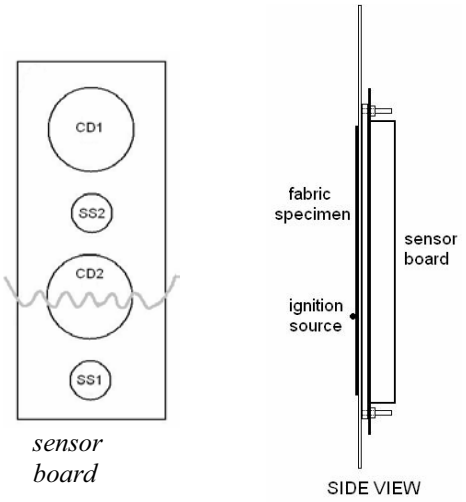

Figure 1: Experimental Apparatus

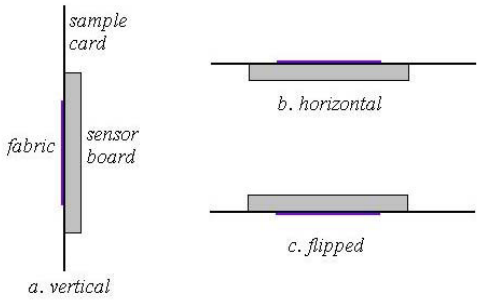

Figure 2: Orientations for 1-g Testing

Results

A variety of testing was done in 1-g to measure heat fluxes and flame spread rates, as well as predicted skin burn injury times. Four fabrics were tested: two 100% cotton samples (mass per unit area of 144 g/m^2 and 176 g/m^2), and two cotton/polyester blends (mass per unit area of 129 g/m^2 and 196 g/m^2). Tests were conducted using three different orientations, shown in Figure 2. Examples of the heat fluxes measured by the two copper disk sensors during tests of the lighter weight cotton fabric mounted in two different orientations are shown in Figure 3. Further details on these ground tests can be found in References [2] and [3].

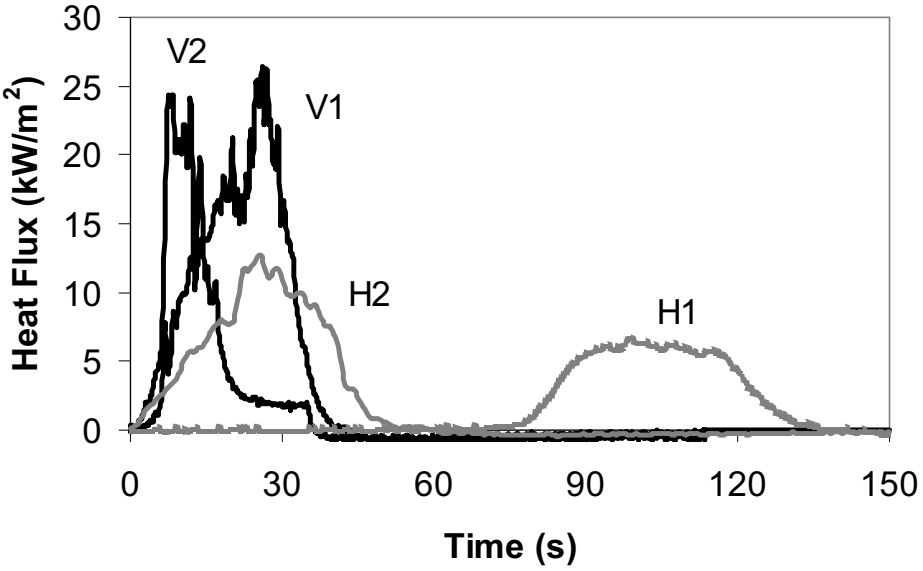

Figure 3: Heat Fluxes Measured By Two Copper Disk Heat Flux Sensors (CD1 and CD2) in Ground Tests of 100% Cotton Fabric (mass per unit area of 144 g/m^2) in Vertical (V) and Horizontal (H) Orientations (Air Gap of 7 mm)

In November, 2003, this new apparatus was used on the KC-135 aircraft for tests of the cotton and cotton/polyester blend fabrics in microgravity. Fabrics were ignited during the pull-up portion of the parabola and the burn behaviour was observed through the 20 s microgravity period. Heat fluxes, flame spread rates and fabric surface temperatures were obtained and skin burn times were predicted.

Examples of heat fluxes obtained for the lighter weight cotton fabric during the KC-135 tests are shown in Figure 4. Heat fluxes drop off substantially during the microgravity period, due to the reduction in flame size, and the absence of convection heat transfer between the fabric and the test sensors. A decrease in heat flux will increase the predicted times required to produce skin burns. For this particular test, the highest average heat flux measured by an individual sensor during the microgravity portion was 3 kW/m^2. It is predicted that a constant heat flux of this magnitude would produce a second degree burn in 53 s. A comparison between this heat flux and the maximum heat fluxes measured during 1-g tests of the same fabric is shown in Table 1, along with a comparison in the predicted times required to produce second degree burns.

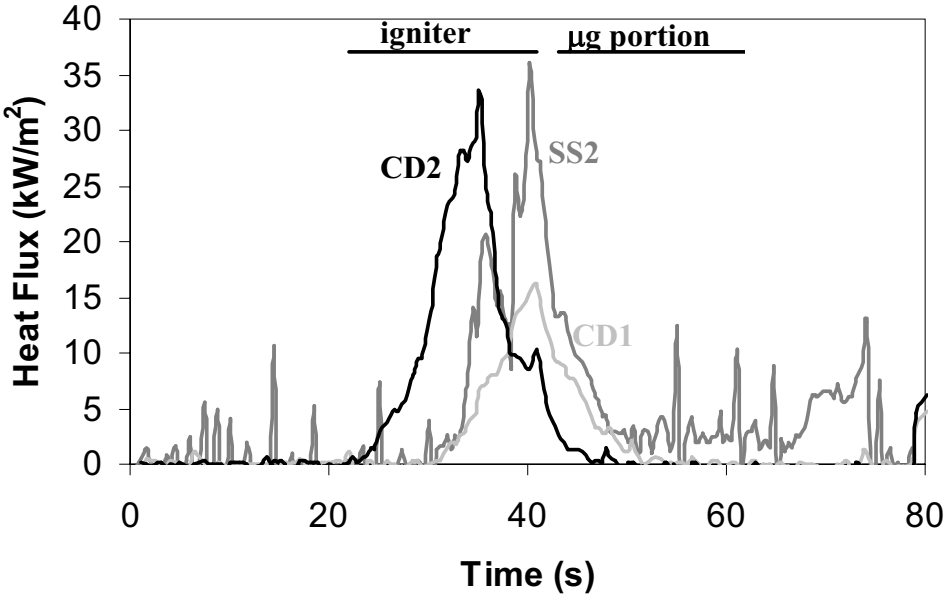

Figure 4: Heat Fluxes Measured by Three Sensors (CD1, CD2 and SS2) during KC-135 Test of 100% Cotton Fabric (mass per unit area of 144 g/m^2) (21% Oxygen Environment, 7 mm Air Gap)

Table 1: Maximum Heat Fluxes and Skin Burn Predictions for 100% Cotton Fabric (mass per unit area of 144 g/m^2) in Various Orientations and Gravity Levels

Orientation	Gravity Level	Max. Heat Flux (kW/m^2)	Predicted Time to Second Degree Burn (s)
Vertical	1-g	28	12
Flipped	1-g	17	37
Horizontal	1-g	13	41
Vertical	μ-g	3	53

Conclusions and Future Work

Preliminary results indicate that heat fluxes in microgravity are lower than those in 1-g, and that predicted times required to produce skin burn injury are longer in microgravity than in 1-g. Future work will include comparing flame spread rates in microgravity and under earth's gravity. Heat flux data and skin burn injury estimates will also be obtained under earth's gravity at other orientations in between those shown in Figure 2. The data generated in all of these experiments will be used in the development of models to predict the flame spread over fabrics, and the resulting heat fluxes and skin burn injury. Other factors that affect fabric flammability (e.g., oxygen concentration and air flow) will also be investigated.

Acknowledgements

The authors would like to thank the Canadian Space Agency, the Natural Sciences and Engineering Research Council of Canada, the University of Saskatchewan's College of Graduate Studies and Research and Department of Mechanical Engineering, and Zonta International for financial support. They would also like to thank the NASA Glenn Research Center's Microgravity Combustion Science Division for the providing the opportunity to conduct these experiments aboard the KC-135 aircraft.

References

[1] Cavanagh, J.M., Torvi, D.A., and Gabriel, K.S., "Experimental Study of Clothing Flammability and Associated Skin Burn Damage in Microgravity", 7th International Workshop on Microgravity Combustion and Chemically Reacting Systems", Cleveland, OH, June 3-6, 2003, pp. 325-328.

[2] Cavanagh, J.M., M.Sc. Thesis, University of Saskatchewan, Saskatoon, SK (in progress).

[3] Cavanagh, J.M., Torvi, D.A., Gabriel, K.S., and Ruff, G.A., "Flammability Tests of Cotton in Microgravity and Normal Gravity", Combustion Institute Canadian Section Spring Technical Meeting, Kingston, ON, May 9-12, 2004 (Paper #2, Session C, pp. 1-6).

Project Description

- experimental study of flame spread over fabrics and the resulting skin burn injury which can occur
- working with researchers at NASA Glenn Research Center
- test environments
  - 1-g, μ-g
- test fabrics
  - cotton, cotton/polyester

Apparatus

- an insert to fit in NASA's KC-135 Spacecraft Fire Safety Facility (SFSF) rig

fabric specimen

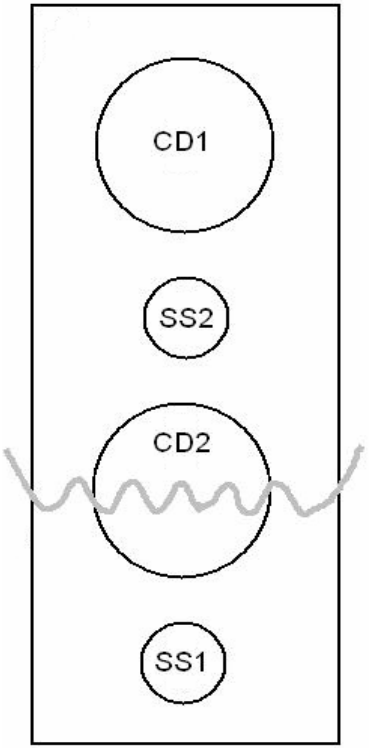

sensor board

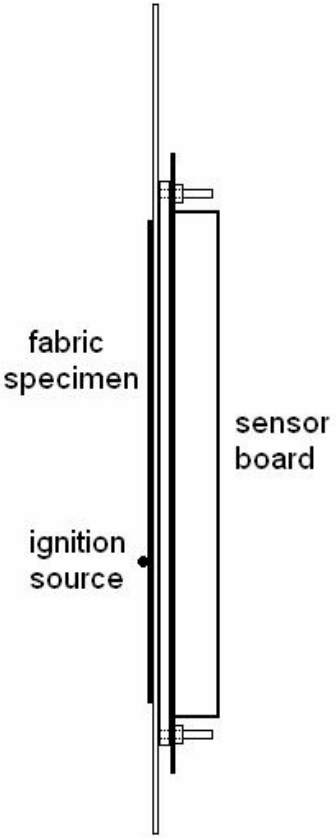

SIDE VIEW

Heat Flux Gauges

- Copper Disk
  - lumped heat capacity analysis
  - Stoll 2° burn criterion

- Skin Simulant
  - semi-infinite solid analysis
  - Henriques' burn integral
  - kpc similar to human skin

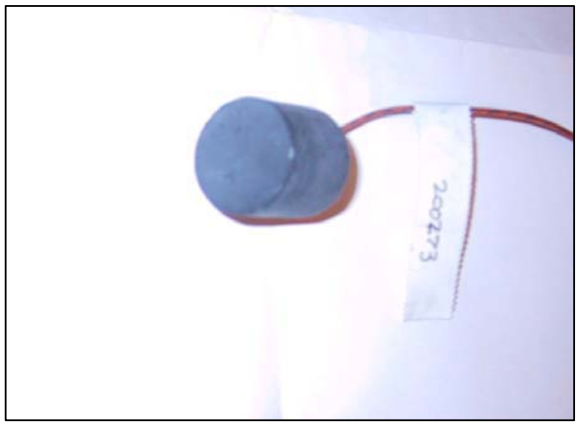

Test Fabrics

Fabric Type	Mass (g/m^2)	Thickness (mm)	Description
lightweight cotton (LC)	***144***	***0.43***	***cotton T-shirt***
heavyweight cotton (HC)	176	0.74	cotton golf shirt
lightweight blend (LB)	129	0.52	cotton/poly T-shirt
heavyweight blend (HB)	196	0.76	cotton/poly golf shirt

1-g Heat Fluxes: LC at various orientations, 7 mm air gap

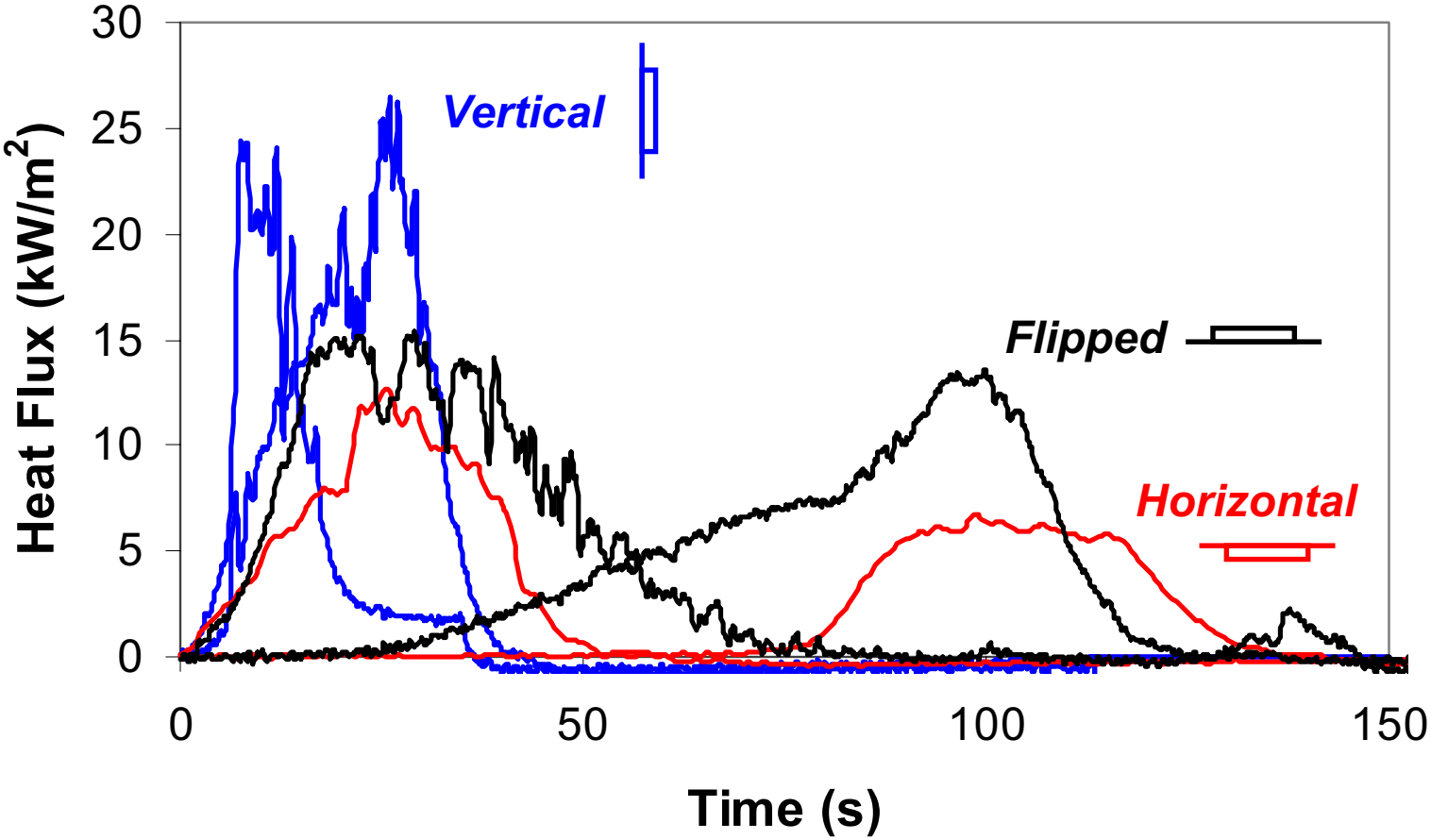

μ-g Heat Fluxes: LC, 21% 0_2, 7 mm air gap

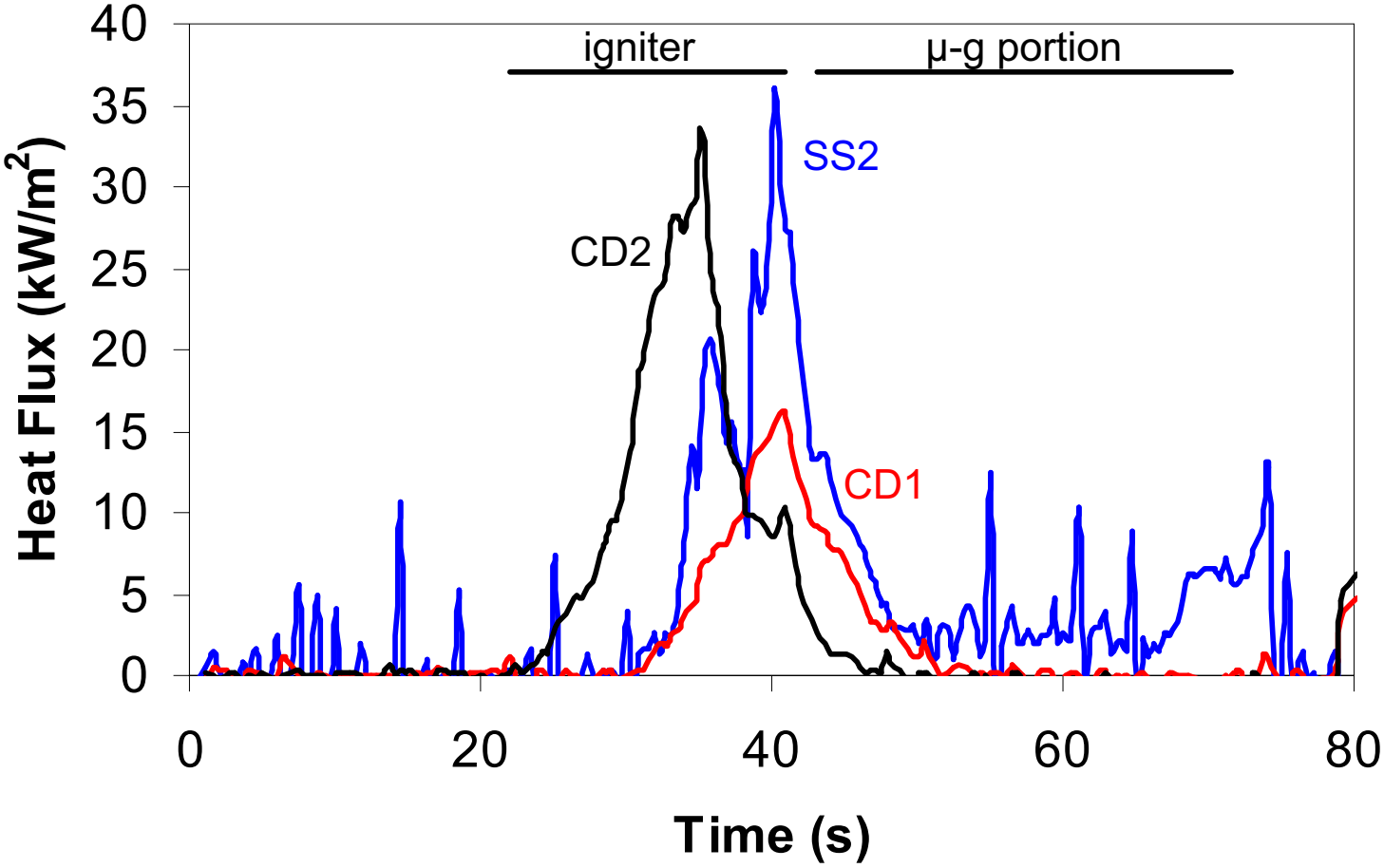

IR Image of Fabric Burning in μ-g

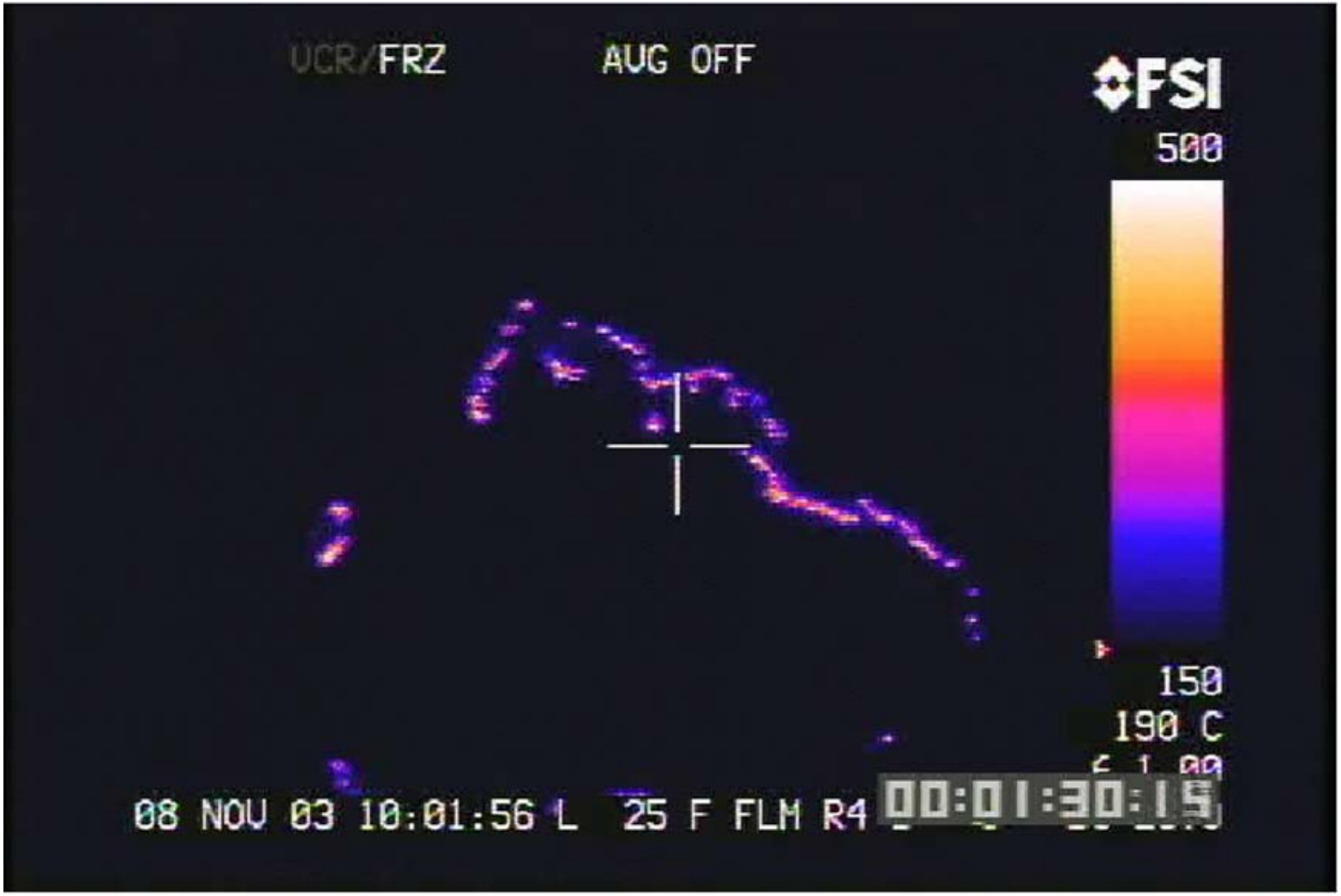

Preliminary Results

- lower flame spread rates in μ-g
- lower heat fluxes in μ-g

Orientation	Gravity Level	Max. Heat Flux	2nd Degree Burn Time
Vertical	1-g	28 kW/m^2	12 sec
Flipped	1-g	17 kW/m^2	37 sec
Horizontal	1-g	13 kW/m^2	41 sec
Vertical	μ-g	3 kW/m^2	53 sec

Future Work

- analyze μ-g flame spread
- complete μ-g, 1-g, and 2-g flame spread, heat flux and skin burn injury analysis
- make recommendations for further testing

Acknowledgements

National Aeronautics and Space Administration

Canadian Space Agency

Zonta International

Natural Sciences & Engineering Research Council Canada

U. Saskatchewan: College of Graduate Studies
Department of Mechanical Engineering

EPS (ELECTRIC PARTICULATE SUSPENSION) MICROGRAVITY TECHNOLOGY PROVIDES NASA WITH NEW TOOLS

Gerald M. Colver,* Nate Greene, and Hua Xu
Department of Mechanical Engineering
Iowa State University
Ames, IA 50011
*gmc@iastate.edu
Ph. 515-294-7572

EPS (Electric Particulate Suspension) microgravity technology provides NASA with new tools:

- A portable diagnostic tool for **fire safety**
- Small scale utility for **combustion testing** of powders on International Space Station and (Mars) Rovers.
- Device for **burning/testing magnesium in CO_2** atmosphere of Mars
- Control of **heat transfer** in vacuum and gas enclosures in space environments

The Electric Particulate Suspension is a fire safety ignition test system being developed at **Iowa State University** with **NASA support** for evaluating combustion properties of powders, powder-gas mixtures, and pure gases in microgravity and gravitational atmospheres (quenching distance, ignition energy, flammability limits). A separate application is the use of EPS technology to control heat transfer in vacuum and space environment enclosures. In combustion testing, ignitable powders (aluminum, magnesium) are introduced in the EPS test cell and ignited by spark, while the addition of inert particles act as quenching media.

As a combustion research tool, the EPS method has potential as a benchmark design for quenching powder flames that would provide NASA with a new fire safety standard for powder ignition testing. The EPS method also supports combustion modeling by providing accurate measurement of flame-quenching distance as an important parameter in laminar flame theory since it is closely related to characteristic flame thickness and flame structure.

In heat transfer applications, inert powder suspensions (copper, steel) driven by electric fields regulate heat flow between adjacent surfaces enclosures both in vacuum (or gas) and microgravity. This simple E-field control can be particularly useful in space environments where physical separation is a requirement between heat exchange surfaces.

EPS (Electric Particulate Suspension) microgravity technology provides NASA with new combustion tool:

Iowa State University research supported by NASA Office of Biological and Physical Research; NASA Glenn Research Center National Center for Microgravity Research on Fluids and Combustion

Gerald M. Colver*
Professor of Mechanical Engineering

Nate Greene, Hua Xu
Graduate Students

David Shoemaker, Hashim Al-Zain
Undergraduates

Department of Mechanical Engineering
Iowa State University
Ames IA 50011
*gmc@iastate.edu

Strategic Research to Enable NASA's Exploration Missions

EPS (powders/gases) Combustion Cell APPLICATIONS:

WHAT IS AN EPS (Electric Particulate Suspension):

- Particulate clouds formed electrostatically using high voltage ~10-30kV between parallel plates
- E-field controls particle dynamics produces more uniform clouds of particles in **microgravity**
- Ignition by sparking

ISU's EPS method is fundamentally simple. It utilizes a cylindrical test section enclosure comprised of two parallel plate electrodes (15 to 20 cm diameter) and Pyrex glass tubing for the insulated sides (Teflon and quartz are also used).

Features of EPS:
- Uniform Cloud Density and Simple Parallel Plate Test Section (no gas dispersion injection)
- Small powder sample few ~ mg
- Ignition testing of both gases and gas-powder mixtures
- Particle concentration easily measured by weight or laser attenuation
- Testing in virtually any space environment-microgravity to standard 1g+ (electric field overcomes gravity)

3,4,5 Tiered EPS Configuration For KC-135/DropTower Tests

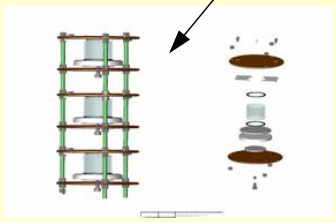

Portable Fire Safety Measurements

- Flammability limits – fuel curves
- Quenching distance
- Ignition energy

Laboratory or Hostile Space

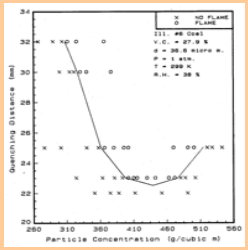

Small scale utility for combustion testing in space environments

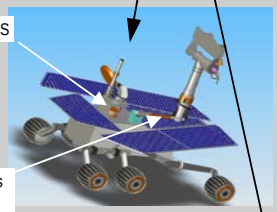

MARS ROVER
Burning/testing magnesium in CO2

Combustion Integrated Rack (CIR)

ISS US Lab Module

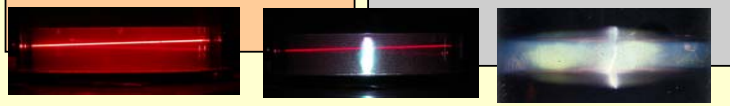

EPS Suspension → Ignition → Burn

Fundamental research tool for Powder Flames Research in Microgravity:

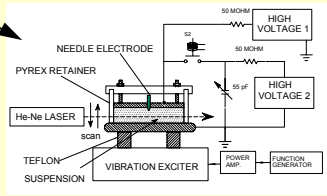

RESEARCH OBJECTIVES:

- To compare quenching distance/flame velocity for combustible powders using ISU's EPS method and McGill's flow dispersion technique
- To evaluate inert particle concentration (copper) on combustible gas flame quenching using EPS method
- To quantify the effect particle-gas slip velocity on flame quenching of gas/powder flames using EPS method
- To characterize particle velocity distribution (PVD) using the EPS method

EPS Heat transfer control in space environments

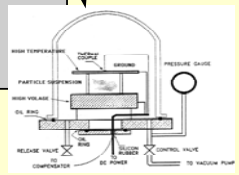

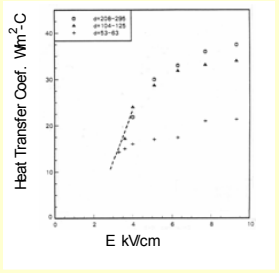

LUNAR SURFACE ENVIRONMENT LABORATORY

Joshua E. Colwell, Mihály Horányi, Scott Robertson, Stein Sture, Susan Batiste, and Zoltan Sternovsky
LASP, University of Colorado, Boulder CO 80309-0392, josh.colwell@lasp.colorado.edu, 303-492-6805, Fax: 303-492-6946

The lunar surface is covered with a layer of fine dust, or lunar regolith, that is produced by the continuous bombardment of the surface by the interplanetary micrometeoroid flux. The dust on the lunar mare is an angular, basaltic material with a mean particle size of about 100 μm and a broad size distribution extending down to at least 1 μm. The relatively low lunar gravity makes it easy for small disturbances to the surface to kick up large amounts of dust which travel higher and farther than in terrestrial gravity. In addition, the airless lunar surface leads to a plasma sheath on the night side due to solar wind ions and a photoelectron sheath on the day side due to photoemission of electrons by the solar UV flux. The dust on the lunar surface charges in this plasma environment and levitates and moves across the surface (Figs. 1-2). Any mission to the surface of the Moon, manned or unmanned, operates in this contaminating environment.

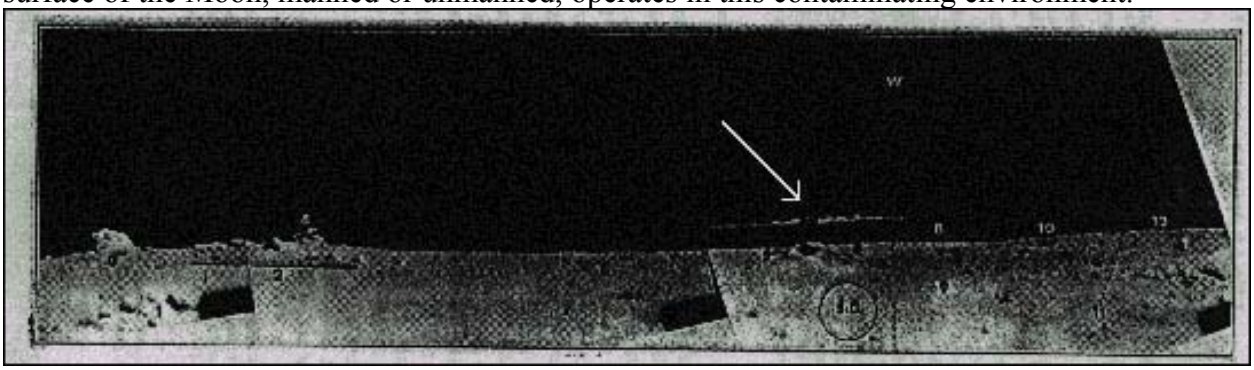

Figure 1: Surveyor photograph of the lunar horizon showing a cloud of small particles suspended 1 m above the surface (indicated by arrow). The circle labeled "S.D." indicates the apparent size and direction to the Sun [1]. NASA photo.

We have studied the charging, levitation, and transport of dust over planetary surfaces both experimentally and numerically [2-4]. We have reproduced the stably levitating dust clouds seen on the Moon (Fig. 1) in our laboratory experiments. We have also studied the response of planetary regolith to gentle impacts in a reduced gravity environment [5, 6].

In addition to dust contamination the charged particle environment at the lunar surface represents a potential hazard to astronauts. The night side of the Moon has a very different plasma environment than the day side due to the return flow of solar wind ions to the negatively charged surface. This results in a plasma sheath near the surface which can lead to even stronger electric fields near the surface than the dayside photoelectron sheath. As the Moon passes through the Earth's magnetotail there are additional charged particle fluences at the lunar surface. Characterization of this charged particle environment should precede extended astronaut stays on the Moon.

In situ resource utilization, including radiation and micro-meteorite shielding of human-outposts, will require excavation of the lunar surface. The unique angular nature of regolith

grains which become interlocked and densified by the lunar quakes complicates soil-movement techniques. Implementing vibrating excavating tools to loosen and dilate regolith for construction purposes will provide an efficient method to achieve regolith movement [7].

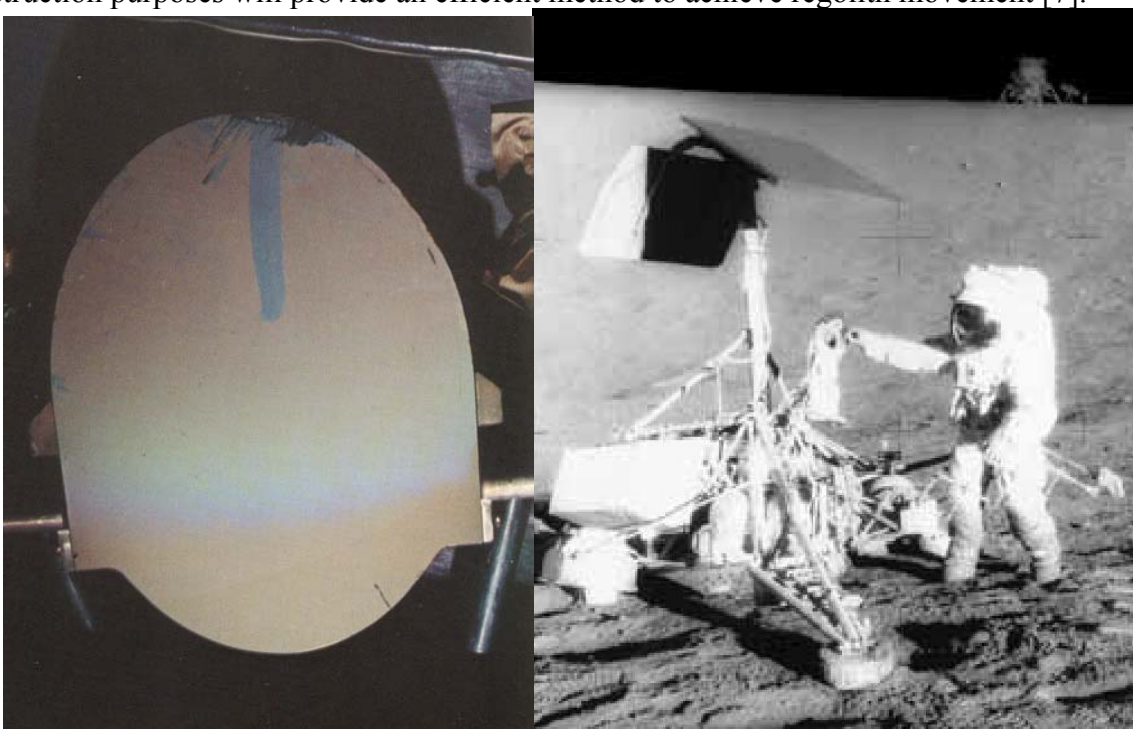

Figure 2: (left) An astronaut's glove print on the camera mirror of Surveyor 3 reveals the amount of dust that accumulated on the mirror after 31 months on the lunar surface; (right) an astronaut's spacesuit is coated with lunar dust up to the knees as he works at the Surveyor 3 spacecraft with the Apollo 12 LM in the background. NASA photos.

A lunar lander with instrumentation to measure near-surface plasma properties, regolith properties, and active experiments to study the response of surface dust to spacecraft activity in a variety of conditions and to test dust mitigation technologies would resolve many of the open questions surrounding the lunar surface environment, facilitating future manned and unmanned missions and surface experiments.

REFERENCES

[1] Rennilson, J. J., and D. R. Criswell, *The Moon*, **10**, 121-142 (1974).

[2] Sickafoose, A. A., J. E. Colwell, M. Horányi, and S. Robertson, *J. Geophys. Res.*, **107**, 1408 (2002).

[3] Sternovsky, Z., A. A. Sickafoose, J. E. Colwell, S. Robertson, and M. Horányi, *J. Geophys. Res.*, **107**, 5105 (2002).

[4] Robertson, S., A. A. Sickafoose, J. E. Colwell,and M. Horányi, *Physics of Plasmas*, **10**, 3874 (2003).

[5] Colwell, J. E., and M. Taylor, *Icarus*, **138**, 241 (1999).

[6] Colwell, J. E., *Icarus*, **164**, doi: 10.1016/S0019-1035(03)00083-6 (2003).

[7] Klosky, J. L., S. Sture, H. Ko, and F. Barnes, "Vibratory Excavation and Anchoring Tools for the Lunar Surface," *Space '96: The 5th International Conference and Exposition on Engineering, Construction and Operations in Space*, ASCE (1996).

NASA/CP—2004-213205/VOL2

Lunar Surface Environment Laboratory

Joshua E. Colwell, Mihály Horányi, Scott Robertson, Stein Sture,

Susan Batiste, and Zoltan Sternovsky

LASP, University of Colorado, Boulder CO

josh.colwell@lasp.colorado.edu, 303-492-6805, Fax: 303-492-6946

Cleveland, June 2004

Strategic Research to Enable NASA's Exploration Missions Conference

Lunar Surface

- The lunar regolith consists of fine-grained dust or lunar soil. Low lunar gravity allows small disturbances to the surface to eject large amounts of dust which travel higher and farther than in terrestrial gravity (Fig. 4) [5,6].
- The airless lunar surface leads to a plasma sheath on the night side due to solar wind ions and a photoelectron sheath on the day side due to photoemission of electrons by the solar UV flux. Dust on the lunar surface charges in this plasma environment, levitates, and moves across the surface (Figs. 1-3).
- The charged particle environment at the lunar surface represents a potential hazard to astronauts. The night side of the Moon has a very different plasma environment than the day side due to the return flow of solar wind ions to the negatively charged surface.
- As the Moon passes through the Earth's magnetotail there are additional charged particle fluences at the lunar surface. Characterization of this charged particle environment should precede extended astronaut stays on the Moon.

Lunar Surface (cont.)

- The unique angular nature of regolith grains which become interlocked and densified by the lunar quakes complicates soil-movement techniques. Implementing vibrating excavating tools to loosen and dilate regolith for construction purposes will provide an efficient method to achieve regolith movement [7].
- In situ resource utilization, including radiation and micro-meteorite shielding of human-outposts, will require excavation of the lunar surface (Figs. 5-7).
- Mobility mechanisms require well-defined vehicle-regolith interaction.
- A dedicated Lunar Surface Environment Laboratory or instrument package can address these technological issues to insure safe and efficient astronaut and unmanned activity on the lunar surface for extended duration visits to the Moon.

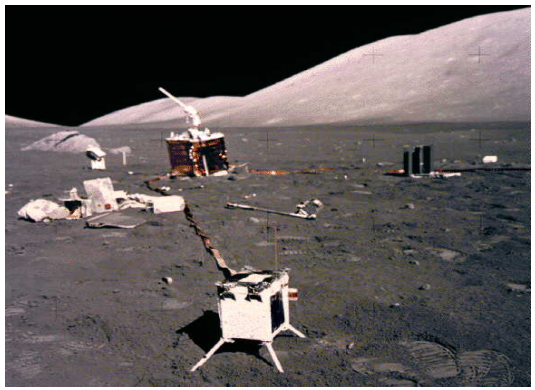

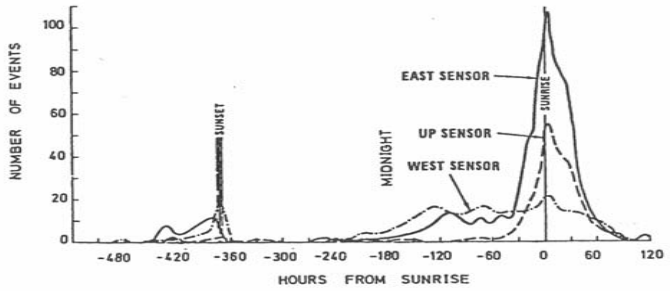

Figure 1: When we return to the Moon, we must understand and mitigate the dust and radiation environment for safe and successful missions on the lunar surface.

Evidence of dust levitation and transport above the lunar surface. Top and right: LEAM experiment and data show degradation of dust sensors facing east, suggesting transport of dust from east to west across the terminator.

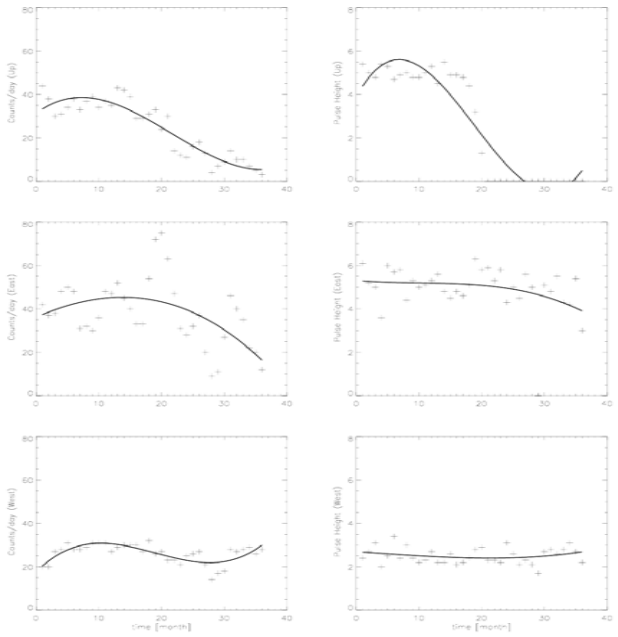

Physics of Dust Levitation

- Photoemission of electrons from a surface creates a photoelectron sheath or a kind of electron exosphere above the surface.
- A surface in a plasma, such as the solar wind, will develop a plasma sheath if photoemission is weak or absent. The plasma sheath generates an electric field, E.
- The surface and dust grains beneath a plasma sheath have a negative charge due to collection of the faster electrons in the plasma.
- The surface bias allows particles to lift off the surface (electrostatic repulsion overcomes adhesion).
- Once in the sheath dust can achieve stable levitation due to the balance of the electric and gravitational force.

Levitation of Dust on the Moon

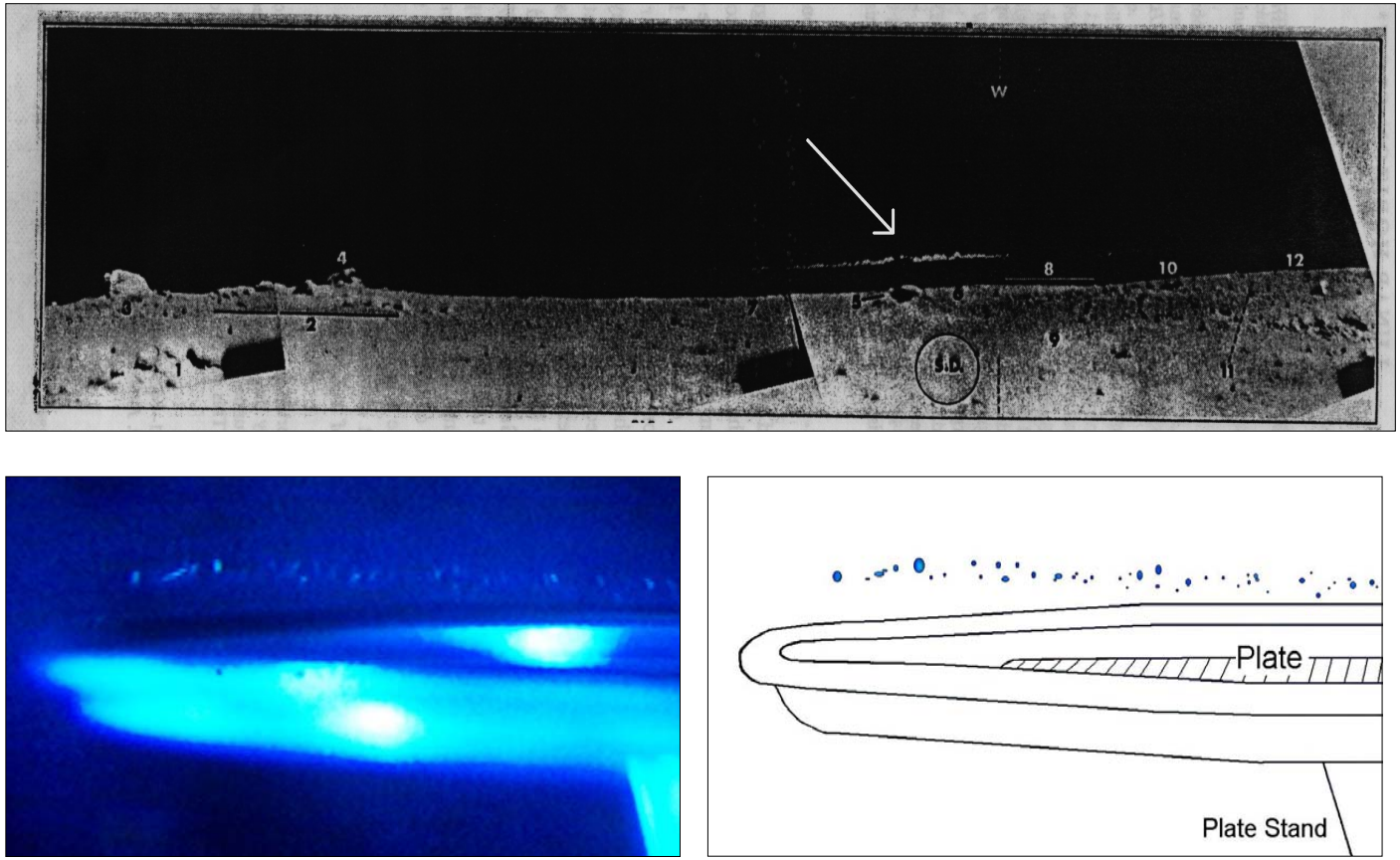

Figure 2: Image of dust levitated over the lunar surface by electrostatic forces (top) [1], and levitated dust grains in LASP dust environment laboratory.

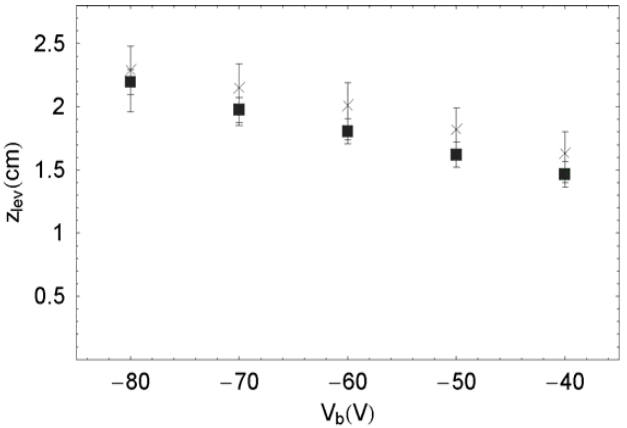

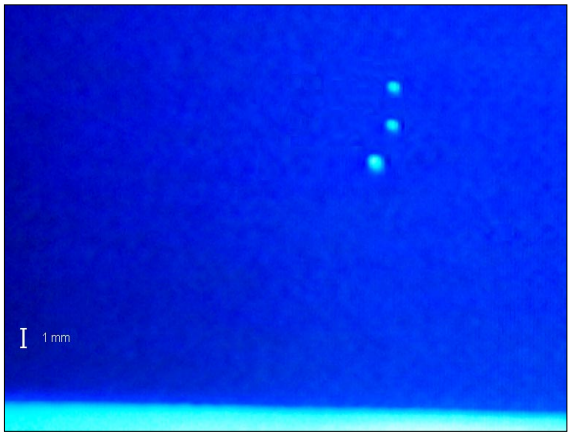

Figure 3: A comparison of theoretically derived and experimentally measured dust levitation heights in a plasma device at LASP (left). Superposition of three images showing a single stably levitating dust particle under three different plasma conditions (right).

Experiments were performed in the plasma device shown at right [2,3,4].

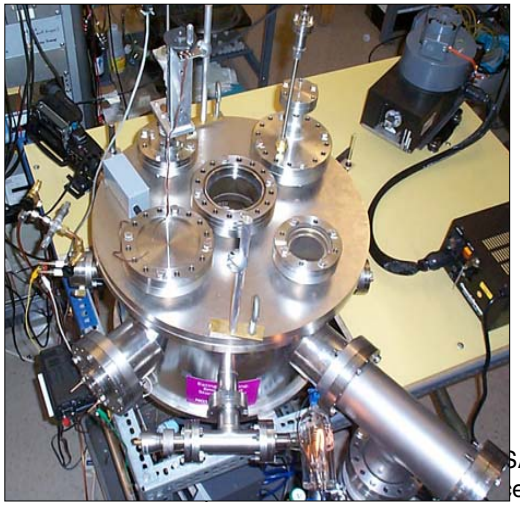

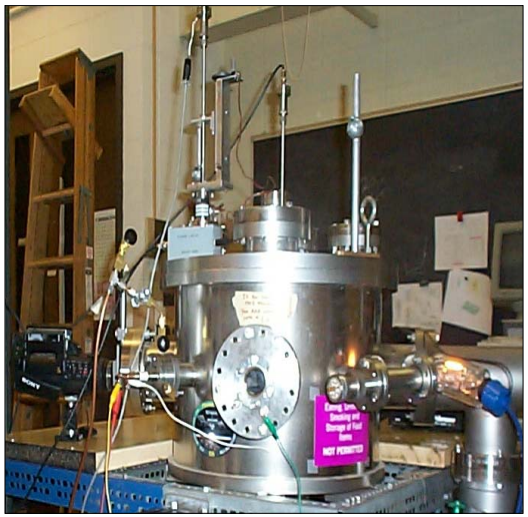

Cleveland, June 2004

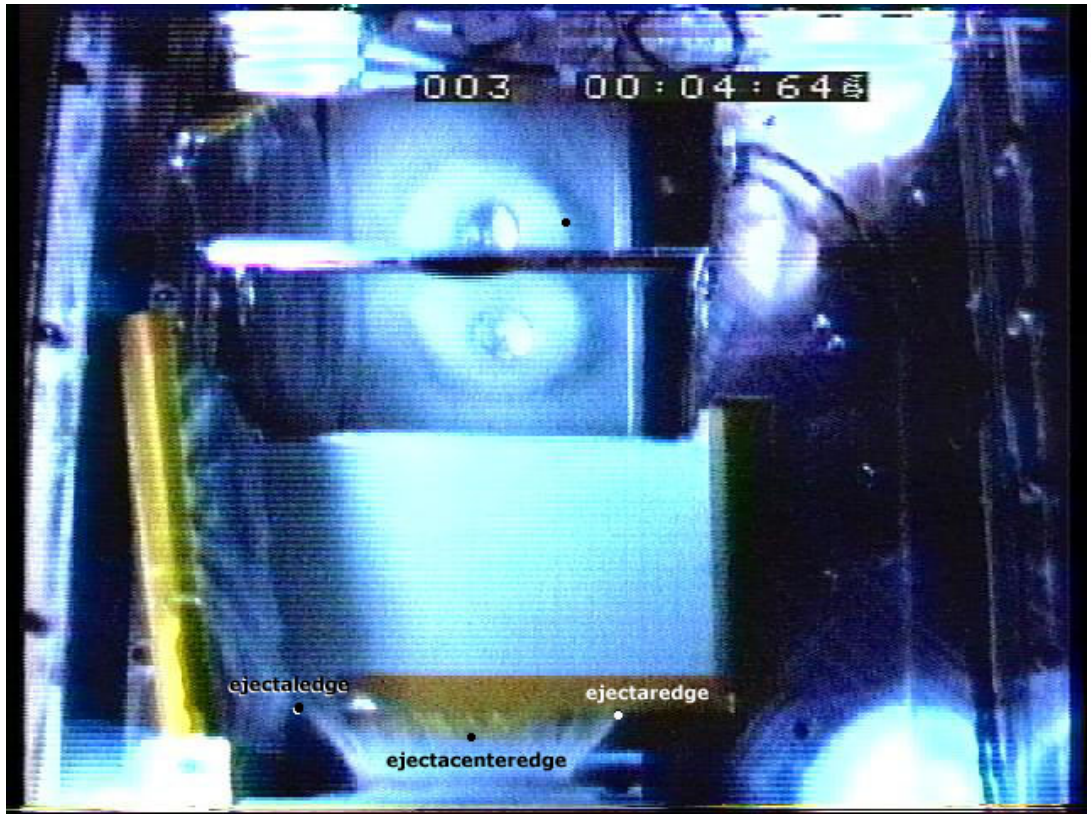

Figure 4: Impact experiments in microgravity (COLLIDE, PRIME) have demonstrated that regolith is ejected even in very gentle collisions when the surface gravity is low [5,6]. The impact shown is at a speed comparable to that of an object falling from a height of 1 m on the Moon. A large amount of particles are displaced in such an impact in reduced gravity conditions, presenting a source of contaminating material for equipment in use on the lunar surface.

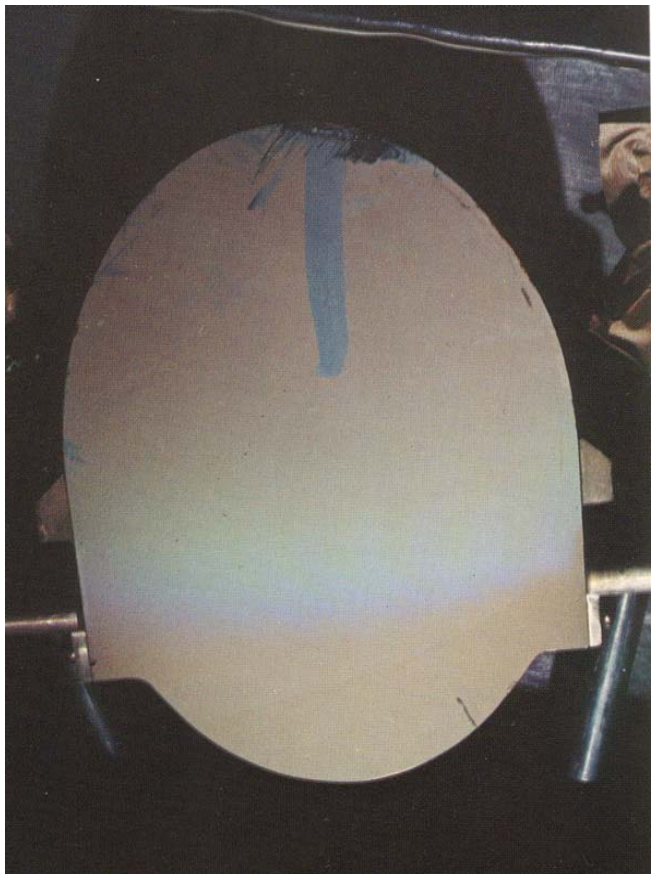

Figure 6 (right): Micrometeoroid bombardment can pose a hazard for long duration missions.

Figure 5 (left) : Dust hazards on the Moon: a mirror is coated with dust after 31 months on the lunar surface.

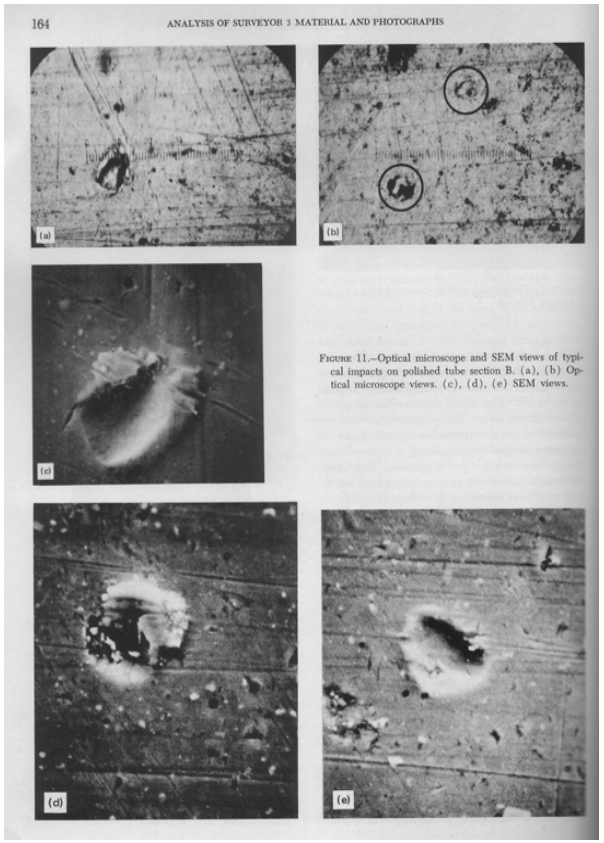

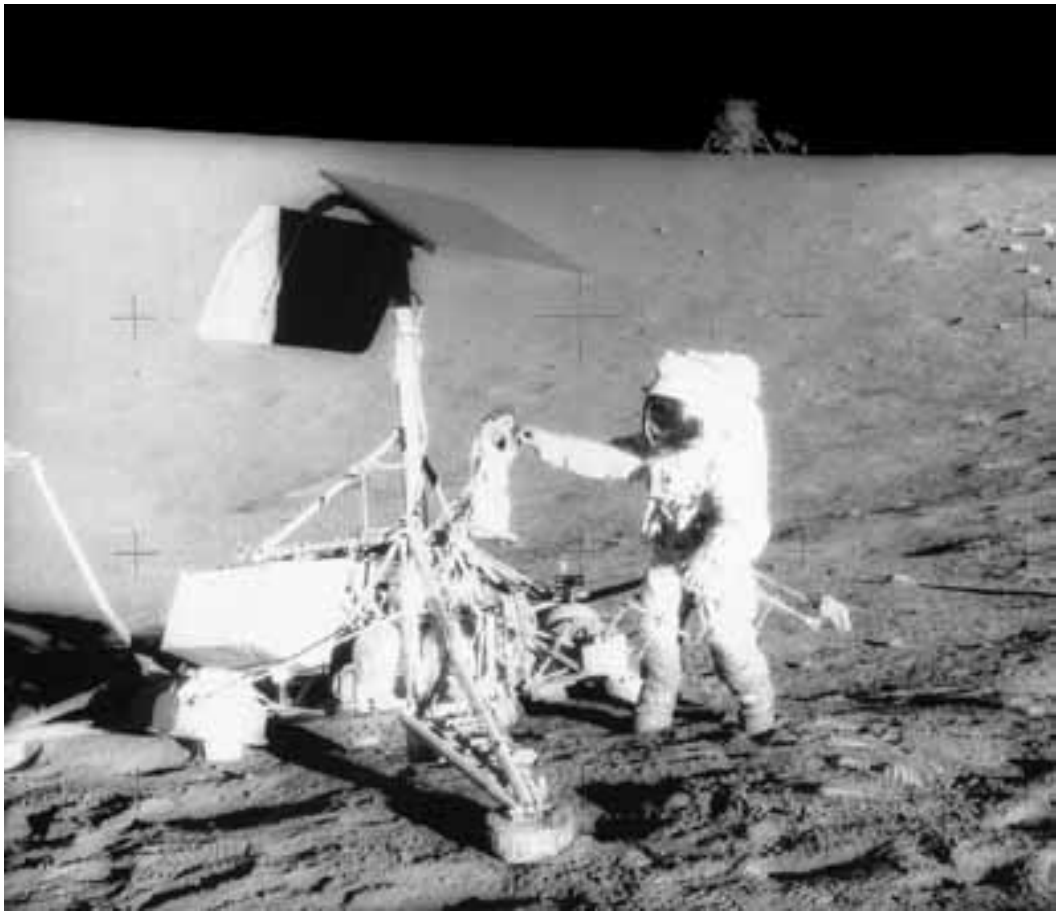

Figure 7: Astronaut Charles Conrad Jr. (Apollo 12) retrieves equipment from Surveyor 3 in November 1969, 31 months after the spacecraft had landed on the surface. Conrad's spacesuit is coated with lunar regolith material from the knees down. Surveyor equipment showed many signs of damage and contamination due to dust (see also Figs. 5-6). The Lander is visible in the background; for longer-term missions and in-situ resource utilization, mobility mechanisms such as rovers will need to be reassessed.

Mission Profile

- Multi-instrument lander.
- Surface operation for several months.
- Study radiation and dust environment through:
  - Diurnal cycle
  - Earth magnetotail passages
  - Solar flares
- Measure dust dynamics and contamination.
- Active soil mechanics experiments:
  - Dust levitation and dynamics in response to surface activity
  - Regolith movement: bulldozing and augering techniques
  - Mechanics of mobility on the surface

Measurements

- Electron energy and density
- Ion energy and density
- Surface electric fields
- Micrometeoroid bombardment rate
- Behavior of dust in different plasma environments
- Response of dust to surface activity
- Regolith-engineering parameters
- Vehicle-regolith interaction characteristics
- Energy requirements for regolith movement

Lunar Lander Instrumentation

- **Plasma Package:**
  - E-field probes
  - Emissive Langmuir probe
- **Dust Package:**
  - Micrometeoroid impact detector
  - Surface manipulator arm
  - Witness plate
- **Camera Package:**
  - Image horizon glow, dust on witness plate, surface
- **Regolith Mechanics & Engineering Package:**
  - Augering and bulldozing tools
  - Instrumentation of Lander, manipulator arm, tools
    - Measure regolith parameters
    - Measure vehicle-regolith interaction
    - Optimize excavation energy requirements

References

[1] Rennilson, J. J., and D. R. Criswell, *The Moon*, **10**, 121-142 (1974).

[2] Sickafoose, A. A., J. E. Colwell, M. Horányi, and S. Robertson, *J. Geophys. Res.*, **107**, 1408 (2002).

[3] Sternovsky, Z., A. A. Sickafoose, J. E. Colwell, S. Robertson, and M. Horányi, *J. Geophys. Res.*, **107**, 5105 (2002).

[4] Robertson, S., A. A. Sickafoose, J. E. Colwell, and M. Horányi, *Physics of Plasmas*, **10**, 3874 (2003).

[5] Colwell, J. E., and M. Taylor, *Icarus*, **138**, 241 (1999).

[6] Colwell, J. E., *Icarus*, **164**, doi: 10.1016/S0019-1035(03)00083-6 (2003).

[7] Klosky, J. L., S. Sture, H. Ko, and F. Barnes, "Vibratory Excavation and Anchoring Tools for the Lunar Surface," *Space '96: The 5th International Conference and Exposition on Engineering, Construction and Operations in Space*, ASCE (1996).

CRITICAL VELOCITIES IN OPEN CAPILLARY CHANNEL FLOWS (CCF)

Michael E. Dreyer, Uwe Rosendahl, Antje Ohlhoff

Center of Applied Space Technology and Microgravity (ZARM)
University of Bremen, Am Fallturm, D-28359 Bremen, Germany
e-mail: dreyer@zarm.uni-bremen.de, Fax: +49-421 218-2521, Phone: +49-421 218-4038

ABSTRACT

We consider a forced liquid flow in an open capillary channel with free liquid surfaces under low gravity conditions. The channel consists of two parallel plates as shown in Figure 1. The gap distance, the width of the plates and the length of the channel are denoted with a, b and l, respectively. The liquid flows along the x-axis and forms free surfaces at the sides between the plates. The flow is maintained by external pumps and the free surface deforms according to the pressure along the flow path. In case of steady flow the capillary pressure of the free surface balances the differential pressure between the liquid and the ambient constant pressure gas phase. A maximum flow rate is achieved when the adjusted volumetric flow rate exceeds a certain limit leading to a collapse of the free surfaces. The aim of the considerations is to determine the profile of the gas/liquid interface, the maximum flow rate of the steady flow and the corresponding critical flow velocity. The maximum flow rate depends on the geometry of the channel and the properties of the liquid, specified by three dimensionless parameters, the OHNESORGE number $\mathrm{Oh} = \sqrt{\rho\nu^2/(2\sigma a)}$, the aspect ratio $\Lambda = b/a$ and the dimensionless length $\tilde{l} = \mathrm{Oh}l/(4a)$ (ρ is the density, ν the kinematic viscosity and σ the surface tension of the fluid).

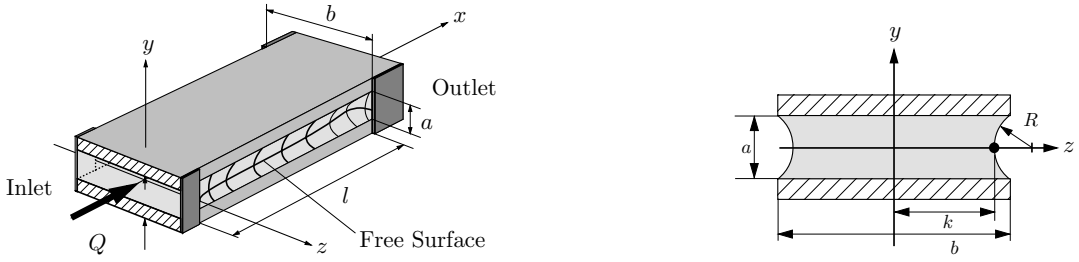

Figure 1: Schematic drawing of the flow through a capillary channel consisting of two parallel plates (left). The cross section area A perpendicular to the flow direction x (right).

We expect that the flow rate limitation occurs due to choking, which is known from compressible gas flows and open channel flows under normal gravity. The theory of choked flow predicts a limiting velocity corresponding to a characteristic signal velocity of the flow. Once that this critical velocity is reached the mass flow is maximum and cannot be increased further. Analogous to these phenomena we introduce the capillary SPEED INDEX $S_{ca} = v/v_{ca}$ where v is the mean liquid velocity and v_{ca} the speed of longitudinal small amplitude waves in open capillary channels. The maximal flow rate Q_{crit} is expected for $S_{ca} = 1$.

The experimental investigations were performed in the drop tower Bremen [1,3] and aboard the sounding rocket TEXUS-37. During the TEXUS experiment the flow rate was increased in small steps up to the critical value and the surface collapse was observed by

video cameras. The data evaluation yields the contour line of the liquid surfaces $k(x)$ as defined from Fig. 1 and the maximum flow rate of the steady flow which are well predicted by numerical model computations [2,4]. Furthermore a good agreement between the

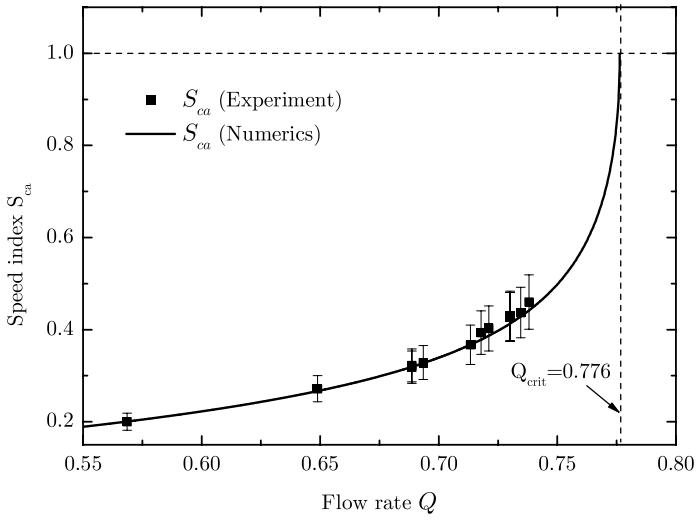

Figure 2: Capillary SPEED INDEX S_{ca} at the smallest cross section of the flow as function of the adjusted flow rate Q for the TEXUS experiment.

experimental data and numerical calculation of S_{ca} were found as depicted in Fig. 2. The numerical S_{ca} tends exactly towards unity for the numerical maximum flow rate, $Q_{crit}^{num} = 0.776$, which confirms the influence of the SPEED INDEX on the flow limitation. Experimentally, a maximum flow rate of $Q \simeq 0.95\, Q_{crit}^{num}$ was reached. A closer approach to the limit might be difficult from the experimental point of view since a small variation of Q leads to a large variation of S_{ca}. The final 5 % of flow rate changes S_{ca} by 50 %. Close to the limit very small increments in Q are required to increase the flow in quasi-static manner avoiding strong non-steady effects.

The experiment has been selected (94 NRA-7) to be conducted in the Microgravity Science Glovebox aboard the ISS. The Science Concept Review has been passed in 2002 and a feasability study (A) was conducted in 2003. A breadboard phase (B0) is currently underway testing detailed technical solutions with respect to the fluid handling, the video observation and the experiment control. The predefinition phase (B) is planned for this year. The experiment should be ready for flight in 2007. The funding of this work by means of the German Federal Ministry for Education and Research (BMBF) through the German Aerospace Center DLR under contract 50 WM 0241 is greatfully acknowledged.

1 M. E. Dreyer, U. Rosendahl, H. J. Rath, Experimental Investigation on Flow Rate Limitations in Open Capillary Vanes, AIAA 98–3165, 1998

2 U. Rosendahl, B. Motil, A. Ohlhoff, M. E. Dreyer, H. J. Rath, Critical Velocity in Open Capillary Channel Flows, AIAA-2001–5021, 2001

3 U. Rosendahl, A. Ohlhoff, M. E. Dreyer, H. J. Rath, Investigation of Forced Liquid Flows in Open Capillary Channels, Microgravity Science and Technology XIII/4, 2002

4 U. Rosendahl, A. Ohlhoff, M. E. Dreyer, Choked flows in open capillary channels: theory, experiment and computations, submitted to: Journal of Fluid Mechanics (JFM)

CRITICAL VELOCITIES IN OPEN CAPILLARY CHANNEL FLOWS (CCF)

Michael E. Dreyer, Uwe Rosendahl, Antje Ohlhoff

Center of Applied Space Technology and Microgravity (ZARM)
University of Bremen, Am Fallturm, D-28359 Bremen, Germany
e-mail: dreyer@zarm.uni-bremen.de, Fax: +49 421 218 2521

Abstract

Forced liquid flows through open capillary channels with free liquid surfaces are and will be investigated under low gravity conditions. If a certain critical flow rate is exceeded, the flow does not remain steady, the surfaces collapse and gas ingestion occurs at the outlet. To investigate the nature of this effect in an extended range of the describing characteristic numbers and in different geometries, the experiment has been selected by 94 NRA-7 and will be conducted in the Microgravity Science Glovebox aboard the ISS. This paper presents the status of the experiment setup based on a feasibility study (A) conducted in 2003 and the results of a breadboard phase (B0) which is currently underway. This paper is comprehensible with the attached slides only.

1 Introduction

The Capillary Channel Flow experiment (CCF) is concerned with flow rate limitations in open capillary channels under low gravity conditions. An open capillary channel is a structure which establishes a liquid flow at low Bond numbers, i.e. when the capillary pressure caused by the surface tension forces dominates in comparison to the hydrostatic pressure induced by gravitational or residual accelerations. The cross section of the flow path is totally or partly confined by free surfaces.

As an example the capillary channel consisting of two parallel plates is shown on slide **2**. At both ends the plates are connected to ducts of closed perimeter. The flow enters the channel via an inlet, passes the open section (free surface flow) and leaves at the outlet. For an internal pressure p lower than ambient pressure p_a the free liquid surfaces are concave at any cross section. The pressure decreases in flow direction and the curvature of the surfaces increases, thus the flow path constricts. A steady flow is only obtained for a flow rate below a critical value ($Q < Q_{crit}$). For that case the differential pressure $p_a - p$ is compensated by the capillary pressure of the free surface. For $Q > Q_{crit}$ the liquid surfaces collapse at the channel outlet and the flow transits from steady single phase flow to unsteady two phase flow.

The aim of the experiment is to determine the maximum flow rate Q_{crit} of the steady flow as well as the profiles of the gas/liquid interface k in the $y = 0$ plane (slide **3**) in dependence of the flow rate Q. Both properties are required to verify our theoretical model [4]. From this model we conclude that the limitation of the steady flow is caused by choking, a phenomenon which was up to now only known from one-dimensional flows in gas dynamics, liquid flows in open channels under terrestrial conditions and in flexible tubes. Choking occurs when the fluid velocity v locally reaches a limiting wave speed. In compressible gas duct flows the characteristic limiting wave speed is defined by the speed of sound v_s. The characteristic number is the Mach number ($\mathrm{Ma} \equiv v/v_s$), and the maximum flow passes through a duct

when Ma = 1. In gravity dominated open channel flows the speed of shallow water waves v_{sw} corresponds to the limiting velocity. The flow is characterized by the FROUDE number (Fr $\equiv v/v_{sw}$), and choking occurs for Fr = 1. A close analogy exists between both flow types since the pressure induced variation of density influences the gas flow in the same manner as the pressure induced change of cross sectional area influences the open channel flow. As a consequence, the specific characteristic wave speeds can be derived from the same universal form. In analogy to these flows a capillary SPEED INDEX $S_{ca} \equiv v/v_{ca}$ may be introduced where v is the mean liquid velocity and v_{ca} the speed of longitudinal small amplitude waves in open capillary channels. In case of choking S_{ca} is expected to tend towards unity (slide **4**). If $v = v_{ca}$ is reached at the smallest cross section A_{min} of the flow path, a further decrease of the pressure downstream does not cause an increase of the flow rate upstream and the flow is choked. Gas ingestion must occur at the outlet to obey the mass conservation law.

Experiments with parallel plate channels were performed in a drop tower [1,2,3] and aboard the sounding rocket TEXUS-37 [2,4]. The evaluated surface profiles and the corresponding flow rates are in good agreement with the predictions of the numerical computations. Furthermore the numerical calculations as well as the TEXUS experiment data clearly confirm the choking effect indicated by $S_{ca} \rightarrow 1$ for $Q \rightarrow Q_{crit}$ [4].

The results of this work can be applied to liquid and/or propellant management problems for weakly or strongly reduced gravity environments. The capillary channels (or vanes) in connection with the dominating surface tension forces are used to pump and/or position the liquid as well as to achieve a connection between different liquid bodies, i.e. between the bulk in the tank and the reservoir (slide **5**). The task of a refillable reservoir is to provide bubble-free propellant for the thruster(s). The critical flow rates in the channels must be known to avoid the rupture of the connection. Weak accelerations resulting from the motion of the spacecraft or a gravitating body may influence these limits. On the other hand, the rupture may be caused on purpose to prevent the undesired withdrawal or leaking from the reservoir. The capillary channels may be formed by many geometries: grooves (heat pipes), wedges, galleries (shuttle RCS), sponges, wicks and other porous media.

To investigate the nature of open capillary channel flows in an extended range of the describing characteristic numbers and for different channel geometries the experiment has been selected by 94 NRA-7 and will be conducted in the Microgravity Science Glovebox (MSG) aboard the ISS. The Science Concept Review has been passed in 2002 and a feasibility study (phase A) was conducted in 2003. A breadboard phase B_0 is currently underway testing detailed technical solutions with respect to the fluid handling, the video observation and the experiment control. The predefinition phase B is planned for this year. The experiment should be ready for flight in 2006. The following sections present the status of the experiment.

2 Experiment Setup

To achieve a high degree of flexibility the experiment was designed as a modular system consisting of the Fluid Management System (FMS), the Board Computer (BC) and the Test Units (TU) (slide **6**). The FMS is equipped with the required components to establish the flow (pumps, plunger, valves) while the TU contains the test channel, a phase separation chamber (PSC), a compensation tube (CT), cameras for the video observation as well as the necessary illumination. The experiment control, the sampling of the housekeeping data as well as the communication with the MSG interfaces and the ground station (PI site) is performed by the BC. For the investigation of the selected channel geometries (parallel plate channel, groove

channel, wedge-shaped channel and a liquid bridge) and the different channel dimensions the TU must be exchangeable. This enables the use of the set-up for others projects with similar research objectives since only different test units must be designed and installed.

Slide **7** shows a schematic drawing of the experiment setup which essentially consist of a main and a secondary fluid loop. The main loop supplies the phase separation chamber (PSC) and withdraws the liquid from the test channel. The volume adjustment is obtained by the cylindrical compensation tube (CT). Via the plunger K2 the liquid volume of the fluid loop can be controlled. The flow is established by two shunted gear pumps (P1 and P2). By means of the plunger K1 a modulation of the flow rate is enabled. The secondary loop is required to control the gas volume inside the PSC and to vent the CT by the plunger K3. A tank with a porous medium serves as separator in case a two phase flow occurs inside the vent line.

The test unit is shown on slide **8**. It consists of the test channel which is covered by slide bars on both sides to establish variable flow lengths and to close the duct in case of any malfunction of the FMS. The phase separation chamber provides bubble-free test liquid to the test channel. The channel and the PSC are connected by a nozzle which is in each case designed to achieve the best flow condition for the theoretical model. The test channel and the compensation tube are observed by 3 video cameras, two cameras for a detailed view and a high temporal and spatial resolution of the surface profiles, and one camera for the general view. The test area is illuminated with diffuse light from the background. A double housing prevents the leakage of the test liquid (actual choice HFE-7500 from 3M) into the MSG.

In total 7 test units are planned (slide **9**):

- 2 for parallel plate channels with aspect ratios $\Lambda = 2.5$ and $\Lambda = 5$, plate distances $a = 5; 10$ mm, plate breadth $b = 25$ mm, and adjustable lengths 25 mm $< l <$ 130 mm
- 2 for groove channels with the same dimensions which can be easily achieved in the same test unit by closing one side with the slide bar
- 3 for the wedge-shaped channel, with 3 different half angles $\alpha = 15; 45; 75$ degree and free surface lengths of $a = 10; 15; 40$ mm
- 2 for a liquid bridge of length $l = 1; 5; 12.5$ mm freely suspended between inlet and outlet of radius $R_0 = 5; 25$ mm

The required volumetric flow rate is 4.5 ml/s $< Q <$ 30 ml/s.

The phase separation chamber is shown on slide **10**. Inside the PSC eight concentric vanes are mounted which are covered by a fine woven sieve. For the process of phase separation a main gas bubble is established between the vanes. It will remain centered between the tips of the vanes. The two phase flow which enters the PSC in case of the surface collapse at $Q > Q_{crit}$ is turned around by a rebounding plate and passes the main gas bubble laterally. In doing so the single bubbles may drift towards the main bubble and coalesces there. Remaining small bubbles will be captured by the sieve, thus only single phase flow will be provided to the test channel.

3 Experiment performance

Prior to the experiment the TU has to be integrated with the help of an astronaut. Initially the gate valves C8 and C9 are closed and the PSC is filled with the test liquid up to the connectors to the FMS. To establish the gas bubble the valves C1, C6, and C8 are opened

and gas is injected into the center of the PSC by means of K3. The liquid volume is displaced into the CT causing a slight overpressure inside the vent line and the separator tank. By opening the valve C7 and removing the plunger K3 this overpressure is released. C6 is closed at that state. To fill the channel the gate valve C9 is opened and a liquid flow occurs from the CT into the channel. The flow is driven by the different capillary pressures of the liquid menisci inside the CT and the gap of the channel. When the liquid contacts the suction head at the outlet of the channel it is withdrawn by the pumps and the liquid circulation is established. After that the experiment procedure starts to determine the maximal flow rate and the contour data. For this purpose the flow rate is increased in coarse increments until the collapse of the surface is observed. Then the flow rate is decreased by small increments. At dedicated flow rates the images of the surface profiles will be captured, processed and send to the ground.

4 Video observation and onboard image processing

For the video observation of the channel two high speed cameras with a resolution of 1240 $\times$ 1028 pixel at a frame rate of 250 Hz are planned. Since the handling of the video data requires large resources it is performed by a separate computer to avoid an overload of the BC leading possibly to an uncontrolled state of the experiment. One of the video systems proposed by the current breadboard phase B_0 is equipped with a compact separate unit containing the RAM for the video images (PHOTRON high speed cameras Fastcam Ultima 1024). With this video system the MSG Laptop Computer (MLC) can be used for the control of the video system including image download and image processing. This assumes that the current MLC is replaced by the IBM Thinkpad A31p which is currently discussed. Using the commercial software MathLab the evaluation of the surface profile can be performed aboard the MSG.

The funding of this work by means of the German Federal Ministry for Education and Research (BMBF) through the German Aerospace Center DLR under contract 50 WM 0241 is gratefully acknowledged. The authors wish to thank the project scientist Brian Motil from NASA Glenn Research Center for his kind support.

References

1 M. E. Dreyer, U. Rosendahl, H. J. Rath, Experimental Investigation on Flow Rate Limitations in Open Capillary Vanes, AIAA 98–3165, 1998

2 U. Rosendahl, B. Motil, A. Ohlhoff, M. E. Dreyer, H. J. Rath, Critical Velocity in Open Capillary Channel Flows, AIAA-2001–5021, 2001

3 U. Rosendahl, A. Ohlhoff, M. E. Dreyer, H. J. Rath, Investigation of Forced Liquid Flows in Open Capillary Channels, Microgravity Science and Technology XIII/4, 2002

4 U. Rosendahl, A. Ohlhoff, M. E. Dreyer, Choked flows in open capillary channels: theory, experiment and computations, Journal of Fluid Mechanics (accepted)

Introduction and Background

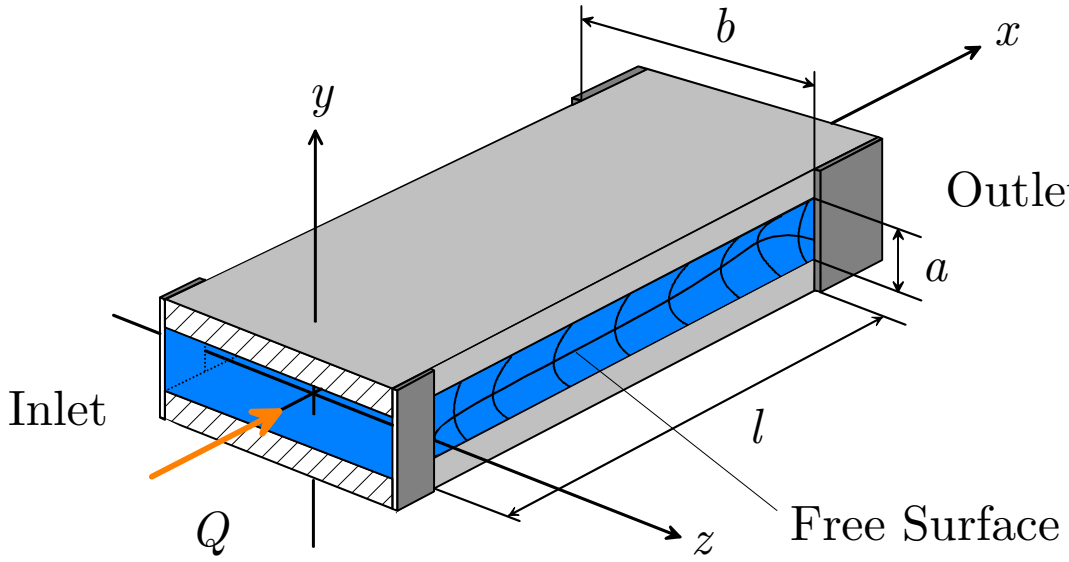

Constant flow rate applied

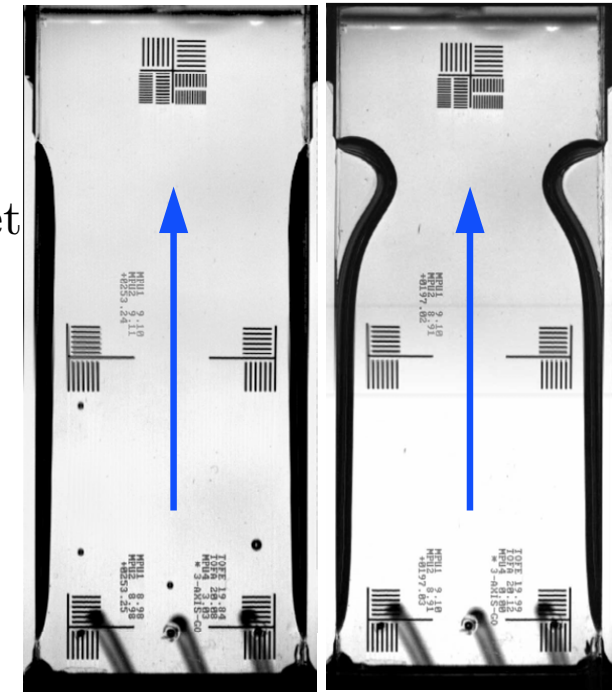

Steady flow Non-steady flow

Gas ingestion at the side(s)

Example of a capillary channel

Liquid withdrawn at the outlet, liquid provided at the inlet

Introduction and Background

Seeking for solutions of
- the limiting volume flux

$$Q_{crit} = g\left(\mathrm{Oh}, \Lambda, \tilde{l}\right)$$

- and the free surface shape

$$k(x) = f\left(\mathrm{Oh}, \Lambda, \tilde{l}, Q\right)$$

- limited to static contact angles $\gamma_s = 0$

$$Q = \frac{Q^*}{A_0 v_c};\ A_0 = ab;\ v_c = \sqrt{\frac{2\sigma}{a\rho}};\ k = \frac{2k^*}{a}$$

$$\mathrm{Oh} = \sqrt{\frac{\rho\nu^2}{2a\sigma}};\quad \Lambda = \frac{b}{a};\quad \tilde{l} = \frac{\mathrm{Oh}}{4a} l$$

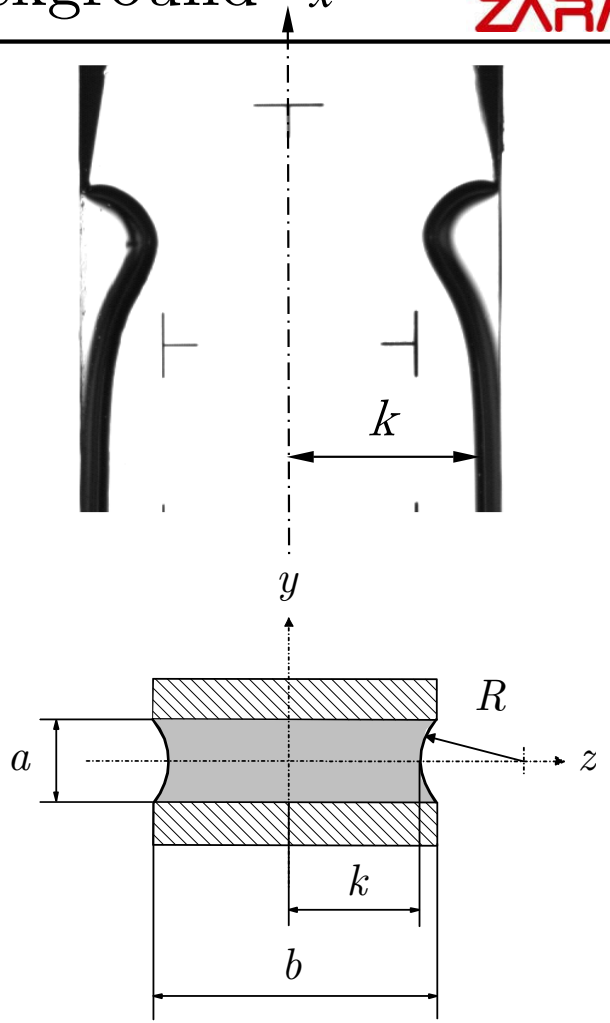

Results – capillary speed index

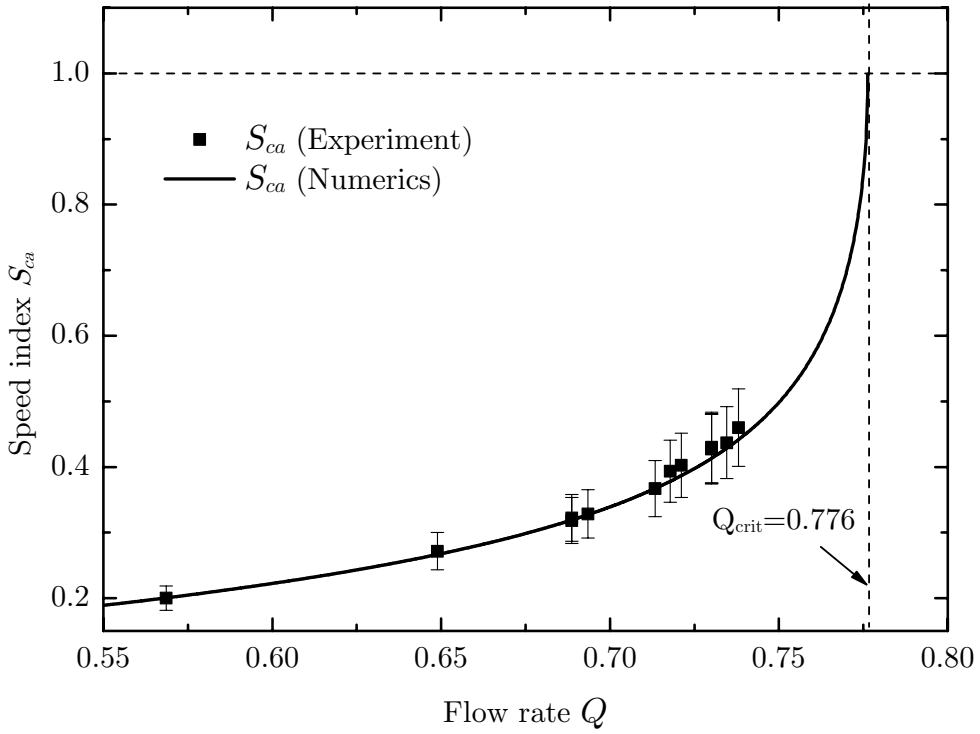

$$v_{ca} = \frac{1}{R}\sqrt{A\frac{dR}{dA}};\; S_{ca} = QR\sqrt{\frac{1}{A^3}\frac{dA}{dR}\frac{dR}{dk}}$$

Simplified approach using only one radius of curvature

$$v = \frac{Q}{A_0}$$

$$v_{rel} = v_{ca} - v = v_{ca}\left(1 - S_{ca}\right)$$

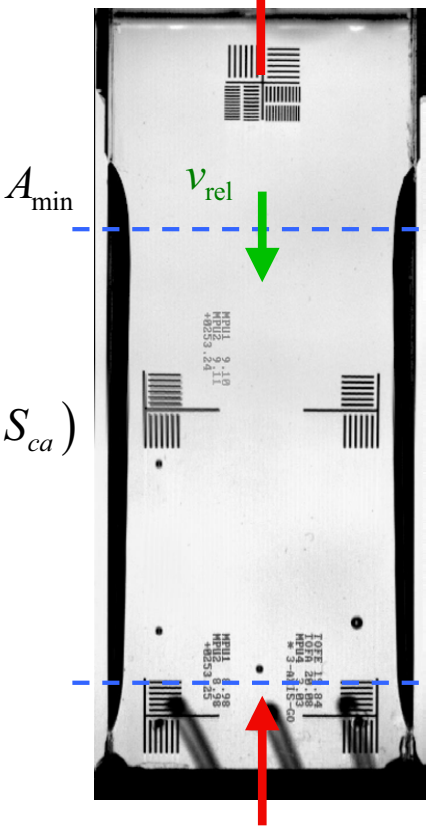

Applications of the work

1. Liquid/propellant management for weakly or strongly reduced gravity environments

2. Open capillary channels can be used for connecting the bulk with a reservoir from where the liquid will be withdrawn

3. Critical flow rates must be know to avoid rupture of the connection

4. Rupture on purpose may be used to avoid the undesired withdrawal of liquid from reservoirs

5. Capillary channels may be formed by many geometries:
grooves, wedges, galleries, sponges, wicks, porous media

Model of a surface tension tank for drop tower tests

Surface tension tank with refillable reservoir

Surface tension tank without refillable reservoir

Courtesy of EADS ST Bremen

Experiment Arrangement

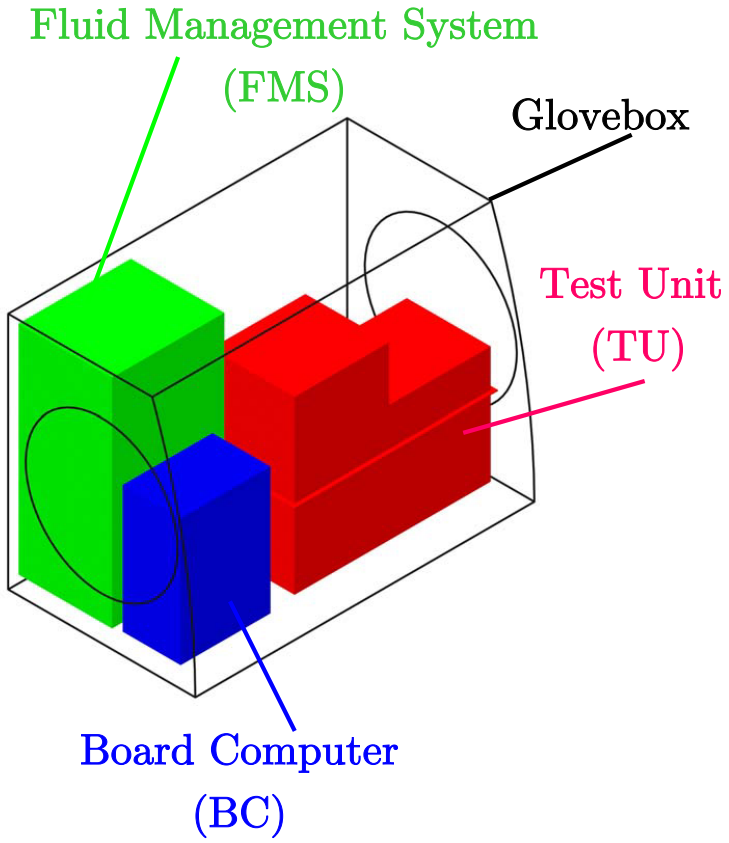

- The experiment is designed as a unit operation system in the Microgravity Science Glovebox (MSG)
  - board computer and fluid management system are permanent units
  - the test unit is exchangeable
  - the replacement requires astronaut involvement

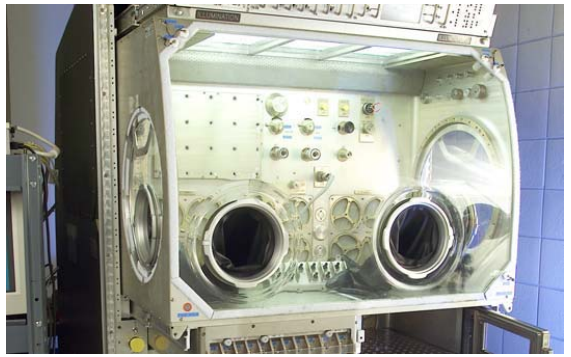

Principle Draft

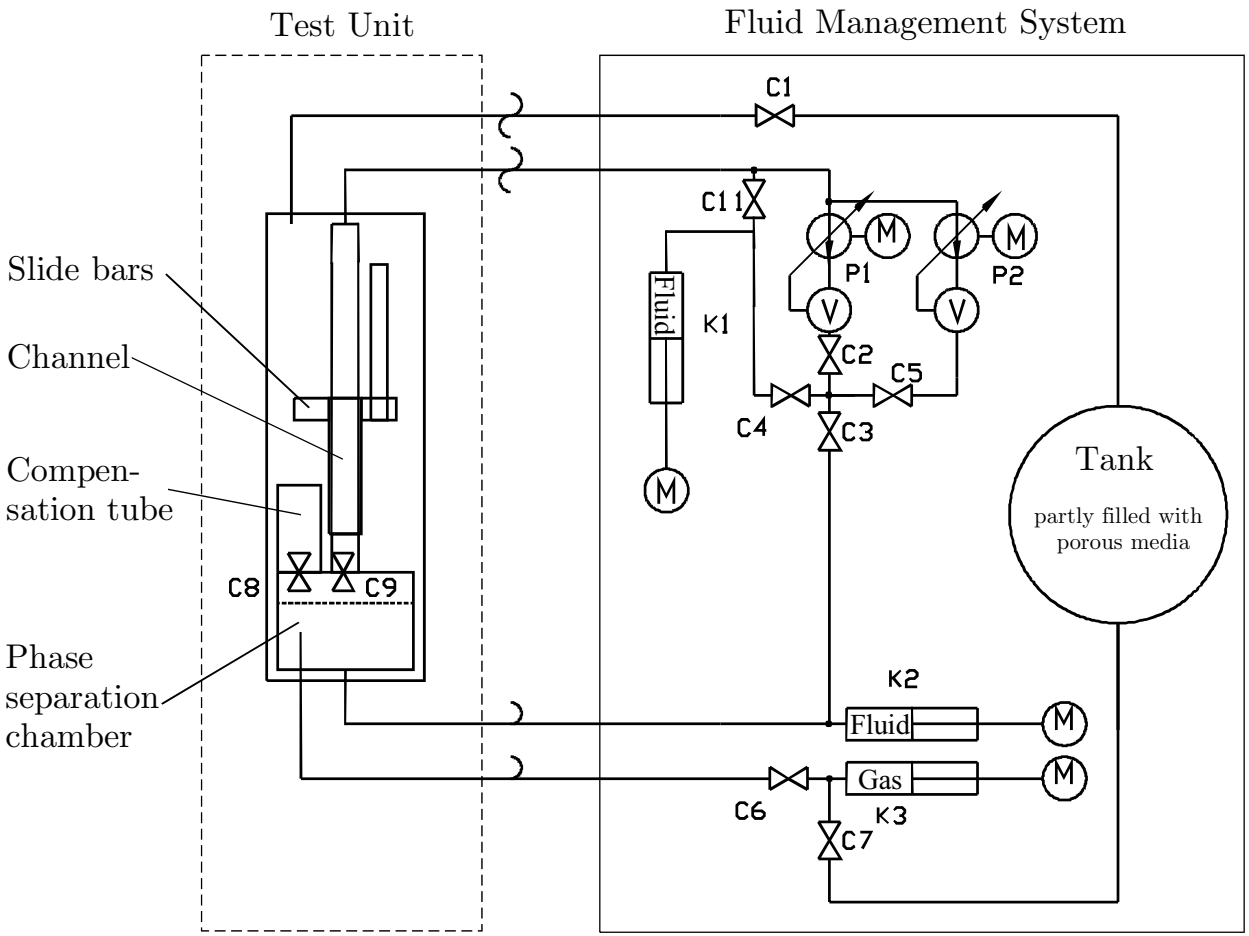

- C1-C11: valves
- P1-P2: pumps
- K1-K3: plungers
- V: flow meter
- M: motor

Test Unit (TU) Set-Up

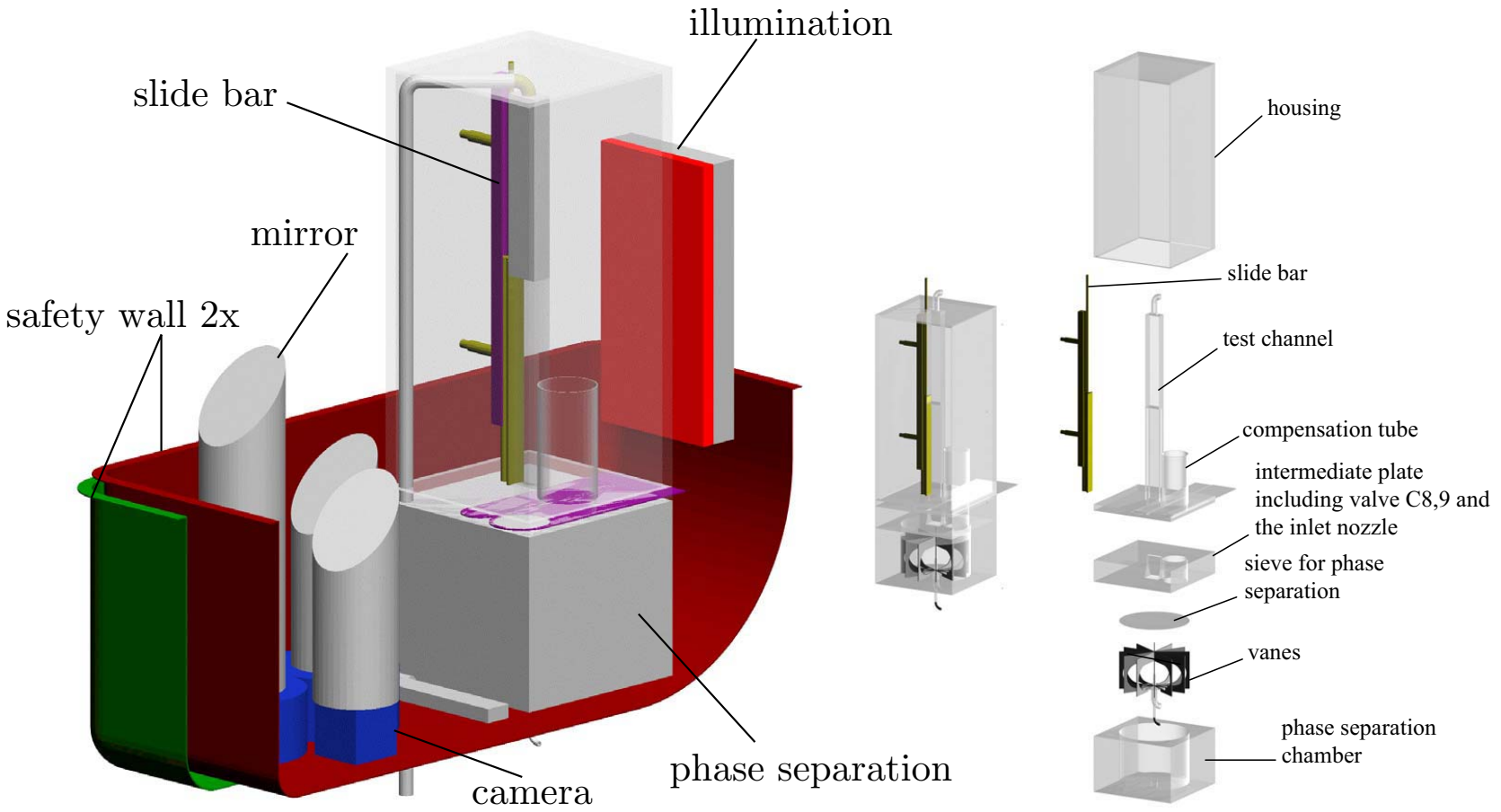

Test Unit (TU) Set-Up

- **Planned channel geometries**
  - 2 parallel plate channels
  - 2 groove channels (same unit)
  - 3 wedge channels
  - 2 liquid bridges
  - Test cell length is continuously adjustable due to 2 independent slide bars

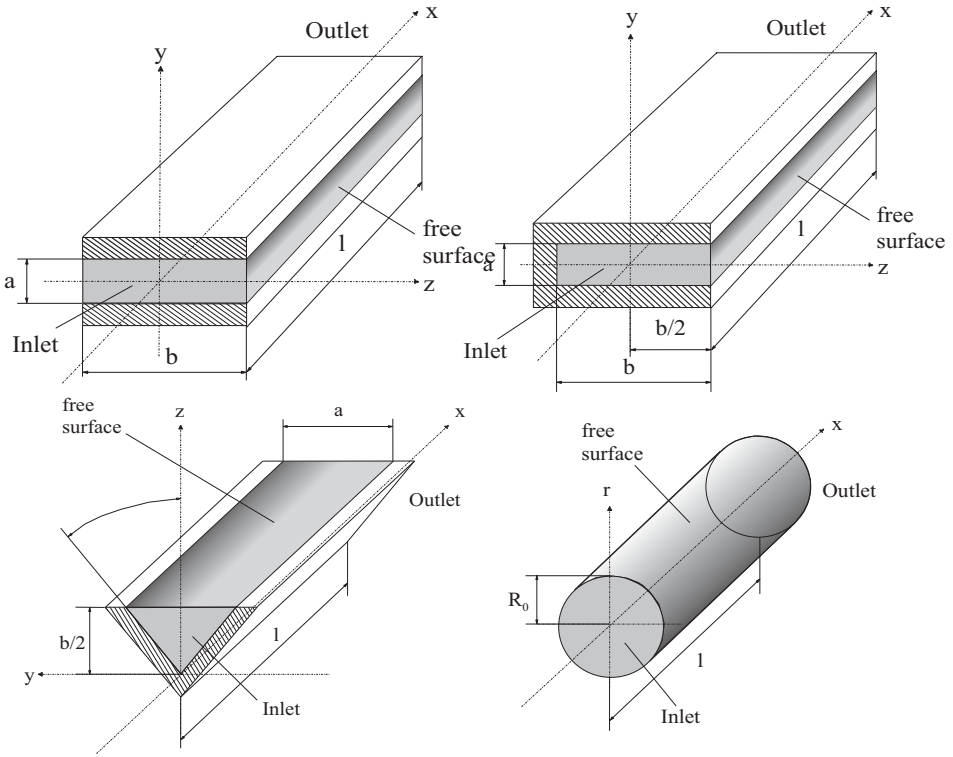

- **Characteristic values**

$$a = 5\ldots40 \text{ mm},\ b = 25 \text{ mm},\ L = 25\ldots130 \text{ mm}$$

$$\alpha = 15^\circ; 45^\circ; 75^\circ,\ R_0 = 5; 25 \text{ mm};\ Q = 4.5\ldots30 \text{ ml/s}$$

Phase Separation Chamber (PSC)

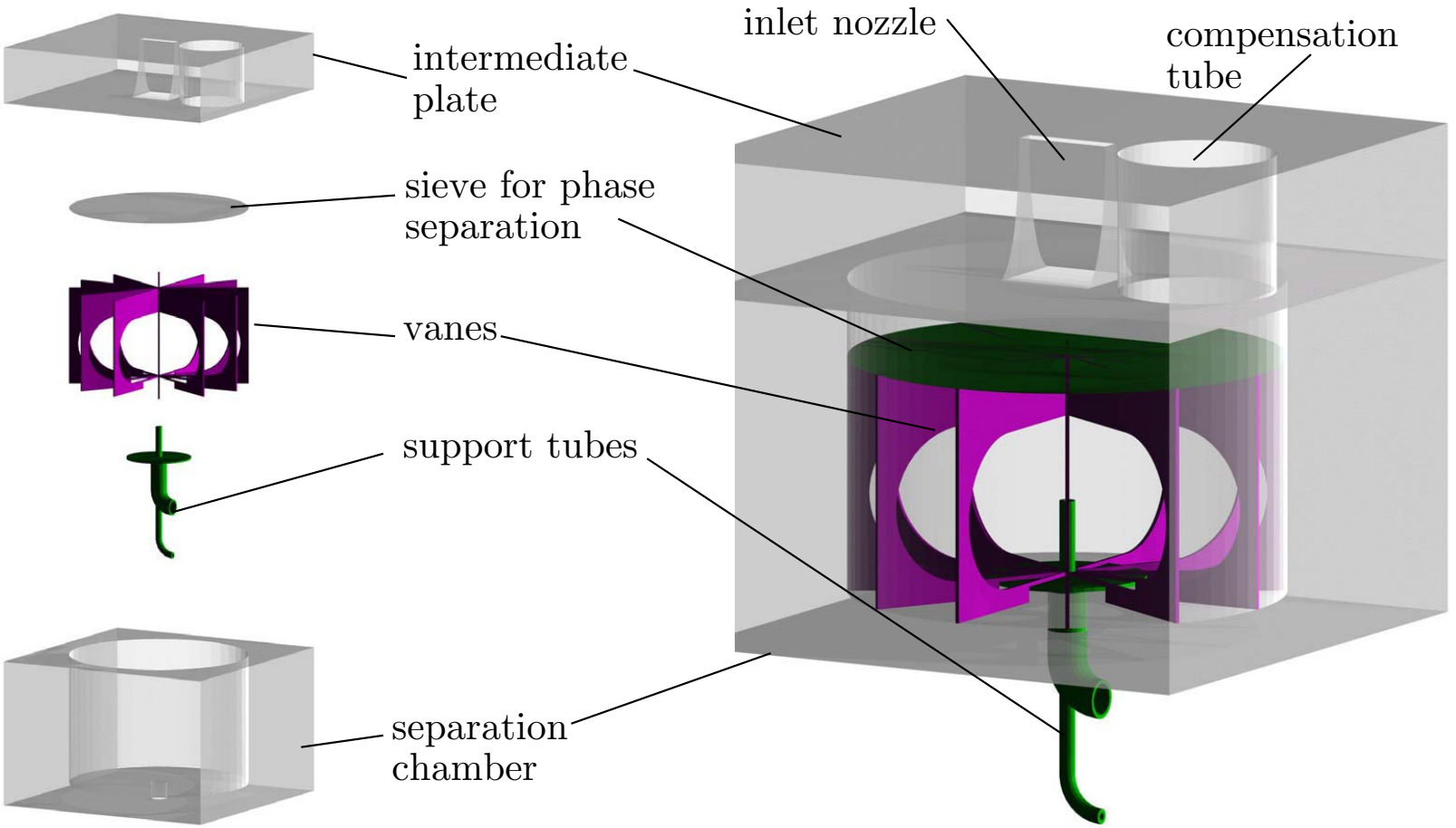

Project Orientation

- The Droplet Combustion Experiment (DCE) is a continuing flight experiment with a lengthy history exploring fundamental properties of diffusive combustion behaviors in sphero-symmetric systems. While the present program is studying isolated liquid droplet combustion of n-heptane, decane, methanol, and ethanol, other fuel liquids and spherical flammable solids can be researched similarly.
- In aligning ongoing research with interests of the Advanced Human Support Technology (AHST) effort, the DCE program is reorienting its flight experiment plans and modeling support more directly with fire safety issues for manned space flight.
- For standard fire suppression techniques, a suppressant jet is impinged upon a combustion event. In considering these techniques for space applications, it is necessary to analyze the effect of suppressant transport to both the near-field and far-field of the region of interest. A significant amount of attention has been paid to the former (Katta et al., 2004) with less paid to the latter.
- Fire prevention can also be implemented by modifying the atmospheric composition of the living environment so as to reduce the likelihood of a self-sustaining combustion event.
- Finally, the flammability properties of materials can also be modified by the addition of materials which suppress ignitability, enhance charring of surfaces, or chemically inhibit self-sustained burning.

Transient Sphero-symmetric, Multi-component Droplet Combustion Model

Mass Conservation:

$$\frac{\partial}{\partial t}(\rho_g)+\frac{1}{r^2}\frac{\partial}{\partial r}(r^2\rho_g v_r)=0$$

Species Equations:

$$\frac{\partial(\rho_g Y_{g,i})}{\partial t}+v_r\frac{\partial(\rho_g Y_{g,i})}{\partial r}=-\frac{1}{r^2}\frac{\partial}{\partial r}(r^2\rho_g Y_{g,i}V_{r,i})+\omega_{g,i}$$

Energy Conservation:

$$\frac{\partial(\rho_g C_{p,g}T_g)}{\partial t}+v_r\frac{\partial(\rho_g C_{p,g}T_g)}{\partial r}=\frac{1}{r^2}\frac{\partial}{\partial r}(r^2\lambda_g\frac{\partial T_g}{\partial r}-q_R)$$
$$-\sum_{i=1}^{n}\frac{\partial\rho_g(Y_{g,i}V_{r,i}C_{p,g,i})T_g}{\partial r}-\sum_{i=1}^{n}\omega_{g,i}H_{g,i}$$

Net Radiative Heat Flux

Gas Phase:
- Multicomponent molecular diffusion
- Detailed Kinetics
- Spectral (non-luminous) thermal radiation
- UV flame emission

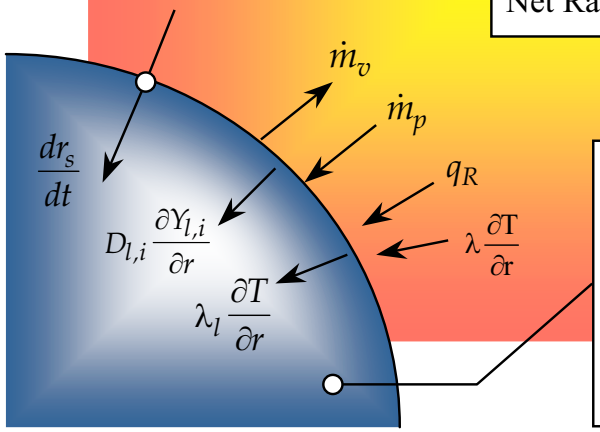

Droplet Interior:

$$\frac{\partial(\rho_l C_{p,l}T_l)}{\partial t}=\frac{1}{r^2}\frac{\partial}{\partial r}\left(r^2\lambda_l\frac{\partial T_l}{\partial r}\right)$$

$$\frac{\partial Y_{l,i}}{\partial t}=\frac{1}{r^2}\frac{\partial}{\partial r}\left(r^2 D_{l,i}\frac{\partial Y_{l,i}}{\partial r}\right)$$

Sphero-symmetry offers significant advantages in terms of numerical modeling and inclusion of robust physical and chemical models.

Experimental Comparison

- Simulation of suspended droplets of n-decane, 15 % oxygen in nitrogen at 90.5 mmHg with an initial diameter of approximately 1.7 mm. Experimental work conducted by Dietrich et al.
- The numerical model reproduces the burning rate over the droplet lifetime within the experimental uncertainties, with divergence at small diameters likely a result of the effects of the support fiber.
- Extinction behavior observed in the experiment is also captured in the model results, as characterized by the sudden break in the D^2 vs. time plot.

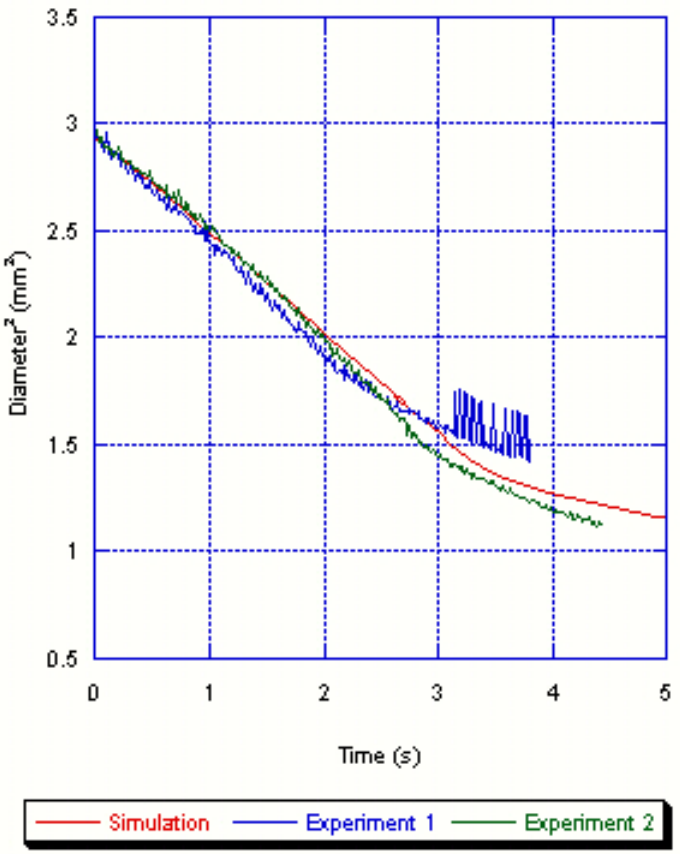

Heterogeneous Flame Suppression by Far-Field Dilution

- A series of isolated 1 mm radius droplets were simulated with identical initial temperature profiles in air at 1 atm. At t = 0.01 s, the ambient, as described by the edge of the numerical system at a distance of 20 droplet diameters is instantly changed to simulate the addition of CO_2 to the listed mole fraction.
- The Stefan flux essentially acts to create a resistance that diffusion must overcome, isolating the burning droplet from environmental changes.
- Even in cases where extinction is observed, at least 90% of the fuel droplet is consumed.

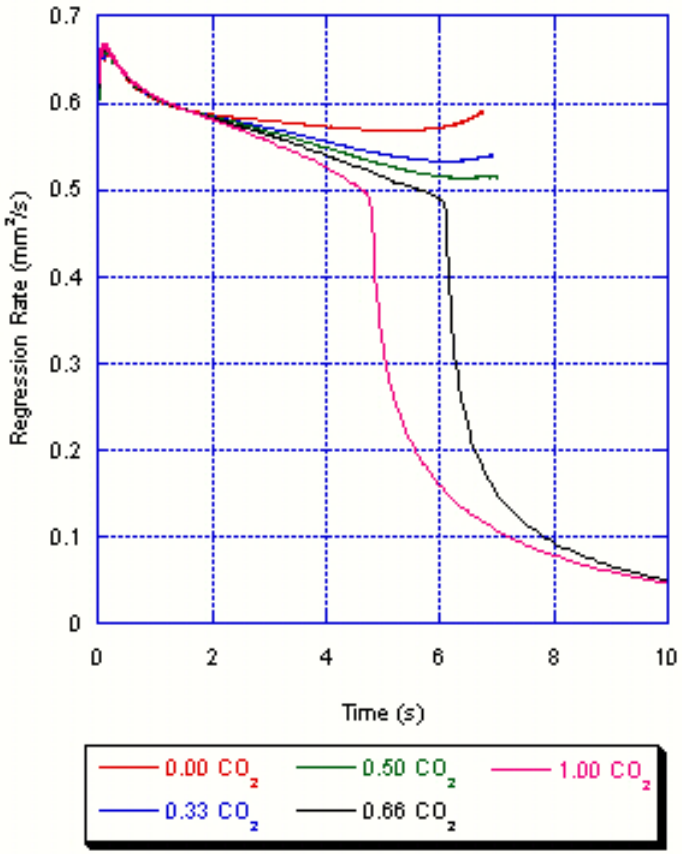

Flame Suppression via Diluent Substitution

- Numerical combustion experiments for isolated droplets of n-heptane were used to explore the effect of modifying the initial ambient atmospheric composition while maintaining the ambient at 1 atm, 300 K with the mole fraction of oxygen constant across all cases. Individual trials are cataloged by ambient percentage of CO_2 by mole.
- The ambient atmosphere in the system was varied from 21% O_2 in 79% N_2 to 21% O_2 in 79% CO_2. The initial temperature profile supplied for ignition was the same for all of the simulations.

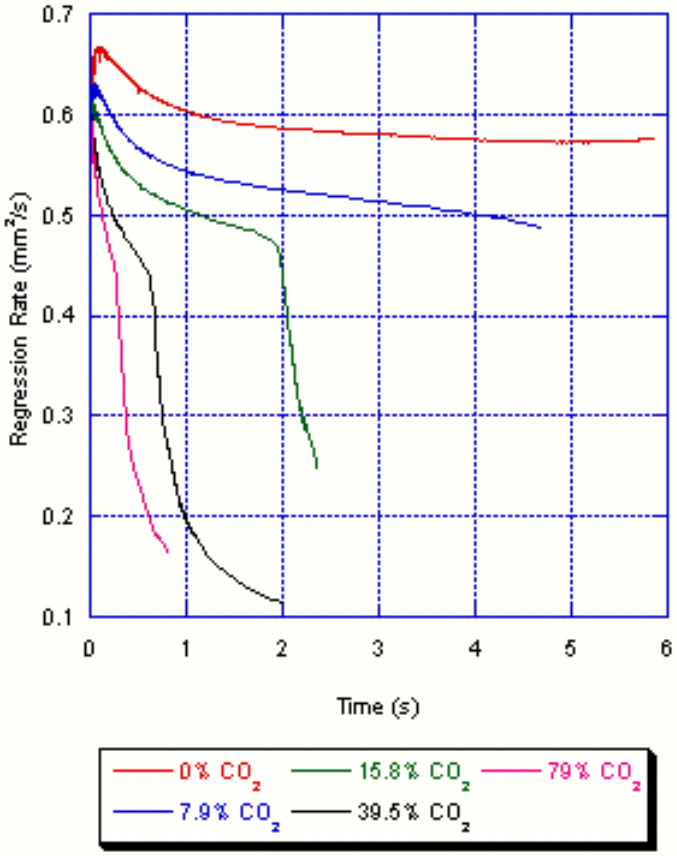

Radiative Effects Versus Thermal Dilution Effects

- Artificial non-reactive diluent species with hybrid properties of nitrogen and carbon dioxide gases were considered in additional numerical experiments.
- All simulations were calculated with identical initial temperature profiles for 1 mm radius n-heptane droplets in 1 atm gas containing 21% oxygen.
- While the higher heat capacity and slower diffusive transport resulting from carbon dioxide substitution for nitrogen reduces burning rate, the spectral radiative behavior modifications of the gas phase by diluent substitution appears to dominate the heat loss phenomenology.

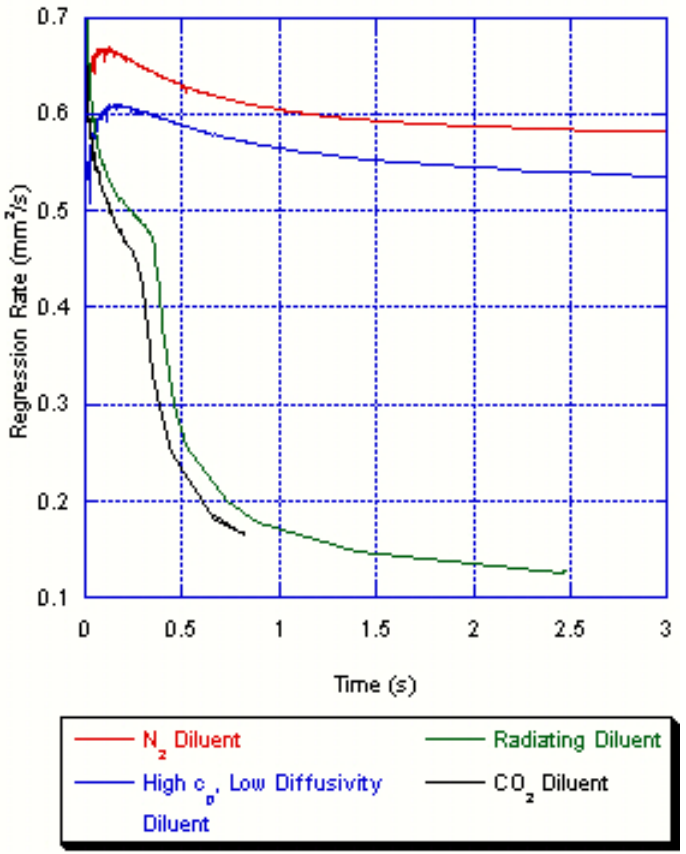

Diluent Substitution Effects of Extinction

- Extinction here is defined as the location in time where the droplet burning rate undergoes a rapid decline.
- A clear trend emerges towards higher temperatures at the start of extinction, implying an active suppressant action on the part of CO_2. This value becomes numerically noisy due to finite time stepping on a rapidly changing variable.
- Due to the dramatically shorter burning times observed at higher mole fractions of CO_2, extinction diameter increases rapidly with CO_2 content. The extinction diameter asymptote is associated with the total amount of heat supplied to the droplet for ignition.

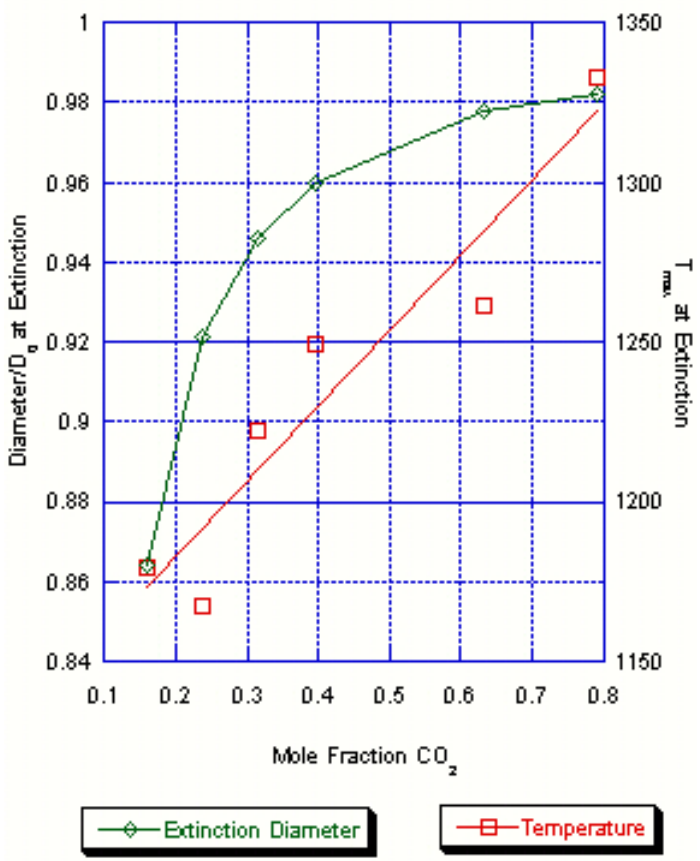

Effect of Far-field Radiation

- Numerical results indicate that in cases where remote, hot (>800 K) solid boundaries of the combustion environment exist, the overall burning rate of the droplet can be increased significantly by net radiative exchange
- Additional work needs to determine how effective carbon dioxide flame suppression remains in systems where significant thermal release has already occurred and how adjacent compartments may interact
- The present simulations are inspired by numerical modeling of experimental work conducted by B.D.Shaw and coworkers at UC Davis for 280 μm diameter droplets in hot-ducted freely-falling, isolated droplet combustion experiments

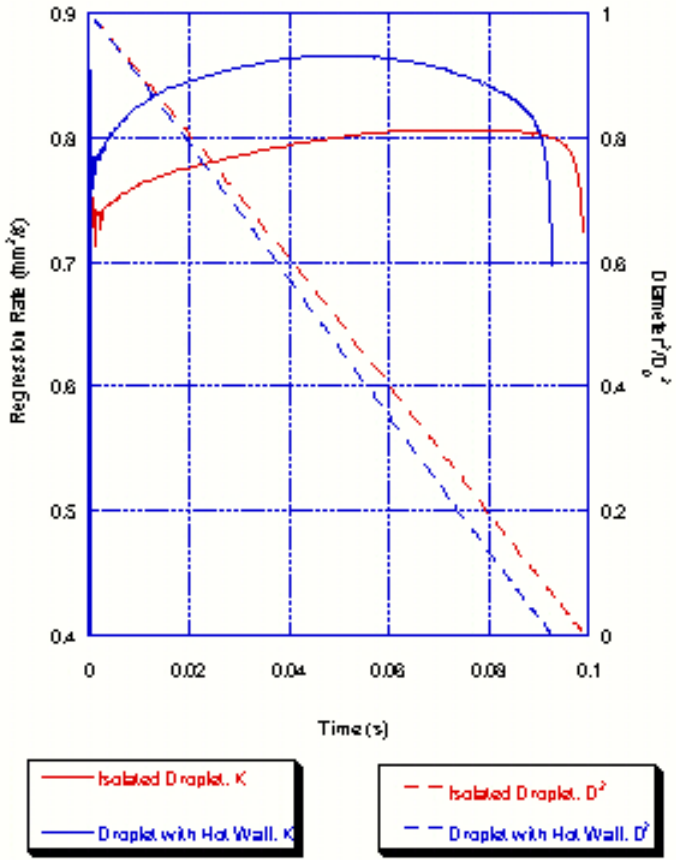

Isolated Liquid Droplet Combustion: Inhibition and Extinction Studies

F. L. Dryer , K.G. Kroenlein and A. Kazakov
Princeton University
Princeton, NJ

F.A. Williams
University of California
San Diego, CA

V. Nayagam
National Center for Microgravity Research
Cleveland, OH

Conference-Workshop on Strategic Research to Enable NASA's Exploration Missions
Marriott Downtown at Key Center, Cleveland, Ohio

June 22, 2004

Summary

- Introduction of fire suppressants to the ambient environment surrounding a heterogeneous diffusion flame may be an inefficient technique for fire safety in systems without buoyant flows.
- Carbon dioxide substitution for nitrogen diluent leads to significant modifications of the sphero-symmetric burning behavior of isolated n-heptane droplets, partly through increased heat capacity within the gaseous diffusion flame, but mostly because of modifications in spectral radiative coupling in the gas phase.
- Effects of longer time scale phenomena such as sooting and slow gas-phase/droplet convection remain to be determined.
- Similar methodologies can be applied to evaluate the effects and efficacy of chemical inhibitors in the liquid and gas phases.

This work was supported at Princeton University under NASA Cooperative Agreement NCC3 735.

WIND-DRIVEN RIVULET BREAK-OFF IN CONDITIONS RANGING FROM 0G TO 1G

R. Ettema, J.S. Marshall, and G. McAlister
IIHR—Hydroscience and Engineering
University of Iowa
Iowa City IA 52242

A study has been performed of the wind-driven breakup of rivulets on a horizontal plate subject to different normal gravitational states, ranging from zero-gravity to terrestrial gravity conditions (1g), and also including some data for partial gravity conditions (between 0.1g and 0.38g). The experiments were conducted both in our laboratory at the University of Iowa and on board the NASA KC-135, parabolic-flight aircraft. The wind-driven rivulets exhibit a break-off phenomenon over a broad range of flow rates, in which a "head" at the tip of the rivulet breaks off periodically to form a droplet that advects down the plate. The rivulet break-off phenomena is found to be sensitive to the normal gravitational force acting on the plate. For instance, the frequency of rivulet break-off is nearly an order of magnitude greater in the 0g condition than it is for the same flow in the 1g condition. During the rivulet break-off event, a droplet detaches from the end of the rivulet and advects downstream on the plate. The detached droplet shape and behavior are observed to be quite different between the 0g and 1g cases. It is furthermore found in all cases examined that wind-driven rivulet and droplet flows are markedly different from gravitationally-driven flows (e.g., flow down an inclined plate). These differences arise primarily from the role of form drag on the droplets and on the raised ridge of the rivulet head near the moving contact line.

Wind-Driven Rivulet Break-off in Conditions Ranging from 0g to 1g

Investigators
Principal Investigators: R. Ettema and J.S. Marshall
Student: G. McAlister

Department of Mechanical and Industrial Engineering
Department of Civil and Environmental Engineering
IIHR-Hydroscience and Engineering, The University of Iowa

Research Objective

The objective of the project is to understand the effect of different gravitational states on the break-off of wind-driven rivulets and the subsequent dynamics of droplet flows generated by rivulet break-off on a horizontal surface.

Approach

Experiments with wind-driven rivulets have been performed in the laboratory using the "rivulet wind-tunnel" device sketched in Figure 1. Water is injected through a 2 mm hole in the bottom Plexiglas plate and carried down the wind tunnel by the aerodynamic force exerted by the wind flow. Both water and air flow rates are adjustable. Experiments with microgravity and different partial gravity conditions (0g, 0.1g, 0.16g, 0.25g, 0.38g) were performed on board the KC-135. Experimental results were compared to analytical predictions obtained by balancing surface tension and aerodynamic drag forces.

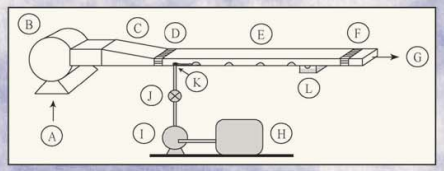

Figure 1. Sketch of the rivulet wind tunnel showing (A) air inlet, (B) blower, (C) contraction, (D) honeycomb, (E) test section, (F) honeycomb water trap, (G) air outlet, (H) collapsible water storage tank, (I) positive-displacement pump, (J) needle valve, (K) water inlet hole, (L) water collection box.

Terrestrial Gravity Results

Whereas gravity-driven flow exhibits the usual meandering rivulet behavior (which has been recorded numerous times in previous literature), the shear-driven rivulet flow exhibits an entirely different behavior. The wind-driven rivulet travels downstream a short distance, and then is observed to stop and form a "head" at its downstream end. The head grows progressively larger as it receives liquid from the rivulet flow. At a certain point, the head breaks off of the rivulet and progresses downstream as a droplet. At the time of break-off, the end of the rivulet moves downstream a short distance and then the process repeats itself. A model for rivulet head detachment was developed by balancing the surface tension and aerodynamic forces on the droplet, which yields the droplet break-off period and the area on the substrate plate covered by the head at break-off as

$$T_{breakoff} = \frac{2\pi}{3Q}\left(\frac{8\sigma}{\rho\pi U^2 C_D}\right)^3 C, \qquad A_{crit} = \pi D\left(\frac{8\sigma}{\rho\pi U^2 C_D}\right)^2, \qquad (1)$$

where Q is liquid flow rate, U is mean wind velocity, C_D is aerodynamic drag coefficient on the head, σ is surface tension, and C and D are empirical coefficients which are functions of the gravitational acceleration. Numerical computations for aerodynamic force on a hemisphere lying on a flat surface have been performed, which indicate that $C_D \sim 0.6$ for the range of Reynolds numbers used in the experiments. The predictions (1) are shown to be in excellent agreement with the terrestrial gravity experiments in Figure 2.

The detached droplet reshapes itself in accordance with the airflow pressure distribution and surface tension and bottom shear forces. The droplet travels downstream at an approximately constant speed with a characteristic double-lobed shape that is elongated in the cross-stream direction (Figure 3). The liquid layer is significantly thicker within the lobes at the ends of the elongated droplet than within the center of the droplet. Droplets will frequently bifurcate within the thin middle section, forming two smaller droplets. These smaller droplets in turn adopt the characteristic elongated double-lobed shape, but they travel much more slowly than the original droplet and sometimes stop entirely. Faster-moving droplets also collide with slower-moving droplets, forming a single larger droplet that moves faster than the droplet constituents prior to the collision. Sufficiently far downstream, the liquid flow progresses by a random series of droplet bifurcations and collisions.

Following the detachment of a "head", the rivulet progresses downstream a fixed distance and the process repeats itself. The rate of downstream rivulet progressing can be correlated as depending inversely on the liquid flow rate and linearly on the rivulet break-off period, as shown in Figure 4.

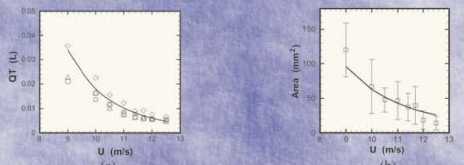

Figure 2. (a) Data for the product of rivulet break-off period T and water flow rate Q versus air speed U for the terrestrial gravity (1g) case, for values of water flow rate of Q = 10 mL/min (squares), 15 mL/min (deltas), 20 mL/min (circles), and 40 mL/min (diamonds). (b) Data for average area covered by droplet just after rivulet break-off as a function of air speed. The solid curves in (a) and (b) are theoretical predictions.

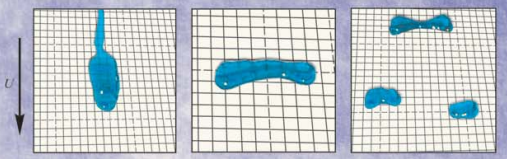

Figure 3. Photographs for wind-driven flow with terrestrial gravity showing (a) rivulet just before break-off of a droplet, (b) close-up view of the elongated double-lobed form of a detached droplet, and (c) a larger droplet overtaking two smaller droplets.

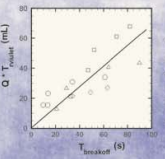

Figure 4. Correlation for the average time $T_{breakoff}$ for the attached rivulet head to progress 300 mm downstream from the inlet versus rivulet break-off period $T_{breakoff}$ for the terrestrial gravity experiments, with water flow rates Q = 5 mL/min (crosses), 10 mL/min (squares), 15 mL/min (deltas), 20 mL/min (circles), and 40 mL/min (diamonds).

Microgravity and Partial Gravity Results

The rivulet break-off and subsequent droplet flow occurs for all gravitational states examined, but the characteristics of the flow are markedly different between the terrestrial gravity and microgravity conditions. The most striking difference is that the period of rivulet break-off is about an order of magnitude shorter in zero gravity than it is in terrestrial gravity. This difference is due to the rivulet head having a raised, nearly hemispherical shape in microgravity, which has much larger aerodynamic drag with the same liquid volume compared to the flattened shape on the head in terrestrial gravity (as observed in Figure 3a). The rivulet break-off period is well predicted for all gravitational states by Eqn. (1) with modification of the coefficient C to account for the effect of gravity on rivulet head shape, as shown in Figure 5 for zero gravity and in Figure 6 for various partial gravity states.

The detached droplets in microgravity retain a nearly hemispherical shape and do not bifurcate, as observed in the terrestrial gravity condition. Because of the absence of bifurcation, all droplets have nearly the same size and velocity for a given liquid and air flow rate condition, and droplets appear to retain approximately uniform spacing with no collisions as they progress downstream (as shown in Figure 7).

In the zero-gravity condition, the droplets at certain times exhibited an interesting "inch-worming" phenomenon that was not observed in terrestrial gravity or in the partial gravity states. The inch-worm progression is initiated with a droplet with a short "tail" propagating on the substrate surface. The onset of the inchworm motion is typified by elongation and flattening of the front lobe of the droplet. Transport of water from the flattened front lobe into the tail section leads to formation of a large rear lobe preceded by a small front lobe at the half-cycle point. The water from the tail then suddenly sloshes back to the front lobe and the droplet simultaneously lurches forward. The inchworm motion is found to be more prevalent for higher wind speeds, above 11 m/s, and the inchworm cycle tends to repeat several times before the droplet returns to a steadily propagating state. The period of oscillation for the inchworm oscillation varies between 0.6 sec and 1 sec, and appears not to be particularly sensitive to the air or water flow rates.

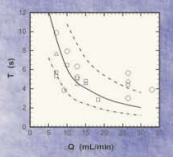

Figure 5. Period T of rivulet break-off in zero-gravity versus the water discharge rate Q, for cases with Q = 10.3 mL/min (squares), 11.4 mL/min (deltas), 11.9 mL/min (circles), and 12.5 mL/min (diamonds). The curves give the theoretical predictions for cases with U = 10 m/s, (dashed), 11 m/s (solid) and 12 m/s (dashed-dotted).

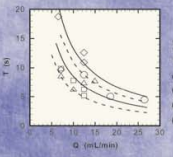

Figure 6. Period of rivulet break-off for partial-gravity cases as a function of water flowrate with air speed held constant at 11 m/s, for cases with 0 g (squares), 0.16 g (gradients), 0.26 g (circles), and 0.38 g (diamonds). Curves are predictions from Eqn. (1) with C = 0.05, (lower dashed), 0.07 (lower solid), 0.09 (upper dashed), and 0.11 (upper solid), respectively.

Figure 7. Periodic shedding showing two nearly hemispherical droplets with a third about to break off from the end of the rivulet for zero-gravity case (Q = 15 mL/min, U = 11.8 m/s).

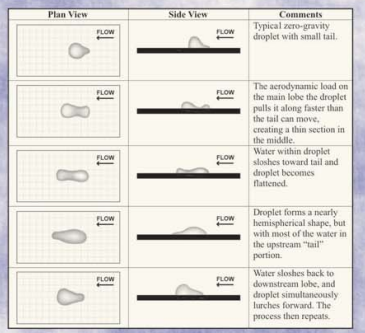

Figure 8. Typical sequence illustrating the inchworm phenomenon for zero-gravity droplet flows.

Publications

McAlister, G., Ettema, R. and Marshall, J.S., "Wind-driven rivulet break-off and droplet flows in microgravity and terrestrial gravity conditions," *Journal of Fluids Engineering* (submitted, 2004).

Marshall, J.S. and Wang, S., "Contact-line fingering and rivulet formation in the presence of surface contamination," *Computers and Fluids* (submitted, 2004).

Marshall, J.S. and Ettema, R., "Contact-line instabilities of driven liquid films," *Advances in Fluid Mechanics (Instability of Flows*, edited by M. Rahman), WIT Press, Southampton, England (in press, 2004).

McAlister, G., "The breakup of sheet flow to rivulets and rivulets to droplets," M.S. thesis, University of Iowa, Iowa City (2003).

Wang, S., "Contact-line receptivity and rivulet initiation in the presence of droplets and surface contamination," M.S. thesis, University of Iowa, Iowa City (2002).

Wang, S. and Marshall, J.S., "Effect of normal body force on fingering instability of a liquid sheet driven by shear stress or gravity," Joint ASME-European Fluids Engineering Summer Conference, Montreal, July 14-18 (2002).

MELTING AND SOLIDIFICATION IN A RECTANGULAR CAVITY UNDER ELECTROMAGNETICALLY SIMULATED LOW GRAVITY

M. Faghri
Department of Mechanical Engineering
University of Rhode Island
Kingston, Rhode Island, USA

M. Charmchi
Department of Mechanical Engineering
University of Massachusetts
Lowell, Massachusetts, USA

A low gravity environment has been simulated numerically and experimentally, via an electromagnetic field, by studying the transport phenomena associated with the melting and solidification of an electrically conducting phase change material (gallium) inside a three-dimensional rectangular enclosure. Both transverse electric and magnetic fields are used to generate a Lorentz force, which is used to counteract the effects of gravity and thus simulate low-gravity environment. The problem is formulated as one-domain by employing an enthalpy-based transformation of the energy equation. The governing equations are then discretized using a control-volume-based finite difference scheme. Experimentally, the solid thickness is measured via ultrasonic techniques and the solid/melt interface is mapped using florescent light shadowgraphy through a transparent window. The experimental data consist of temperature history, ultrasonic detection of the interface, florescent light shadowgraphy and solid phase volume fraction. The experimental results show the presence of the magnetic filed had a marked effect on melting and natural convection whereas phase change convection was noticeable in the solidification. The numerical results show that the application of an electromagnetic filed can be used to simulate key melting characteristics found for actual low gravity. However, the resulting three-dimensional flow field in the melted region differs from actual low gravity. The application of an electromagnetic field creates a flow reversal phenomenon not found in actual low gravity. Flow distortions exist when an electromagnetic field is applied but their intensity is significantly lower than the distortions found when only a magnetic filed is applied.

TRANSITION FROM FORWARD SMOLDERING TO FLAMING IN SMALL POLYURETHANE FOAM SAMPLES

A.C. Fernandez-Pello, A. Bar-Ilan, O.M. Putzeys, and G. Rein
Department of Mechanical Engineering
University of California, Berkeley
Berkeley CA 94720

D.L. Urban
NASA Glenn Research Center
Cleveland, OH 44135

Experiments are also conducted on the effect of the flow velocity and oxygen concentration, and of a thermal radiant flux, on the transition from smoldering to flaming in forward smoldering of small parallelepiped samples of polyurethane foam with a gas/solid interface. Because the microgravity experiments are planned for the International Space Station, the foam samples had to be limited to a sample size that is too small for smolder to self propagate because of heat losses to the surrounding environment. Thus, the smolder propagation and the transition to flaming had to be assisted by reducing the heat losses to the surroundings and increasing the oxygen concentration in a range of 30% - 40% by volume. The former is attained by maintaining three of the sample lateral-sides at elevated temperature, and exposing the fourth side to an upward flow and to a radiant flux. It is found that decreasing the flow velocity and increasing its oxygen concentration, and/or increasing the external radiant flux enhances the transition to flaming, and reduces the delay time to transition. Below an oxygen mole fraction of 0.35, no transition is observed for any duct flow velocity. At an oxygen mole fraction of 0.35, transition is observed only for duct flow velocities of 0.25 m/s, while at an oxygen mole fraction of 0.40, transition is observed for all duct flow velocities below 2.0 m/s. Similarly, for a radiant heat flux of 7.25 kW/m^2, transition is only observed at a duct flow velocity of 0.25 m/s. However at a radiant heat flux of 8.75 kW/m^2 transition is observed for all duct flow velocities below 2.0 m/s. The results show that smolder propagation and the transition to flaming can occur in relatively small fuel samples if the external conditions are appropriate. Combined with observations from high speed video and schlieren photography, the results also indicate that transition to flaming occurs in the char left behind by the smolder reaction, and it has the characteristics of a gas-phase ignition induced by the smolder reaction, which acts as the source of both gaseous fuel and heat. A simplified energy balance analysis on the smolder front region is able to predict the boundaries between the transition/no transition regions, as shown in Fig 1.

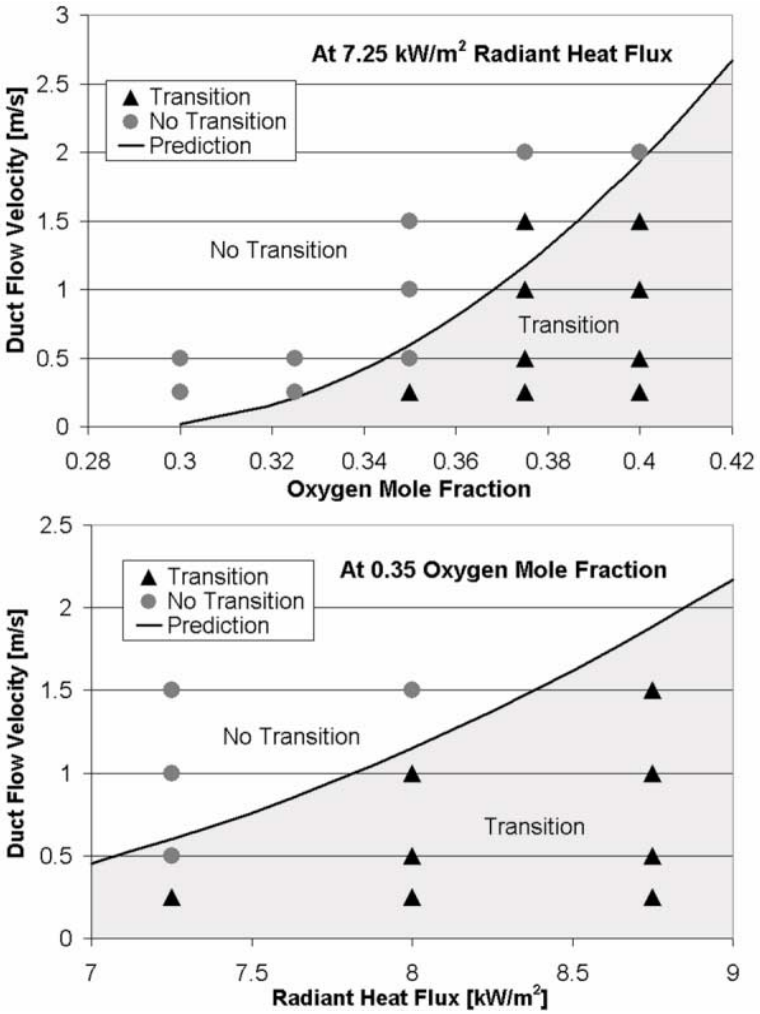

Fig 1. Comparison of experimental results with the energy balance analysis predictions of transition/no transition regions as a function of (a) oxygen mole fraction. (b) radiant heat flux.

PI contact information**:**
Prof. A. Carlos Fernandez-Pello
Department of Mechanical Engineering
6105A Etcheverry Hall
University of California
Berkeley, CA 94720-1740
Phone: (510) 642-6554
Fax: (510) 642-6163
Email: ferpello@me.berkeley.edu

PROGRESS ON ACOUSTIC MEASUREMENTS OF THE BULK VISCOSITY OF NEAR-CRITICAL XENON (BVX)

Keith A. Gillis, Iosif I. Shinder, and Michael R. Moldover
Process Measurements Division, National Institute of Standards and Technology,
Gaithersburg, MD 20899-8360

We plan to determine the bulk viscosity of xenon 10 times closer [in reduced temperature $\tau = (T\text{-}T_c)/T_c$] to its liquid-vapor critical point than ever before. (T_c is the critical temperature.) To do so, we must measure the dispersion and attenuation of sound at frequencies 1/100 of those used previously. In general, sound attenuation has contributions from the bulk viscosity acting throughout the volume of the xenon as well as contributions from the thermal conductivity and the shear viscosity acting within thin thermoacoustic boundary layers at the interface between the xenon and the solid walls of the resonator. Thus, we can determine the bulk viscosity only when the boundary layer attenuation is small and well understood. We present a comparison of calculations and measurements of sound attenuation in the acoustic boundary layer of xenon near its liquid-vapor critical point.

We used a novel, compact, acoustic resonator designed specifically for these measurements (Fig. 1). We measured the frequency response of this resonator filled with xenon at its critical density ρ_c in the reduced temperature range $10^{-3} < \tau < 10^{-1}$. From the frequency-response data, we obtained the resonance frequency and the attenuation for six resonant modes in the range 0.10 kHz $< f <$ 7.5 kHz. Using the known thermo-physical properties of xenon, we predict that the attenuation at the boundary first increases and then saturates when the effusivity of the xenon exceeds that of the solid. [The effusivity is $\varepsilon \equiv (\rho C_P \lambda_T)^{1/2}$, where C_P is the isobaric specific heat and λ_T is the thermal conductivity.] The model correctly predicts (±1.0 %) the quality factors Q of resonances measured in a steel resonator (ε_{ss} = 6400 kg·K^{-1}·s$^{-5/2}$); it also predicts the observed increase of the Q, by up to a factor of 8, when the resonator is coated with a polymer (ε_{pr} = 370 kg·K^{-1}·s$^{-5/2}$). The measured acoustic dissipation in near-critical xenon shows a prominent plateau for the Helmholtz mode and, to a lesser extent, for the longitudinal modes (Fig. 2). These results are the first direct

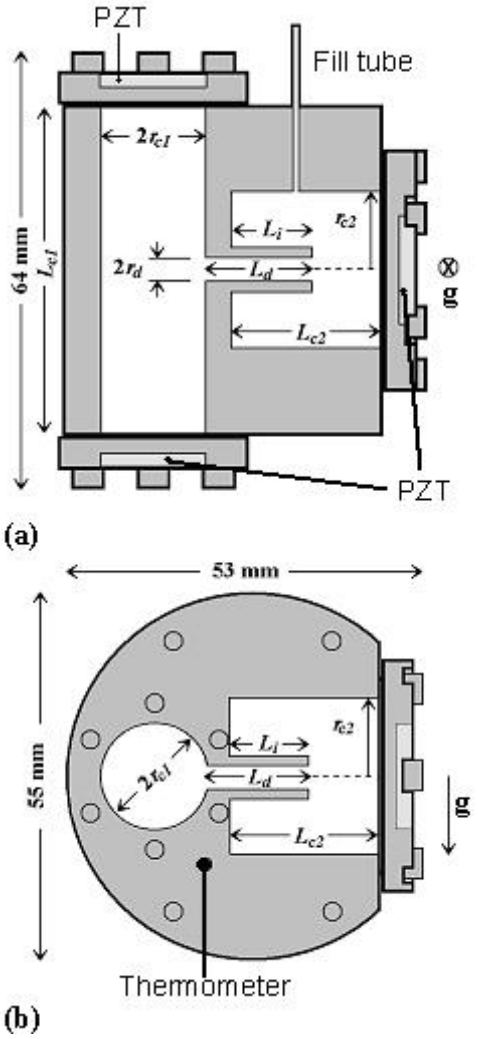

Figure 1. Acoustic resonator

evidence of thermal boundary dissipation being limited by the thermophysical properties of the solid wall.

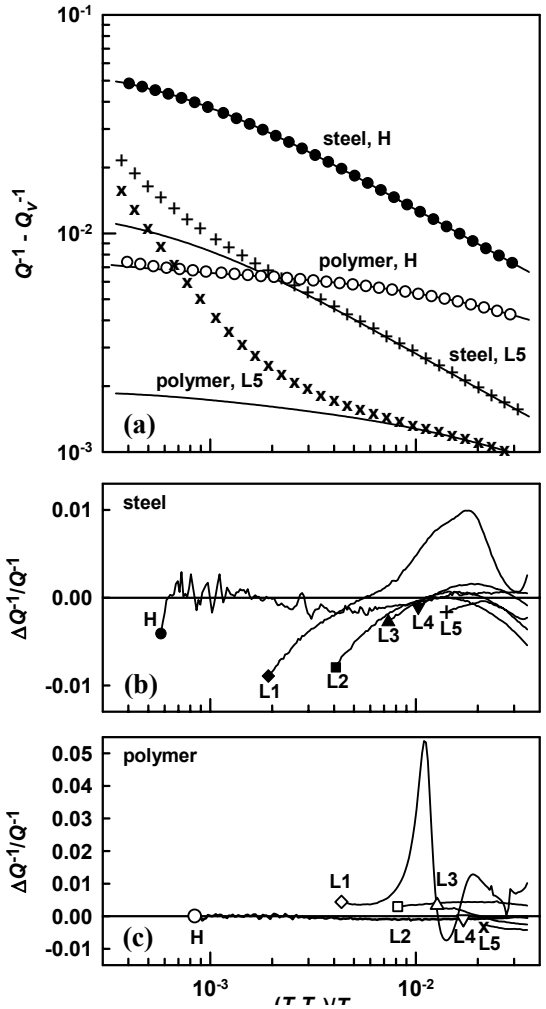

Figure 2. (a) Dissipation due to bulk viscosity and the thermal boundary layer versus reduced temperature. Theory for thermal boundary dissipation (———). The fractional deviations of the measured dissipation from theory versus reduced temperature for all the modes in the steel (b) and polymer-coated (c) resonators. Only data for which the dissipation from bulk viscosity was less than 0.8 % of the total dissipation is shown.

We observed an 8-fold reduction in the thermal boundary dissipation (as predicted) after coating a steel resonator with a low-effusivity polymer. (See Fig. 2a.) Such a reduction in thermal dissipation will be necessary in order to measure the low-frequency dissipation from bulk viscosity close to the critical point in future experiments.

To analyze the data, we formulated a theory for acoustic dissipation in a fluid that is bounded by a rigid wall with the condition that the temperature and heat flux across the boundary be continuous. The theory is valid both near to and far from the critical point; it includes volume and surface dissipation from thermal conduction, shear viscosity, and bulk viscosity.

We measured the speed of sound in xenon as a function of reduced temperature in the range $0.0006 < \tau < 0.03$. Using the measured sound speed and attenuation, the isothermal susceptibility from Ref. [1], and $(\partial P/\partial T)_\rho$ from Ref. [2], we derived C_V, C_P, and the background terms for the thermal conductivity. These derived properties were used to determine the amplitude $A^+ = 18.01$ for the singular part of C_V (with $\alpha = 0.110$) and the correlation length amplitude $\xi_0^+ = 0.1866$ nm. Although the data do not extend far into the asymptotic region, the agreement with other values is remarkable.

The onset of bulk viscosity is evident from the excess dissipation (over the thermal and viscous dissipation) indicated by the upturn at low τ of the measured dissipation shown in Fig. 2a. It is also evident that the dissipation from the bulk viscosity increases as the frequency increases in qualitative agreement with theory. The onset of bulk viscosity is more evident in the polymer-coated resonator because the thermal dissipation is smaller than it is in the bare-steel resonator.

[1] H. Güttinger and D.S. Cannell, Phys. Rev. A **24**, 3188-3201 (1981).
[2] H.L. Swinney and D.L. Henry, Phys Rev A **8**, 2566-2617 (1973).

Progress on acoustic measurements of the bulk viscosity of near-critical xenon (BVX)

Keith A. Gillis (Co-I), Iosif I. Shinder, Michael R. Moldover (PI)

National Institute of Standards and Technology, Gaithersburg, MD 20899

and Gregory A. Zimmerli (Co-I)

NASA Glenn Research Center, Cleveland, OH 44135

We plan to determine the bulk viscosity of xenon 10 times closer [in reduced temperature $\tau = (T-T_c)/T_c$] to its liquid-vapor critical point than ever before. (T_c is the critical temperature.) To do so, we must measure the dispersion and attenuation of sound at frequencies 1/100 of those used previously. We will determine the bulk viscosity ζ (also "second viscosity" or "dilational viscosity") from measurements of sound attenuation α_λ and dispersion using a novel, compact, acoustic resonator designed specifically for this purpose.

In general, sound attenuation has contributions from the bulk viscosity acting throughout the volume of the xenon and contributions from the thermal conductivity and the shear viscosity acting within thin boundary layers near the resonator wall. Thus, we can best determine the bulk viscosity when the boundary layer attenuation is small and well understood. We present a comparison of calculations and measurements of sound attenuation in the acoustic boundary layer of xenon near its liquid-vapor critical point.

The liquid-vapor critical point

The critical point is the highest temperature and pressure at which liquid and vapor can coexist in the same container. For xenon T_c=16.584 °C, P_c= 5.84 MPa

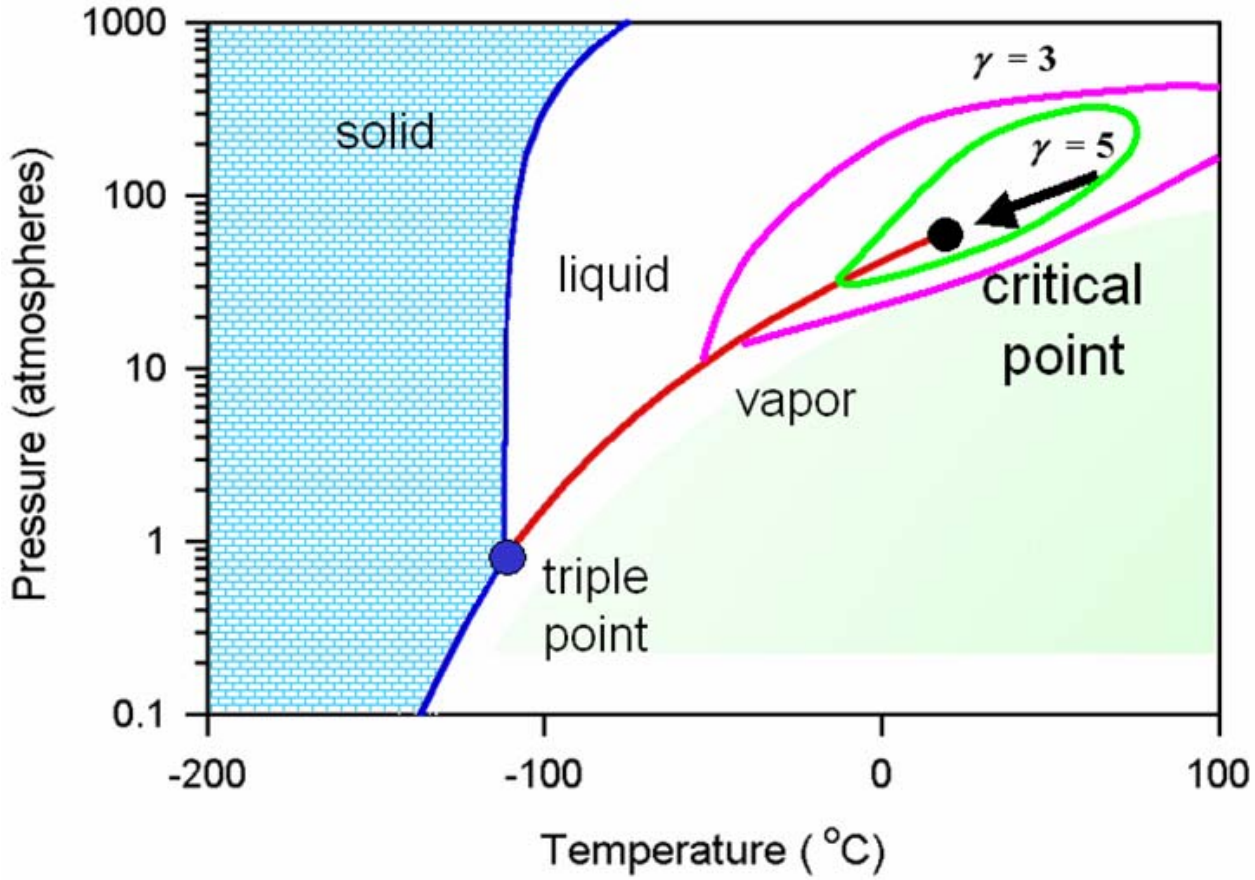

As the critical point is approached: the sound speed → 0; the bulk viscosity ζ diverges; γ= C_p/C_v diverges. Attenuation in the thermal boundary layer is proportional to γ and therefore poses a potential problem. Conventional acoustic theory assumes γ≈ 1 and attenuation is a small perturbation.

Accomplishments

- We extended acoustic theory to include near-critical fluids, heat flow in solid wall, and bulk viscosity.
- We were the first to observe direct evidence of thermal boundary dissipation being limited by thermophysical properties of the solid wall.
- We demonstrated an 8-fold reduction in thermal boundary dissipation after coating steel with a polymer.
- We derived C_V, C_P, and background thermal conductivity from our measured speed of sound.
- We observed the onset of dissipation due to bulk viscosity.

Helmholtz mode

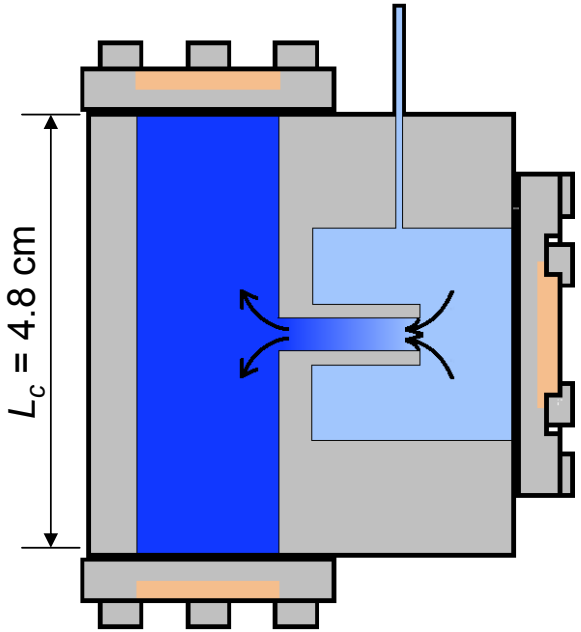

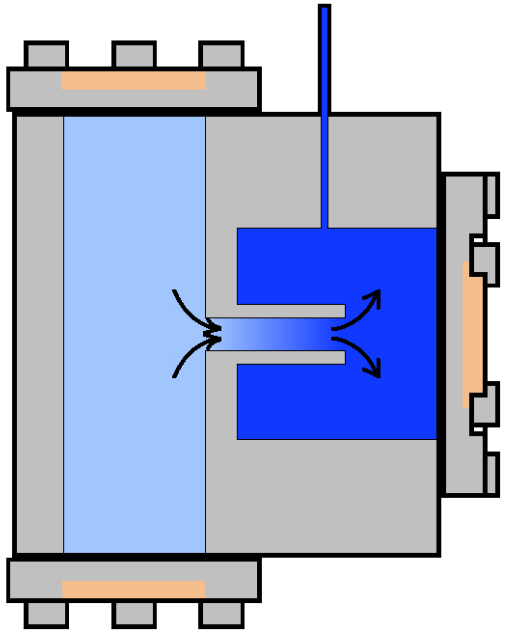

ωt $\omega t + \pi$

r_d = 0.2 cm
L_d = 1.5 cm

$$k_H = 0.1226\,\mathrm{cm}^{-1} \Rightarrow \lambda = 51.0\,\mathrm{cm} \approx 34 L_d$$

In it's fundamental acoustic mode, the gas oscillates between two chambers through a small tube (radius = r_d and length = L_d). The wavelength of this mode is about 10 times the size of the resonator or 34 times the tube length. We measure the response as a function of frequency to determine the resonance frequency and Q. For xenon at its critical density, the frequency of this mode varies from 127 Hz at 3 mK above T_c to 240 Hz at 3 K above T_c.

We use resonators of this type (called double-Helmholtz resonators) to measure the viscosity of dilute gases. See K.A.Gillis, J.B. Mehl, and M.R. Moldover, "Theory of the Greenspan Viscometer," JASA 114, 166-173 (2003)

Longitudinal modes

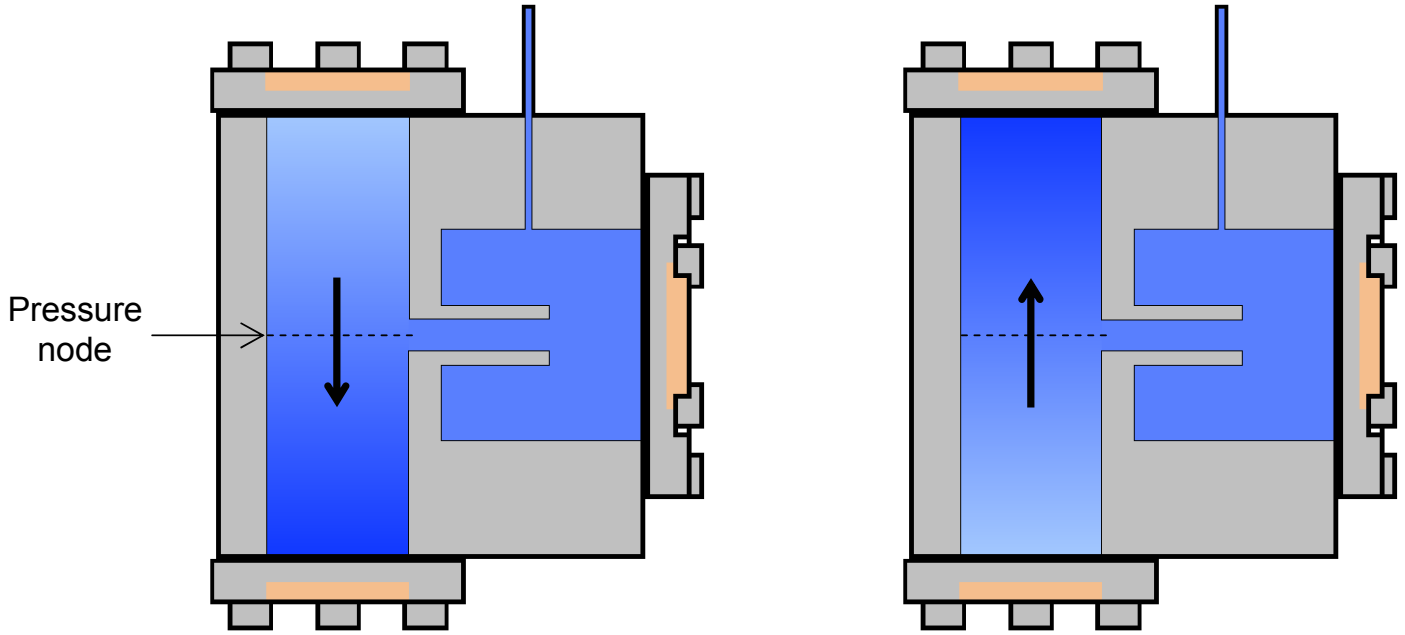

ωt $\omega t + \pi$

$$k_{L1} = 0.6536\,\mathrm{cm}^{-1} \Rightarrow \lambda = 9.6\,\mathrm{cm} = 2L_c$$

We deduce the sound speed and the acoustic attenuation from the resonance frequency and Q for a given mode.

To measure dispersion, we also study the first 5 longitudinal modes of the longer chamber. Like the Helmholtz mode these modes are non-degenerate and well separated because of the asymmetric resonator design. All 6 modes span a factor of 27 in frequency at a given temperature. The acoustic data span a factor of 60 in frequency over the full temperature range.

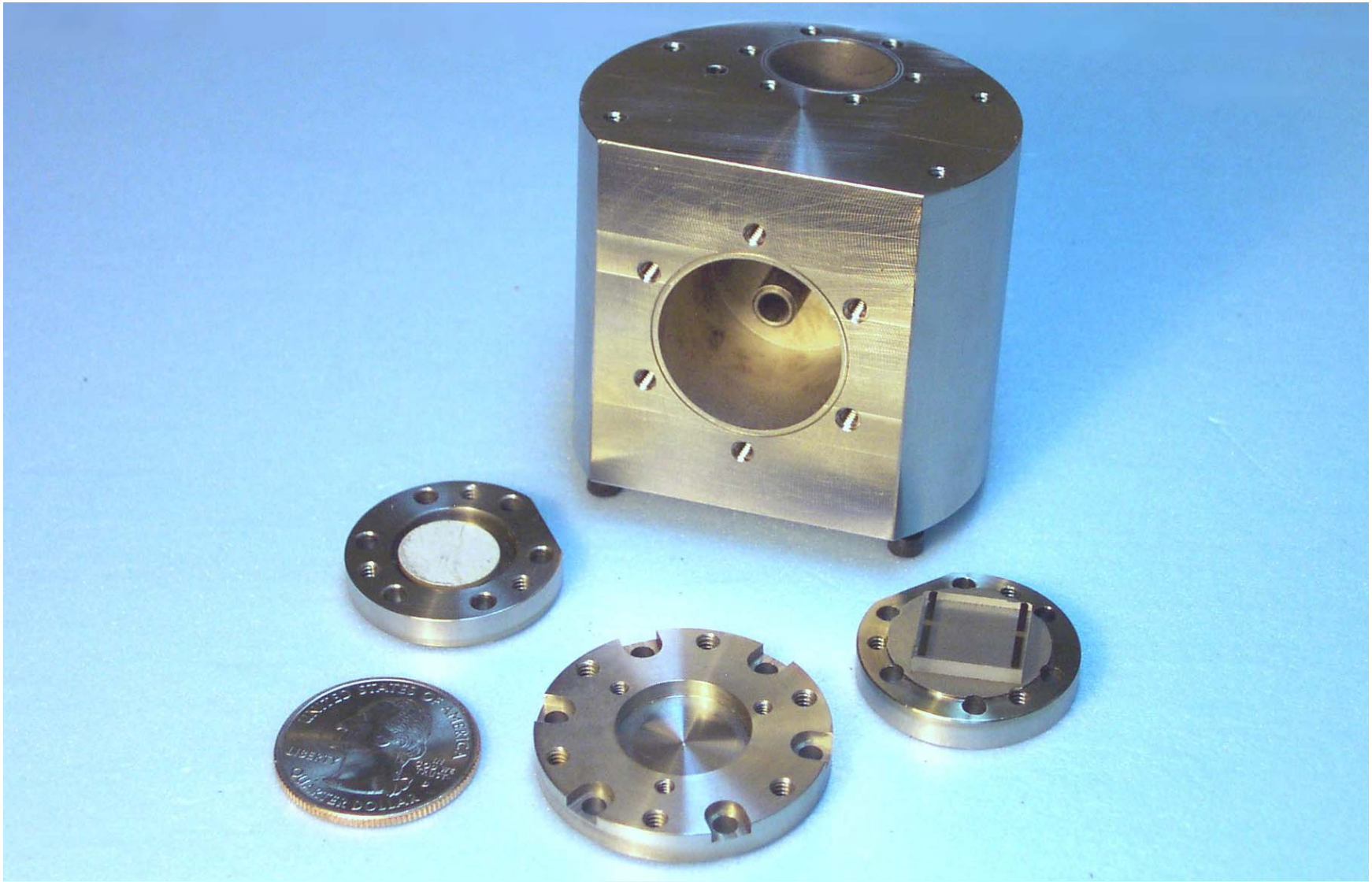

The 2 chambers and the connecting tube were machined as one piece from a block of stainless steel. The high rigidity is crucial for studies of dense fluids. Piezoceramic disks were attached to the outside of the flanges in order to drive and detect sound waves in the fluid. Two similar resonators were used. One resonator was coated with a polymer to reduce the thermal conduction between the xenon and the resonator wall. The other resonator was left as bare steel.

Acoustical Spectrum of Resonator

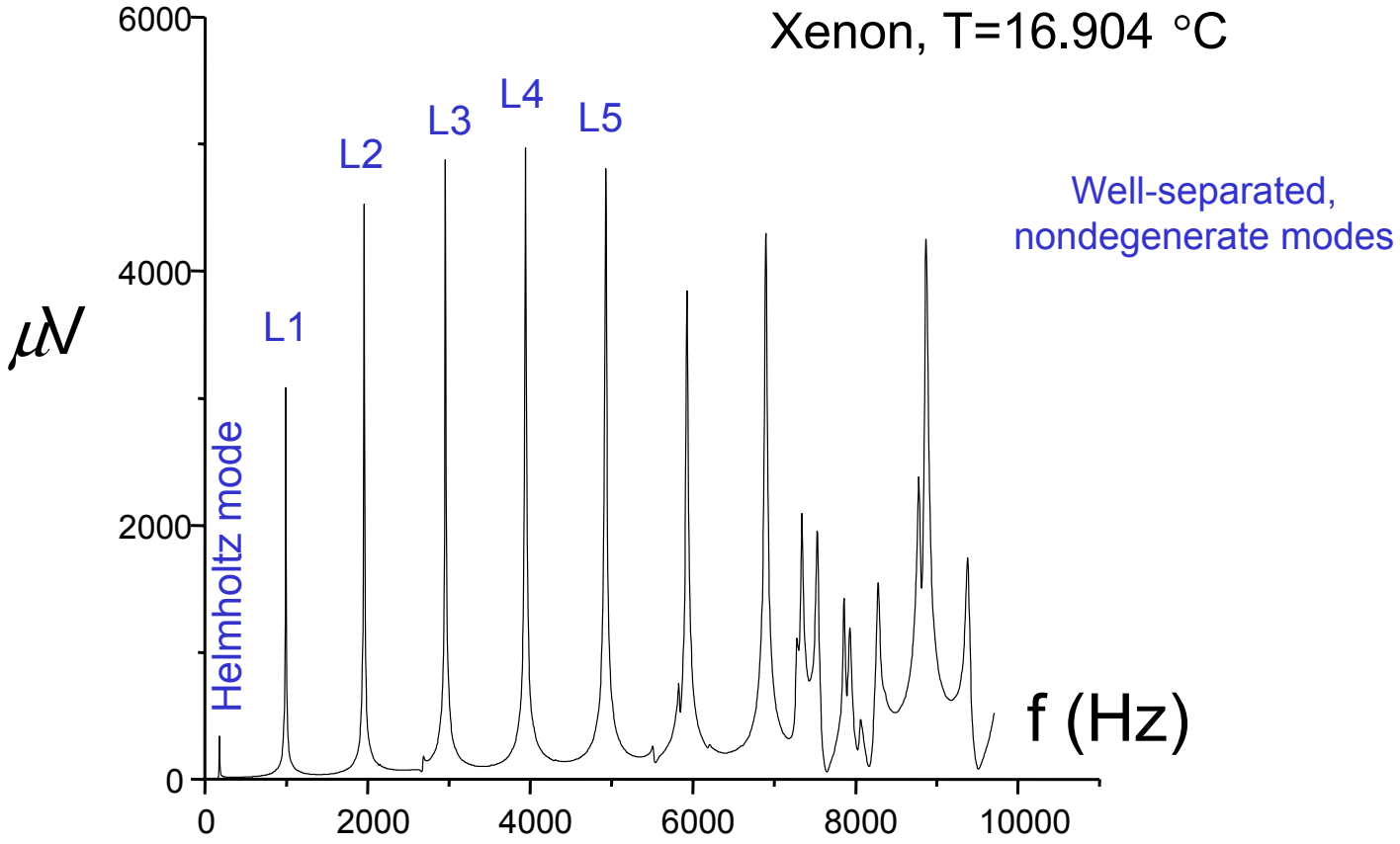

The graph shows the amplitude of the detector signal as a function of frequency. The Helmholtz mode and the longitudinal modes of the chamber (L1-L5) are clearly visible and well-separated. Isolated, non-degenerate modes are necessary for accurate modeling.

From dilute gas to the critical isochore

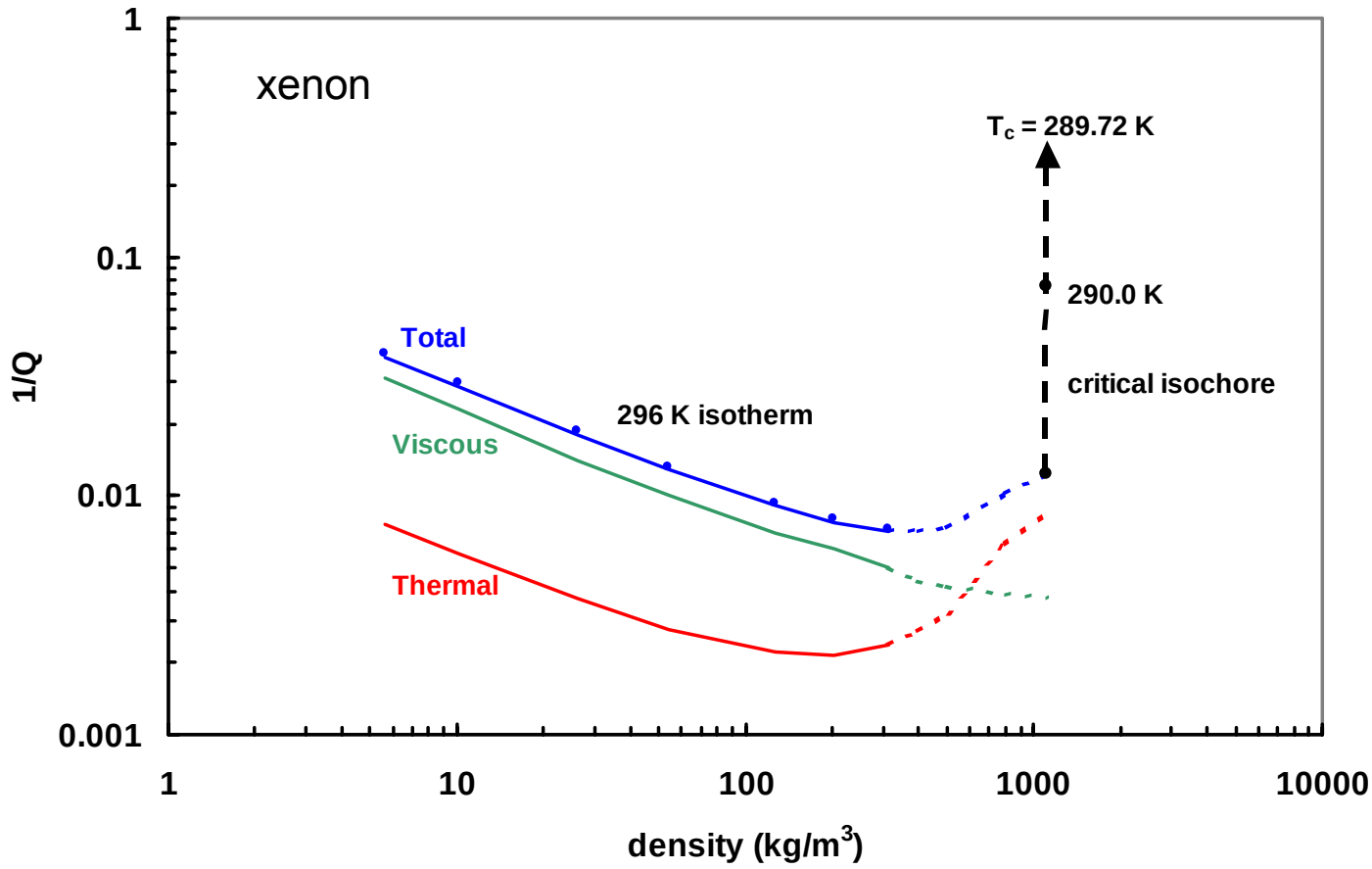

This graph shows the measured dissipation (1/Q) as the density increases from ambient conditions to the critical density (1116 kg/m^3) at constant temperature (blue curve). The contributions from viscosity and thermal conductivity within the boundary layers, calculated from the model, are shown in green and red. Viscous dissipation dominates at low density. Thermal dissipation dominates at high density due to the large γ. The black dashed line shows the dramatic increase in 1/Q as the temperature is lowered to T_c along the critical isochore.

Dependence of dissipation on thermal properties of the wall

thermal conduction | shear viscosity | bulk viscosity

$$Q^{-1} \approx (\gamma - 1)\frac{q_T \delta_T}{1+\vartheta} + q_v \delta_v + \frac{\omega\zeta}{\rho c^2} + \ldots$$

ε = effusivity

$$\vartheta \propto \frac{\varepsilon}{\varepsilon_{\text{solid}}}$$

$$\delta_T \approx \sqrt{\frac{2D_T}{\omega}} \qquad \delta_v = \sqrt{\frac{2\eta}{\rho\omega}}$$

boundary layer thicknesses

$$\frac{\varepsilon}{\varepsilon_{\text{solid}}} = \frac{\left(\rho C_P \lambda_T\right)^{1/2}}{\left(\rho C_P \lambda_T\right)^{1/2}_{\text{solid}}}$$

	$\varepsilon_{\text{solid}}$ $(\text{kg}\cdot\text{K}^{-1}\cdot\text{s}^{-5/2})$
perfect solid	∞
copper	37000
steel	6400
polymer (parylene)	370

To lowest order, the dissipation is due to the sum of 3 contributions: thermal and viscous dissipation at the interface between xenon and the wall plus a volume dissipation due to bulk viscosity. The thermal dissipation reaches its maximum value when the ratio ϑ of the effusivity of xenon ε to the effusivity of the solid wall ε_{solid} equals one. Lower ε_{solid} means the thermal dissipation saturates at a lower value farther from T_c. See K.A. Gillis, I.I. Shinder, and M.R. Moldover, "Thermoacoustic boundary layers near the liquid-vapor critical point," (in press Phys. Rev. E, July 2004).

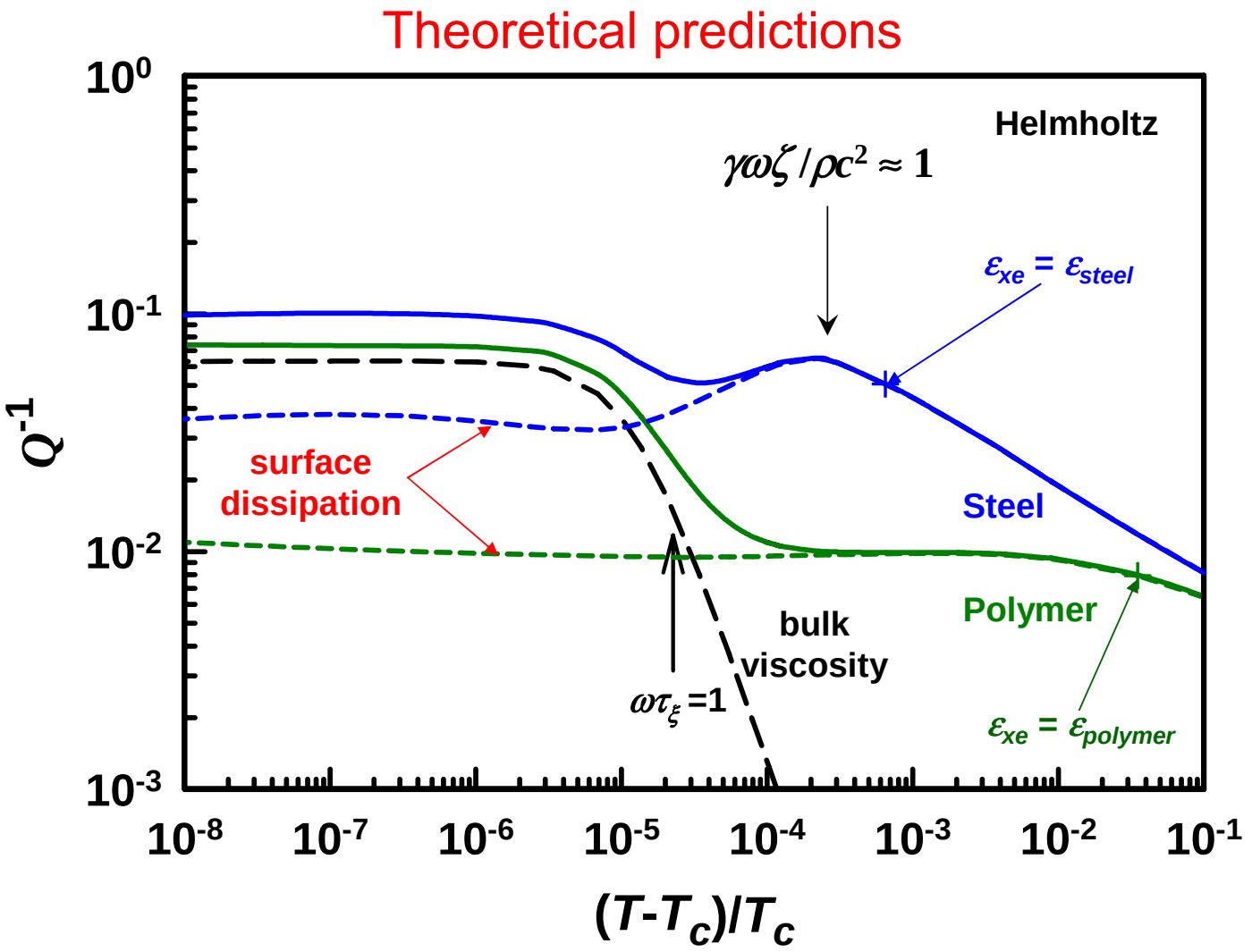

Predicted dissipation as a function of reduced temperature in bare steel and polymer-coated resonators. The crosses indicate where the effusivity ε of xenon equals the effusivity of the solid. The surface dissipation from viscosity and heat conduction is shown with short dashed curves. The contribution from bulk viscosity ζ in the volume is shown with a long dashed curve. The relaxation of fluctuations gives rise to bulk viscosity and has characteristic time τ_ξ. The condition $\gamma\omega\zeta/\rho c^2 \approx 1$ indicates where the boundary layer becomes highly compressible.

Comparison of measurements with theory

Xenon near its critical point

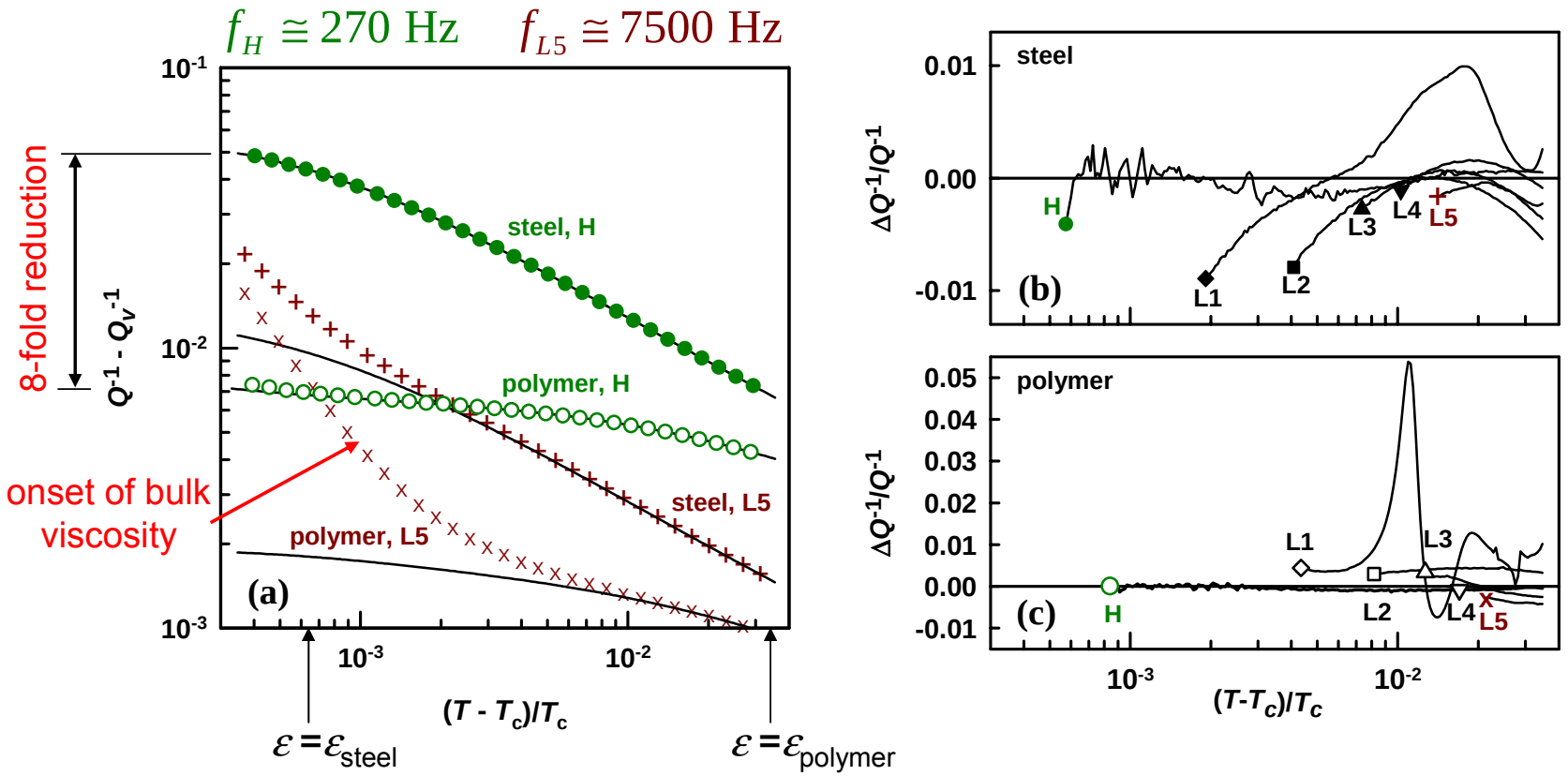

(a) ***Dissipation due to bulk viscosity and the thermal boundary layer versus reduced temperature. Theory for thermal boundary dissipation (———). The fractional deviations of the measured dissipation from theory versus reduced temperature for all the modes in the steel*** **(b)** ***and polymer-coated*** **(c)** ***resonators. Only data for which the dissipation from bulk viscosity was less than 0.8 % of the total dissipation is shown.***

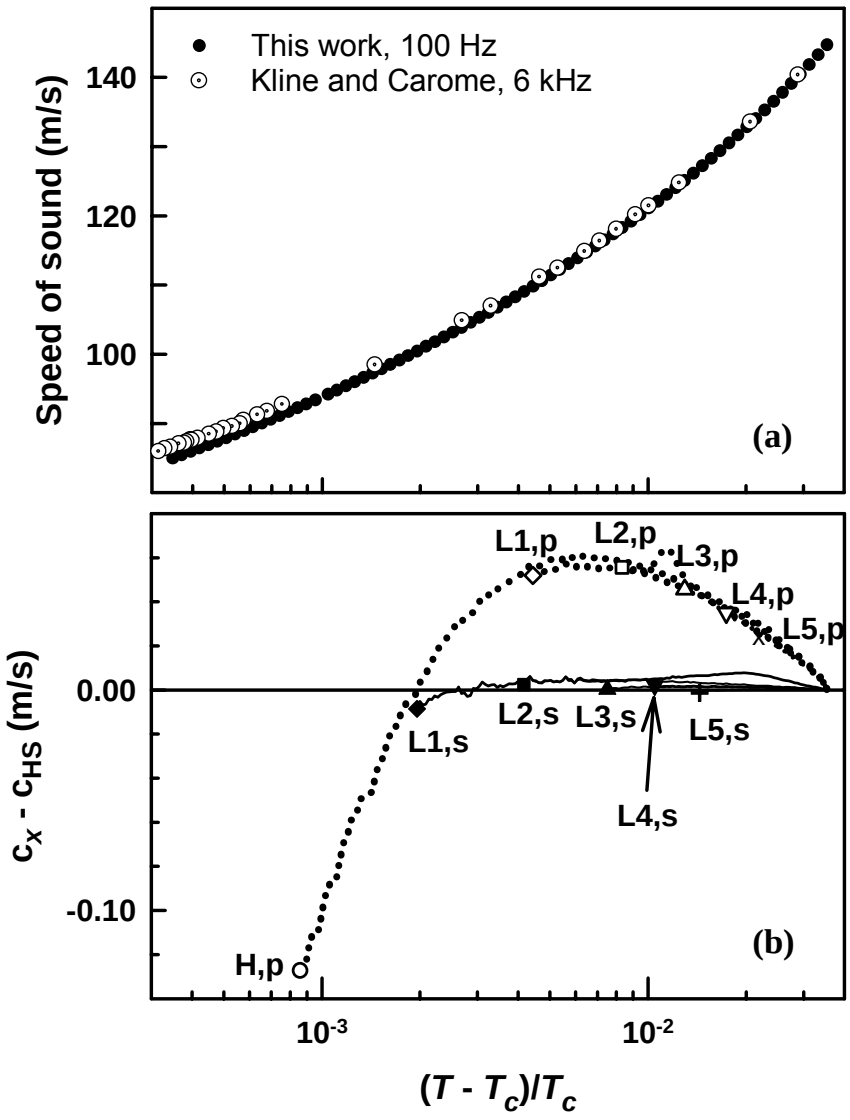

Speed of sound in xenon near its critical point

(a) ***The speed of sound c_{HS} determined from the Helmholtz mode with bare stainless steel plotted versus the reduced temperature. The speed of sound measured by Kline and Carome at 6 kHz.***

(b) ***Deviations of the speed of sound determined from each mode from c_{HS} shown in the upper graph.***

Consistency among modes ~0.01%

Consistency between resonators ~0.1%

Studying Biological Rhythms of Person's Skin-Galvanic Reaction and Dynamics of Light Transmission by Isomeric Substance in Space Flight Conditions

e-mail: vladimir.v@nt-ftlg.com
vladimir.p@nt-ftlg.com
Phone: (919) 942-9241
Fax: (919) 942-9241

General substantiation

1. State of the Question. Novelty and Practical Value of the Research.

Intensity and amplitude of human functional systems and human most important organs are wavelike, rhythmic by nature. These waves have constant periodicity, phase and amplitude. The mentioned characteristics can vary, however their variations have a pronounced reiteration in the course of time. This indicates a hashing of several wave processes and their interference. Stochastic changes in wave processes characteristics of a human organism are explained either by "pulsations" associated with hashing (superposition) of several wave processes and their interference, or by single influence of environmental physical factors on a human organism.

Human beings have respectively periods of higher and lower efficiency, state of health and so on, depending not only of environmental factors, but also of "internal" rhythmic factor. Sometimes peaks and falls periodicity of some or other characteristics is broken. Disturbance of steady-state biological rhythms is usually accompanied by reduction of activity steadiness of the most important systems of a human organism. In its turn this has an effect on organism's adaptation to changing living conditions as well as on general condition and efficiency of a human being. The latter factor is very important for space medicine.

Biological rhythmology is a special branch of biology and medicine, it studies rhythmic activity mechanisms of organs, their systems, individuals and species. Appropriate researches were also carried out in space medicine.

Some or other rhythmical processes are attributable to all living substances of our planet. Such processes are observed in all organisms –from unicellular algae to human organism – concerning both the whole organism as well as its separate cells. The majority of biological rhythms is probably not conditioned by periodic environmental effects, but it is subjected to some unknown biological clock. This rhythm mechanism does not simply respond to external stimulations, but it adapts itself to the external environment in a finer and more expanded manner, since necessary preparatory reactions take place in living organism before changing of external conditions, for example before it gets dark. Synchronization of a great number 400 of human organism's functional parameters changing rhythmically during one circadian period can be only explained by existence of such biological clock. However, the biological clock was not found both in organisms of all levels and in its separate cells. There is another striking fact – biological rhythms of hundreds millions of cornfield spikelets are strictly synchronized with each other. This field is not though an entire organism. Striking accuracy of observed rhythms gives an idea that there is nevertheless some periodically changing geophysical or cosmic environmental factor, which constantly "informs" plants and animals about the course of time.

In 1973-1974 V.P.Glushko advanced a hypothesis that if such factor existed, it could be found out through its influence on a lifeless inert matter. Such factor was discovered during synchronous

experiments with plants and isomer solutions. It was indicated by high coefficient of correlation between 24 hours' light absorption by lamina of a living plant and dynamics of light transmission through an isomer solution. Such factor turned to be a gravitational field, namely – gravitational perturbations (waves) going from the center of our Galaxy. The report on this work was given at "Problems of Plants Photo Energy" All-Union Conference held in Almaty in 1974 and at "Magnetic Fields in Medicine and Biology" International Conference held in Kaliningrad in 1975.

Authors' group V.P.Glushko, R.A.Gareev and A.N.Startsev gave a report on profound correlation between 24 hours' dynamics of person's psychophysiologic state and 24 hours' dynamics of light dispersion through isomer solutions, at the first Worldwide Aerospace Congress held in Moscow in 1995. It was there stated a hypothesis that a psychophysiologic state of an astronaut situated at a space station depends not only on already known space flight factors, such as zero-gravity, smells, sounds, electromagnetic noise of equipment, psychological and other so-called "internal" space flight factors, but it depends also on external factors such as gravity waves frequency variation resulted by Doppler effect, i.e. waves initiating biological rhythms. Initiating signal's frequency variation "disturbs" a biological rhythm of the organism and this has to influence on the whole astronaut's organism. Frequency variation of the signal initiating biological rhythm cannot be in principle simulated at the planet's surface, but this occurs naturally during space flight.

"*Tangr – 2"* space experiment held in 1998 and elicited the fact that T.Musabayev, an astronaut showed biological rhythms of skin-galvanic reaction shortened in time by 5-8% in comparison with similar rhythms registered on the Earth. **Mathematical processing of results of measurements was done by "Institute of theoretical and applied mathematics of the Ministry of a science - academy of sciences of Republic Kazakhstan».** The above said researches (3 experiments, each lasting for 3 hours with registration at intervals of a minute) were carried out after astronauts of 25-th expedition had spent about 3 or 4 months at "*Mir"* orbital station; i.e. after the period of critical adaptation to zero gravity and specific living environment existed at the orbital station. **Results of work are published in the collective monography «Space researches in Kazakhstan», under edition of academician M.M.Sultangazin, Almaty, year 2002. Section 5.12, «The Medical and biologic researches connected to flights of the Kazakhstan cosmonauts», page 446 - 460. And as in the collection of works the 2-nd international scientific - practical conference «The Science and education at the present stage of development of a society». Almaty, year 2003, page 72 - 73. Authors: Gareyev R.A., Fajzulina S.R., Glushko V.P., of the name: «The Psychophysical condition of the cosmonaut to KGR parameter during the period after-flight's rehabilitations».**

New Technologies of Physicotechnical Laboratory "GLUSHKO" will congregate to continue the begun researches. It is supposed to study out dynamics variation of "rhythms" of optical properties of isomer solutions situated both in space flight, as well as on the planet's surface. This will greatly contribute to resolving question about biological rhythms mechanism and its properties. If we evolve the hypothesis about a space factor initiating biological rhythms, it will be clear that there is not life as such outside the spatial region where this factor operates. This work is topical for pilot cosmonautics not only in view of the above-mentioned, but also in view of the knowledge about degree of dependence of biological clock's "course speed" on spacecraft's traverse speed after signal frequency has varied as a result of Doppler effect, as well as the knowledge about possibility of their disalignment.

ELECTROSTATIC RELEASE OF FINE PARTICLES ADHERED TO SURFACES ON THE MOON OR MARS

John Goree
Department of Physics and Astronomy
The University of Iowa
Iowa City, IA 52246
Phone: 319-335-1843; Fax: 319-335-1753

The adhesion of fine particles to surfaces is a concern for human exploration of the Moon and Mars. Airlocks, EVA suits, and photovoltaic cells have surfaces where dust can be an unwanted contaminant. When a particle rests on a surface, it is held in place by a van-der-Waals attraction, but this adhesion can be overcome by several mechanisms. One such mechanism for the Moon and Mars environments is the application of electrostatic forces. These forces occur spontaneously on the Moon. They could also be applied deliberately for the purpose of cleaning surfaces on the Moon or Mars.

The Moon, unlike Mars, has no atmosphere. Instead, it is immersed in interplanetary plasma, which consists of free electrons and protons at a low number density. The Moon disturbs this plasma, so that there is an electric field perpendicular to the Moon's surface. This electric field applies a vertical force to any electrically-charged fine particle.

Particles are known to become charged and levitated on the Moon. This was discovered in Apollo missions, where a thin cloud of dust was seen floating above the lunar horizon. Particles can be charged either photoelectrically by exposure to solar UV, or by collection of free electrons and ions from the surrounding plasma. This can lead to levitation, if the particle can first overcome van-der-Waals adhesion to surfaces such as a rock, a photovoltaic cell, or another dust particle.

Laboratory experiments have demonstrated that one mechanism for overcoming adhesion is an electrostatic force. Dielectric particles on a surface are charged due to exposure to plasma, or UV. In a pile of particles, two neighboring particles can acquire charges of the same polarity, thereby applying an interparticle repulsion sufficient to overcome the adhesion. This particle release occurs with a surprising speed that remains unexplained.

On Mars, there is an atmosphere of neutral gas instead of a natural plasma. However, it is possible to purposefully produce a localized plasma by ionizing the thin Martian atmosphere. This can be done by applying a voltage to an antenna or electrode. It is worth studying whether such a plasma could be used for cleaning surfaces. A similar method has been developed previously for the semiconductor industry to clean particulate contaminants from semiconductor wafer surfaces.

Another application for these principles is ion thruster technology. Fine particles can flake from interior surfaces of an ion-thruster's plasma source. When these particles overcome adhesion from the surface, they move about and become lodged in the grids that accelerate ions, causing a malfunction by shorting the grids. For this reason, it is of interest to study the plasma-generated electrostatic forces that overcome adhesion of particles to surfaces.

It is proposed to carry out laboratory experiments and possibly parabolic flights with lunar gravity conditions, to study these electrostatic mechanisms, using plasma sources and a UV lamp.

SUPPRESSION OF LOW STRAIN RATE NONPREMIXED FLAMES BY AN AGENT*

A. Hamins, M. Bundy, C.B. Oh, and J. Park
The National Institute of Standards and Technology
Building and Fire Research Laboratory
Gaithersburg, MD 20899-8663

I.K. Puri
Department of Mechanical Engineering
University of Illinois at Chicago
Chicago, IL 60607-7022

The extinction and structure of non-premixed methane/air flames were investigated in normal gravity and microgravity through the comparison of experiments and calculations using a counterflow configuration. From a fire safety perspective, low strain rate conditions are important for several reasons. In normal gravity, many fires start from small ignition sources where the convective flow and strain rates are weak. Fires in microgravity conditions, such as a manned spacecraft, may also occur in near quiescent conditions where strain rates are very low. When designing a fire suppression system, worst-case conditions should be considered. Most diffusion flames become more robust as the strain rate is decreased. The goal of this project is to investigate the extinction limits of non-premixed flames using various agents and to compare reduced gravity and normal gravity conditions.

Experiments at the NASA Glenn Research Center's 2.2-second drop tower were conducted to attain extinction and temperature measurements in low-strain non-premixed flames. Extinction measurements using nitrogen added to the fuel stream were performed for global strain rates from 7 s^{-1} to 50 s^{-1}. The results confirmed the "turning point" behavior observed previously by Maruta et al. in a 10 s drop tower. The maximum nitrogen volume fraction in the fuel stream needed to assure extinction for all strain rates was measured to be 0.855 ± 0.016, associated with the turning point determined to occur at a strain rate of 15 s^{-1}. The critical nitrogen volume fraction in the fuel stream needed for extinction of 0-g flames was measured to be higher than that of 1-g flames.

Flame temperature measurements were attained in the high temperature region of the flame (T > 1200 K) using visible emission from a (12.5 ± 0.5) μm filament positioned axially along the burner centerline. This method was used to obtain the time varying temperatures as the flame transitioned to microgravity conditions and as the flame extinguished. Temperature measurements showed that a peak flame temperature of approximately 1400 (± 100) K for a global strain rate of 20 s^{-1} for conditions when the flame was very near extinction (99% of the required nitrogen volume fraction for extinction in microgravity). The measured flame temperature profiles were a function of the strain rate, the concentration of N_2 and the presence of buoyancy forces. The lower the global strain rate, the greater the changes in the flame as it transitioned from 1-G to μ–G.

A two-dimensional flame simulation using a three step chemical mechanism was developed here and compared favorably to the extinction and temperature measurements in both normal and microgravity. One-dimensional flame computations using OPDIFF could not predict the flame shape or the extinction limits accurately at *low strain rates* in 0-G or 1-G due to multi-dimensional heat loss and the effects of buoyancy. The two-dimensional model (see Figure below) showed that at low strain rates, the 1-G flame extinguishes from the outer flame edge inwards towards the central axis, whereas the 0-G flame

extinguishes from the centerline out. Differences in the details of 0-G and 1-G flame structure are important in interpreting the results of the microgravity extinction experiments.

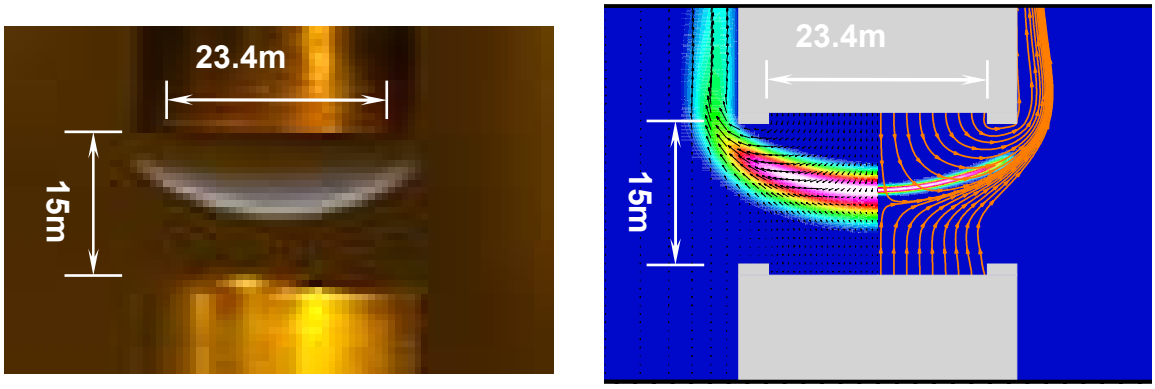

Figure 1. Comparison of photograph and simulation of a near-extinction counterflow diffusion flame at a strain rate of 20 s^{-1} in 1-G with the fuel stream composed of 79 % N_2 and 21 % CH_4 flowing from the bottom duct. The right hand side of the simulation shows the calculated heat release rate and streamlines and the left hand side shows the calculated temperature and velocity contours.

Suppression of Low Strain Rate Nonpremixed Flames by an Agent

A.Hamins, M.Bundy, C.B. Oh, J.Park
National Institute of Standards and Technology, Gaithersburg, MD

I.K. Puri
Dept. Mechanical Engineering, University of Illinois at Chicago, Chicago, IL

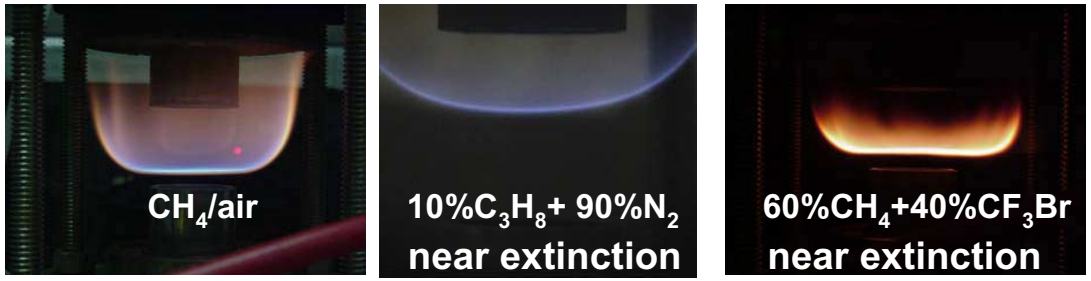

Supported by the NASA Microgravity Combustion Research Program;
Dr. Sandra L. Olson, Technical Monitor.

NIST
National Institute of Standards and Technology
Technology Administration, U.S. Department of Commerce

BUILDING AND FIRE RESEARCH LABORATORY

Motivation

- unwanted fires are typically non-premixed
- low strain rate flame conditions prevail for a fire on a space platform

Objective

Investigate the structure and suppression limits of low strain rate non-premixed flames.

Experimental Variables

suppressant type: N_2, CO_2, CF_3Br

configuration (suppressant in fuel or air stream)

buoyancy (1-g and μ-g)

global strain rate

air/fuel velocity ratio

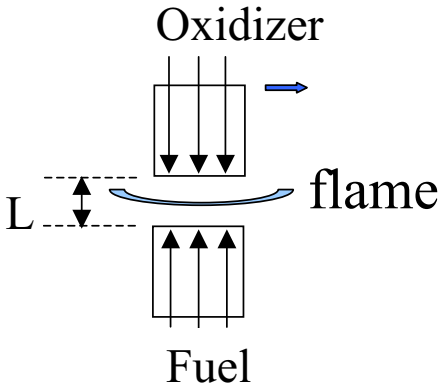

counterflow configuration

Approach: numerical

- 1D *Oppdif* simulations of 0-g flame structure and suppression
- 2D simulations of 0-g and 1-g flame structure and suppression

1D Model: Oppdif	2D Model *
detailed chemistry & transport	3 step global reaction
no buoyancy term	buoyancy term
optically thin radiation model	optically thin radiation
predicts extinction	predicts extinction

*** C.B. Oh, C.E. Lee and J. Park, "Numerical Investigation of Extinction in a Counterflow Nonpremixed Flame Perturbed by a Vortex", *Combust. Flame*, 2004, to appear.**

Approach: experimental

- 2.2 s drop tower experiments
- measurements of flame temperature & critical agent requirements
- comparison of simulations and measurements

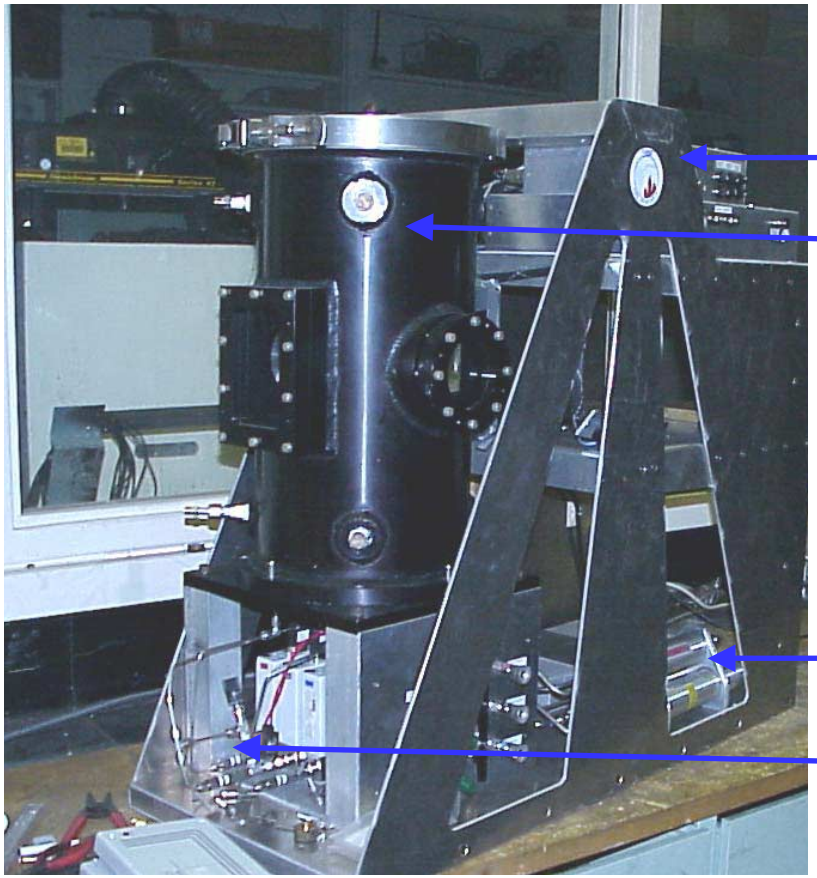

electronics/on-board computer

combustion chamber

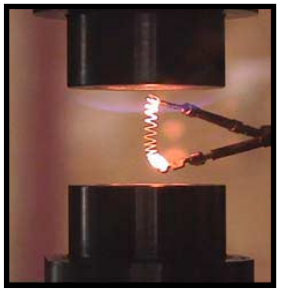

burner & retractable igniter

gas cylinders

pressure flow controllers/ critical flow orifices

Flame Extinction Limits in 0-g and 1-g

Agent (N_2) added to Fuel (CH_4) Stream

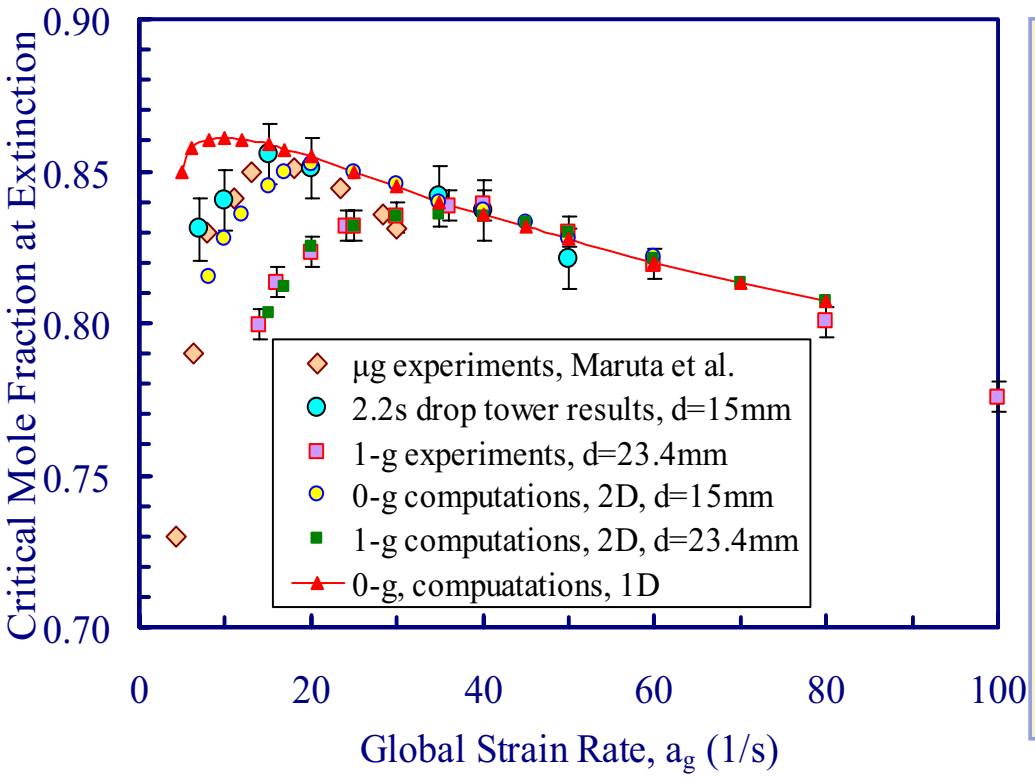

- New extinction measurements agree with Maruta et al, 1998.
- 2D model results agree with 0-g and 1-g measurements.
- 0-g flames are more robust than 1g flames at low strain.
- Muti-dimensional effects exist at low strain rate, which effects extinction limit.

$$a_g = \frac{2|u_O|}{L}\left(1+\frac{|u_F|\sqrt{\rho_F}}{|u_O|\sqrt{\rho_O}}\right)$$

1-g Flame Shape and Temperature Profile

Experiment

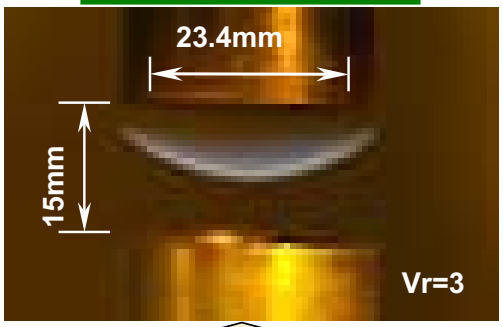

a_g = 20 (1/s)

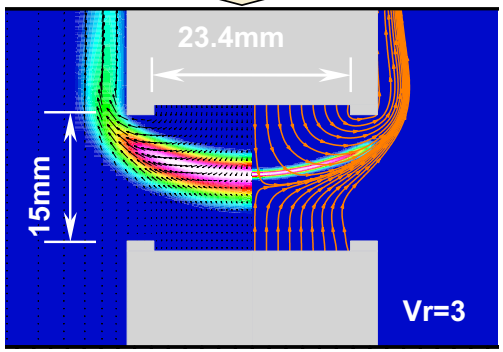

Computation

LHS : Temperature and Velocity Vector
RHS : Heat Release Rate and Stream Line

Fuel ➔ CH_4:N_2 = 21:79 by volume
a_g=20 (1/s), Vr = 3

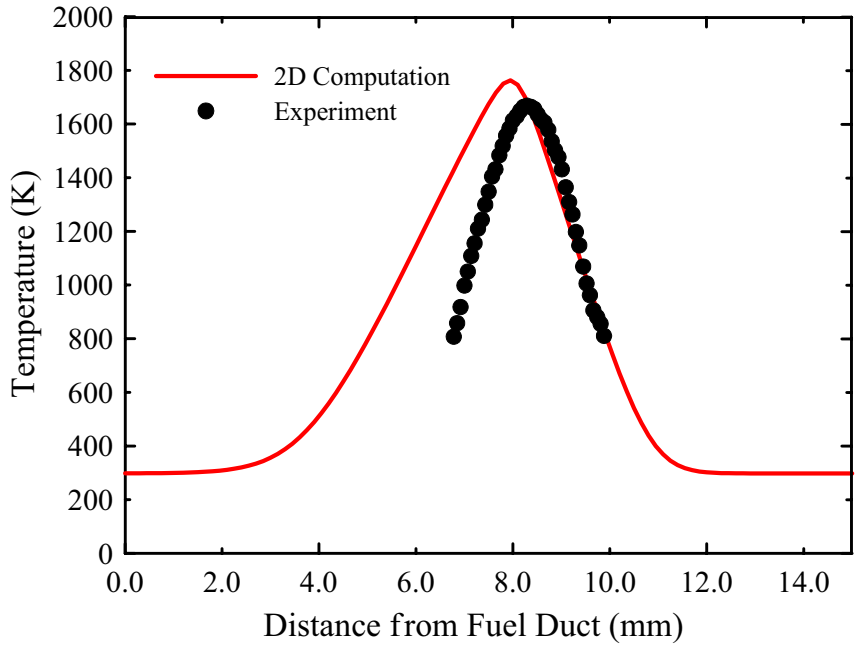

Comparison of Centerline Temperature

Extinction Process in 0-g Flame; a_g=20 (1/s)

Nitrogen fuel stream volume fraction increasing from 0.79 ➔ 0.855

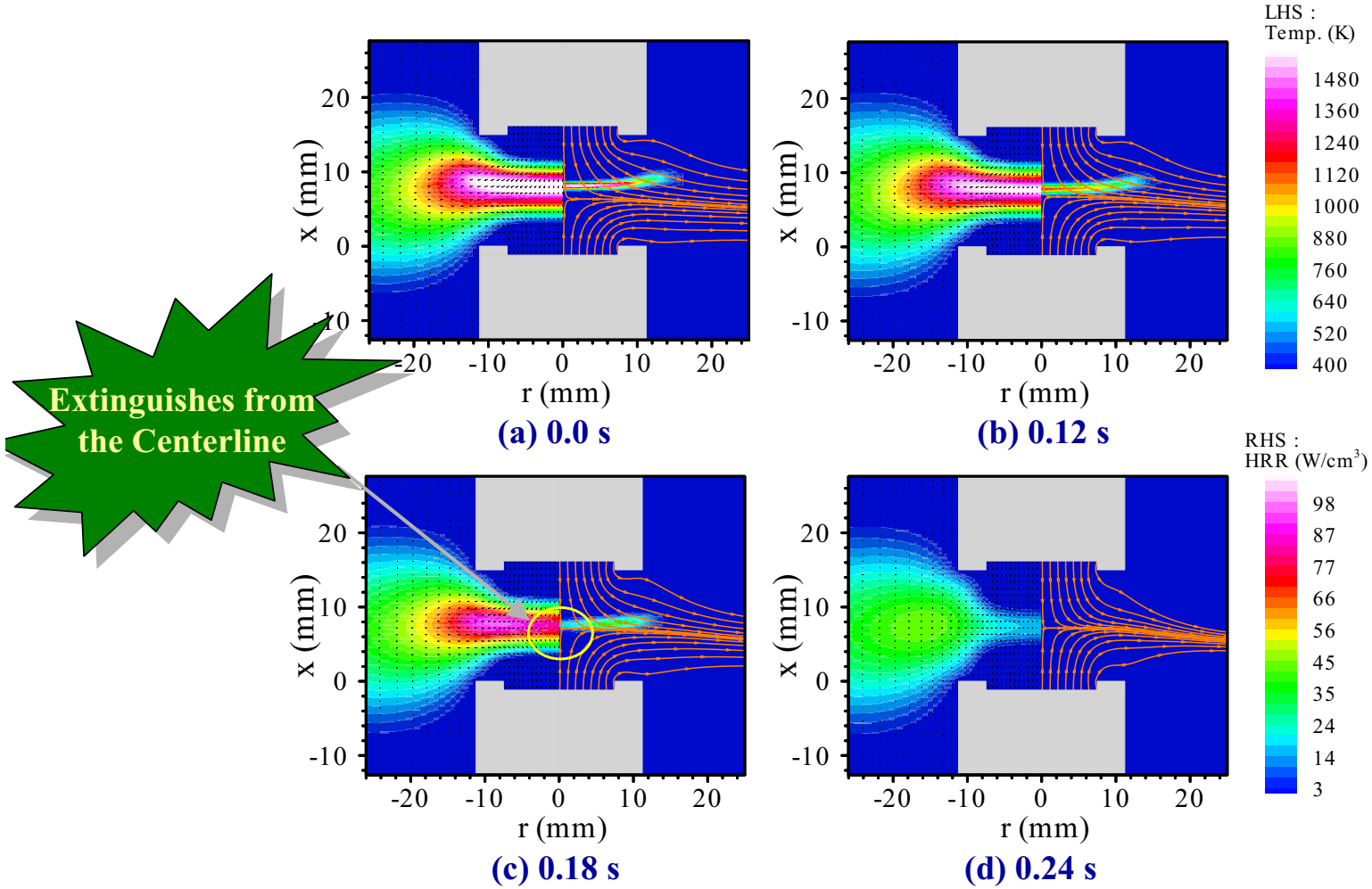

Extinction Process in 1-g Flame; a_g=20 (1/s)

Nitrogen fuel stream volume fraction increasing from 0.79 ➔ 0.825

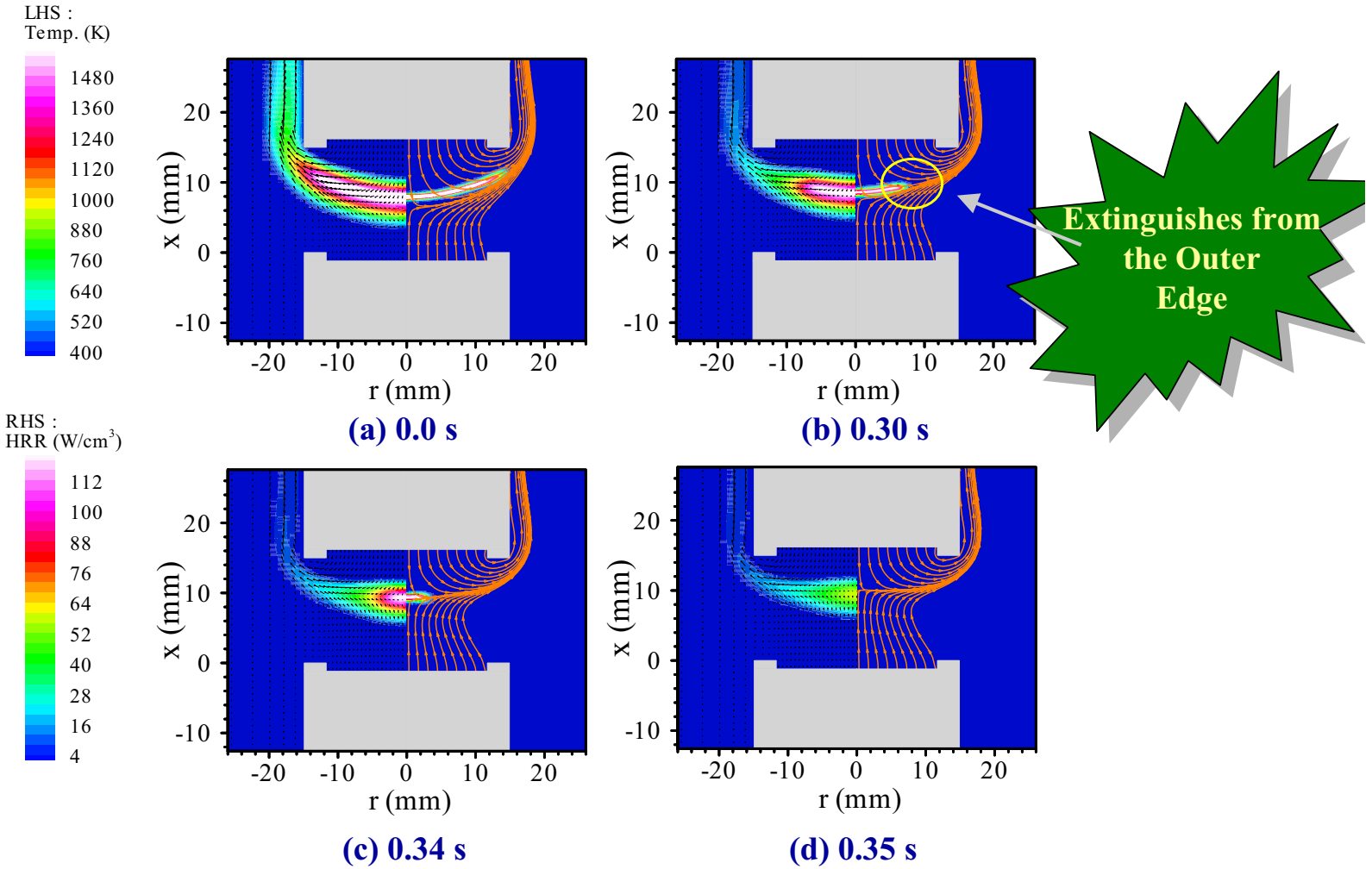

Conclusions

- 2D computations of 0-g and 1-g flames are in good agreement with experimental results.
- At low strain rate, 1g flame extinguishes from the outer flame edge, while 0g flame extinguishes from the centerline.
- 1D computations cannot predict the flame shape and extinction limit reasonably at low strain rates due to muti-dimensional heat loss.
- New extinction measurements in 2.2 s reported here are in good agreement with 10 s JAMIC results (Maruta et al, 1998).
- Critical nitrogen volume fraction in the fuel stream needed for extinction of 0-g flames is higher than that of 1-g flames.

BUOYANCY EFFECTS IN STRONGLY-PULSED, TURBULENT DIFFUSION FLAMES

J.C. Hermanson
University of Washington, Box 352400, Seattle, WA 98195
Ph: (206)616-2310 Fax: (206)543-0217 email jherm@aa.washington.edu

H. Johari and E. Ghaem-Maghami
Worcester Polytechnic Institute,
Worcester MA 01609

D.P. Stocker and U. G. Hegde
NASA Glenn Research Center,
Cleveland, OH 44135

The objective of this experiment is to better understand the combustion behavior of pulsed, turbulent diffusion flames by conducting experiments in microgravity. The fuel jet is fully-modulated (i.e., completely shut off between pulses) by an externally controlled valve system leading to enhanced fuel/air mixing compared to acoustically excited or partially-modulated jets[1].

Experiments are conducted both in laboratories at UW and WPI and in the GRC 2.2s Drop Tower. A single fuel nozzle with diameter d = 2 mm is centered in a combustor 20 × 20 cm in cross section and 67 cm in height. The gaseous fuel flow (ethylene or a 50/50 ethylene/nitrogen mixture by volume) is fully-modulated by a fast-response solenoid valve with injection times from τ = 4 to τ = 300 ms. The nominal Reynolds number based on the fuel velocity during injection, U_{jet}, is 5,000. A slow oxidizer co-flow properly ventilates the flame[2] and an electrically heated wire loop serves as a continuous ignition source. Diagnostic techniques include video imaging, fine-wire thermocouples and thermopile radiometers, and gas sampling and standard emissions instruments (the last in the laboratory only).

The normalized flame lengths of fully-modulated diffusion flames consisting of isolated, non-interacting structures at low duty cycle, α (i.e., low jet-on fraction) are shown in Fig. 1. The flame length scales well with the parameter $P(1+\psi)^{1/3}$, where $P \equiv (U_{jet}\tau/d)^{1/3}$ and ψ is the stoichiometric air/fuel ratio[1]. The linear scaling persists to $P \approx 8$ where a transition from compact puffs to elongated flame structures begins. The visually-observed celerity of flame puffs near burn-out is generally less in microgravity than in normal gravity and the flame puffs in microgravity generally take a longer time to burn out. These two effects appear to be offsetting, with the result that the flame length of isolated, compact puffs in the linear scaling region is insensitive to buoyancy. By contrast, the mean length of flames with elongated, isolated structures ($P > 8$) does increase as buoyancy is removed.

The flame length in fully-modulated diffusion flames can also be significantly impacted by the off-time (or duty cycle) as shown in Fig. 2. Decreasing the off-time causes the discrete fuel puffs to give way to more closely-packed, interacting flame structures, which lead in turn to a longer flame length. This effect is greatest for the most compact puffs with the shortest injection time (lowest values of P). An example of a microgravity flame at a duty cycle sufficiently high to result in significant structure-structure interaction is shown in Fig. 3.

The combination of increasing flame puff size and decreasing puff celerity with downstream distance changes the separation between puffs, effectively increasing the duty cycle locally. This effect is greater in microgravity than in normal gravity due to the lower celerity in the former case, suggesting that the change in flame length with increasing injection duty cycle is correspondingly greater in microgravity. This is in qualitative agreement with the experiments.

Buoyancy appears to have a strong effect on the thermal characteristics of fully-modulated turbulent diffusion flames[3]. The cycle-averaged centerline temperatures are generally higher in the microgravity flames than in normal gravity, especially at the flame tip where the difference was as much as 200 K. The highest average centerline temperature (Fig. 4) appears to decrease, then to become roughly constant as P is increased. The transition occurs at $P \approx 8$ (similar to value for the transition in flame length mentioned previously).

The highest emission indices of CO and unburned hydrocarbons (UHC) were found for compact, isolated puffs and were roughly an order of magnitude higher than emissions from elongated flames[4]. The levels of CO, UHC, and NOx for all fully-modulated flames approached the low, steady-flame values for a duty cycle of approximately $\alpha \geq 0.4$, with a flame length significantly shorter than that of the steady flame. All emissions data were acquired in 1-g; the emissions levels of flames in microgravity have not yet been investigated.

This work is sponsored by NASA Glenn Research Center under Agreements NCC3-673 and NNC04AA37A.

References

[1] Hermanson, J.C., Dugnani, R., and Johari, H., *Comb. Sci. Tech.* **155**, 203-225, 2000.
[2] Hermanson, J.C., Usowicz, J., Johari, H., and Sangras, R., *AIAA Journal* **40** (7), 2002.
[3] Page, K.L., Stocker, D.P, Hegde, U.G., Hermanson, J.C. and Johari, H., *Third Joint Meeting of the U.S. Sections of The Combustion Institute*, Chicago, IL, March, 2003.
[4] Johari, H., Ghaem-Maghami, E., and Hermanson, J.C., *Combustion Science and Technology,* in press, 2004.

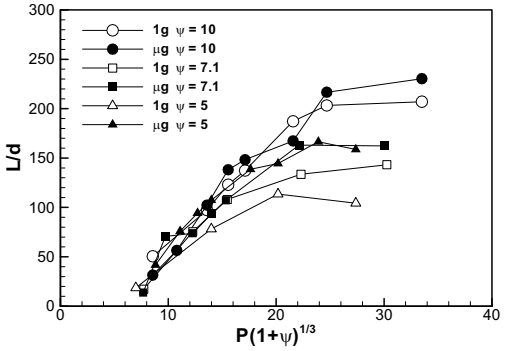

Fig. 1 Normalized flame length for fully-modulated flames.

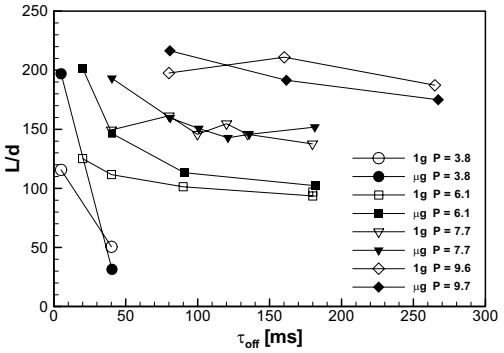

Fig. 2 Effect of injection off-time on normalized flame length for fully-modulated flames for $\psi = 10$.

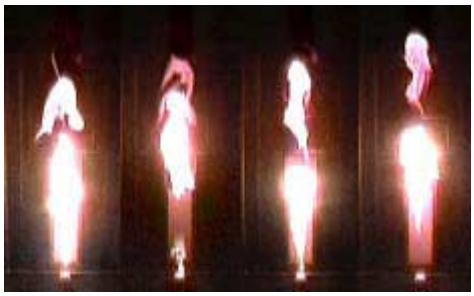

Fig. 3 Sequence of fully-modulated flames in microgravity showing the merging of large-scale turbulent structures. $P = 7.6$, $\alpha = 0.5$.

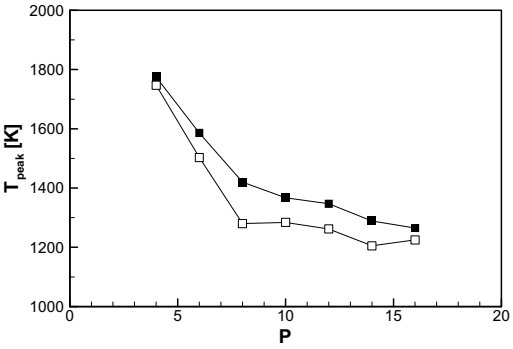

Fig. 4 Highest values of the average centerline temperature.

PROBLEM STATEMENT

Fundamental issues in turbulent, non-premixed flames include the nature of the interaction between the dominant large-scale structures and the implications of these dynamics for air entrainment, the air/fuel mixing, combustion temperatures, and exhaust emissions. In normal gravity, the evolution of the turbulent structure of pulsed diffusion flames is governed by a combination of momentum-driven and buoyant instabilities. The removal of buoyancy in microgravity can thus be expected to have a significant effect on the characteristics of fully-modulated flames, as well as on steady flames.

APPROACH

This research employs a fully-modulated fuel injection approach in both normal- and microgravity. In this approach the fuel is completely shut off between pulses, positively controlling the generation and interaction of the large-scale turbulent flame structures. By regulating both the injection time as well as the jet off-time and thereby the injection duty cycle (the jet-off fraction of each pulsing cycle as set by the fuel valve controller), it is possible to study turbulent flames under conditions ranging from isolated structures, to interacting structures, to steady flames. Diagnostic techniques include video imaging of the visible flame, thermocouple temperature measurement, and measurement of stable emissions species.

Specific issues include the effects of buoyancy on large-scale structure growth, the nature of the dynamic interaction between neighboring structures, and the implications for air entrainment, air/fuel mixing, combustion temperatures, and exhaust emissions.

COMBUSTOR CONFIGURATION AND FLOW CONDITIONS

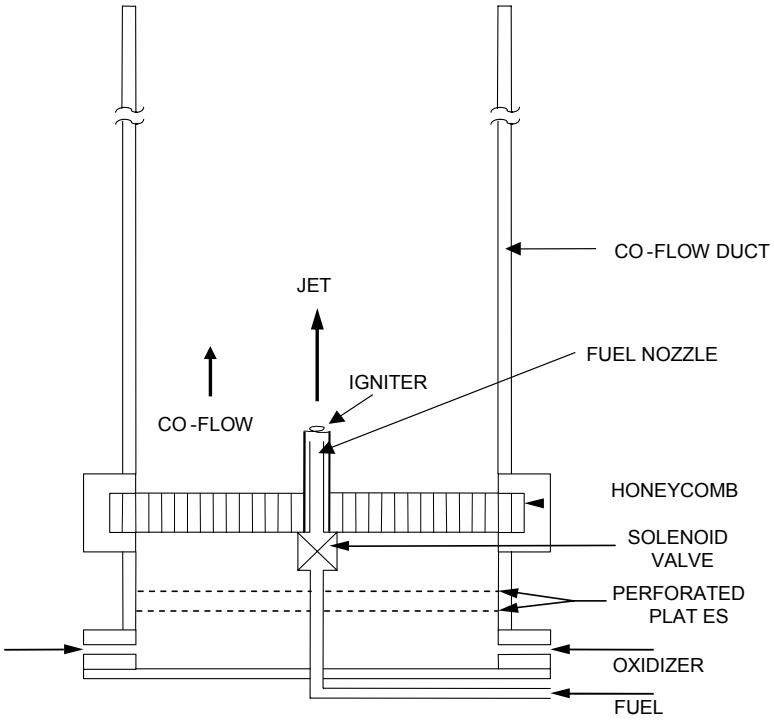

- Nozzle: 2 mm i.d.
- Combustor X- section: 20 x 20 cm
- Duct height: 56 cm
- Fuels: 50/50 C_2H_4/N_2; C_2H_4
- Fuel flow: Re_d = 5000
- Injection time: τ = 4 to 300 ms
- Jet off-time: τ_{off} = 4 to 500 ms
- Duty cycle: 0.02 – 0.9
- Co-flow: 21/79 O_2/N_2 ; 30/70 O_2/N_2
- Air/fuel ratio ψ = 5-14.3
- Co-flow : $\approx$ 0.5% of jet velocity
- Reactants: unheated
- Pressure: $\approx$ 1 atm

Puff injection parameter $P = (U_{jet}\,\tau/d)^{1/3}$ *where* U_{jet} = jet-on injection velocity

TURBULENT DIFFUSION FLAMES IN MICROGRAVITY

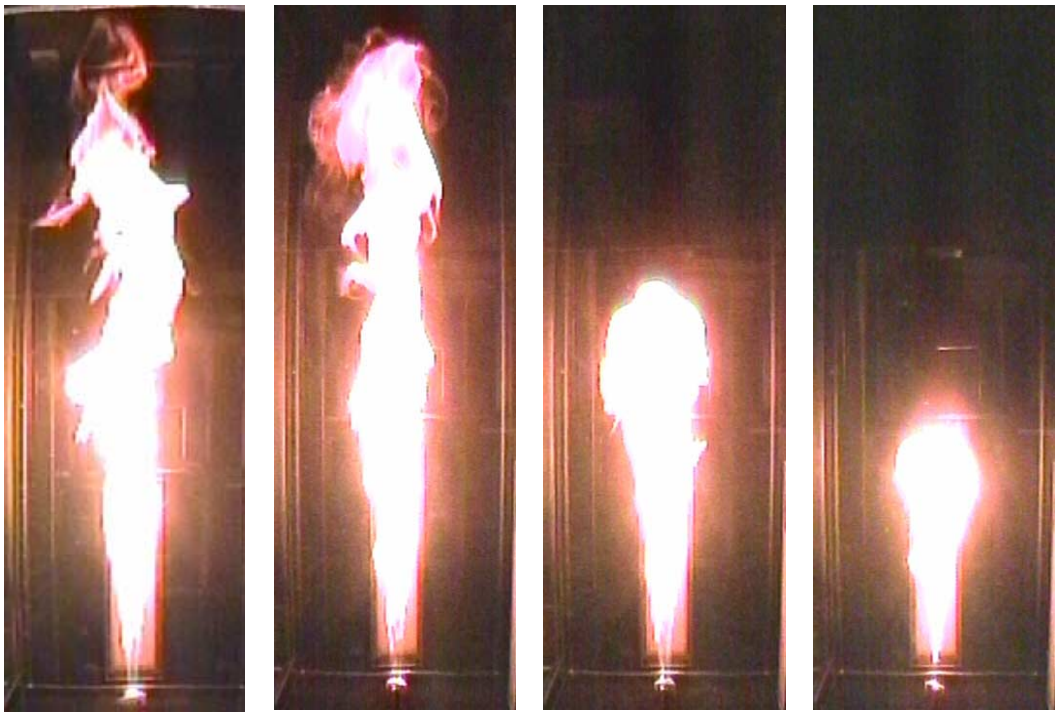

a) b) c) d)

Turbulent ethylene/(30% oxygen in nitrogen) diffusion flames in microgravity near the end of the injection interval. a) Steady flame, b) fully-modulated flame with injection time τ = 300 ms, P = 15; c) fully-modulated flame with τ = 200 ms, P = *13*; d) fully-modulated flame with τ = 40 ms, P = *7.7*. The vertical extent of all images is 55 cm.

FULLY-MODULATED FLAME SEQUENCES

Top, 1g; bottom, μg.

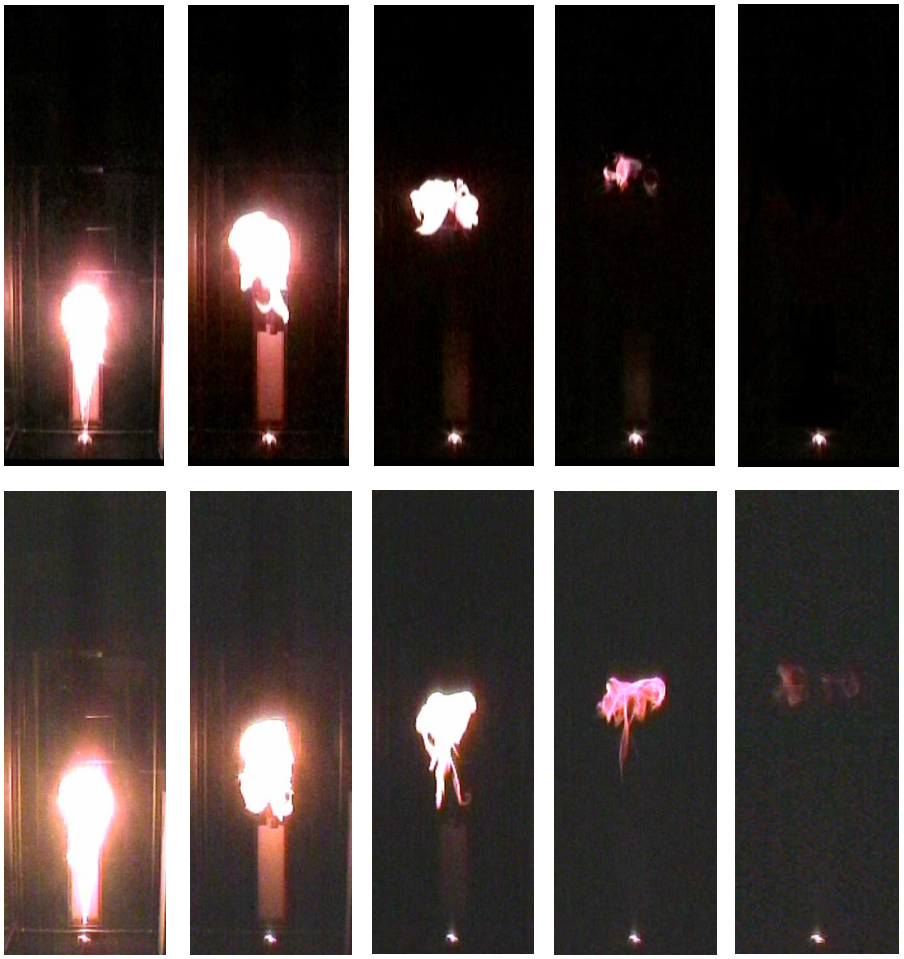

Fully-modulated ethylene/(30% oxygen in nitrogen) flames for τ = 40 ms, P = 7.7. Time between images 33 ms. The sequences proceed from left to right. The image heights are 56 cm.

The celerity of the visible flame puff near burn-out is lower in microgravity than in normal gravity. These isolated microgravity flame puffs also exhibit a longer time to burn-out than puffs in normal gravity.

$P \approx 8$ is the approximate upper limit for puff-like flame structure; for higher P more elongated structures result.

MEAN FLAME LENGTH OF ISOLATED, FULLY-MODULATED DIFFUSION FLAME STRUCTURES

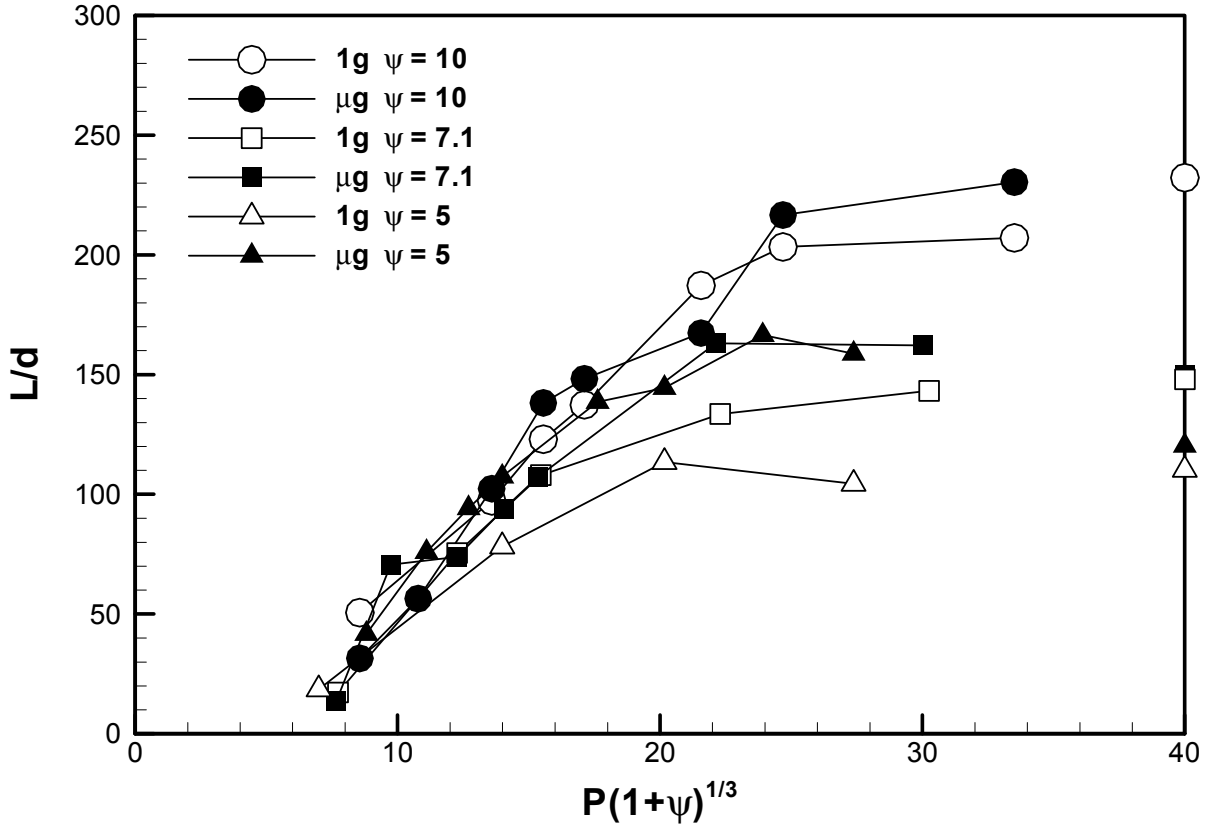

The flame lengths for steady flames are shown at $P(1+\psi)^{1/3} = 40$ for reference. The length of isolated (i.e., long off-time) fully-modulated flame puffs scales as $L/d \sim (1+\psi)^{1/3} P$ for $P \leq 8$.

MEAN FLAME LENGTH OF FULLY-MODULATED DIFFUSION FLAMES WITH INTERACTING STRUCTURES

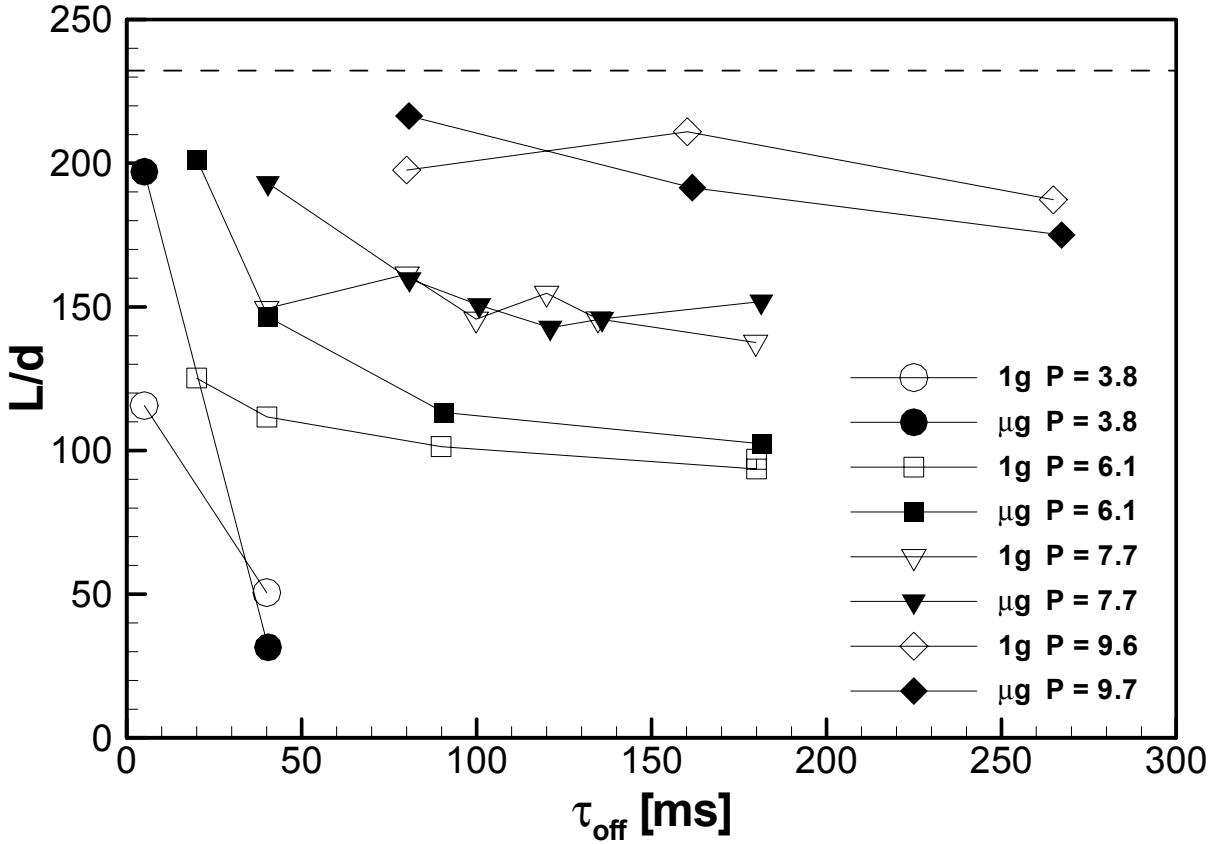

ψ = 10. The dashed line shows the length of steady flames. The flame length of puffs with the shortest injection time (smallest *P*) are influenced most by the interaction with nearby puffs as the off-time is decreased.

COMBUSTION TEMPERATURES AND EMISSIONS OF FULLY-MODULATED DIFFUSION FLAMES

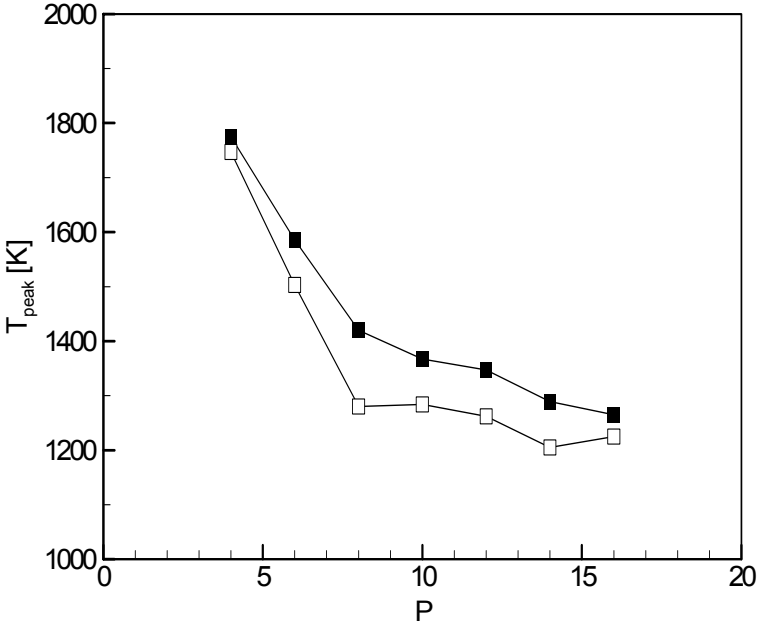

Peak values, along the flame axis, of the cycle-averaged centerline temperature as a function of *P*. ψ = 7.1. Normal gravity (open symbols) and microgravity (solid symbols). A transition in temperature is apparent at $P \approx 8$.

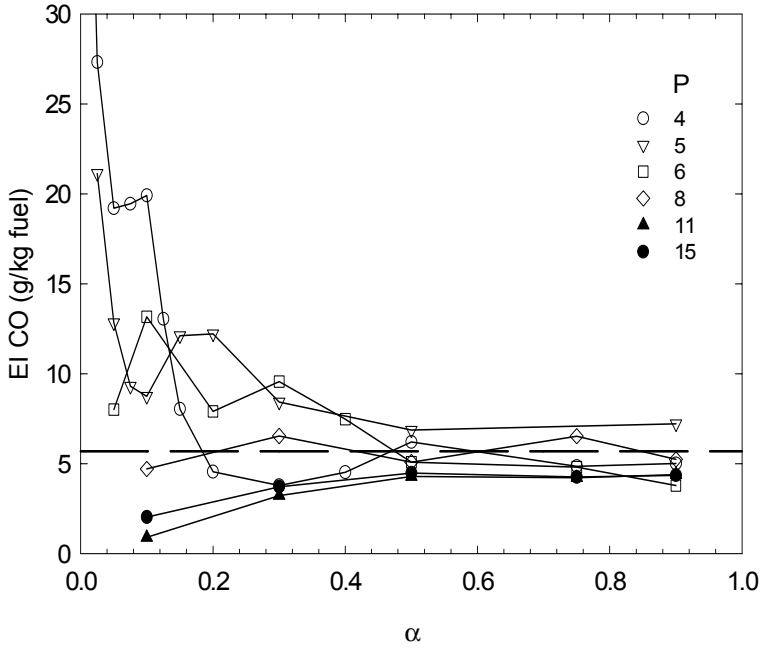

Exhaust CO emissions of fully-modulated flames in normal gravity. ψ = 14.3. For all injection times low CO emissions comparable to that of the steady flame (dashed line) are achieved for duty cycles of $\alpha \geq 0.5$.

SUMMARY OF KEY RESULTS

- The mean flame length of isolated puffs in microgravity appears comparable to that of similar puffs in normal gravity, and scales in both cases with $P(1+\psi)^{1/3}$ up to a value of $P \approx 8$. $P \approx 8$ is the approximate upper limit for puff-like flame structure; for higher P more elongated structures result. The flame lengths for steady-state flames were also not significantly impacted by the elimination of buoyancy in microgravity. The flame length of isolated, elongated flame structures ($P > 8$) however does increase with the removal of buoyancy.

- In contrast to the case of isolated flame puffs, the flame length of interacting, fully-modulated puffs can be significantly impacted by the removal of buoyancy, with an increase is flame length most apparent for the shortest injection times.

- Buoyancy has a strong effect on the time-averaged centerline temperatures of fully-modulated flames, with the temperatures in μg generally higher than in 1g.

- The highest exhaust emission indices of CO (also unburned hydrocarbons) were found for compact, isolated puffs and were roughly an order of magnitude higher than emissions from elongated flames. The levels of all emissions for fully-modulated flames approached the low, steady-flame values for a duty cycle of approximately 0.4. The emissions levels of fully-modulated turbulent jet flames in microgravity are not known at present.

MAJOR CONCLUSIONS

- For some injection conditions, buoyancy has a significant impact on the mean flame length and, by implication, on the rate of oxidizer entrainment and mixing. The largest impact of buoyancy occurs for compact, interacting puffs. The lack of sensitivity of flame length to buoyancy for isolated, fully-modulated flame puffs is believed to be related to offsetting changes in flame puff celerity and time to burnout for the microgravity versus normal gravity cases.

- Several characteristics of fully-modulated flames appear to undergo a transition for a value of the injection parameter of approximately $P = 8$. For injection times corresponding to higher values of P the following occur: 1) a transition from compact, puff-like structures to more elongated structures, 2) a deviation from a linear scaling of flame length with $(1+\psi)^{1/3} P$ for isolated structures, and 3) a change in the time-averaged centerline temperatures, leading to a value less sensitive to injection time than for the case of low P.

- As the duty cycle is increased the emissions levels of fully-modulated flames approach those of steady flames. At the same time, the flame length can be significantly shorter than that of the steady flame (by as much as 50%). The fully-modulated injection technique thus appears to have the potential to provide for compact, low-emissions turbulent jet diffusion flames.

Flammability Configuration Analysis for Spacecraft Applications

David Hirsch

Flammability of Flight Hardware - Technical Requirements

- NASA-STD-6001
- NSTS 1700.7B - Safety Policy and Requirements for Payloads Using the Space Transportation System
- SSP 30233 - Space Station Requirements for Materials and Processes

Flammability of Flight Hardware - Technical Requirements

NSTS 1700.7B -

- **tailors NASA-STD-6001 by exempting materials used in small quantities (< 0.1 lb or 10 in in manned crew compartments and < 1 lb and/or 12 linear inches for external materials)**
- **requires a flammability assessment per NSTS 22648**

Flammability of Flight Hardware - Technical Requirements (Continued)

SSP 30233

- **requires Material Usage Agreements (MUA) for hardware containing materials failing NASA-STD-6001 requirements.**
- **MUA's are supported by analysis per NSTS 22648**

Flight Hardware Configuration Flammability Assessment - NSTS 22648

- Evaluate the overall hardware configuration
- Evaluate the way in which the hardware will be used
- Identify the major materials to be assessed
- Determine fire propagation paths
- Evaluate ability of containers to contain fire

Material Usage Agreements SSP 30233 Flammability Rationale Codes - Examples

Code	Rationale
104	sandwiched between non-flammable material and no Ignition source (IS) or propagation path (PP)
105	minor usage; no IS or PP
106	used in a sealed container

MUA's - SSP 30233 Flammability Rationale Codes - Examples (Continued)

Code	Rationale
108	off the shelf equipment having material acceptable in configuration; no IS or PP
112	overcoated with a non-flammable material

TWO-FLUID MODEL AND INTERFACIAL AREA TRANSPORT IN MICROGRAVITY CONDITION

Mamoru Ishii[♣], Xiaodong Sun, and Shilp Vasavada
School of Nuclear Engineering, Purdue University, West Lafayette, Indiana

The objective of the present study is to develop a two-fluid model formulation with interfacial area transport equation applicable for microgravity conditions. The new model is expected to make a leapfrog improvement by furnishing the constitutive relations for the interfacial interaction terms with the interfacial area transport equation, which can dynamically model the changes of the interfacial structures. In the first year of this three-year project supported by the U.S. NASA, Office of Biological and Physics Research, the primary focus is to design and construct a ground-based, microgravity two-phase flow simulation facility, in which two immiscible fluids with close density will be used.

In predicting the two-phase flow behaviors in any two-phase flow system, the interfacial transfer terms are among the most essential factors in the modeling. These interfacial transfer terms in a two-fluid model specify the rate of phase change, momentum exchange, and energy transfer at the interface between the two phases. For the two-phase flow under the microgravity condition, the stability of the fluid particle interface and the interfacial structures are quite different from those under normal gravity condition. The flow structure may not reach an equilibrium condition and the two fluids may be loosely coupled such that the inertia terms of each fluid should be considered separately by use of the two-fluid model. Previous studies indicated that, unless phase-interaction terms are accurately modeled in the two-fluid model, the complex modeling does not necessarily warrant an accurate solution.

Traditionally, the interfacial area concentration, one of the parameters characterizing the interfacial structure, is specified by empirical correlations that are based on the two-phase flow regimes and regime transition criteria. In view of this, the focus of many studies for the microgravity two-phase flow was on identifying the flow regime transition or transition criteria. However, this approach has the following shortcomings:

1. The flow regime transition criteria are algebraic relations for steady-state fully-developed flows. They do not fully reflect the true dynamic nature of changes in interfacial structures. Hence the effects of the entrance and developing flow cannot be taken into account correctly, nor the gradual transition between the flow regimes. Under the microgravity conditions, the flow structure may not reach an equilibrium configuration. Therefore, the flow regime dependent constitutive relations developed for the steady-state fully-developed two-phase flow are not suitable.
2. The method based on the flow regime transition criteria is a two-step method, which requires the flow regime transition criteria and the regime dependent closure relations for the interfacial area.

[♣] PI: School of Nuclear Engineering, 400 Central Drive, Purdue University, West Lafayette, IN 47907; email: ishii@ecn.purdue.edu; Tel: 765-494-4587; Fax: 765-494-9570.

3. The flow regime dependent correlations and criteria may be valid only in limited parameter ranges for certain specific operational conditions. When applied to the microgravity two-phase flow conditions, these models may cause significant discrepancies and artificial discontinuities.

To better represent the effects of the interfacial structure and the flow regime transition, the use of the dynamic equation to characterize the interfacial area transport has been proposed and is currently being pursued. Based on the current developments in the normal gravity two-phase flow, the interfacial area transport equation can be considered a rational choice in providing a closure relation for the interfacial area concentration for the microgravity two-phase flow. Through mechanistic modeling of various fluid particle interactions, the interfacial area transport equation can closely model the two-phase flow evolution across the flow regime transition boundaries, and thus prevent artificial discontinuities. Furthermore, the recent studies suggest the significance of investigation on particle interaction mechanisms in the evolution of two-phase structures (Colin et al., 1991; Hewitt, 1996; Takamasa et al., 2002). It is expected that the interfacial area transport equation can significantly improve the current capability of the two-fluid model from both scientific and practical viewpoints.

To benchmark the theoretical model, ground-based tests by employing two immiscible fluids with similar density is being performed to simulate the microgravity condition in the first phase of this research. A detailed scaling analysis is being performed to closely simulate the gas-liquid two-phase flow in the microgravity condition. Both the global and local two-phase flow parameters will be acquired by the state-of-the-art instrumentation, namely, multi-sensor conductivity probes, multi-sensor void-meter, and LDA system, along with detailed flow visualization and image analysis. Following the first stage experiment, the second stage experiment is to be performed with the gas-liquid two-phase flow in the in-flight or drop-tower microgravity facilities.

Currently, the design of the test facility has been basically completed. Through a detailed preliminary study, water and Therminol 59, which has a density of 971 kg/m^3 at 20^{o}C, have been chosen as the two fluids to simulate microgravity environment on ground. Round pipes with 25.4 and 304.8 mm internal diameter have been selected as the test sections. The construction of the facility is expected to be completed and tested by the end of September 2004.

REFERENCES

Colin, C., Fabre, J. and Dukler, A.E., 1991, "Gas-liquid Flow at Microgravity Conditions-1. Dispersed Bubble and Slug Flow," *Int. J. Multiphase Flow*, 17, pp. 533-544.

Hewitt, G.F., 1996, "Multiphase Flow: The Gravity of the Situation," *NASA-CP-3338*, Proc. of the Third Microgravity Fluid Physics Conf., July 13-15, 1996, pp. 3-23.

Takamasa, T., Iguchi, T., Hazuku, T., Hibiki, T. and Ishii, M., 2002, "Interfacial Area Transport of Bubbly Flow under Microgravity Environment," To be published in *Int. J. Multiphase Flow*.

NASA/CP—2004-213205/VOL2

Two-fluid Model and Interfacial Area Transport under Microgravity Condition

Workshop on Strategic Research to Enable NASA's Exploration Missions
June 22-23, 2004, Cleveland, Ohio

M. Ishii, X. Sun and S. Vasavada
Thermal-Hydraulics and Reactor Safety Laboratory
School of Nuclear Engineering, Purdue University

Supported by:
National Aeronautics and Space Administration
Office of Biological and Physical Research
(Managed by the NASA Glenn Research Center)

Research Motivation

- Need of Gas-liquid Two-phase Flow Systems for Future Manned Deep Space Exploration
  - Advanced life support operations
  - Power generation
  - Propulsion
- Limited Understanding of Two-phase Flows under a Microgravity Environment
  - No apparent characteristic internal length scale
  - Flow may not reach an equilibrium configuration
- Predictive Models for Two-phase Flows Developed for Earth Application: Inadequate for a Microgravity Environment
- Previous Research Concentrated on Flow Regime Identification, Pressure Drop Prediction, Pool and Flow Boiling, and Corresponding Scaling Studies

Research Objectives

- To Develop Framework of the Two-fluid Model Formulation with Interfacial Area Transport Equation (IATE) Applicable to Space Microgravity Conditions
- To Perform Liquid-liquid Experiments on Ground to Simulate Two-Phase Flows under Microgravity Conditions
  - To Establish a database of key two-phase flow parameters
- To Develop the IATE Applicable to Microgravity Conditions
  - To model the constitutive relations for the IATE through mechanistic modeling of fluid particle interactions
  - To Investigate the relative motion between phases
- To Study Scaling Issues between Earth and Microgravity Two-phase Flows (Optional)

Technical Approach

- Theoretical Approach
  - Two-fluid Model with IATE
  - Mechanistically modeling of fluid particle interactions
- Experimental Study
  - Simulation of microgravity two-phase flows in earth based on liquid-liquid experiments
    - Two immiscible fluids with similar density
  - Focus on low and medium inertia regions
  - Two sizes of test sections: 2.5 and 30.5 cm ID round Pyrex glass pipes
  - Advanced instrumentation
    - Electrical: Multi-sensor conductivity probe and Impedance void probe
    - Optical: Laser Doppler anemometry and High-speed photography

Two-fluid Model

- Two-fluid Model (Vernier and Delhaye, 1968; Kocamustafaogullari, 1971; Ishii, 1975; Drew and Lahey, 1979)
  - Considers each phase separately
  - Macroscopic fields of one phase are coupled to the other phase
  - Interfacial transfer terms in the conservation equations
- (Interfacial Transfer): ~ (Interfacial Area Conc.) ×(Driving Potential)
- a_i: Interfacial Area Concentration

$$a_i = \frac{\text{Interfacial Area}}{\text{Mixture Volume}}$$

  - Characterizes the geometric "capacity" for interfacial transfer
- Conventional Approach for a_i: Flow Regime-dependent Correlations/Models
  - Flow regime identified by flow regime map or regime transition criteria (Bubbly, Slug, Churn, …)
  - Difficulty of modeling effects of entrance, flow development, and phase change

Interfacial Area Transport Equation

- Dynamic Approach for Interfacial Structure Modeling, Consistent with the Two-fluid Model (Ishii, '75)
- To Predict Evolution of Interfacial Structures Dynamically
- Foundation of IATE (Ishii and Kocamustafaogullari, '95)
- One-group IATE (Wu et al., '98; Kim, '99)

$$\frac{\partial a_i}{\partial t}+\nabla\cdot\left(a_i\vec{v}_i\right)=\frac{2a_i}{3\alpha}\left[\frac{\partial\alpha}{\partial t}+\nabla\cdot\left(\alpha\vec{v}_g\right)-\eta_{\mathrm{ph}}\right]+\sum_j\phi_j+\phi_{\mathrm{ph}}$$

  - Fluid particle interactions: Coalescence and Disintegration

    (Focus of the current research)
  - Phase change: Nucleation and Condensation

Experimental Study

- Working Fluids
  - Water and Therminol 59 (Alkyl Substituted Aromatic with a density of 971 kg/m^3 at 20^{o}C, 2.7% difference with water)
  - Relatively easy separation based on gravity
  - Interfacial tension measurement (Technique based on Rashidnia *et al.*, '94): $0.037^{+4\%}_{-9\%}$ N/m

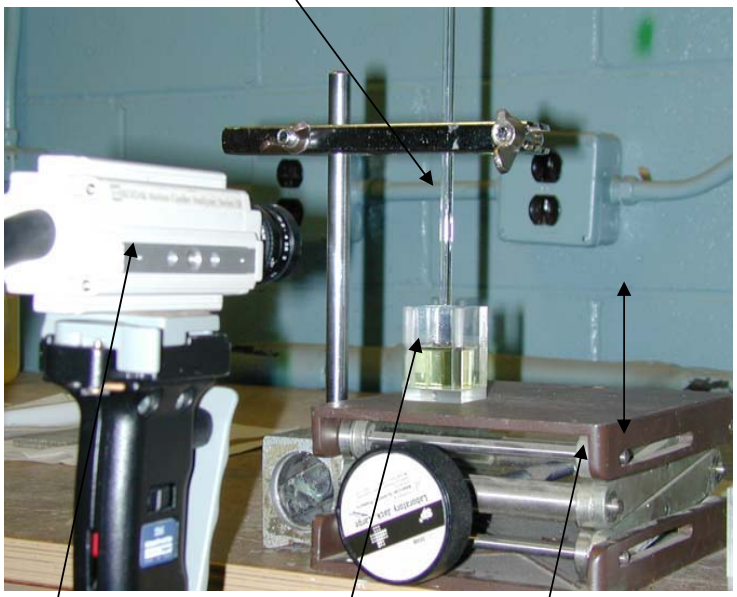

Present setup for interfacial tension measurement

Therminol 59 "bubbles" injected into stagnant water

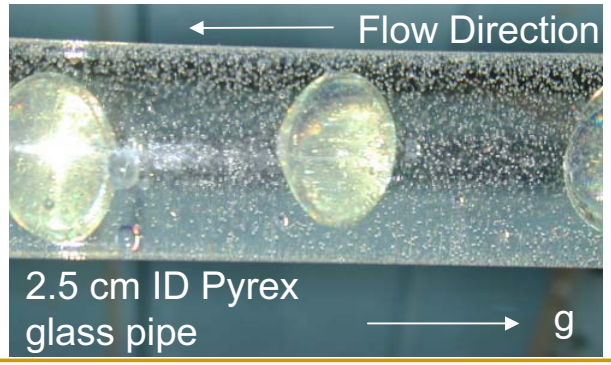

Experimental Facility and Instrumentation

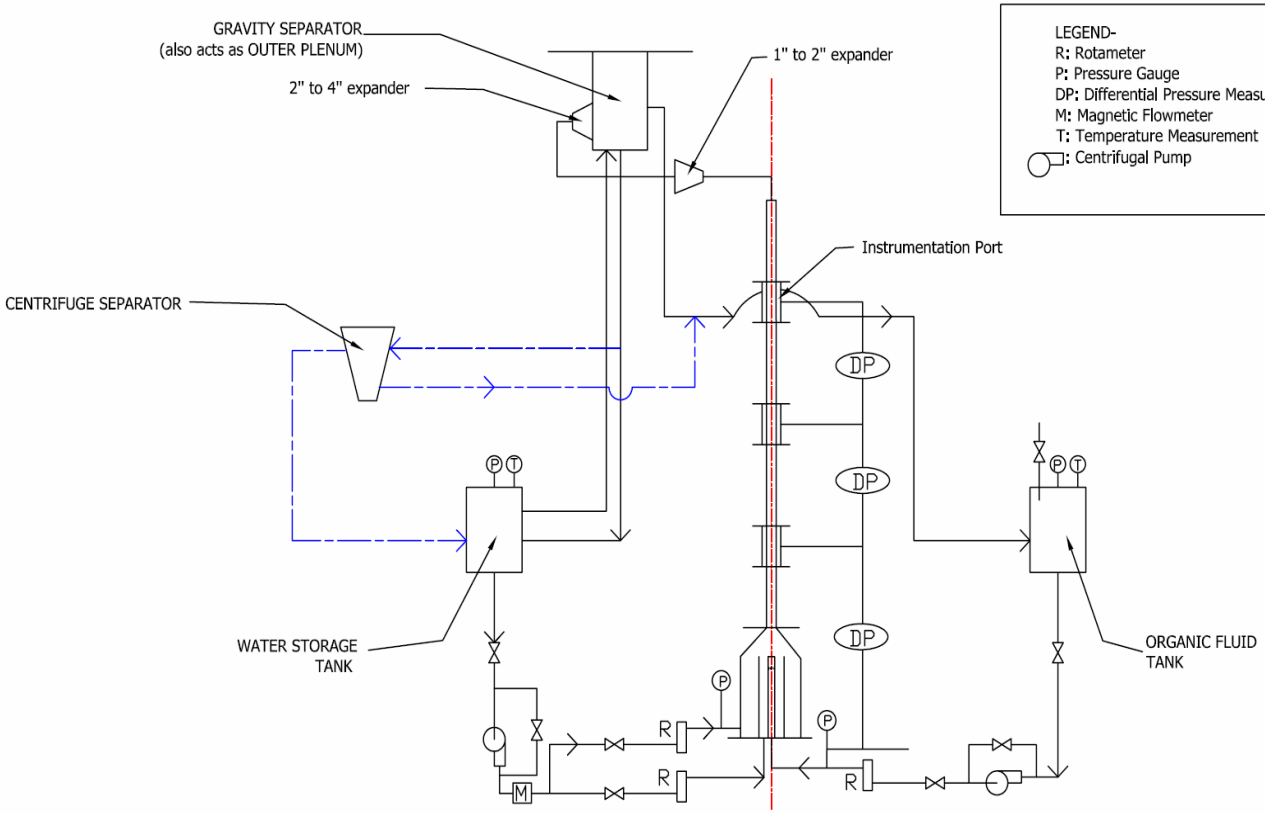

Schematic of the experimental facility for 2.5 cm ID test section

Impedance void probe

Instrumentation and Data Acquisition

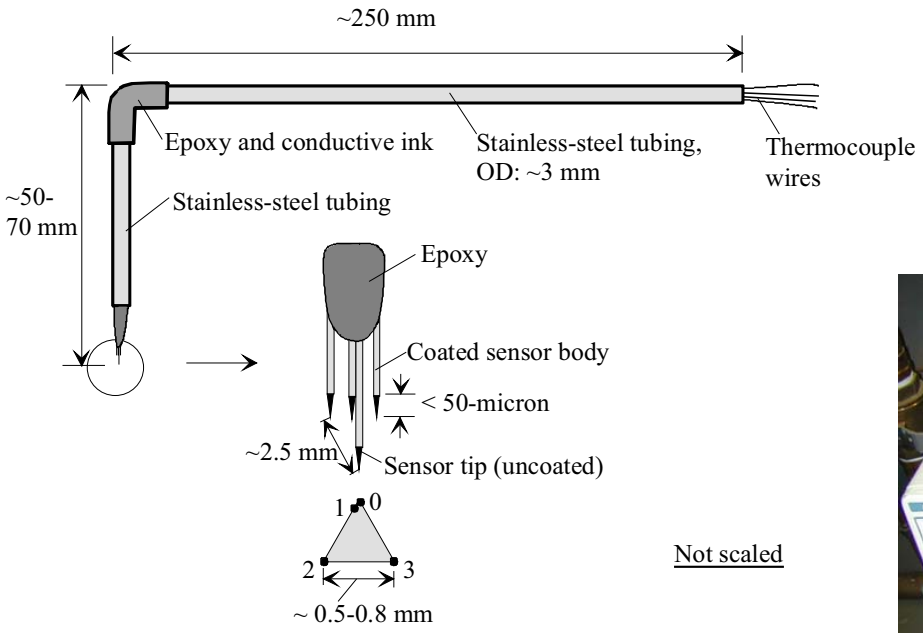

Schematic of four-sensor conductivity probe

Data acquisition

Four-sensor conductivity probe can measure local time-averaged fluid fraction, interfacial area concentration, fluid particle velocity and size

Current Status

- Literature survey has been carried out
- Technical approach has been preliminarily developed
- Possible fluid particle interaction mechanisms have been identified
- Working fluids have been selected
- Experimental facility design has been completed
- Instrumentation has been selected and the applicability has been preliminarily tested
- Surface tension parameter between the working fluids has been measured in house
- Major components of the facility have been purchased or machined
- Construction of the facility is ongoing

Aeolian sand transport with collisional suspension

James T. Jenkins,[1] José Miguel Pasini,[1] and Alexandre Valance[2]

[1] *Department of Theoretical and Applied Mechanics, Cornell University, Ithaca, NY 14853*
[2] *Groupe Matière Condensée et Matériaux, Université Rennes1, Campus Beaulieu-Bât11A, 35042 Rennes cedex*

Aeolian transport is an important mechanism for the transport of sand on Earth and on Mars. Dust and sand storms are common occurrences on Mars and windblown sand is responsible for many of the observed surface features, such as dune fields. A better understanding of Aeolian transport could also lead to improvements in pneumatic conveying of materials to be mined for life support on the surface of the Moon and Mars.

The usual view of aeolian sand transport is that for mild winds, saltation is the dominant mechanism, with particles in the bed being dislodged by the impact of other saltating particles, but without in-flight collisions. As the wind becomes stronger, turbulent suspension keeps the particles in the air, allowing much longer trajectories, with the corresponding increase in transport rate. We show here that an important regime exists between these two extremes: for strong winds, but before turbulent suspension becomes dominant, there is a regime in which in-flight collisions dominate over turbulence as a suspension mechanism, yielding transport rates much higher than those for saltation. The theory presented is based on granular kinetic theory, and includes both turbulent suspension and particle-particle collisions. The wind strengths for which the calculated transport rates are relevant are beyond the published strengths of current wind tunnel experiments, so these theoretical results are an invitation to do experiments in the strong-wind regime.

In order to make a connection between the regime of saltation and the regime of collisional suspension, it is necessary to better understand the interaction between the bed and the particles that collide with it. This interaction depends on the agitation of the particles of the bed. In mild winds, collisions with the bed are relatively infrequent and the local disturbance associated with a collision can relax before the next nearby collision. However, as the wind speed increases, collision become more frequent and the agitation need not decay completely. In the regime of collisional suspension, the particles near the surface of the bed are assumed to be in a state of constant agitation. We indicate the conditions at the bed corresponding to the limits of saltation and collisional suspension and outline experiments, simulations, and modeling that have been undertaken to bridge these limits.

Aeolian sand transport with collisional suspension

James T. Jenkins and José Miguel Pasini
Department of Theoretical and Applied Mechanics, Cornell University, Ithaca, NY 14853, USA

Alexandre Valance
Groupe Matière Condensée et Matériaux, Université Rennes1,
Campus Beaulieu–Bât 11A, 35042 Rennes cedex, France

Aeolian transport is an important mechanism for the transport of sand on Earth and on Mars. Understanding the natural process can also yield insight on improving the pneumatic conveying of materials to be mined for life support on the Moon and Mars. For mild winds, a few particles are in the air, but as the wind becomes stronger, the concentration of particles aloft increases, until in-flight particle collisions start to play a role. Along with this, particle-bed collisions become more frequent, and the bed behavior may change drastically, from an essentially quiescent bed to a dense agitated system. We present here a combination of experiments, simulations, and modeling that has been undertaken to understand the transition from weak to very strong winds. In particular, a collisional model that includes turbulent suspension shows that particle-particle collisions may dominate over turbulence as a suspension mechanism. Results from collisionless saltation simulations are also used to obtain an upper bound for the relaxation time of the bed.

I. INTRODUCTION

Dust and sand storms are common occurrences on Mars, and windblown sand is responsible for many of the observed surface features, such as dune fields. A better understanding of aeolian transport could also lead to improvements in pneumatic conveying of materials to be mined for life support on the surface of the Moon and Mars. Understanding the dominant mechanisms for long-term transport can also lead to understanding ancient wind regimes [1].

Figure 1 shows the different scales involved in aeolian sand transport: from dune fields that affect local winds to the few centimeters above the bed where most of the transport takes place. This study deals with the processes in the latter part. This separation of the global and local processes is possible due to the difference in scales between dune evolution times (months to centuries) and local saturation times (seconds). A dune evolution model must then combine the knowledge at all levels to predict the evolution of the surface topography [2, 3].

The usual view of aeolian sand transport is that for mild winds, saltation is the dominant mechanism, with particles in the bed being dislodged by the impact of other saltating particles, but without in-flight collisions. As the wind becomes stronger, turbulent suspension keeps the particles in the air, allowing much longer trajectories, with the corresponding increase in transport rate. We show here that between these two extremes we may have another important suspension mechanism: particle-particle collisions. This mechanism yields transport rates much higher than those predicted for saltation. The theory presented is based on granular kinetic theory, and includes both turbulent suspension and particle-particle collisions.

In order to make a connection between the regime of saltation and the regime of collisional suspension, it is necessary to better understand the interaction between the bed and the particles that collide with it. This interaction depends on the agitation of the particles of the bed. In mild winds, collisions with the bed are relatively infrequent and the local disturbance associated with a collision can relax before the next nearby collision. How-

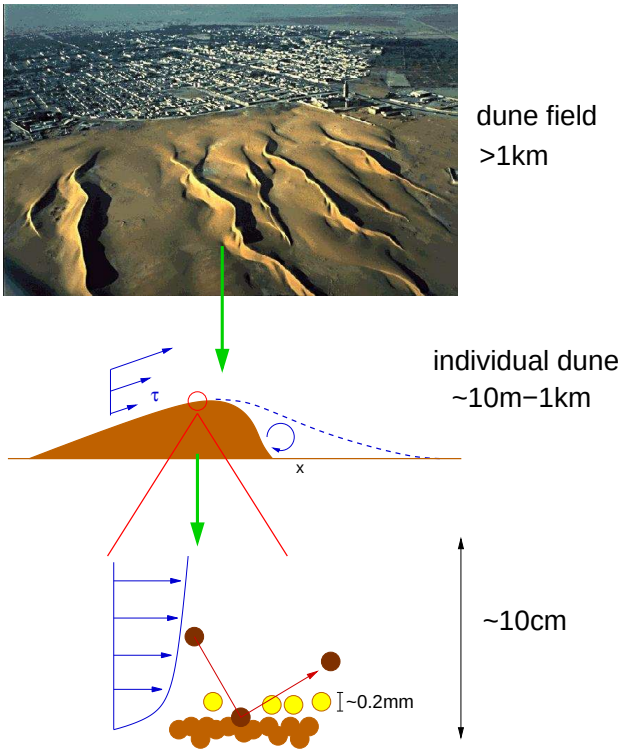

FIG. 1: Scales involved in the evolution of dunes. Upper photograph: Landsat picture of dunes encroaching on Nouakchott, the capital of Mauritania.

ever, as the wind speed increases, collisions become more frequent and the agitation need not decay completely. In the regime of collisional suspension, the particles near the surface of the bed are assumed to be in a state of constant agitation. The wind strengths for which the calculated transport rates are relevant are at the limit of current current wind tunnel experiments, and the difference between the theory and the experiments is used to provide bounds for the relaxation time of the bed. Thus these results are an invitation to do experiments in the strong-wind regime.

In order to fix notation, the grain diameter is d, gravity is g, and the Shields parameter is θ. The Shields parameter is a dimensionless measure of the free-stream stress: it is the free stream stress normalized by the buoyant weight per unit area of a solid layer of particle material one diameter in thickness.

II. BED IMPACT PROCESSES: SPLASH

For weak winds the particle-bed impacts are infrequent enough that the local agitation introduced by a previous impact has had enough time to decay. In this regime the bed impact process is described by the *splash function*, introduced by Ungar and Haff [4]. Given an impacting particle speed, the splash function gives the expected number of ejected particles and their distribution function. It also gives the distribution for the rebound of the impacting particle. In terms of dilute kinetic theory, the splash function is a complicated wall kernel with memory for the Boltzmann equation (see e.g. [5]).

Experiments on the impact of one grain on different beds were performed in Rennes. First, for two-dimensional granular packings [6], where ordering is an important issue. More recently, impacts on a 3–D disordered bed have been studied [7]. The rebound statistics agree well with those used by Werner [8]. These ongoing experiments are yielding important information on the velocity distribution of the ejecta, and also the ejection time-delay distribution. For $d = 6$ mm particles, the most probable delay is about 0.02 s, or

$$t_{\rm delay} \approx 0.8\sqrt{\frac{d}{g}}.$$

We use this as an order-of-magnitude estimate of the relaxation time of the bed.

III. WEAK WINDS: SALTATION COMPUTATION

For weak winds, the particles in the saltation cloud are few, and they do not collide with each other. We present here computations based on collisionless saltation, following Werner [8]. We solve for the velocity distribution $f(\boldsymbol{v}; y)$ of the grains. The splash function of Ref. [8] is

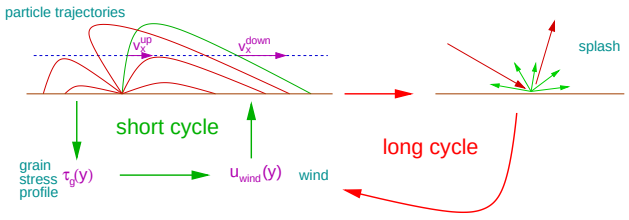

FIG. 2: Integration scheme for the saltation computation.

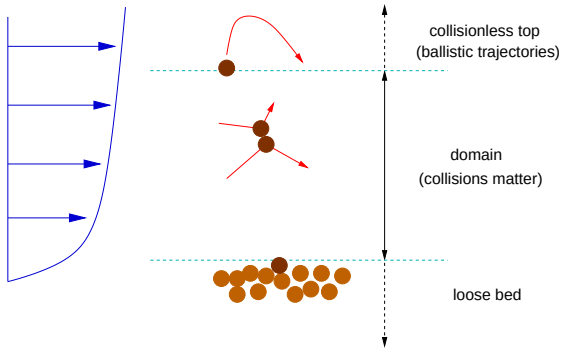

FIG. 3: Division of the domain into collisional and boundary conditions.

a boundary condition for this problem, and the integration method is the following iterative scheme sketched in Fig. 2.

IV. STRONG WINDS: COLLISIONAL MODEL

For strong winds, the number of particles in the air increases, and the particles are driven into collisions with each other. In this study the whole process is divided into three subdomains, as shown in Fig. 3. The middle section is the collisional part, where the model equations are solved. The top and bottom sections are solved in an approximate analytical fashion to yield boundary conditions (for details, see Ref. [9]).

For the middle section the unknown fields are the particle concentration profile $c(y)$, the wind velocity $U(y)$, the particle velocity $u(y)$, the particle stress $s(y)$, the granular temperature $T(y)$, the particle energy flux $q(y)$, and the collisional layer thickness h. *Note that the thickness of the collisional region is obtained as part of the solution.* Since the flow is steady and fully developed, the total shear stress is constant across the system, and it is partitioned into grain- and wind-borne stress. The equations for the particle phase are closed using granular kinetic theory, and the particles interact with the wind through viscous drag. Turbulent fluctuations in the gas are also included in a very simple way, so that the two suspension mechanisms (particle pressure gradient and turbulent suspension) can compete.

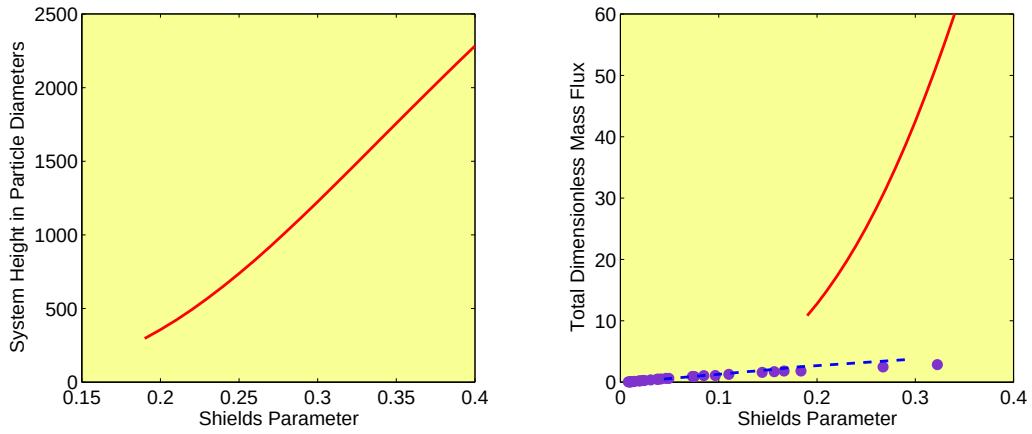

FIG. 4: Height of the collisional layer and dimensionless transport rate for 170 μm grains. Collisional model (solid line), saltation computation (dashed line), and wind tunnel experiments (circles, from Fig. 4b in Ref. [11], courtesy of K. Rasmussen).

Boundary conditions

At the bed we assume that the wind is so strong that it remains agitated bed [10]. This gives boundary conditions for the concentration (random loose packing), the wind and particle velocities (no slip for both), and the flux of particle fluctuation energy.

The particle concentration decreases strongly with increasing distance to the bed. Thus far enough from the bed we assume that the system becomes so rarefied that collisions between particles are neglected, and the trajectories are dominated by drag and gravity. This defines a characteristic particle pressure at the top of the collisional layer. The collisionless layer on top is solved analytically in an approximate way and this, together with the characteristic value of the pressure, gives boundary conditions for the particle stress and the flux of particle fluctuation energy.

V. RESULTS

Figure 4 shows the thickness of the collisional layer and the corresponding transport rate for the collisional model, for particles with $d = 170$ μm. It also shows the transport rate obtained from the collisionless saltation computation, and wind tunnel experiments from Ref. [11]. The collisionless saltation results correspond well to the wind tunnel results. The collisional model, on the other hand, overpredicts the transport rate. This mismatch is used to estimate an upper bound for the relaxation time of the bed.

The collisional model also gives enough particles aloft so that the gradient of particle pressure dominates over turbulent suspension throughout the domain.

Relaxation time for the bed

The validity of the collisional model depends on the validity of its boundary conditions. However, the splash process is a complicated dynamic behavior of a disordered granular packing. In particular the validity of the bottom boundary condition depends on how fast the bed relaxes. In other words, *the relaxation time of the bed will define how strong the wind needs to be to have an agitated bed.*

The mismatch between the experimental results and the collisional model is most likely due to the bottom boundary condition: we are assuming that the collisions with the bed are so frequent that it does not have time to return to a quiescent state. The results imply that in the wind tunnel experiments the wind is still not strong enough to break down the vailidy of the splash function concept. Preliminary simulational results of 3–D splash on disordered beds by L. Oger show that the impact of a fast particle on the bed produces ejecta at an average distance of approximately three particle diameters from the impact site (L. Oger, private communication). We use this estimate, together with the results from the collisionless computation, to obtain the average time interval between collisions of fast particles (those that will produce ejecta) on an area of the bed surface. This yields an upper bound for the bed relaxation time. Using the saltation results for $d = 170$ μm and $\theta = 0.29$:

$$t_{\text{bed relaxation}} < 2\sqrt{\frac{d}{g}}.$$

As experiments at higher Shields parameters become available, more stringent bounds can be imposed on this important parameter.

VI. CONCLUSIONS AND OUTLOOK

A combination of approaches to understand the transition from weak to strong winds were undertaken. In particular, we presented a model that includes both collisions between particles and turbulent suspension. The profiles obtained in this model show that particle-particle collisions can dominate over turbulence as a suspension mechanism.

The transport rates predicted with the collisional model are much larger than those yielded by a standard collisionless simulation and by wind tunnel experiments. This indicates that the splash function concept is still valid up to the wind speeds probed. This mismatch is used to obtain an upper bound for the relaxation time of the bed. On the other hand, the 3–D splash experiments provide the time delay between the impact and ejection of particles. This delay provides a rough lower bound for the relaxation time.

These results, together with the estimate found in Ref. [12], indicate that in-flight collisions may become important while the splash function concept is still valid. This gives two avenues for extending the models presented here:

- For the collisionless saltation computation, in-flight collisions may be included in a perturbational manner. This development is under way. Together with these calculations, further understanding of the relaxation time at the bed is required for defining the validity ranges of each approach. Molecular dynamics simulations of 3–D beds, such as those being performed by L. Oger, are especially useful to isolate the relevant processes involved.

- For the collisional model, the agitated boundary condition at the bed [10] may be replaced by a different one that allows for jumps in particle speed, concentration, and granular temperature. To perform this extension without introducing free unknown parameters, the development of these boundary conditions must be bounded by experiment.

To complement these research lines, the 3–D splash experiments are being extended to obtain more extensive information on the rebound and ejection properties of the bed.

Acknowledgments

This research was sponsored by grant NAG3-2353 from the Office of Biological and Physical Research of the National Aeronautics and Space Administration. The authors benefited from the hospitality of the Isaac Newton Institute, Cambridge, UK, during the final stages of the work. The authors would like to thank Dan Hanes, for providing the trajectory simulations that helped to derive the top boundary conditions, Keld Rasmussen for providing us with the experimental results included here, and Luc Oger for discussing his 3–D splash simulations with us.

[1] K. D. Adams, Sedimentology **50**, 565 (2003).
[2] G. Sauermann, K. Kroy, and H. J. Herrmann, Phys. Rev. E **64**, 031305 (2001).
[3] A. R. Lima, G. Sauermann, H. J. Herrmann, and K. Kroy, Physica A **310**, 487 (2002).
[4] J. E. Ungar and P. K. Haff, Sedimentology **34**, 289 (1987).
[5] C. Cercignani, *Mathematical Methods in Kinetic Theory* (Plenum Press, New York, 1990), 2nd ed.
[6] F. Rioual, A. Valance, and D. Bideau, Europhys. Lett. **61**, 194 (2003).
[7] D. Beladjine, Rapport de Stage de DEA, Groupe Matière Condensée et Matériaux, Université Rennes1, Campus de Beaulieu Bâtiment 11A CS 74205, 263 av. du géneral Leclerc, 35042 Rennes Cedex (2003).
[8] B. T. Werner, J. Geol. **98**, 1 (1990).
[9] J. M. Pasini and J. T. Jenkins (2004), submitted to Philos. Trans. R. Soc. Lond. A.
[10] J. T. Jenkins and E. Askari, J. Fluid Mech. **223**, 497 (1991).
[11] J. D. Iversen and K. R. Rasmussen, Sedimentology **46**, 723 (1999).
[12] M. Sørensen and I. McEwan, Sedimentology **43**, 65 (1996).

TWO DIMENSIONAL TURBULENCE IN PRESENCE OF POLYMER

Yonggun Jun, Jie Zhang, and Xiao-Lun Wu
Department of Physics and Astronomy
University of Pittsburgh
Pittsburgh, Pennsylvania 15260

The phenomenon of drag reduction by adding a small amount of long-chain polymers to turbulent flow has been studied for a long time but is not fully understood. We investigated the effect of the dilute polymer concentration and the energy injection rate upon the drag reduction and the turbulent structures in fully-developed 2D turbulent flow. Our measurements were performed in a freely suspended soap film. The Particle Imaging Velocimetry (PIV) is used to determine the velocity field and the local topological structures. The local topology is characterized by the Jacobian determinant $\Lambda(x, y) = (\omega^2 - \sigma^2)/4$, where $\omega(x,y)$ is the local vorticity, and $\sigma(x,y)$ is the local strain rate. We found that large coherent structures were suppressed by polymers and the energy dissipation due to polymer suddenly increased around polymer concentration 10 wppm. The shape of the PDF of the local topology $P(\Lambda)$ is changed for higher polymer concentrations.

TRANSITION FROM IGNITION TO FLAME GROWTH UNDER EXTERNAL RADIATION IN THREE DIMENSIONS (TIGER-3D)

Takashi Kashiwagi, Yuji Nakamura, Sandra L. Olson, and William Mell

This study focuses on localized ignition by external radiant flux and subsequent flame growth over thin polymeric materials (plastic and paper) in microgravity. Two transition stages were observed. The first transition stage covers the period from the onset of ignition to the formation of stabilized flame near the ignited area. This is followed by the second transition of the flame growth stage from the initial stabilized flame to sustained fire growth away from the ignited area. For the first stage, ignition experiments of thin PMMA sheets were conducted using a CO_2 laser as an external source in the 10 s drop tower. The results of front side surface ignition and of backside surface ignition were observed. The effects of imposed flow velocity, sample thickness, and ambient oxygen concentration on ignition are obtained. Numerical study was conducted to investigate to understand and predict ignition behavior observed in the experiments. For the second stage, numerical study is being conducted to describe the effects of gravity on heat release rate of a PMMA sheet. The gravity level was varied from zero to normal gravity. The preliminary results show that the maximum heat release occurs at around 0.02 g.

NASA/CP—2004-213205/VOL2

Transition from Ignition to flame Growth under External Radiation in 3D

Takashi Kashiwagi, NIST/U. of Maryland
Yuji Nakamura, Nagoya University
William E. Mell, NIST
Sandra L. Olson, NASA Glenn RC

This work is supported by NASA under C-32090-K and NCC3-919

Objectives

- **Understand localized ignition processes of polymeric materials (plastic and paper) and subsequent flame growth in microgravity.**
- **Determine the effects of gravity (from 0 g to normal g)**
- **Determine the effects of sample thickness**
- **Determine the effects of imposed flow velocity**
- **Determine the effects of oxygen concentration at various atmospheric pressures**

Approach

- **Two transition stages**
  - **First transition stage**: From onset of ignition to formation of anchored flame
  - **Second transition stage**: Flame growth from localized, anchored flame
- **First transition stage**: Experiments in the 10 s drop tower at JAMIC and 3 D numerical calculation.
- **Second transition stage**: Numerical calculation.

Experiments

- CO_2 laser as an external radiant source
- PMMA(0.2 mm & 0.4 mm thick) and Paper (60 g/m2, 120 g/m2, and 240 g/m2)
- Air and 35% O2/65%N2
- Imposed flow velocity (up to 20 cm/s)

Numerical Calculation

- 3-D time-dependent Navier-Stokes equations

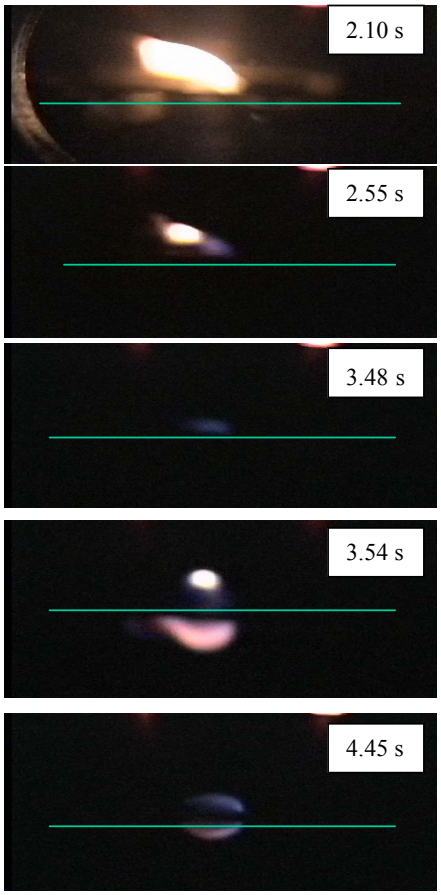

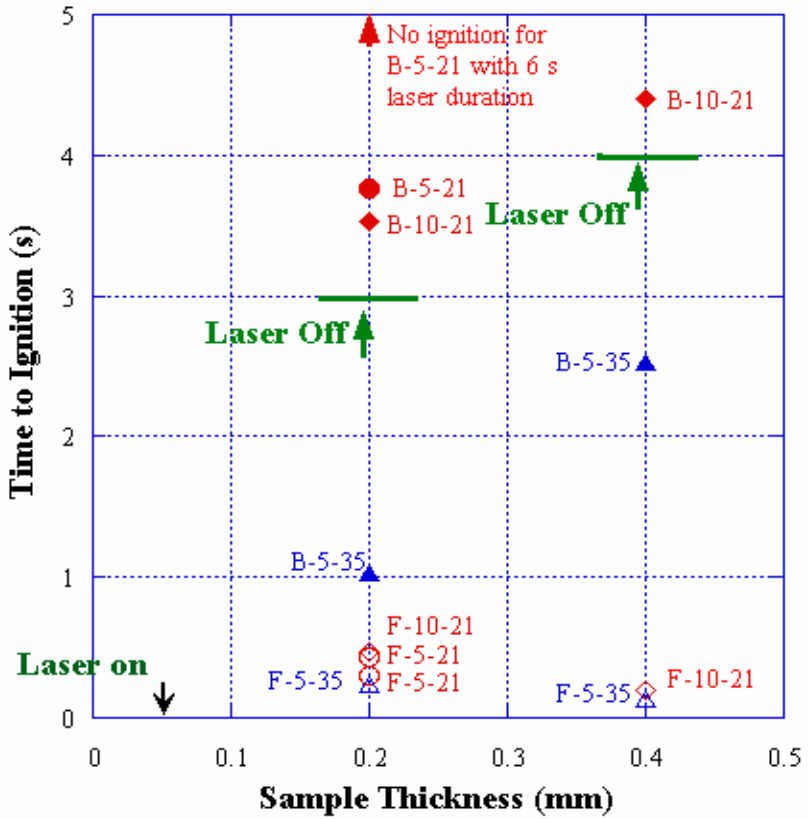

PMMA(0.2mm), air, 5cm/s from right

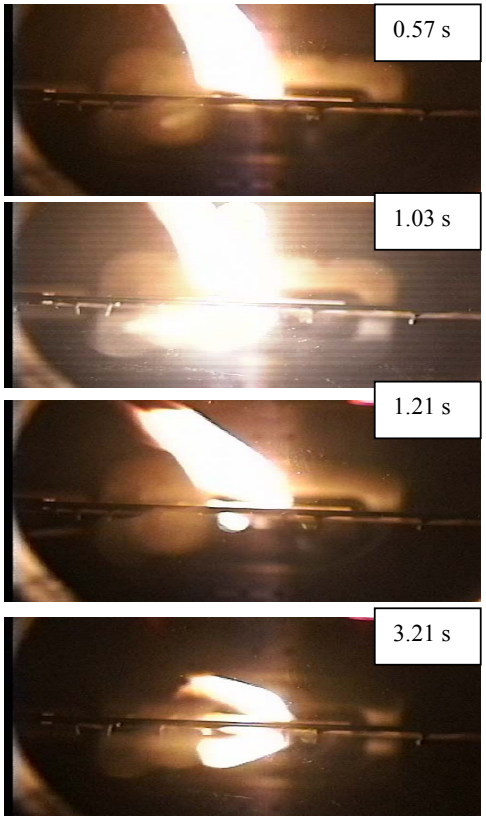

PMMA(0.2mm), 35% O_2 at 5 cm/s from right

PMMA(0.2mm), air at 5 cm/s with 6 s laser duration. t=0.06 s before laser termination

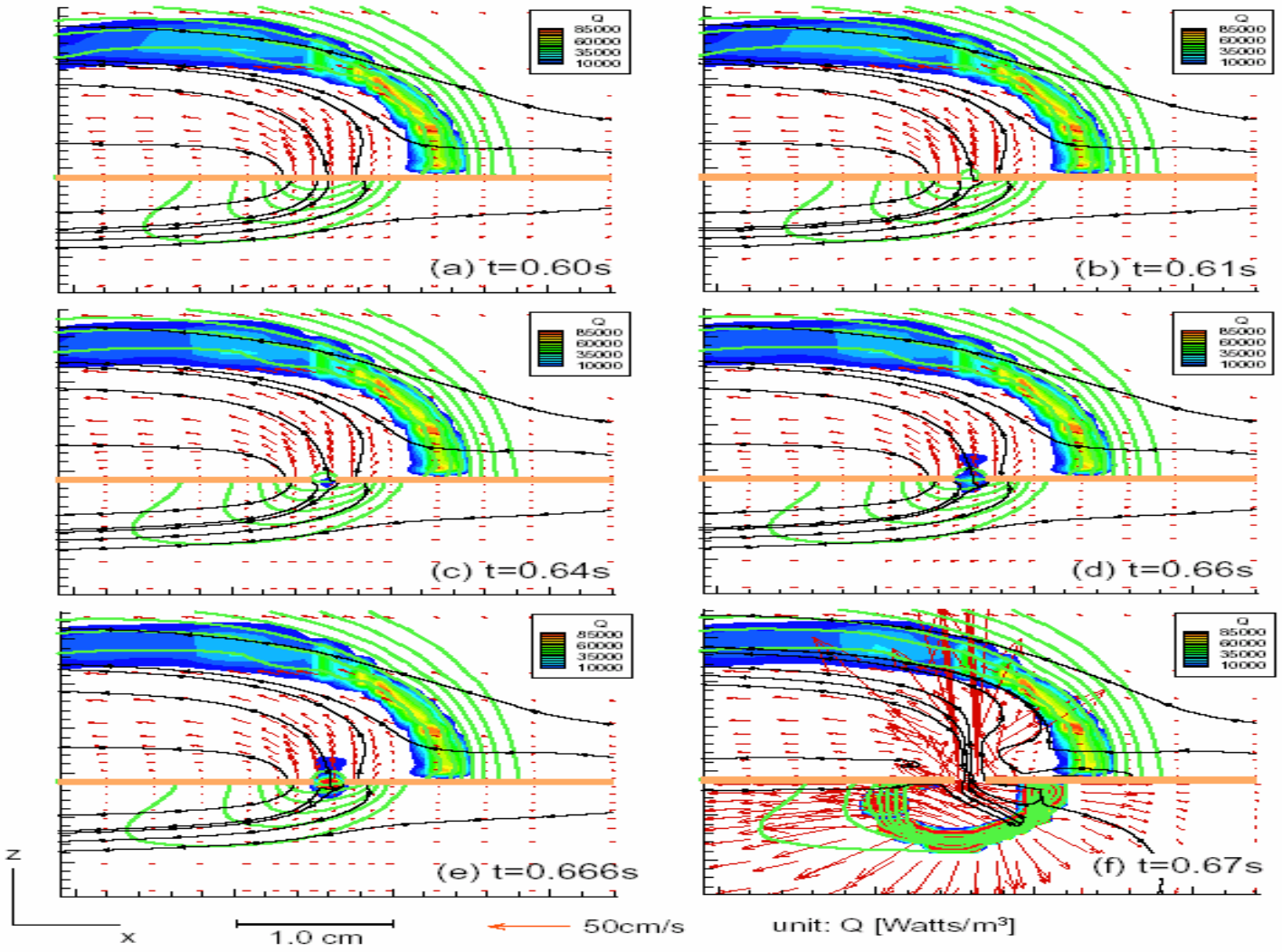

Numerical results: heat release rate (Q), oxygen mass fraction (green), stream line (black), flow vectors (red arrow), PMMA (orange sheet)

Second Transition Stage

- **Effects of gravity on flame growth and heat release rate – Preliminary results**

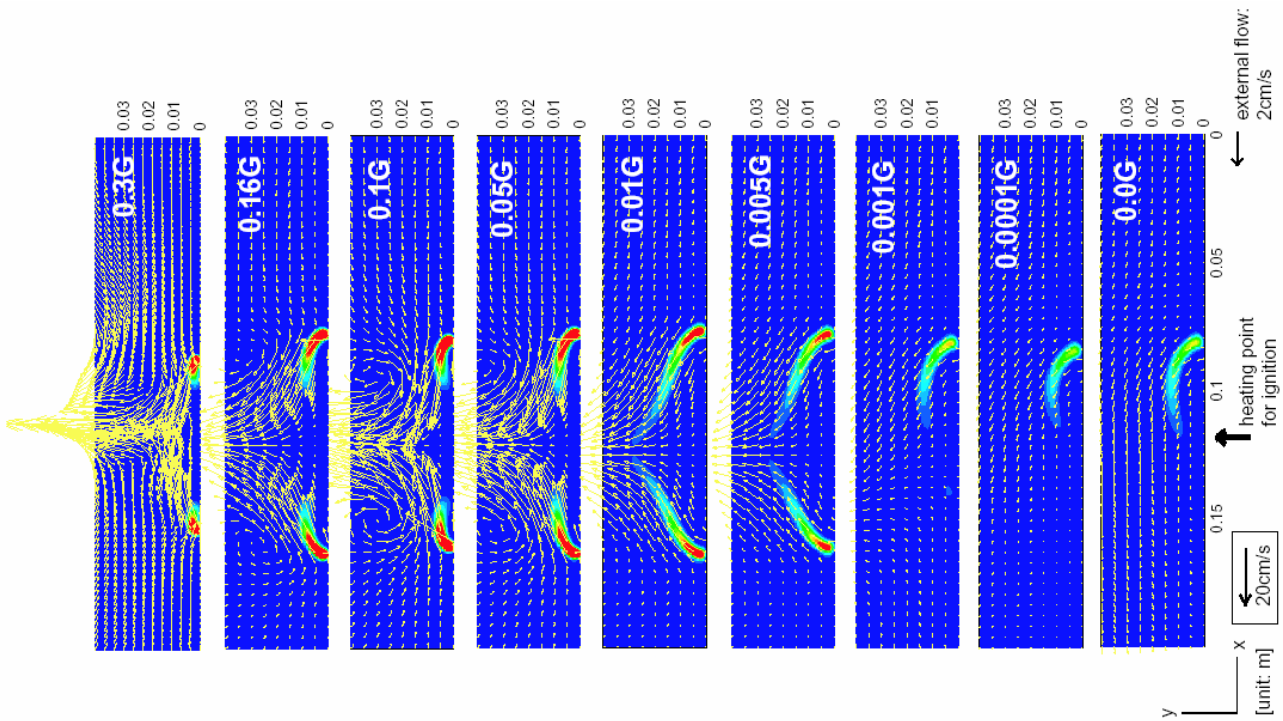
0.2G
0.16G
0.1G
0.05G
0.01G
0.005G
0.001G
0.0001G
0.0G
0.03
0.02
0.01
0
0.15
0.1
0.05
0
x
y
[unit: m]
20cm/s
heating point
for ignition
external flow:
2cm/s

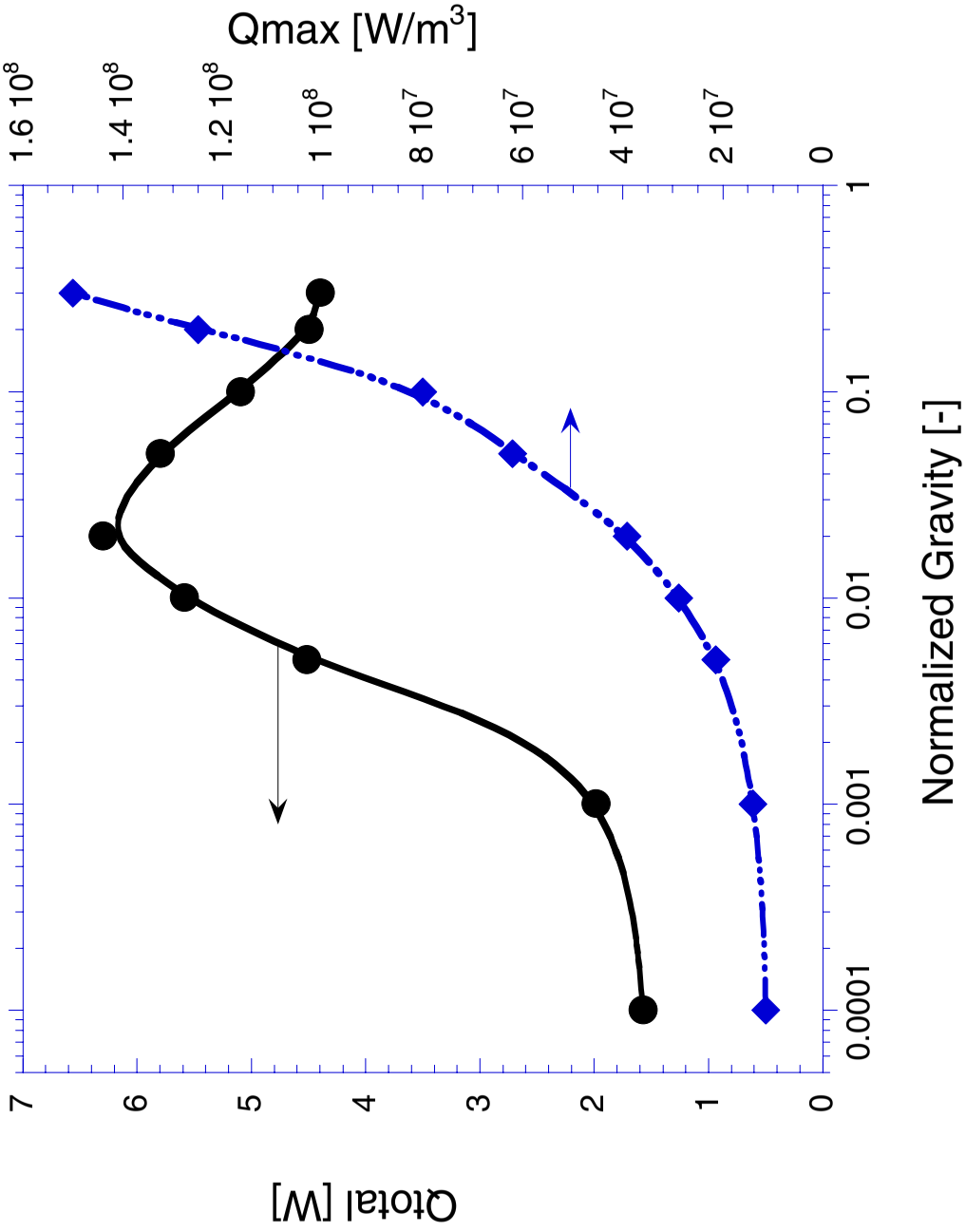
Qmax [W/m3]
1.6 10^8
1.4 10^8
1.2 10^8
1 10^8
8 10^7
6 10^7
4 10^7
2 10^7
0
Qtotal [W]
0
1
2
3
4
5
6
7
Normalized Gravity [-]
0.0001
0.001
0.01
0.1
1

ISOLATED LIQUID DROPLET COMBUSTION: INHIBITION AND EXTINCTION STUDIES

A. Kazakov, K.G. Kroenlein, and F.L. Dryer
Princeton University, Princeton, NJ

F.A. Williams
University of California, San Diego, CA

V. Nayagam
National Center for Microgravity Research, Cleveland, OH

NASA's new space exploration initiative calls for an expansion of human presence into space, and many of the technologies envisioned for these efforts involve fire risks including oxygen generating systems, power-generation equipment, propellant production systems, and waste-management technology and other essentials for life support. The flammability characteristics of materials and methods of sensing the imminence of fires, as well as mitigating those fires which might occur all require detailed information as to how flammability and extinction processes are affected by reduced gravitational body forces and ambient environments that can be significantly different that those on earth. The effects of these differences have not been fully characterized under conditions that supply sufficient results to determine the best means of optimizing fire safety related issues. Both experiments and modeling results can provide insights to developing optimal approaches and to defining fire safety related materials criteria and sensing/control methodologies.

Liquid flammables produce particular fire safety problems when liquids under pressure are released (formation of aerosols) and/or spills occur accidentally into inhabitable environments on earth as well as under reduced gravity conditions. Methodologies involving the inert dilution of the atmosphere to reduce oxygen index beyond what will support combustion (without precluding biological activity), addition of flame and ignition inhibitors to the liquid phase, and/or addition of flame and ignition inhibitors to the gas phase are individually, and in concert, techniques for enhancing fire safety on earth. Investigations in earth's gravitational field have shown that the effectiveness of a particular methodology is at least locally coupled with natural convective effects produced by the ignition and combustion event. The variation of this coupling in reduced gravity conditions can change the relative effectiveness of various approaches, in some cases eliminating their consideration.

A simple example from our earlier work is that in drop tower investigations, we found that isolated droplets of n-heptane would continue to burn at reduced oxygen indices created by nitrogen dilution that were much lower than the limiting value in earth's gravity field. In fact, the limiting value under microgravity conditions appeared to be below that necessary to sustain biological activity. This critical result has not been completely investigated, nor has similar research on limiting oxygen index ever been conducted (either experimentally or numerically) using isolated droplet combustion under reduced gravity in combination with the use of inhibiting additives and other inerts such as helium. The combination of helium with inhibiting additives either in the liquid or gas phase, appears to have promise for reducing the fire potential in inhabitable environments during human exploration endeavors. Experiments such as these are easily accommodated within the range of parameters available in the Multi-Droplet Combustion Apparatus (MDCA) being readied for use on the International Space Station (ISS). Experimental measurements permit assessment of ignition, burning rate, flame characteristics, and

extinction against which the other more complex geometric configurations can be compared. Indeed MDCA facilities and methodologies could also be adapted to investigate spherical solid material combustion properties. It has also been well established that slow convective flows under reduced gravitational environments can drastically alter the combustion and extinction characteristics of liquid droplets, and sphero-symmetric modeling studies are presently being expanded to consider two dimensional steady convection field conditions surrounding an isolated burning droplet.

To preliminarily assess the feasibility and potential mechanisms of fire suppression by CO_2 in non-buoyant systems, we recently conducted a series of numerical experiments involving CO_2 dilution. A 2-mm n-heptane droplet was ignited under normal ambient conditions (air at 1 atm) and was computed for sufficient times to establish an initial flame structure (~10 ms). After that, the simulation was restarted with different far-field gas compositions, composed of varying amounts of CO_2 and air. As expected, at elevated levels of CO_2 in the far field, burning rate decreased, and at high levels of CO_2, flame extinction was observed. The extinction event correlated with flame-zone concentrations of CO_2 near 27% and appears to result from reduced temperature and chemical rates within the flame structure as a result of an increase in local heat capacity. As CO_2 delivery to the flame zone controls the system dynamics, the absolute location of the computationally-defined "far-field" dominates the overall system response in terms of the necessary characteristic time associated with CO_2 diffusion into the flame structure. The implication is that highly-localized delivery mechanisms may be required to extinguish an isolated heterogeneous combustion event. The suppression of flame propagation, on the other hand, is a more feasible use of introducing high heat capacity diluents. In low gravity environments, forced convection may have significant influence on the effectiveness of diluents on extinction processes.

Isolated droplet combustion experiments and modeling with and without relative gas phase convection can be utilized to evaluate the influence of convection of the effectiveness of various fire suppression methodologies. Future efforts using isolated droplet burning experiments and numerical modeling tools can:

1. Map flammability boundaries including Limiting Oxygen Index (LOI) for well-characterized combustion events under varying gravitational accelerations.
2. Measure the effects of inert-substituted environments on the burning rates, flame structure, and extinction conditions, as functions of gas phase composition, including substituted diluents, dilution by increased diluent addition, and the presence of additives that may chemically inhibit combustion.
3. Experimentally investigate fuel additives that could lead to fire-safe fuels while operating as efficient propulsion source.
4. Investigate the effects of slow convection on the above characterizations.
5. Develop predictive numerical codes and chemical kinetic schemes to model flammability boundaries as a function effective gravitational acceleration and the unique ambient conditions encountered in space exploration applications.

ELECTRIC-FIELD-DRIVEN PHENOMENA FOR MANIPULATING PARTICLES IN MICRO-DEVICES

Boris Khusid
New Jersey Institute of Technology
University Heights, Newark, NJ 07102
Phone: 973-596-3316; Email; khusid@adm.njit.edu

Andreas Acrivos
The City College of New York
140th Street & Convent Avenue
New York, NY 10031
Phone: 212-650-8159; Email: acrivos@scisun.sci.ccny.cuny.edu

Compared to other available methods, ac dielectrophoresis is particularly well-suited for the manipulation of minute particles in micro- and nano-fluidics. The essential advantage of this technique is that an ac field at a sufficiently high frequency suppresses unwanted electric effects in a liquid. To date very little has been achieved towards understanding the micro-scale field-and shear driven behavior of a suspension in that, the concepts currently favored for the design and operation of dielectrophoretic micro-devices adopt the approach used for macro-scale electric filters. This strategy considers the trend of the field-induced particle motions by computing the spatial distribution of the field strength over a channel as if it were filled only with a liquid and then evaluating the direction of the dielectrophoretic force, exerted on a single particle placed in the liquid. However, the exposure of suspended particles to a field generates not only the dielectrophoretic force acting on each of these particles, but also the dipolar interactions of the particles due to their polarization. Furthermore, the field-driven motion of the particles is accompanied by their hydrodynamic interactions. We present the results of our experimental and theoretical studies which indicate that, under certain conditions, these long-range electrical and hydrodynamic interparticle interactions drastically affect the suspension behavior in a micro-channel due to its small dimensions.

Electric-field-driven Phenomena for Manipulating Particles in Micro-Devices

Boris Khusid[1] and Andreas Acrivos[2]

[1] *New Jersey Institute of Technology, University Heights, Newark, NJ 07102*
Email: khusid@adm.njit.edu
[2] *The City College of New York, 140th Street & Convent Avenue, New York, NY 10031*
Email: acrivos@scisun.sci.ccny.cuny.edu

Compared to other available methods, ac dielectrophoresis is particularly well-suited for the manipulation of minute particles in micro- and nano-fluidics. The essential advantage of this technique is that an ac field at a sufficiently high frequency suppresses unwanted electric effects in a liquid (for water, in particular, in the MHz-frequency range). To date very little has been achieved towards understanding the micro-scale field- and shear driven behavior of a suspension in that, the concepts currently favored for the design and operation of dielectrophoretic micro-devices adopt the approach used for macro-scale electric filters. This strategy considers the trend of the field-induced particle motions by computing the spatial distribution of the field strength over a channel as if it were filled only with a liquid and then evaluating the direction of the dielectrophoretic force, exerted on a single particle placed in the liquid. However, the exposure of suspended particles to a field generates not only the dielectrophoretic force acting on each of these particles, but also the dipolar interactions of the particles due to their polarization. Furthermore, the field-driven motion of the particles is accompanied by their hydrodynamic interactions.

We present the results of our experimental and theoretical studies [1-4] which indicate that, under certain conditions, these long-range electrical and hydrodynamic interparticle interactions drastically affect the suspension behavior in a micro-channel due to its small dimensions. As we shall demonstrate, this leads to the formation and propagation of the concentration front in suspensions subject to a high gradient electric field. This phenomenon provides a new method for strongly concentrating particles in focused regions of micro-devices. Potential applications of the field-driven phenomena for advanced life support and environmental monitoring & control systems for long-duration missions include a wide range of electro-micro-devices for multiphase separation, bubble manipulation, monitoring particulate and microbial background environment, etc. However, our experiments aboard the NASA research aircraft KC-135 [4] revealed that an unexpectedly pronounced effect of a relatively weak gravity imposes certain limitations on the use of ground-based tests for predicting the operation of electro-technologies in micro-gravity.

Principal publications

1. Bennett, D., Khusid, B., Galambos, P., James, C.D., Okandan, M., Jacqmin, D., and Acrivos, A., Field-induced dielectrophoresis and phase separation for manipulating particles in microfluidics. *Appl. Phys. Lett*., (2003) **83**(23), 4866
2. Markarian, N., Yeksel, M., Khusid, B., Farmer, K., Acrivos, A., Limitations on the scale of an electrode array for trapping particles in microfluidics by positive dielectrophoresis, *Appl. Phys. Lett.,* (2003) **82** (26), 4839; Particle motions and segregation in dielectrophoretic micro-fluidics, *J. Appl. Phys*., (2003) **94**(6), 4160
3. Kumar, A., Qiu, Z., Acrivos, A., Khusid, B., and Jacqmin, D., Combined negative dielectrophoresis and phase separation in nondilute suspensions subject to a high-gradient ac electric field. *Phys. Rev. E*, (2004) **69**, 021402
4. Markarian, N., Yeksel, M., Khusid, B., Kumar, A., and Tin, P., Effects of clinorotation and positive dielectrophoresis on suspensions of heavy particles. *Phys. Fluids*, (2004) **16**(5), 1826

Dielectrophoretic Particle Concentrator

40 µm (W)×6 µm (H)×570 µm (L) **10 Vptp, 15-30 MHz**

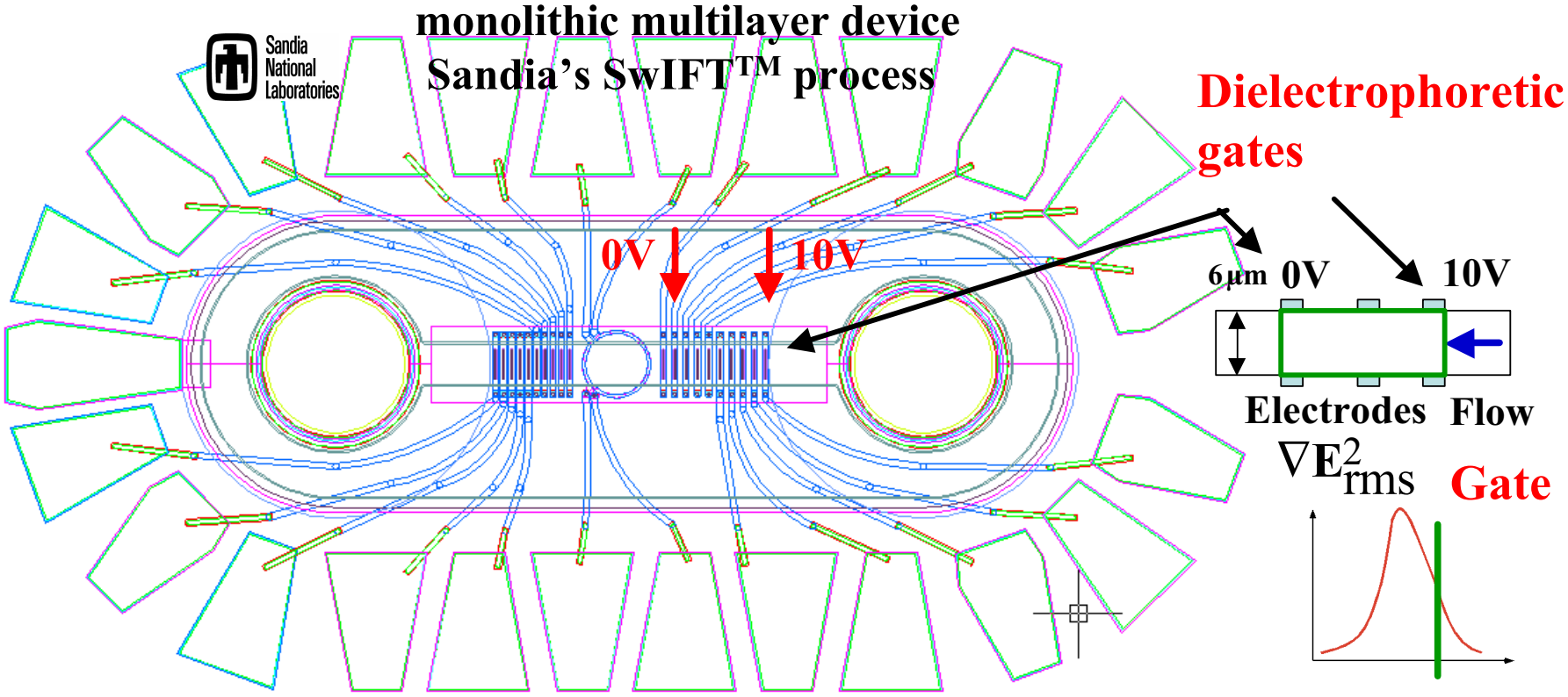

Source: **Bennett, Khusid, Galambos, James, Okandan, TRANSDUCERS'03, Boston, MA**

Experimental Results

1 μm polystyrene spherical beads in DI water, 0.1% (v/v)

Particle polarization $\beta = -0.45 - 0.27i$

Flow rate 0.24 pL/s to 9.6 pL/s; Re~10^{-5}- 10^{-3}

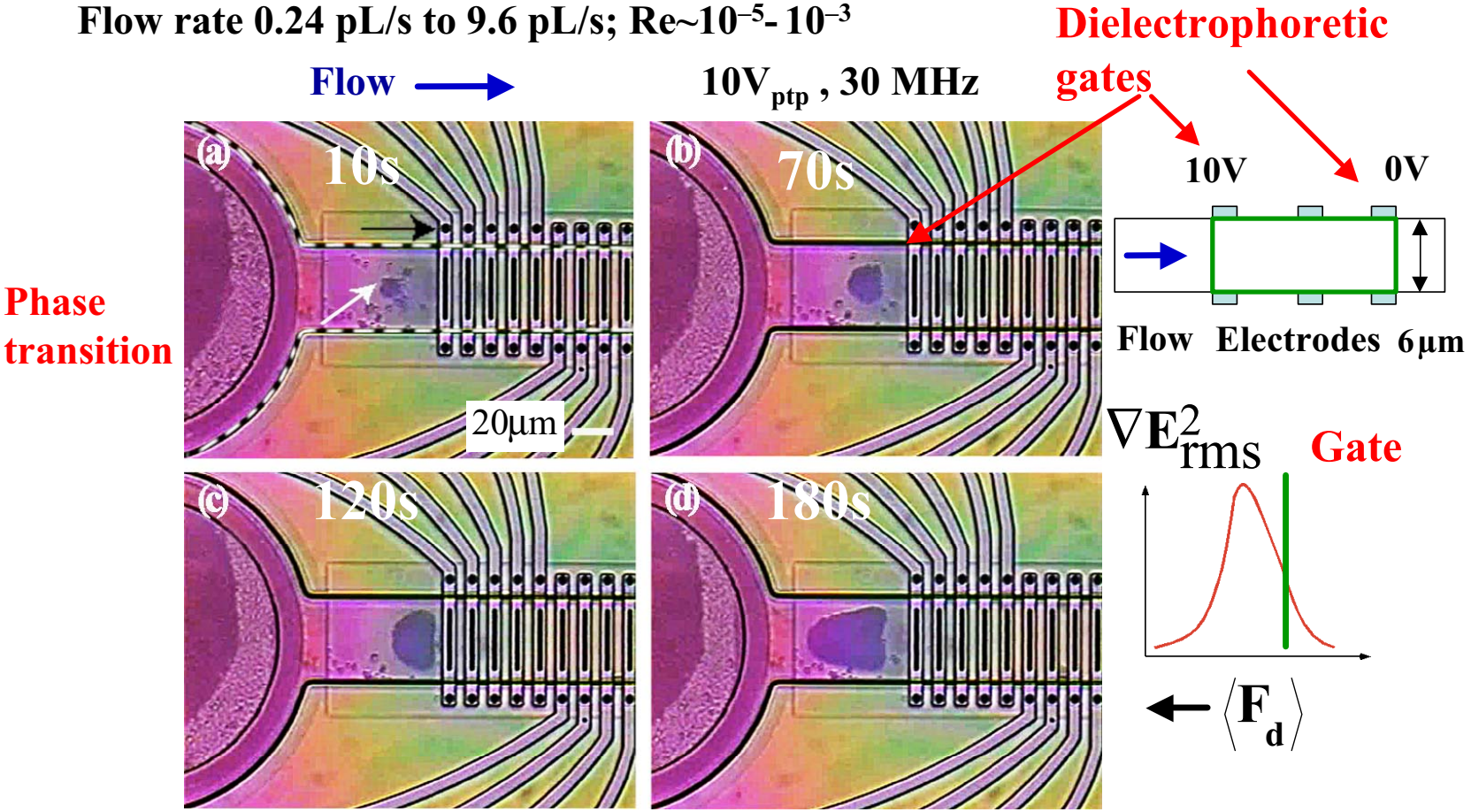

Source: Bennett, Khusid, Galambos, James, Okandan, Jacqmin, Acrivos, Appl Phys Lett, 83, 2003

Flowing Heterogeneous Mixture

Beads and bacterial cells (heat-killed staphylococcus aureus)

10 V_{ptp}, 15 MHz **Flow rate 0.24 pL/s to 9.6 pL/s**

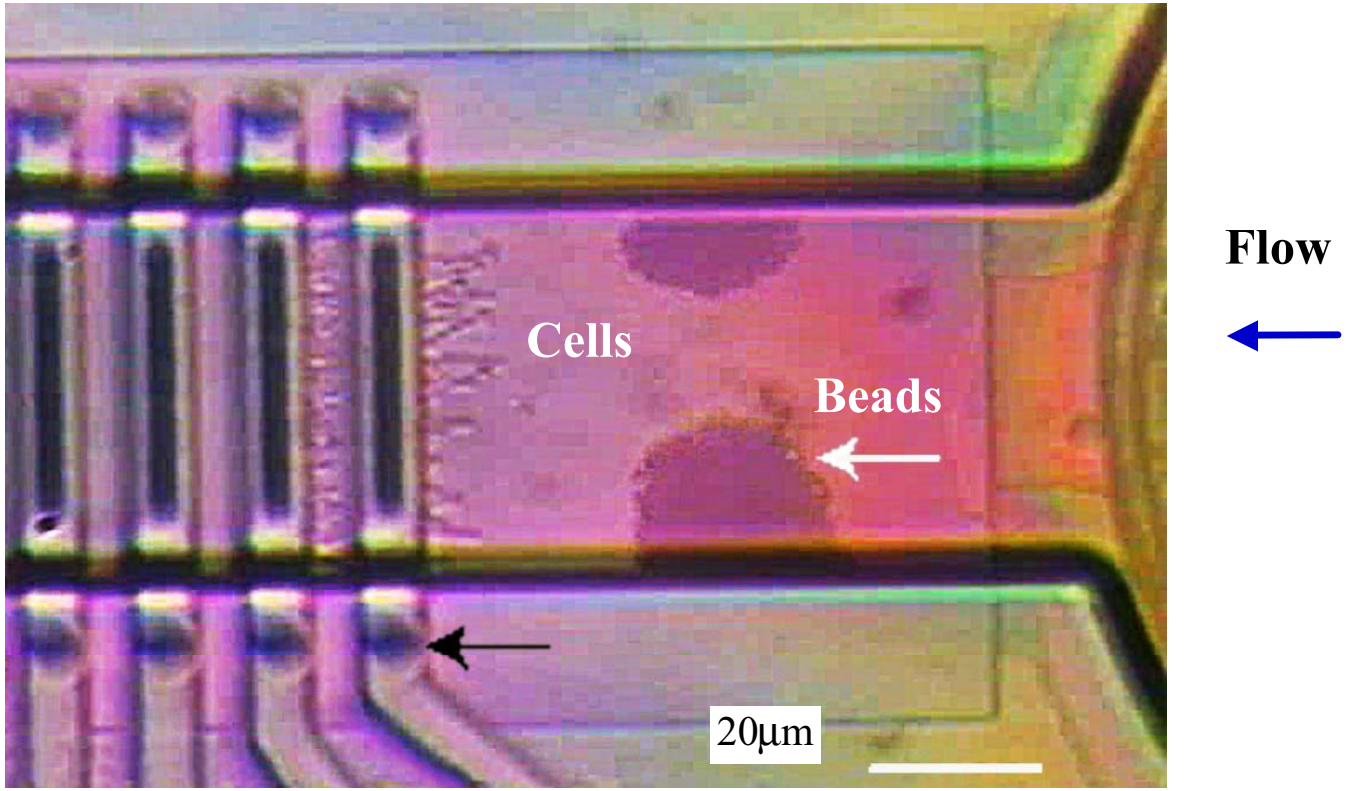

Source: Bennett, Khusid, Galambos, James, Okandan, Jacqmin, Acrivos, Appl Phys Lett, 83, 2003

Modeling

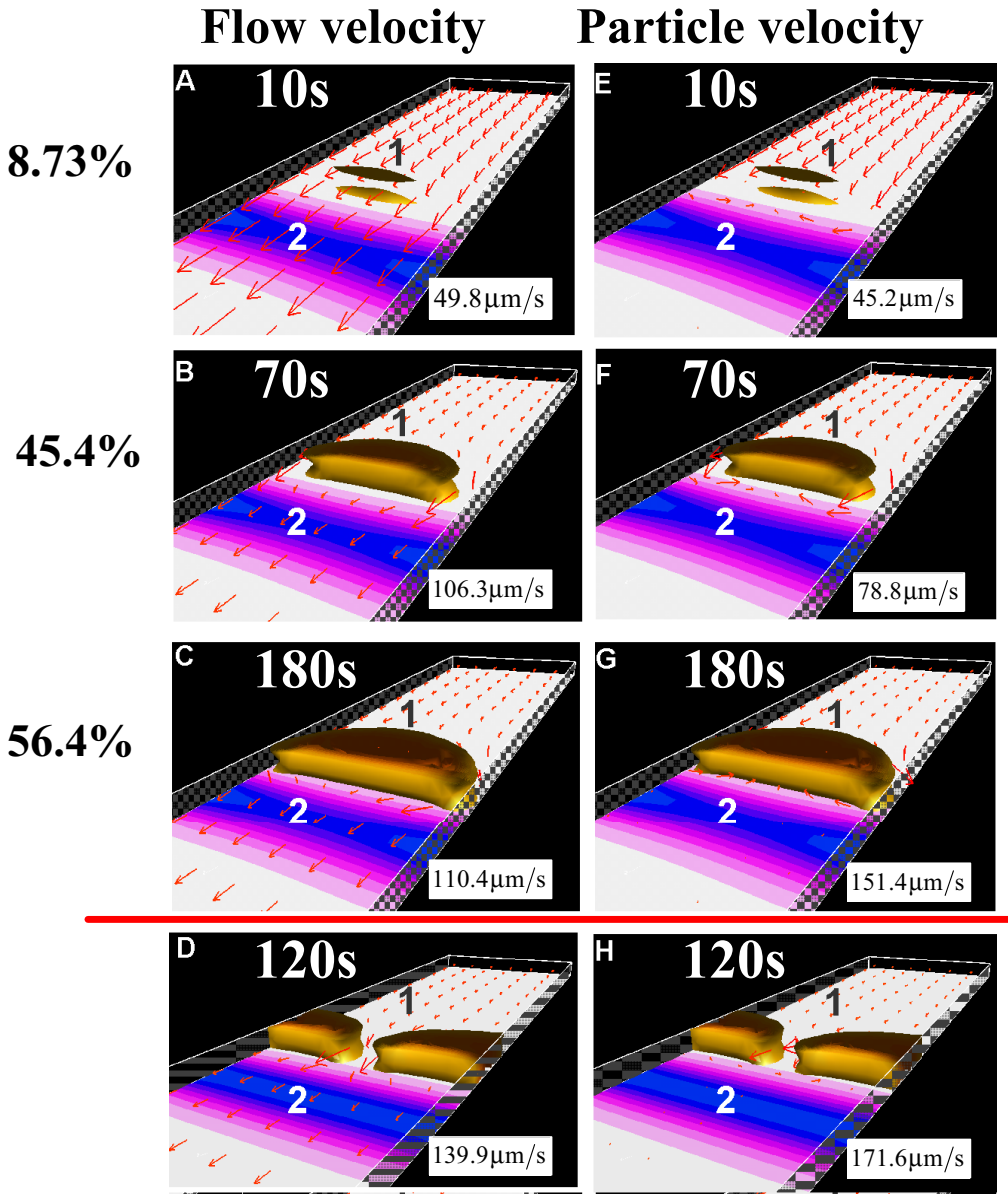

Single bolus

0.1%(v/v)-suspension

Flow rate 8.64 pL/s

Voltage $10V_{ptp}$

Average flow velocity 36 µm/s

1, concentration

2, field strength

Two boluses

Source: Bennett, Khusid, Galambos, James, Okandan, Jacqmin, Acrivos, Appl Phys Lett, 83, 2003

Field-induced Segregation

Top view, 10%

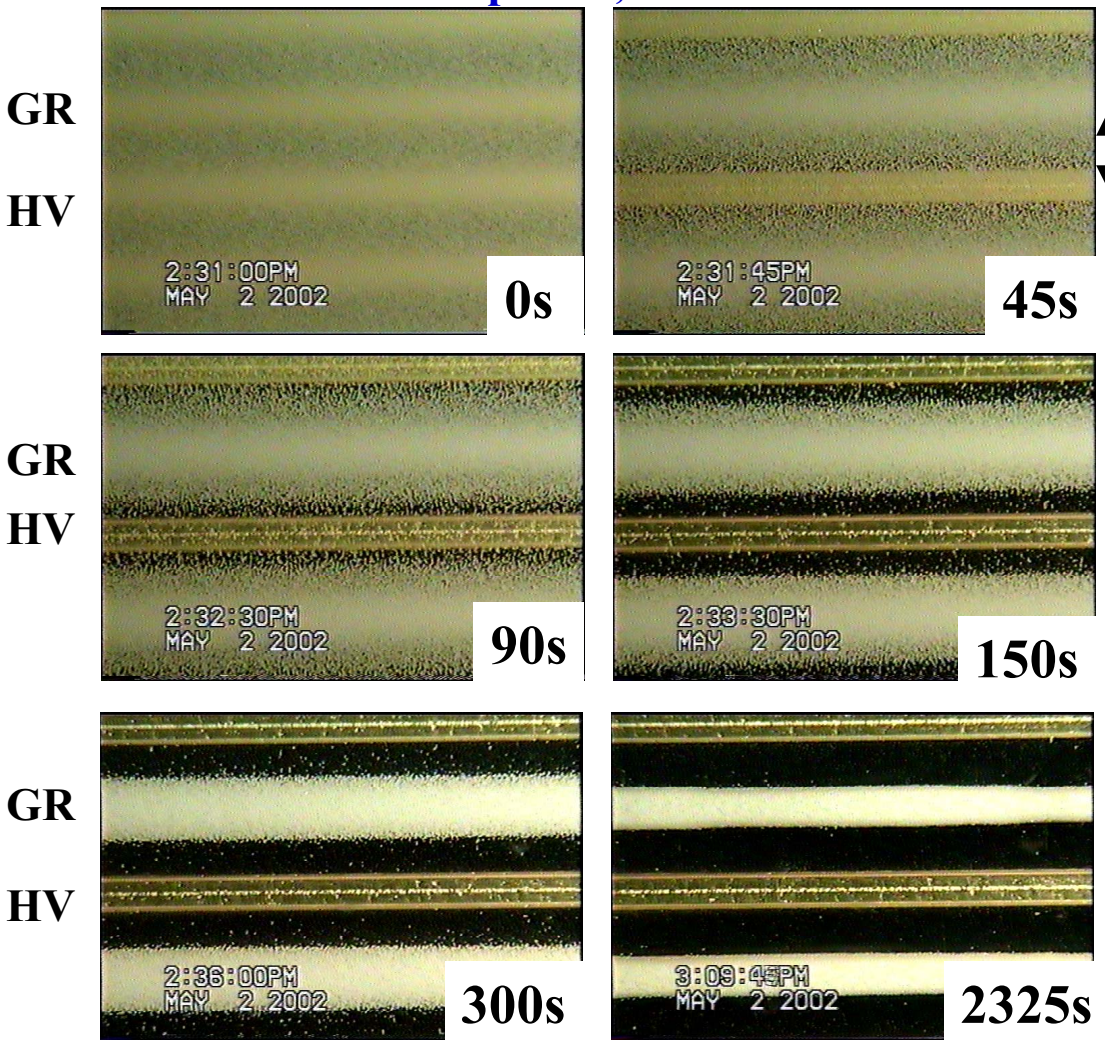

Neutrally buoyant polyalphaolefin spheres in corn oil

$Re(\beta) = -0.15$

for 100-1000 Hz

5kv, 100Hz, without flow

$V_{rms}/d = 2.5$ **kV/mm**

Electric-field strength

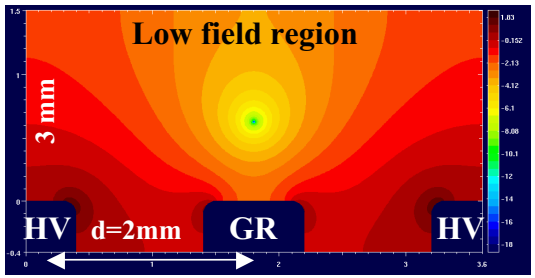

Source: Kumar, Qiu, Khusid, Jacqmin, Acrivos, Phys. Rev. E, 69, 2004

Comparison with Experiments

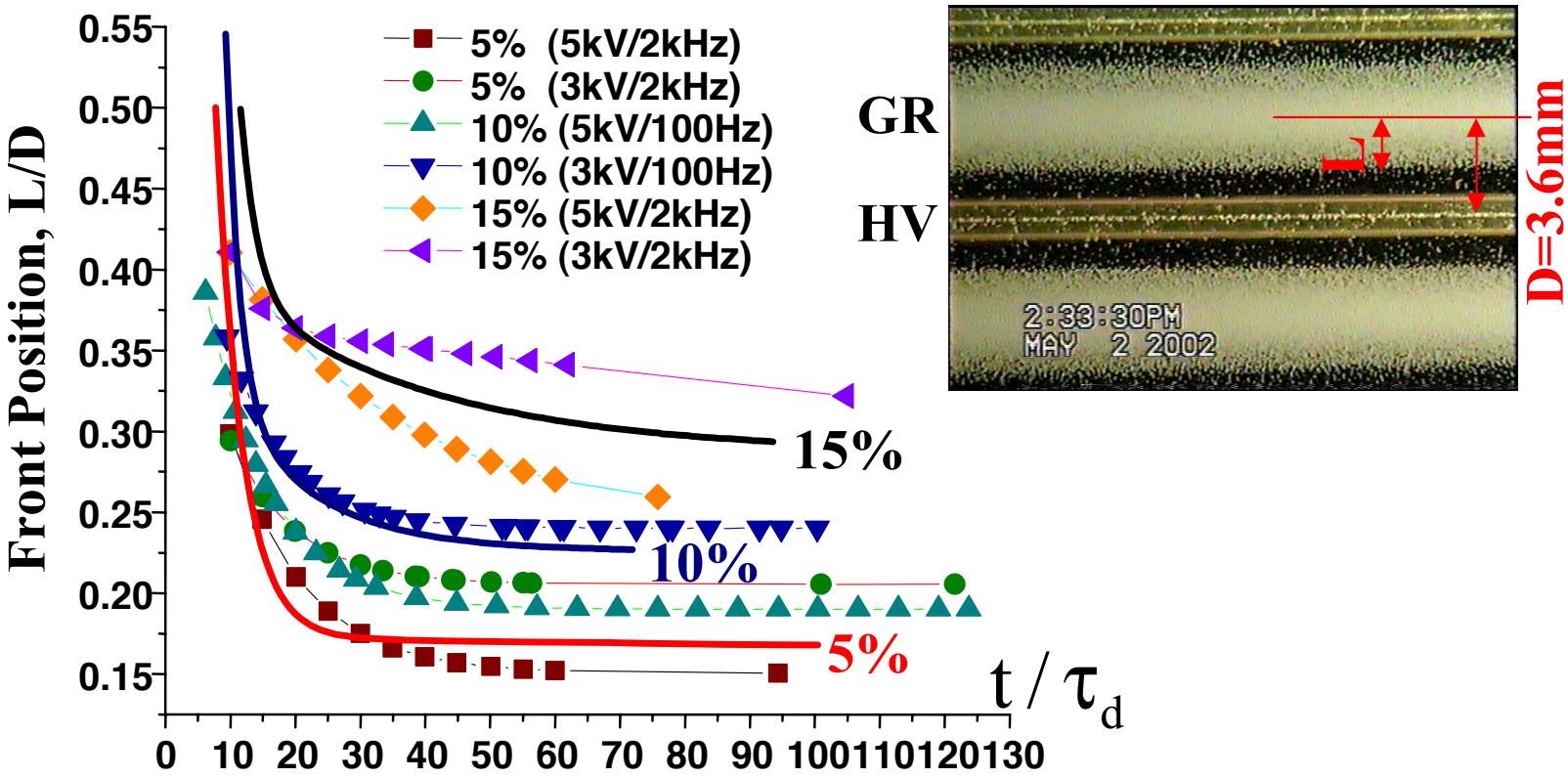

Dielectrophoretic time $$\tau_d = \frac{3d^4\eta_f}{a^2\varepsilon_0\varepsilon_f\left|\mathrm{Re}(\beta(\omega))\right|V_{rms}^2}$$

Source: **Kumar, Qiu, Khusid, Jacqmin, Acrivos, Phys. Rev. E, 69, 2004**

Multi- Channel Apparatus

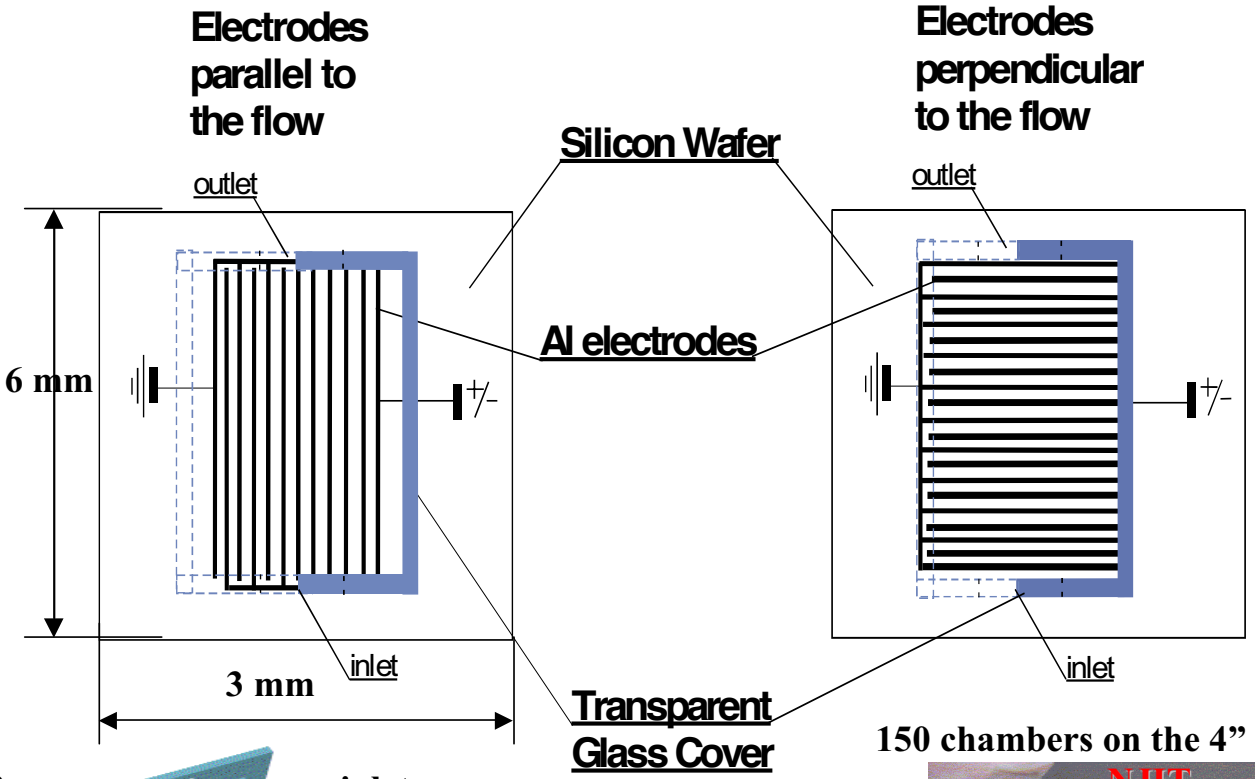

Electrode spacing = 2, 5, 10 µm

H = 30 µm

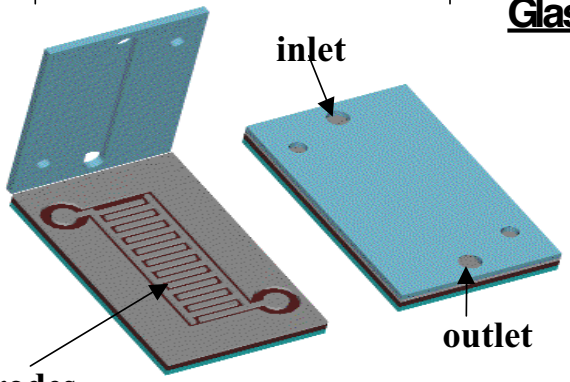

150 chambers on the 4” wafer

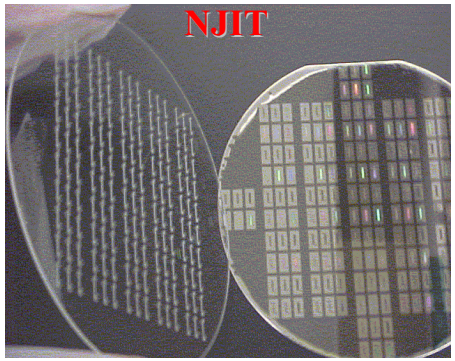

Source: Markarian, Yeksel, Khusid, Farmer, Acrivos, Appl Phys Lett, 82, 2003

KC-135 Experiment

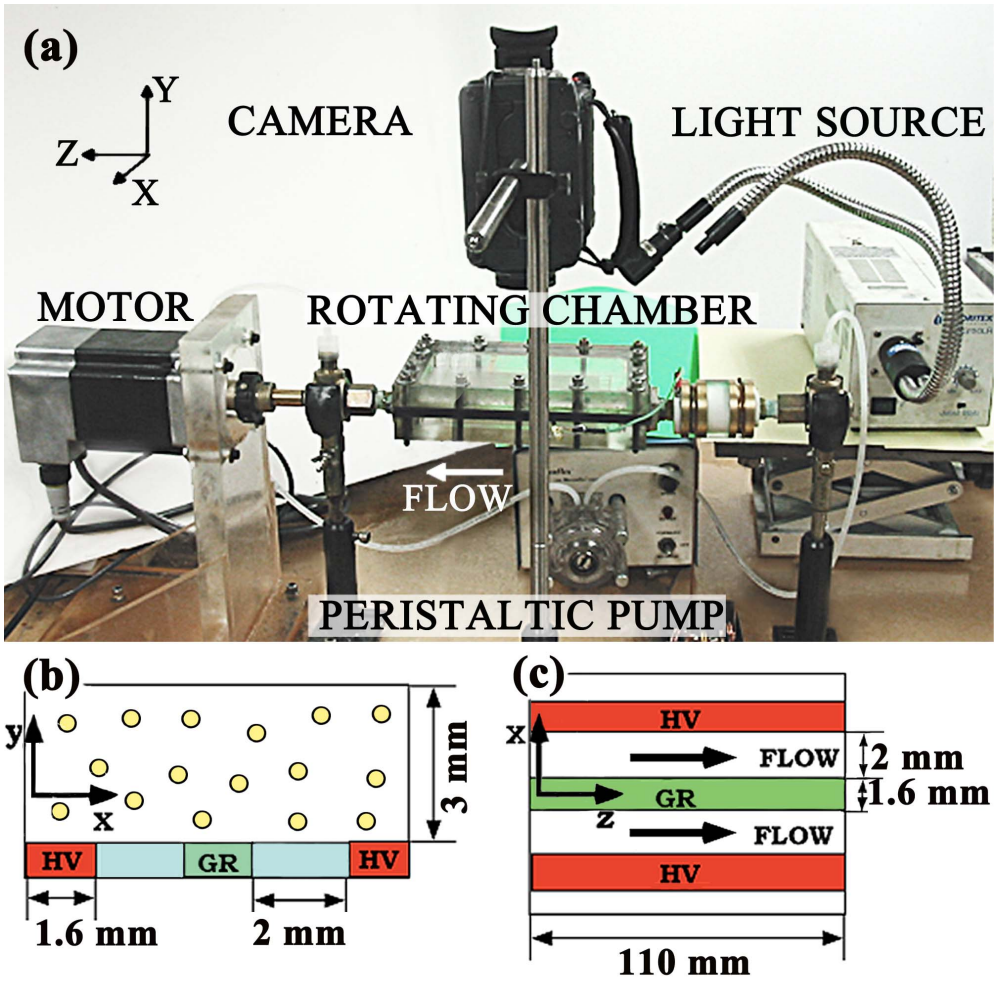

Source: Markarian, Yeksel, Khusid, Kumar, Tin, Phys. Fluids, 16, 2004

Dielectrophoresis in Microgarvity

5kv, 100Hz,

Aggregation patterns, 10s

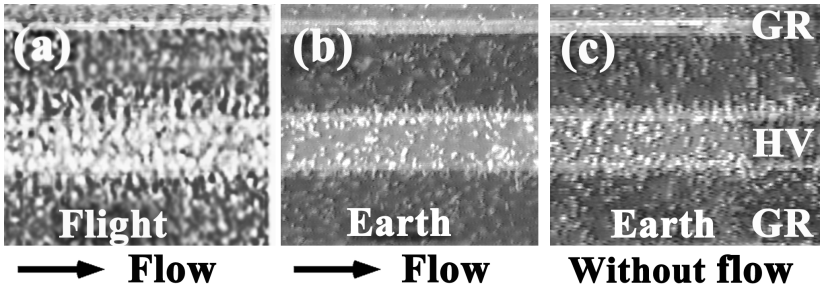

Bristle length

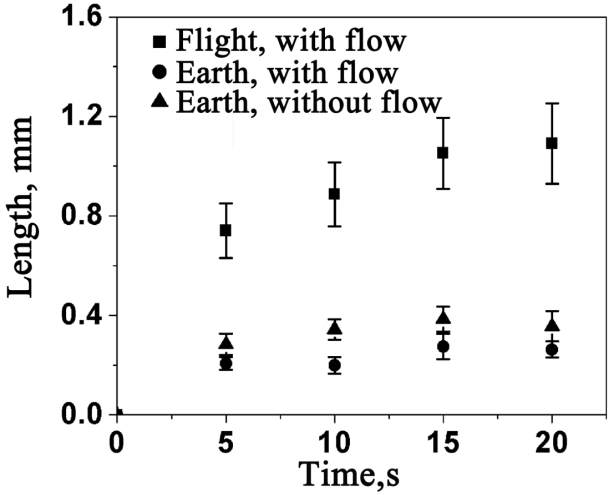

Particle accumulation

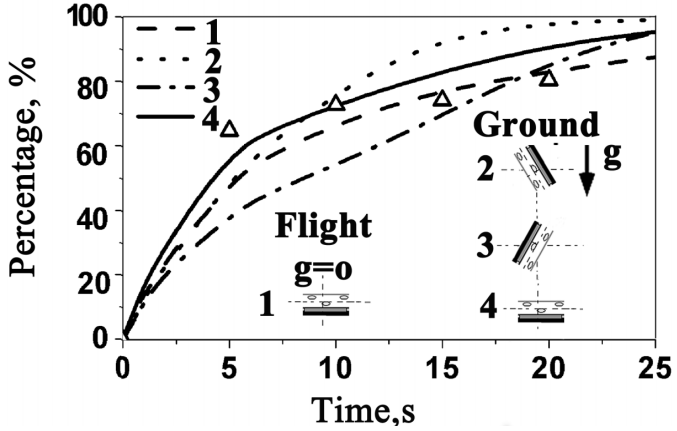

Computations and flight experiments

Air bubbles

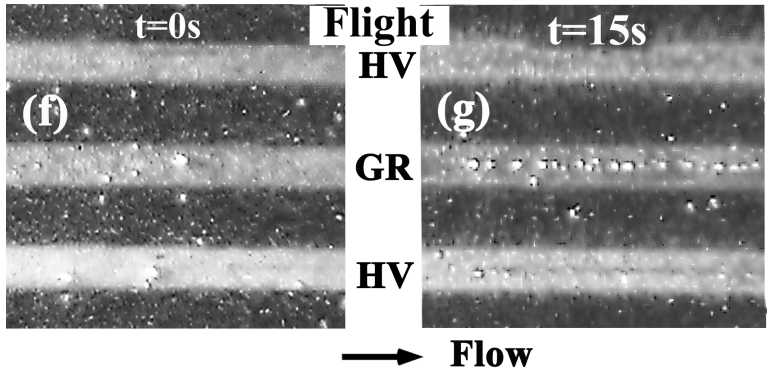

Source: Markarian, Yeksel, Khusid, Kumar, Tin, Phys. Fluids, 16, 2004

Microsensor Technologies for Plant Growth System Monitoring

Chang-Soo Kim
Depts. of Electrical & Computer Eng. and Biological Sciences
Univ. of Missouri-Rolla

- Critical need of precise control of root zone; wetness, oxygen, nutrients, temperature.
- Ideal sensor configuration; miniaturization, multiple, array, low power, robustness.
- Thin film flexible microsensor strips for dissolved oxygen and wetness detection.
- Flexible microfluidic substrate for rhizosphere monitoring and manipulation.

Experimental setup with a porous tube growth system

- Dissolved oxygen microsensor strip
  (3-electrode amperometric measurement by enwrapping the porous tube surface)

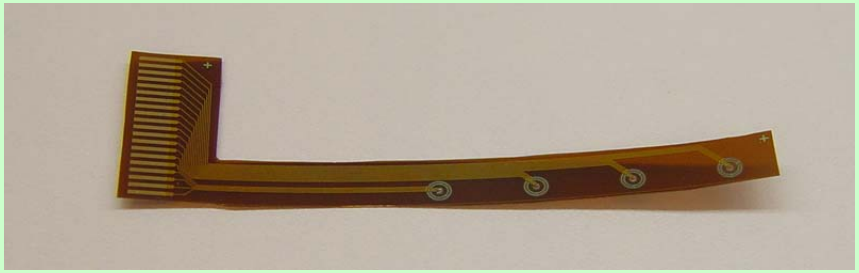

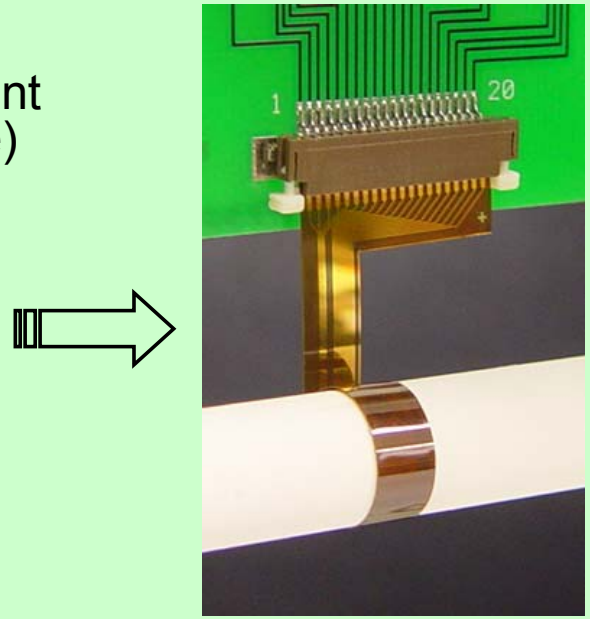

3 inches

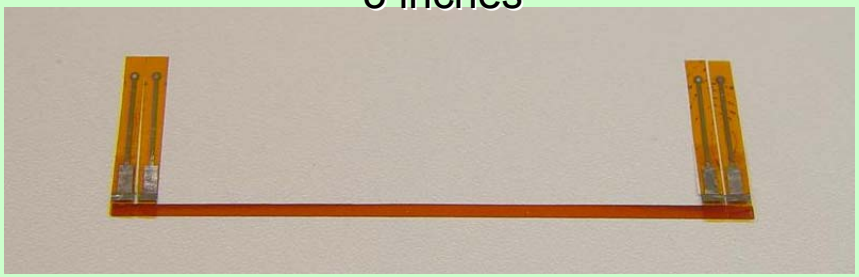

- Wetness sensor strip (4-electrode conductivity measurement along the porous tube surface)

Dissolved oxygen measurement on the porous tube surface

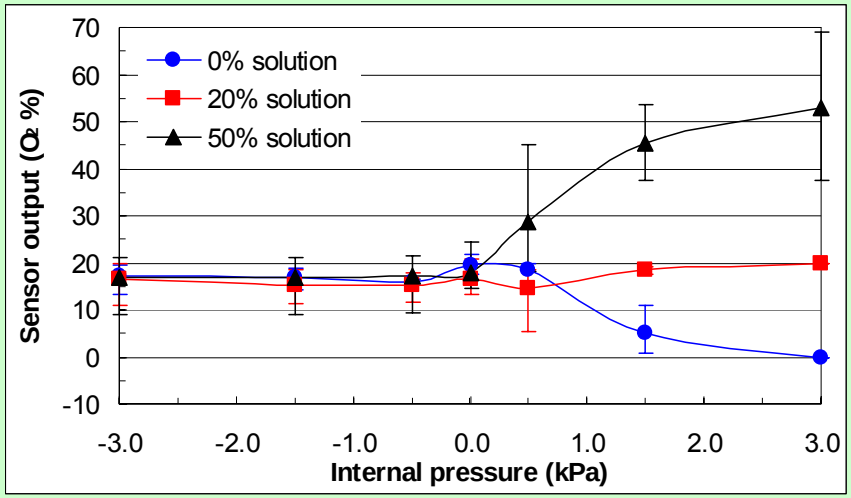

- With a commercial oxygen probe;
- Reflecting O_2 value of inner sol. at (+) pressures.
- Convergence to 20% value (air-sat. value) at (-) pressures.

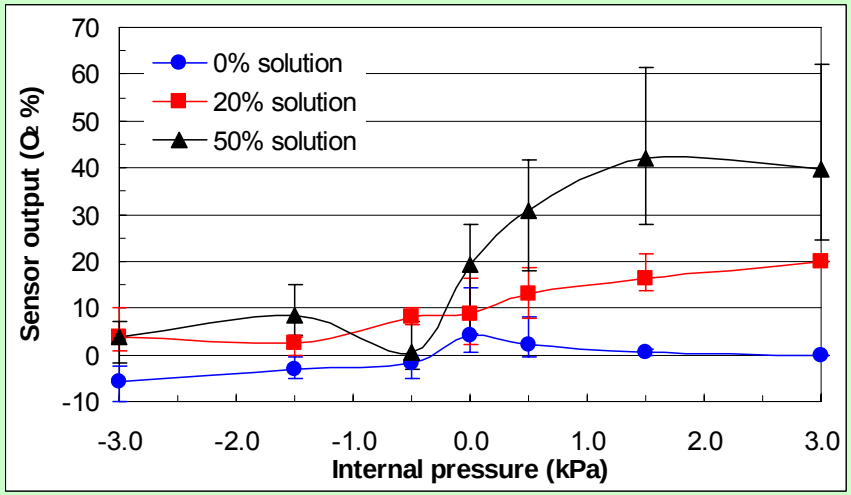

- With a microsensor array;
- Reflecting O_2 value of inner sol. at (+) pressures.
- Scattering around 0% value at (-) pressures (due to surface dryness and absence of sensor permeable membrane).

Wetness measurement on the porous tube surface

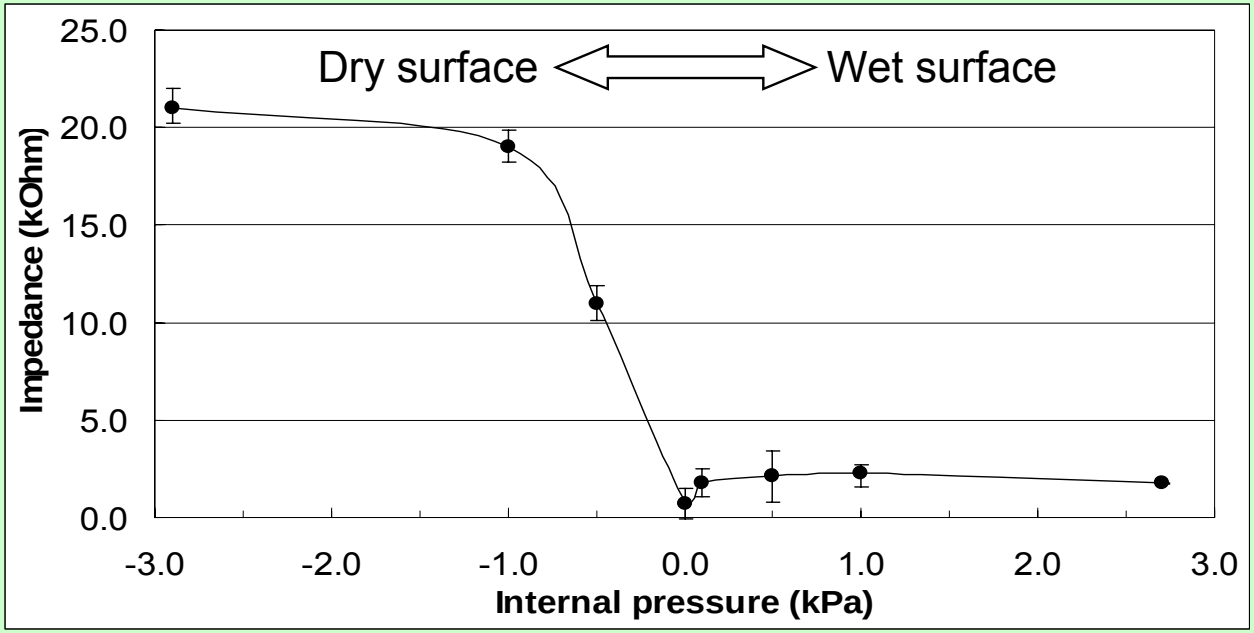

- A steep decrease of surface impedance at the transition from (-) to (+) pressure.

Experimental setup with a particulate growth system (Turface® 1-2 mm size particulate)

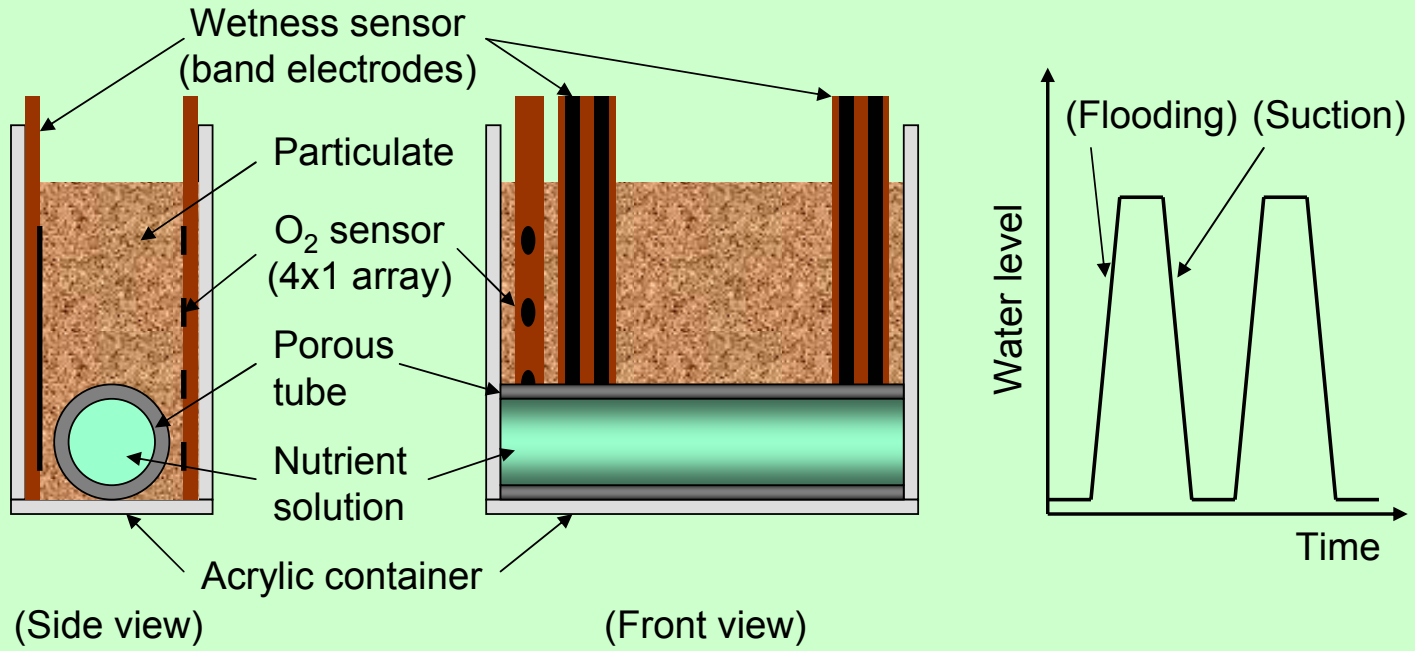

- Dissolved oxygen and wetness measurements within an unsaturated Turface® media.
- Repeated flooding and suction of nutrient solution using the embedded porous tube.

Dissolved oxygen measurements within the particulate

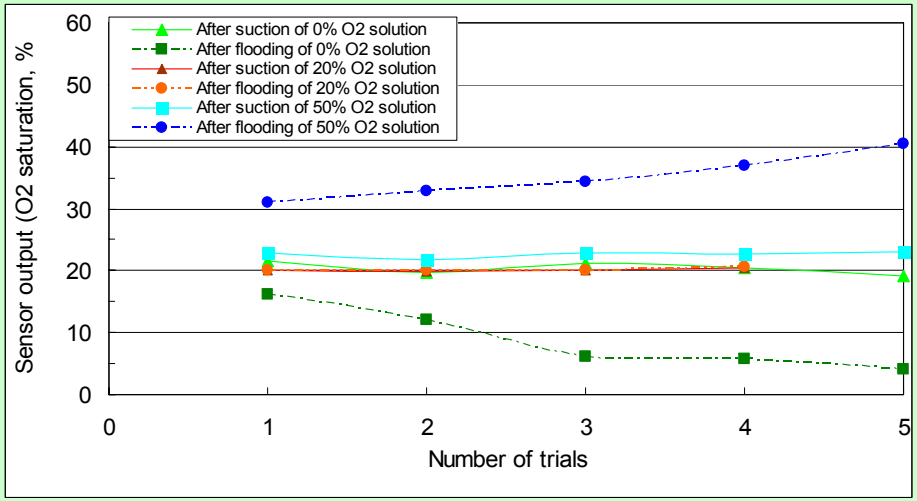

- With a commercial oxygen probe;
- Convergence to O_2 value of inner sol. with repeated flooding.
- Convergence to 20% value (air-sat. value) with suction.

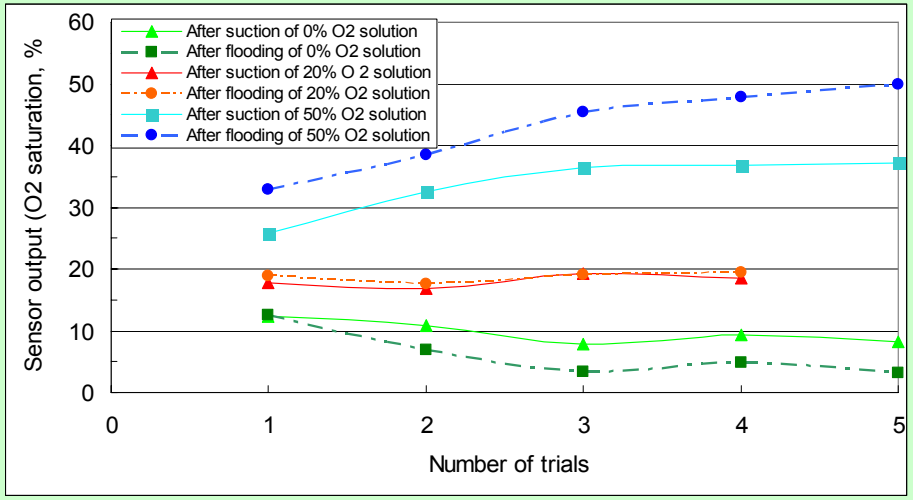

- With a microsensor array;
- Better reflection of O_2 value of inner sol. with repeated flooding.
- Better reflection of O_2 value of inner sol. with repeated suction.

Wetness measurement within the particulate

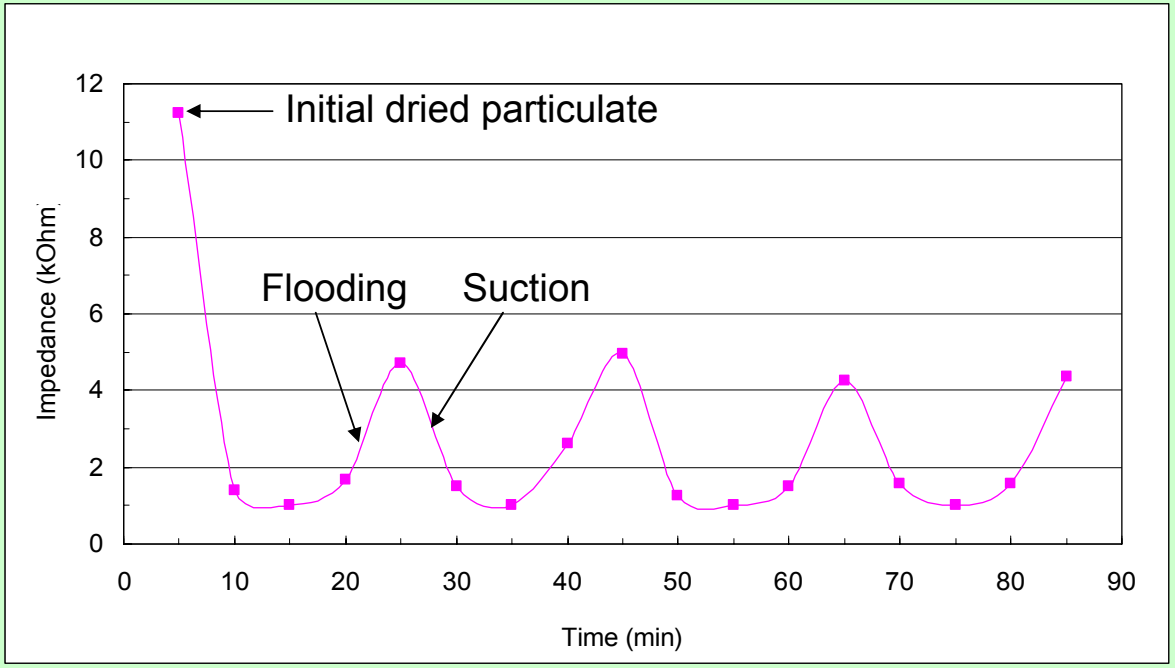

- Variations of the impedance due to repeated solution flooding and suction.

Flexible microfluidic substrate for rhizosphere monitoring and manipulation

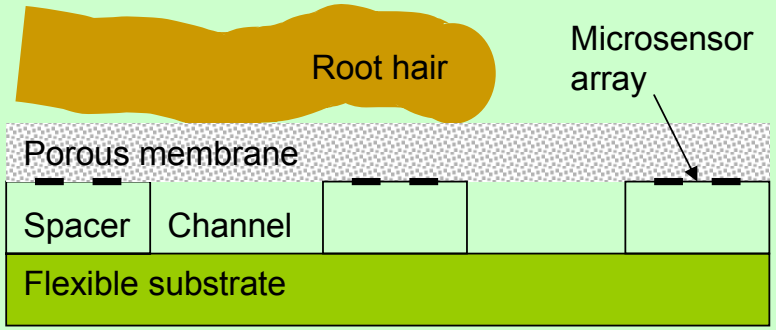

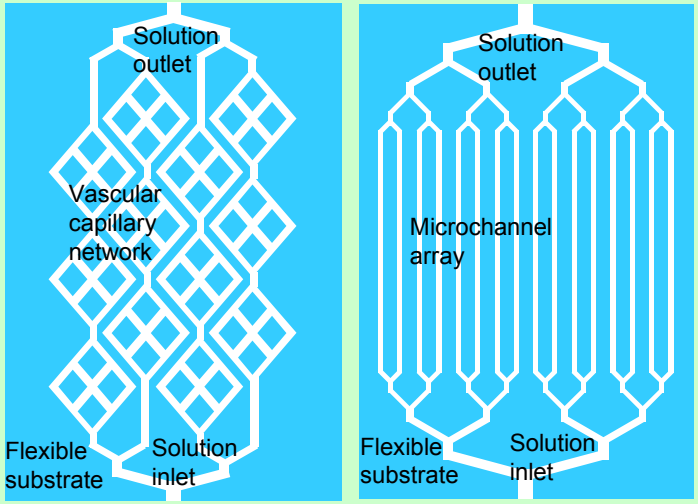

- Root hair growth on the surface of a porous membrane with underlying microfluidic channels and microsensor arrays.
- Exemplary layout of planar microfluidic substrates.

Conceptual growth system using flexible microfluidic rhizosphere substrate

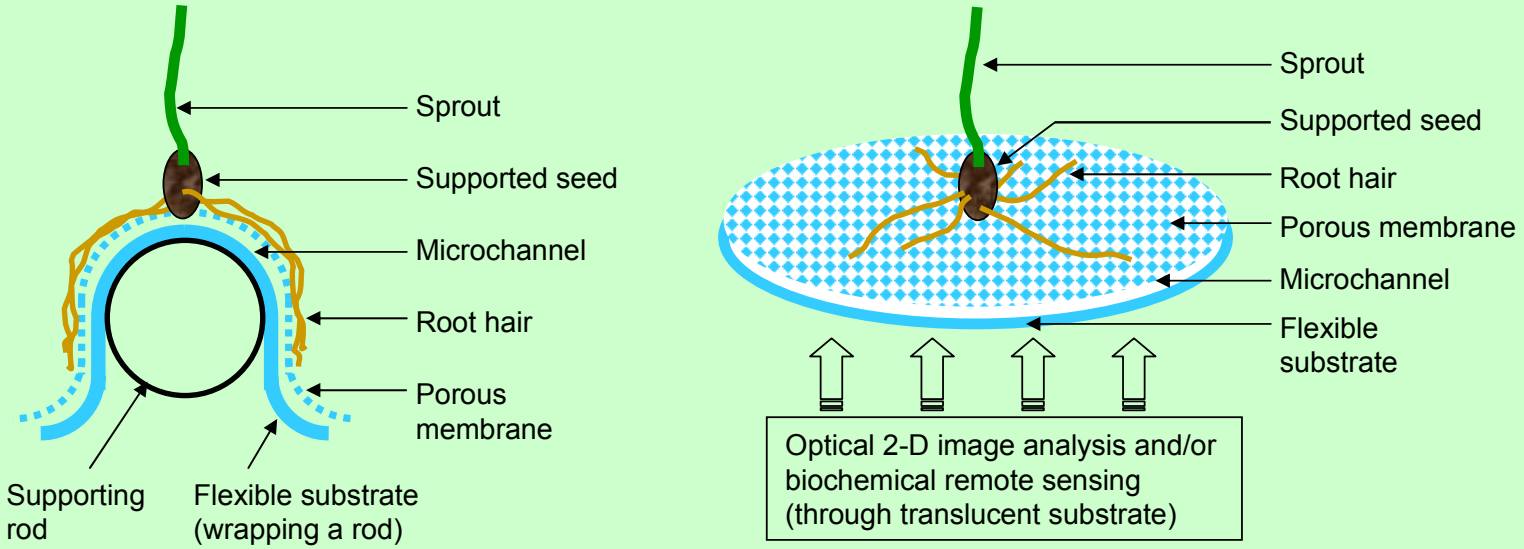

- Rhizosphere manipulation using embedded microchannels (e.g. change of nutrient solution composition).
- Rhizosphere *in situ* monitoring using embedded microsensor arrays or remote optical sensors.
- Root growth pattern analysis using optical imaging.

Summary

- Demonstration of feasibility of microsensor for porous tube and particulate growth systems.
  - Dissolved oxygen.
  - Wetness.

- Flexible microfluidic substrate with microfluidic channels and microsensor arrays.
  - Dynamic root zone control/monitoring in microgravity.
  - Rapid prototyping of phytoremediation.
  - A new tool for root physiology and pathology studies.

Acknowledgement: NASA grant NAG9-1423

Spray Cooling Processes for Space Applications

John P. Kizito*, Randy L. Vander Wal, Gordon Berger
National Center for Microgravity Research, NASA Glenn Research Center, 21000 Brookpark Rd, Cleveland, OH 44135
*Tel 216 433 2275, Fax 216 433 3793, John.Kizito@grc.nasa.gov
and
Gretar Tryggvason
Worcester Polytechnic Institute

Abstract

The present paper reports ongoing work to develop numerical and modeling tools used to design efficient and effective spray cooling processes and to determine characteristic non-dimensional parametric dependence for practical fluids and conditions. In particular, we present data that will delineate conditions towards control of the impingement dynamics of droplets upon a heated substrate germane to practical situations.

INTRODUCTION

Current data on droplet dynamics is scarce for the sizes and velocities typical of practical applications. In particular, improved understanding of drop breakup dynamics is needed to optimize the desired behavior of impinging drops in practical situations such as spray combustion in diesel engines, rocket engines, agricultural and medical sprays, spray painting, printed circuit manufacturing, aircraft icing and spray cooling of high heat-flux electronic components.

While much more representative of practical applications, the small spatial scales and rapid time-scales prevent detailed measurement of the internal fluid dynamics and liquid property gradients produced by impinging upon surfaces. Realized through the extended spatial and temporal scales afforded by a microgravity environment, an improved understanding of drop breakup dynamics is sought to understand and ultimately control the impingement dynamics of droplets upon surfaces in spray cooling.

Our long term goal is to investigate the mechanism(s) for droplet breakup and the effects of relative droplet-surface temperature, ambient pressure and impingement angle on spray cooling processes. Furthermore, we are developing numerical models that are benchmarked against experimental data capable of predicting droplet-wall dynamics. In practical applications, droplet sizes range from 10 - 100 microns with velocities extending from 1 to beyond 10 m/s. These small spatial scales and short temporal scales prohibit detailed study of the internal fluid dynamics and temperature profiles during droplet-wall interaction.

In the past, direct numerical simulations applying the full Navier-Stokes equations to problems that contain free interfaces which are highly deformable have been difficult and computationally time consuming. To this end, a number of investigators have produced numerical results involving droplet-wall interactions with small parameters far below the

splashing threshold. Therefore, the primary objectives of this paper is to report ongoing work on numerical, experimental, and modeling tools used to investigate the physical mechanism leading to different "splashing modes" and to determine how that process influences spray cooling.

The complete droplet and heated wall interaction problem is highly dependent on the simultaneous coupling of many effects none of which can typically be ignored. The modeling of mass, momentum and energy transport must include surface tension [1], discontinuous material properties and complicated liquid-vapor interface dynamics. We use a two-dimensional axisymmetric front-tracking finite difference code for fluid flow that enables the simulation of problems involving complex motion of the large interface deformations and topology changes with or without a temperature field. The method is based on a finite difference approximation of the Navier-Stokes and energy equations on an unmoving, structured grid and an explicit tracking of the liquid interface on a moving, unstructured grid. The method is an extension of techniques already developed for isothermal, multifluid flows without phase change in both two and three dimensions by Unverdi and Tryggvason [2]. The multifluid code has also been used to investigate the collision of drops, thermal migration of drops and the motion of clouds of bubbles [3,4,5].

THEORETICAL CONSIDERATIONS

Formulation and Numerical Method

Consider a domain consisting of a fluid droplet as shown in **Figure 1**.

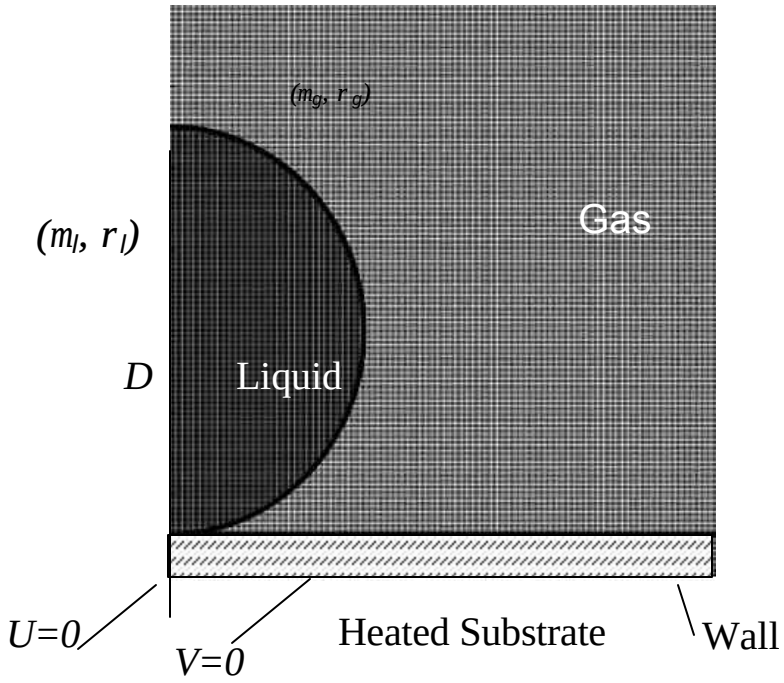

Figure 1 Schematic illustration of computational domain and boundary conditions.

For simplicity, let the material properties of the phases be constant but different within each phase. The basic equations that describe the laws of conservation of mass, momentum, and energy for each phase and jump conditions across the interface are given below. The equations

are solved using the front tracking method where the equations of motion are discretized by the finite difference method on a Cartesian non-uniform staggered mesh. Our approach involves treating the liquid boundary surface as an imbedded interface by adding the appropriate source terms to the conservation laws (momentum, energy and mass). These source terms are in the form of delta functions localized at the interface and are selected in such a way so as to satisfy the correct matching conditions at the phase boundary.

Scaling Analysis

The momentum equation can be non-dimensionalized and normalized to give parameters which describe the process. We normalize the momentum equation by dividing through by the inertia term. The resulting equation will contain the following parameters: Reynolds number, *Re*, Weber number, *We*, Peclet number, *Pe*, density, thermal conductivity, aspect and viscosity ratios described as:

$\mathrm{Re} = \frac{\rho UD}{\mu}$, $We = \frac{\rho U^2 D}{\sigma}$, $Pe = \frac{\rho c_p UD}{k}$, $\frac{\rho_l}{\rho_g}, \frac{k_l}{k_g}, \frac{c_{pl}}{c_{pg}}, \frac{D}{L}$ and $\frac{\mu_l}{\mu_g}$.

The characteristic time is given as T_R seconds: $T_R = \frac{D}{U}$

Where, *D* is the diameter of the initially spherical drop, L is the domain size and U is the impact velocity. The temperature is scaled by the maximum difference. For the example presented here, a drop diameter *D = 0.00196* m, impact velocity *U=2.17 m/s*, and T_R*= 0.0009 seconds.* The temperature difference was held at 10 degrees for all simulated cases *(*$\Delta T = 10$*).*

Table 1. Ethanol Property Parameters

Thermal capacity cp J/(kg K)	Thermal conductivity k W/(m K)	Surface tension σ (N/m)	Density (mass) ρ kg/m^3	Dynamic viscosity μ·10^6 Pa.s
2840	0.18	0.023	789.3	1200

Table 2. Representative Non-Dimensional Parameters

Re	*We*	*Pe*	$\frac{\rho_l}{\rho_g}$	$\frac{k_l}{k_g}$	$\frac{c_{pl}}{c_{pg}}$	$\frac{D}{L}$	$\frac{\mu_l}{\mu_g}$
2824.	317.8	53201.	681	6.92	2.82	0.25	64.9

Numerical Test Matrix

Table 3 summarizes the parameters used for the numerical simulation cases.

Table 3. Numerical Parameters for the simulated experiments

Case	*Re*	*We*	*Pe*	*k* ratio	*m* ratio	*r* ratio
1	2777.8	316.9	53201	6.92	64.9	681
5	27.8	3.17	50	2	25.7	10
9	277.8	31.7	5	200	257.	10
11	277.8	316.9	500	2	257.	10

Problem definition

Axisymmetric representation permits simulation of half of the domain as shown in **Figure 1**. The initial height of the liquid film is of the same order of magnitude as the diameter of the drop. The drop diameter D at a velocity U approaches a substrate at temperature T_b. The subscript l represents the liquid and g represents the gaseous phase. We assume a no slip and no penetration boundary condition at the wall. We have found that a grid size of 400x400 is adequate to capture the physics.

EXPERIMENTAL METHODS

Figure 2 illustrates our basic experimental approach. A Kodak EktaPro HG 2000 high-speed camera was manually triggered and recorded the droplet impact at 2000 frames/sec for half of the imaging field. The exposure time was set at 28 ms while using a 105 mm Nikkor lens set at an aperture of 32 to minimize motion blurring and to provide a large depth of field. A halogen lamp illuminated the impact site through a single sheet of Roscoe 111 diffusion film to provide uniform high intensity back lighting. An Incandescent lamp was used to provide back-illumination. A droplet deployment device was positioned above a heated billet. The inertial-based release mechanism included interchangeable needles to hold different volumes of a wide variety of liquids with many different physical properties. Droplets were measured volumetrically and manually placed on the needle with a syringe. A droplet size of 0.197 cm in diameter (4 µL volume) was chosen because the liquid maintained a spherical shape throughout the free fall, negating concerns of an uneven impact. The liquid was then deployed by way of a simple manual trigger that released a rubber band in tension at the top of the mechanism. The relaxing rubber band then moved the needle quickly upward, pulling it out of the liquid droplet and releasing the droplet to fall onto the film below.

Droplet velocities were increased or decreased by translating the release mechanism vertically and taking advantage of gravitational acceleration. All velocities were measured using XCAP 2.0, an image acquisition and analysis program from EPIX. Measured velocities have an error of ± 0.15 m/s based on the pixel size and 0.5 ms image spacing.

The temperature of the heated billet is held constant during the droplet impact. Visualization of the droplet-wall interaction is achieved through a combination of high speed video and repetitive stop action photography whereby images at different stages of evolution are captured from separate but equivalent events.

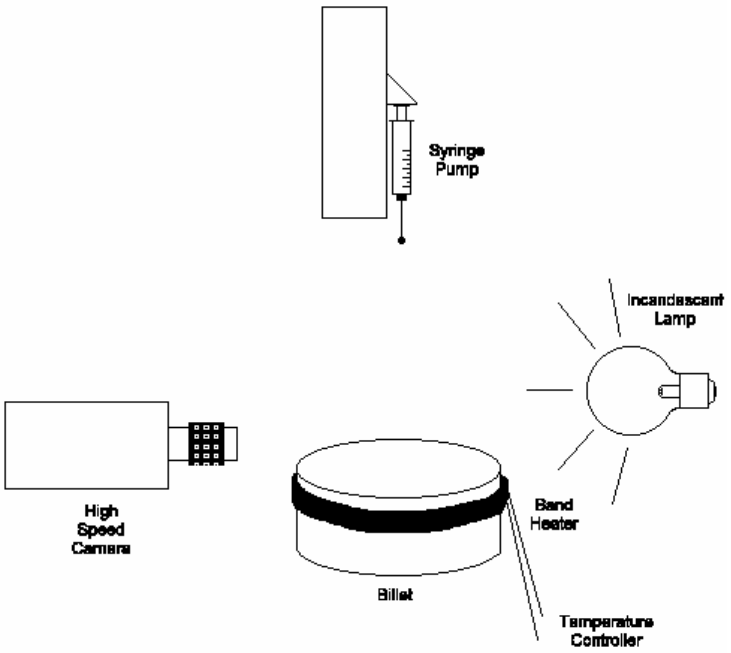

Figure 2 Schematic illustration of experimental setup.

The fluids used include alkanes (HPLC grade heptane and hexadecane and anhydrous decane) and alcohols (spectrophotometric grade methanol and n-propanol and reagent grade butanol), whose properties were gathered experimentally. Deionized water was obtained from a Millipore AFS filtration system. The properties of the glycerol solution were measured using a Cannon-Fenske (Reverse Flow) viscometer and Cahn tensiometer. Table 1 contains relevant properties of a sample fluid used in this study.

RESULTS

An example of our experimental data is presented below in Figures 3. These images are of a relatively high viscosity fluid (*Re*=620, and *We*=104), hexadecane impacting a mirror-polished surface. At a higher impact velocity, 3.15m/s (*Re*=1436, and *We*=559), the droplet forms splashed products.

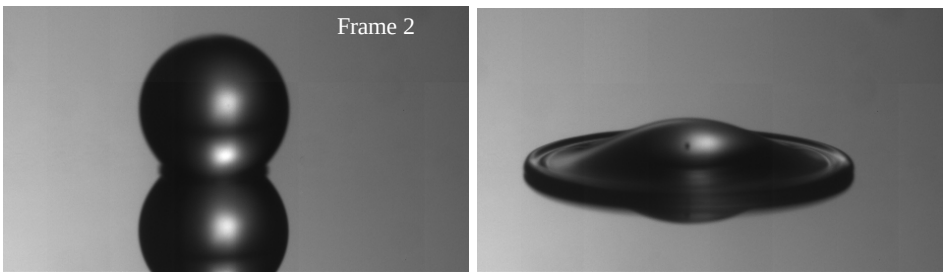

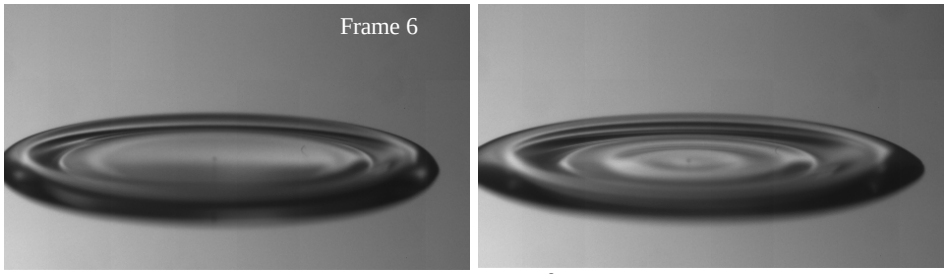

Figure 3. Hexadecane impacting a mirror-polished surface at 1.36m/s (*Re*=620, and *We*=104). The images were acquired using a high-speed camera at 2000 frames per second.

The droplet interaction with a heated substrate was computed for a variety of parameters listed in table 1. The computational domain was 4 times the droplet diameter in each direction and was resolved by a grid of 400x400 nodes (the results were independent of the grid size). The computational results are shown in Figure 4 and denoted by case number. Figure 4 shows numerical simulations of a droplet-wall interaction.

Figure 4 shows results of collision of cold droplet with a heated substrate at dimensionless time, t = 20 for the parameters listed in Table 3. The isotherms are shown on the left and the corresponding velocity vector map is shown on the right. These cases show the effect of viscosity, surface tension, and thermal diffusivity represented by *Re*, *We*, and *Pe* respectively. Other parameters that represent the fluid property ratios were varied. The parameters were changed by an order of magnitude to determine the mechanism that allows maximum heat transfer between a cold droplet and a heated wall. The assessment is mostly qualitative; determined by the extent of spreading and the concentration of isotherms next to the heated substrate (thermal boundary layer formation). The concentration of isotherms indicates increased thermal energy transport to the droplet.

For all cases, the motion of the droplet draws cold gas towards the heated substrate. As the droplet approaches the heated wall, it displaces the ambient gas from the substrate depending on the control parameter. The droplet will come into contact with the wall and then deform interchanging the energy between kinetic and surface energies. Depending on the magnitude of the initial kinetic energy and the exchange dynamics between kinetic and surface energy, the droplet will either rebound or remain in contact with the surface. The effect of surface tension is to minimize surface area. When kinetic energy reaches a minimum, a surface tension force causes the flattened droplet to retract to its former spherical shape thus causing the droplet to rebound and leave the substrate. The amount of heat transferred depends on the interaction time and the extent of droplet spread.

Let's use case 1 as the basis of comparison for all numerical simulation data in Figure 4. The parameters for case 1 were exactly marched with the experimental parameters shown in table 2. Numerical experiments show that the density ratio is not sensitive to the droplet shape. The isotherms shown in case 1 are closer to each other because of the high *Pe* number. The isotherms shown in case 1 are closer to each other because of the high *Pe* number. The effect of increasing the impact velocity is apparent when case 1 is compared with case 5. At low impact velocity, the droplet remains spherical and hardly displaces any air from the heated substrate. In addition, the heat transfer in case 5 is poor because of minimal interaction with the substrate. The effect of low *We* number is evident in case 9. The droplet undergoes a small deformation

which leads to a shortened droplet-wall interaction time and a much quicker rebound. The shorter stay at the heated wall will result in diminished cooling effect by the droplet.

The effect of increasing the fluid viscosity is demonstrated by case 11. Here, the *Re* number is reduced while the *We* number is held constant. The spread extent decreases and the droplet deforms to a disc-like shape. This case provides for the best heat transfer profile because of increased surface area of the fluid in contact with the heated substrate. In addition, the center of the droplet is not drained of its liquid, consequently there is more fluid heat capacity available.

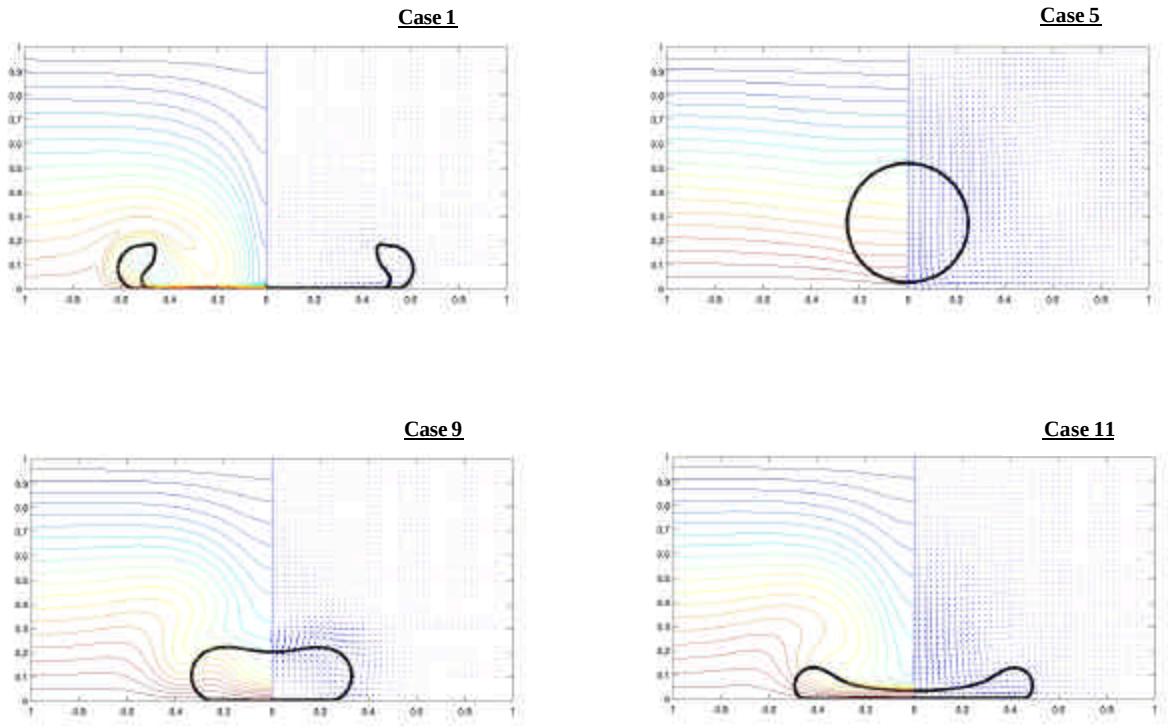

Figure 4. Collision of a cold droplet with a heated substrate at dimensionless time, t = 20 for the parameters list in Table 3. The isotherms are shown on the left and the corresponding velocity vector map is shown on the right.

CONCLUSIONS

We have presented numerical and experimental data used to investigate the physical mechanism leading to "splashing modes" and to determine parametric non-dimensional number dependencies for impinging droplets on spray cooling. The data shows that for non-evaporating drop approaching and interacting with a heated substrate, maximum heat is transferred when the droplet has the widest extent of spread on the substrate and does not form a crown or splashed

products. Therefore, it is important to know and map splash regimes in order to design effective droplet cooling devices.

ACKNOWLEDGEMENTS

This work was supported by a NASA NRA 98-HEDs-03 fluid physics award administered through NASA cooperative agreement NCC3-975 with The National Center for Microgravity Research on Fluids and Combustion (NCMR) at The NASA-Glenn Research Center. The authors gratefully acknowledge Steven D. Mozes and Premal D. Patel for assistance with the experiments. Also, we are grateful to Dr Asghar Esmaeeli for assistance with the numerical code.

REFERENCES

1. Gupta N. R., Balasubramaniam R. and Stebe K. J. (2002) "Rapidly Expanding Viscous Drop from a Submerged Orifice at Finite Reynolds Numbers", Ann. New York Academy Sci. An. N.Y. Acad. Sci. 974:398-409
2. Unverdi, S. O. and Tryggvason, G. (1992) "A front-tracking method for viscous, incompressible", multi-fluid flows. J. Comp. Phys. 100: 25-37
3. Nobari, M. R., Jan, Y.J., and Tryggvason, G. (1996) "Head on collision of drops - numerical investigation", Phys. Fluids 8, 29-42.
4. Nas, S. and Tryggvason, G. (1993) "Computational investigation of thermal migration of bubbles and drops", In Fluid Mechanics Phenomena in Microgravity, AMD 174/FED 175, pp. 71-83. ASME: New York.
5. Esmaeeli, A. and Tryggvason, G. (1996) "An inverse energy cascade in 2-dimensional low Reynolds number bubbly flows", J. Fluid Mech. 314: 315-330.

EFFECTS OF GRAVITY ON BUBBLE FORMATION IN AN ANNULAR JET

R.A. Koepp, R.N. Parthasarathy and S.R. Gollahalli
School of Aerospace and Mechanical Engineering
The University of Oklahoma
Norman, OK 73019
E-mail: rparthasarathy@ou.edu; Phone: 405-325-1735

The effects of gravity on the bubble formation in an annular jet were studied. The experiments were conducted in the 2.2-second drop tower at the NASA Glenn Research Center. Terrestrial gravity experiments were conducted at the Fluid Dynamics Research Laboratory at the University of Oklahoma. Stainless steel tubing with inner diameters of 1/8" (gas inner annulus) and 5/16" (liquid outer annulus) served as the injector. A rectangular test section, 6" x 6" x 14" tall, made out of half-inch thick Lexan was used. Images of the annular jet were acquired using a high-speed camera. The effects of gravity and varying liquid and gas flow rates on bubble size, wavelength, and breakup length were documented.

In general, the bubble diameter was found to be larger in terrestrial gravity than in microgravity for varying Weber numbers (0.05 – 0.16 and 5 – 11) and liquid flow rates (1.5 ft/s – 3.0 ft/s). The wavelength was found to be larger in terrestrial gravity than in microgravity, but remained constant for varying Weber numbers. For low Weber numbers (0.05 – 0.16), the breakup length in microgravity was significantly higher than in terrestrial gravity. Comparison with linear stability analysis showed estimated bubble sizes within 9% of experimental bubble sizes. Bubble size compared to other terrestrial gravity experiments with same flow conditions showed distinct differences in bubble size, which displayed the importance of injector geometry on bubble formation.

Effects of Gravity on Bubble Formation in an Annular Jet

R. A. Koepp, R. N. Parthasarathy, and S. R. Gollahalli
School of Aerospace and Mechanical Engineering
University of Oklahoma
Norman, OK

Acknowledgments:
John McQuillen, Brian Motil
NASA GRC

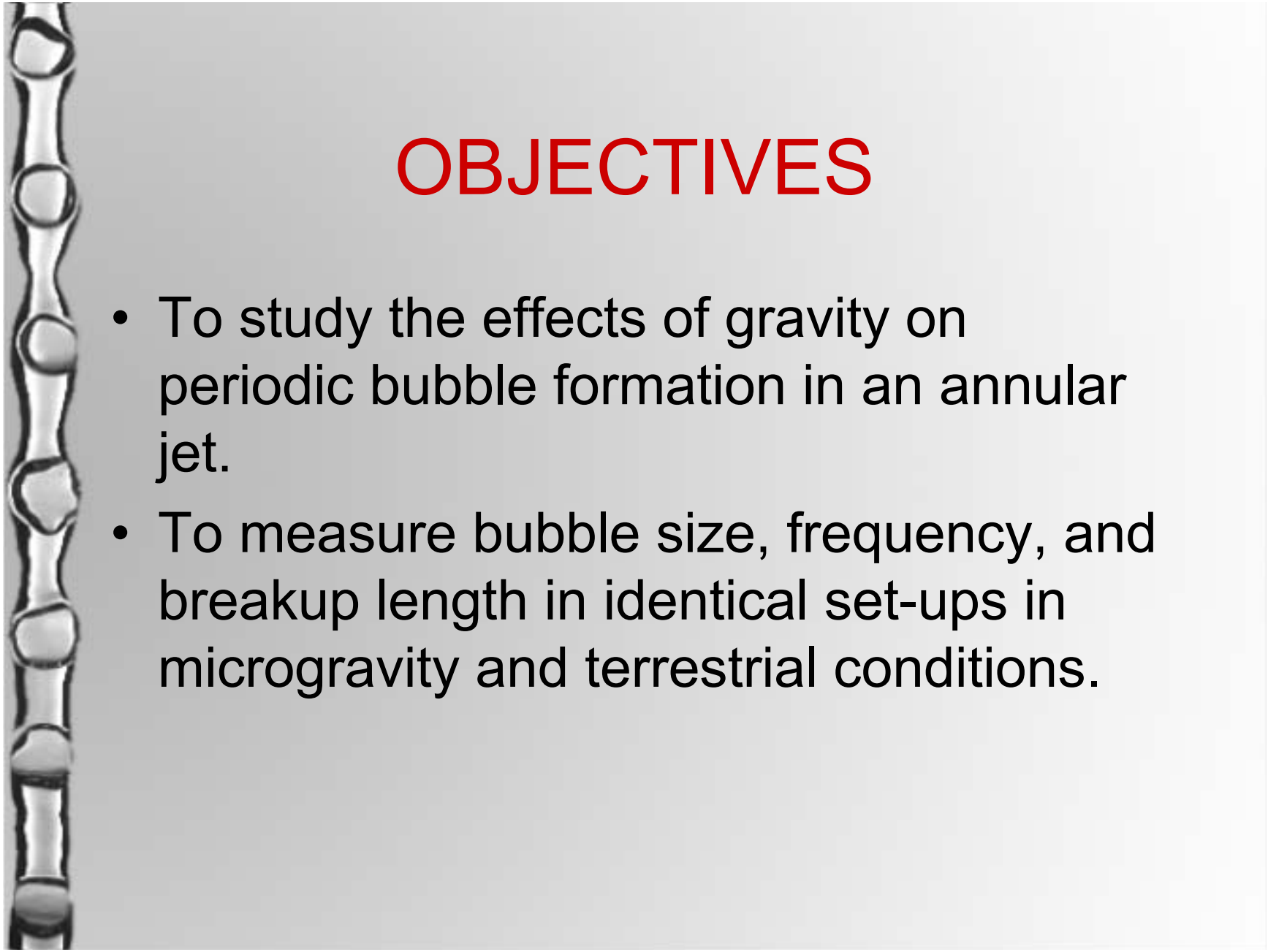
OBJECTIVES
• To study the effects of gravity on periodic bubble formation in an annular jet.
• To measure bubble size, frequency, and breakup length in identical set-ups in microgravity and terrestrial conditions.

SET-UP

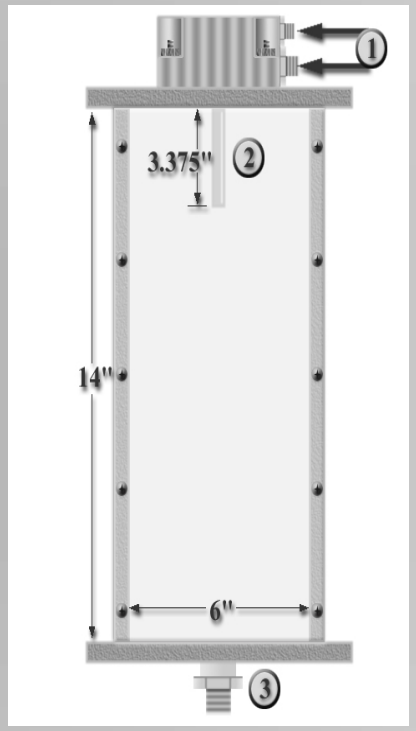

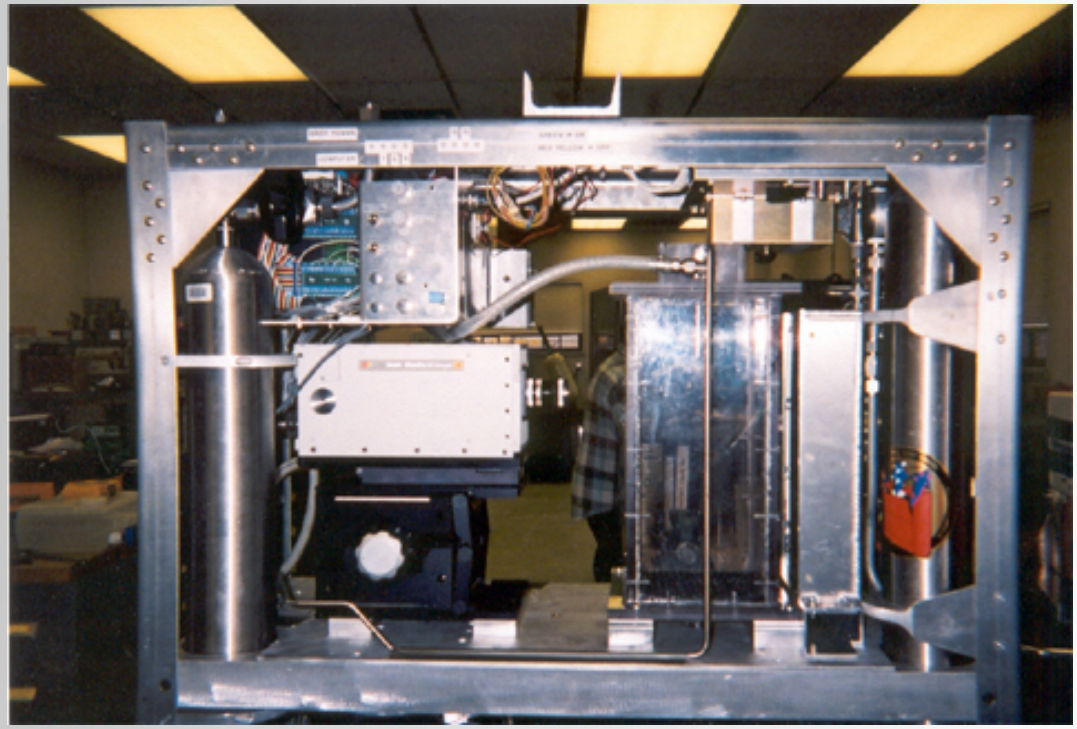

We = 0.05

$U_l / U_g = 0.4$

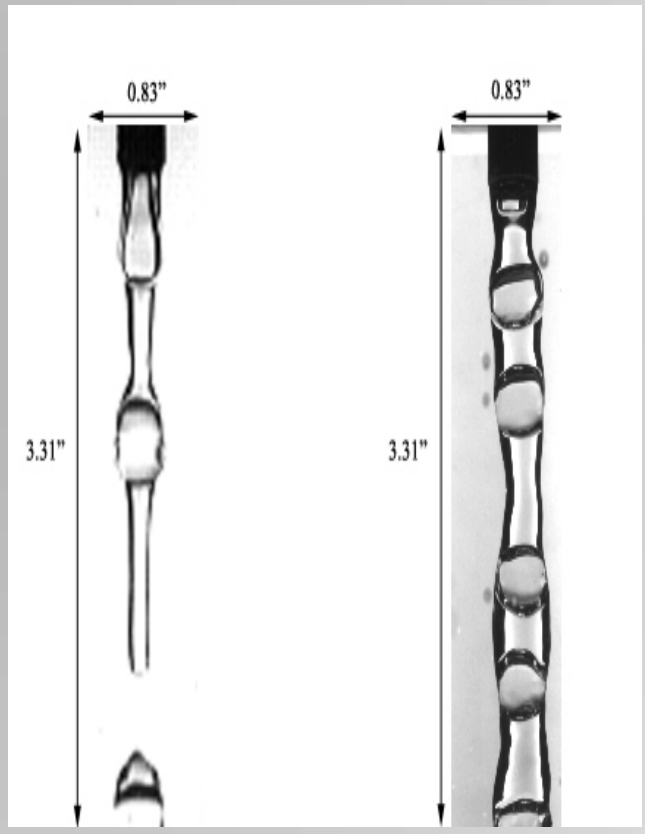

$U_l / U_g = 0.6$

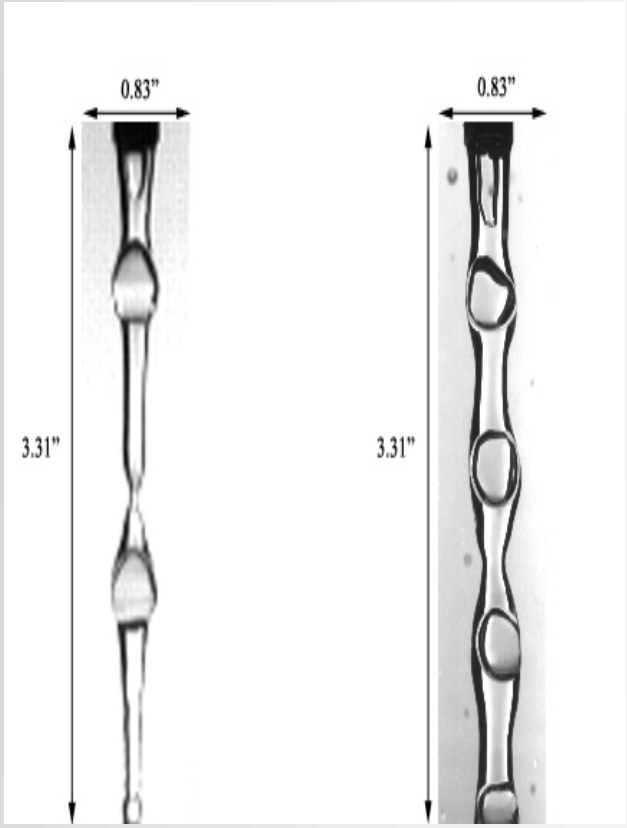

We = 5

$U_l / U_g = 0.05$

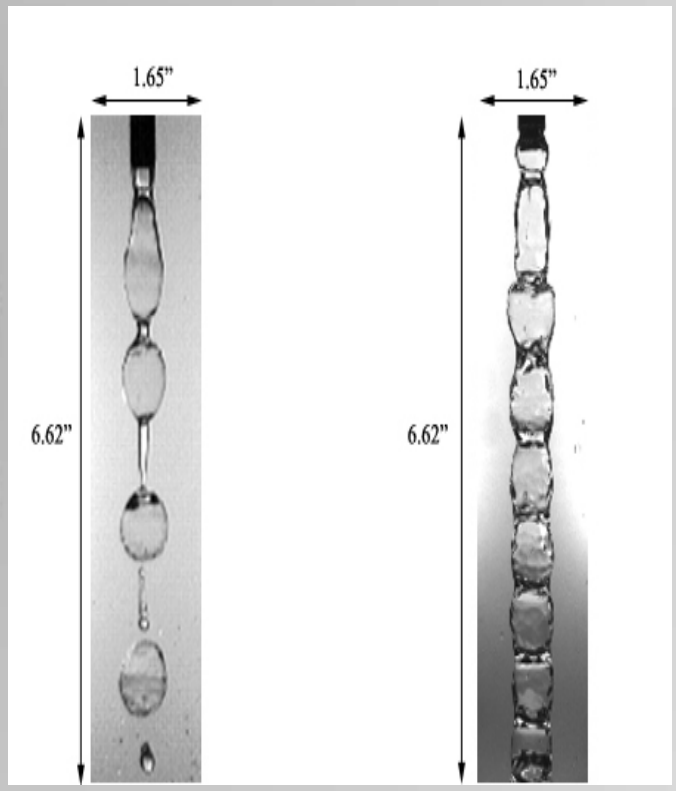

$U_l / U_g = 0.09$

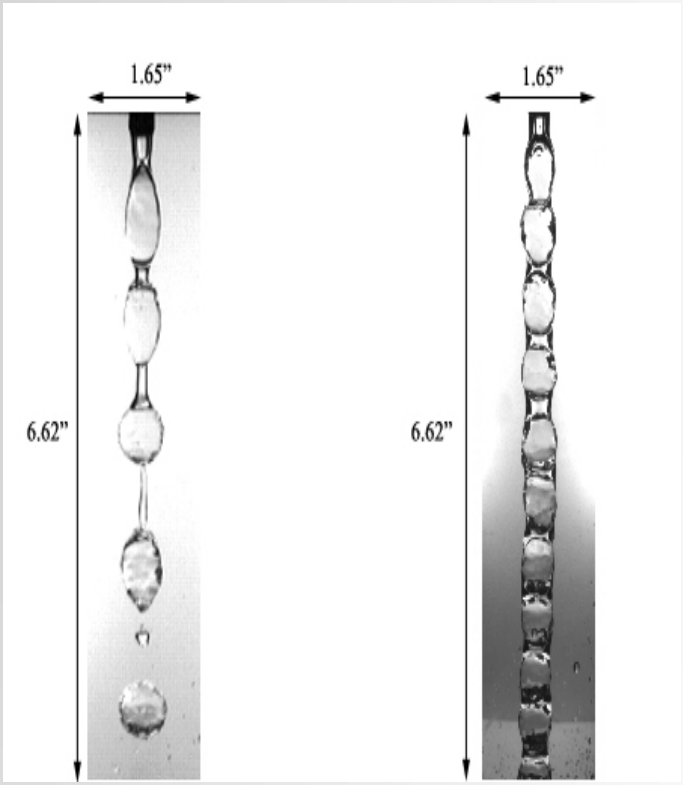

We = 10.5

$U_l / U_g = 0.03$

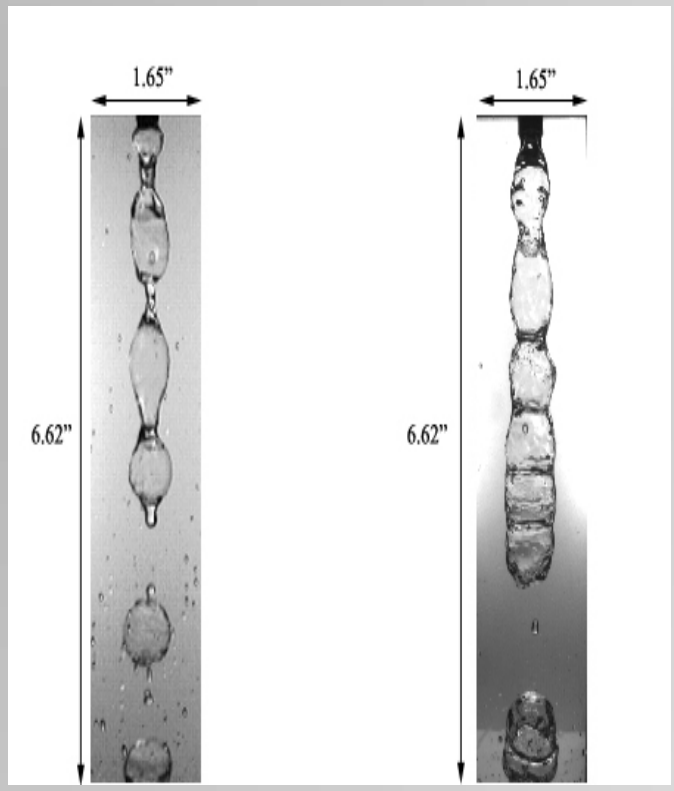

$U_l / U_g = 0.07$

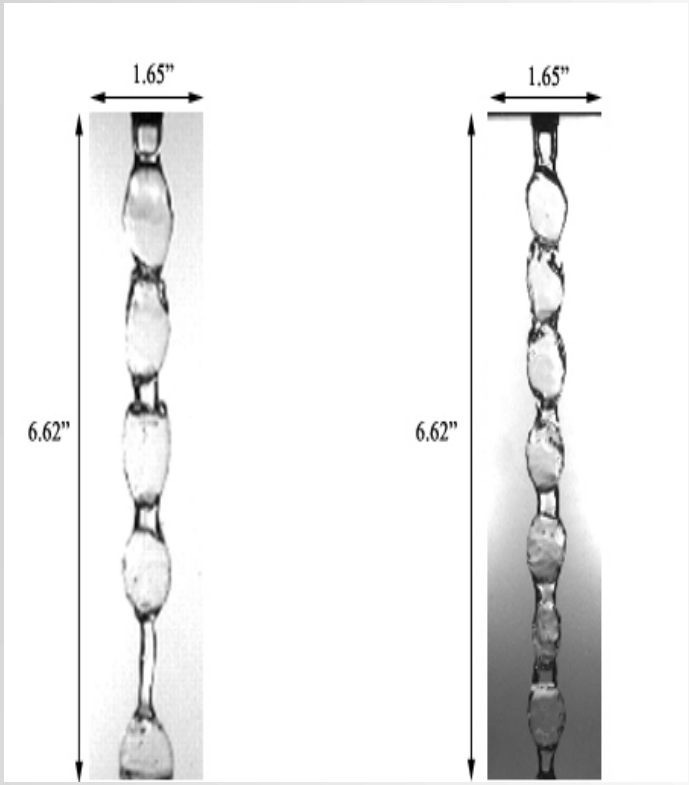

Normalized Bubble Size

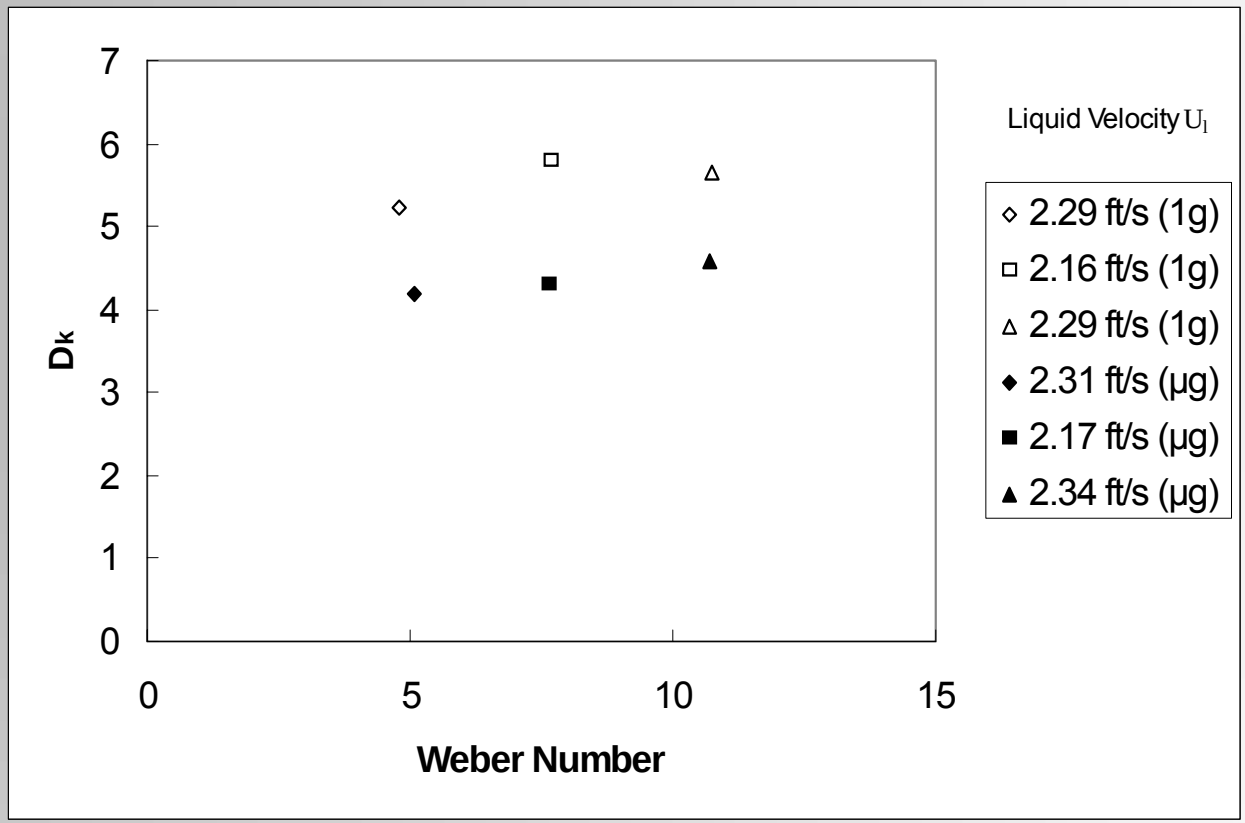

Normalized Breakup Length

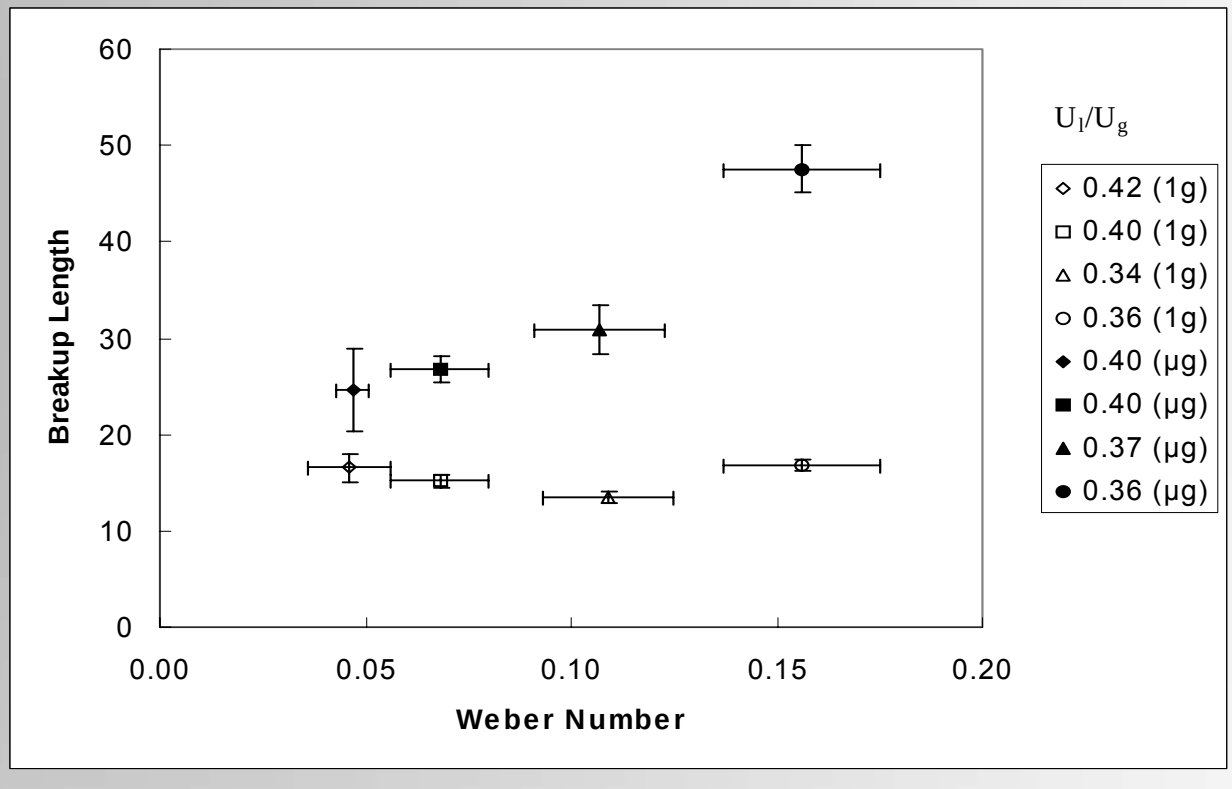

Conclusions

Bubble size was larger in normal gravity than in microgravity due to reduced relative velocities and buoyancy effects.

Wavelength was larger in normal gravity due to the stretching of the jet.

Acceleration due to gravity caused the jet to thin and pinch off leading to shorter breakup lengths in normal gravity.

Breakup was not observed in microgravity at large Weber numbers.

A STUDY OF COLLOIDAL CRYSTALLIZATION

Wesley M. Kopacka, Andrew D. Hollingsworth, and William B. Russel
Department of Chemical Engineering, Princeton University 08544

Paul M. Chaikin
Department of Physics, Princeton University 08544

One of the still open problems in condensed matter physics today is that of crystallization.[1] The ability to accurately study atomic or molecular crystallization is hindered by the incredibly small length and time scales involved compared to many of the experimental techniques available today. On the biological front, determining the structure of the more than 80,000 proteins in the human body is limited by our inability to crystallize proteins effectively. As a result, only 4000 human protein structures have been solved. Nanotechnologies such as photonic band gap materials and photothermal nanosecond light-switches rely heavily on being able to control crystallization to achieve particular packing structures, spacings, and sizes. A firm understanding of the thermodynamic and kinetic driving forces is therefore essential in fabricating products with specific properties. Model systems to study the physics behind the phase behavior, structure, and dynamics of crystallization are needed to shed light to the various applications being studied today.

Colloidal suspensions may be considered ideal model systems because of the significant amount of knowledge and advances that have occurred in colloid science. In addition, colloidal length and time scales can be easily explored with many common instruments used today. Colloids are already being used to model protein crystallization and are the precursors for most nano-devices being developed. However, current research on the crystallization of high-density model colloidal suspensions has yet to produce definitive conclusions on the kinetics for nucleation and growth mechanisms in the various phases. Results for different "model" systems often differ, raising questions as to whether the system is actually a well-defined "model", experimental techniques are inaccurate, or assumptions are incorrect. Recently, microgravity experiments on colloidal crystallization[2,3] revealed dendrites in the coexistence regime and crystallization in the usually "glassy" region of the hard sphere phase diagram, both of which were never before observed in ground-based experiments. This posed yet another question as to the role that gravity plays in crystallization. Although it would be ideal to perform these experiments in a microgravity environment where the effects of convection and buoyancy are not present, a suitable alternative is to index- and density-match the particles and solvent to which the equivalence of a milligravity environment is achieved. The presence of crystals well into the glass regime has been observed recently in a ground-based experiment in which index and density matching was utilized to simulate milligravity.[4] Performing experiments in these conditions will also provide insight and direction for studies using the PCS+ (Physics of Colloids in Space+) aboard the International space station in 2005.

My research details a thorough, quantitative analysis of the kinetics of hard sphere colloidal crystallization, reducing the effect of gravity by density-matching the particles and solvent. The primary tool is the PHaSE (Physics of Hard Spheres Experiment) multi-functional light scattering apparatus flown on board two MSL-1 (Microgravity Science Laboratory-1) missions

in 1997, STS-83 and STS-94, which now resides in the Princeton Materials Institute at Princeton University. Recently, experiments have also been performed using the PCS+ instrument, an upgraded version of the PHaSE instrument that will be used for the mission currently scheduled to fly at the end of 2005. Nucleation and growth can be followed accurately over long periods of time with the PHaSE/PCS+ instruments and index/density-matched suspensions. The following phenomena are being studied: (1) the growth mechanisms in the coexistence regime, (2) the formation of dendrites near freezing, and (3) the crystallization of "glassy" samples. The exhaustive quantitative studies of these phenomena under milligravity conditions fill an important void in the scope of crystallization behavior previously studied under normal gravity and future micro-gravity data from the PCS+ mission.

[1] Cheng, "Colloidal hard sphere crystallization and glass transition," Thesis, **1998**.
[2] Zhu, Li, Rogers, Meyer, Ottewill, STS-73 Space Shuttle Crew, Russel, & Chaikin, *Nature*, 387: 883-885, **1997**.
[3] Cheng, Zhu, Russel, Meyer, & Chaikin, *Applied Optics*, 40(24): 4146-4151, **2001**.
[4] Kegel, *Langmuir*, 16: 939-941, **2000**.

CONTACT INFORMATION

Mr. Wesley M. Kopacka
Graduate Student

Princeton University
Department of Chemical Engineering
A-217 Engineering Quadrangle
Princeton, NJ 08544

wkopacka@princeton.edu
609-258-2123 (office)
609-258-6878 (fax)

A Study of Hard Sphere Colloidal Crystallization

Wesley M. Kopacka[1], Paul M. Chaikin[2], and William B. Russel[1]

[1]*Dept. of Chemical Engineering,* [2]*Dept. of Physics*
Princeton University, Princeton, NJ 08544

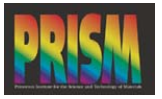

Objective

To probe in quantitative detail the kinetics of nucleation and growth of hard sphere crystals

...to understand three novel features deduced from the PHaSE experiment:

1) Coarsening of crystallites during the growth phase
2) Growth of dendritic crystallites at conditions just above the freezing transition
3) Crystallization of glassy phases in reduced gravity

Hard Spheres

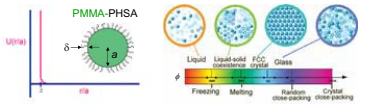

PMMA: poly(methyl methacrylate), a ~ 300 nm
PHSA: poly(12-hydroxystearic acid), δ ~ 10 nm

ϕ – volume fraction
r – distance
U – interparticle potential

- Hard sphere-like potential:
  - ✓ Steric stabilization – establish repulsive force 'near contact'
  - ✓ Refractive index-matching – minimize attractive van der Waal forces
- Density-matching – minimize sedimentation
  - ✓ Ability to perform long-time kinetic studies (t > 1 week)
  - ✓ Gravitational heights between typical 1g and μg environments

Formulation

Gravitational height, h

$$h = \frac{k_B T}{m_b g}$$

Solvents	1g	μg
cis/trans-decalin & tetralin	20 μm	20 m
???	20 mm	

$k_B T$ – thermal energy
m_b – buoyant mass of particle

Abbreviations:
- Decahydronaphthalene (decalin)
- Tetrahydronaphthalene (tetralin)
- Tetrachloroethylene (TCE)

- Decalin and tetralin typically used to index-match PMMA-PHSA particles
- 3rd solvent needed to match density as well → tetrachloroethylene

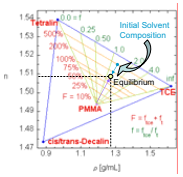

- Density-matching NOT trivial
- Tetralin and TCE swell PMMA
- Particles and solvent initially prepared mis-matched to account for changing properties as particles swell
- Centrifugation & light scattering techniques used to quantify swelling & ρ/n-matches
- Analytical expressions used to quantify shift in physical properties
- Free volume included to account for non-ideal mixing

$$n' = \frac{n_{pmma}(1-v) + n_s(f_s + x_s v) + n_{tet}(f_{tet} + (1-x_s)v)}{1 + f_s + f_{tet}}$$

$$\rho' = \frac{\rho_{pmma}(1-v) + \rho_s(f_s + x_s v) + \rho_{tet}(f_{tet} + (1-x_s)v)}{1 + f_s + f_{tet}}$$

v – free volume
n – refractive index
ρ – density
f_i – volumetric swelling factor
x_i – fraction of free volume occupied by tetralin

Dilute Characterization

Static Light Scattering (SLS):

- Dilute suspensions exposed to laser light for given amounts of time
- Time-averaged scattered intensity probed over various angles
- Rayleigh ratio used to quantify the 'scattering strength' of the particles

$$R(q) = N\frac{I(q)}{I_o}r^2 = Nk^4a^6\left(\frac{m^2-1}{m^2+2}\right)^2 P(q)S(q)$$

= 1, in dilute limit

$I_o \rightarrow$ Incident intensity
$N \rightarrow$ Particle number density
$r \rightarrow$ Distance from scatterer to detector
$a \rightarrow$ Particle radius
$k \rightarrow$ Propagation constant $= 2\pi n_s/\lambda_o$
$m \rightarrow$ Relative refractive index $= n_p/n_s$
$q \rightarrow$ Wavenumber $= \frac{4\pi n_s}{\lambda_o}\sin\left(\frac{\theta}{2}\right)$

for a spherical particle...

$$P(q) = \frac{9}{(aq)^6}\left[\sin aq - aq\cos aq\right]^2$$

with a finite distribution of particle sizes...

$$\overline{P(q)} = \int_0^\infty a^6 P(a,q)G(a)da$$

$R(q) \rightarrow$ Rayleigh ratio
$I(q) \rightarrow$ Scattered intensity
$P(q) \rightarrow$ Particle form factor
$S(q) \rightarrow$ Structure factor

Dynamic Light Scattering (DLS):

- Probes fluctuations in scattered intensity → directly related to Brownian motion of the particles
- Intensity autocorrelation function, $g^{(2)}$, calculated over many decay times, τ

$$g^{(2)}(q,\tau) = \frac{\langle I(q,t)I(q,t+\tau)\rangle}{\langle I(q,t)\rangle^2} \rightarrow \lim_{\tau\to 0}\frac{d\ln g^{(2)}(q,\tau)}{d\tau} = -2q^2 D_{eff}(q)$$

$$G(a) = \frac{1}{\sqrt{2\pi}\delta}\exp\left[-\frac{(a-\bar{a})^2}{2\delta^2}\right]$$

$g^{(2)}(q,\tau) \rightarrow$ Normalized intensity-intensity autocorrelation function
$G(a) \rightarrow$ Gaussian PSD

$$D_{eff}(q) = \frac{k_B T}{6\pi\mu a_{eff}} = \frac{\int_0^\infty a^6 P(a,q)D_s(a)G(a)da}{\int_0^\infty a^6 P(a,q)G(a)da}$$

$D_s(a) \rightarrow$ Stokes-Einstein diffusion coeff.
$\mu \rightarrow$ Solvent viscosity

Characterization Results

- Results for PMMA-PHSA, batch ADH005

Case 1: ADH005 in non-swelling decalin
Case 2: ADH005 in an equilibrated index and density-matching solvent mixture of decalin, tetralin, and TCE

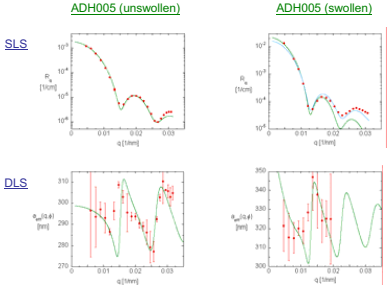

a = 292.0 nm
σ = 6.8 %

a = 322.3 nm
σ = 7.2 %

PHaSE/PCS+ Hardware

- Static light scattering performed on two high volume fraction suspensions
- 532 nm double-pumped, continuous-wave, 100 mW, Nd-YAG solid-state laser
- Beam enters test section via fiber optic cable, passes through collimator, then enters sample cell
- Lens on sample cell focuses scattered light onto fluorescent screen
- Images collected via a CCD camera for analysis

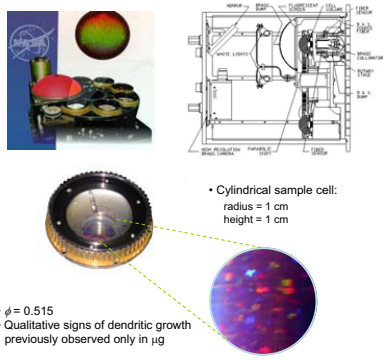

- ϕ = 0.515
- Qualitative signs of dendritic growth previously observed only in μg

Scattering Data

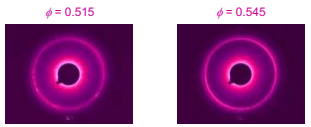

- CCD images of two samples taken ~ 15 hours after shear melting
- Images collected from the PCS+ hardware

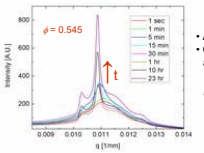

- As ϕ increases from the dilute limit, $S(q) \neq 1$
- Crystal structure and kinetics studied by analyzing evolution of $S(q)$ curves over time

$$S(q) = I(q)/CP(q)$$

$C \rightarrow$ instrument factor

Extracting Crystal Parameters

- A Gaussian is fit to the main Bragg peak – the profile of which is related to crystal parameters

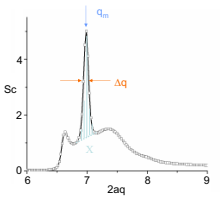

- Crystal volume fraction:
$$\phi_c(t) = \frac{2}{9\pi^2\sqrt{3}}\left[q_m(t)a\right]^3$$
- Average crystal size:
$$L(t) = \pi\kappa/\Delta q(t)a, \quad \kappa = 1.155$$
- Crystal fraction:
$$X(t) = c\int_{q_1}^{q_2} S_c(t)\,dq$$
- Number density of crystals:
$$N_c(t) = X(t)/L^3(t)$$

- For a given crystal size and interparticle spacing, different crystal packings result in different peak profiles
- Colloidal crystals are known to 'age' over time, that is, become more FCC-weighted during coarsening
- After determining the proper crystal packing, peak profiles can then determine the correct crystal parameters to compare data over all times

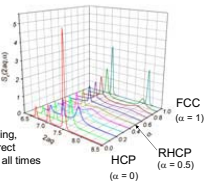

α → faulty stacking probability

Conclusions

- Index and density-match formulation/characterization developed to a high degree of accuracy
- Gravitational heights of h ~ 1 – 2 cm achievable
- Visible evidence of dendritic growth indicates crystallization phenomena similar to that found in microgravity

Future Work

- Develop analysis method to quantitatively extract kinetic parameters
- Perform crystallization studies for volume fractions 0.50 < ϕ < 0.60
- Compare 'milli-gravity' data to data obtained from previous mg and 1g studies

Acknowledgements

- NASA Images:
  - http://microgravity.grc.nasa.gov/6712/comflu/PHaSE_intro.html
  - Stephanie Grasson and Gayle DiBiasio (Graphics Dept.)
  - Emery Adanich (Imaging Technology Center)
- Particle synthesis by Andrew D. Hollingsworth
- Funding by NASA GSRP – grant no. NGT5-50407

GSRP Graduate Student Researchers Program

POSITIONING OF SIMULATED VAPOR BUBBLES IN MICROGRAVITY BY THE KELVIN FORCE

John Kuhlman[+], Donald D. Gray[*], Shannon Glaspell[#], Paul Kreitzer[#], Charlie Battleson[#], Michelle Lechliter[#], Michael Campanelli[#], Nicholas Fredrick[#], Christopher Sunderlin[#], Brianne Williams[#]
West Virginia University, Morgantown, WV 26506

[+]Professor, and [#]Undergraduate Student, Department of Mechanical and Aerospace Engineering
[*]Professor, Department of Civil and Environmental Engineering

INTRODUCTION

Experiments were performed in July 2003 in the NASA "Weightless Wonder" KC-135 aircraft through the Reduced Gravity Student Flight Opportunities Program, to study the influence of the magnetic Kelvin force on the behavior of air bubbles in a paramagnetic liquid in microgravity (μ-g). This aircraft, which flies through a series of parabolic arcs providing about 20 seconds of μ-g per parabola, allowed a unique environment in which to study the resultant phenomena. The experiment was conceived, designed, constructed, and performed by the WVU student team and their advisors.

When there is no dominant body force such as gravity to produce a buoyant force, vapor bubbles that form may remain adjacent to heat rejection surfaces, rather than be driven away due to buoyancy. This reduces the heat exchange rates and can cause burnout or damage the surface that needs to be cooled. The experiment modeled one possible method for repelling the vapor bubbles on a heat rejection surface in μ-g. In the presence of a non-uniform magnetic field, a body force, known as the Kelvin force, is exerted on all magnetically permeable materials. Diamagnetic and paramagnetic fluids are repelled from and attracted to magnetic fields, respectively. The Kelvin force is approximately three orders of magnitude larger for liquids than for gases, leading to a magnetic buoyancy force on bubbles in a liquid.

HYPOTHESIS

This experiment used the Kelvin force to control the position of air bubbles in a 4.9 molar solution of manganese chloride $MnCl_2$ (simulated coolant), which is a paramagnetic liquid. Air bubbles were injected into the bottom of two geometrically identical tanks, one fitted with a 2,000 gauss permanent magnet at the bottom of the tank, and one without a magnet. The Kelvin force exerted on the liquid has been estimated to be approximately 0.28 g. The resulting bubble formation, detachment, and motion were video taped for both tanks under identical gravitational accelerations. In μ-g, it was expected that the Kelvin force would attract the liquid towards the magnet located at the bottom of the tank, thereby driving the air bubbles (simulated vapor bubbles) away from the bottom of the tank.

RESULTS

Results indicated that air bubbles within the magnet tank could be repelled from the magnet surface through the use of the Kelvin force to attract the liquid to the surface. This conclusion was valid for all parabolas for which the free surface of the $MnCl_2$ solution did not invert in the tanks due to small negative-g conditions, and for which the air flow rate was large enough to cause bubbles to flow into both tanks during the microgravity portion of each parabola. Several types of flows were observed during the course of the experiment due to variations in gravity levels onboard the KC-135, as well as variations in air flow from the syringe pump.

For the first type of flow that was recorded, it was observed that as the air bubbles flowed into the geometrically identical tanks at identical flow rates, the control tank (no magnet) allowed the bubbles to become relatively large (~1 cm) before breaking away from the bottom surface of the tank and slowly floating toward the free surface. In the magnet tank, however, the air bubbles were observed to remain smaller (~2-3 mm) and to be more numerous, to detach from the bottom of the tank, and to be forced toward the free surface much more quickly. Sample captured video images of this flow type are shown in Fig. 1 (Day 1, Parabola 33, 8 mm camera) and Fig. 2 (Day 1 Parabola 33, NAC HSV-500C high speed camera at 500 fps).

The second type of flow that was observed also supported the general conclusion that the Kelvin force could repel the air bubbles from the surface of the magnet. However, for this flow situation, bubbles were not pushed completely to the free surface in the magnet tank. Instead, bubbles were forced away from the magnet surface and remained within the fluid at some distance from the magnet surface. This was caused by negative fluctuations in gravity that reduced the momentum of the air bubbles moving toward the free surface, causing a change in direction. Often, in this circumstance, the control tank bubbles would rest on the tank bottom.

For several parabolas, there was a period of negative gravity. The free surface within the tanks would invert, preventing bubble formation. Sometimes, the negative gravity would "prime" the syringe pump, allowing the bubbles to more easily flow into the tanks once the liquid had returned to the bottoms of the tanks. The data collected from these parabolas was not discarded if there were periods of zero gravity either directly before or after the inversion, and bubbles were observed in both tanks once the period of inversion ended.

The double syringe pump used for the experiment was expected to function in microgravity similar to how it did with Earth gravity. However, once in flight, the lower flow rates (below approx. 1 mL/min) were found to be inadequate under microgravity conditions to drive out the liquid solution that entered the air supply tubes during the 1.8-g pull out portions of the parabolas. Generally, better results were obtained at the higher air flow rates (5-15 mL/min).

The recorded data from the WVU Crossbow model CXLO4LP3 three-axis accelerometer and on-board NASA accelerometers provided useful information as to the duration and variations of gravity levels experienced during the experiment. Fig. 3 shows an example of measured gravitational acceleration levels from the Crossbow accelerometer data (with a raw output voltage of 2.32-2.33 volts corresponding to zero-g; see voltage display in Fig. 2) for an entire parabola. Fig. 4 zooms in on a typical period of zero gravity; computed mean and RMS values are listed.

The apparatus functioned as designed for 28 of the 67 total zero-g parabolas flown over the 2-day period, where bubbles were observed simultaneously in both tanks and the liquid was not inverted. For these 28 parabolas, the Kelvin force successfully repelled the bubbles from the bottom of the tank for all but one, or possibly two cases. At least 18 other parabolas had bubbles in one tank or the other, with bubble size and motion consistent with the other 28 parabolas. The remaining 21 parabolas had syringe pump flow rates that were too low to generate air bubbles.

Fig. 1: Flow Type 1 (Day 1 Parabola 33, 8 mm camera).

Fig. 2: Flow Type 1 (Day 1 Parabola 33, high speed).

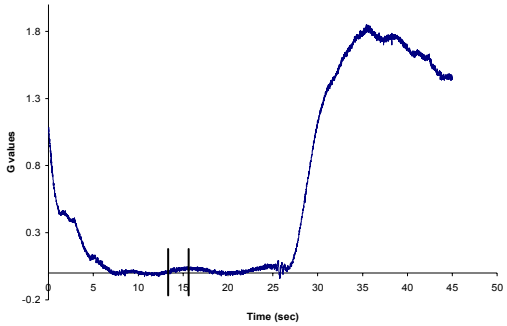

Fig. 3: Accelerometer Data (Day 1, Parabola 33).

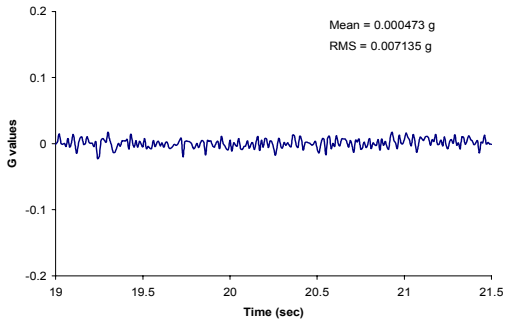

Fig. 4: Accelerometer Data (zoomed in on zero-g portion).

POSITIONING OF SIMULATED VAPOR BUBBLES IN MICROGRAVITY BY THE KELVIN FORCE

John Kuhlman[+], Donald D. Gray[*], Shannon Glaspell[#], Paul Kreitzer[#], Charlie Battleson[#], Michelle Lechliter[#], Michael Campanelli[#], Nicholas Fredrick[#], Christopher Sunderlin[#], Brianne Williams[#]

West Virginia University, Morgantown, WV 26506

[+]Professor; [#]Undergraduate Student, Department of Mechanical and Aerospace Engineering

[*]Professor, Department of Civil and Environmental Engineering

INTRODUCTION

Experiments were performed in July 2003 in the NASA "Weightless Wonder" KC-135 aircraft through the Reduced Gravity Student Flight Opportunities Program, to study the influence of the magnetic Kelvin force on the behavior of air bubbles in a paramagnetic liquid in microgravity (μ-g). This aircraft, which flies through a series of parabolic arcs providing about 20 seconds of μ-g per parabola, allowed a unique environment in which to study the resultant phenomena. The experiment was conceived, designed, constructed, and performed by the WVU student Microgravity Research Team and their advisors.

When there is no dominant body force such as gravity to produce a buoyant force, vapor bubbles that form may remain adjacent to heat rejection surfaces, rather than be driven away due to buoyancy. This can reduce the critical heat flux and can cause burnout or damage the surface that needs to be cooled. The experiment modeled one possible method for repelling the vapor bubbles from a heat rejection surface in μ-g. In the presence of a non-uniform magnetic field, the Kelvin body force is exerted on all magnetically permeable materials. Diamagnetic and paramagnetic fluids are repelled from and attracted to magnetic fields, respectively. The Kelvin force is approximately three orders of magnitude larger for liquids than for gases, leading to a magnetic buoyancy force on bubbles in a liquid.

RELATED WORK

Sanada, et al. (2003) recently studied the motion of chains of individual, small (0.5-2.5 mm dia.), equal-size air bubbles rising in initially stagnant water under conditions of Earth gravity. Bubble trajectories had a zig-zag or helical component about the vertical axis that generally increased in magnitude as bubble diameter or bubble generation frequency was increased. Average liquid velocities along the bubble train trajectory were measured via PIV; the liquid jet generated by the bubble train also deviated further from the vertical direction as bubble size and frequency increased.

Lee, et al. (1997) observed vapor bubble formation in pool boiling of R-113 under μ-g conditions for a series of 5 space flights under the NASA GAS program. Bubble formation and motion were recorded using a high-speed film camera. The observed motion of bubbles away from nucleation sites on the heater surface, the migration of these bubbles along the heater surface, and subsequent bubble coalescence, were all ascribed to Marangoni convection effects. Boiling heat transfer in μ-g was enhanced relative to one-g levels at lower heat fluxes, but critical heat flux was reduced significantly in μ-g.

The present experiment was conceived to determine whether or not the magnetic Kelvin force could be utilized in μ-g to remove small air bubbles from the bottom of a tank filled with a paramagnetic liquid. It was expected that air bubble behavior under conditions of μ-g might have some similarities with the work of Lee, et al. (1997) when no Kelvin force was present, but might change to a behavior somewhat like that observed by Sanada, et al. (2003) under the influence of the Kelvin force.

APPARATUS

This experiment used the Kelvin force to control the position of air bubbles in an unheated 4.9 molar aqueous solution of manganese chloride ($MnCl_2$), a paramagnetic liquid. Air bubbles were injected into the bottom of two geometrically identical tanks, one with a 2,000 gauss permanent magnet forming the bottom of the tank, and one without a magnet. Tanks were

5.4 cm x 5.4 cm in cross section, while liquid depth was 3.7 cm. Air bubbles were injected into the tanks through 1.5 mm diameter holes drilled at the centers of each tank floor. Airflow rates were set using a dual piston syringe pump, and varied between 0.1-25 mL/min; the majority of parabolas had flow rates of 5-10 mL/min.

The double syringe pump did not function in μ-g as it did in Earth gravity. Once in flight, the lower flow rates (below approx. 1 mL/min) were found to be inadequate under μ-g conditions to drive out the liquid solution that entered the air supply tubes during the 1.8-g pullout portions of the parabolas. Generally, better results were obtained at the higher airflow rates (5-25 mL/min).

The Kelvin force exerted on the liquid has been computed to be approximately 0.28 g, based on measurements of the magnetic induction with a gauss meter, and the average of two published values of the volumetric magnetic susceptibility of room temperature saturated aqueous solutions of $MnCl_2$ (Andres, 1976; Mahajan, et al., 1998). The resulting bubble formation, detachment, and motion were video taped for both tanks under identical gravitational accelerations. In μ-g, it was expected that the Kelvin force would attract the liquid towards the magnet located at the bottom of the tank, thereby driving the air bubbles (simulating vapor bubbles in pool boiling) away from the bottom of the tank.

RESULTS

Results indicate that air bubbles within the magnet tank were repelled from the magnet surface because the Kelvin force attracted the liquid to the magnet surface. This conclusion is valid for all but one or two parabolas for which the free surface of the $MnCl_2$ solution did not invert in the tanks due to small negative-g conditions, and for which the airflow rate was large enough to cause bubbles to flow into both tanks during the μ-g portion of each parabola.

Two bubble flow patterns were observed during the course of the experiment, due to variations in gravity levels onboard the KC-135, as well as to variations in airflow from the syringe pump. For flow pattern 1, as the air bubbles flowed into the geometrically identical tanks at identical flow rates, the control tank (no magnet) allowed the bubbles to become relatively large (~1 cm) before breaking away from the bottom surface of the tank and either remaining at the bottom of the tank or slowly moving toward the free surface. In the magnet tank, however, smaller (~2-4 mm), more numerous air bubbles were observed. These bubbles detached from the bottom of the tank, and were forced toward the free surface much more quickly. Sample video images of this flow pattern are shown in Fig. 1 (Day 1, Parabola 33, 8 mm camera) and Fig. 2 (Day 1 Parabola 33, NAC HSV-500C high speed camera at 500 fps).

The second flow pattern also supported the general conclusion that the Kelvin force could repel the air bubbles from the surface of the magnet. However, for flow pattern 2, bubbles were not pushed completely to the free surface in the magnet tank. Instead, bubbles were forced away from the magnet surface and remained within the fluid at some distance from the magnet surface. This was caused by negative fluctuations in gravity that reduced the momentum of the air bubbles moving toward the free surface, causing them to stop or reverse direction. In this circumstance, the control tank bubbles were larger and remained on the tank bottom.

Fig. 1: Flow Pattern 1 (Day 1 Parabola 33, 8 mm camera). **Fig. 2:** Flow Pattern 1 (Day 1 Parabola 33, high speed).

For several parabolas, there were periods of negative gravity, causing the free surfaces to invert, preventing bubble formation. Sometimes, this period of negative gravity would "prime" the syringe pump, removing any liquid that had flowed into the air supply tubes connecting the syringe pump to the tanks during the previous 1.8-g pullout. This allowed the bubbles to more easily flow into the tanks once the liquid had returned to the bottoms of the tanks. The data collected from these parabolas was not discarded if there were periods of slightly positive μ-g either directly before or after the inversion, and if bubbles were observed in both tanks once the period of inversion ended.

The recorded data from the WVU Crossbow model CXLO4LP3 three-axis accelerometer and on-board NASA accelerometers recorded the gravity levels experienced during the experiment. Fig. 3 shows an example of gravitational acceleration levels for an entire parabola from the Crossbow accelerometer. (A raw output voltage of 2.32-2.33 volts corresponds to g = 0; see voltage display in Fig. 2.) Fig. 4 zooms in on the period of μ-g indicated in Fig. 3; the computed mean and RMS values are listed.

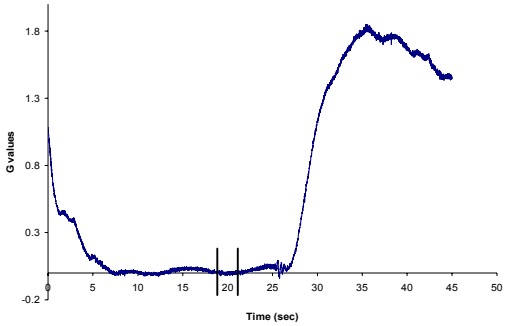

Fig. 3: Accelerometer Data (Day 1, Parabola 33).

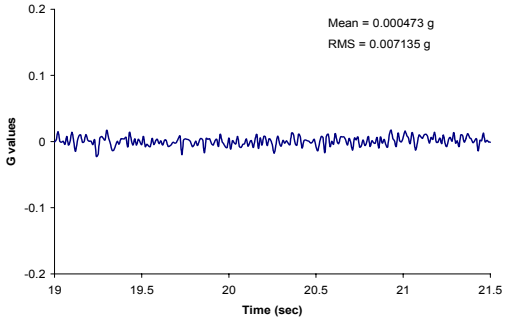

Fig. 4: Accelerometer Data (zoomed in on zero-g portion).

A total of 67 μ-g parabolas were flown over a 2-day period. There were 28 parabolas during which bubbles were observed simultaneously in both tanks and the liquid was not inverted. For these 28 parabolas, the Kelvin force successfully repelled the bubbles from the bottom of the tank for all but one, or possibly two cases. At least 18 other parabolas had bubbles in one tank or the other, with bubble size and motion consistent with the other 28 parabolas. No conclusion could be drawn for the remaining 21 parabolas, which had syringe pump flow rates that were too low to generate air bubbles.

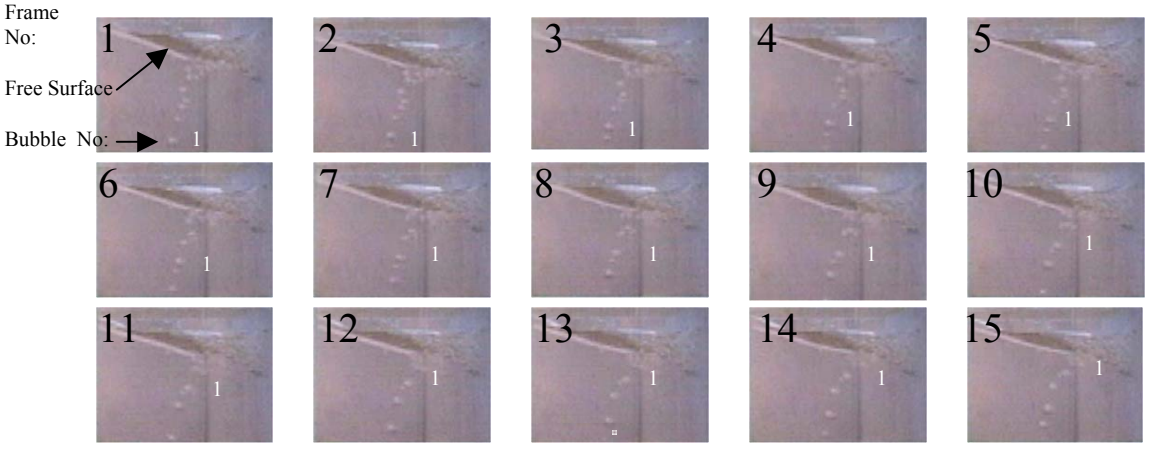

Fig. 5: Sample Video Images from 0.5 sec of 8mm Video Tape for Magnet Tank: Day 1, Parabola 11.

Some limited quantitative analysis of the present bubble behavior has been performed using 8mm video tape from Day 1, Parabola 11. Fig. 5 shows 15 successive frames (covering 0.5 s) of the liquid in the tank fitted with the magnet. (Compare with RHS of Fig. 1.) Also indicated is the location of the initial

bubble analyzed in this series of frames. Lateral and vertical bubble chords were measured and averaged; these average bubble diameters are plotted versus distance from the bottom of the magnet tank in Fig. 6. Most bubbles were between 3 to 4 mm, with one smaller bubble (No. 2) having a diameter of approximately 2 mm. The average bubble diameter was 3.4 mm. Bubble centroids were also measured and used to compute bubble velocities; the average bubble velocity was 43 mm/sec, although there was considerable scatter in these results. Bubble generation frequency was 7-8 bps. (It was noted in every parabola that the liquid free surface was inclined during the periods of μ-g, with the deeper liquid towards the aircraft right wing.; the cause of this is not known.)

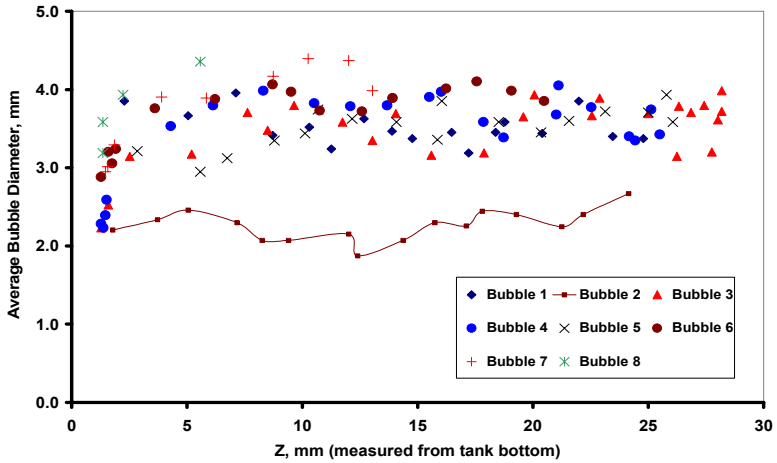

Fig. 6: Average Bubble Diameter versus Distance from Tank Bottom for Magnet Tank: Day 1, Parabola 11.

Bubble diameter (Fig. 6) and velocity were used to compute Reynolds number and drag force. Also, the magnetic induction and magnetic susceptibility were used to compute the magnitude of the Kelvin force and the magnetic Bond number. At the computed Reynolds number of 28, a drag coefficient of 2.2 was calculated based on correlations for solid spheres; this gave an average drag force of about 30 μN. The Kelvin force on a bubble adjacent to the magnet surface was computed to be approximately 20 μN, which was judged to be in good agreement with the computed drag force. The magnetic Bond number was about 0.1-0.05 adjacent to the magnet surface, showing that surface tension forces were significantly larger than the Kelvin force for these bubbles. This is consistent with the observation that the bubbles appeared to be nearly spherical. Note that the Kelvin force falls off rapidly with distance from the tank bottom.

Significantly larger bubbles were observed in the tank without a magnet (no Kelvin force). Average bubble diameter for the same 8 mm video sequence was 12 mm; this bubble remained attached to the tank bottom for the entire parabola.

This work was partially supported by the WV NASA Space Grant Consortium, the WVU College of Engineering and Mineral Resources, and the Depts. of Mechanical and Aerospace Engineering and Civil and Environmental Engineering.

REFERENCES

Andres, U. Ts., 1976: "Magnetic Liquids", Materials Science and Engineering, Vol. 26, pp. 269-275.

Lee, H. S., Merte, Jr., H., and Chiaramonte, F., 1997: "Pool Boiling Curve in Micro-gravity", Journal of Thermophysics and Heat Transfer, Vol. 11, No. 2, pp. 216-212.

Mahajan, M. P., Tsige, M., Taylor, P. L., and Rosenblatt, C., 1998: "Paramagnetic Liquid Bridge in a Gravity-Compensating Magnetic Field", Physics of Fluids, Vol. 10, No. 9, September, pp. 2208-2211.

Sanada, T., Watanabe, M., and Fukano, T., 2003: "Study on Single Bubble Chains in Stagnant Water", Proc. ASME FEDSM03, 4th Joint ASME JSME Fluids Engineering Conference, Honolulu, Hawaii, July 6-10.

NASA/CP—2004-213205/VOL2

Positioning of Simulated Vapor Bubbles in Microgravity by the Kelvin Force

7th Microgravity Fluid Physics and Transport Phenomena Conference
Cleveland OH, June 22-23, 2004

John Kuhlman+, Donald D. Gray*, Charlie Battleson#, Shannon Glaspell#, Paul Kreitzer#, Michelle Lechliter#, Michael Campanelli#, Nicholas Fredrick#, Christopher Sunderlin#, Brianne Williams#
West Virginia University, Morgantown, WV 26506-6106

+Professor, and #Undergraduate Student, Dept. of Mechanical and Aerospace Engineering
*Professor, Dept. of Civil and Environmental Engineering

Sponsored by WV NASA Space Grant Consortium
WVU College of Engineering and Mineral Resources
WVU Dept. of Mechanical and Aerospace Engineering
WVU Dept. of Civil and Environmental Engineering

INTRODUCTION

The influence of the magnetic Kelvin force on the behavior of air bubbles in a paramagnetic liquid in microgravity (μ-g) was studied in July 2003 aboard the NASA "Weightless Wonder" KC-135 aircraft through the Reduced Gravity Student Flight Opportunities Program. The experiment was conceived, designed, constructed, and performed by the WVU student Microgravity Research Team and their faculty advisors.

When there is no dominant body force such as gravity to produce a buoyant force, vapor bubbles that form may remain adjacent to heat rejection surfaces, rather than be driven away due to buoyancy. This can cause burnout or damage the device that needs to be cooled.

This experiment modeled one possible method for repelling the vapor bubbles on a heat rejection surface in μ-g. In the presence of a non-uniform magnetic field, the Kelvin body force is exerted on all magnetically permeable materials. Diamagnetic and paramagnetic fluids are repelled from and attracted to magnetic fields, respectively. The Kelvin force is approximately three orders of magnitude larger for liquids than for gases, leading to a magnetic buoyancy force on bubbles in a liquid in the presence of a spatially varying magnetic field.

HYPOTHESIS

This experiment used the Kelvin force to control the position of air bubbles in a 4.9 molar aqueous solution of manganese chloride $MnCl_2$ (simulated coolant), which is a paramagnetic liquid. Air bubbles were injected into the bottom of two geometrically identical tanks, using a dual piston syringe pump. The base of one tank was a 2,000 gauss permanent magnet; the second (control) tank was identical in shape, but without a magnet. The Kelvin force exerted on the liquid has been estimated to be approximately 0.28 g, based on magnetic field strength measurements.

The resulting bubble formation, detachment, and motion were video taped simultaneously for both tanks under identical gravitational accelerations. In μ-g, it was expected that the Kelvin force would attract the liquid towards the magnet located at the bottom of the tank, thereby driving the air bubbles (simulated vapor bubbles) away from the bottom of the tank.

RESULTS

A total of 67 μ-g parabolas were flown over a 2-day flight period. For 28 parabolas, bubbles were observed simultaneously in both tanks and the liquid was not inverted. For these 28 parabolas, the Kelvin force successfully repelled the bubbles from the bottom of the tank for all but one, or possibly two cases. At least 18 other parabolas had bubbles in one tank or the other, with bubble size and motion consistent with the previously described 28 parabolas. The remaining 21 parabolas had syringe pump flow rates that were too low to generate air bubbles in either tank. These results support the hypothesis that air bubbles within the magnet tank were repelled from the magnet surface by the Kelvin force.

Two flow patterns were observed, due to variations in gravity levels onboard the KC-135, and in air flow from the syringe pump. In pattern 1 the air bubbles flowed into the geometrically identical tanks at identical flow rates; in the control tank (no magnet) the bubbles became relatively large (~1 cm) before detaching from the bottom surface of the tank and remaining there or slowly floating toward the free surface. In the magnet tank the air bubbles were observed to remain smaller (~2-4 mm), to be more numerous, to detach from the bottom of the tank, and to be forced toward the free surface much more quickly. Sample video images of this flow pattern are shown in Fig. 1 (Day 1, Parabola 33, 8 mm camera) and Fig. 2 (Day 1, Parabola 33, NAC HSV-500C high speed camera at 500 fps).

SAMPLE VIDEO IMAGES

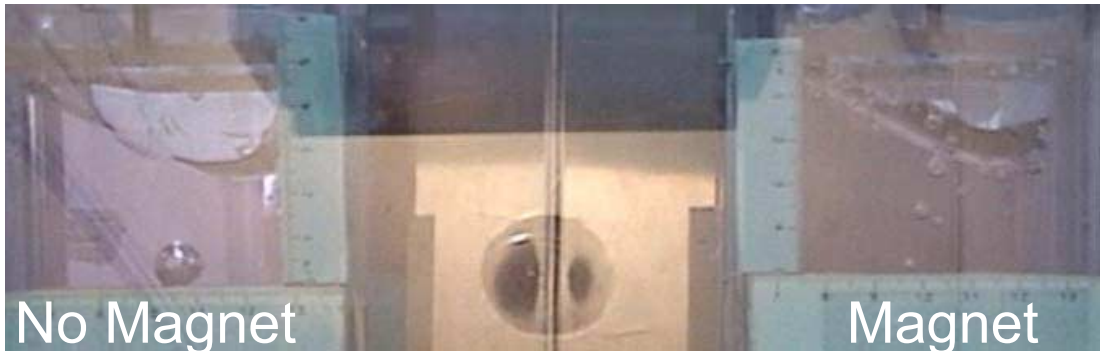

Fig. 1: Flow Pattern 1 (Day 1 Parabola 33, 8 mm camera).

Fig. 2: Flow Pattern 1 (Day 1 Parabola 33, high speed).

RESULTS (Cont'd)

The second pattern of flow that was observed also supported the general conclusion that the Kelvin force could repel the air bubbles from the surface of the magnet. However, for flow pattern 2, bubbles were not pushed completely to the free surface in the magnet tank. Instead, bubbles were forced away from the magnet surface and remained within the liquid at some distance from the magnet surface. This was most likely due to negative fluctuations in gravity that reduced the momentum of the air bubbles moving toward the free surface, causing them to stop or to change direction. Often, in flow pattern 2, the control tank bubbles would rest on the tank bottom.

PROBLEMS ENCOUNTERED

1. For several parabolas, there were a periods of (small) negative gravity. This caused the free surface within the tanks to invert, preventing bubble formation. Sometimes, this negative gravity would "prime" the syringe pump, allowing the bubbles to more easily flow into the tanks once the liquid had returned to the bottoms of the tanks.

2. The double syringe pump used for the experiment did not function in microgravity as it did in Earth gravity. Some of the liquid solution entered the air supply tubes between the syringe pump and the tanks during the 1.8-g pullout portions of the parabolas. Generally, higher air flow rates (5-25 mL/min) were required to clear these tubes during the μ-g portion of each parabola.

SAMPLE ACCELERATION RESULTS

The WVU Crossbow model CXLO4LP3 three-axis accelerometer and the on-board NASA accelerometers recorded the gravity levels experienced during the experiment. Fig. 3 shows an example of measured gravitational acceleration levels for an entire parabola from the Crossbow accelerometer (with a raw output voltage of 2.32-2.33 volts corresponding to zero-g; see voltage display visible in Fig. 2). Fig. 4 zooms in on the period of μ-g in Fig. 3; the computed mean and RMS values are listed.

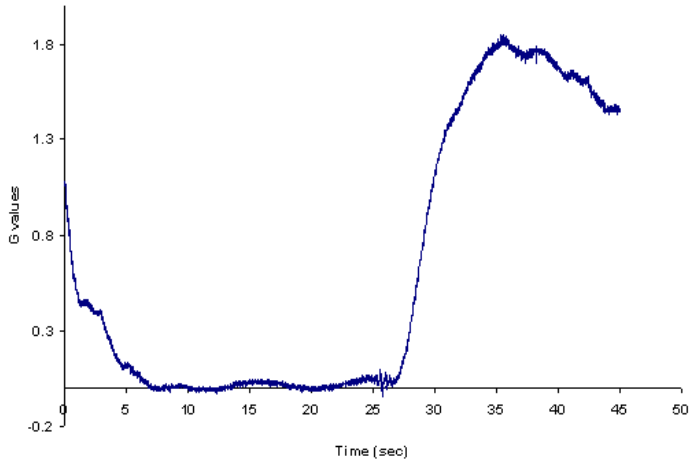

Fig. 3: Accelerometer Data (Day 1, Parabola 33)

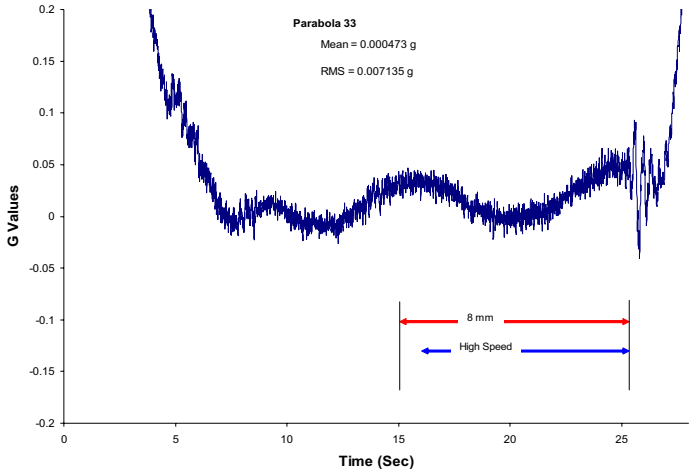

Fig. 4: Accelerometer Data (zoomed in on zero-g portion)

Day 1, Parabola 11: Sample 8 mm Video of Magnet Tank

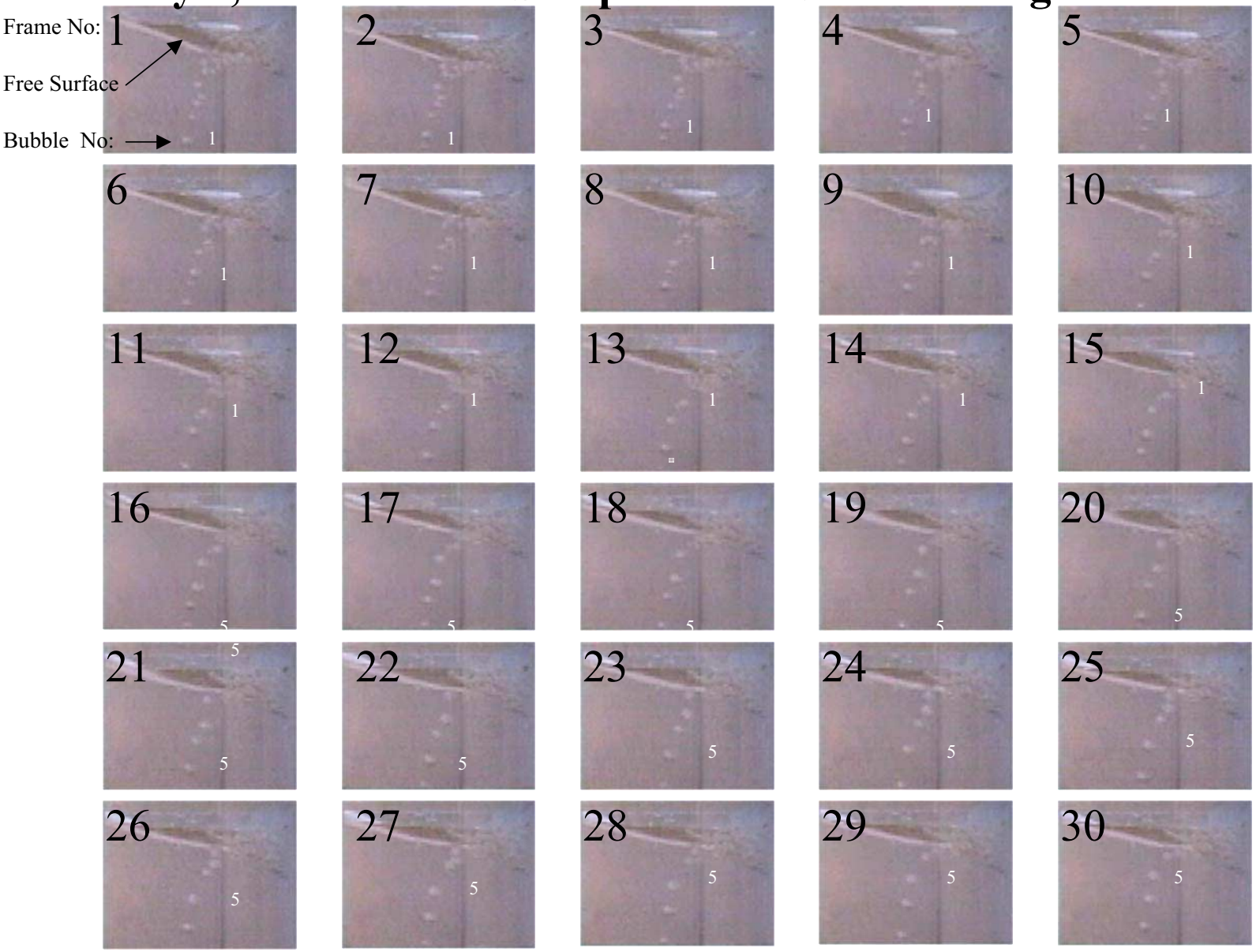

Day 1, Parabola 11: Bubble Diameter and Velocity, Computed From Sample 8 mm Video of Magnet Tank

(Previous Slide)

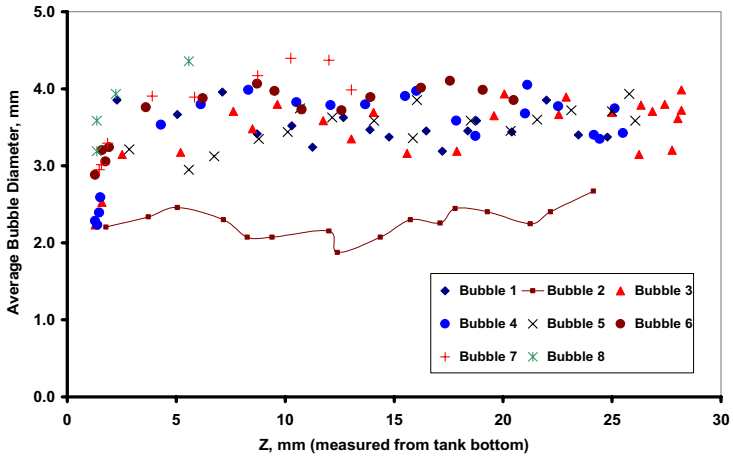

Average Bubble Diameter

(Avg. Diameter = 3.4 mm;
at 7-8 bubbles/sec)

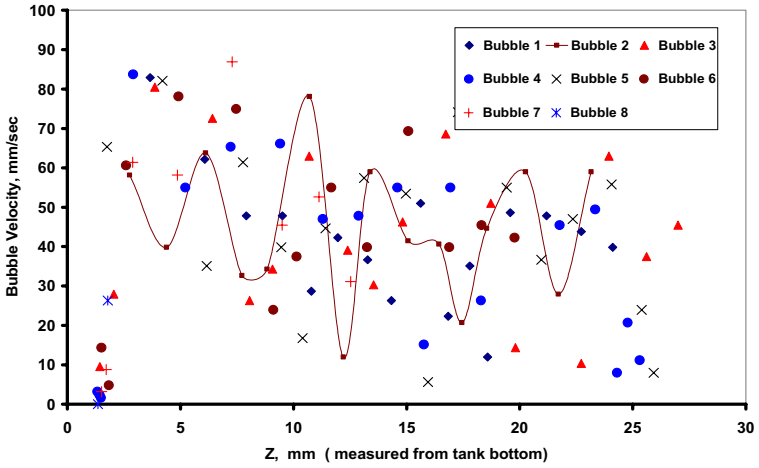

Bubble Velocity

(Avg. Velocity = 43 mm/sec,
but with much scatter)

Day 1, Parabola 11: Sample 8 mm Video of No Magnet (Control) Tank

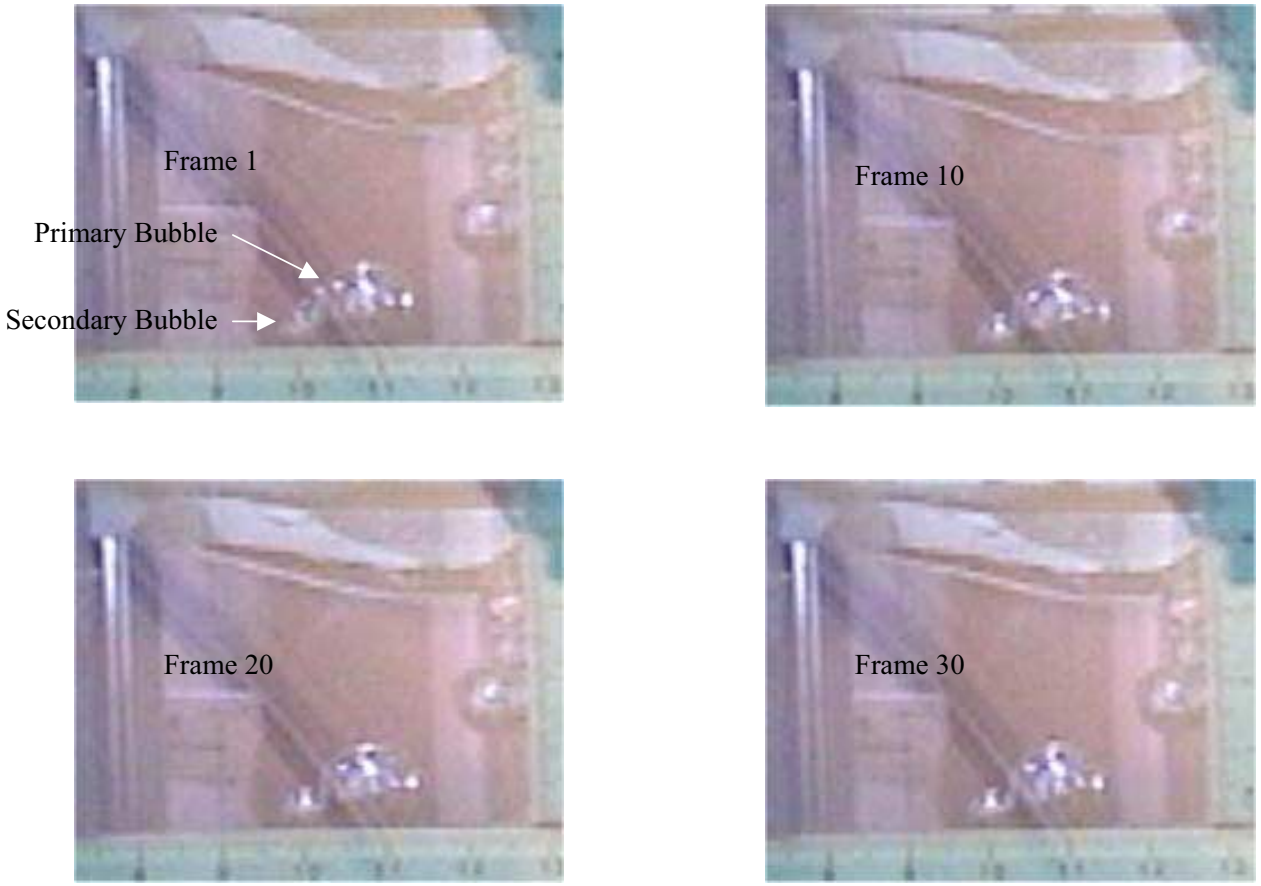

A Large Primary Bubble and a Smaller Secondary Bubble Remain at Bottom of Tank for Entire Parabola

AC ELECTROKINETIC JETS AND SPRAYS FOR SPACE APPLICATIONS

Dmitri Lastochkin, Ping Wang, and Hsueh-Chia Chang
Department of Chemical and Biomolecular Engineering
University of Notre Dame
Notre Dame, IN 46556

New mechanisms for ejecting drops and bubbles using high-frequency AC electric fields are reported for: (i)-generating micron-sized liquid drops of electrolytes in air and (ii)-generating a micron-sized bubble jet in an electrolyte within a microfluidic device.

(i) AC Electro-sprays: The new AC electrospray ejects drops from a meniscus at the tip of a capillary filled with the liquid to be sprayed. A needle electrode is inserted into the capillary such that its tip is just behind the meniscus. The other electrode is on the air side a short distance beyond the meniscus. When a high voltage (1000 V to 2000 V) AC field is activated, a micro-jet forms intermittently at the meniscus and ejects drops. Unlike DC electro-sprays, these drops are larger and are electro-neutral. In contrast, DC electro-spray, which is widely used in the pharmaceutical industry in conjunction with a mass spectrometer for drug testing, generates only charged liquid drops. The electro-neutral drops generated by the current high-frequency AC electro-spray immediately extend the utility of electro-sprays to a much wider area of potential application. Its negligible current and wattage also imply that the spray can be driven by miniature and portable power packs and without consuming much power from the on-board power sources. DC electrosprays are currently used to position and stabilize space crafts. The larger drop size and the electro-neutral drops of the AC spray should allow more precise and yet stronger manipulation actions. Possible other space applications include dispensing contents of biochips and medical diagnostic chips into on-board analytical instrument.

(ii) Micro-bubble Jet Pump. A new micron-sized bubble jet in an electrolyte within a microfluidic device is reported. An intense (1000 V) AC high-frequency electric field is established between two orthogonal line electrodes (less than 25 microns in diameter) with a large peak-to-peak voltage drop. This intense field at the tip triggers a local electrolysis reaction that generates small bubbles at the tip at high speeds. The field also shapes each air bubble into a sharp cone and then pinches it off at high rates to form a jet consisting of a stream of fast-moving bubble train. These bubbles stream off the cone tip at velocities higher than 10 cm/second and drag the surrounding liquid with it. This produces a two-phase jet of bubble and liquid with a linear velocity in excess of 10 cm/second. The jet also drives a high-intensity vortex around it. The streaming bubbles are less than 10 microns in diameter and quickly dissolve into the electrolyte. The bubbles hence do not accumulate within the micro-fluidic device. The metal loss from the electrode due to reaction and the resulting contamination are also negligible. The jet can be used as a microfluidic pump to transport fluids in micro-heat exchangers, fuel cells, CPU cooling, biochips in space crafts and space stations. It functions well in micro-gravity environments and is hence ideal for space applications. It does not contaminate the liquid and requires only a miniature power source ideal for space application.

PHOTOREGULATED ELECTRON TRANSFER AT BIO-INORGANIC INTERFACES

Nikolai Lebedev[(1,2)], Scott A. Trammell[(1)] Anthony Spano[(2)]
[(1)]US Naval Research Laboratory, [(2)]University of Virginia

Efficient connection between bio- and inorganic materials is crucial for the development of new generation of photo-, chemo- and bio-sensors, power sources, information processing devices, and ultimately will lead to the construction of integrated bio-computer hybrids. The main problem in the construction of such bioinorganic devices is the electrical connection between biomolecules and semiconductors or metals, and viability of the protein after immobilization. In the present work using genetically engineered proteins and specifically synthesized organic linkers, we were able to construct self-assembling aligned biomolecular surfaces on various metals and semiconductors, including gold, ITO, glasses, porous SnO_2, carbon nanotubes, and in artificial lipid membranes. Using bacterial photosynthetic reaction centers (RCs) as an active protein, we were able to demonstrate that after immobilization on the surfaces this protein can operate as a photosensor, optical switch, or photovoltaic device for local power generation. Our experimental results have shown that after binding to an electrode, photosynthetic RCs are able to undergo efficient photoinduced charge separation, operate as a photorectifier and transfer current only in only one, protein orientation-dependent direction. Part of the protein (H-subunit) acts as an insulator and must be removed for substantial improvement of the protein performance. Electron transfer in the constructed devices follows a tunneling mechanism and can be described by integrated Marcus' formalism. It shows an exponential dependence of the rate of electron transfer on the distance between RC and electrode and demonstrates rather low reorganization energy.

Two ways of oriented binding of photosynthetic RC to electrode and the structure of the linkers

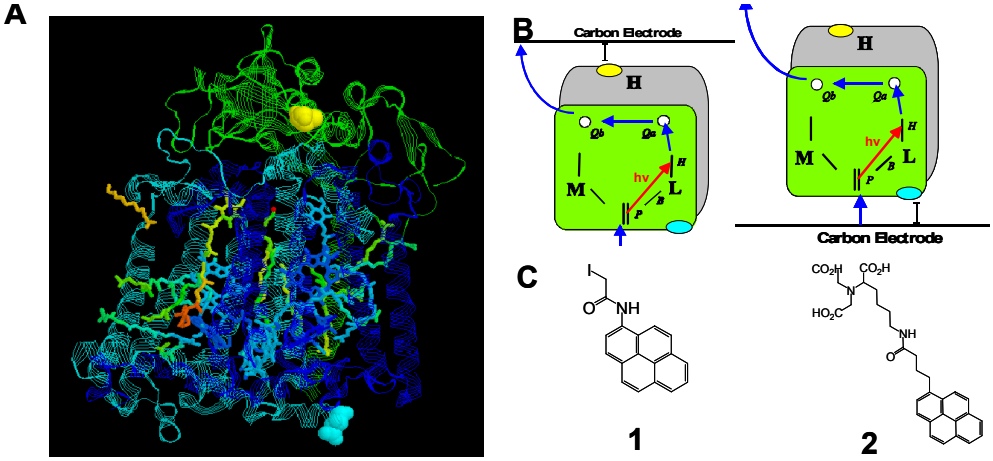

Effect of protein orientation on the efficiency and direction of photocurrent at the electrode:

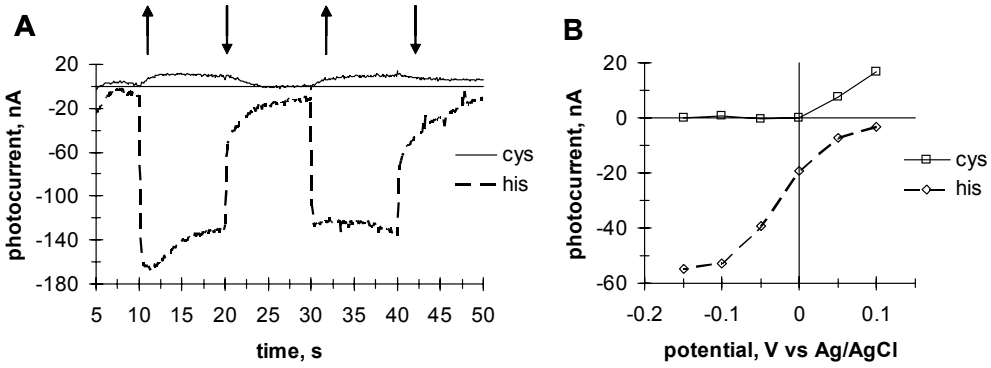

Effect of the distance and driving force on the efficiency of electron transfer between RC and the electrode:

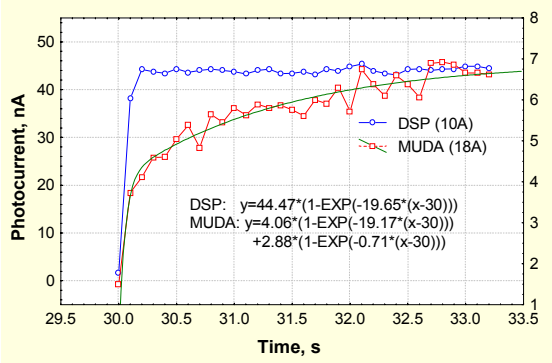

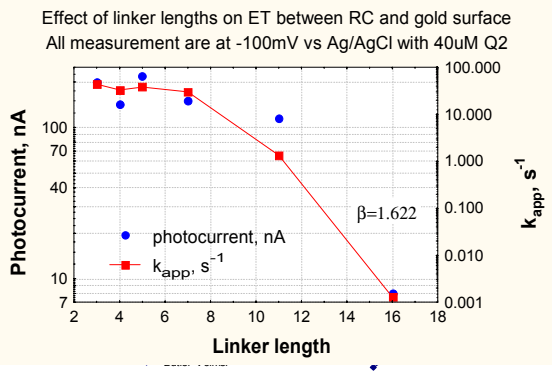

$$k = \frac{2\pi}{h}\left|H_{DA}\right|^2 (FC)$$

$$\left|H_{DA}\right|^2 \propto \exp\left[-\beta\left(R-Ro\right)\right]$$

$$FC \propto \exp\left[-\frac{(\lambda - \Delta Go)^2}{4\lambda RT}\right]$$

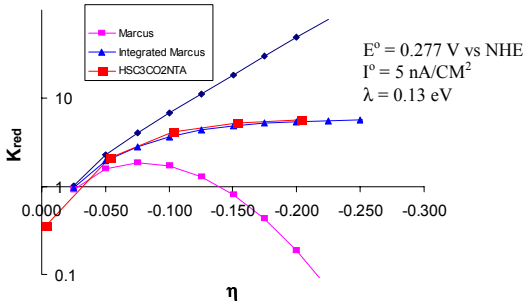

Construction of a Protein-based High Power Density Photovoltaic Device

Nikolai Lebedev, Scott Trammell
US Naval Research Laboratory
Anthony Spano
University of Virginia

NASA Strategic Planning Conference
June 22-23, 2004

Problem: About 50% of the weight of most current autonomous devices dedicated to the power source

Our Goal: Construction of ultra-light weight high-power density photovoltaic and quantum electronic device based on photosynthetic proteins

The main focus area: Efficient junction between photosynthetic RC and electrodes.

Why Photosynthetic RC:

- The size of the active unit (photosynthetic reaction center, RC) is about 7 nm
- The quantum yield of internal light energy conversion in RC is ~99%
- RC generates local voltage of ~ 10^6 V/cm
- RC does not require bias voltage for ET
- RC has broad spectral sensitivity (300-1000nm)
- RC has fast operation time <200 ps (~5 GHz)
- Genetic manipulation with photosynthetic reaction centers allows for precise control of the protein structure and ET pathway
- Biological production leads to cheap ultra pure material with 100% identity of the components

Structure of photosynthetic RC

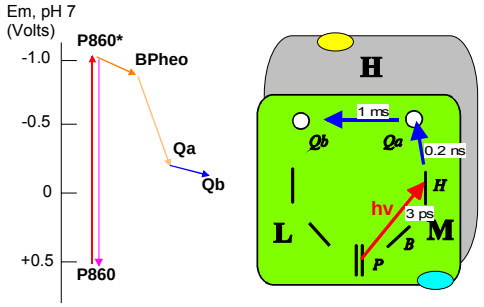

How the protein can be bound to an electrode?

Active amino acids:

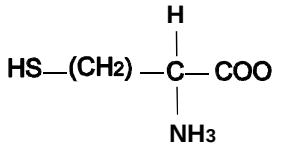

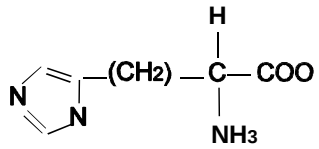

Support-binding groups:

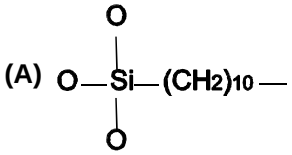

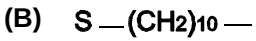

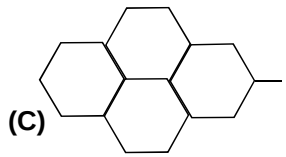

Protein-binding groups:

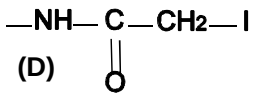

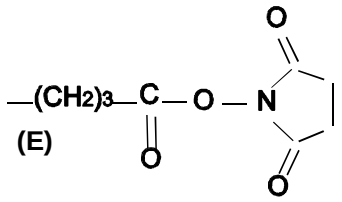

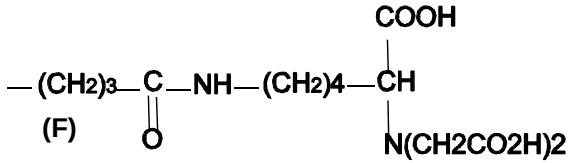

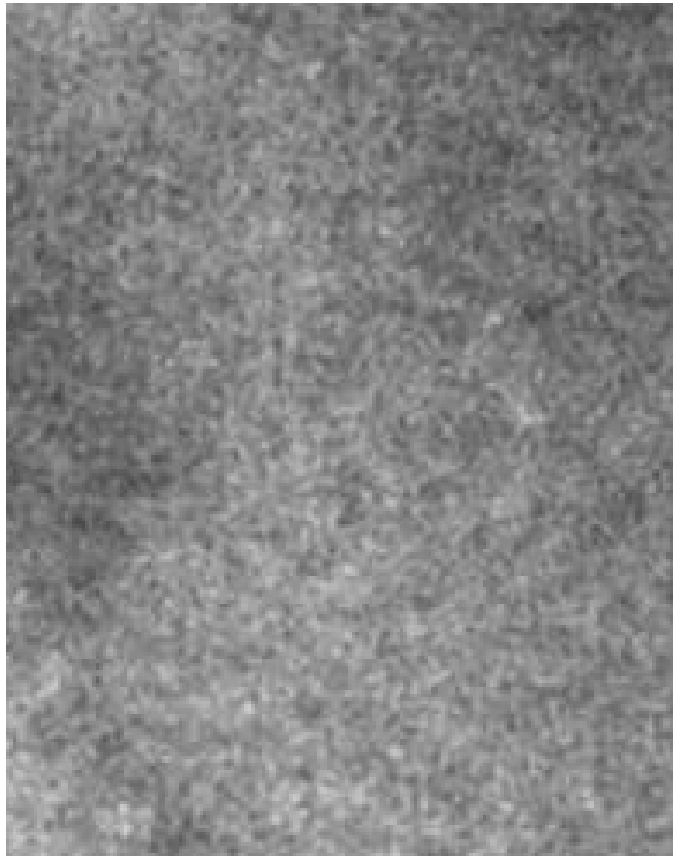

TEM of RC monolayer on carbon surface
(x 320 000)

The Effects of RC Orientation

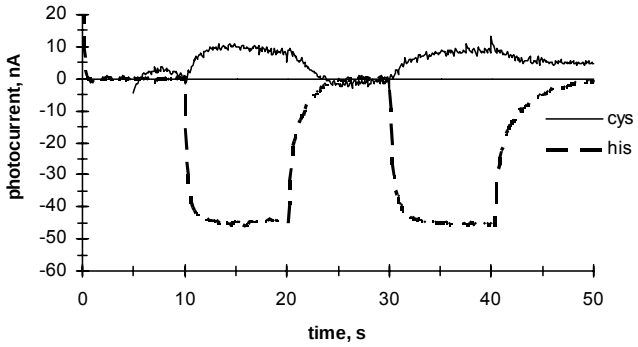

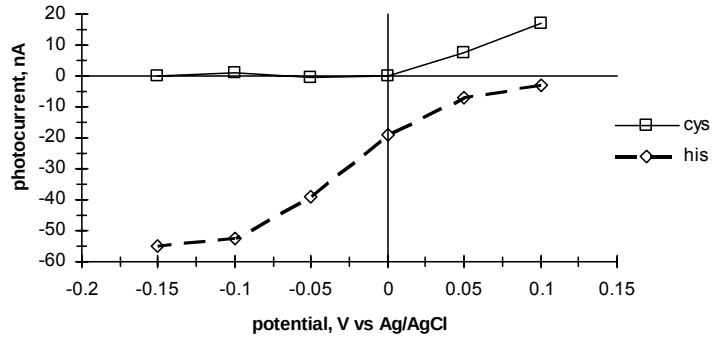

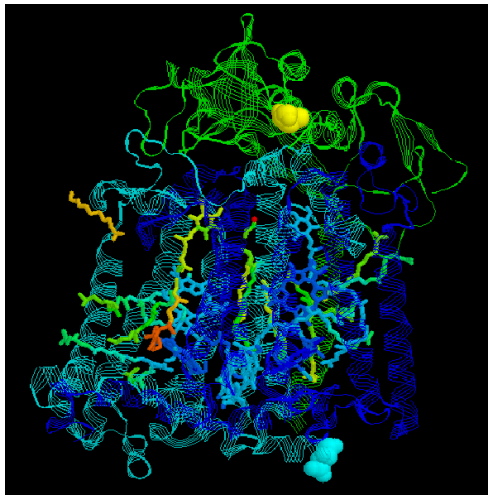

cysteine (Cys) =

polyhistidine tag =

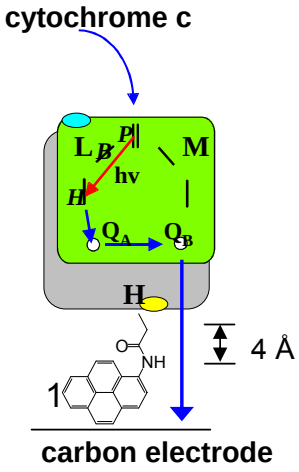

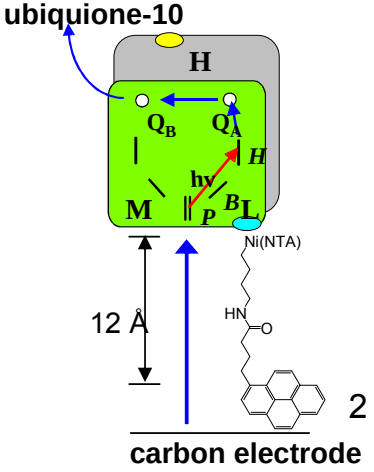

Control of ET between RC and Electrode

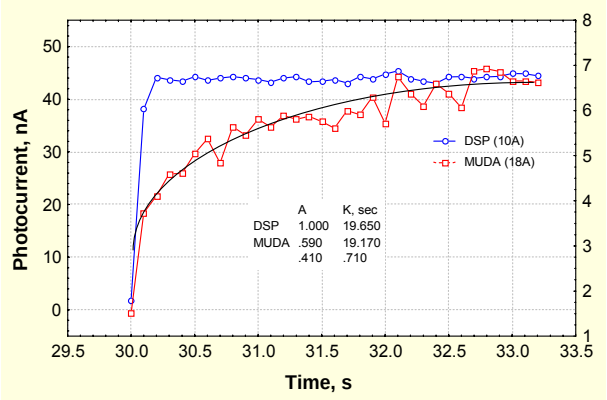

$$k = \frac{2\pi}{\mathrm{h}}\left|\mathrm{H_{DA}}\right|^2(\mathrm{FC})$$

$$\left|\mathrm{H_{DA}}\right|^2 \propto \exp\left[-\beta\left(R\text{-}Ro\right)\right]$$

$$\mathrm{FC} \propto \exp\left[-\frac{(\lambda - \Delta Go)^2}{4\lambda RT}\right]$$

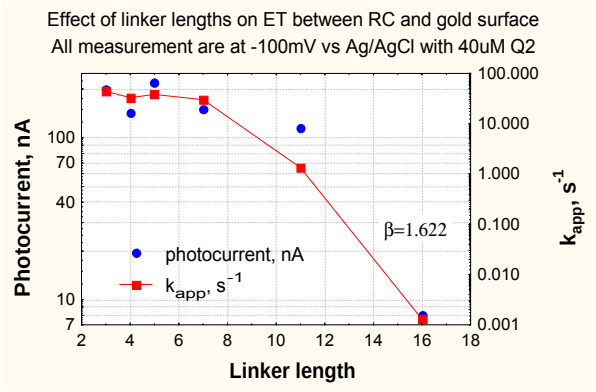

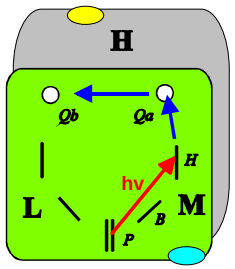

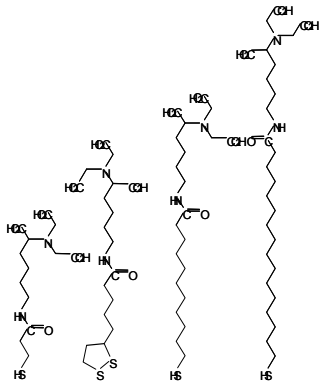

DSP Thioctic acid MUDA MHDA

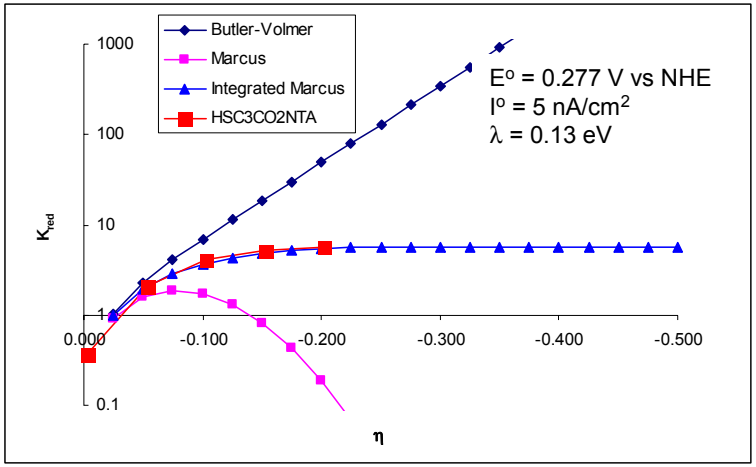

Modeling of ET between RC and Electrode

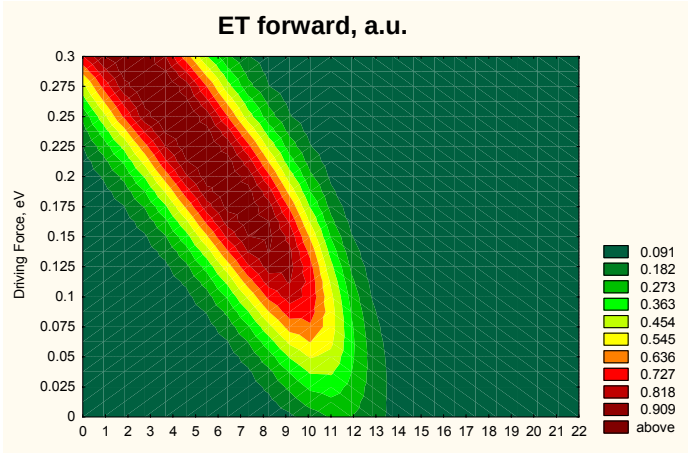

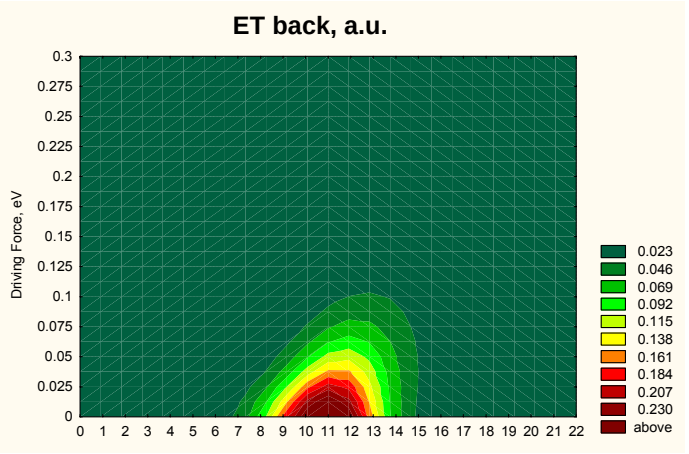

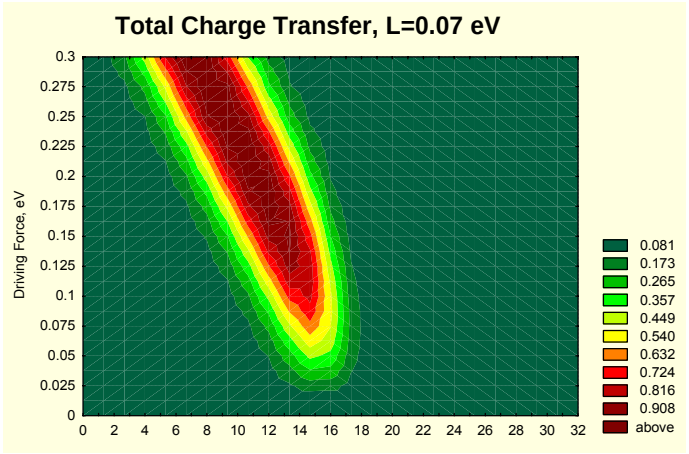

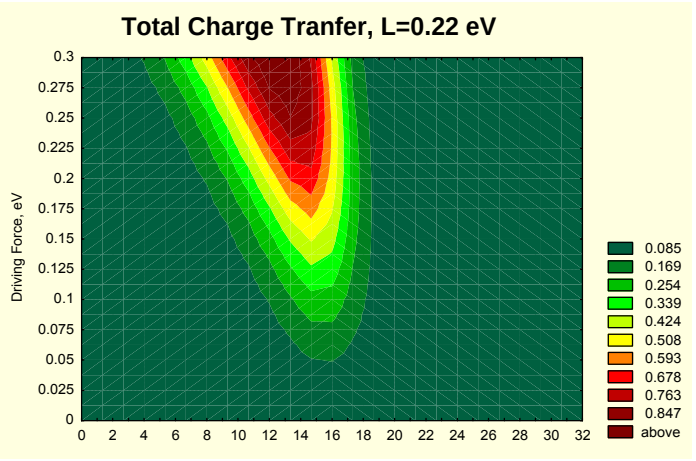

Self-Assembling Photo-Sensor

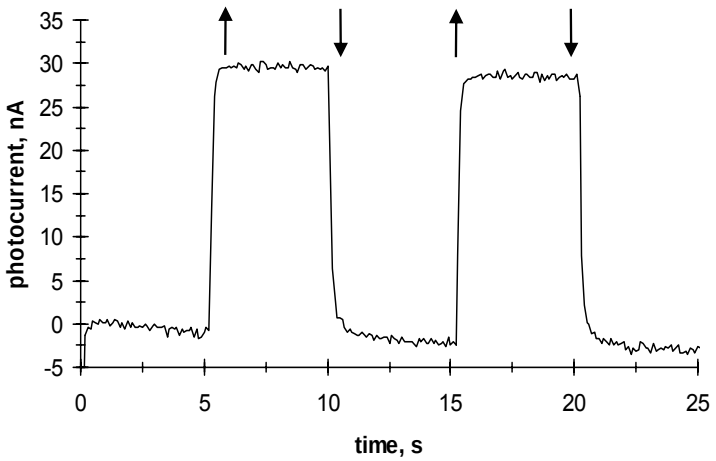

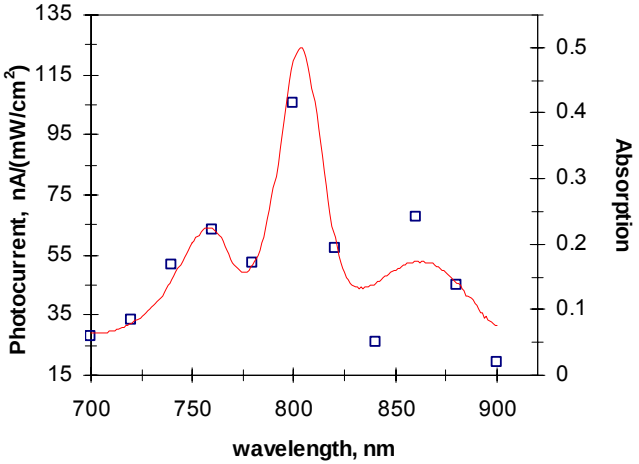

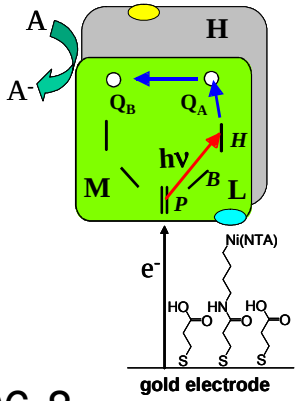

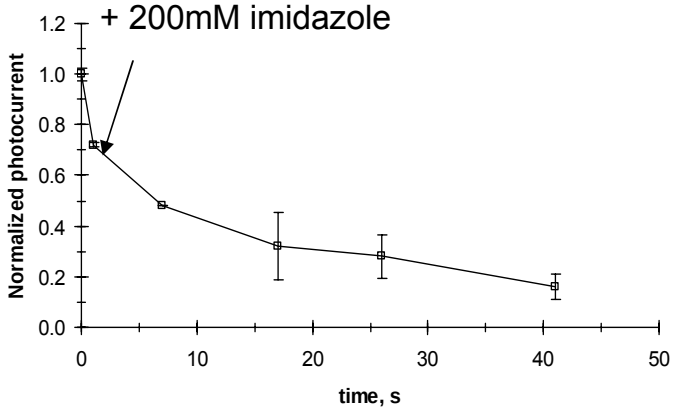

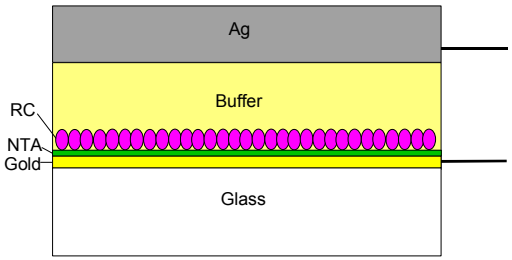

Lebedev, Trammell & Spano

Solid-State Photo-Cell

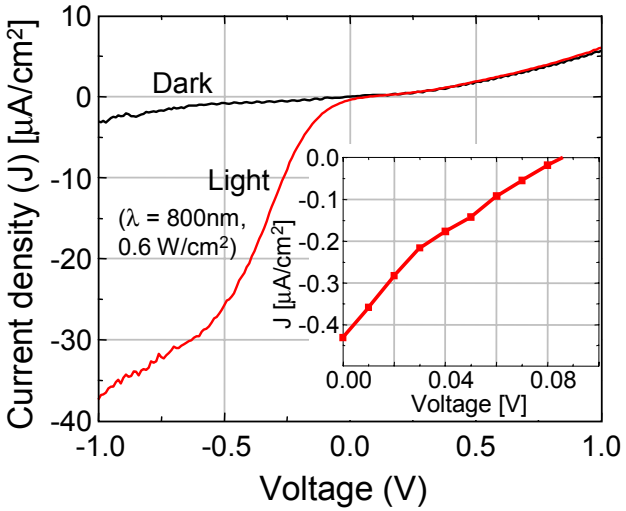

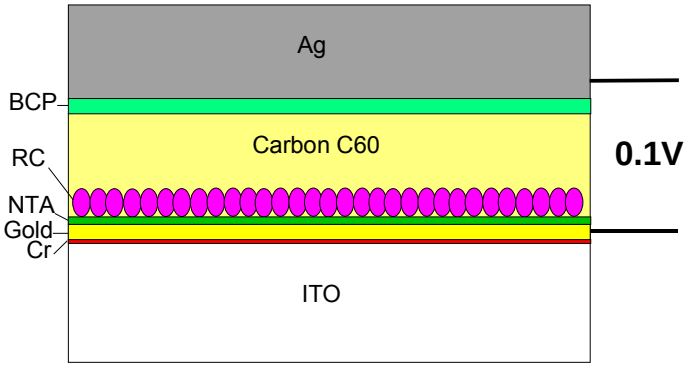

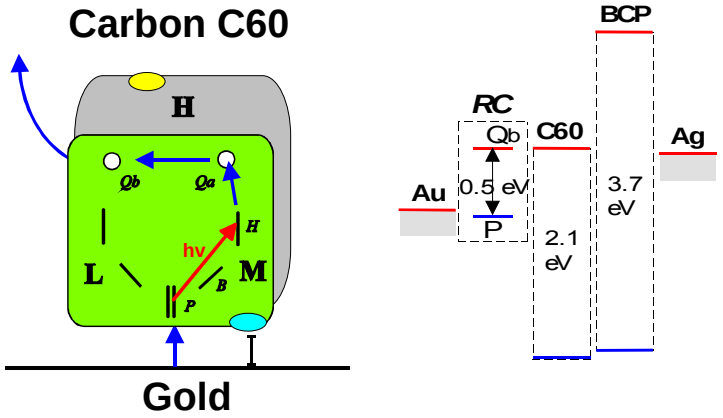

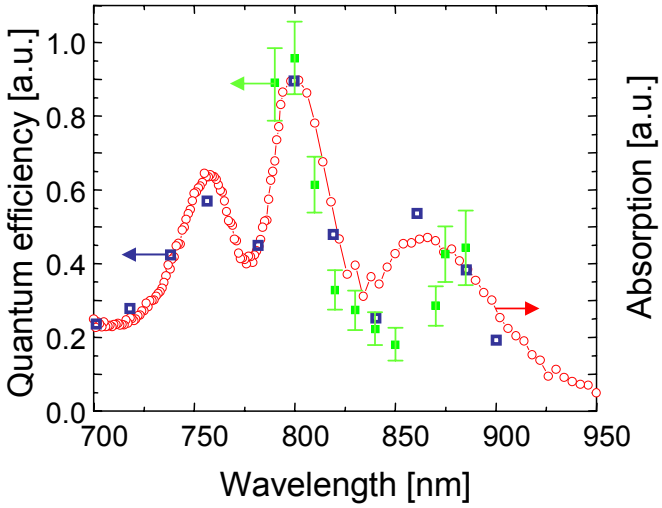

406-9

(in collaboration with Marc Baldo, MIT)

Photoactive RC-CNT Arrays

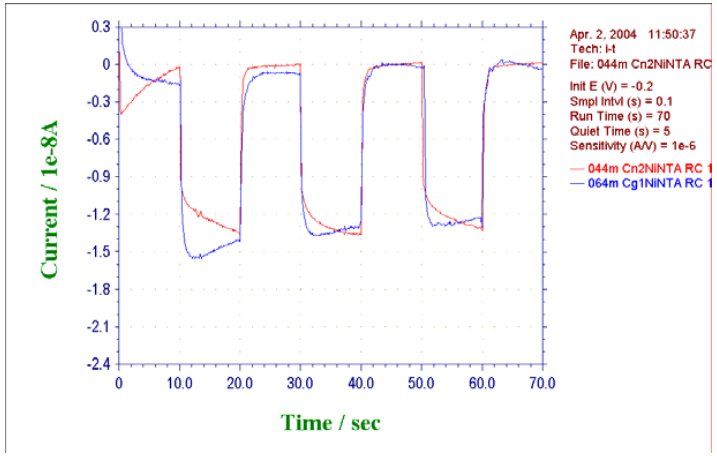

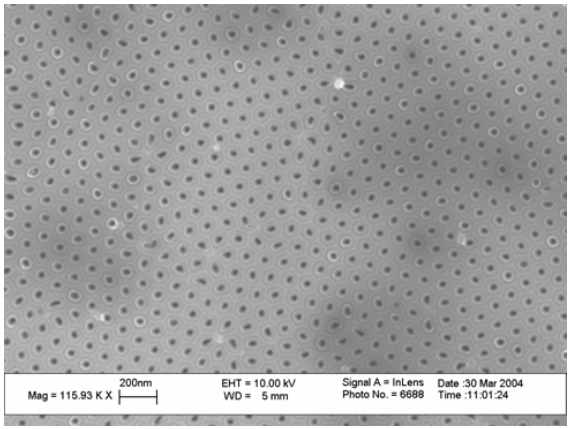

SEM of CNT, Low Magnification

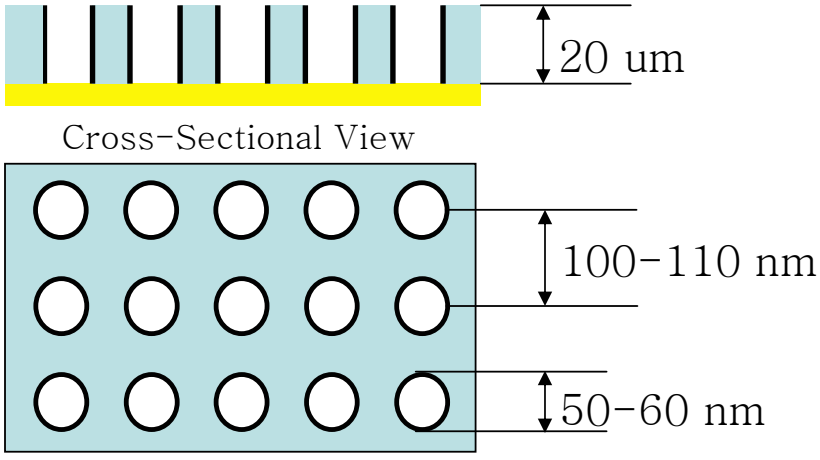

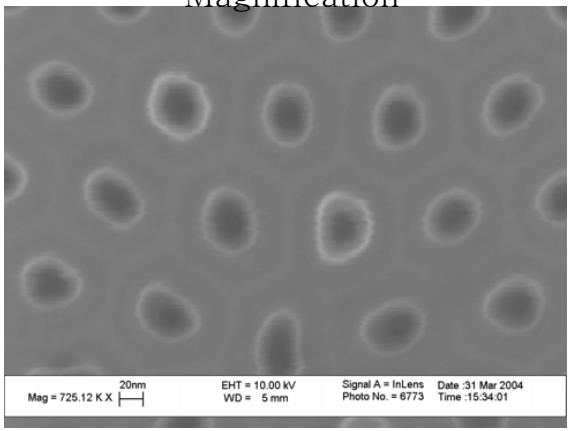

SEM of CNT, High Magnification

406-10

(in collaboration with Jimmy Xu, Brown U.)

NASA/CP—2004-213205/VOL2

Expected Power Conversion Efficiency in Photosynthetic RC:

Power Output (W) = i_{sc} x V_{oc} x ff

Current density (i_{sc})
= k_{et} e C s = 10^{9} 10^{-19} 10^{12} 10^{-3} =0.1 A/cm^2
Output Voltage (V_{oc}) = 0.5 V
Fill factor (ff) = 0.5

W_{max} = 25 mW/cm^2
(for modern Si-based devices W_{max}=10 mW/cm^2)

NASA/CP—2004-213205/VOL2

Conclusions:

Our results demonstrate that photosynthetic proteins can be bound to electrodes and serve as efficient light energy to electric current converters

To increase the system performance a number of specific questions must be solved including modification of the rate and pathways of electron transfer, increase efficiency of light harvesting, etc.

MIMICKING MICROGRAVITY IN BIO- AND NANO-COLLOIDAL SYSTEMS USING SUPERCRITICAL CARBON DIOXIDE

C. Ted Lee, Jr.
Department of Chemical Engineering, The University of Southern California
925 Bloom Walk, HED 207, Los Angeles, CA, 90089-1211
Phone: (213) 740-2066, Fax: (213) 740-8053, tedlee@usc.edu

Density modulation of highly-compressible supercritical carbon dioxide ($scCO_2$) will be used to minimize density differences in $scCO_2$-surfactant mixtures, thereby providing a simple, ground-based approach for approximating microgravity conditions in colloidal and interfacial systems. Density matching will allow investigation of the effects of microgravity on the surface phenomena of complex fluids, suspensions, and multiphase systems, with specific emphasis on interactions between nanometer-sized colloids and nanocolloidal aggregation. Recently, a variety of nanometer-scale surfactant morphologies have been discovered in $scCO_2$ – including spherical and cylindrical microemulsions. By adjusting the density of CO_2 to match that of the water/surfactant phase, the effects of gravity vanish, allowing an investigation of the impact of microgravity on the fluid dynamics and interfacial phenomena of colloidal systems. Specifically, the influence of effectively-reduced gravity on electrostatic and intermolecular interactions, colloidal aggregation, and the *microemulsion* critical point can be realized. It has been known since the early 20th century that gravity effects strongly couple with the critical phenomena of pure fluids, fluid mixtures, and colloidal systems – a result of large concentration (i.e., density) gradients that develop at the critical point due to molecular or colloidal aggregation. This proposal will allow critical phenomena to be studied independent of gravity in a ground-based experiment.

We have investigated the effect of mimicking microgravity in water-in-CO_2 microemulsions, as shown in Figure 1.

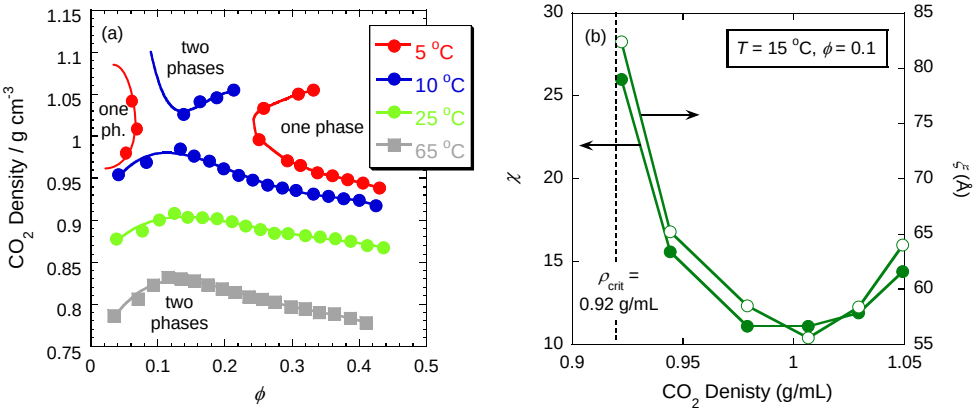

Figure 1. (a) Phase behavior of W/C microemulsions as a function of CO_2 density, temperature, and droplet volume fraction, ϕ, and (b) osmotic susceptibility χ and correlation length ξ determined from neutron scattering

Matching the density of CO_2 to that of water and, thereby, diminishing buoyancy effects has a profound influence on the microemulsion properties. For example, the microemulsion phase-behavior data demonstrate a rather unique phenomenon, namely the coupling of two *microemulsion critical points* to form a so-called "hourglass" cloud-point curve at a water-matched CO_2 density of approximately 1.0 g/mL and a temperature of 5 °C. Furthermore, the onset of nanodroplet clustering can been seen from the osmotic susceptibility (χ) and correlation length (ξ) determined from neutron scattering. As the microemulsion critical point is approached both χ and ξ diverge to large values. This well-known phenomenon can be understood by recalling that the correlation length is a measure of the average size of the aggregated droplet clusters. Thus, the cluster size diverges as the critical point is approached. Interesting, however, is the minima observed for both the osmotic susceptibility and correlation length at a CO_2 density of approximately 1.0 g/mL. These minima may be a result of coupling the effects of gravity with the critical phenomena, due to the large density gradients that develop with cluster formation. Under the influence of gravity, larger droplet clusters are expected to settle at faster rates, thus, sweeping past and incorporating smaller clusters, potentially resulting in an enhancement of the critical/clustering phenomena. Thus, the observed minima in the susceptibility (interaction strength) and correlation length (cluster size) likely results from diminished gravity effects under simulated (i.e., density matched) microgravity. Indeed, previous space-based studies have revealed that under microgravity conditions in the absence of sedimentation, unique colloidal ordering and crystallization – of which colloidal clustering is the first step – can be observed in systems that show no such abnormalities under earth gravity.

Knowledge of the microemulsion critical phenomena will serve as a gateway to allow study of colloidal critical phenomena under simulated microgravity in our laboratory. Furthermore, the discovery of the microemulsions phases mentioned above has laid the groundwork for the formation of more complex, liquid crystalline phases in surfactant-scCO_2 systems. These surfactant morphologies hold promise in ground-based studies of protein crystallization, where density matching to reduce buoyancy-driven convection will result in a process that is diffusion-dominated, thereby potentially producing large, high quality crystals of membrane proteins. It is important to point out that the phenomena of microemulsion criticality and protein crystallization both involve nanocolloidal aggregation, whether to form droplet fractals or protein crystals. Indeed, the fundamental similarly between these two seemingly-different processes points to the importance a ground-based technique for studying mimicking microgravity could have on future NASA missions, as well as for technological advancement here on Earth.

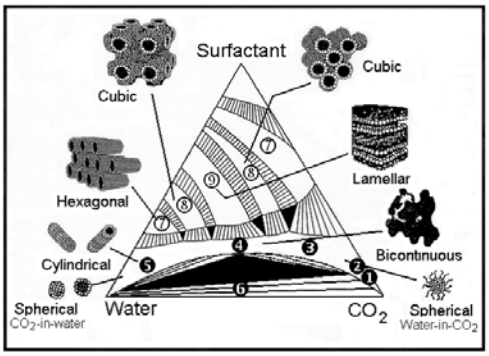

Figure 2. Schematic illustration of the various surfactant phases expected in surfactant/water/CO_2 systems that could be used to crystallize proteins under microgravity.

Abstract

Density modulation of highly-compressible supercritical carbon dioxide ($scCO_2$) will be used to minimize density differences in $scCO_2$-surfactant mixtures, thereby providing a simple, ground-based approach for approximating microgravity conditions in colloidal and interfacial systems. Density matching will allow investigation of the effects of microgravity on the surface phenomena of complex fluids, suspensions, and multiphase systems, with specific emphasis on interactions between nanometer-sized colloids and nanocolloidal aggregation. Recently, a variety of nanometer-scale surfactant morphologies have been discovered in $scCO_2$ – including spherical and cylindrical microemulsions. By adjusting the density of CO_2 to match that of the water/surfactant phase, the effects of gravity vanish, allowing an investigation of the impact of microgravity on the fluid dynamics and interfacial phenomena of colloidal systems. Specifically, the influence of effectively-reduced gravity on electrostatic and intermolecular interactions, colloidal aggregation, and the *microemulsion* critical point can be realized. This will allow critical phenomena to be studied independent of gravity in a ground-based experiment. Furthermore, the discovery of the microemulsions phases mentioned above has laid the groundwork for the formation of more complex, liquid-crystalline phases in surfactant-$scCO_2$ systems. These surfactant morphologies hold promise in ground-based studies of protein crystallization, where density matching to reduce buoyancy-driven convection will result in a process that is diffusion-dominated, thereby potentially producing large, high quality crystals of membrane proteins. It is important to point out that the phenomena of microemulsion criticality and protein crystallization both involve nanocolloidal aggregation, whether to form droplet fractals or protein crystals. Indeed, the fundamental similarly between these two seemingly-different processes points to the importance a ground-based technique of mimicking microgravity could have on future NASA missions, as well as for technological advancement here on Earth.

- Advantages of CO_2:
  - nontoxic, nonflammable
  - environmentally benign
  - tunable solvent
  - can bridge the fluorocarbon-hydrocarbon solubility gap
  - low critical temperature and pressure

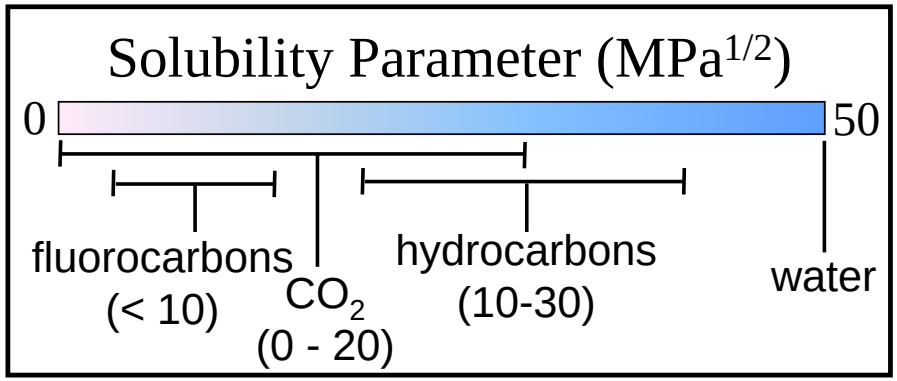

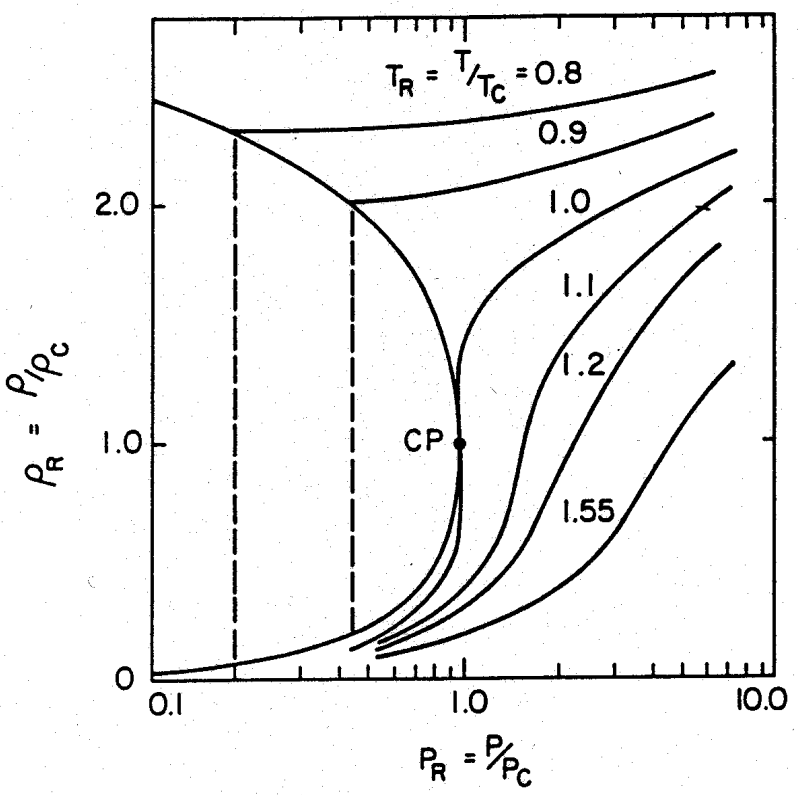

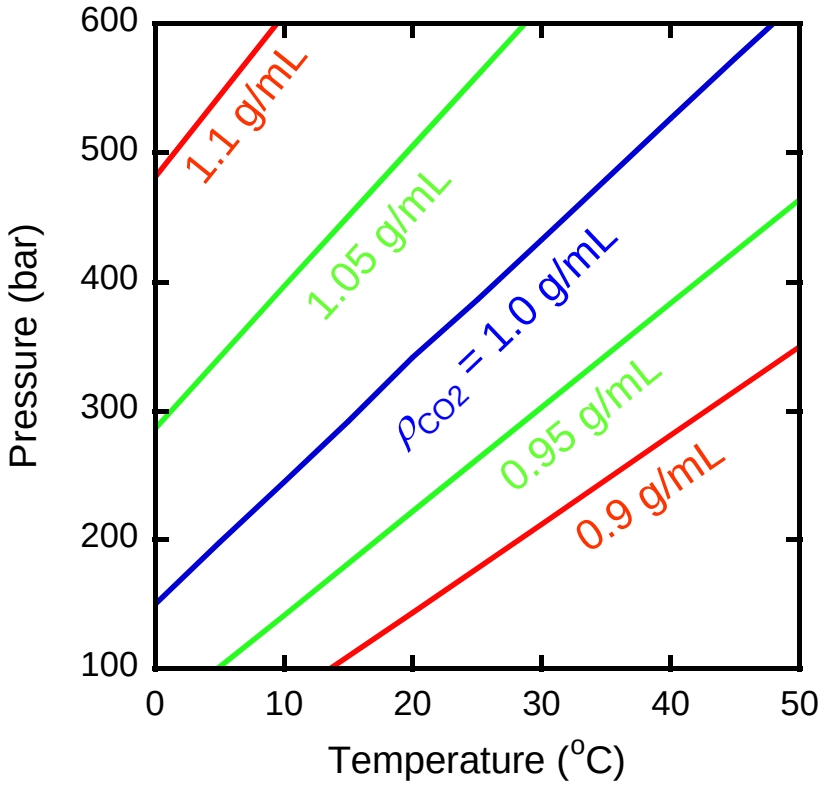

Motivation for Density-Responsive Surfactant Systems

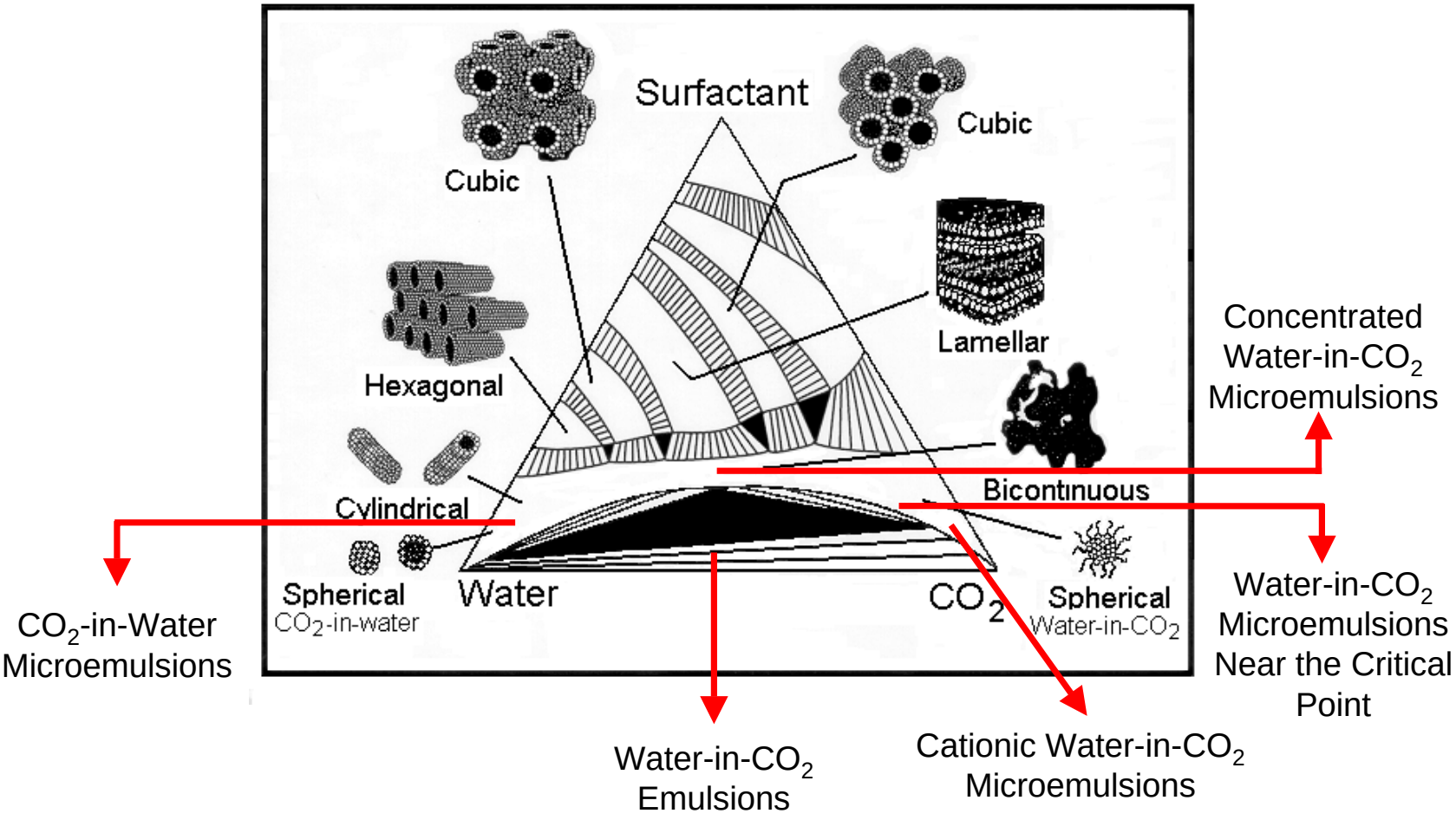

Water-in-CO_2 Emulsions

- Emulsion stability maximum under “microgravity” conditions

Surfactant:

CF_3-(O-CF_2-$CF(CF_3)$)$_n$-$COO^-NH_4^+$ (n ~ 14)

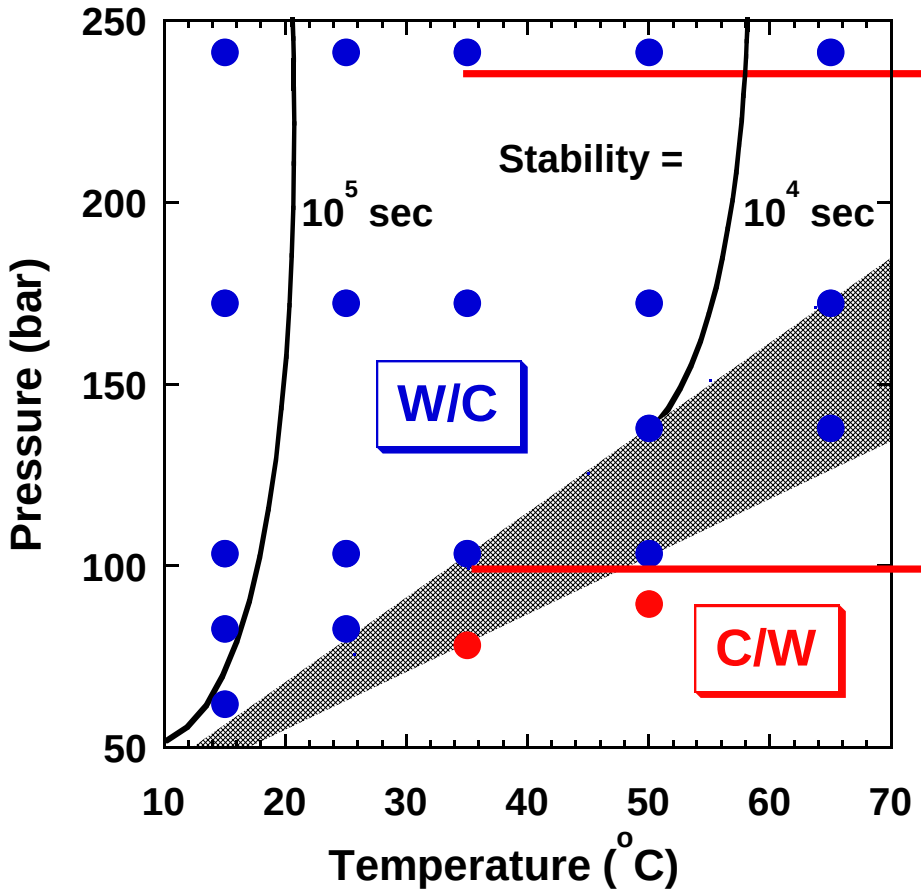

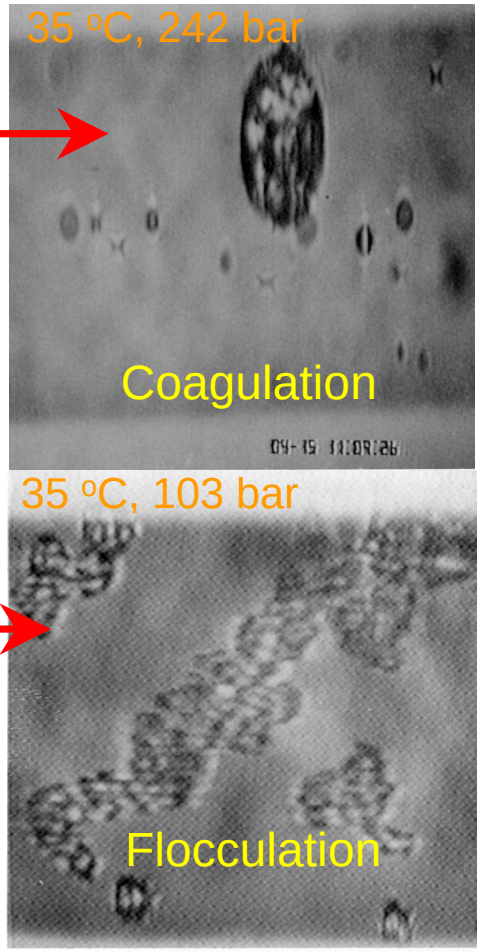

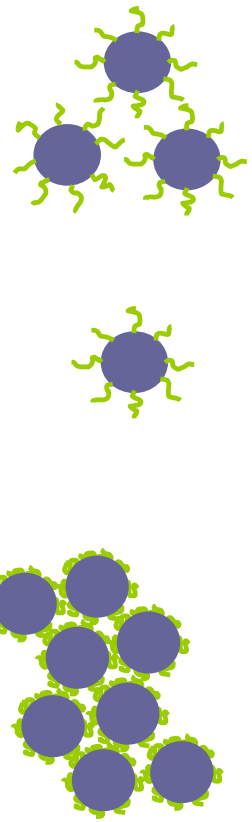

↔ 10 μm

Critical Water-in-CO_2 Microemulsions

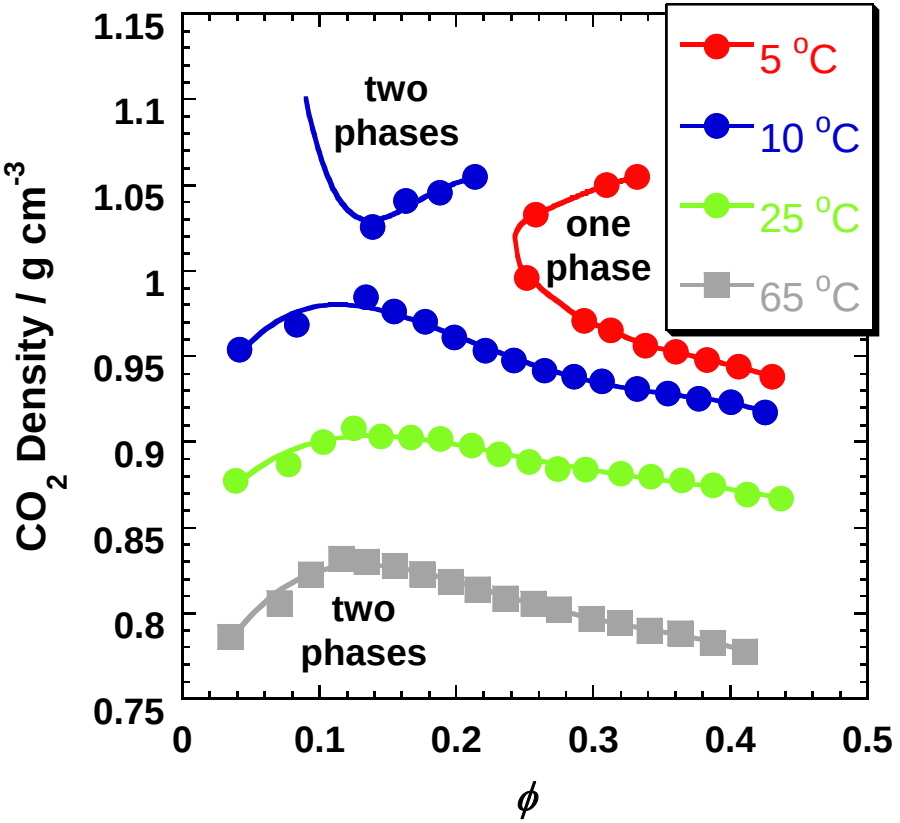

- Droplet interactions are minimum at ρ ~ 1.0 g/mL

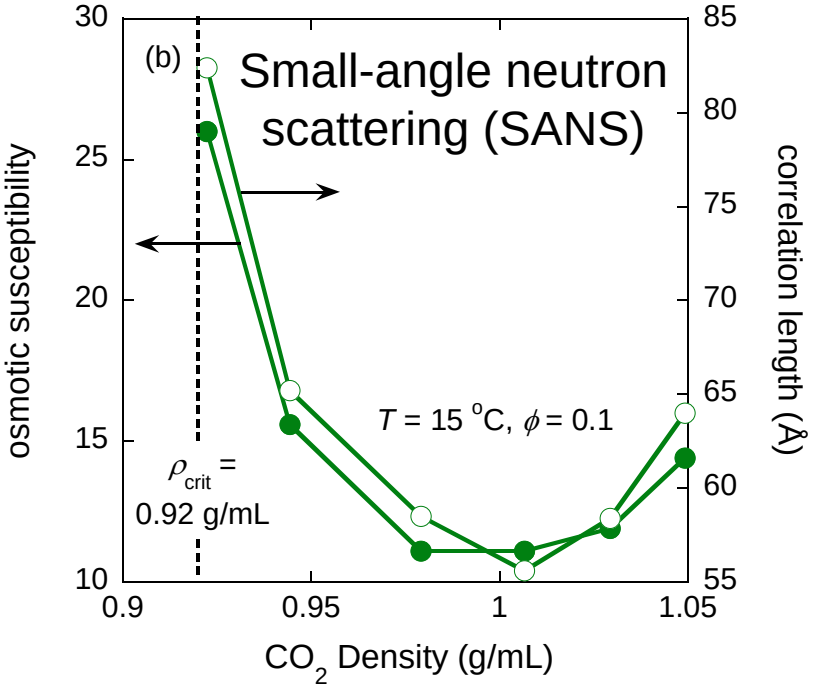

CO_2-in-Water Microemulsions

$$D_0 = \frac{k_B T\left[\ln(d/L) + f(d/L)\right]}{3\pi\eta L}$$

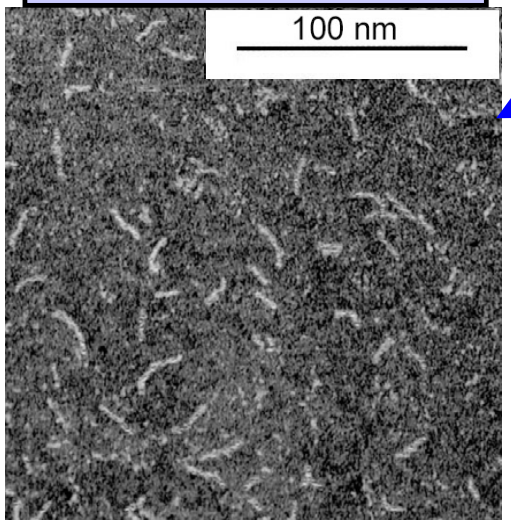

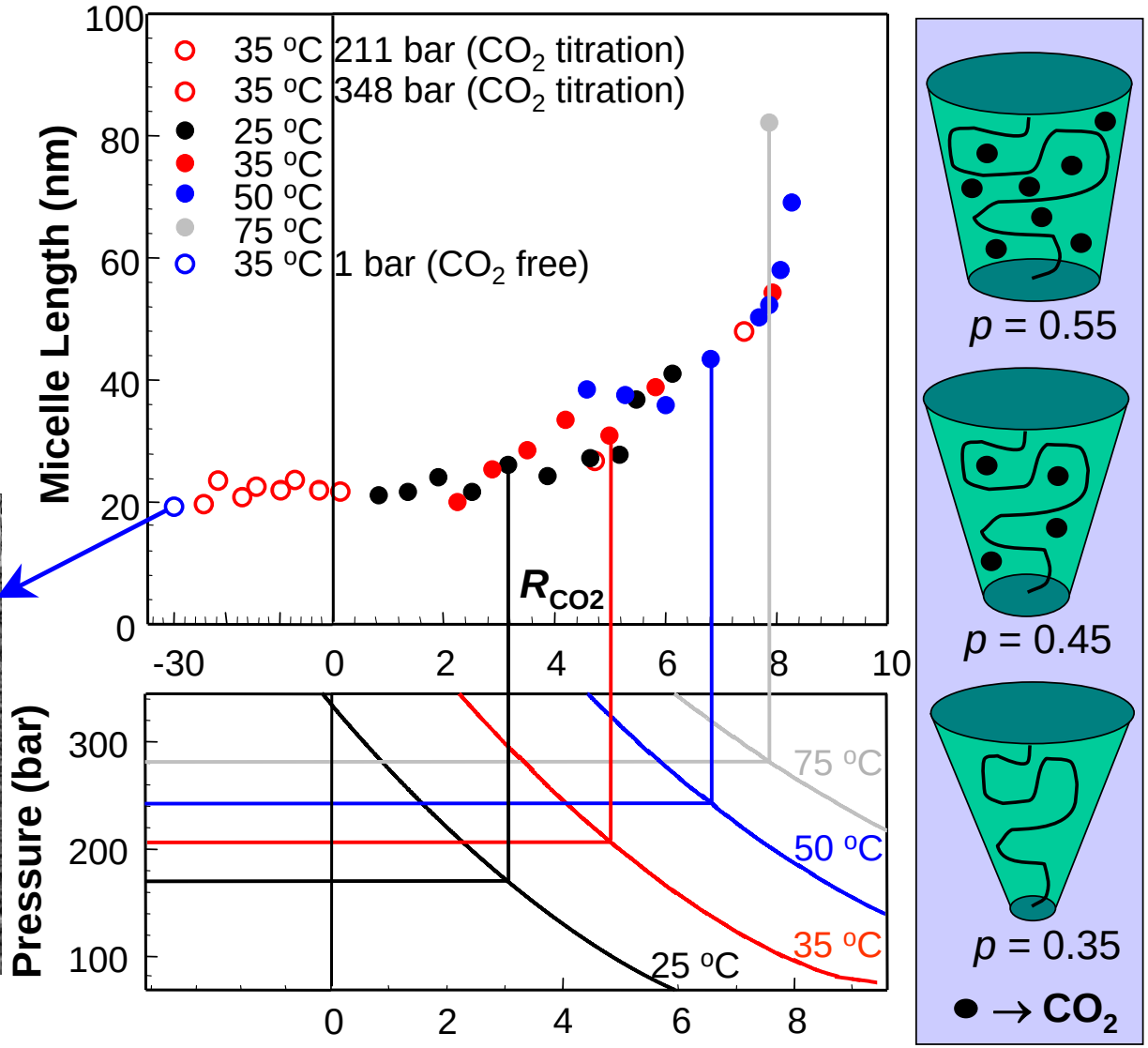

Solubilization in CO_2-Swollen Micelles

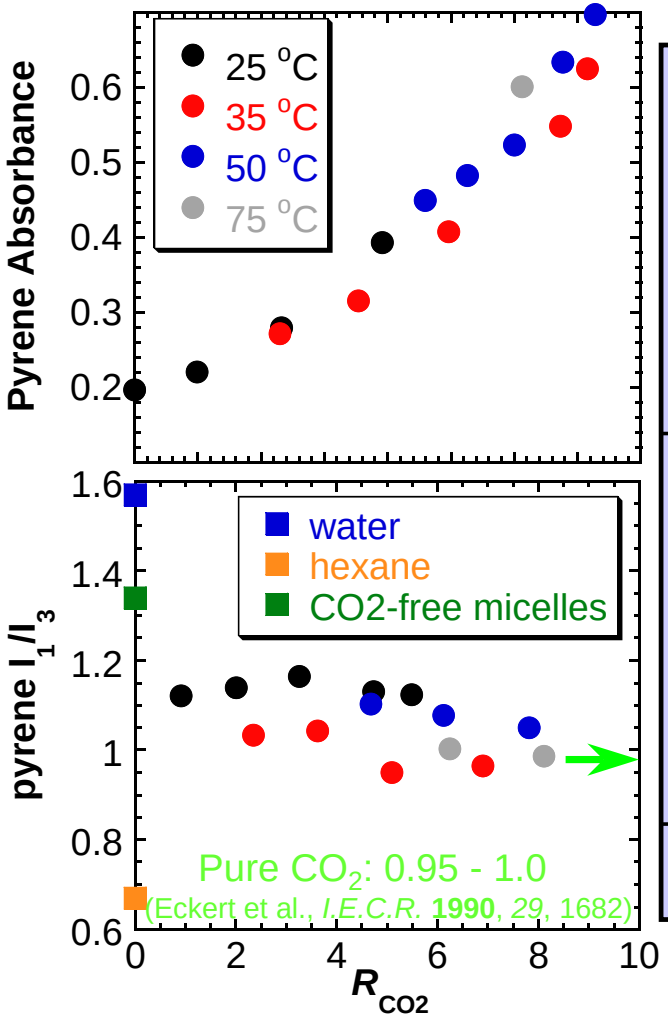

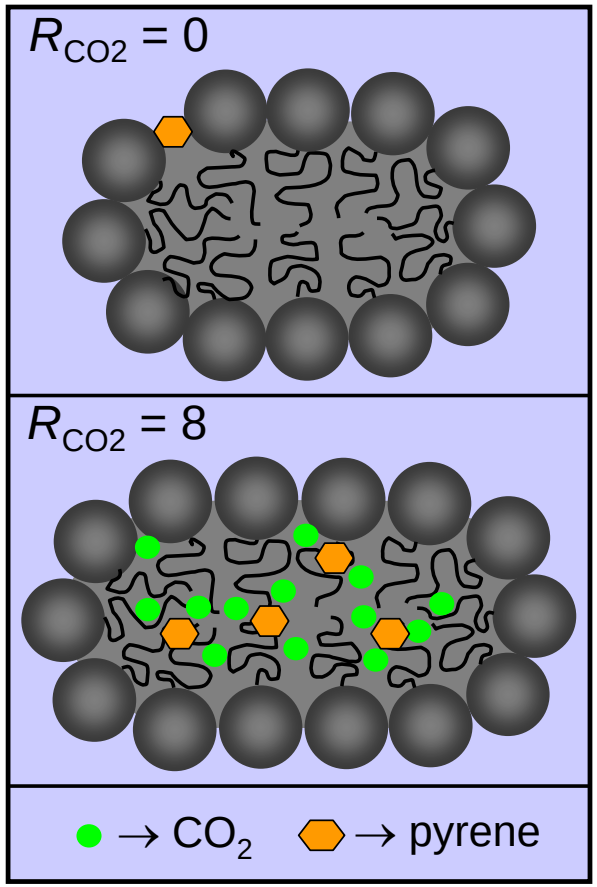

- Addition of CO_2 allows for the solubilization of ***hydrocarbon*** solutes into ***fluorocarbon*** micelles
- Potential to act as a ***universal solvent***

Catanionic Water-in-CO_2 Microemulsions

$\phi = 0.01$, $P = 346$ bar

W_o	T	R_w
19.4	90	16.0
19.4	65	19.1
19.4	35	20.2
32.1	90	31.6
38.1	90	35.9
38.1	65	35.0

Surfactant (quaternary ammonium salt):

F-$(CF(CF_3)$-CF_2-$O)_n$-$CF(CF_3)$-C(O)-NH-$CH_2N^+(CH_3)_3$-$OOCCH_3$

$$R_W = \left(\frac{3v_W}{a_H}\right) W_o + \left(\frac{3v_H}{a_H}\right)$$

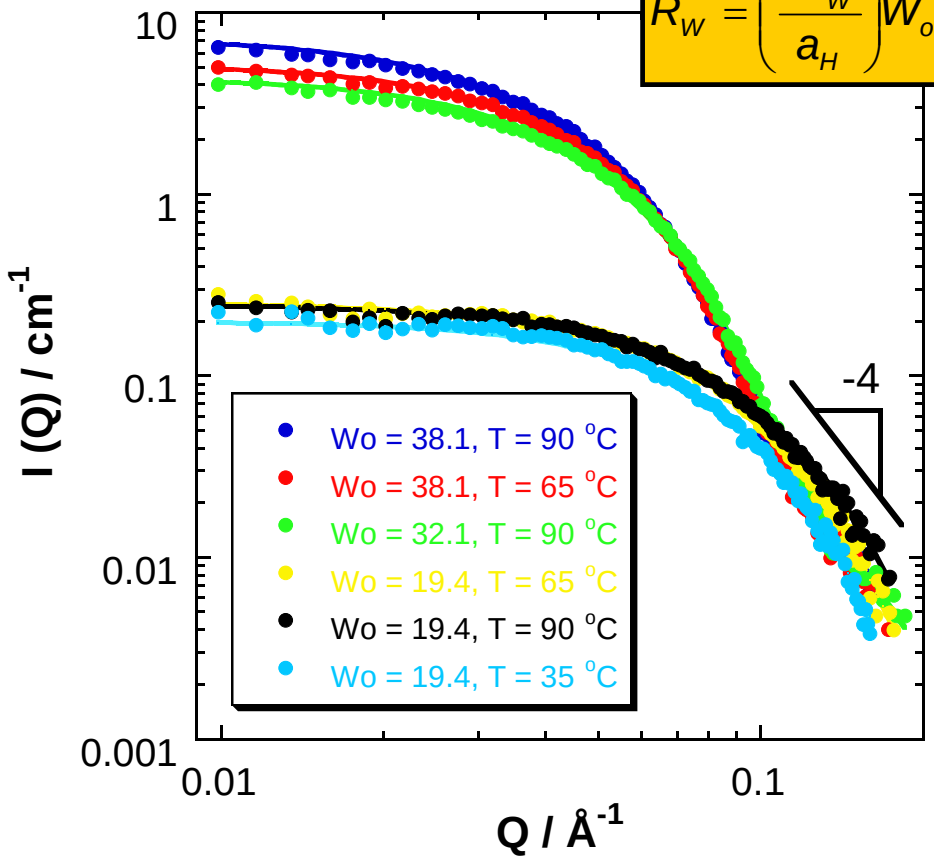

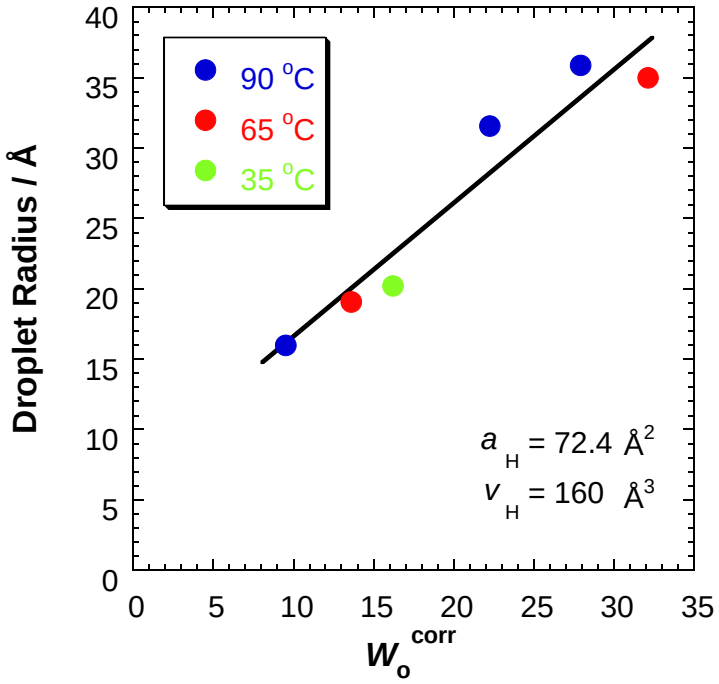

THERMOACOUSTIC CONVECTION AND TRANSPORT IN GASES AND NEAR-CRITICAL FLUIDS UNDER NORMAL AND MICRO-GRAVITY CONDITIONS

Yiqiang Lin, Zhiheng Lei, and Bakhtier Farouk*
Department of Mechanical Engineering and Mechanics, Drexel University, Philadelphia, PA.
*e-mail: bfarouk@coe.drexel.edu; fax: 215 895 1478; phone: 215 895 2287
Elaine S. Oran
Naval Research Laboratory, Washington, D.C

ABSTRACT

The recently initiated research project is aimed at studying thermoacoustic and buoyancy-driven transport in gases and near-critical fluids at normal and reduced gravity environments. Large-scale detailed computational models are being developed to simulate and understand the complex phenomena, and thereby analyze the heat and mass transport in gases and near-critical fluids under both microgravity and normal gravity conditions. Normal and reduced gravity experiments are being designed where careful measurements and visualization studies will be carried out to characterize thermoacoustic waves in gases and near-critical fluids. Ground-based reduced gravity experiments will be carried out in the 2.2 s drop tower at the Glenn Research Center.

When a compressible fluid is suddenly exposed to a localized heat flux, part of the fluid in the immediate vicinity of the boundary expands. This gives rise to a rapid increase in the local pressure, leading to the production of pressure waves called thermoacoustic waves. Thermal convection induced or augmented by acoustic waves is termed as 'thermoacoustic convection'. In real gases, the heat transfer and fluid dynamic effects of thermoacoustic waves are only significant when the heat addition is rapid and the gravitational effects are reduced. We shall investigate the thermoacoustic wave characteristics in different real gases in normal and reduced gravity environmnents. Preliminary solutions of two-dimensional thermoacoustic wave generation and propagation in a nitrogen-filled (at normal temperature and pressure conditions) squre enclosure is shown in Figures 1(a) - 1(d). The left wall was rapidly heated (with a linearly varying temperature profile along the vertical axis).

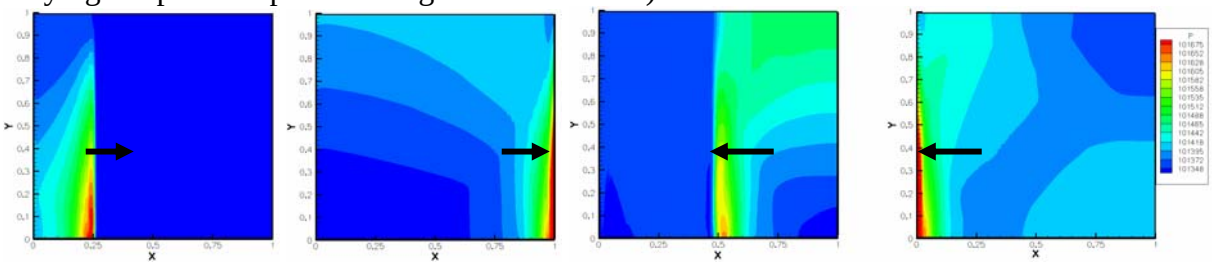

(a) (b) (c) (d)

Figure 1. Thermoacoustic wave propagation in nitrogen due to rapid heating of the left wall

In near-critical fluids, the highly compressible nature coupled with the high density significantly enhances heat and mass transfer due to any temperature perturbation and the resulting thermoacoustic wave. This effect is also known as the *Piston Effect.* This effect is difficult to study in normal gravity, as even very small temperature increase in supercritical fluid

gives rise to large buoyancy effects (high Rayleigh Number) due to the very small values of thermal diffusivity of near critical fluids. Interesting property variations of carbon dioxide near its critical point are shown in Figures 2(a) and 2(b).

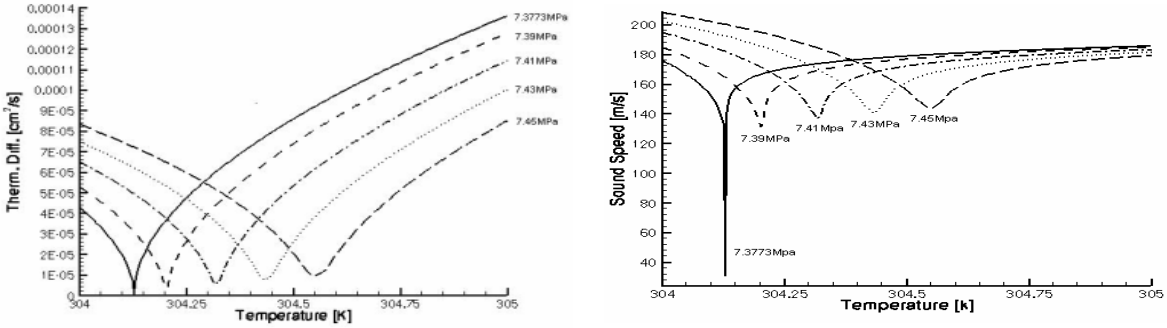

(a) (b)

Fig. 2 Thermal diffusivity and the sound speed of near-critical carbon dioxide[1]

Mildly supercritical fluids (at pressures and temperatures slightly above the critical point) exhibit specific behaviors that make them attractive for both fundamental science and industrial applications. The generation and propagation of thermoacoustic waves in slightly supercritical carbon dioxide will be investigated by solving the fully compressible form of the Navier-Stokes equations. The thermodynamic properties of the slightly supercritical carbon dioxide will be calculated using the NIST standard reference database 12[1].

A schematic of the proposed experimental set up for studying thermoacosutic waves in real gases is shown below in Figure 3. The thermoacoustic waves will be generated and propagated inside a cylinder. A resistance-capacitance circuit will be used to rapidly heat a thin foil that constitutes one end of the cylinder. By carefully choosing the foil, the capacitor and the discharge voltage, we can get different temperatures in the foil and different heating rates.

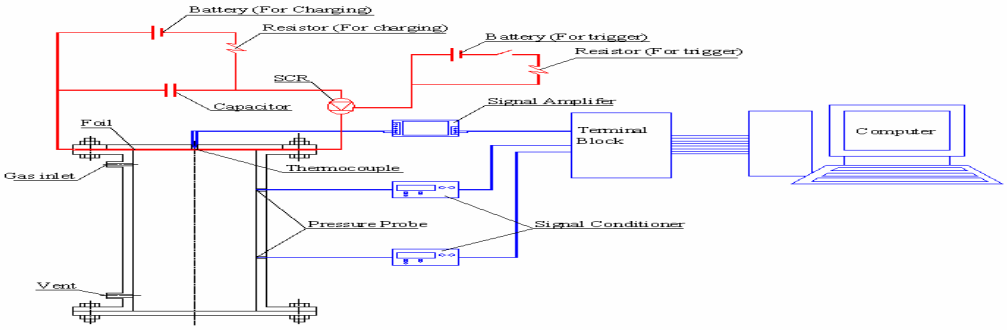

Fig. 3. Schematic of the experimental set up to study thermoacoustic waves in real gases

Experiments will be first carried out under normal gravity conditions. Similar experiments are also planned for enclosures filled with mildly super-critical carbon dioxide. For both real gases and super-critical fluids, experiments will be carried out at ground based reduced gravity experimental facilities.

References

1. Lemmon, E. W., Peskin, A. P., McLinden, M. O., and Friend, D. G. 2000. NIST Thermodynamic and Transport Properties of Pure Fluids, U.S. Department of Commerce, Gaithersburg, MD.

FLUID PHYSICS AND TRANSPORT PHENOMENA IN A SIMULATED REDUCED GRAVITY ENVIRONMENT

J. Lipa
Physics Department
Stanford University
Stanford, CA 94305

We describe a ground-based apparatus that allows the cancellation of gravity on a fluid using magnetic forces. The present system was designed for liquid oxygen studies over the range 0.001 - 5 g's. This fluid is an essential component of any flight mission using substantial amounts of liquid propellant, especially manned missions. The apparatus has been used to reduce the hydrostatic compression near the oxygen critical point and to demonstrate inverted phase separation. It could also be used to study pool boiling and two–phase heat transfer in Martian, Lunar or near-zero gravity, as well as phenomena such as Marangoni flow and convective instabilities. These studies would contribute directly to the reliability and optimization of the Moon and Mars flight programs.

PI name: John Lipa
Physics Department, Stanford University, Stanford CA 94305
e-mail address : jlipa@stanford.edu
phone number 650-723-4562

FLUID PHYSICS AND TRANSPORT PHENOMENA IN A SIMULATED REDUCED GRAVITY ENVIRONMENT

J. Lipa
Physics Department
Stanford University
Stanford, CA 94305

We describe a ground-based apparatus that allows the cancellation of gravity on a fluid using magnetic forces. The present system was designed for use with liquid oxygen over the range 0.001 - 5 g's. This fluid is an essential component of any flight mission using substantial amounts of liquid propellant, especially manned missions. The apparatus has been used to reduce the hydrostatic compression near the oxygen critical point and to demonstrate inverted phase separation. It could also be used to study pool and film boiling, and two–phase heat transfer and flow in Martian, Lunar or near-zero gravity, as well as phenomena such as Marangoni flow, convective instabilities and the effects of interfacial forces. These studies would contribute directly to the reliability and optimization of the Moon and Mars flight support systems. Systems using higher magnetic fields can be built to study other fluids, including water.

INTRODUCTION

In recent years the magnetic levitation of many ordinary substances against the earth's gravity field has been demonstrated[1]. Materials from wood to water to small living creatures have been freely suspended in air against gravity for significant periods. This effect can be used to perform a wide range of interesting fluid studies, including convection with a variable driving force and thermal stratification effects, two phase flow and heat transport and film boiling to name a few. In some cases the magnetic field requirements are sufficiently modest that the materials can be levitated indefinitely using superconducting magnets or in the case of a few materials such as oxygen and bismuth, with permanent magnets. This capability opens up exciting research opportunities previously only accessible in space. An essential property of magnetic levitation of a single component material is that the force is applied to all molecules equally, canceling gravity in the bulk, as opposed to applying surface forces as is done in a rotating bioreactor, for example. On the other hand, the levitation of complex objects involves cancellation of gravity only on average, in a similar fashion to buoyancy. In this paper we describe some work conducted with a liquid oxygen levitator and point out some future directions that could be of value to the Moon and Mars program.

With current technology, magnetic levitation is in principle achievable for any material with a susceptibility greater than about $\pm\ 3.5\text{x}10^{-10}$ m^3/kg. This limit is set by the design constraints of high field magnets, and could be lowered in the future, as new magnet technologies are developed. The levitating force is proportional to the susceptibility times $B\nabla B$, where B is the magnetic field intensity and ∇B is its gradient, and must of course be directed upwards. For most materials susceptibilities are in the range ± 1 to $5\text{x}10^{-10}$ m^3/kg, requiring quite high fields and gradients to achieve levitation, if it can be done. The high fields complicate experiment design and tend to restrict the choice of fluids to those of low atomic weight, but fortunately include water, oxygen and hydrogen, the fluids most likely to be used on deep space manned missions. Liquid oxygen is an exceptional case, having an extremely high susceptibility of $2.41\text{x}10^{-7}$ m^3/kg at 90K. This implies typical levitation values of $B\nabla B$ that are 300 times smaller than for water. In the poster charts below, we show some photos of an oxygen levitation demonstration using a small samarium-cobalt permanent magnet.

The goal of the system described here was to perform an improved investigation of critical phenomena entering deep into the asymptotic region by making use of magnetic levitation to reduce the hydrostatic compression of a fluid. A magnetic technique to cancel the hydrostatic pressure variations in a small column of liquid helium to the 1% level was demonstrated at JPL[2]. A similar magnet was also used at Brown University[3] to levitate large drops of helium. These experiments needed very large $B\nabla B$ values to achieve levitation due to the small value of the susceptibility of helium. The resulting magnet design constraints severely limit the sample volume where accurate cancellation of gravity can be achieved. In contrast, a much more effective cancellation of the hydrostatic pressure over larger volumes can be accomplished with a sample of liquid oxygen in relatively modest magnetic fields using wide bore solenoids and carefully designed gradient coils. We note that the magnetic effects on oxygen were demonstrated[4] at the Bitter Magnet Laboratory at MIT many years ago. Since biological material is composed primarily of water, and the other components have similar susceptibilities, it can typically be levitated.

OXYGEN LEVITATION

We have built a magnetic levitation system that is capable of canceling the effect of gravity on an oxygen sample to about 0.1%, a capacitance cell with associated electronics for local fluid density measurements, and a thermal enclosure designed to achieve a thermal stability and homogeneity of about 1 microdegree when operating near 154 K. The levitation system consists of a solenoid and a gradient coil configured to provide a lift force uniformity of about 0.1% over a disk-shaped volume 1 mm high and 1 cm in diameter. The uniform field and the gradient can be adjusted independently. To minimize the perturbations to the field distribution all components within the bore of the magnet are fabricated from non-magnetic materials. A schematic view of the apparatus is shown in the charts below.

The cell contains a narrow gap capacitor formed from aluminum films deposited on sapphire. The structure was designed to be very stable mechanically and have low sensitivity to pressure. The capacitor gap was located below the center of the cell about 1 mm from the bottom, and it was 0.5 cm in diameter. By applying a pulsed dc bias to the plates the effect of electrostriction on the fluid can be observed, allowing the compressibility to be estimated. The internal height of the cell was 3 mm and the large spaces were filled with copper blocks.

A significant component of the apparatus is the thermal control system. We designed a system to achieve a stability and homogeneity of about 10^{-8} near the critical point, allowing good operation at the resolution goal of $t \sim 10^{-7}$. This is at about the level obtained in state-of-the-art thermal controllers such as those used on the Zeno and CVX flight experiments. The mechanical portion of the control system is a multi-shell enclosure operated in a high vacuum. A photograph of the partially disassembled system with the shells removed is shown below. The temperatures of the stages were measured using calibrated thermistors and conventional high resolution ac bridge techniques involving high stability ratio transformers.

Recently, we used the levitator system to reduce the hydrostatic compression of oxygen near its critical point, allowing a new investigation of thermodynamic phenomena in this region. The effect of the levitator is to cancel gravity on each volume element within a fluid, mimicking the conditions of space flight on the ground. A basic problem in the study of second order phase transitions is that fluids are the only materials free of distortion due to impurity and stress inhomogeneities, but near the transition, the compressibility diverges, causing distortion due to hydrostatic compression. Space experiments, which eliminate the hydrostatic effect, have become one of the few ways that much progress can be made in this field. Wilson's application[5] of the renormalization group calculation scheme to the problem of the critical point led to predictions for the exponents and many 'universal' amplitude ratios in the model. These predictions for fundamental thermodynamic quantities are currently the most accurate ones in

the entire field of bulk critical phenomena in statistical physics. The project described here was designed to improve the testing of these predictions.

The sample density was measured by monitoring the change in capacitance between the aluminum electrodes plates due to the fluid filling the gap. A commercial capacitance bridge with a resolution $\Delta C/C \sim 10^{-7}$ is used for the measurements. In a figure below we show some typical electrostriction data obtained as the sample cools at constant average density close to critical. This curve shows three regions. Well above the critical temperature the fluid responds quickly to the square wave voltage applied to the plates. As the transition temperature is approached the amplitude of the response is seen to increase as expected since it is proportional to the compressibility. Very close to the transition a sharp increase in the thermal relaxation time is observed possibly due to the presence of two fluid phases within the capacitor gap. With further cooling the time constant is reduced and the density deviation from the original value increases rapidly. Typically, this region corresponds to a branch of the coexistence curve. Commonly, the density will change rapidly once more as the temperature is lowered further and the opposite branch of the coexistence curve will be traced out. A figure below shows some initial measurements of the compressibility in the critical region. From separate coexistence curve measurements it appears that for this set of data the mean density of the sample is within 1% of critical, and possibly much closer. The data shows some rounding for $t < 5 \times 10^{-6}$. Also shown are results obtained with the magnet turned off. Significantly more rounding is observed. This demonstrates that the magnetic levitation system is capable of reducing the effect of gravity at the critical point.

MOON AND MARS MISSION SUPPORT

In the mission support arena, three acceleration environments are of primary interest: the levels seen on the Moon and Mars, and the level encountered during transit. Clearly, in low gravity situations, the magnetic manipulation of fluids is relatively straightforward. For example, for water, a $B\nabla B$ of only 1.4 T^2/m is needed to hold the fluid against milli-g accelerations. In unmanned vehicles, it is easy to achieve micro-g accelerations when thruster firing is avoided. In that situation, liquid hydrogen can be controlled at $B\nabla B \sim 5 \times 10^{-4}$ T^2/m. At this level, surface tension forces over radii of 0.1 m compete with the magnetic force. An obvious application for long space voyages, say to Mars, is the controlled venting of cryogenic propellants without the need for fine mesh screens within the tanks. In some cases, permanent magnets could be used near the venting orifice. Magnetic separation of the phases would avoid the 'blow-through' problem with meshes since the separation would be intrinsically stable. Any loss of control due to transient forces would be recovered from automatically.

The effective gravity environments on the Moon and Mars are 0.17g and 0.39g respectively. The table below[6] shows some representative values for the $B\nabla B$ values required to create various artificial gravity environments for some commonly used liquids. A lift force of 1g – 0.39g = 0.61g is needed to create the equivalent artificial gravity environment for Mars in an Earth based laboratory. Since the created effective gravity is linear in $B\nabla B$, the table can be used to determine arbitrary gravity compensations for the fluids listed.

Another potential application is low dissipation pumping, using time varying magnetic attraction. The inertia of the fluid could be used to draw fluid into a multi-stage magnetic attraction system and expel it in a region of repulsive force. The technique described here can also be used to suppress or enhance convection in certain fluids. This would allow the study of stratification effects encountered, for example, in cooled propellant tanks. Magnetic forces could also be used to apply artificial gravity in small regions for critical applications. For example phase separation in a small boiler could be enhanced, possibly simplifying the design in other areas.

In addition, the magnetic levitation technique could be of significant value to other studies of convection and thermally induced flows. This would allow the study of many flow phenomena

in the environments of interest without tying up the extremely scarce microgravity resources currently available. In the case of intermediate g values, magnetic cancellation of gravity gives us the only way to look at flow phenomena for more than a few seconds without actually going to the Moon or Mars. For studying the behavior of oxygen as a typical fluid in Martian gravity, for example, an accessible volume of more than 50cc would be possible, more than enough for many experiments. Applications in other fields are also quite possible, for example, protein crystal growth[7] and biological studies[3].

ACKNOWLEDGMENTS

We wish to thank the NASA office of Life and Microgravity Sciences and Applications for its support with grant # NAG8-1431.

REFERENCES

1: A. Geim, Physics Today, **51**, 36 (sept. 1998).
2: M. Larson, F-C. Liu, and U.E. Israelsson, Czech. J. of Phys. **46** part S1, 179 (1996).
3: M. A. Weilert, D. L. Whitaker, H. J. Maris and G. M. Seidel, J Low Temp. Phys. **106**, 101 (1997); M. A. Weilert, D. L. Whitaker, H. J. Maris and G. M. Seidel, Phys. Rev. Lett. **77**, 4840 (1996).
4: H.H. Sample and L.G. Rubin, Cryogenics, 18, 223 (1978).
5: K.G. Wilson, Phys. Rev. B 4, 3174 (1971).
6: J.A. Lipa and U.E. Israelsson, Space 98: Proc. of the Sixth Internat. Conf. and Exposit. on Eng., Construct., and Ops in Space, edited by R. Galloway and S. Lokaj, p. 225-231 (1998).
7: J.A. Lipa, The use of Magnetic Forces to Suppress Convection in the Crystallization Process, Proc. 38th AIAA meeting, Reno (Jan. 2000).

		Earth	Moon	Mars	Low gravity
Substance	Susceptibility (m^3/kg)	B∇B (1g) (T^2/m)	B∇B (0.17g) (T^2/m)	B∇B (0.39g) (T^2/m)	B∇B (.001g) (T^2/m)
Hydrogen	-1.99E-09	-492	-81	-194	-0.49
Helium	-4.73E-10	-2074	-342	-817	-2.07
Water	-7.21E-10	-1360	-224	-536	-1.36
Nitrogen	-4.29E-10	-2287	-377	-901	-2.29
Oxygen	2.41E-07	4.07	0.67	1.60	4.07E-03
Neon	-3.34E-10	-2934	-484	-1156	-2.93
Argon	-4.91E-10	-1998	-330	-787	-2.00

Susceptibilities and magnetic levitation forces as a function of g for some fluids. Transport phenomena and fluid mechanics could be studied for all these materials in simulated Moon and Mars gravities and for all except Neon in simulated zero gravity. To get the actual magnetic lift force needed to simulate the Moon's gravity on Earth for example, for a particular fluid, subtract the entry under Moon from that under Earth.

For materials other than oxygen the sample size is somewhat restricted depending on the accuracy required in the gravity simulation. Typical simulations to 1% accuracies are possible in 1 cc spherical regions.

MAGNETIC LEVITATION

Gravitational effects in fluids come about because the gravitational force acts on every atom in the sample. If this force can be compensated by another force acting on the atoms, then we have simulated microgravity and the gravitational effects should be reduced. We use the magnetic force, B x grad(B), acting on the oxygen molecule magnetic dipole to compensate gravity. Since oxygen has an unusually high magnetic dipole moment, only moderate (1 – 3 Tesla) magnetic fields and modest field gradients are needed. This allows a relatively large working space with small residual forces without the need for state-of-the-art solenoids. In fact, levitation can be achieved with permanent magnets (see demonstration photos).

- *Magnetic levitation has space exploration applications which include intermediate gravity simulation, fluid management, pool boiling studies of fluid propellants in low gravity, thermal stratification effects, long term bone loss studies, low gravity simulation for small living things, three-dimensional cell cultures.*
- *It has scientific applications in suppressing gravity effects in fluids: the removal of hydrostatic compression at critical points and the lambda point, the suppression of convection in Marangoni flow studies (thermocapillary effect), reduced convection in protein crystal growth.*

- *It has industrial applications in magnetic bearing systems, Maglev vehicles, and projectile launchers, and possibly protein structure analysis.*

LIQUID OXYGEN LEVITATION DEMONSTRATION

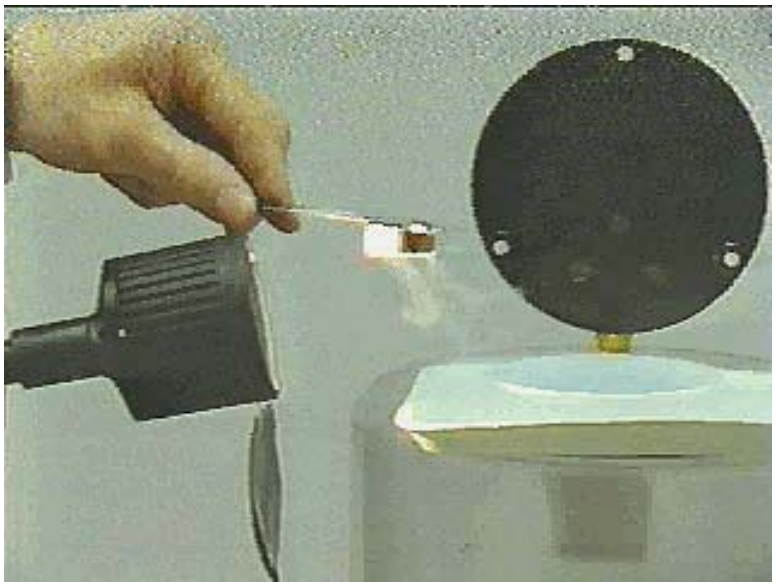

This photo shows the setup used to demonstrate liquid oxygen magnetic levitation: cylindrical magnet attached to steel ruler; tray of cryogenic fluids; circular black screen; lamp.

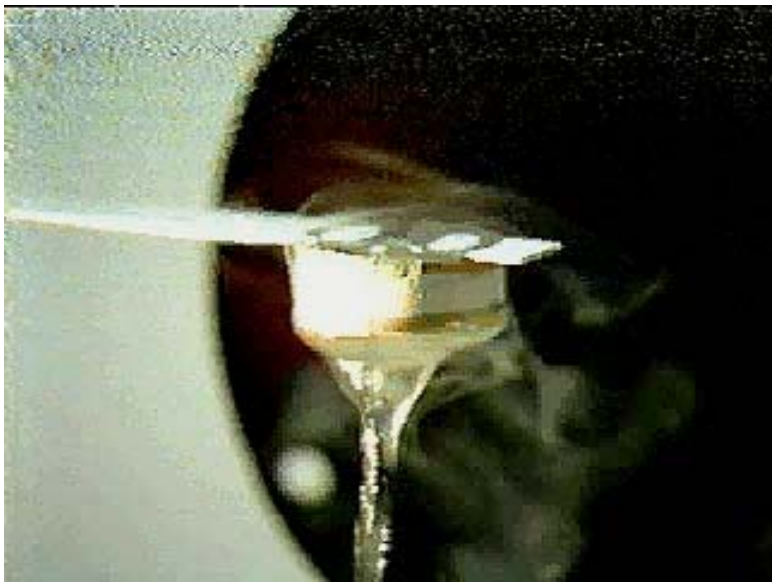

This photo shows the removal of a large droplet of liquid oxygen from the bath and the subsequent draining of excess fluid that is not supported against gravity.

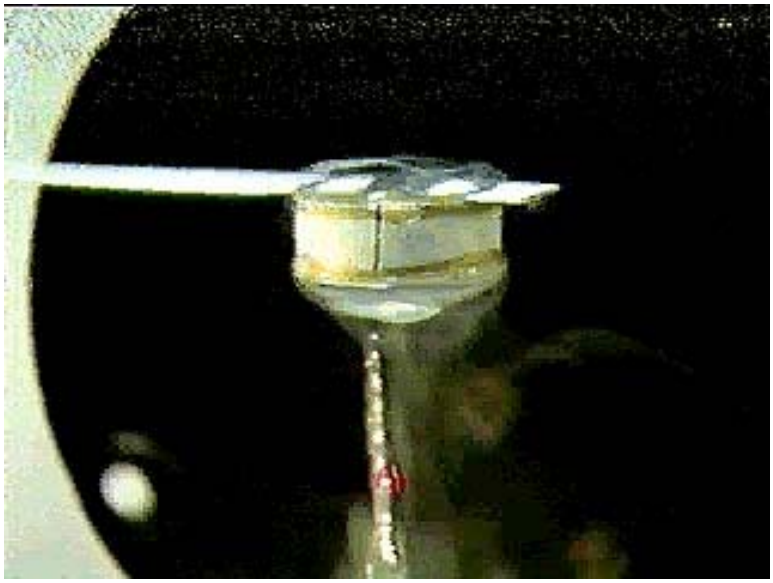

This shows the cessation of the draining event and the formation of a stable droplet attached to the magnet.

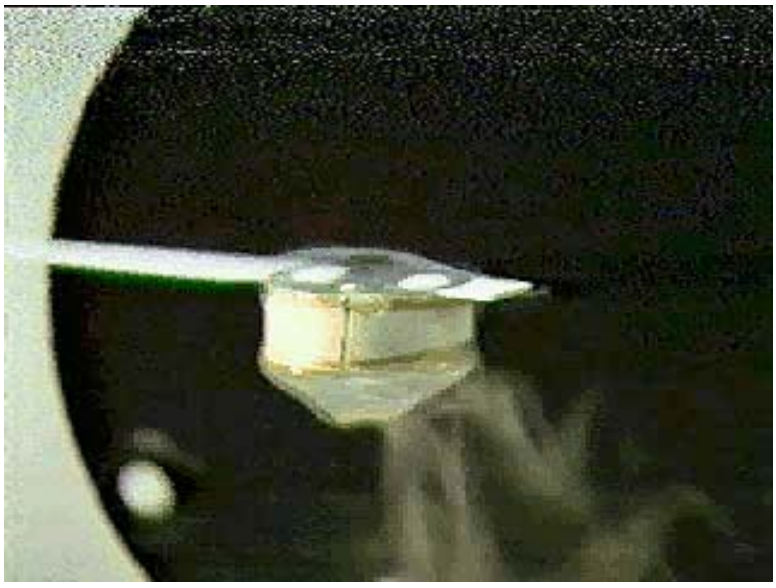

Stable levitation of liquid oxygen with a permanent magnet! Liquid nitrogen will NOT do this.

This picture shows the top view of stable magnetic levitation of a live frog in a high field hybrid magnet. Many common materials can now be levitated.

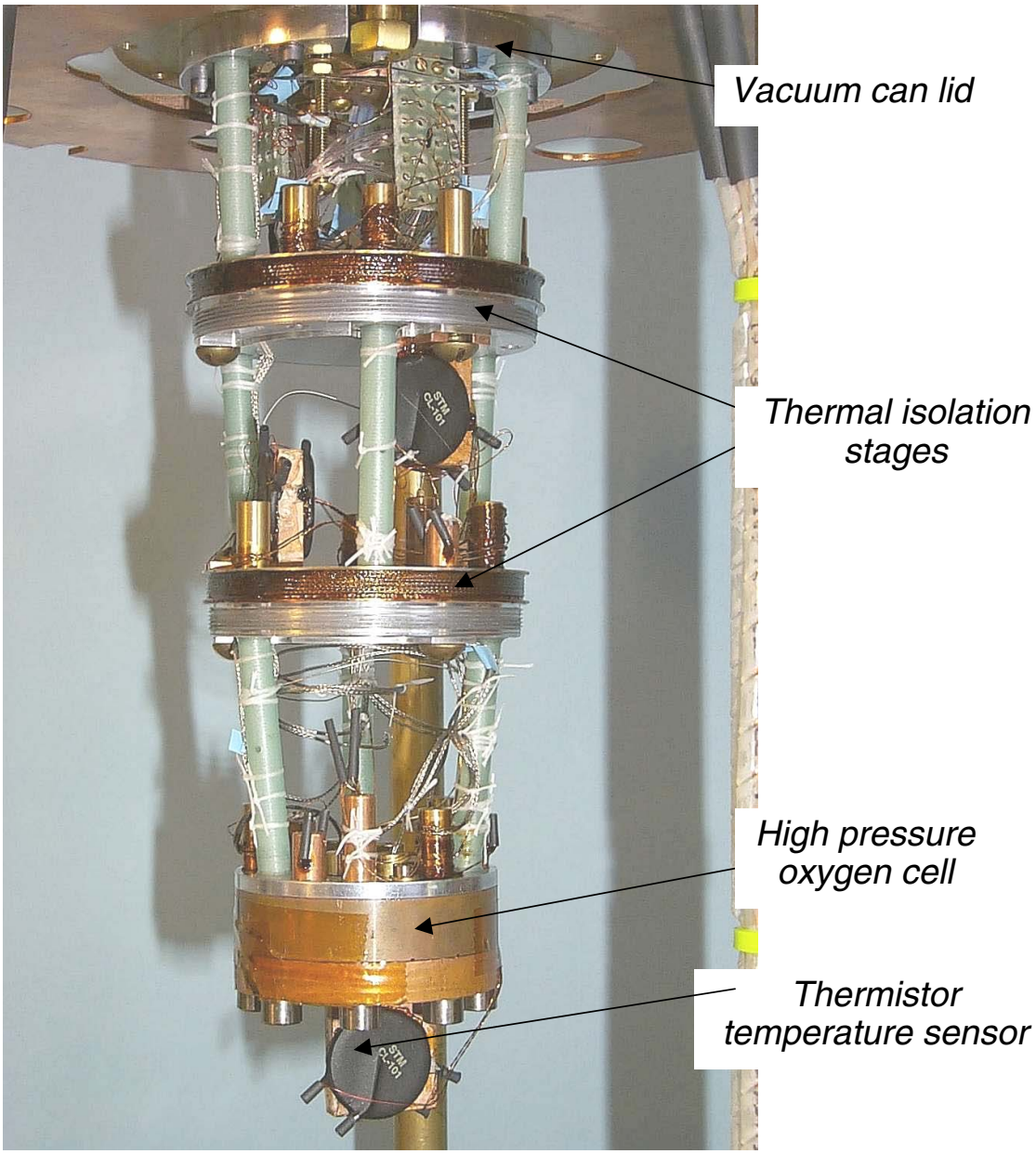

Internal view of thermal control system and oxygen cell used in critical point studies at Stanford. Two thermal shields and the vacuum can have been removed.

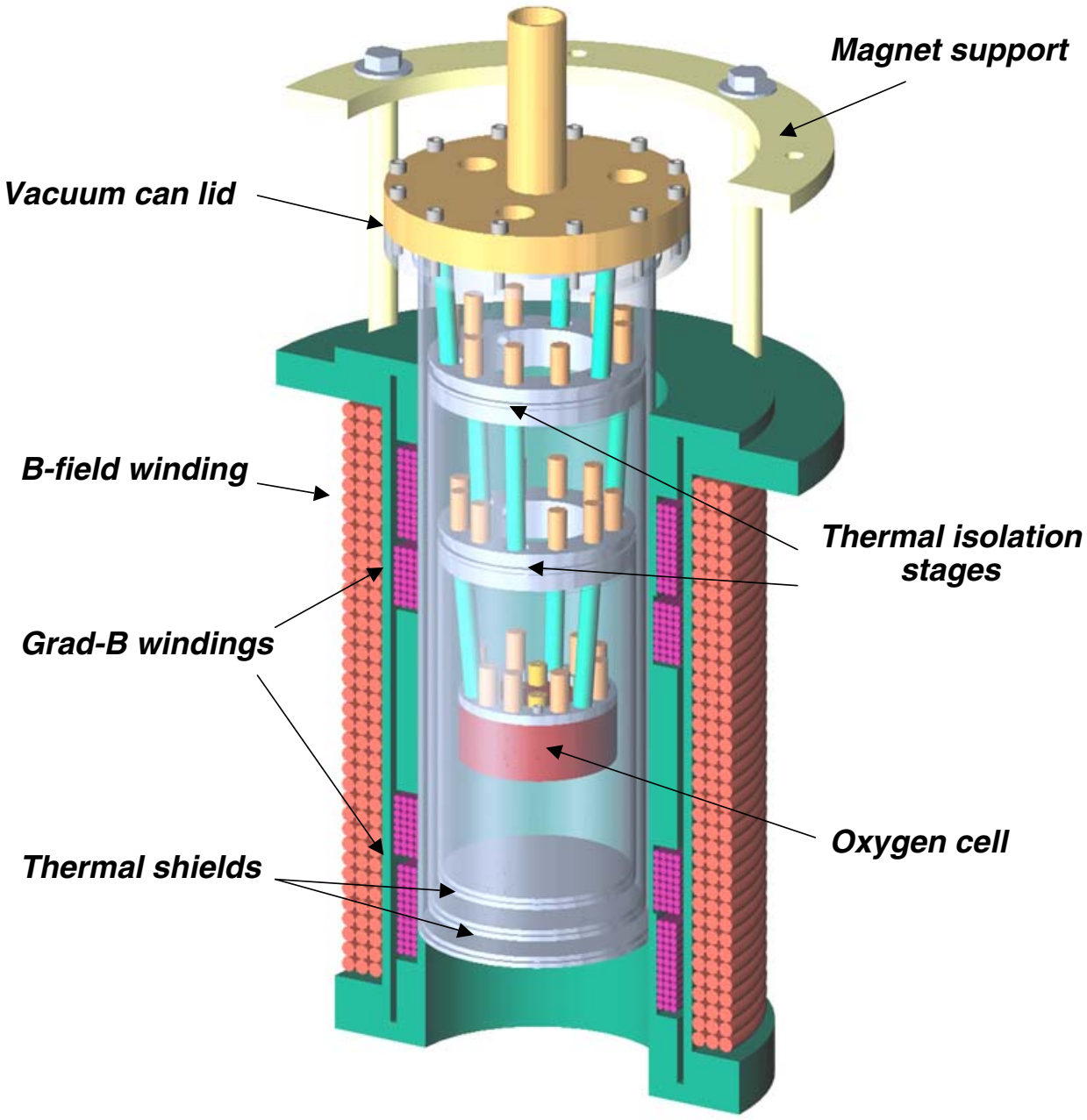

Schematic cross-section of oxygen levitator

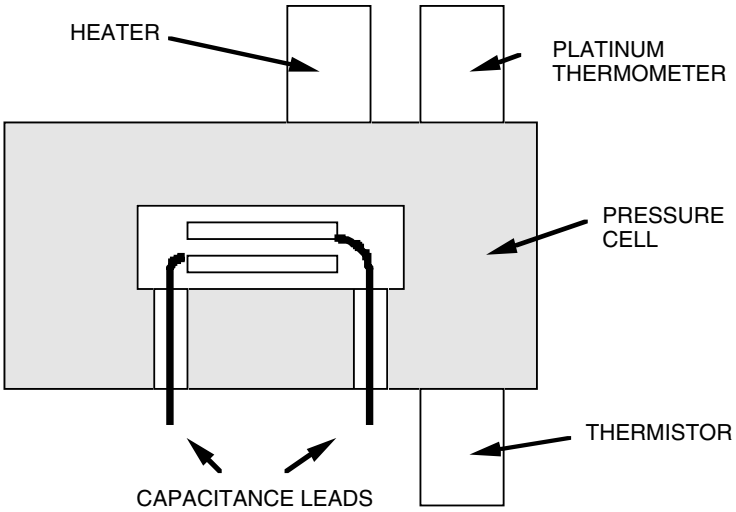

Simplified sketch of oxygen sample cell designed for operation near the critical point (~150K, 50 bars). Gap between sapphire capacitance plates is 0.004 cm.

Near the critical point of a fluid the compressibility diverges, leading to a flattening of the pressure – density isotherms. This causes a significant averaging of the states of the fluid in a finite height sample on earth, making accurate measurements near the critical point very difficult. Magnetic levitation can help reduce this effect.

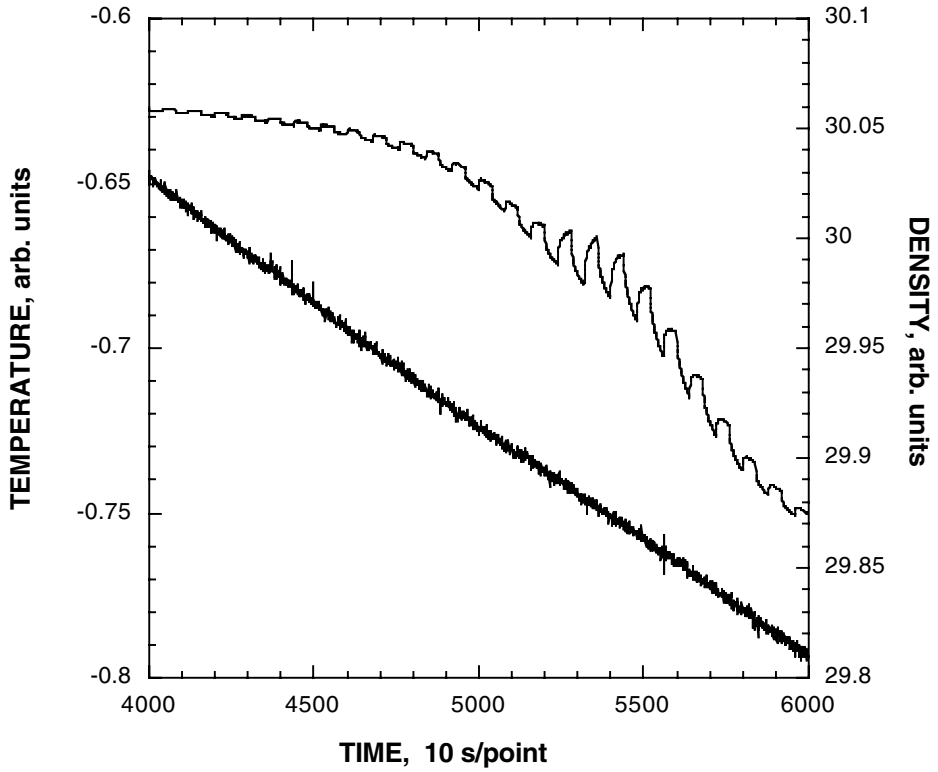

Upper curve: typical electrostriction data obtained as the sample cools at constant average density close to critical. This curve shows three regions. Well above the critical temperature the fluid responds quickly to the square wave voltage applied to the plates. As the transition temperature is approached the amplitude of the response is seen to increase as expected since it is proportional to the compressibility. Very close to the transition a sharp increase in the thermal relaxation time is observed possibly due to the presence of two fluid phases within the capacitor gap. With further cooling the time constant is reduced and the density deviation from the original value increases rapidly. Typically, this region corresponds to a branch of the coexistence curve. Lower curve: sample temperature vs time

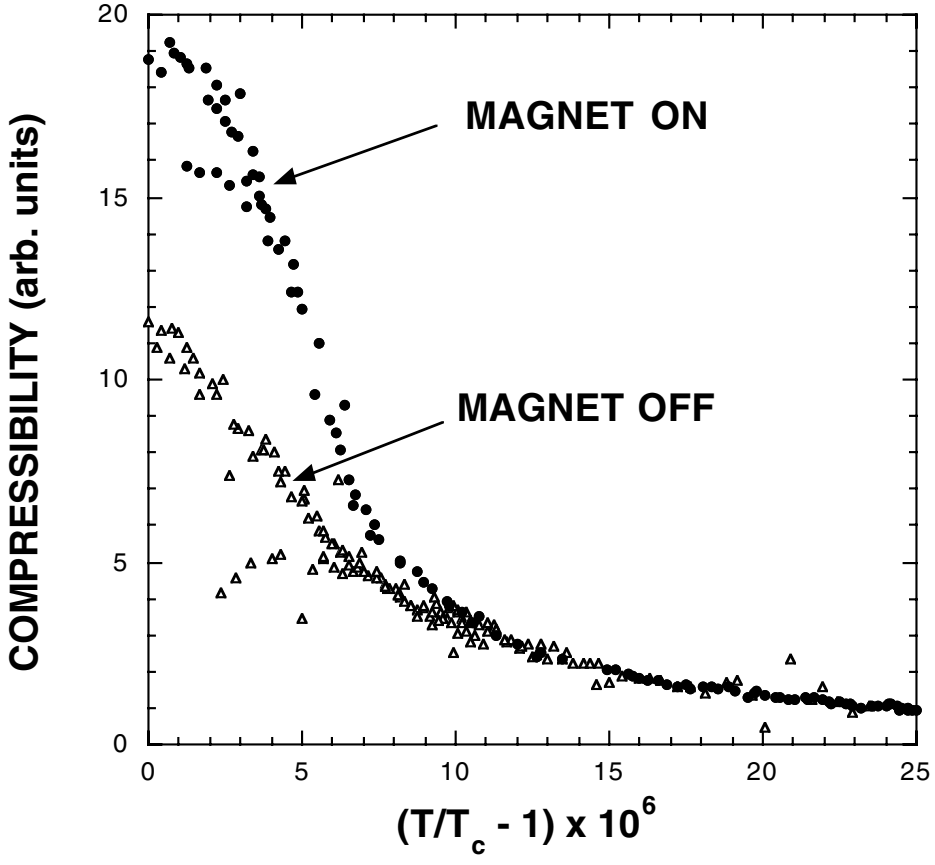

Compressibility of oxygen vs temperature just above the critical point showing the reduction of gravitational effects with magnetic suspension of the fluid. In zero gravity the compressibility should show divergent behavior at the critical temperature.

A CONTINUOUS MICROCULTURE DEVICE FOR MONITORING THE EFFECTS OF SPACE ENVIRONMENTS ON LIVING SYSTEMS

R. Martineau, M. Piccini, and B. Towe
Harrington Department of Bioengineering
Arizona State University
Tempe, AZ, USA

We report our development of a microculture device that continuously cultures genetically engineered bacterial cells and monitors their response to environmental/chemical stimuli. Responses include changes in culture turbidity, pH, production of fluorescent proteins, and bioluminescence. Cells are maintained in a 10µl glass capillary by infusing microliter quantities of media and reagents using novel, miniature pumps and valves. Metabolic wastes are removed and nutrients delivered through microdialysis. Microbore tubing (150 µm i.d.) forms the fluidic interconnects between components and optical monitoring is accomplished using light emitting diodes as excitation sources and photodiodes as detectors. The system is housed in conventionally machined acrylics with dimensions of 3.0 x 8.9 x 0.6 cm^3. On-board electronics support data acquisition, power delivery, microfluidic component driving, and computer interfacing. All microfluidic components and media are on-board. The device uses a single link to a computer and contains media for a few days.

Applications for the device include the testing of potentially stressful stimuli (microgravity, radiations, etc.) for effects on life as well as automated biological assays. Ultimately, we aim to create an array of cultures which contains cells that are selectively responsive to fundamental stressors and to fingerprint an environment by probing bacterial responses via reporter fusions to stress-response pathways.

A Continuous Microculture Device for Monitoring the Effects of Space Environments on Living Systems

R. Martineau, M. Piccini, B. Towe
Harrington Department of Bioengineering
Arizona State University, Tempe, AZ, USA

Abstract

We report our development of a microculture device that continuously cultures genetically engineered bacterial cells and monitors their response to environmental/chemical stimuli. Responses include changes in culture turbidity, pH, production of fluorescent proteins, and bioluminescence.

Cells are maintained in a 10μl glass capillary by infusing microliter quantities of media and reagents using novel, miniature pumps and valves. Metabolic wastes are removed and nutrients delivered through microdialysis. Microbore tubing (150 μm i.d.) forms the fluidic interconnects between components and optical monitoring is accomplished using light emitting diodes as excitation sources and photodiodes as detectors. The system is housed in conventionally machined acrylics with dimensions of 3.0 x 8.9 x 0.6 cm^3. On-board electronics support data acquisition, power delivery, microfluidic component driving, and computer interfacing. All microfluidic components and media are on-board. The device uses a single link to a computer and contains media for a few days.

Applications for the device include the testing of potentially stressful stimuli (microgravity, radiations, etc.) for effects on life as well as automated biological assays. Ultimately, we aim to create an array of cultures which contains cells that are selectively responsive to fundamental stressors and to fingerprint an environment by probing bacterial responses via reporter fusions to stress-response pathways.

Effects of Stress on Living Systems

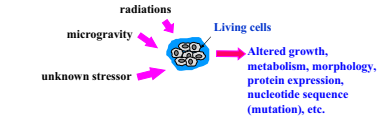

Monitoring Effects of Stress Optically

Responses to stress can be monitored according to multiple paradigms: optical density can indicate cell growth and specific metabolic byproducts, fluorescence probes can be coupled to protein expression to track specific protein systems, and luminescence proteins can be engineered to produce light under a wide variety of circumstances, both inducible and constitutive.

Colorimetric Optical Cells

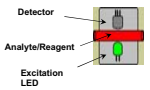

Simple optical cells are effective in performing absorbance-based assays which can monitor carbon dioxide production, pH, and cell numbers. We are currently developing fluorescence cells for detecting protein expression, such as GFP, to monitor the activity of specific protein systems in continuously cultured cells.

Bioluminescence Detection

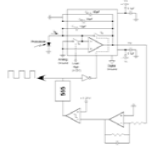

Low-light level detection is achieved using a blue enhanced photodiode in conjunction with a current sensing and integrating circuit illustrated above. The output is a TTL level pulse train whose frequency is proportional to luminescence intensity.

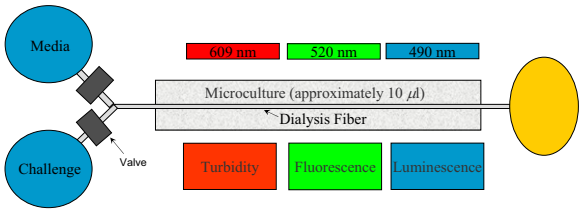

Flow schematic of microculture device. Media and reagents are pumped through the flow path using the passively pressurized membrane pumps (described at right.) Flow is regulated through miniature valves with integrated flow sensing. Media perfuses the cell culture through a dialysis membrane which extracts wastes and delivers nutrients. Optical detection is accomplished by looking through the culture directly or its effluent.

Continuous Monitoring of Bacterial Stress Responses

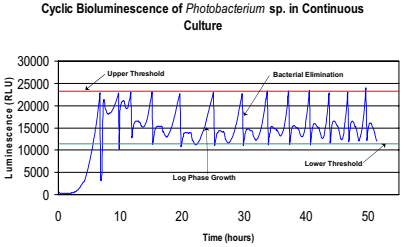

Experimental data showing reproducible cycling of bacterial bioluminescence over a 2 day period. Cycling is accomplished via bacterial elimination through flushing of the microculture with fresh media. Here we created a luminescence saw-tooth in order to continuously culture bacteria in a log phase state. Our assumptions are that period measurements of the waveform will allow for more sensitive and reproducible detection of stressors.

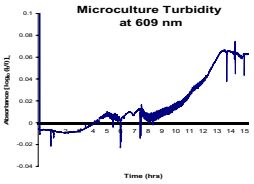

Culture turbidity in the microculture device is monitored using an absorbance cell. *E. coli* cells were periodically infused with fresh media using a pulsatile flow scheme. Approximately 10 μL were infused every 5 minutes. Monitoring cell biomass accumulation serves as an important control and adjunct to other detection techniques.

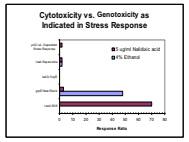

LaRossa and Van Dyk, *Bacterial Stress Responses, Chapter 29*, ASM Press, 2000.

Stress Fingerprints

A potentially powerful approach to the study of hazardous environments is demonstrated in the bar graph shown at left from LaRossa and Van Dyk. Here, the proteins required for bioluminescence induction (right) were coupled to known bacterial stress response gene systems to provide insight into the nature of toxicity. For example, ethanol induces bacterial cells to produce heat shock proteins, whereas Nalidixic acid induces activity in the DNA-repair circuits (recA system).

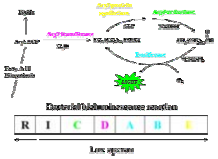

Illustration of the bioluminescence reaction.

Membrane Pumps

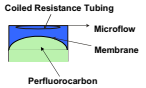

Perfluorocarbon mixtures combine to create a passively pressurized compartment, which pushes against a membrane to dispense culture media and other reagents. The segmented flow rate is controlled by varying the reservoir pressure, the tubing resistance, and the on-time of the valve.

Shape-Memory Alloy Valves with Integrated Flow Sensor

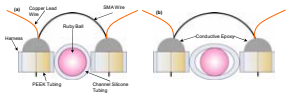

Nitinol™ wires are used to stretch a silicone tube away from a ruby ball plug to allow the passage of fluids. A downstream thermocouple allows for flow sensing. Valve is depicted in the closed (a) and open (b) states.

Single Microculture Device

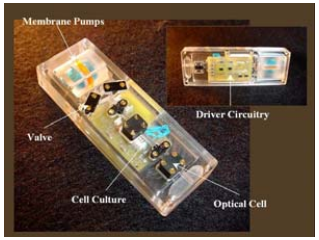

Bioreporter Array

Arrays of the devices, each containing bacteria with various gene fusions, can be used to create a continuous bioreporter system with the potential capability of fingerprinting unknown environments. That is, the response of life on the molecular level can be tracked, resulting in a greater understanding of the nature and mechanism of toxicity.

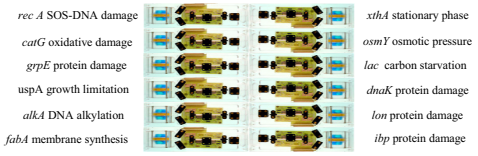

References

[1] Towe, B.C., R.L. Martineau, C.G. Cooney, M.E. Piccini, P. Daydiff, and V. Stout, "A Microfluidic Bioreporter System for Space Flight Monitoring", 25th Annual International Conference of the EMBS, Proceedings, 2003.

[2] C.G. Cooney, B.C. Towe, and C.R. Eyster ,"Optical pH, oxygen, and carbon dioxide monitoring using a microdialysis approach," Sens Act B, vol. 69, pp183-188, 2000.

EFFECT OF VARIED AIR FLOW ON FLAME STRUCTURE OF LAMINAR INVERSE DIFFUSION FLAMES

M.A. Mikofski*
University of California Berkeley, USA
mikofski@me.berkeley.edu

L.G. Blevins, T.C. Williams, and C.R. Shaddix
Sandia National Laboratories, USA

The structure of laminar inverse diffusion flames (IDFs) of methane and ethylene in air was studied using a cylindrical co-flowing burner. Inverse diffusion flames are similar to normal diffusion flames, except that the relative positions of the fuel and oxidizer are reversed. Several flames of the same fuel flow-rate yet various air flow-rates were examined. Flame heights were obtained using visible images and measurements of hydroxyl (OH) laser-induced fluorescence (LIF). Radiation from soot surrounding the IDF was found to mask the reaction zone in visible images. As a result, flame heights determined from visible images were overestimated. The height of the reaction zone as indicated by OH LIF was shown to be a more relevant measure of height. The concentration and position of polycyclic aromatic hydrocarbons (PAHs) and soot were observed using LIF and laser-induced incandescence (LII). PAH LIF and soot LII indicated that PAH and soot are present on the fuel side of the flame, and that soot is located closer to the reaction zone than PAH. Ethylene flames produced significantly higher PAH LIF and soot LII signals than methane flames, which is consistent with the sooting propensity of ethylene.

Photographs of ethylene IDFs, shown in Fig. 1, demonstrate that flame height scales with air flow-rate. Radiating soot almost entirely covers each ethylene flame, and only a small portion of the blue region is visible near the base of each flame. Fig. 2 shows OH and PAH LIF of ethylene IDFs. The upside-down U shape in each panel of Fig. 2 is OH LIF, which indicates the location of the reaction zone. PAHs are present on the outer (fuel) side of the reaction zone. Fig. 3 shows soot LII images for the ethylene IDFs. PAH LIF is vaguely present in the LII images. The soot and PAH are present on the fuel side of the reaction zone, but the soot is closer to the reaction zone than the PAH.

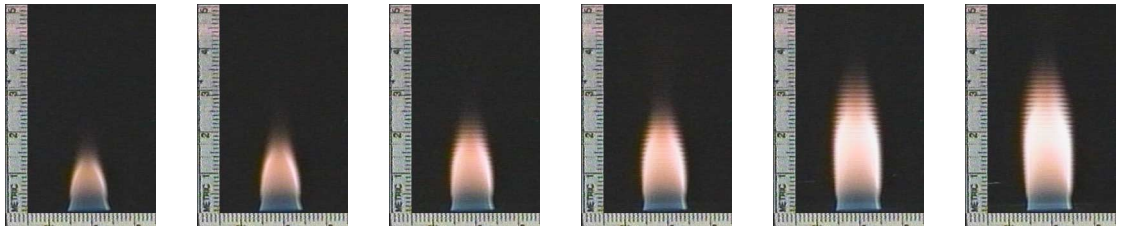

Figure 1. Visible images of ethylene IDFs.

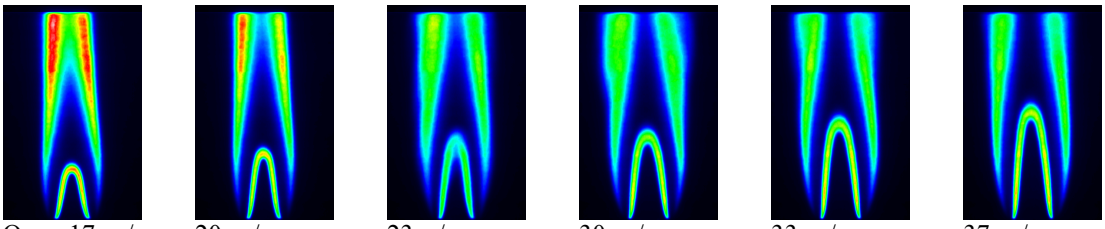

Q_{air} = 17 cc/s 20 cc/s 23cc/s 30 cc/s 33 cc/s 37 cc/s

Figure 2. OH and PAH LIF of ethylene IDFs.

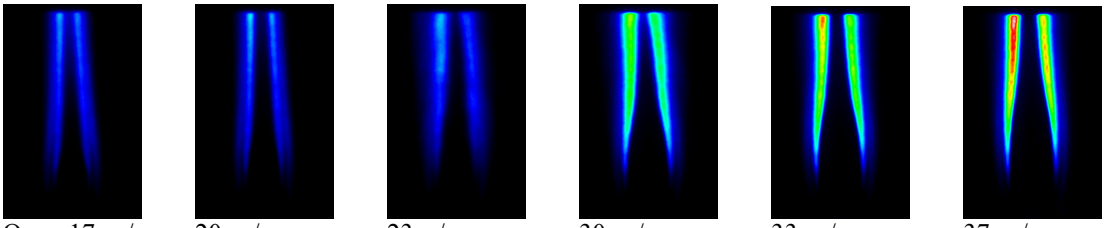

Q_{air} = 17 cc/s 20 cc/s 23cc/s 30 cc/s 33 cc/s 37 cc/s

Figure 3. PAH LIF and soot LII of ethylene IDFs.

LIGHT SCATTERING AND DIRECT VISUALIZATION STUDIES OF ANISOMETRIC COLLOIDAL AGGREGATES AND GELS

Ali Mohraz and Michael J. Solomon
Department of Chemical Engineering, University of Michigan, Ann Arbor, MI 48109-2136
(mjsolo@umich.edu)

ABSTRACT

Suspensions of anisometric colloids find widespread technological applications in areas such as the manufacturing of ceramics and the production of polymer/clay nanocomposites. Although often the functional properties of the final products rely on the anisometric shape of the colloids, the fundamental role of this parameter in mediating the microstructure and rheology of aggregated structures such as colloidal gels is poorly understood. To experimentally assess the effect of particle geometry on the morphology of such amorphous structures, colloidal boehmite rods of approximately monodisperse dimensions and aspect ratios in the range 5-30 have been synthesized. Aggregation is induced by the addition of electrolytes to aqueous suspensions and the structure of fractal aggregates in both the DLCA and RLCA regimes is characterized over three decades of the scattering vector by combined ultra-small, small, and wide-angle light scattering. The microstructure of rod aggregates in the DLCA regime shows an unexpected dependence on the geometry of primary particles [1], in contrast with the universal behavior of colloidal spheres. Monte Carlo simulations of rod aggregation corroborate this finding and the underlying mechanism for this unforeseen deviation is understood in light of the interaction of Brownian motion and anisotropic excluded volume of primary particles [1]. Furthermore, as the rod aspect ratio is increased, the structural distinction between the DLCA and RLCA aggregates is diminished. The implication of these structural anomalies in the internal dynamics of fractal networks is investigated by photon correlation spectroscopy.

Direct visualization of three-dimensional structure by confocal laser scanning microscopy (CLSM) provides a powerful means for investigating the effect of particle shape and orientation of the structure and dynamics of colloidal suspensions. Stable suspensions of fluorescent colloidal spherocylinders and ellipsoids in organic solvents have been prepared by the adaptation of literature methods. The sterically-stabilized polymeric colloids have been dispersed in density and refractive-index matching mixed organic solvents suitable for CLSM studies. Image processing algorithms for location of the centroid position and orientation angle of individual particles have been developed. By means of these methods, we investigate the distribution of rod orientations in suspensions and gels.

[1] Mohraz, A. D.B. Moler, R.F. Ziff and M.J. Solomon, "Effect of monomer geometry on the fractal structure of colloidal rod aggregates," *Physical Review Letters* **92**(15) 155503 1-4 (2004).

CHARACTERIZING MECHANICAL PROPERTIES OF SIMULANT SOILS USING WAVE VELOCITY TECHNIQUE

Masami Nakagawa
Colorado School of Mines

We will present two in-house projects which will have direct relevance to in-situ space resources utilization. One of the aims of the first project is to measure mechanical properties of packed particles of different sizes and materials by measuring the wave velocity using piezoelectric sensors. Our results include preliminary measurements under microgravity environment using the NASA GRC drop tower facility. The second project is the feasibility study of mechanical properties of small scale assemblies of wet/cohesive granular materials by using micromanipulators. One of the driving questions for the second project is how to define mechanical properties of an assembly containing only a small number of particles but still behave as a collective solid. We can test the validity of extending our results of mesoscopic systems to predictions about macroscopic behavior, and so provide an alternative to bulk testing of precious extraterrestrial samples.

DIRECT NUMERICAL SIMULATION OF GAS-LIQUID SYSTEMS IN VARIABLE GRAVITY ENVIRONMENTS

Jean-Christophe Nave, Sanjoy Banerjee
Dept. of Mechanical Engineering, University of California, Santa Barbara, CA, USA, 93106
banerjee@engineering.ucsb.edu, phone: (805) 893-3456, fax: (805) 893-4731

Liquid films are present in many processes that occur in space applications. It is important to understand interfacial behavior as gravity becomes less important because, depending on the flow regime, interface motion may change dramatically. For instance, we observe enhancement of waves in film flow, when gravity decreases. An understanding of the influence of gravity as a controlling mechanism related to interface structure is important for both fundamental and design purposes. For instance, large topology changes of the gas liquid interface are responsible for enhancement of transfer processes. The types of problems studied here are of interest for condensers and evaporator performance in microgravity.

The numerical simulations presented here show different regimes in both gravity and micro-gravity environments where deformation of the gas/liquid interface is important. We use a finite difference method on a staggered grid, and the projection method to solve the Navier-Stokes equations. In order to deal with large density ratios, we use a ghost fluid method [1], This method allows for a sharp treatment of the interface and also, for first order accurate treatment of surface tension forces. Time integration is performed using a 3rd order Runge-Kutta TVD scheme. The numerical challenges associated with the problem of simulating gas/liquid systems are numerous. The aspect ratio of the waves demands that the physical domain be long, forcing us to use very fine nodalization. Also, the high density ratio between the gas phase and the liquid phase leads to poor convergence of the equations. We have developed a solution technique for the Poisson pressure equation that is quite efficient in this situation. We use a BiConjugate Gradient Stabilized method along with a Incomplete Lower/Upper preconditioner. Using periodic boundary conditions, we present two cases of a horizontal liquid film being driven by a pressure gradient, one with wall normal gravity, the other one with zero gravity.

The different simulations are performed in three-dimension and the interface is implicitly tracked using a level set method. Figure 1 shows interfacial waves on falling films at low Reynolds numbers (Re) that agree with experiments, providing validation of the methods. In order to illustrate the behavior of the physical system under different gravity conditions, some results, in which a high Re film on a shallow inclined plane (~0.25 degree) driven by gravity (Figure 2), are first shown. The interface stays quite flat while bulk vortices due to turbulence generated by wall shear, disrupt it. The effect of gravity in stabilizing the interface is apparent by comparison with Figure 3. Note that waves are steeper when the wall normal component of gravity is set to zero, as it is in this Figure.

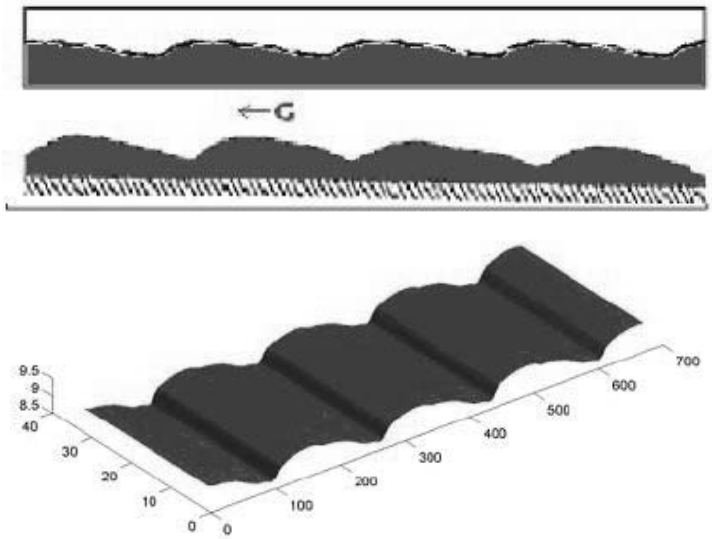

Figure 1: Comparison of simulation (top) and experiment (middle), and 3D view (Bottom)
Flow rate= 0.19 cm2/s, Wave Length= 0.85 cm, Wave velocity= 18.78 cm/s (Simulation)
Flow rate= 0.201 cm2/s, Wave Length= 0.8 cm, Wave velocity= 21.7 cm/s (Experiment)

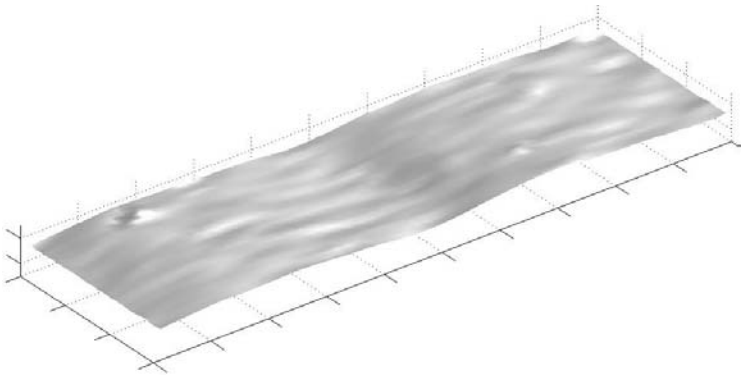

Figure 2: Interface deformations (bumps) from impinging coherent structures (looking at an angle from the top) at Re=1060.

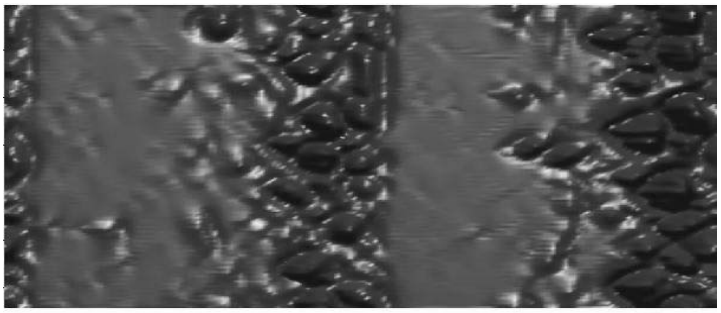

Figure 3: Interface deformation in absence of wall normal gravity at Re=1060 (looking down). Note 3D interfacial wave structure.

References

[1] Fedkiw, R. and Liu, X.-D.(1998), The Ghost Fluid Method for Viscous Flows, *Progress in Numerical Solutions of Partial Differential Equations*, Arachon, France, edited by M. Hafez

[2] P.L. Kapitza, 1945, "Experimental Study of Ondulatory Flow Conditions", D.Ter Haar, ed., Collected Papers of P.L. Kapitza, (Pergamon, Oxford, 1965).

A New Test Method For Material Flammability Assessment in Microgravity & Extraterrestrial Environments

S.L. Olson*, H. D. Beeson[+], J.P. Haas[+], and J.S. Baas[+]

*NASA Glenn Research Center, Cleveland, OH 44135
[+] NASA White Sands Test Facility, Las Cruces, NM

The standard oxygen consumption (cone) calorimeter (described in ASTM E 1354 and NASA STD 6001 Test 2) is modified to provide a bench-scale test environment that simulates the low velocity buoyant or ventilation flow generated by or around a burning surface in a spacecraft or extraterrestrial gravity level. The Equivalent Low Stretch Apparatus (ELSA) uses an inverted cone geometry with the sample burning in a ceiling fire (stagnation flow) configuration.

For a fixed radiant flux, ignition delay times for characterization material PMMA are shown to decrease by a factor of three at low stretch, demonstrating that ignition delay times determined from normal cone tests significantly underestimate the risk in microgravity.

The critical heat flux for ignition is found to be lowered at low stretch as the convective cooling is reduced. At the limit of no stretch, any heat flux that exceeds the surface radiative loss at the surface ignition temperature is sufficient for ignition.

Regression rates for PMMA increase with heat flux and stretch rate, but regression rates are much more sensitive to heat flux at the low stretch rates, where a modest increase in heat flux of 25 kW/m^2 increases the burning rates by an order of magnitude.

The global equivalence ratio of these flames is very fuel rich, and the quantity of CO produced in this configuration is significantly higher than standard cone tests.

These results [2] demonstrate the ELSA apparatus allows us to conduct normal gravity experiments that accurately and quantifiably evaluate a material's flammability characteristics in the real-use environment of spacecraft or extra-terrestrial gravitational acceleration. These results also demonstrate that current NASA STD 6001 Test 2 (standard cone) is not conservative since it evaluates materials flammability with a much higher inherent buoyant convective flow.

A Better Test Method is Needed

NASA's current method of material screening determines fire resistance under conditions representing a worst-case for normal gravity flammability - the Upward Flame Propagation Test (Test 1[1]). The applicability of Test 1 to fires in microgravity and extraterrestrial environments, however, is uncertain because the relationship between this buoyancy-dominated test and actual extraterrestrial fire hazards is not understood.

Unlike Test 1, the NASA STD 6001 Test 2 [1] standard oxygen consumption (cone) calorimeter (also described in ASTM E 1354) provides quantitative data on ignition delay times and burning rates of materials. However, it currently lacks any pass-fail criteria. In addition, it too is buoyancy-dominated.

The objective of this research is to modify the well-instrumented standard cone configuration to provide a reproducible bench-scale test environment that simulates the buoyant or ventilation flow that would be generated by or around a burning surface in a spacecraft or

extraterrestrial gravity level. We will then develop a standard test method with pass-fail criteria for future use in spacecraft materials flammability screening. (For example, dripping of molten material will be an automatic fail.)

Scaling Arguments

The ELSA concept is based upon scaling analysis that demonstrates buoyant stretch and forced stretch can be equated. This means that through scaling we can burn materials over a wide range of gravity levels.

Equivalent stretch rates can be determined as a function of gravity, imposed flow, and geometry. For purely buoyant stagnation flow, the equivalent stretch rate is $a_b = [(\rho_e-\rho^*)/\rho_e][g/R]^{1/2}$ [6,7], where the density difference from the average flame temperature to ambient is used, g is gravity, and R is the radius of curvature of the sample. For purely forced flow, the equivalent stretch rate is characterized by either $a_f = 2\tilde{U_\infty}R$ for a cylinder[6], or $a_f = U_{jet}/d_{jet}$ for a jet impinging on a planar surface[9]. U_∞ is the velocity of the ambient stream or the jet, R is the radius of curvature of the cylinder, and d_{jet} is the diameter of the jet. A generalized expression for stretch rate which captures mixed convection includes both buoyant and forced stretch is defined[6] as $a_{equivalent} = a_f(1+ a_b^2/a_f^2)^{1/2}$. The inherent buoyant stretch for the current ELSA holder is ~4 s^{-1} based on a correlation of regression rates for cylinders and flat disks. This correlation also allows us to determine that the normal cone buoyant stretch rate is 33 s^{-1}] by extrapolating the correlation to the 'ideal' burning rate (heat flux from flame to surface only) for clear PMMA from [11].

The stretch rate is simply the velocity gradient as the flow decelerates toward the fuel surface. The velocity gradient for flame spread problems has been shown to be the important flow parameter [Wichman, 1983], and the flame is spreading deep within the boundary layer where the velocity gradient is almost constant. For forced flow velocities of up to 20 cm/s (spacecraft ventilation), the velocity gradient (stretch rate) is of the same order for small fires. Thus a test method which varies the velocity gradient (stretch rate) will capture the essential flammability behavior of flame spread as well as stagnation point fires.

To demonstrate this scaling with experimental results, the ignition delay results of FIST [4] at different flow rates, including natural convection, are added to the ignition delay –stretch plot by estimating the Blasius boundary layer velocity gradient at the surface for the free stream flow based on their experiment geometry. The correlation holds up very well over a wide range of velocity gradient in cm/s per cm (flame stretch rate, s^{-1}). While the normal cone flow field is not well characterized, the flame is stabilized near a surface with a cross flow (entrained air), and velocity gradients in a laminar boundary layer near the surface are constant. For a 5 cm surface (1/2 sample) with an average velocity gradient near the surface of 33 s^{-1}, the average entrained cross flow would be ~20 cm/s, which is reasonable.

References

1)D. Mulville, *Flammability, Odor, Offgassing, and Compatibility Requirements and Test Procedures for Materials in Environments that Support Combustion*, NASA-STD-6001, (1998).

2) Olson, S.L., Beeson, H.D., Haas, J.P., and Baas, J.S.; *An Earth-Based Equivalent Low Stretch Apparatus For Material Flammability Assessment in Microgravity & Extraterrestrial Environments*, Proceedings of the Combustion Institute, 30, to appear, (2004).

[3] Wichman, I.S., "*Flame Spread in an Opposed Flow with a Linear Velocity Gradient,*"Combustion and Flame**,** 50, 28 (1983).

[4] Roslon, Olenick, Walther, Torero, Ross, and Fernandez-Pello, *"Microgravity Ignition Delay of Solid Fuels in Low Velocity Flows"*, AIAA J., V. 39, No. 12, 2336-2342, (2001).

Developing a Test Method for Material Flammability Assessment in Microgravity & Extraterrestrial Environments
(Earth, Lunar, Martian, Microgravity, and anywhere between)

S.L. Olson,
NASA Glenn Research Center, Cleveland, OH 44135
H. D. Beeson, J.P. Haas, and J.S. Baas
NASA White Sands Test Facility, Las Cruces, NM

Objectives: **To develop a 1g standardized test method that captures the reduced gravity ignition and burning behavior of a material through application of scaling laws. This program fulfills a very real need for an accurate and efficient materials screening test for future materials to be used in our exploration vehicles and habitats.**

Equivalent Low Stretch Apparatus:

The standard oxygen consumption (cone) calorimeter (described in ASTM E 1354 and NASA STD 6001 Test 2)[1] is modified to burn in a ceiling fire configuration to provide a low velocity buoyant or ventilation flow generated by or around a burning surface. This low velocity flow is of the same order as that found in a spacecraft or extraterrestrial gravity level. The **Equivalent Low Stretch Apparatus (ELSA)** uses an inverted cone geometry with the sample burning in a ceiling fire (stagnation flow) configuration, as shown in Figure 1. The 'stretch' is the flow deceleration rate as it impinges on the fuel. So stretch is really a velocity gradient, with units of cm/s per second, or s^{-1}.

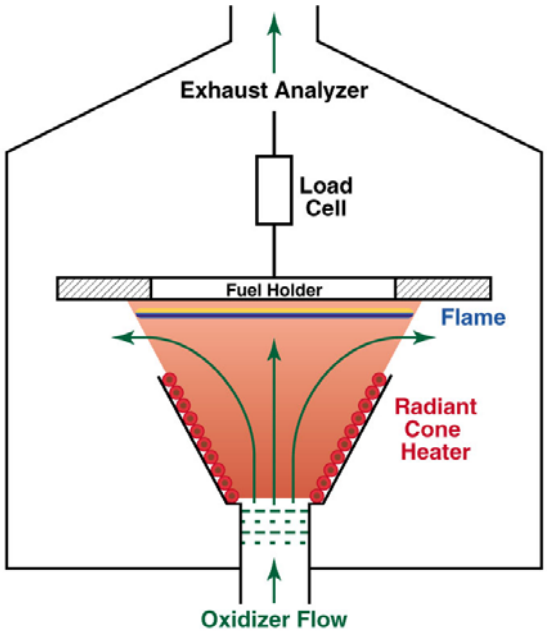

Figure 1: Concept of ELSA apparatus, showing fuel sample suspended above radiant cone heater and oxidizer flow jet. The enclosure reflects the WSTF Controlled Atmosphere Cone Calorimeter facility[1].

Summary:

We have successfully demonstrated [2] that ELSA accurately and quantifiably evaluates a materials flammability characteristics (ignition delay time, burning rate, critical heat flux for ignition, heat release rate, CO production rate, etc) over a range of flows representative of reduced gravity flow environments, including Lunar, Martian, and microgravity. The irradiated cone heat flux levels were tested over the range of expected radiant exchange of burning adjacent materials.

These results also demonstrate that current NASA STD 6001 Test 2 (standard cone) is not conservative since it evaluates materials flammability with a much higher inherent buoyant convective flow. Test 2 overestimates ignition delay times (~3x) and underestimates CO concentrations (~10x) generated by reduced gravity fires. The critical heat flux for ignition is reduced at low stretch (~4x).

Results:

Ignition delay time, defined as the time between when the sample is exposed to the radiant heater and sustained ignition, was measured as a function of forced and buoyant flow at 10 kW/m^2 and 25 kW/m^2 flux levels, as shown in Figure 2.

For a fixed radiant flux, ignition delay times are shown to decrease with decreasing equivalent velocity gradient, or g level. The difference between a normal (1g) cone ignition delay time (high equivalent velocity gradient ~ 33s^{-1}) and ignition delay times at very low equivalent velocity gradients is a factor of three, demonstrating that ignition delay times determined from normal cone tests significantly ***overestimate*** the ignition delay times of materials in microgravity or in partial gravity extraterrestrial environments. In addition, at the 10 kW/m^2 flux level, the ignition delay time at low g levels approaches the value of the 1g normal cone at 25 kW/m^2, indicating the sensitivity of low g flames to even weak levels of external flux.

The critical heat flux for ignition is an important fire safety measurement for materials evaluation. At low gravity, radiation from a small adjacent burning material may be sufficient to ignite a material. This was observed on Mir [3] in their Skorost facility, where a burning molten ball of fuel at the end of a rod of one material heated an adjacent rod to vaporization temperatures (bending, bubbling). The flame from the first rod then acted as the gas-phase pilot for the premixed cloud developed between the two rods. The premixed flame propagated through the cloud and ignited the heated second rod.

For the ELSA apparatus, we can estimate the critical net heat flux by extrapolating ignition delay time data at different heat flux to the zero stretch (no flow) limit. The ignition delay time for a semi-infinite solid is related to the heat flux and surface ignition temperature[4] by an inverse square root relationship.

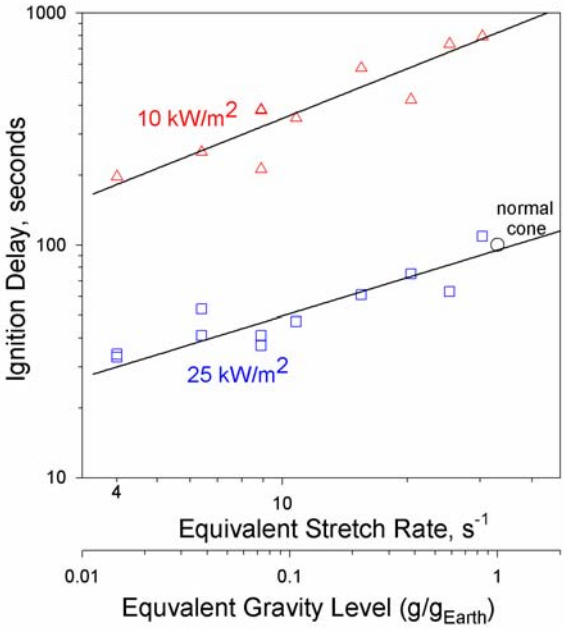

Figure 2: Ignition delay time plotted as a function of equivalent velocity gradient or equivalent gravity level. Normal cone data (1g) [4] is included for 25 kW/m^2.

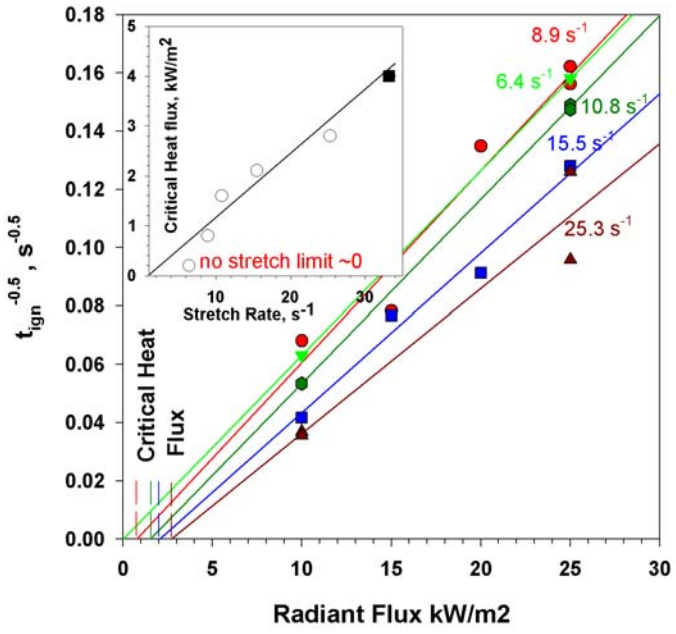

Figure 3: Heat Flux derived from extrapolation of $t_{ign}^{-0.5}$ =0. The critical net heat flux at the limit of no flow is effectively zero. Inset data: circles are this work, square datapoint [4].

As shown in Figure 3, an inverse square root dependence on heat flux and ignition delay time is found in ELSA tests all stretch rates tested. The critical heat flux for ignition is where the linear fit to the data crosses the x axis (infinite ignition delay time). The inset plots the critical net heat flux values found for each stretch rate, and a roughly linear dependence is found. The zero flow heat flux is so low that **for all practical purposes, any heat flux that just slightly more than offsets the experimental heat losses such as surface radiation is sufficient to ignite the material. This agrees with the model of Rhodes and Quintiere [4] in the limit of no convection.**

As shown in Figure 4, regression rates for PMMA increase with heat flux and stretch rate, but regression rates are much more sensitive to heat flux at the low stretch rates, where a modest increase in heat flux of 25 kW/m^2 increases the burning rates by an order of magnitude.

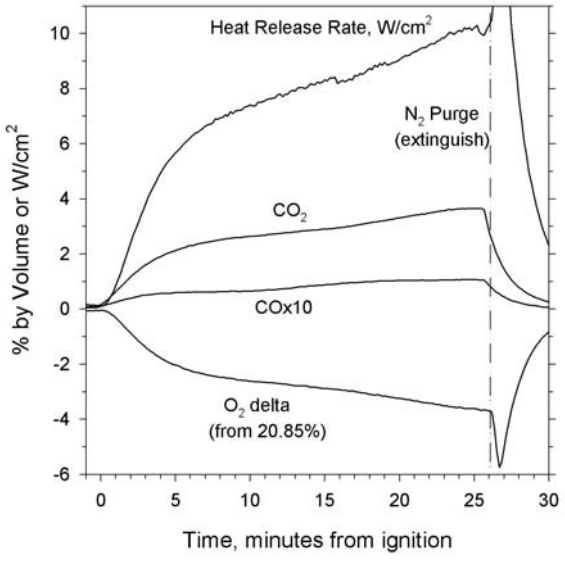

Figure 5: Oxygen consumption, CO, CO2, and Heat Release Rate from WSTF-ELSA test [2].

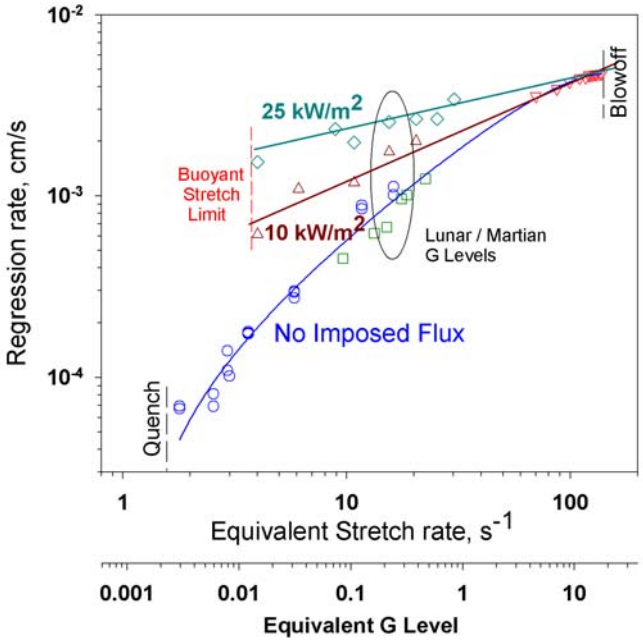

Figure 4: PMMA regression rates for three levels of imposed heat flux from radiant cone heater, plotted as a function of equivalent stretch rate or velocity gradient. Data: ◊Δ this work, ○[6], ▽[7], □[8]. Using scaling, the equivalent gravity shows that Lunar and Martian G levels fall in the mid-range of flammability.

The quantity of CO produced in these low stretch flames is nearly a factor of ten time higher than standard cone tests. As shown in Figure 5, the heat release rises to 10 W/cm^2, or 100 kW/m^2. CO and CO_2 concentrations rise as well, with CO reaching a maximum of 0.1% (1000 ppm) by the end of the test. The CO concentrations in this configuration of 1000 ppm are nearly a factor of ten higher than standard cone tests (25kW/m^2, 24 liters/sec), which have CO concentrations from 0.012-0.015 % [5]. Exposure to 1000 ppm of CO for longer than 30 minutes causes nausea, mental confusion, headache, staggering, and heart palpitations.

Scaling Arguments:

The ELSA concept is based upon scaling analysis that demonstrates buoyant stretch and forced stretch can be equated. This means that through scaling we can assess how materials will burn over a wide range of gravity levels.

The stretch rate is simply the velocity gradient as the flow decelerates toward the fuel surface. The velocity gradient for flame spread problems has been shown to be the important flow parameter[9], and the flame is spreading deep within the boundary layer where the velocity gradient is almost constant (Fig. 6). For forced flow velocities of up to 20 cm/s (spacecraft ventilation), the velocity gradient (stretch rate) is of the same order for small fires, as shown in the inset to Fig. 6. Thus a test method which varies the velocity gradient (stretch rate) will capture the essential flammability behavior of flame spread as well as stagnation point fires.

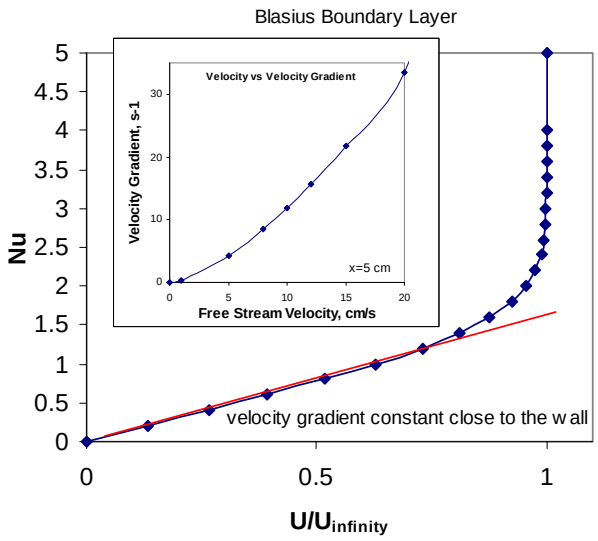

Figure 6: Linear Velocity profile in boundary layer showing constant velocity gradient ('stretch') within boundary layer. At low free stream velocities, the gradient is of the same order. as shown in the inset.

To demonstrate this scaling with experimental results, the ignition delay results of FIST[10] at different flow rates, including natural convection, are added to the ignition delay –stretch plot in Figure 7 by estimating the Blasius boundary layer velocity gradient at the surface for the free stream flow based on their experiment geometry. The correlation holds up very well over a wide range of velocity gradient in cm/s per cm (flame stretch rate, s^{-1}).

While the normal cone flow field is not well characterized, the flame is stabilized near a surface with a cross flow (entrained air), and velocity gradients in a laminar boundary layer near the surface are constant. For a 5 cm surface (1/2 sample) with an average velocity gradient near the surface of 33 s^{-1}, the average entrained cross flow would be ~20 cm/s, which is reasonable.

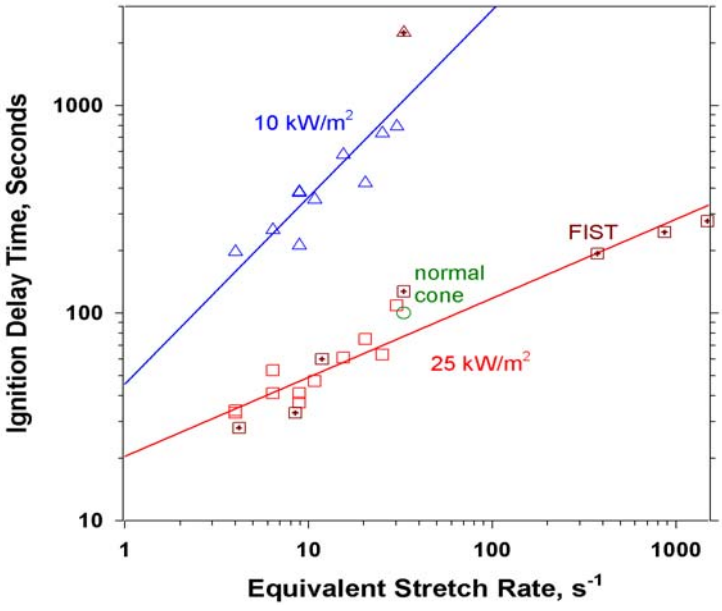

Figure 7: Using boundary layer velocity gradient scaling, FIST [10] KC-135 and 1g ignition delay time data is plotted with ELSA data, and shows good agreement in the trends.

Theoretical predictions of stagnation flames in mixed convective environments by Foutch and T'ien (1987)[11] indicate that it should be possible to understand a material's burning characteristics in the low stretch environment of spacecraft (non-buoyant, but with some movement induced by fans and crew disturbances) by understanding its burning characteristics in an equivalent Earth-based stretch environment (induced by normal gravity buoyancy and/or forced convection). Experimental results with a buoyant low stretch flame [6] demonstrated the transition from a robust flame at stretch rates of 10-20 s^{-1} to a quenched flame at very low stretch (1-2 s^{-1}) in air.

Equivalent stretch rates can be determined as a function of gravity, imposed flow, and geometry. For purely buoyant flow, the equivalent stretch rate is $a_b = [(\rho_e - \rho^*)/\rho_e]\,[g/R]^{1/2}$ [6,11], where the density difference from the average flame temperature to ambient is used, g is gravity, and R is the radius of curvature of the sample. For purely forced flow, the equivalent stretch rate is characterized by either $a_f = 2U_\infty/R$ for a cylinder[11], or $a_f = U_{jet}/d_{jet}$ for a jet impinging on a planar surface[7]. U_∞ is the velocity of the ambient stream or the jet, R is the radius of curvature of the cylinder, and d_{jet} is the diameter of the jet. A generalized expression for stretch rate which captures mixed convection includes both buoyant and forced stretch is defined[11] as $a_{equivalent} = a_f(1+ a_b^2/a_f^2)^{1/2}$. The system has been designed so that the nozzle diameter, sample size, and distance between the two are all of the same order, so that the stretch rate does not vary significantly across the sample.

The contributions of the buoyant stretch on the equivalent stretch rate were evaluated by correlating regression rate data for flat disks of various radii [12] and cylindrical samples with reported stretch rates [6] . The correlation, shown in Figure 8, allows us to determine the inherent buoyant stretch for ELSA to be ~4 s^{-1} by matching the regression rates for cylinders and flat disks. Note that this correlation worked even through the range of radii where Rayleigh-Taylor instabilities were found at larger radii (>8cm)[12]. On the Moon (0.16g) or Mars (0.38g), the *same size* samples would burn with buoyant stretch rates of ~1.4 $^{s-1}$ and 2.2 $^{s-1}$ respectively in the ELSA test configuration.

This correlation also allows us to determine that the normal cone buoyant stretch rate is 33 s^{-1} by extrapolating the correlation fit in Fig. 8 to the 'ideal' burning rate (heat flux from flame to surface only) for clear PMMA from [13].

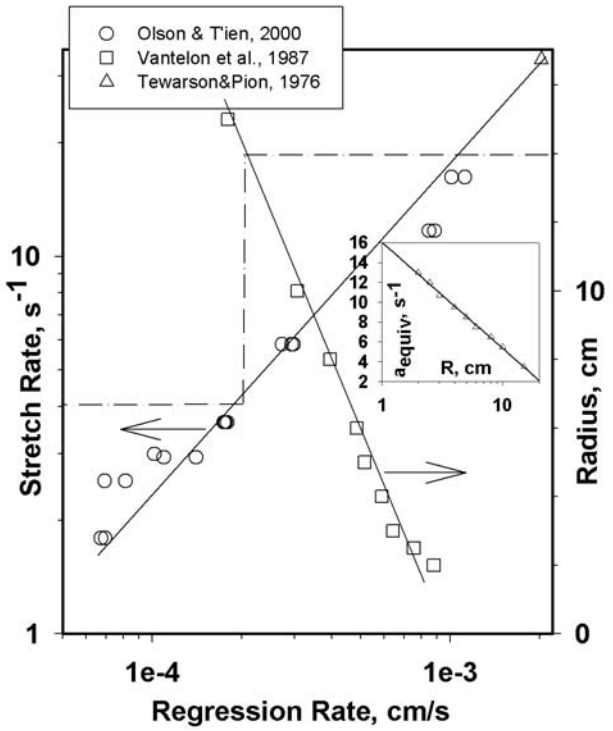

Figure 8: Correlation of flat disk radius with equivalent buoyant stretch [6, 12]. Regression rates for cylinders and flat disks were correlated, and the equivalent stretch rate for the 14 cm radius ELSA holder was determined from the linear relation found between radius of the disk and equivalent stretch rate. Equivalent stretch for normal cone geometry[13] was determined for 'ideal' burning conditions with flame heat flux only.

A New Test Method is Needed:

NASA's current method of material screening determines fire resistance under conditions representing a worst-case for normal gravity flammability - the Upward Flame Propagation Test (Test 1[1]). However, Test 1 does not provide any quantitative indication of the margin of safety of a material. Unlike Test 1, the NASA STD 6001 Test 2 [1] standard oxygen consumption (cone) calorimeter (also described in ASTM E 1354) provides *quantitative* data on ignition delay times and burning rates of materials, but it currently lacks any pass-fail criteria. In addition, it too is buoyancy-dominated. **ELSA retains the quantitative data of Test 2, but adds flow control to the test.**

Materials Screening Tests

Measurement	Test 1	ELSA	FIST/LIFT	LOI	Measurement Utility
Ignition delay time (video)		X	X		A measure of resistance to ignition under test conditions. Provides information on how long detectors have to detect degradation and how long crew has to respond before material will ignite.
Spread Rate (video)			X		How fast fire will grow. Provides information on how rapidly the situation will deteriorate. Important for detection time and crew response time.
Burning Rate (load cell)		X			Mass burning rate, how much fuel actually burns. A different, complementary measure of how fast a fire will grow and how rapidly the situation will deteriorate. Important for detection time and crew response time.
Limiting oxygen concentration (fundamental)	Upward LOI < test atm	X	X	downward	Atmosphere needed to extinguish fire. Important to know to evaluate extinguisher efficacy on fire.
Limiting Flow imposed or buoyant	Buoyant con-current	X	X (FIST)/ buoyant flow horizontal spread (LIFT)	Buoyant opposed	Provides information on flow environments to avoid (fundmental LOI flow environment) and minimum flow for 'quiescent' extinction (is it practical?).
Toxic products (gas sensors)		X			Species concentrations per unit of fuel or oxidizer burned. Provides information on how toxic the atmosphere is to the crew, and how much of what chemicals need to be scrubbed post-fire.
Heat Release Rate via Oxygen Consumption		X			1g standard fire measurement. Provides a measure of how much energy the fire is producing (growth rate) as well as a measure of how much oxygen is being consumed. Excessive oxygen consumption will result in non-viable atmosphere for crew.
Global Equivalence Ratio		X			Overall stoichiometry of fire, based on burning rate and oxygen consumption rate. Provides a measure of how much flammable vapor is being produced that may result in premixed gaseous flame propagation leading to flashover.
Critical Heat Flux for Ignition		X	X		A measure of material resistance to radiative ignition/flashover. Derived from ignition delay time data.

X = currently measured in test

ELSA Test Variables and Measurements:

The *primary variables* include

- stretch rate,
- radiant flux level,
- oxygen concentration (higher than air for exploration),
- fuels (PMMA, practical)

Additional variables to be considered as well are total pressure (low pressure for exploration), diluents (extinguishment tests), and piggyback fire safety systems such as exhaust combustion product detectors, retardants, and others.

Measurements to be recorded for each test include

- ignition delay time (video),
- mass loss rate (load cell),
- heat release rate (O2 consumption), and
- combustion product generation rates (CO, CO_2, THC, soot) for toxicity assessment.

Performance-based Pass/Fail Criteria for Materials Tested in ELSA

Ignition delay time criteria: the ignition delay time is at least TBD minutes under TBD end-use environmental conditions (O2, heat flux, flow, g), so that detectors have time to detect incipient fire and crew has time to respond to the situation so that no ignition or fire spread occurs and also long enough so for crew action to egress and evacuate the atmosphere is possible before excessive fire spread/flashover occurs. [CEV, Moon, Mars environments]

Critical heat flux criteria: critical heat flux for ignition is sufficiently TBD high that material does not ignite when exposed to burning adjacent materials [=f(surface temperatures, view factor)].

Burning rate, , oxygen consumption, or heat release rate criteria: burning rate/spread rate/oxygen consumption/heat release rate is sufficiently low under TBDend-use environmental conditions (O2, heat flux, flow, g), so that the crew has time take action (use suppressant) before contaminating the atmosphere beyond the point of viable life support or generating enough flammable vapor to cause a premixed gas flame leading to flashover (global equivalence ratio).

Toxic products criteria: Pyrolysis products toxicity and production rates are sufficiently low – (TBD based on module volume and production rate) that the crew has time to take action (deactivate system, use suppressant, turn on air cleaning) prior to being negatively influenced by the products.

ELSA Deliverables / Products:

1) A practical and scientifically rigorous materials screening test method at TRL level 9 (fully demonstrated and operational) for use in materials screening for future exploration vehicles and extraterrestrial habitats.
2) A peer-reviewed archive of scientific papers to rigorously demonstrate the validity of the test method. [6,14,2].
3) A flight system verification test to demonstrate the validity of the scaling arguments that form the basis of this test method. (TRL level 8 test).

References

1)D. Mulville, *Flammability, Odor, Offgassing, and Compatibility Requirements and Test Procedures for Materials in Environments that Support Combustion*, NASA-STD-6001, 1998.

2) Olson, S.L., Beeson, H.D., Haas, J.P., and Baas, J.S.; "An Earth-Based Equivalent Low Stretch Apparatus for Material Flammability Assessment in Microgravity and Extraterrestrial Environments", *Proceedings of the Combustion Institute*, V. 30, July, 2004, to appear.

3) A.V. Ivanov, et. al, NASA Contract NAS3-97160 final report, Russian Space Agency, Keldysh Research Center, Moscow 1999, also NASA CP-1999-208917, pp. 47-50.

4) B.T. Rhodes, and J.G. Quintiere, *Fire Safety Journal* 26, (1996) 221-240.

5) F.-Y. Hsheih, S.E. Motto, D.B. Hirsch, and H.D. Beeson, *Proceedings of the International Conference on Fire Safety* 18, (1993), 299-325.

6) S.L.Olson, and J.S. T'ien, *Combustion and Flame*, 121, (2000) 439-452.

7) J.S. T'ien,, S.N. Singhal. D.P. Harrold and J.M.Prahl.; *Combustion and Flame* 33,(1978) 55-68.

8) H. Ohtani, K. Akita, and T. Hirano, *Combust. Flame* 53, (1983) 33-40.

9) Wichman, I.S., "Flame Spread in an Opposed Flow with a Linear Velocity Gradient", *Combustion and Flame*, V.50, 28 (1983).

10) Roslon, Olenick, Walther, Torero, Ross, and Fernandez-Pello, *"Microgravity Ignition Delay of Solid Fuels in Low Velocity Flows"*, AIAA J., V. 39, No. 12, 2336-2342, (2001).

11) D.W. Foutch,, and J.S. T'ien, *AIAA Journal* 25, No. 7, (1987) 972-976.

12) J.P. Vantelon., A. Himdi, and F. Gaboraiud, ; *Combust. Sci. and Tech*., 54, (1987) 145-158.

13) Tewarson, A., and Pion, R.F.; *Combust. Flame* 26, (1976) 85-103.

14) S.L. Olson, and J.S.T'ien, *Fire and Materials*, 23, (2000) 227-237.

Most Probable Fire Scenarios in Spacecraft and Extraterrestrial Habitats - Why NASA's Current Test 1 Might Not Always Be Conservative

S.L. Olson, NASA Glenn Research Center

NASA's current method of material screening determines fire resistance under conditions representing a worst-case for normal gravity flammability - the Upward Flame Propagation Test (Test 1[1]). Its simple pass-fail criteria eliminates materials that burn for more than 12 inches from a standardized ignition source. In addition, if a material drips burning pieces that ignite a flammable fabric below, it fails.

The applicability of Test 1 to fires in microgravity and extraterrestrial environments, however, is uncertain because the relationship between this buoyancy-dominated test and actual extraterrestrial fire hazards is not understood. There is compelling evidence that the Test 1 may not be the worst case for spacecraft fires, and we don't have enough information to assess if it is adequate at Lunar or Martian gravity levels.

Microgravity Flames do Strange Things

Flames in microgravity are known to preferentially spread upwind (ie opposed flow) [2], not downwind (i.e. concurrent flow) as in the normal gravity upward flammability screening Test 1. Over most of the range of air ventilation rates (5-20 cm/s) comparable to spacecraft ventilation, upstream flame spread was the only viable flame. Only when the flow becomes strong enough (estimated to be $\geq$ 10 cm/s), will at least a partial downstream flame become viable. Numerical and experimental results [7] predict an upstream flame only at 5.0 cm/s, an upstream flame and two localized edge flames propagating downstream at 10.0 cm/s, and both an upstream and downstream flame at 20.0 cm/s.

This propensity to spread upwind does not only occur for thin materials, but also occurs for thicker materials and other shapes. For example, experiments were conducted aboard the Mir space station using plastic cylinders. The intent was to burn them with a concurrent flame spread similar to that of Test 1. However, rather than spread along the rod, the flame stabilized at the front tip of the rod and burned like a candle flame at the end of a fat wick [3,4],

Under the right flow conditions in space, things will burn that won't burn on Earth. This is most clearly demonstrated by a flammability map [5,6]. In the opposed flow flame spread flammability map for a cellulose fuel, the LOI, or limiting oxygen index on Earth in opposed flow is 16.5% O_2. However, if the flow is on the order of spacecraft ventilation (5-20 cm/s), flames can be sustained even at 14 % O_2. Thus a normal gravity measure of flammability does not guarantee that the material won't burn in space.

Some preliminary work on independent opposed and concurrent flame spread was conducted in a glovebox experiment [8]. The flame spread results in the cabin air (~21% O2) show that the quenching region spans from +0.5 to -2 cm/s, so even correcting for the small spread rate, the concurrent flame has a higher flow flammability boundary than the opposed flow flame.

On the Moon or Mars (0.17g and 0.38 g, respectively), where buoyant flows will be greater than 20 cm/s, the concurrent flame spread will be viable simultaneously with any opposed flow flame. Experiments conducted aboard the KC-135 [9] demonstrate the faster burning of concurrent flames in partial gravity environments. These higher flow test conditions are on the blowoff side of the flammability boundary.

If a fire is initiated, and the crew takes steps to extinguish it, the first line of defense is to turn off the flow. As demonstrated by the data above, the flame cannot survive indefinitely without a supply of fresh oxygen. Once the fire is out, the crew would reactivate the flow to clean up any residual smoke.

However, experiments have shown that even a very slight air flow of a fraction of a cm/s [4] is sufficient to allow the flame to survive. These flames can become almost undetectable (small, non-luminous) and yet persist for many minutes [10, 11] for a fingering flame spread observed under very weak ventilation. The tiny flamelet (~6 mm x 2mm) spread steadily, albeit slowly, for 80 seconds. When the flow was turned up 100-fold to 50 cm/s, the flame did not blow out as one would expect, but flared up into a much larger spreading flame. The fingering behavior is unique to low gravity. The formation of these different flame structures is due to changes in lateral diffusive flux of oxygen from the outer flow to the flame, convective flow patterns and oxygen shadow caused by oxygen consumption at the upstream flamelet. These types of behaviors must be known and understood so that the crew can watch for them.

References

1)D. Mulville, *Flammability, Odor, Offgassing, and Compatibility Requirements and Test Procedures for Materials in Environments that Support Combustion*, NASA-STD-6001, 1998.

2) K.B. McGrattan, T. Kashiwagi, H.R.Baum, and S.L. Olson, S.L.;.*Combust. Flame*, 106, (1996) 377-391.

3) Y.Halli, and J.S. T'ien, , NBS-GCR-86-507, 1986.

4) A.V. Ivanov, et. al, NASA Contract NAS3-97160 final report, Russian Space Agency, Keldysh Research Center, Moscow 1999, also NASA CP-1999-208917, pp. 47-50.

5) S.L. Olson,, *Comb. Science and Tech*. 76 (1991) 233-249.

6) T'ien, J.S., SIBAL Science Requirements Document, 2002.

7) Prasad, K., Olson, S.L., Nakamura, Y., and Kashiwagi, T.; "Effect of Wind Velocity on Flame Spread in Microgravity", the *Proceedings of the Combustion Institute, V. 29,* pp 2553-2560, July, 2002.

8) Olson, S.L., Kashiwagi, T., Fujita, O., Kikuchi, M., and Ito, K.; "Experimental Observations of Spot Radiative Ignition and Subsequent Three-Dimensional Flame Spread over Thin Cellulose Fuels", *Combustion and Flame*, V. 125, pp. 852-864, 2001.

9) Sacksteder, K.R., Ferkul, P.V., Feier, II, Kumar, A., and T'ien, J.S., "Upward and Downward Flame Spreading and Extinction in Partial Gravity Environments, Seventh International Workshop on Microgravity Combustion and Chemically Reacting Systems, NASA/CP-2003-212376/Rev1, pp141-144, 2003.

10) Wichman, I.S., ATHINA Science Requirements Document, 2004.

11) Olson, S.L., Baum, H.R., and Kashiwagi, T.; "Finger-like Smoldering over Thin Cellulosic Sheets in Microgravity", *Twenty-Seventh Symposium (International) on Combustion*, pp. 2525-2533, 1998.

Most Probable Fire Scenarios in Spacecraft and Extraterrestrial Habitats - Why NASA's Current Test 1 Might Not Always Be Conservative

S.L. Olson, NASA GRC

NASA's current method of material screening determines fire resistance under conditions representing a worst-case for normal gravity flammability - the Upward Flame Propagation Test (Test 1[1]). Its simple pass-fail criteria eliminates materials that burn for more than 12 inches from a standardized ignition source. In addition, if a material drips burning pieces that ignite a flammable fabric below, it fails.

The applicability of Test 1 to fires in microgravity and extraterrestrial environments, however, is uncertain because the relationship between this buoyancy-dominated test and actual extraterrestrial fire hazards is not understood. There is compelling evidence that the Test 1 may not be the worst case for spacecraft fires, or at Lunar or Martian gravity levels. This poster is a summary of what we know about the most likely forms a fire will take in space. (Please see reference list for cited works presented here).

Microgravity flames go the wrong way

Flames in microgravity are known to preferentially spread upwind (ie opposed flow) [2], not downwind (i.e. concurrent flow) as in the normal gravity upward flammability screening Test 1. Over most of the range of air ventilation rates (5-20 cm/s) comparable to spacecraft ventilation, upstream flame spread was the only viable flame. Figure 1 shows an image of a thin cellulose sample ignited in the middle. The blue half-dome flame is spreading upstream – into the fresh air. The downstream half of the dome is not viable because the oxygen has been consumed by the upstream side of the flame.

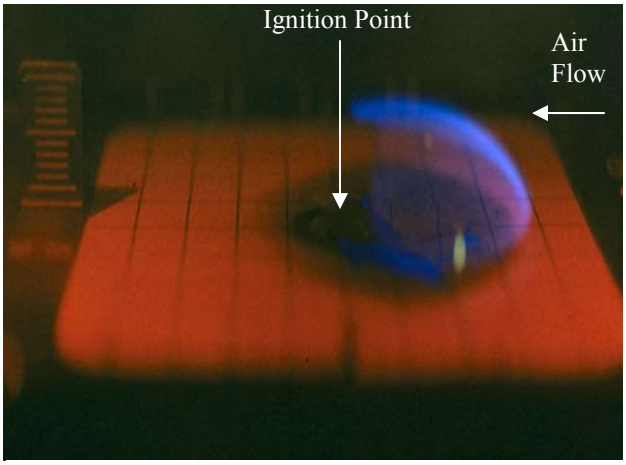

Figure 1: When ignited in the middle, the flame preferentially spreads upstream at low speed airflows

Only when the flow becomes strong enough (estimated to be ≥ 10 cm/s), will at least a partial downstream flame become viable. Numerical and experimental results [7]. predict an upstream flame only at 5.0 cm/s, an upstream flame and two localized edge flames propagating downstream at 10.0 cm/s, and both an upstream and downstream flame at 20.0 cm/s.

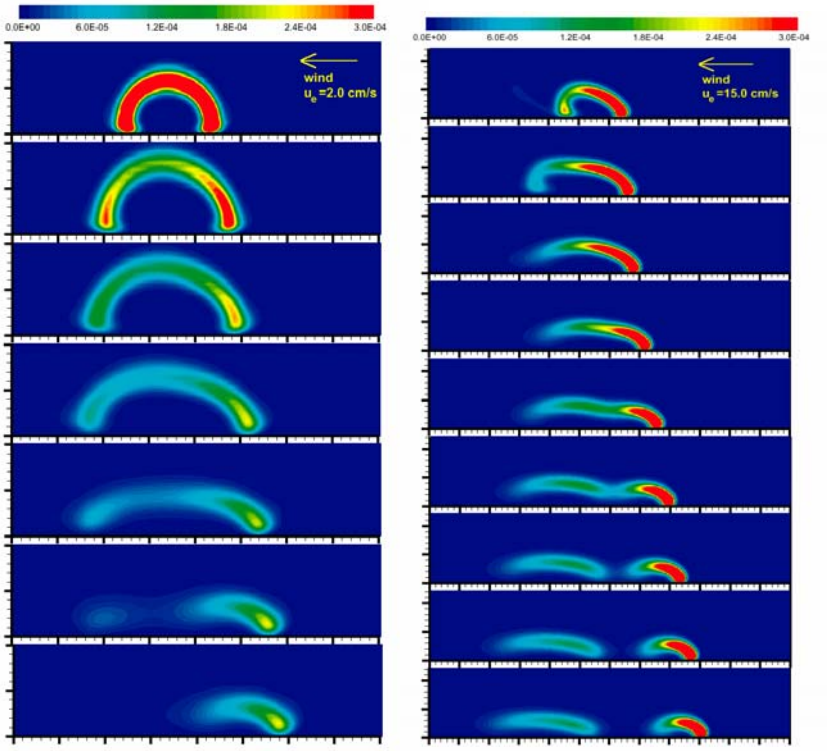

Figure 2: Computational Results of ignition and transition to flame spread for 5 cm/s (left) and 20 cm/s (right). The downstream flame is not viable at low wind velocities, but the two flames separate successfully at 20 cm/s as the thin fuel burns out in the middle. Notice even then how much weaker the downstream flame is. [7]

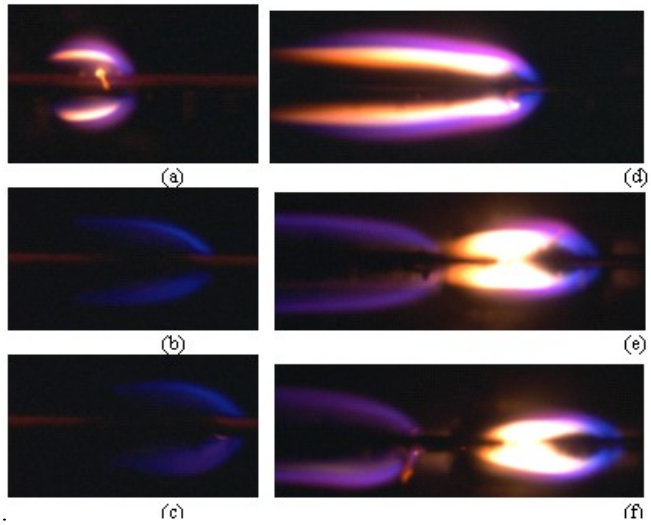

Figure 3: Color images of the edge view for flame spread in microgravity conditions obtained from the drop tower experiments. Figures 3. a, b and c are for an imposed flow velocity of 5 cm/s at t=2 s (a), 6.5 s (b) and 9.5 s (c) from the onset of external radiation. Figures 3. d, e and f are for an imposed flow velocity of 20 cm/s at t=4 s (a), 8 s (b) and 9.5 s (c) from the onset of external radiation. The flow is from right to left and the flames are propagating in air. Notice the similarities in the flame separation between these images and the computations of Figure 2.[7]

The computations and experimental results [7] at 5 cm/s and 20 cm/s are shown in Figures 2 and 3.

This propensity to spread upwind does not only occur for thin materials, but also occurs for thicker materials and other shapes. For example, experiments were conducted aboard the Mir space station using plastic cylinders. The intent was to burn them with a concurrent flame spread similar to that of Test 1. However, rather than spread along the rod, the flame stabilized at the front tip of the rod and burned like a candle flame at the end of a fat wick [3,4], as shown in Figure 4.

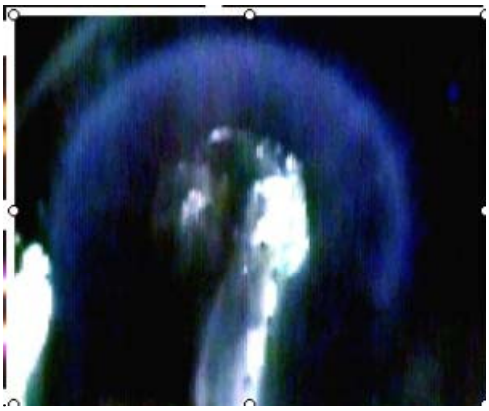

Figure 4: Candle-like flame burning at the upstream end of a plastic rod [4].

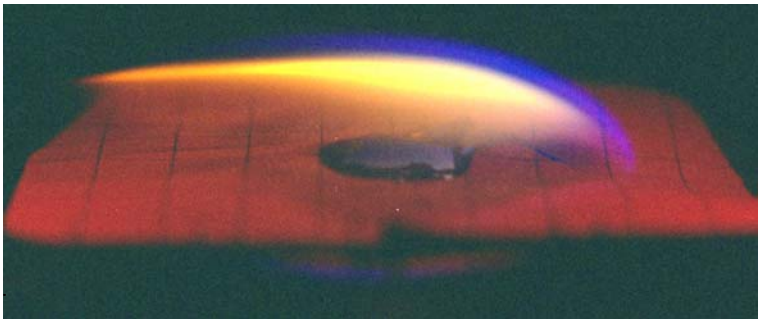

Figure 5: 3D flame spread with only upstream spread and a long downstream tail.

It is conceivable that a thermally thick sample would result in only one flame propagating upstream, with a long tail instead of the two flame structure for a thermally thin sample (because fuel burnout does not occur). [Takashi Kashiwagi, private communication]. Flame would look similar to Fig. 5.

Things burn in space that don't burn on Earth

Under the right flow conditions in space, things will burn that won't burn on Earth. This is most clearly demonstrated by a flammability map [5,6]. Figure 5 shows the opposed flow flame spread flammability map for a cellulose fuel. The LOI, or limiting oxygen index on Earth for this material in opposed flow is 16.5% O_2. **However, if the flow is on the order of spacecraft ventilation (5-20 cm/s), flames can be sustained even at 14 % O_2. Thus a normal gravity measure of flammability does not guarantee that the material won't burn in space.**

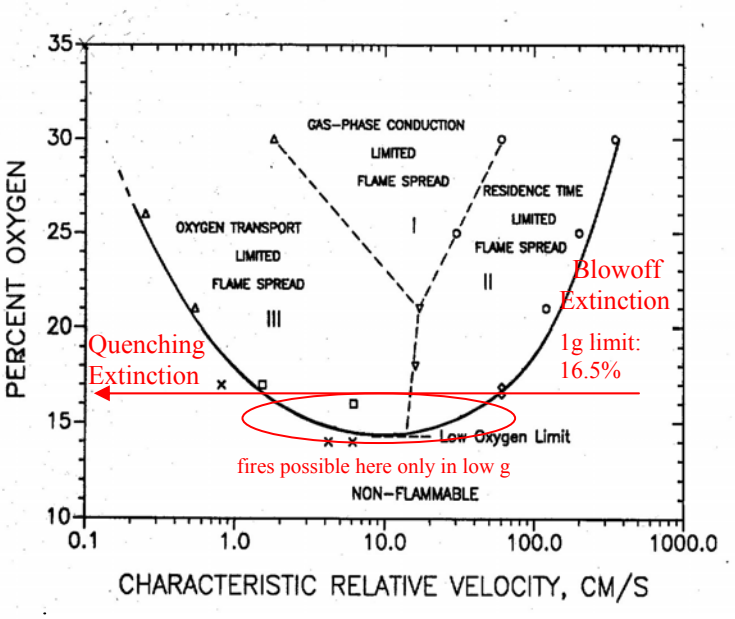

Figure 5: Experimentally-based flammability map for opposed flow flame spread over cellulose [5].

Shown in Figure 6 are 2D numerical predictions [6] of opposed flow vs concurrent flow flame spread (not simultaneous as described above).

As can be seen in Fig. 6, the fundamental LOI occurs at very low free stream velocities, which are in the range of spacecraft ventilation velocities (5-20 cm/s). Thus a 1g upward (concurrent) flame spread test, where buoyant flows are higher than 20 cm/s, is not conservative for these environments.

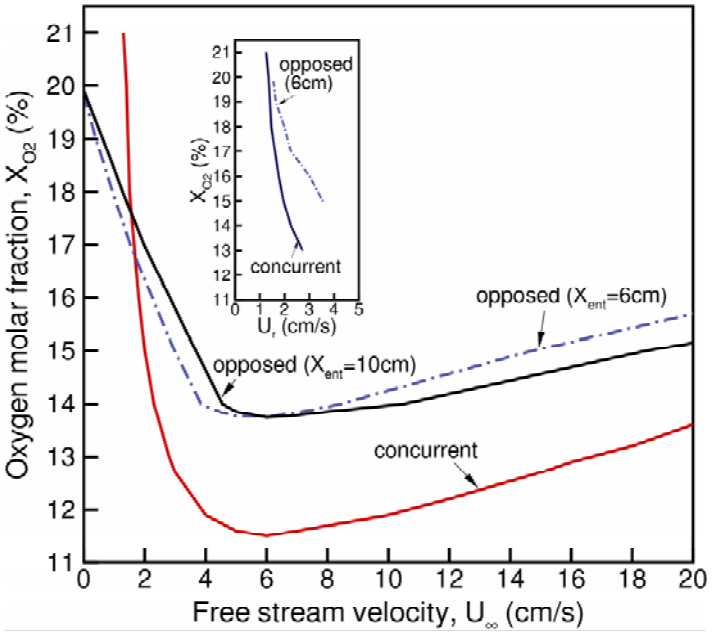

Figure 6: 2D theoretical flammability boundaries for independent opposed and concurrent flame spread. Notice the concurrent boundary extends to much lower oxygen concentrations than the opposed boundary except at very low speed forced flows, where the trend is reversed. [6]

These predictions show that oxygen limits (including the fundamental limit) are lower for the concurrent flame than for the opposed flames except in the very low velocity range. 3D computations are underway, and the extinction boundaries are expected to shift somewhat due to the importance of lateral oxygen transport, especially at low flows and low oxygen concentrations.

In the very low velocity range, oxygen supply is limiting. Therefore opposed spread, by moving against the oxygen flow, acquires a higher rate of oxygen transport into the flame, thus can have a lower oxygen limit. This point is illustrated further by plotting the flammability map using the relative velocity (between the flame and the flow) as the abscissa, shown in the inset of Fig. 6. Experiments are planned for ISS to measure the concurrent-only flame spread limits to verify these predictions.

Some preliminary work on independent opposed and concurrent flame spread was conducted in a glovebox experiment [8]. The flame spread results in the cabin air (~21% O2) are shown in Figure 7. The quenching region spans from +0.5 to -2 cm/s, so even correcting for the small spread rate, the concurrent flame has a higher flow flammability boundary than the opposed flow flame. This contradicts the inset of Figure 6, where the concurrent flame, once corrected for flame spread rate, has a comparable flammability limit.

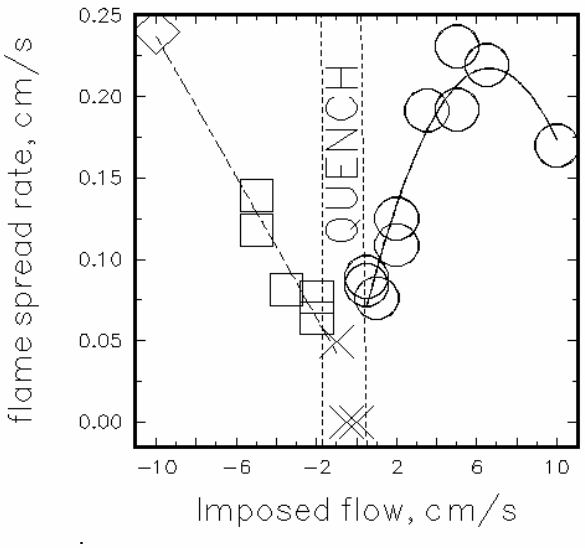

Figure 7: Flame spread rates in shuttle cabin air plotted against imposed flow. Negative flow is concurrent flow, whereas positive flow is opposed flow.

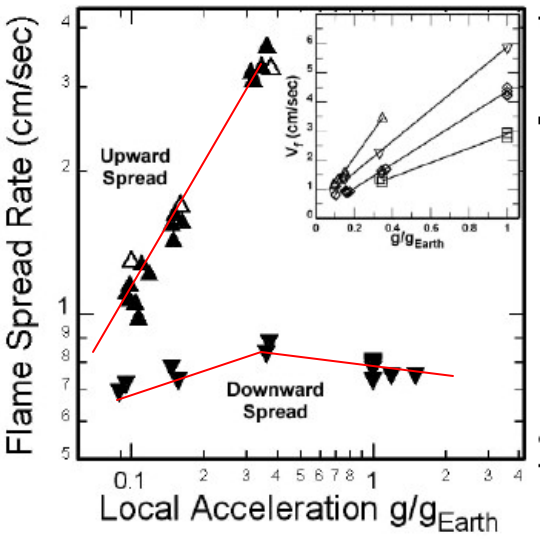

Figure 8: Upward and downward flame spread rates for narrow samples (2 cm) in low pressure (4 psia) air at various gravity levels. Closed symbols are experiments, open symbols are numerical simulations. Inset is 1 cm wide samples [9].

On the Moon or Mars (0.17g and 0.38 g, respectively), where buoyant flows will be greater than 20 cm/s, the concurrent flame spread will be viable simultaneously with any opposed flow flame. Experiments conducted aboard the KC-135 [9] demonstrate the faster burning of concurrent flames in partial gravity environments, as shown in Figure 8. These higher flow test conditions are on the blowoff side of the flammability boundary (Figure 5). Thus while upward burning here is worse than downward burning, the **normal gravity upward test is still not conservative because the minimum flammability is at low velocities only achievable in reduced gravity (Fig. 6).**

Flames Do Strange Things in Space

If a fire is initiated, and the crew takes steps to extinguish it, the first line of defense is to turn off the flow. As demonstrated by the data above, the flame cannot survive indefinitely without a supply of fresh oxygen. Once the fire is out, the crew would reactivate the flow to clean up any residual smoke.

However, experiments have shown that even a very slight air flow of a fraction of a cm/s [4] is sufficient to allow the flame to survive. **We cannot rely on quiescence to extinguish flames, because even the slightest flow *O*(mm/s) will support flames.** These flames, which near the limit will likely be flamelets, can become almost undetectable (small, non-luminous) and yet persist for many minutes[10], as shown in Figure 9 for a fingering flame spread observed under very weak ventilation (5 mm/s). The tiny flamelet (~6 mm x 2mm) spread steadily, albeit slowly, for 80 seconds. When the flow was turned up 100-fold to 50 cm/s, the flame did not blow out as one would expect, but flared up into a much larger spreading flame.

Figure 9: A tiny flame at 0.5 cm/s flares up within seconds when the flow is suddenly increased. Flow enters from right.

This fingering flamelet behavior, currently being studied as part of an ISS flight experiment, (Fig 10, 11) occurs near the quenching extinction boundary. The formation of these different flame structures is due to changes in lateral diffusive flux of oxygen from the outer flow to the flame, convective flow patterns and oxygen shadow caused by oxygen consumption at the upstream flamelet.

Flamelet fingering occurs in either opposed-flow spread (flame spreading against the wind) or concurrent spread (with the wind) under weak ventilation conditions. The fingering nature of the two spread modes is different, however, as shown in Figure 10.

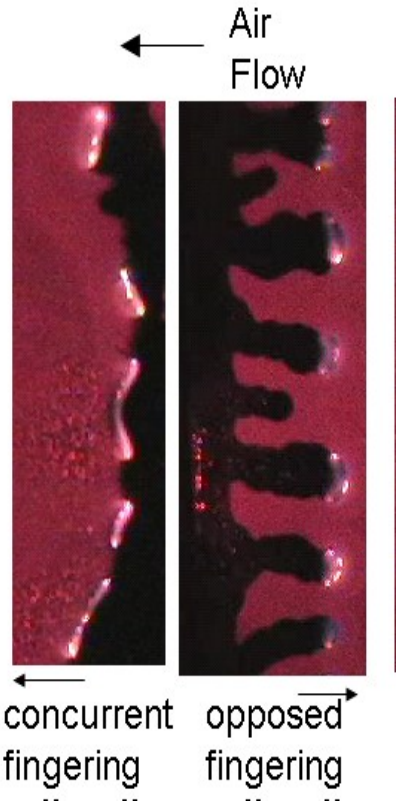

Figure 10: Concurrent flamelet fingering tends to travel along the edges of the unburned material like caterpillars eating a leaf, whereas opposed flamelet fingering tends to tunnel into the pristine fuel. While the concurrent flamelets spread more slowly than the opposed flamelets, overall, they consume more of the fuel. [10]

If ignited in the middle of the fuel, the predominant mode is opposed flow spread, because the upstream-most flame will consume the oxygen and any downstream reactions are unable to survive in the vitiated air [7]. However, if ignited at the upstream edge, then concurrent flamelets can survive since the fresh oxidizer reaches them directly. However, they stabilize on the edge of the burning material and cannot tunnel into the material very far before turning back upstream toward the fresh oxidizer.

These types of flaming and smoldering must be better understood so that we can gain confidence that we can detect these hard-to-detect fires and fully-extinguish them so that they do not flare up into a large fire.

Figure 11: Smoldering fingering [11] has also been seen in microgravity. 1 cm grid. Flow enters from right. Large circle is ignition point.

References

1)D. Mulville, *Flammability, Odor, Offgassing, and Compatibility Requirements and Test Procedures for Materials in Environments that Support Combustion*, NASA-STD-6001, 1998.

2) K.B. McGrattan, T. Kashiwagi, H.R.Baum, and S.L. Olson, S.L.;.*Combust. Flame*, 106, (1996) 377-391.

3) Y.Halli, and J.S. T'ien, , NBS-GCR-86-507, 1986.

4) A.V. Ivanov, et. al, NASA Contract NAS3-97160 final report, Russian Space Agency, Keldysh Research Center, Moscow 1999, also NASA CP-1999-208917, pp. 47-50.

5) S.L. Olson,, *Comb. Science and Tech*. 76 (1991) 233-249.

6) T'ien, J.S., SIBAL Science Requirements Document, 2002.

7) Prasad, K., Olson, S.L., Nakamura, Y., and Kashiwagi, T.; "Effect of Wind Velocity on Flame Spread in Microgravity", the *Proceedings of the Combustion Institute, V. 29,* pp 2553-2560, July, 2002.

8) Olson, S.L., Kashiwagi, T., Fujita, O., Kikuchi, M., and Ito, K.; "Experimental Observations of Spot Radiative Ignition and Subsequent Three-Dimensional Flame Spread over Thin Cellulose Fuels", *Combustion and Flame*, V. 125, pp. 852-864, 2001.

9) Sacksteder, K.R., Ferkul, P.V., Feier, II, Kumar, A., and T'ien, J.S., "Upward and Downward Flame Spreading and Extinction in Partial Gravity Environments, Seventh International Workshop on Microgravity Combustion and Chemically Reacting Systems, NASA/CP-2003-212376/Rev1, pp141-144, 2003.

10) Wichman, I.S., ATHINA Science Requirements Document, 2004.

11) Olson, S.L., Baum, H.R., and Kashiwagi, T.; "Finger-like Smoldering over Thin Cellulosic Sheets in Microgravity", *Twenty-Seventh Symposium (International) on Combustion*, pp. 2525-2533, 1998.

INTERFACIAL INSTABILITIES DURING EVAPORATION

Ozgur Ozen
University of Florida

Interfacial instabilities in the presence of vapors have traditionally been investigated by others who have assumed that the vapor phase is infinitely deep and passive, i.e. vapor fluid dynamics has been ignored. However, when we look at many engineering processes, such as heat pipes and coating technologies where interfacial instabilities take place, we might imagine that the assumption of an infinitely deep vapor layer, or at least that of a passive vapor, is inappropriate.

We have looked at a variety of problems where a liquid is in contact with a gas (sometimes even its own vapor) and investigated the role of the active gas phase on the interfacial instability. We have especially focused on the evaporative instabilities where the instability mechanism is more complicated. In order to understand the physics of these instabilities, calculations were done employing the techniques of linear stability analysis and the dominant balance method. The theoretical results and interpretations are also backed by experiments in bilayer fluid systems using IR imaging for flow visualization.

MICROFLUIDIC BIOCHIP DESIGN

Charles Panzarella

As humans prepare for the exploration of our solar system, there is a growing need for miniaturized medical and environmental diagnostic devices for use on spacecrafts, especially during long-duration space missions where size and power requirements are critical. In recent years, the biochip (or Lab-on-a-Chip) has emerged as a technology that might be able to satisfy this need. In generic terms, a biochip is a miniaturized microfluidic device analogous to the electronic microchip that ushered in the digital age. It consists of tiny microfluidic channels, pumps and valves that transport small amounts of sample fluids to biosensors that can perform a variety of tests on those fluids in near real time. It has the obvious advantages of being small, lightweight, requiring less sample fluids and reagents and being more sensitive and efficient than larger devices currently in use. Some of the desired space-based applications would be to provide smaller, more robust devices for analyzing blood, saliva and urine and for testing water and food supplies for the presence of harmful contaminants and microorganisms. Our group has undertaken the goal of adapting as well as improving upon current biochip technology for use in long-duration microgravity environments.

In addition to developing computational models of the microfluidic channels, valves and pumps that form the basis of every biochip, we are also trying to identify potential problems that could arise in reduced gravity and develop solutions to these problems. One such problem is due to the prevalence of bubbly sample fluids in microgravity. A bubble trapped in a microfluidic channel could be detrimental to the operation of a biochip. Therefore, the process of bubble formation in microgravity needs to be studied, and a model of this process has been developed and used to understand how bubbles develop and move through biochip components. It is clear that some type of bubble filter would be necessary in Space, and several bubble filter designs are being evaluated.

Another area of current research is DNA hybridization on solid surfaces. In DNA hybridization, short single strands of DNA, called oligonucleotides (oligos), are bonded to a solid substrate such as glass, and then fluid containing unknown DNA flows over it. The bound DNA are called the probes, and the suspended DNA are called the targets. A fluorescent molecule is attached to each target DNA. If the target and probe DNA complement each other, they will hybridize (zip up), and then the fluorescent molecules will emit detectable light when stimulated by a laser. The intensity of the fluorescent signal relates to the degree of surface hybridization and can be used as a means of identifying the unknown DNA. This is the basis of many commercial DNA microarrays such as the GeneChip made by Affymetrix, which can contain hundreds of thousands of oligo spots and are used primarily for studying gene expression.

Another application of this technique currently under consideration is the identification of microorganisms from their unique genetic signature. This is particularly important to NASA because such a device could be used to test for contaminated food and water supplies onboard distant spacecraft or outposts. The basic principle would be to deposit an array of oligo spots that uniquely identify the organisms most commonly suspected for contamination. Then, the process of surface hybridization could be used to see if any of the DNA from the unknown samples match the known DNA. The exact details of this process have not yet been completely worked out, but a number of companies such as HealthSpex are working on prototype devices.

There are a number of problems that need to be solved before this process becomes practical. First, the list of desired microorganisms needs to be determined, and from the genome of every organism on that list,

short DNA sequences (oligos) need to be selected that are capable of uniquely identifying them. The DNA from the sample needs to be extracted, purified and possibly amplified before passing over the immobilized probes.

In order to make the device as small as possible, it would be desirable to integrate the sample preparation, transport and detection processes into a single miniaturized device. In the ideal device, microfluidic channels would transport small amounts of sample fluid over the probe sites, and optical sensors integrated directly into the microchip would detect the hybridization.

Current research efforts are focusing on the optimization of this type of biosensor. The critical question is whether the fluorescent signal itself can provide enough information to uniquely identify the unknown organisms. This depends first and foremost on the proper choice of the oligo probes. They must be unique enough to differentiate the unknown organism from any other organism. This depends on where in the genome the oligo is selected and how long it is. It is generally believed that a length of about 25-30 nucleotide pairs is a good choice for gene expression analysis, but it is not clear that this would be the optimal length for microbial identification.

One problem that arises is how to distinguish between perfect complementary hybridization and single-base-pair mismatch hybridization. Without this ability, it would be impossible to differentiate between closely related organisms. One way of alleviating this problem is to apply a temperature gradient along the substrate and exploit changes in the kinetics of the hybridization process with temperature. Each complementary oligo pair has a unique melting temperature (the temperature at which half the available oligos are paired), and the melting temperature between a perfect match and a single mismatch can often be as large as 10 degrees Celsius. The melting temperature depends on the composition of the oligo as well as its length. If the position of the oligo spot on the substrate corresponds to its melting temperature, then different surface hybridization patterns can be used to distinguish between complementary and non-complementary duplexes.

In order to examine all of these issues, a computational model of DNA hybridization in a microchannel has been developed. Assuming the kinetics of the hybridization process are known, it can be used to optimize the design of the detector to improve its sensitivity and specificity for the set of microorganisms under consideration. In addition to the choice of oligo, other factors that can be varied include the channel dimensions, flow rate, inlet concentrations, sensor area and temperature profile. This model is used to predict the degree of hybridization and the unique surface concentration pattern for each case. In order to help with the problem of oligo selection, software has been developed that can compute the thermodynamic properties of the oligos such as their entropy, enthalpy, Gibbs free energy and melting temperature from known empirical data. It is also able to calculate the changes in these properties due to mismatches. This software is integrated directly into the model.

DETECTION AND PREVENTION OF CARDIAC ARRHYTHMIAS DURING SPACE FLIGHT

Dilip Pillai and David S. Rosenbaum
MetroHealth Campus, Case Western Reserve University
2500 MetroHealth Drive
Cleveland, Ohio 44109
(216) 778-2273
dpillai@metrohealth.org

Kathy J. Liszka
The University of Akron

David W. York, Michael A. Mackin, and Michael J. Lichter
NASA Glenn Research Center

There have been reports suggesting that long-duration space flight might lead to an increased risk of potentially serious heart rhythm disturbances. If space flight does, in fact, significantly decrease cardiac electrical stability, the effects could be catastrophic, potentially leading to sudden cardiac death. It will be important to determine the mechanisms underlying this phenomenon in order to prepare for long-term manned lunar and interplanetary missions and to develop appropriate countermeasures.

Electrical alternans affecting the ST segment and T-wave have been demonstrated to be common among patients at increased risk for ventricular arrhythmias. Subtle electrical alternans on the ECG may serve as a noninvasive marker of vulnerability to ventricular arrhythmias. We are studying indices of electrical instability in the heart for long term space missions by non-invasively measuring microvolt level T-wave alternans in a reduced gravity environment. In this investigation we are using volunteer subjects on the KC-135 aircraft as an initial study of the effect of electrical adaptation of the heart to microgravity. T-wave alternans will be analyzed for heart rate variability and QT restitution curve plotting will be compared for statistical significance.

Our hypothesis is that prolonged exposure to microgravity will alter T wave alternans measurements, decrease heart rate variance, increase QT dispersion, decrease heart rate recovery and alter QT restitution curve. A recently published study has shown that long duration spaceflights prolong cardiac conduction and repolarization. They concluded that long duration flight is associated with QT interval prolongation and may increase arrhythmia susceptibility. We propose using computer technology as a noninvasive clinical tool to detect and study clinically significant TWA during standard exercise testing using electrode systems specifically adapted for the purpose of obtaining and measuring TWA.

The equipment we will use for this operational and follow-on biomedical testing is the FDA approved Cambridge Heart Heartwave Diagnostic System modified to use a laptop computer versus a desktop unit developed for a hospital lab setting. The unique features of this ECG unit are the microvolt sensitivity, the back lead which is used to derive 3D electrical vectors of the heart, and the proprietary Cambridge Heart analysis and display software. The unit measures microvolt T-wave alternans using seven proprietary micro-V alternans sensors and seven standard electrodes placed in the standard 12-lead configuration, as well as four Frank vector positions. The micro-V sensors reduce the effects of muscle noise and baseline wander when used in conjunction with specialized signal processing techniques.

Protocols will be observed for preflight, in-flight, postflight and KC-135 flight data collection. The KC-135 flights will help with early operational research testing techniques. The purpose of the operational experiment is to correlate cardiac parameters with blood pressure and gravity levels to determine how the data fits historical ground data. The complete experiment has both operational and biomedical research component. IRB approval of the study will be obtained. Informed consent will be obtained from the participants.

The T wave alternans test results can be positive, negative or indeterminate. The test has an excellent negative predictive value and therefore, those who test negative are at a low risk for sudden cardiac death. Those who test positive may be at risk of susceptibility to ventricular arrhythmias. A statistical analysis of the land-based, low gravity, Martian trajectory and Lunar trajectory environment measurements will be made and determined if there is any significant difference between the recordings.

A population of approximately 15 healthy men and 5 healthy women subjects, representative of the astronaut cohort will be asked to voluntarily participate in this study. Their blood pressure and ECG/TWA will be measured pre-flight and in-flight. Prior to flight, subjects will be asked to participate in an orientation session. Still photos will be taken of the skin where the conductive gel is used for the multi-segment sensors. Photos will be recorded preflight, immediately postflight, and several times during the proceeding week until it has been determined that any skin reaction has disappeared or that no rash is present and will not appear.

A Fast Fourier Transform (FFT) spectral analysis uses the vector magnitude ECG signal recorded from three orthogonal leads over a predetermined minimum number of ECG beats. The analysis yields two measurements: the alternans magnitude and alternans ratio. These are obtained using the Cambridge Heart CH2000 Cardiac Diagnostic System instrument. A positive T-Wave alternan test is the presence of sustained alternans with an amplitude at least 1.9 microvolt and alternans ratio of = 3.0. A quantitative analysis of this data will be performed and presented in a chart form listing each subject's (no name, just subject's number) systemic blood pressure and ECG for pre-flight and in-flight. This data will be compared with ground-based studies and used to develop further medical protocols and possible countermeasures.

The goal of this research is to perform operational testing in low gravity of an advanced ECG with microvolt resolution and 3D localized features to account for altered heart position associated with the low gravity environment of space. Once operational feasibility is proven medical protocols will be developed to determine if advanced ECG testing (including T-wave alterations and Q-T dispersions) can be performed in low gravity. The purpose of the operational experiment is to correlate cardiac parameters with blood pressure and gravity levels to determine how the data fits historical ground data. The complete experiment has both operational and biomedical research component. The first flight week, May 17, 2004, will be operational testing. A research plan will be developed for testing beginning on the August 2, 2004 flight week. An early operational and research objective will be to determine if a series of TWA tests of 20-40 seconds (30-60 beats) can be correlated to produce the same result as one consecutive 128 beat test.

THE EFFECT OF GRAVITY MODULATION ON FILTRATIONAL CONVECTION IN A HORIZONTAL LAYER

Natalya Popova
Department of Mathematics
University of Illinois at Chicago
Chicago, IL 60607
npopov1@uic.edu

The present paper examines the effect of vertical (transverse) harmonic oscillations of the frequency ω and the amplitude A on the onset of convection in an infinite horizontal layer of fluid saturating a porous medium. Constant temperature distribution is assigned on the rigid impermeable boundaries, so that there exists a vertical temperature gradient. The mathematical model is described by equations of filtrational convection [1,2] in the Darcy-Oberbeck-Boussinesq approximation, introduced in the coordinate system inflexibly fixed to the oscillating horizontal layer.

Mechanical quasi-equilibrium solution to the system is obtained. The linear stability analysis for this solution is performed by using Floquet theory. The system of equations for normal disturbances includes the following nondimensional parameters: the Prandtl number $Pr=\nu/\chi$, the wave number α, the gravitational Grashoff number $Gr=\beta Ch^2 g_0 K/\nu^2$, the vibrational Grashoff number $Gv=Gr\bullet\eta$. Here $\eta=A\omega^2/\varphi g_0$, g_0 is the steady gravity acceleration, φ is the porosity of the medium, ν is the kinematic viscosity of the fluid, χ is the thermal diffusivity, K is the intrinsic permeability of the medium, β is the coefficient of thermal expansion of the fluid, C is the quasi-equilibrium temperature gradient, h is the thickness of the layer. The vibrational Grashoff number does not depend on gravity and describes filtrational convection in weightlessness.

The system for the perturbed quantities is reduced to the single damped Mathieu equation for the temperature perturbations. The behavior of its solution is represented by a Fourier series in time. Employment of the method of continued fractions allows us to derive the dispersion equation for the Floquet exponent σ in the explicit form [3].

This equation is investigated with the focus on the following two problems. First, the Floquet spectrum, which describes the stability of the quasi-equilibrium state, is investigated analytically and numerically for different values of the parameters: frequency ω, amplitude A of oscillations, and the Rayleigh number $Ra=Gr\bullet Pr$. Second, the neutral curves $Gv(\alpha)$ and $Gr(\alpha)$ for the synchronous and subharmonic resonant modes are constructed for different values of ω and A. These curves define the regions of parametric instability. The conditions of weightlessness ($Gr=0$) and microgravity (Gr is small) are examined for each of the problems described above.

Also, for both of these problems, asymptotics are derived for large values of ω using the method of averaging and, for small values of ω, using the WKB method. The results obtained by using the method of continued fractions and the asymptotic methods are in a good agreement.

Analytical and numerical investigation of the problem proves that sufficiently intensive vertical (transverse) translational oscillations can delay or even completely suppress the onset of filtrational convection, i.e. stabilize the system. However, for some values of the vibration parameters, these oscillations can destabilize the system and even induce the convection in the stable system (for instance,

in the case of the negative temperature gradient). Therefore, by means of changing the parameters of vibration – the frequency and the amplitude - we can control convective instability in a layer of fluid saturating a porous medium.

References

1. Nield D., Bejan A., Convection in porous media, Springer-Verlag, New York, 1998.
2. Gershuni G., Zhukhovitskii E., Convective stability of incompressible fluid, "Nauka", Moskva, 1972.
3. Yudovich V., Zenkovskaya S., Novossiadliy V., Shleykel A., Parametric excitation of waves on a free boundary of a horizontal fluid layer, C.R. Mecanique 331, 2003.

THE EFFECT OF GRAVITY MODULATION ON FILTRATIONAL CONVECTION IN A HORIZONTAL LAYER

Natalya Popova
Department of Mathematics, University of Illinois at Chicago
851 S. Morgan Street
Chicago, IL 60607
npopov1@uic.edu

ABSTRACT

The present paper examines the effect of vertical (transverse) harmonic oscillations of the frequency Ω and the amplitude A on the onset of convection in an infinite horizontal layer of fluid saturating a porous medium. Constant temperature distribution is assigned on the rigid impermeable boundaries, so that there exists a vertical temperature gradient. The mathematical model is described by equations of filtrational convection (see [1], [2]) in the Darcy-Oberbeck-Boussinesq approximation, introduced in the coordinate system inflexibly fixed to the oscillating horizontal layer.

Mechanical quasi-equilibrium solution to the system is obtained. The linear stability analysis for this solution is performed by using Floquet theory. The system of equations for normal disturbances includes the following nondimensional parameters: the Prandtl number $\mathrm{Pr}=\nu/\chi$, the gravitational Grashoff number $\mathrm{Gr}=\beta C h^2 g_0 K/\nu^2$, the vibrational Grashoff number $\mathrm{Gv}=\mathrm{Gr}\cdot\eta$, the frequency of oscillations $\omega=\Omega h^2/\nu$. Here $\eta=A\Omega^2/\varphi g_0$ is the nondimensional amplitude of oscillations, g_0 is the steady gravity acceleration, φ is the porosity of the medium, ν is the kinematic viscosity of the fluid, χ is the thermal diffusivity, K is the intrinsic permeability of the medium, β is the coefficient of thermal expansion of the fluid, C is the quasi-equilibrium temperature gradient, h is the thickness of the layer. The vibrational Grashoff number does not depend on gravity and describes filtrational convection in weightlessness.

The system for the perturbed quantities is reduced to the single damped Mathieu equation for the temperature perturbations. The behavior of its solution is represented by a Fourier series in time. Employment of the method of continued fractions allows us to derive the dispersion equation for the Floquet exponent σ in the explicit form (see [3], [4], [7], [8]).

This equation is investigated with the focus on the following two problems. First, the Floquet spectrum, which describes the stability of the quasi-equilibrium state, is investigated analytically and numerically for different values of the parameters: frequency ω, amplitude η of oscillations, and the Rayleigh number $\mathrm{Ra}=\mathrm{Gr}\cdot\mathrm{Pr}$. Second, the neutral curves $\mathrm{Ra}(\alpha)$ and $\mathrm{Rv}(\alpha)$ ($\mathrm{Rv}=\mathrm{Gv}\cdot\mathrm{Pr}$) for the synchronous and subharmonic resonant modes are constructed for different values of ω and η. These curves define the regions of parametric instability. The conditions of weightlessness (Gr=0) and microgravity (Gr is small) are examined for each of the problems described above.

Also, for both of these problems, asymptotics are derived for large values of ω using the method of averaging (see [5], [6]) and, for small values of ω, using the WKB method (see [10]). The results obtained by using the method of continued fractions and the asymptotic methods are in a good agreement.

Analytical and numerical investigation of the problem proves that sufficiently intensive vertical (transverse) translational oscillations can delay or even completely suppress the onset of

filtrational convection, i.e. stabilize the system. However, for some values of vibration parameters, these oscillations can destabilize the system and even induce convection in the stable system (for instance, in the case of the negative temperature gradient or in the case of weightlessness). Therefore, by means of changing parameters of vibration – the frequency and the amplitude - we can control convective instability in a layer of fluid saturating a porous medium.

References

1. Nield D., Bejan A., Convection in porous media, Springer-Verlag, New York, 1998, pp.546.

2. Gershuni G., Zhukhovitskii E., Convective stability of incompressible fluid, "Nauka", Moskva, 1972, pp. 310.

3. Meshalkin L., Sinai Y., Investigation of the stability of a stationary solution of system of equations for the plane movement of an incompressible viscous liquid, Appl. Math. Mech., 1961, 25, 1140-1143.

4. Markman G., Yudovich V., Numerical investigation of the origin of convection in the layer of fluid subjected to the external forces periodic in time, Izv. AN USSR, MZG, 1971, 3, 81-86.

5. Zenkovskaya S., Effect of high-frequency vibration on filtrational convection, Prikl. Math. Tech. Fiz., 1992, 5, 83-88.

6. Zen'kovskaya S., Rogovenko T., Filtration convection in a high-frequency vibration field, Journal of Appl. Mech. Tech. Phys., 1999, 40(3), 379-385.

7. Yudovich V., Zenkovskaya S., Novossiadliy V., Shleykel A., Parametric excitation of waves on a free boundary of a horizontal fluid layer, C.R. Mecanique 331, 2003.

8. Belenkaya L., Friedlander S., Yudovich V., The unstable spectrum of oscillating shear flows, SIAM Journal of Appl. Math., 1999, 59(5), 1701-1715.

9. VanVleck E., On the convergence of continued fractions with complex elements, Trans. Amer. Math. Soc., 1901, 15, 215-233.

10. Naifeh A., Introduction to perturbation techniques, New York, Toronto, 1981, pp. 519.

1 Problem description and basic equations

We consider an infinite horizontal layer of a porous medium saturated by a viscous incompressible fluid. The layer and its boundaries are subjected to vertical harmonic oscillations described by the formula: $z=A\,f(\Omega t)$, where $f(\Omega t)$ is a 2π-periodic function with the zero average. We assume that the porous medium is homogeneous and isotropic, and the boundaries are rigid and impermeable, with the slip allowed. The constant temperature distribution is specified at the boundaries so that there exists a vertical temperature gradient.

We use the filtrational convection equations in the Darcy-Oberbeck-Boussinesq approximation (see [1], [2]). In the Cartesian coordinate system inflexibly fixed to the horizontal layer, with the z-axis directed vertically upwards, these equations have the following form:

$$\frac{1}{\varphi}\frac{\partial \vec{\mathrm{v}}}{\partial t} = -\frac{1}{\rho}\nabla p - \frac{\nu}{K}\vec{\mathrm{v}} + \beta T g(t)\vec{\gamma}, \tag{1}$$

$$\kappa\frac{\partial T}{\partial t} + \vec{\mathrm{v}}\cdot\nabla T = \chi\nabla^2 T, \qquad \nabla\cdot\vec{\mathrm{v}} = 0. \tag{2}$$

Gravitational acceleration $g(t) = g_0 + g_e(t)$, where g_0 is acceleration due to static gravity, and $g_e(t) = (A\Omega^2/\varphi) f''(\Omega t)$ is vibrational acceleration.

We consider boundary conditions of the following form:

$$z = 0: \qquad \mathrm{v}_3 = 0, \qquad T = T_1 = \mathrm{const}, \tag{3}$$

$$z = h: \qquad \mathrm{v}_3 = 0, \qquad T = T_2 = \mathrm{const}. \tag{4}$$

2 Linearized system of equations

System (1) - (4) has a solution corresponding to the following basic state:

$$\vec{v}^0 = 0, \quad T^0 = T_1 - \frac{1}{h}(T_1 - T_2)z, \quad p^0 = \beta\rho\, g(t)\left(T_1 z - \frac{1}{2h}(T_1 - T_2)z^2 \right). \qquad (5)$$

To examine the stability of this basic state by using the linearization method, we introduce the small perturbations ($\vec{u}$, q, θ) of the variables ($\vec{v}$, p, T).

Dimensionless linearized system has the following form:

$$c\frac{\partial \vec{u}}{\partial t} = -\nabla q - \vec{u} + Gr(1 + \eta\, f''(\omega t))\theta\,\vec{\gamma}, \qquad (6)$$

$$\kappa\frac{\partial \theta}{\partial t} - u_3 = \frac{1}{\mathrm{Pr}}\nabla^2\theta, \qquad \nabla\cdot\vec{u} = 0, \qquad (7)$$

where $c = \dfrac{K}{\varphi h^2}$, $Gr = \dfrac{\beta C h^2 g_0 K}{\nu^2}$, $\eta = \dfrac{A\Omega^2}{\varphi g_0}$, $\mathrm{Pr} = \dfrac{\nu}{\chi}$, $C = \dfrac{T_1 - T_2}{h}$, $\omega = \dfrac{\Omega h^2}{\nu}$.

Dimensionless Boundary Conditions are:

$$z = 0, \;\; z = 1: \;\; u_3 = \theta = 0 \qquad (8)$$

3 Dispersion equation for the Floquet exponent σ

At this point we assume that the function $f(\Omega t)$ in the expression for $g(t)$ has the following form: $f(\Omega t) = \cos(\Omega t)$, then $g(t) = g_0 - (A\Omega^2/\varphi)\cos(\Omega t)$.

After separating the x-, y-, and z-variables from the system, we reduce system (6) – (8) to the form of the damped Mathieu equation:

$$\theta''(t) + \left(\frac{m^2}{P} + P\right)\theta'(t) + \left(m^2 - \frac{\alpha^2}{m^2}\mathrm{Ra}(1 - \eta\cos(\omega t))\right)\theta(t) = 0, \qquad (9)$$

where $P = \sqrt{\dfrac{\mathrm{Pr}\,\kappa}{c}}$, $m^2 = \alpha^2 + (\pi l)^2$, $\alpha^2 = \alpha_1^{\,2} + \alpha_2^{\,2}$, $\mathrm{Ra} = \mathrm{Gr}\cdot\mathrm{Pr}$.

For the case of weightlessness ($g_0 = 0$), this equation transforms into

$$\theta''(t) + \left(\frac{m^2}{P} + P\right)\theta'(t) + \left(m^2 + \frac{\alpha^2}{m^2}\mathrm{Rv}\cdot\cos(\omega t)\right)\theta(t) = 0, \qquad \text{where } \mathrm{Rv} = \mathrm{Ra}\cdot\eta.$$

We search for the solutions of equation (9) in the form of the Fourier series

$$\theta(t) = e^{\sigma t} \sum_{n=-\infty}^{+\infty} c_n e^{in\omega t}. \tag{10}$$

Substituting (10) into (9), we obtain an infinite 3-diagonal system of linear algebraic equations

$$M_n c_n = -q(c_{n-1} + c_{n+1}), \qquad n = 0,\pm1,\pm2,... \tag{11}$$

where $M_n = (\sigma + in\omega)^2 + \left(\frac{m^2}{P} + P\right)(\sigma + in\omega) + \left(m^2 - \frac{\alpha^2}{m^2}\mathrm{Ra}\right)$, $q = \frac{\alpha^2 \mathrm{Ra}\,\eta}{2m^2}$.

Using the method of continued fractions to solve this system (see [3],[4],[7],[8]), we obtain the dispersion equation for the Floquet exponent σ in the explicit form:

$$M_0 - \cfrac{q^2}{M_1 - \cfrac{q^2}{M_2 - \cfrac{q^2}{M_3 - \ldots}}} = \cfrac{q^2}{M_{-1} - \cfrac{q^2}{M_{-2} - \cfrac{q^2}{M_{-3} - \ldots}}}. \tag{12}$$

Consider two particular cases for which this equation simplifies to a real form:

1. For the case of $\sigma=0$, corresponding to T-periodic ($T=2\pi/\omega$), or synchronous modes, equation (12) transforms into

$$\mathrm{Re}\left(\cfrac{q^2}{M_1 - \cfrac{q^2}{M_2 - \cfrac{q^2}{M_3 - \ldots}}} \right) = \frac{M_0}{2}. \tag{13}$$

2. For the case of $\sigma = i\omega/2$, corresponding to $2T$-periodic, or subharmonic modes, equation (12) simplifies to

$$\left| M_0 - \cfrac{q^2}{M_1 - \cfrac{q^2}{M_2 - \cfrac{q^2}{M_3 - \ldots}}} \right|^2 = q^2. \qquad (14)$$

We solve equations (13) and (14) numerically to obtain the neutral curves Ra(α) and Rv(α).

4 The case of a rapidly oscillating external force ($\omega \to \infty$)

Represent the amplitude of the oscillations in the form: $\eta = \tilde{A}\omega$, where $\tilde{A} = (A\omega\nu^2/\varphi g_0 h^4)$, and introduce a new "fast" time variable $\tau=\omega t$. Represent the solution to equation (9) in the form:

$$\theta(t) = \bar{\theta}(t) + \frac{1}{\omega}\tilde{\theta}(\tau, t), \qquad (15)$$

where $\bar{\theta}(t)$ is a slowly varying part, which is a function of the "slow" time t only, $\tilde{\theta}(\tau, t)$ is a rapidly oscillating part, which is 2π-periodic in τ, with the zero mean. By using the averaging method (see [5], [6]]) we derive the averaged equation for the slowly varying component $\bar{\theta}(t)$:

$$\bar{\theta}''(t) + \left(\frac{m^2}{P} + P\right)\bar{\theta}'(t) + \left(m^2 - \frac{\alpha^2}{m^2}\mathrm{Ra} + \frac{(\alpha^2 \mathrm{Ra}\tilde{A})^2}{2m^4}\right)\bar{\theta}(t) = 0 \qquad (16)$$

The stability spectrum of this equation can be represented in the explicit form:

$$\sigma^2 + \left(\frac{m^2}{P} + P\right)\sigma + \left(m^2 - \frac{\alpha^2}{m^2}\mathrm{Ra} + \frac{(\alpha^2 \mathrm{Ra}\tilde{A})^2}{2m^4}\right) = 0$$

5 The case of a slowly oscillating external force ($\omega \to 0$)

Represent the amplitude of the oscillations in the form $\eta = \tilde{A}\omega$, where $\tilde{A}$ has the same form as in Section 4. Introduce a new time variable $\tau = \omega t$, a large parameter $\lambda = 1/\omega$, and denote $\theta(t) = \hat{\theta}(\tau)$. Now we apply the WKB method (see [10]) and write the leading-order asymptotic approximation for $\hat{\theta}(\tau)$ in the form:

$$\hat{\theta}(\tau) = \frac{1}{\sqrt[4]{F(\tau)}} \exp\left(-\frac{\lambda}{2}\left(\frac{m^2}{P} + P \right)\tau \pm \lambda \int_0^\tau \sqrt{F(t)}\, dt \right),$$

where $F(\tau) = \frac{1}{4}\left(\frac{m^2}{P} + P \right)^2 - m^2 + \frac{\alpha^2}{m^2}\mathrm{Ra}\left(1 + \frac{\tilde{A}}{\lambda}\cos\tau \right)$, assuming $F(\tau) \neq 0$.

By using 2π-periodicity of $\hat{\theta}(\tau)$ and $F(\tau)$, we obtain the asymptotic equation for the neutral curves $\mathrm{Ra}(\alpha)$, corresponding to synchronous modes:

$$\left(\frac{m^2}{P} + P \right)\pi = \int_0^{2\pi} \sqrt{\frac{1}{4}\left(\frac{m^2}{P} + P \right)^2 - m^2 + \frac{\alpha^2}{m^2}\mathrm{Ra}(1 + \tilde{A}\omega\cos t)}\, dt. \qquad (29)$$

6 Numerical results

In Fig.1 we consider negative Rayleigh numbers, which correspond to heating of the layer from above. The alternating pattern for the instability regions, corresponding to synchronous and subharmonic modes, is evident. Increasing the frequency ω causes these instability regions to move toward lower values of Ra, preserving the same alternating pattern.

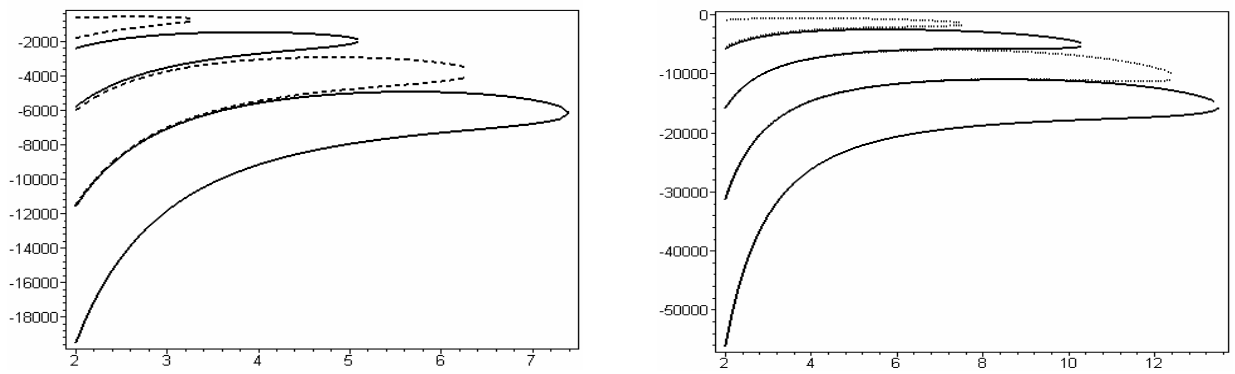

(a) (b)

Figure 1: Graphs of Ra(α) for synchronous (solid line) and subharmonic (dashed line) modes, obtained by the method of continued fractions. In (a) $\omega = 30$, $\eta = 3$, in (b) $\omega = 60$, $\eta = 6$.

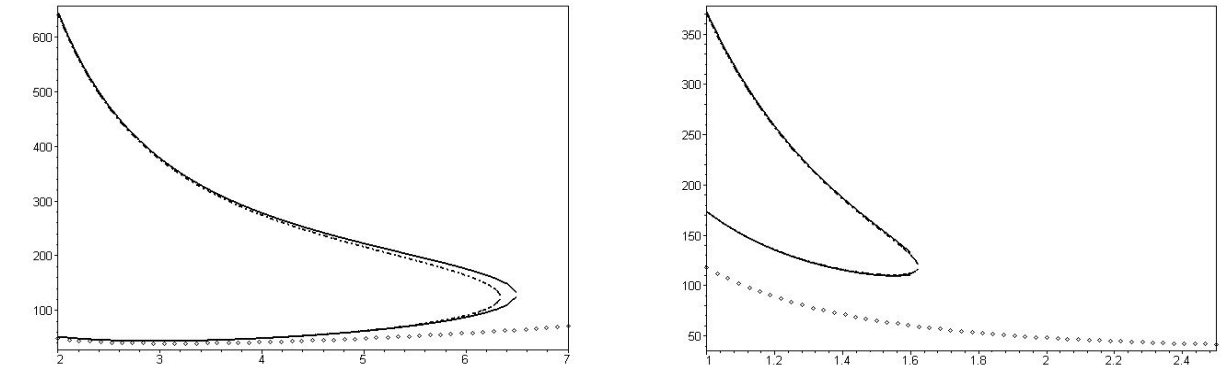

(a) (b)

Figure 2: Graphs of Ra(α) for large ω, obtained by the method of continuous fractions (solid line) and by the method of averaging (dashed line). In graph (a) $\omega = 300$, $\eta = 30$, (b) $\omega = 300$, $\eta = 60$. The individual points in both graphs correspond to the case with no oscillations.

In Fig.2 and 3 we consider positive Rayleigh numbers and synchronous modes only. The instability regions in Fig. 2 move upwards, decrease in size and finally disappear as the ratio of the amplitude and the frequency of oscillations increases.

(a)

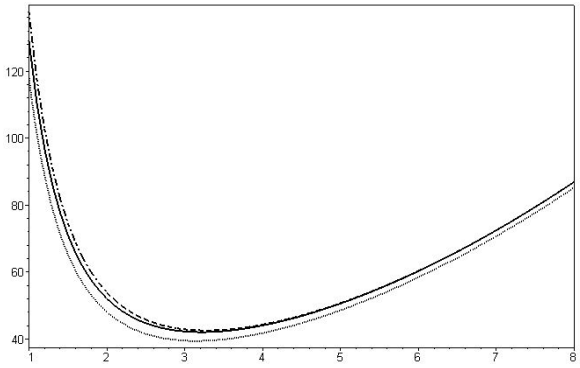

Figure 3: Graphs of Ra(α) for ω =10, η = 2, obtained by the method of continued fractions (solid line) and by the WKB method (dashed line); and for the "no-oscillation" case (dotted line).

(b)

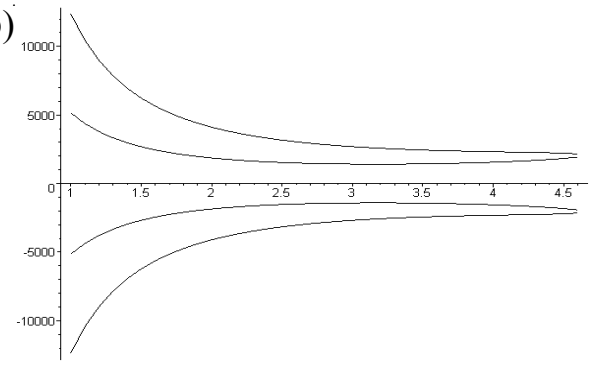

Figure 4: Graphs of Rv(α) obtained by the method of continued fractions for ω=10, g_0=0 (a case of weightlessness).

The "oscillatory" curves in Fig.3 approach very close the curve for the case with no oscillations as the frequency and the amplitude of oscillations decrease. Parameters not specified on the plots are chosen to be Pr=0.733, l=1, κ/c =1.

7 Conclusions

Analytical, asymptotical and numerical investigation of the system indicates that sufficiently intensive vertical oscillations can delay or even completely suppress the onset of filtrational convection, i.e. stabilize the system. However, for some values of parameters, (for instance, for negative Rayleigh numbers or for the case of weightlessness) vertical oscillations can destabilize the system and even induce convection in the stable system. Therefore, vertical vibration can be used to control convective instability in a layer of fluid saturating a porous medium.

A natural extension of the present study will analyze the effect of vertical oscillations on a doubly diffusive convection in porous media.

MINIATURE TIME OF FLIGHT MASS SPECTROMETER

Richard S. Potember, Ph.D.
Applied Physics Laboratory
The Johns Hopkins University
Johns Hopkins Road
Laurel, MD 20723-6099
Phone: 240-228-6251 Fax: 240-228-6904 E-mail: Richard.Potember@jhjuapl.edu

We are developing and testing a small, efficient time-of-flight mass spectrometer to rapidly identify important biomarkers and countermeasures for human space exploration. We are using the time-of-flight mass spectrometer to evaluate critical biomarkers and countermeasures that are indicators of bone loss and repair associated with space travel. This miniature instrument will provide new capabilities in the area of sampling, sample preparation, rapid quantitation of biomarkers and it will allow us to apply our technology to other space based problems such as monitoring the spacecraft environment for chemical and biological contaminants.

Mass spectrometry is a technique for determining the masses of molecules and specific fragmentation products formed during vaporization and ionization. From detailed analysis of the mass distribution of the molecule and its fragments, molecular identification is accomplished. These molecular measurements can be carried out at the attomole (10-18 mole) level of material using specialized laboratory-based instruments. The combination of specific molecular identification and extreme sensitivity makes mass spectrometry one of the most powerful analytical laboratory tools yet developed for detection and identification of chemical and biological substances.

1. Muscle Alterations and Atrophy We have recorded full spectrum mass spectral signature of key target biomarker analytes using the MALDI technique at physiological concentrations found in urine. Sampling from urine has been chosen as a high priority for this project. Compounds investigated included: insulin-like growth factors (IGF-I), Urinary 3-methylhistidine, and estradiol. IGF-I is a potent anabolic factor that mimics most of the growth promoting actions of GH *in vivo*. IGF-1 has also been identified by the Bone Demineralization / Calcium Metabolism Team as an important biomarker.

Another biomarker is urinary 3-methylhistidine. It is a measure of myofibrillar protein degradation. 3-methylhistidine cannot be re-utilized by the body. It is rapidly and quantitatively excreted in the urine. Estradiol is a steroid hormone important for the maintenance of muscle mass and bone density. It is widely speculated that steroid hormones such as estradiol play a central role in the early stages of muscle atrophy and bone demineralization.

We have also used matrix-assisted laser desorption mass spectrometry as a tool to *quantitatively* measure 3-MH in biological fluids. The TOFMS team analyzed various concentrations of 3-methylhistidine in water and in urine to determine the relationship between analyte concentration and analyte molecular ion intensity. The concentrations used in this study were based on 3-methylhistidine concentration typically found in urine, i.e. 20pmole – 3.5nmole. The team examined the utility of two types of internal standards, histidine, a structural analogue, and d_3-3-methylhistidine, a stable-isotope labeled analogue. 3-Methylhistidine (3-MH) samples in water and urine were prepared ranging from 5uM – 10mM, keeping the (3MH)/(histidine) ratio constant at 1:10. Protonated molecular ions for 3MH and histidine could be identified in the corresponding MALDI spectra. A plot of the ratio of relative peak intensities of (3MH)/(d_3-3-MH) versus 3-MH concentration gave a linear response with a correlation coefficient, $R^2 = 0.9799$ and a relative standard deviation of the slope of 4.00%.

2. Bone Demineralization / Calcium Metabolism

We have completed initial laboratory studies with biomarkers specific to bone loss and metabolism. These biomarkers include trivalent hydroxypyridinium crosslinks and creatinine. Trivalent hydroxypyridinium crosslinks are released into the circulation during bone resorption and are excreted as free pyridinolines molecules. In bone and cartilage, the collagen is bound by pyridinoline or deoxypyridinoline crosslinks. Deoxypyridinoline is found exclusively in bone while pyridinoline is found in skin, joint and cartilage. Creatinine is used to extrapolate the status of bone remodeling activity in various metabolic bone conditions.

We have performed a mass spectral analysis of alendronate to determine the mass spectral pattern by MALDI and to add the compound to our library of critical biomarkers. Bisphosphonate administration to the hindlimb of suspended rats and limb immobilization studies in dogs suggest that this compound is an effective countermeasure to bone loss. Alendronate is a member of the bisphosphonate family of drugs used to treat/prevent osteoporosis. We analyzed a commercially available product, Fosamax.

3. Radiation in Space

The risks to personnel in space from the naturally occurring radiation are generally considered to be one of the most serious limitations to human space missions. The consequences of exposure to radiation in space are considered a major limiting factor for long-duration interplanetary space travel for humans. Radiation doses in space may be hundreds of times greater than those experienced on earth. These energetically charged particles can kill cells in the body or cause mutations that may lead to cancer, cataracts, central nervous system damage or other diseases.

We have evaluated three novel peptide cancer biomarkers to demonstrate the utility of MALDI-TOF as a tool for the early detection of carcinomas. The advantage in using it for detection over these other methods is the robust nature of the analyzer. MALDI-TOF mass spectrometry is rapid, sensitive, and tolerant of salts in biological samples.

This work was supported by a grant from the National Space Biomedical Research Association.

PARTIALLY PREMIXED FLAME (PPF) RESEARCH FOR FIRE SAFETY

Ishwar K. Puri*, Suresh K. Aggarwal, Andrew J. Lock, University of Illinois at Chicago
Uday Hegde, National Center for Microgravity Research

ABSTRACT

Incipient fires typically occur after the partial premixing of fuel and oxidizer. The mixing of product species into the fuel/oxidizer mixture influences flame stabilization and fire spread. Therefore, it is important to characterize the impact of different levels of fuel/oxidizer/product mixing on flame stabilization, liftoff and extinguishment under different gravity conditions. With regard to fire protection, the agent concentration required to achieve flame suppression is an important consideration. The initial stage of an unwanted fire in a microgravity environment will depend on the level of partial premixing and the local conditions such as air currents generated by the fire itself and any forced ventilation (that influence agent and product mixing into the fire). The motivation of our investigation is to characterize these impacts in a systematic and fundamental manner.

UIC-NASA PPF Drop Rig

(a) General Description

The UIC-NASA PPF drop rig includes equipment for performing normal- and reduced-gravity partially premixed flame experiments. The rig is equipped with two fuel storage tanks that have a volume of 0.5 L and can be filled to a maximum pressure of 250 psi. Various fuel, oxidizer, and diluent combinations can be stored in these tanks. For safety reasons, the mixtures utilized are outside the flammability limits. Both the inner and outer flows are supplied independently by using mixtures in two separate tanks. The gas flows are metered by on board MKS mass flow controllers that have a maximum range of 5 L/min for the inner flow and 20 L/min for the outer flow and are rated accurate within 1% of their maximum ranges. A variety of burners can be enclosed within a standard NASA supplied chamber. For normal atmospheric tests in the 2.2 Second Drop Tower, the chamber is not sealed.

(b) Diagnostics:

Several diagnostic techniques have been employed in the rig to examine partially premixed flame behavior: (i) A color CCD video camera is used to record the transient visible structure of the flames in normal and microgravity. (ii) Temperature measurements have been made using a thermocouple rake. (iii) Global radiation measurements through the use of a thermopile type radiometer have provided valuable heat loss information. Other diagnostics currently being developed for implementation during the next research phase (2004-2006) are: (i) A rainbow schlieren deflectometry (RSD) system for accurate nonintrusive temperature measurements, and (ii) Light intensity attenuation system for measuring soot loading in the flame.

Example Results

(a) Fundamental Research on Partially Premixed Flames

Our investigations have characterized the behavior of partially premixed flames in microgravity environments through observations of the transient flame structure, temperature profiles, and global radiation. These measurements have supplemented by detailed numerical simulations that have been extensively validated. The gravity-dependent behavior of the flames was characterized in terms of flow dilation, buoyancy, and radiation heat loss. These results will be published in the *Proceedings of the 30th International Symposium on Combustion* [1].

(b) Fire Safety Research

* PI: 842 W. Taylor(MC251),Chicago, IL 60607, ikpuri@uic.edu, Ph:312-355-3317 Fx:312-413-0447

Experiments are underway to investigate flame liftoff and blowout in normal- and microgravity from a fire safety perspective. The premixed fuel-air streams are diluted with nitrogen in order to simulate the entrainment of inert product species into a fire. Nitrogen addition is found to raise the Schmidt number sufficiently to allow for flame liftoff, i.e., that product diluted flames may in some cases detach and cause secondary fires at some distance from the reactant source. The effects of the reactant stoichiometry and flow conditions are being investigated for these lifted flames. In all cases, we find lifted flames to be much more stable in microgravity due to the removal of buoyancy-induced instabilities. In most cases the flame moves closer to the reactant source in microgravity relative to its normal gravity location clearly illustrating that normal gravity results are inadequate to describe microgravity flames and, therefore, fires. Moreover, different fuel/air concentrations have different effects on flame liftoff under the influence of gravity. Preliminary results on these aspects have been presented at the 42nd AIAA Aerospace Sciences Meeting and Exhibit, Reno, Nevada, Jan. 5-8, 2004 [2].

Our experiments also consider the influence of other diluents on these lifted flames, such as carbon dioxide and argon. These diluents are the primary components of non-halon gaseous fire extinguishing agents. The two inert species influence the flames differently. One reason arises from their differing heat capacities. They also inhibit the burning intensity, since they increase the third body concentrations and, therefore, influence the combustion chemistry. The diluents have differing radiation emission properties, which impact the heat losses from these flames. Differences between normal- and microgravity flame lift off and blow off may also be impacted by buoyancy driven instabilities and the contribution of diluent species properties to instability characteristics, such as their amplitude. Our investigation hopes to elucidate these issues in a fundamental manner to facilitate the appropriate fire safety strategies.

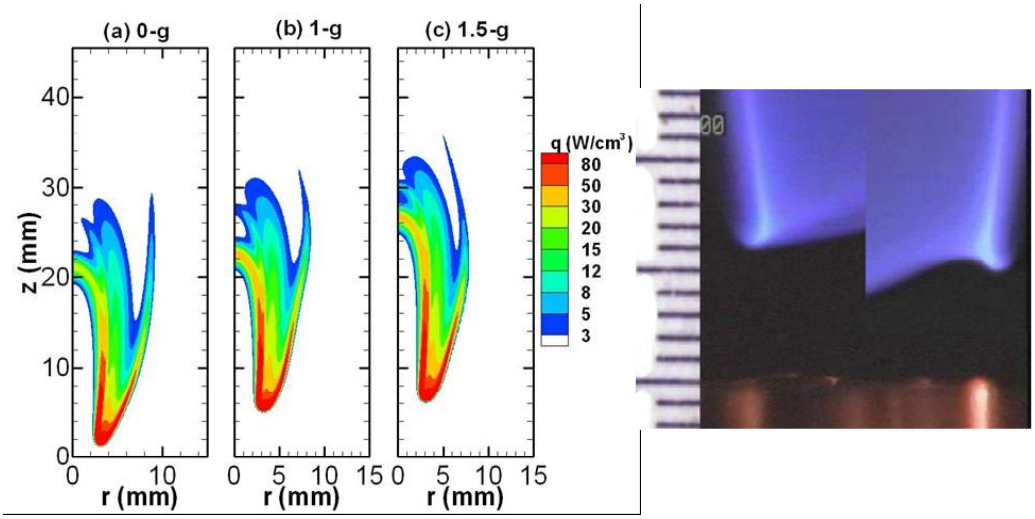

Figure 1: Influence of gravity on the liftoff height of a nonpremixed flame established on a coannular burner. Left: results of detailed numerical simulations. Right: normal- and microgravity experiments.

1 . Lock, A., Ganguly, R., Puri, I. K., Aggarwal, S. K., and Hegde, U., "Gravity Effects on Partially Premixed Flames: An Experimental-Numerical Investigation", to appear in *Proceedings of The Combustion Institute*, 30, 2004.

2. Lock, A., Qin, X., Ganguly, R., Puri, I. K., Aggarwal, S. K., and Hegde, U. "Lifted Partially Premixed Flames in Microgravity", *42nd Annual AIAA Aerospace Science Meeting and Exhibit*, Reno NV, January 2004

PPF Drop Rig

- Flexible and reliable piece of equipment.
- May be used in several microgravity facilities.
- Designed to investigate Partially Premixed Flames (PPFs)
- Flexible diagnostics platform.
- Designed and operated by Professor Ishwar K. Puri (VT), Professor Suresh K. Aggarwal (UIC), and Dr. Uday Hegde (NASA GRC).

- Equipped with two fuel storage tanks.
- Various Fuel/Oxidizer/Diluent combinations are used outside of flammability limits.
- Jet Flames investigated on slot burner and coaxial coflowing burners.
- Precision flow control, data acquisition, and control systems located on-board.

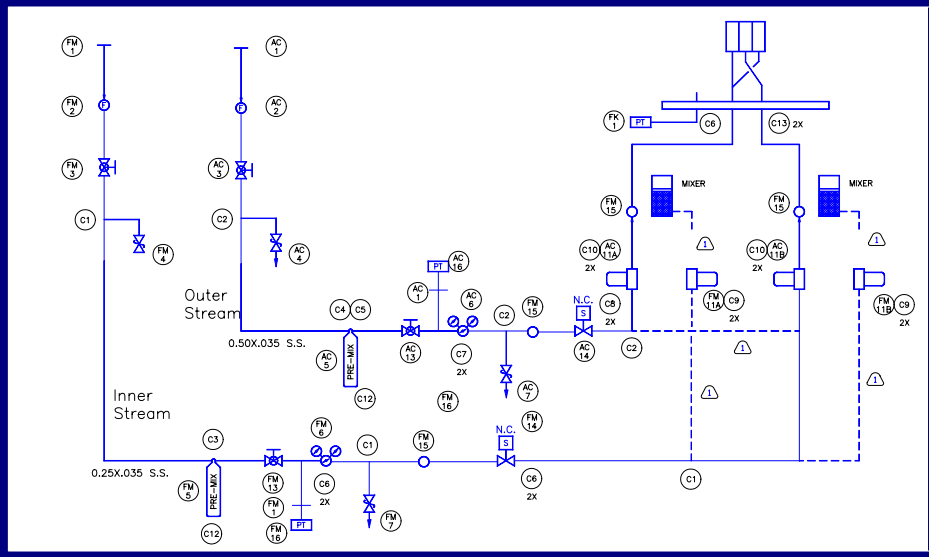

Drop Rig Diagnostics

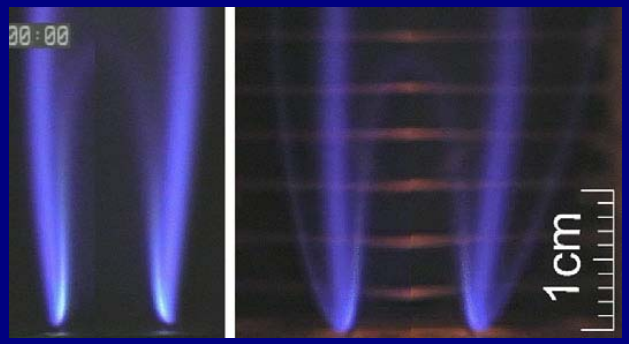

Color CCD Camera

- Focused on flame
- Video remotely recorded

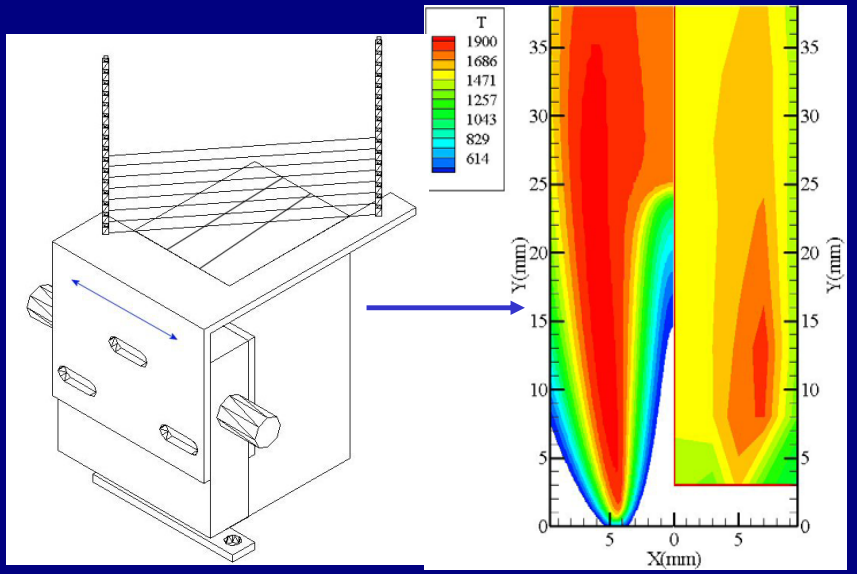

Thermocouple temperature measurements

- Eight type R thermocouples
- Onboard data acquisition
- Results provide direct comparison with simulation

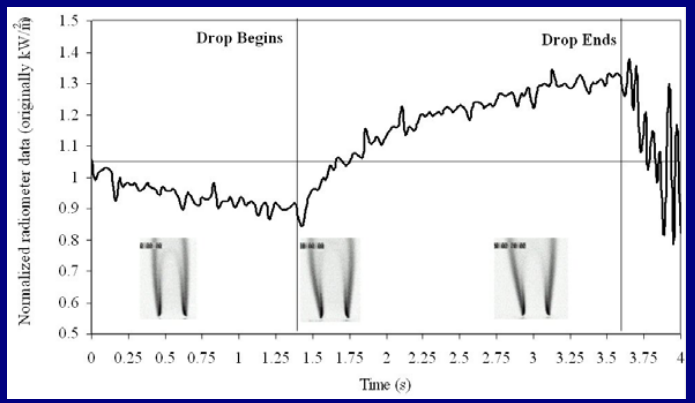

Radiometer global radiation measurement

- Thermopile type radiometer
- Onboard data acquisition via Tattletale
- Results provide insight into global radiation heat loss

Future Diagnostics

Rainbow Schlieren Deflectometry

- Non-intrusive temperature measurement
- Better temperature resolution
- Better temporal resolution
- Laboratory scale system working
- Rig design has been prototyped
- Next phase of rig development

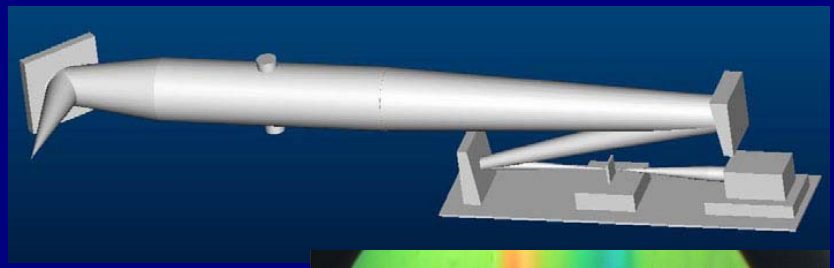

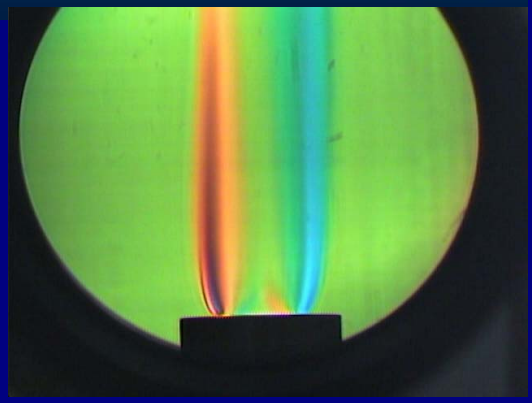

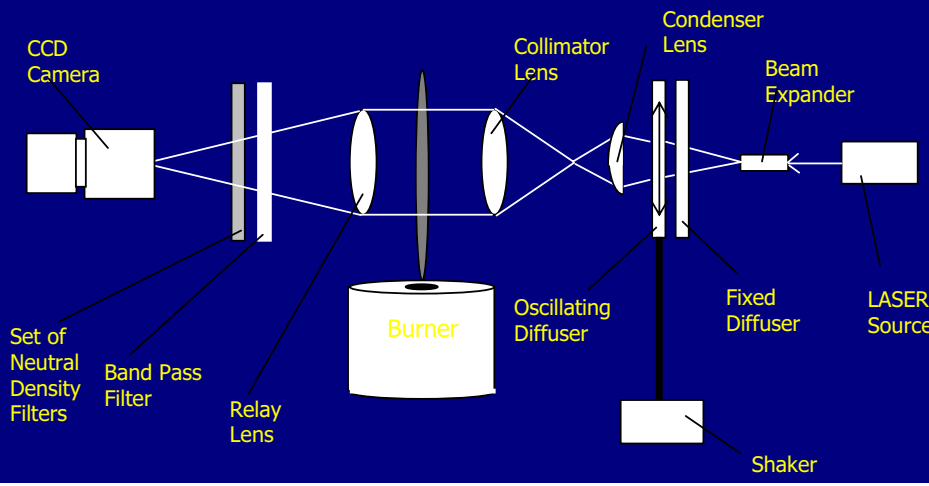

Soot Volume Fraction

- Non-intrusive soot measurement
- Provides 2-D field data
- Good temporal resolution
- Next phase of rig development

Partially Premixed Flames

Characteristics of PPFs

- Non-uniform fuel-air mixing
- Different flammability characteristics from those of fully premixed and nonpremixed
- Produce two or more reaction zones
- Occur naturally in many practical applications
- Partially premixed regions are formed by gaseous fuel leaks and in evaporating liquids

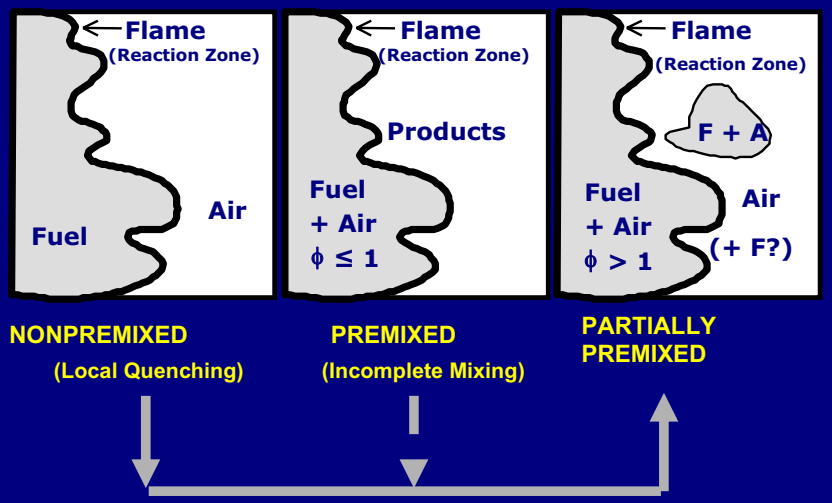

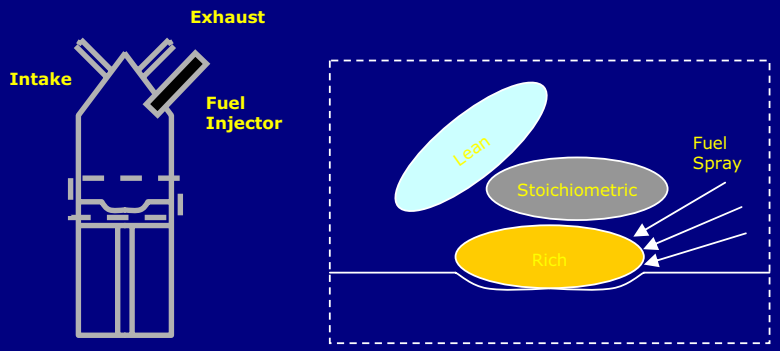

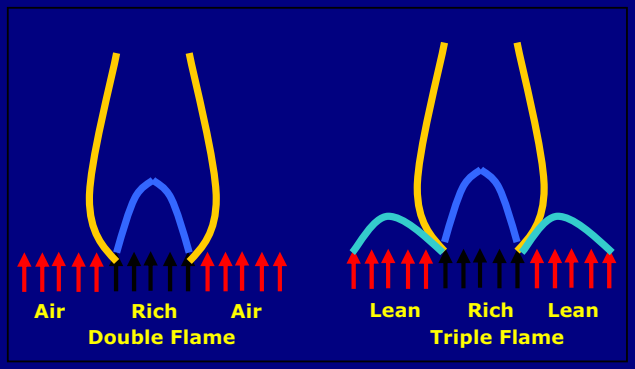

Adapted from Wehrmeyer et al., C&F, 128, 232 – 241 (2002)

Gravity Effect on attached PPFs

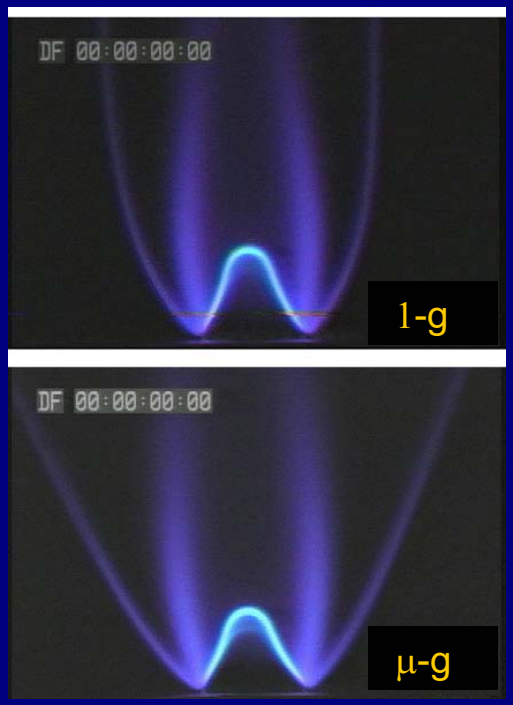

Flame Structure Changes

- Loss of buoyancy spreads flame, larger flame separation
- Tip opening occurs which may allow for partial oxidation components to escape

Flame Temperature Field Changes

- Temperature field spreads with reaction zones
- Mean temperature decreases
- Maximum temperature decrease

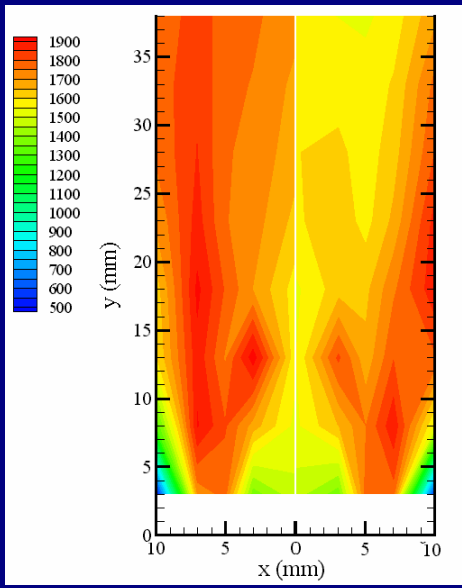

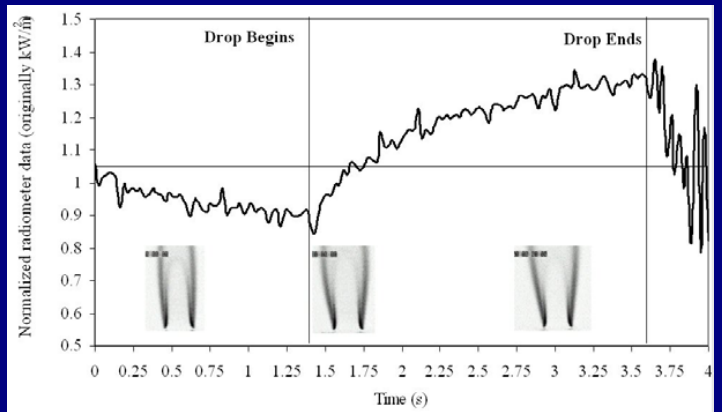

Flame Radiation Heat Loss

- Loss of buoyancy allows for longer residence time
- Flame volume occupies a larger volume
- The radiation heat loss from the flame increases substantially in microgravity

Fire Safety

Gas Leaks Produce Partially Premixed Regions

- Image shows raw rainbow schlieren image of a leaking pipe
- The varying color indicates varying degrees of premixedness
- The partial premixing creates a fuel concentration gradient

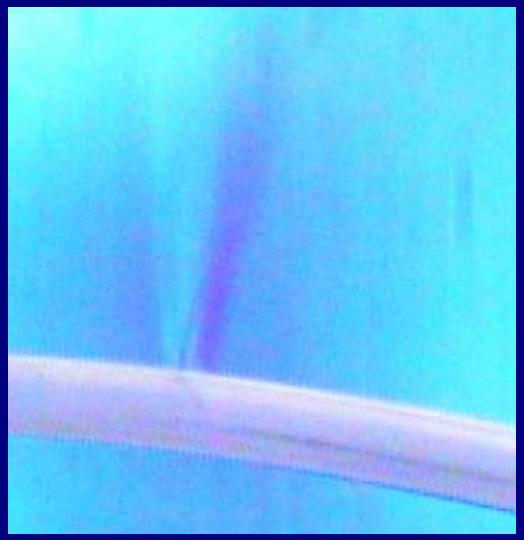

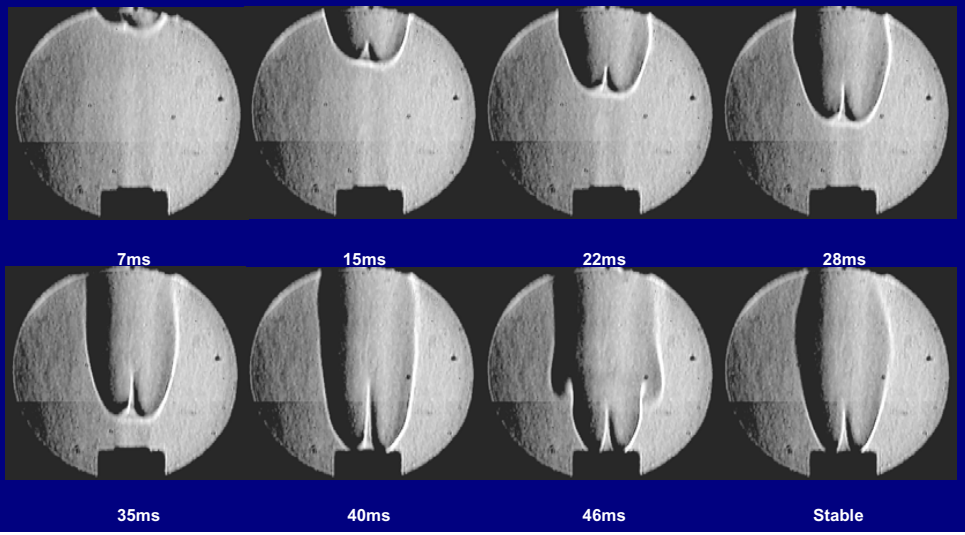

Ignition Above a Partially Premixed Jet

- Flame propagates back to source
- Buoyancy affects the propagation speed
- The flame propagates faster in microgravity

Lifted PPFs

ϕ_{in}=2.5, ϕ_{out}=0, V=50cm/s 25% N_2 Diluent

ϕ_{in}=2.5, ϕ_{out}=0, V=50cm/s 25% Ar Diluent

ϕ_{in}=2.5, ϕ_{out}=0, V=50cm/s 20% CO_2 Diluent

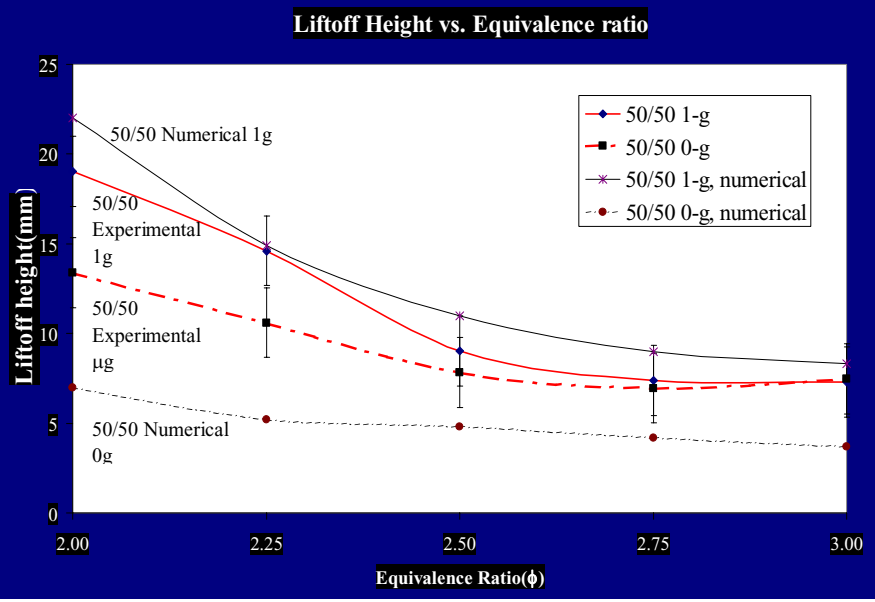

- Introduction of inert diluent raises Schmidt number and allows methane-air PPFs to be lifted
- Different diluents produce different effects
  - N_2, Ar, and CO_2 are common components of non-halon fire suppressants
- Reduction of gravity influences flame liftoff and propagation
- Microgravity flames, but which blow out in normal gravity, may be stabilized

Acknowledgements

- Dr. Kurt Sacksteder: Technical monitor
- Dr. Chun Choi: Rig design and fabrication
- Dan Giles: Experimental assistance
- NASA Grant: NCC3–688
- NASA GSRP: Student Funding

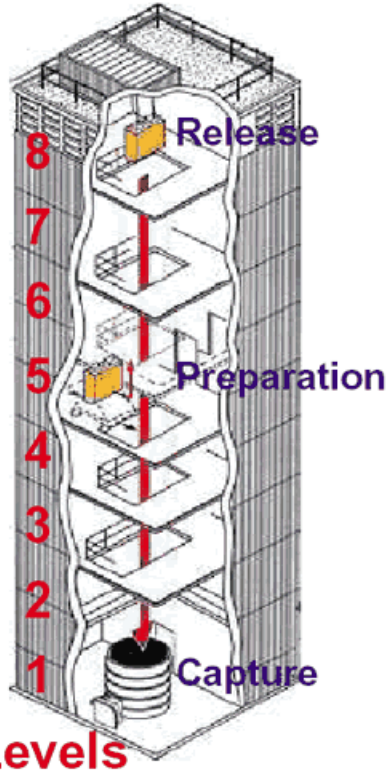

A cutaway drawing of the 2.2 Second Drop Tower, showing the levels on which an experiment package is prepared, released, and captured.

Authors

- **Ishwar K. Puri**
  - Professor and Head of Engineering Science and Mechanics, ***Virginia Tech*** – PI
- **Suresh K. Aggarwal**
  - Professor of Mechanical Engineering, ***University of Illinois at Chicago*** – Co-PI
- **Andrew Lock**
  - Ph.D. Student, ***University of Illinois at Chicago***
- **Uday Hegde**
  - Technical Monitor, ***NASA Glenn Research Center***

EFFECTS OF CHEMICALLY-PASSIVE SUPPRESSANTS ON LAMINAR PREMIXED HYDROGEN/AIR FLAMES

L. Qiao, C.H. Kim, and G.M. Faeth
Department of Aerospace Engineering
University of Michigan
Ann Arbor, Michigan, USA

Fundamental unstretched laminar burning velocities and flame response to stretch, as characterized by Markstein numbers, were considered experimentally and computationally for outwardly-propagating spherical laminar premixed flames. Experimental and computational conditions were as follows: fuel-equivalence ratios of 1.0 and 1.8; pressures of 0.5-1.0 atm; gaseous suppressant including argon, helium, nitrogen and carbon dioxide; and suppressant concentrations in the range of 0-40%, by volume. Predicted flame behavior was obtained from one-dimensional time-dependent numerical simulations treating variable property multi-component transport, with detailed hydrogen/oxygen chemical kinetics from Mueller et al. (1999). The present flames were sensitive to flame stretch, yielding values of unstretched-to-stretched laminar burning velocities in the range 0.5-1.5 for levels of flame stretch well below quenching conditions, e.g., for Karlovitz numbers less than 0.5. The present passive flame suppressants improved in performance in the following order: argon, helium, nitrogen, and carbon monoxide. This order reflects the capability of suppressants to promote quenching of the reaction zone by either increased specific heats or by enhanced conduction heat losses. Finally, the comparison between measurements and predictions was excellent for present conditions, which involved flames not too near quenching conditions where radiant heat losses were modest.

OBJECTIVES

Investigate the effect of chemically-passive flame suppressants on the properties of outwardly-propagating laminar premixed flames:

- Measure fundamental unstretched laminar burning velocities and flame response to stretch (Markstein numbers) for hydrogen/air flames containing various suppressants.
- Use the new measurements to evaluate contemporary models of flame structure based on detailed descriptions of both chemical kinetic mechanisms and transport properties.

Measurements and predictions considered outwardly-propagating spherical laminar premixed flames with helium, argon, nitrogen and carbon dioxide as suppressants.

FLAME/STRETCH INTERACTIONS

- The relationship between the laminar burning velocity, S_L, and the flame stretch, K, is found using the local-conditions hypothesis as follows:

$$S_{L\infty}/S_L = 1 + MaKa$$

where

S_L, $S_{L\infty}$ are the stretched and unstretched values of S_L.

Ma is the Markstein number, L/δ_D.

Ka is the Karlovitz number, KD_u/S_L^2.

and

δ_D is the characteristic flame thickness, D_u/S_L.

D_u is the mass diffusivity of the fuel in the unburned gas.

- Flame stretch interactions can be found from observations of the variation of flame radius as a function of time for freely-propagating spherical flames:

$$S_L = (\rho_b/\rho_u)\,dr_f/dt \qquad K = (2/r_f)\,dr_f/dt$$

where

ρ_b, ρ_u are the densities of the burned and unburned gas.

r_f is the radius of the flame.

EXPERIMENTAL METHODS

- Motion picture shadowgraphs indicated flame stability, rates of propagation and stretch.
- Minimum ignition energies were used to minimize ignition disturbances.
- Measurements were limited to r_f = 5-30mm to provide thin, constant-pressure flames.

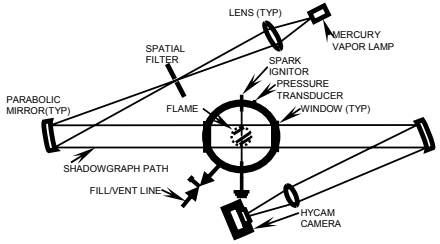

RESULTS AND DISCUSSION

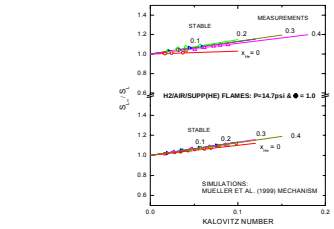

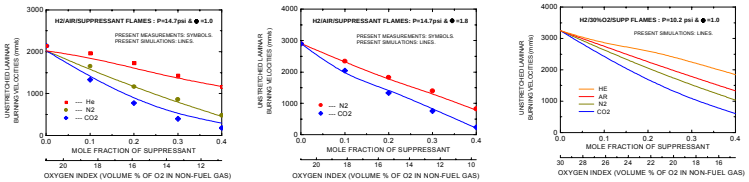

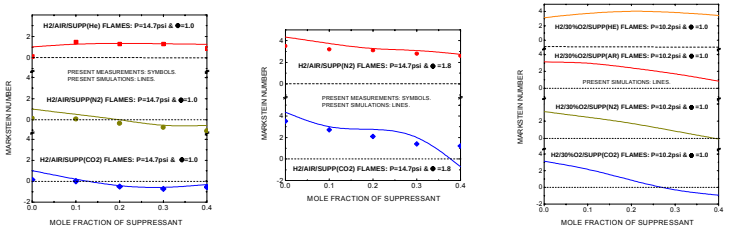

- The predictions of $S_{L\infty}$ and Ma are in excellent agreement with measurements.
- Flame/stretch interactions are substantial for H2/air flames ($S_{L\infty}/S_L$ = 0.5-3.0) but correlate compactly using the local-conditions hypothesis.
- Chemically-passive suppressants increase in effectiveness in the order He, Ar, N2 and CO2, which mainly reflects their progressively increasing specific heats and decreasing thermal conductivities.
- Addition of suppressants generally cause Markstein numbers to decrease which tends to reduce suppressant effectiveness by promoting preferential-diffusion instabilities.

FUTURE WORK

Future work will involve direct measurements of flame extinguishment properties at microgravity:

- Absence of buoyant motion makes fires harder to suppress in spacecraft.
- Numerical simulations are not reliable near low-gravity flammability limits where radiant heat losses affect suppression conditions.

DYNAMIC WETTING OF ROOM TEMPERATURE POLYMER MELTS: DEVIATIONS FROM NEWTONIAN BEHAVIOR

Enrique Ramé
National Center for Microgravity Research

We examine the dynamic wetting of two simple, room temperature polymer melts, polystyrene and polyisobutylene, by observing the liquid-vapor interface formed on the outside of a silica surface forced into a bath of the test fluid at controlled rates. The dynamic interface shapes of these fluids deviate from the prediction of models that include only Newtonian flow behavior. Specifically, near the contact line the fluid interface curvature is enhanced compared to the Newtonian fluid having the same shear viscosity and static wetting behavior. This observation is surprising because neither elasticity nor any other non-Newtonian behavior is detected for these materials using standard rotational rheometry. To probe the cause of the deviation further, we observe the interface shape of analogous model fluids having measurable elasticity in the rheometer and show that elasticity causes qualitatively similar, although larger, deviations from Newtonian behavior. This study demonstrates that fluids which appear Newtonian in standard rheometric characterization may have wetting behavior which deviates from purely Newtonian. We may expect these deviations to appear not only in the interface shape near the moving contact line but also in such key properties as spontaneous spreading times and in flows which control coating processes.

NASA/CP—2004-213205/VOL2

Understanding Material Property Impacts on Co-Current Flame Spread: Improving Understanding Crucial for Fire Safety

Ali S. Rangwala [A], Steven G. Buckley [A] and Jose L. Torero [B]

[A] *Department of Mechanical and Aerospace Engineering, University of California, San Diego, CA*

[B] *School of Engineering and Electronics, University of Edinburgh, Scotland, UK.*

UCSD Jacobs | Mechanical and Aerospace Engineering

Introduction

The prospect of long-term manned space flight brings fresh urgency to the development of an integrated and fundamental approach to the study of material flammability. Currently, NASA uses two tests, the upward flame propagation test and heat and visible smoke release rate test, to assess the flammability properties of materials to be used in space under microgravity conditions. The upward flame propagation test can be considered in the context of the 2-D analysis of Emmons (1956)[1]. This solution incorporates material properties by a "mass transfer number," B in the boundary conditions, given by.

$$B = \frac{(1-\chi)(\Delta H_C Y_{O_2,\infty}) - Cp_\infty (T_{ig} - T_\infty)}{\Delta H_P + Q_C}$$

In this expression for B, the numerator denotes the amount of heat release and the denominator represents the amount of heat needed to gasify the fuel; hence larger values of B represent a greater potential driving force for combustion and a greater potential flammability. Experimental and theoretical calculations of the B number, however, don't give similar results. The primary reason for this appears to be air entrainment, which is not accounted for in the Emmons 2-D model. Current experimental and analysis work aims to provide a more solid foundation for the prediction of material property influence on flammability.

[1] H. Emmons, Z. angew. Math. Mech. 36 (1-2) (1956) 60-71.

Experiment

- Measurements of flame stand-off distance and pyrolysis length enable determination of B in a configuration analogous to NASA's flame spread test (Figures 1, 2, 5)
- Particle image velocimetry measurements illustrate air entrainment from the 3rd dimension, this has been verified using the Fire Dynamic Simulator Code from NIST (Figure 3, 4).

Experimental setup

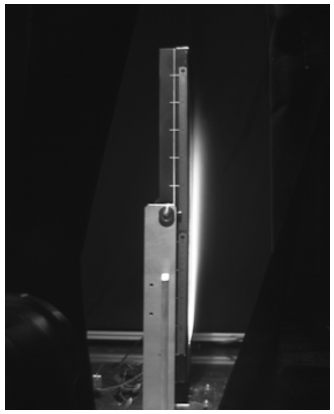

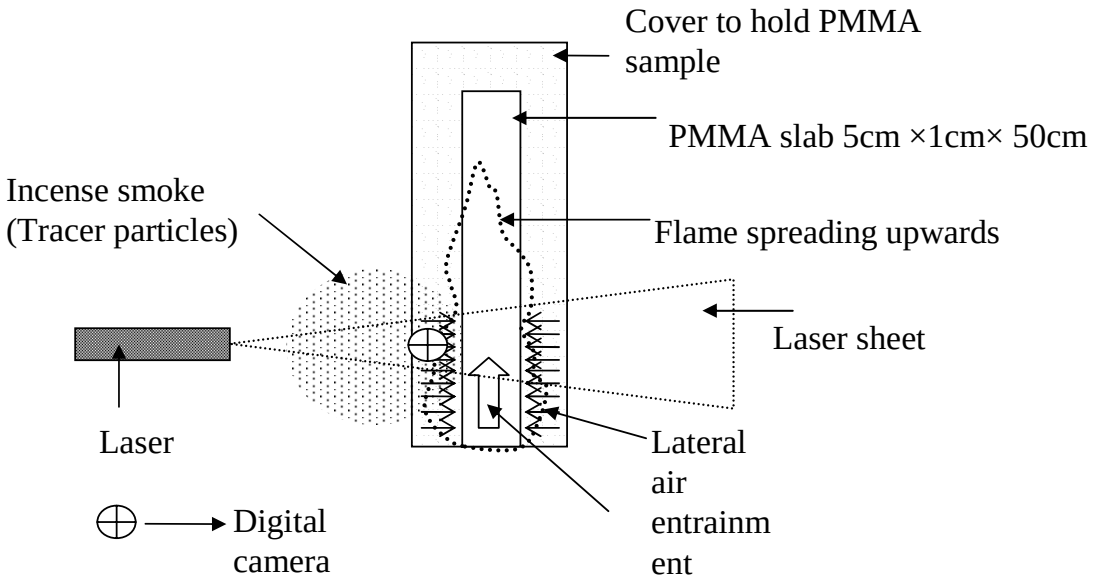

***Fig 1, 2*:** Experimental set up to measure stand off distance is shown by the picture on left hand side. The right hand side above shows the particle image velocimetry (PIV) set up.

Typical stand-off distances measured as a function of time

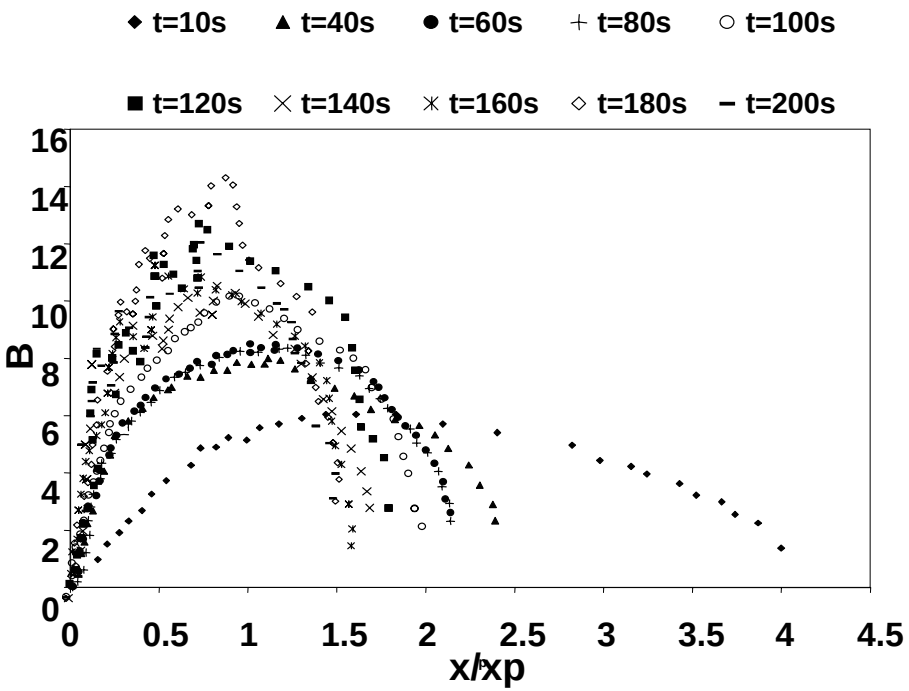

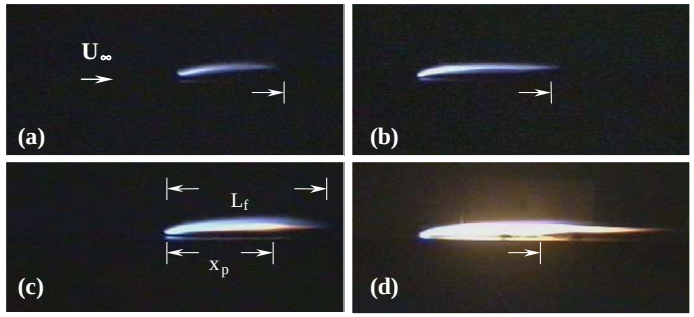

Significance/Findings

The two-dimensional classical boundary layer solution of Emmons[1] is insufficient to describe the buoyantly-driven flame propagation investigated here due to the influence of air entrainment in the 3rd dimension. However, this does not invalidate the significance of the B number or the importance of material properties on flame spread.

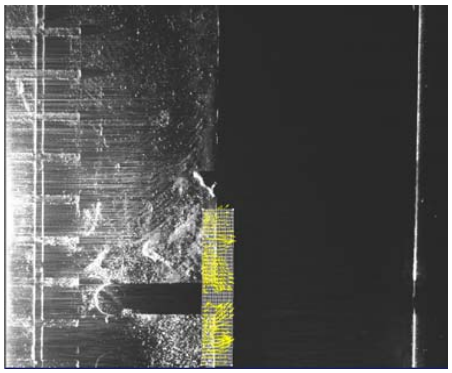

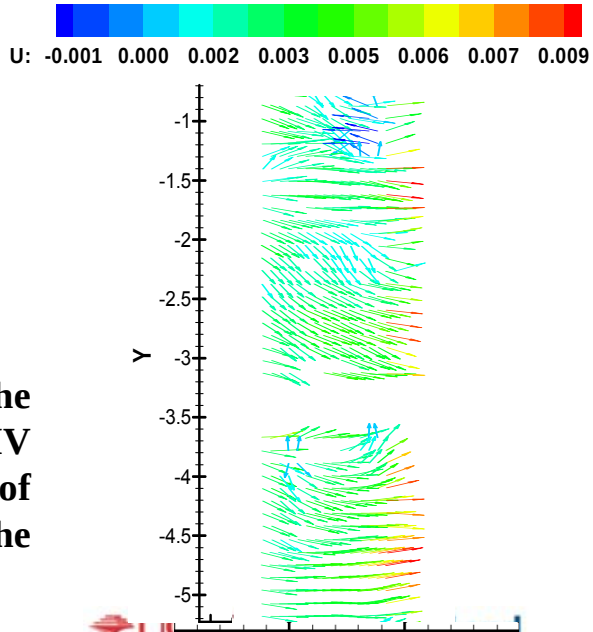

***Fig 3*: Above: the fuel, with the yellow square on the edge of the fuel showing the location of the PIV measurements. The PIV measurements (right) illustrate entrainment from the side of the fuel: Average velocity is 7-10 mm/s at 4 to 5 mm from the surface of the fuel.**

Jacobs | Aerospace Engineering

Experimental and FDS results

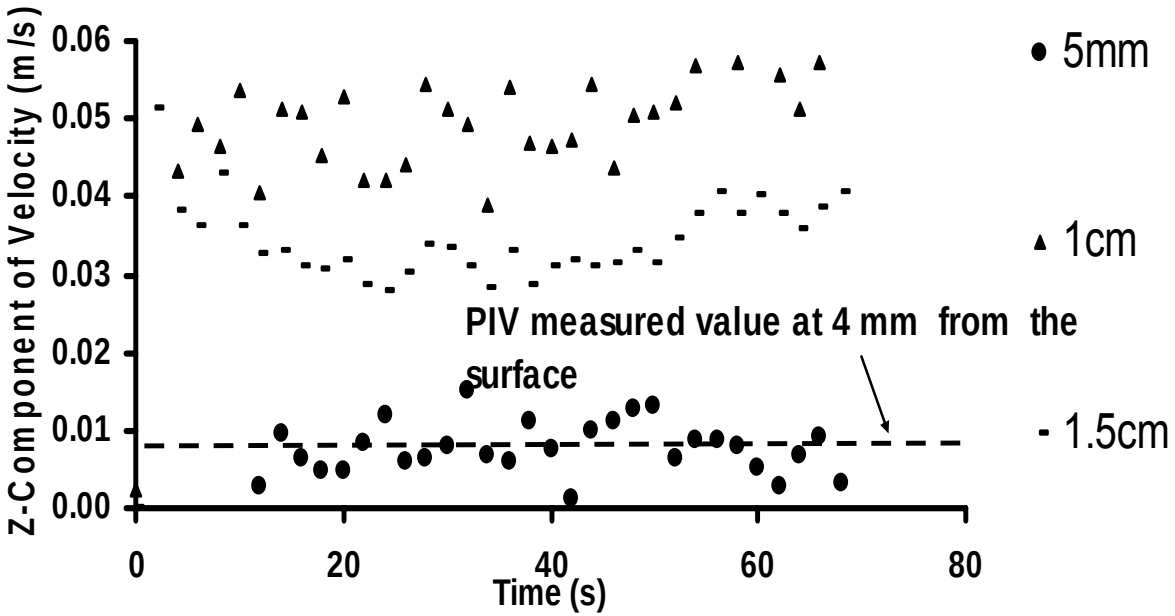

***Fig 4*: The lateral entrainment velocity predicted by FDS (fire dynamic simulator). As the distance from the surface increases the lateral entrainment velocity increases, reaching a maximum value at about 1 cm from the surface before decreasing. The entrainment velocity of 7-10 mm/s we measured from our experiments was a distance of between 4 to 5 mm from the surface of the fuel in good agreement with FDS.**

***Fig 5*: The flame shape has a direct relationship with the B number. Four of the curves with similar shapes are from theory, while the red curve shows the experimentally measured flame shape. The experimentally-determined B number should be a constant, but it is not. The evolution of the B number obtained from the stand off distance shows that theory and experiment don't match.**

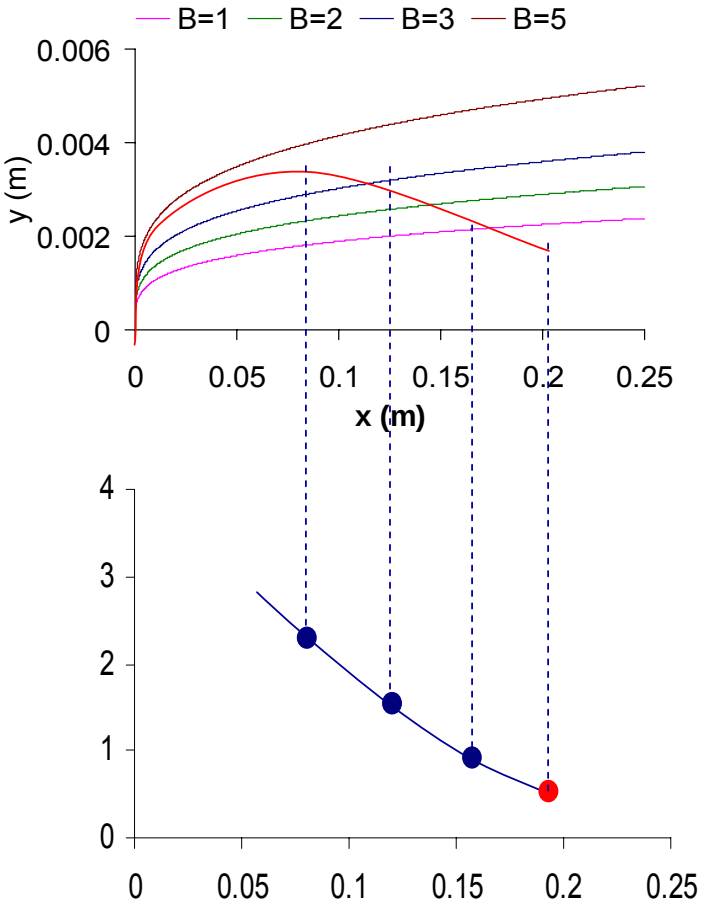

Conclusions to date

- **Lateral flame spread has a significant impact on the upward flame spread problem under study. The traditional Emmons solution is not able to capture the impact of flow in this 3rd dimension and thus modifications are required to apply theory to this problem.**
- **Material properties, such as those embodied in the mass transfer number B, should play a vital role in our understanding of flammability and flame spread**

Continuing Work

- **New experiments are planned to better examine the linkage between the material properties, B number, and flammability.**
- **Direct numerical modeling of the experiments to better quantify flow field.**
- **Analytical solution of the flow in the third dimension**

Acknowledgements

NASA Fire Safety Program of the Bioastronautics Initiative: Grant #NAG-32568

NASA technical contact: Dr. Gary Ruff

Experimental assistance: Dr. Mickey Coutin

STUDY OF CO-CURRENT AND COUNTER-CURRENT GAS-LIQUID TWO-PHASE FLOW THROUGH PACKED BED IN MICROGRAVITY

Shripad T. Revankar and Xiangcheng Kong
School of Nuclear Engineering, Purdue University, West Lafayette, IN 47907

ABSTRACT

The main goal of the project was to develop experiments to obtain data and develop models on the co-current and counter-current gas-liquid two-phase flow through a packed bed in microgravity and characterize the flow regime transition, pressure drop, void and interfacial area distribution, and liquid hold up.

An experimental and analytical modeling program for the study of co-current air-water two-phase down flow in a packed column was developed. A detailed survey of the literature was performed on two-phase flow in packed columns. The literature shows only one set of study from Glenn Research Center NASA is available on two-phase flow in packed bed under microgavity conditions. A large amount of effort was put in the development of instrumentation for the local and global measurement in the packed bed. A two point conductivity probe for the measurement of void fraction in the bed at pore level, a film thickness probe for the measurement of film thickness and drying characteristics of the packing, and a bed wise impedance meter for bed wise void measurement were developed. These probes were calibrated and plans were made for the installation of these probes in the packed bed. A packed bed test facility was designed and constructed. The bed is a cylindrical pipe of diameter 69 mm and height of 1.52m. the bed particles were glass spheres of diameter 6 mm. The bed porosity was 0.377.

Single phase flow characterization of the test loop was performed by flowing air and water in the bed and measuring bed pressure drop. From these measurements single phase constants in Ergun pressure drop equations were calculated.

Two Phase co-current down flow of air-water test were conducted. The flow regime in the bed was observed and recorded with high speed video camera. Flow regime map was developed. Five flow regimes were identified, trickling, wavy, transitional, pulsing and bubble flow. Pressure drop in the bed were also obtained for various flow regimes in the bed. An analytical model was developed for predicting flow regime transition from trickle to pulse mode using two-phase film model.

Packed bed reactors have potential space-based applications in bioregenerative food production, waste treatment, watering and nutrient transport in plant root systems, waste recovery, and extraction from planetary materials. The present research addresses the most important topic of HEDS-specific microgravity fluid physics research identified by NASA ‘s one of the strategic enterprises, OBPR Enterprise. The first two years are devoted to ground based flight definition experimental and modeling program. During the next two years microgravity flight tests are carried out using the ground-based parabolic flight research aircraft.

Reference

Charpentier, J. C., Favier M., 1975, Some liquid holdup experimental data in trickle-bed reactors for foaming and nonfoaming hydrocarbons, *AIChE J.*, Vol. **21**, pp. 1213-1218.Chou T. S., Worley

Jr. F.L., Luss D., 1977, Transition to pulsed flow in mixed-phase co-current downflow through a fixed bed, *Ind. And Eng. Chem., Proc. Design and Dev*., Vol. **16**, pp. 424-429.
Drinkenberg A.A., Blok J. R., Varkevisser J., 1983, Transition to pulsing flow, holdup and pressure drop in packed columns with co-current gas-liquid downflow, *Chem. Eng. Sci.*, **38**, pp.687-699.
Sato Y., T. Hirose, 1973, Flow pattern and pulsation properties of cocurrent gas-liquid downflow in packed beds, *J. Chem. Eng. Jpn.*, **6**, pp. 315-319.

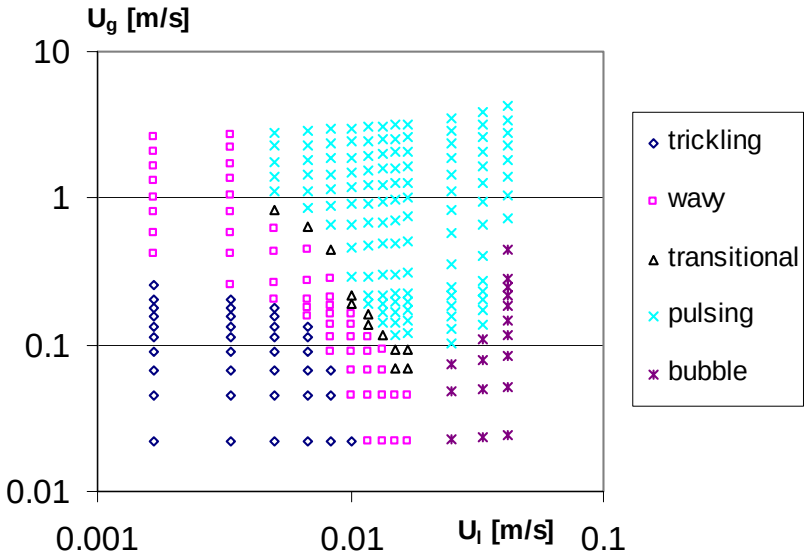

Figure 1 Flow regime map for packed bed of diameter 0.07 m and bed porosity 0.38, air-water co-current downward flow, spherical packing of diameter 6mm

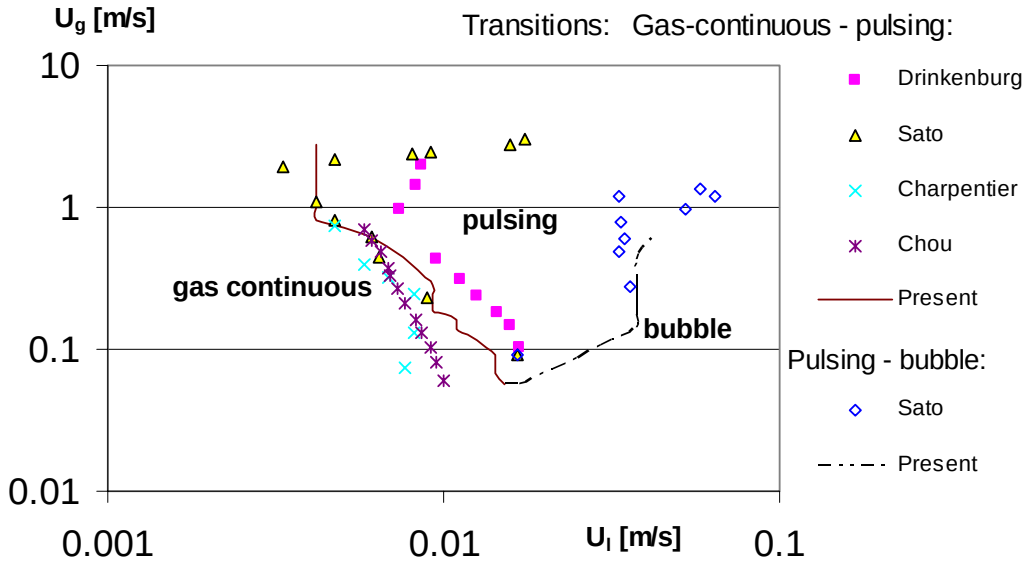

Figure 2. Comparison of flow regime map with data of Chou (1977), Drinckenburg (1983), Sato (1973) and Charpentier (1975).

EFFECTS OF HEAT FLUX, OXYGEN CONCENTRATION AND GLASS FIBER VOLUME FRACTION ON PYROLYSATE MASS FLUX FROM COMPOSITE SOLIDS

D.B. Rich,[1] C.W. Lautenberger,[1] Z. Yuan,[2] and A.C. Fernandez-Pello[1*]
[1]University of California, Department of Mechanical Engineering, Berkeley, 94720 CA USA
[2]NASA Glenn Research Center; Cleveland, OH, 44135 USA
[*]ferpello@me.berkeley.edu

Experimental work on the effects of heat flux, oxygen concentration and glass fiber volume fraction on pyrolysate mass flux from samples of polypropylene/glass fiber composite (PP/G) is underway. The research is conducted as part of a larger project to develop a test methodology for flammability of materials, particularly composites, in the microgravity and variable oxygen concentration environment of spacecraft and space structures. Samples of PP/G sized at 30x30x10 mm are flush mounted in a flow tunnel, which provides a flow of oxidizer over the surface of the samples at a fixed value of 1 m/s and oxygen concentrations varying between 18 and 30%. Each sample is exposed to a constant external radiant heat flux at a given value, which varies between tests from 10 to 24 kW/m^2. Continuous sample mass loss and surface temperature measurements are recorded for each test. Some tests are conducted with an igniter and some are not. In the former case, the research goal is to quantify the critical mass flux at ignition for the various environmental and material conditions described above. The later case generates a wider range of mass flux rates than those seen prior to ignition, providing an opportunity to examine the protective effects of blowing on oxidative pyrolysis and heating of the surface.

Graphs of surface temperature and sample mass loss vs. time for samples of 30% PPG at oxygen concentrations of 18 and 21% are presented in the figures below. These figures give a clear indication of the lower pyrolysis rate and extended time to ignition that accompany a lower oxygen concentration. Analysis of the mass flux rate at the time of ignition gives good repeatability but requires further work to provide a clear indication of mass flux trends accompanying changes in environmental and material properties.

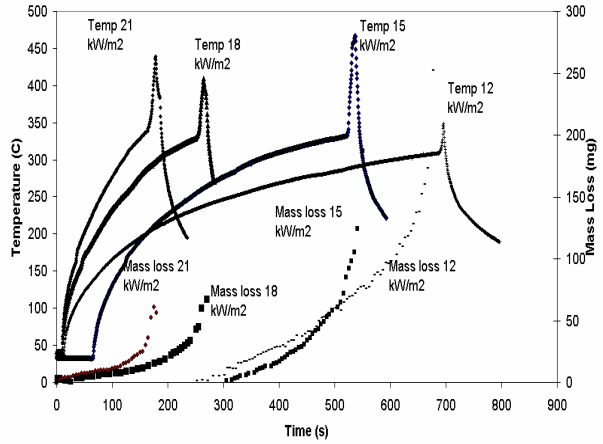

Fig. 1. Comparison of surface temperatures and mass loss values of PP/G 30% at 21% O_2 concentration for varying heat fluxes.

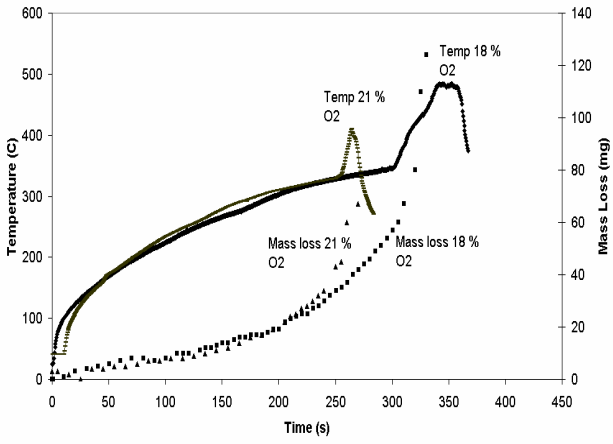

Fig. 2. Comparison of surface temperatures and mass loss values of PP/G 30% at 18 kW/m^2 for varying oxygen concentrations.

THE INTEGRATION OF A SMOKE DETECTOR MODEL WITH LARGE EDDY SIMULATION FIRE MODELING FOR PREDICTING SMOKE DETECTOR ACTIVATION IN MICROGRAVITY

Richard Roby, Wei Zhang, Glenn Gaines, Stephen Olenick, and Michael Klassen
Combustion Science & Engineering, Inc., 8940 Old Annapolis Road Suite L, Columbia, MD, 21045
Phone: 410-884-3266, Fax: 410-884-3267, Email: rroby@csefire.com

Jose L. Torero
Engineering and Electronics, The University of Edinburgh Edinburgh, EH9 3JL, United Kingdom

Fire safety on spacecraft, space stations, and in potential non-terrestrial environments (e.g. Mars) is an important consideration for any mission. Safety of the crews and spacecraft or space station, as well as continuation of the mission is dependent on adequate prevention, detection and suppression of fires in low- and micro-gravity environments. Early detection of fires relies on quickly identifying a fire signature by a detection device placed in an optimum location. Fire signatures and fire flows have been shown to be vastly different on spacecraft and in low-gravity environments; therefore, studies aimed at determining proper detector locations are necessary to provide adequate fire protection in low-gravity environments.

Since it is not practical to perform the large number of experiments necessary to determine optimal placement of detectors in the various low-gravity environments (e.g. the shuttle or varying racks and modules in ISS), a methodology must be developed which will allow for effective detector placement using a minimal number of experiments and a well-validated computational scheme. This study aims to integrate an algorithm that describes the response characteristics of the smoke detectors used in the ISS and the shuttle into a Large Eddy Simulation fire model (FDS [3]). The algorithm is restricted to two parameters, a dwell time and a mixing time, which was originally proposed by Cleary et al. [1]. A full scale room test with convective flows similar to the International Space Station is currently being conducted. Hence initially, experimental data from a multi-room compartment fire was used for validation. Overall, reasonable results were obtained when comparing the predictions to the experimental results. This result shows great potential of the smoke detector modeling combined with CFD (Computational Fluid Dynamics) fire modeling.

The two characteristic parameters that describe smoke model detector activation are: (1) the dwell time (or time lag δt) and the mixing time (τ). Both parameters are a function of the mass flow of smoke into the detector. The dwell time δt was defined as the mass of the smoke within the detector divided by the mass flow rate of smoke (Eq.2), and the mixing time τ was defined as the ratio between the mass of smoke in the sensing chamber divided by and the mass flow rate (Eq.3). Both can also be described by a power law dependence on velocity.

$$\delta t = \frac{L A \rho}{\dot{m}} = \frac{L}{u} \approx \alpha_1 u^{-\beta_1} \tag{1}$$

$$\tau = \frac{\rho V}{\dot{m}} = \frac{L'}{u} \approx \alpha_2 u^{-\beta_2} \tag{2}$$

where V is the sensing chamber volume (V=AL'), A is the effective area of the detector, $\dot{m}$ is the smoke flow rate into the detector and L is the characteristic distance represents smoke entry resistance and $\alpha_1, \alpha_2, \beta_1, \beta_2$ are proportionality constants that account for the detector geometry. The change of the mass of smoke in the sensing chamber volume should equal the difference of the mass fraction as it passes

though the distance L. If the initial mass fraction of smoke in the sensing chamber is zero, the mass fraction of smoke in the sensing chamber is given by:

$$Y_o(t) = \exp\left(-\int_0^t \frac{1}{\tau(t')}\,dt'\right)\left\{\int_0^t \left(\frac{1}{\tau(t')}\cdot \exp\left(\int_0^t \frac{1}{\tau(t')}\,dt'\right)\cdot Y_e(t'-\delta t)\right) dt'\right\} \quad (3)$$

where e represents the entrance of the model detector and o represents the sensing chamber. Y is the mass fraction of smoke.

In this validation case, the test geometry consisted of two compartments (2.4 m x 2.4 m x 2.4 m) connected by a corridor (4.9 m long with 2.4 m high ceiling) [2]. Ionization smoke detectors were used in this testing. In this study, the proportionality constants for ionization detectors [1] were used. A value of 7.6 m^2/g was used as the specific extinction coefficient, which is a typical value for a flaming fire.

Table 1 shows the comparison between experimental data and modeling results of the smoke model detector activation time. The experimental data was averaged from three independent test cases. Figure 1(a, b) provides the predictions of the external obscuration (%/ meter) and the predicted responses (internal obscurations) of the model detectors at five different detector locations. Work is currently ongoing to extend this technique to the detectors in use on the ISS and the Shuttle.

References:

[1] Cleary, T., Chernovsky, A. Grosshandler, W. and Anderson, M. (1999). "Particulate entry lag in spot-type-smoke detectors". Proceedings of the 6th international symposium 1999, pp 779-790.

[2] D'souza, V.T., Sutula, J.A., Olenick, S.M., Zhang, W. and Roby, R.J., (2002). "Predicting smoke detector activation using the fire dynamics simulator". Proceedings of 7th international symposium of fire safety science, 2002.

[3] Fire Dynamics Simulator (Version 4.0)–User's Guide, National Institute of Standards and Technology (NIST), NISTIR 6784. 2003 Ed.

Table 1.—Measured and predicted detector activation times(s) for experimental setup.

Detector	D# 1	D# 2	D# 3	D#4	D# 5
Experiment (sec)	14	31	43	64	60.1
Model Detector I1	18.8	14.1	50.6	50.1	60.1
Model Detector I2	19.0	14.1	52.2	50.6	59.9

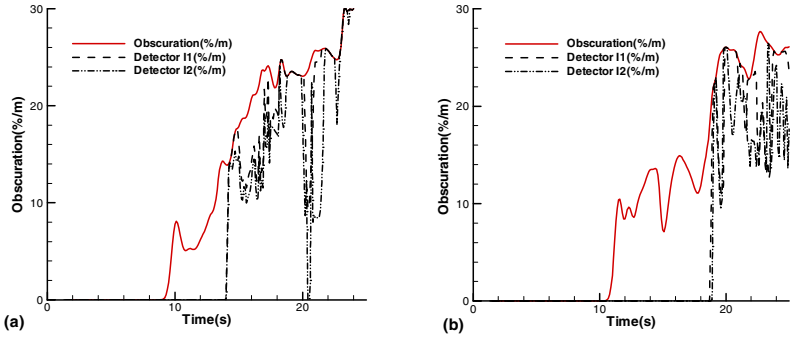

Figure 1.—Predicted obscuration (%/m) and detector (I1 & I2) responses in the fire room.

STUDY OF THE VON-KÁRMÁN VORTEX STREET CLOSE TO ONSET OF SHEDDING

Pedram Roushan and Xiao-Lun Wu
Department of Physics and Astronomy
University of Pittsburgh
Pittsburgh, Pennsylvania 15260

The Bénard-von Kármán vortex street is studied in a flowing soap film channel. The two-dimensional fluid flow in the film allows stable vortex streets to be generated and investigated over a broad range of Reynolds numbers, $10<Re<2000$. Unlike previous studies, which concentrated on the temporal velocity oscillations at a single point in the wake region, the current study focuses on the entire near-wake region using image analysis techniques. The envelope of the von-Kármán vortex street is analyzed for different rod diameters, which span more than two orders of magnitude in their diameters. The parameters that characterize the envelope of the vortex street, such as the growth rate and the saturation amplitude, are measured for different Reynolds numbers. It is found that all of the curves representing the envelope can be collapsed onto a single master curve, suggesting that the shape of the von-Kármán vortex street is universal, independent of Re. We construct a simple model that takes into account the energy transfer into vortices by periodic oscillations of transverse velocity fluctuations beneath the rod. This simple model not only explains the near wake shape of the von-Kármán vortex street, but also allows extraction of useful information about the wake, such as the kinetic energy injected into the fluid and the drag coefficient (C_D).

EVALUATION OF CO_2, N_2 AND HE AS FIRE SUPPRESSION AGENTS IN MICROGRAVITY

Gary A. Ruff and Michael Hicks
NASA Glenn Research Center

Richard Pettegrew
National Center for Microgravity Research

The U.S. modules of the International Space Station use gaseous CO_2 as the fire extinguishing agent. This was selected as a result of extensive experience with CO_2 as a fire suppressant in terrestrial applications, trade studies on various suppressants, and experiments. The selection of fire suppressants and suppression strategies for NASA's Lunar and Martian exploration missions will be based on the same studies and normal-gravity data unless reduced gravity fire suppression data is obtained. In this study, the suppressant agent concentrations required to extinguish a flame in low velocity convective flows within the 20-sec of low gravity on the KC-135 aircraft were investigated. Suppressant gas mixtures of CO_2, N_2, and He with the balance being oxygen/nitrogen mixtures with either 21% or 25% O_2 were used to suppress flames on a 19-mm diameter PMMA cylinder in reduced gravity. For each of the suppressant mixtures, limiting concentrations were established that would extinguish the flame at any velocity. Similarly, concentrations were established that would not extinguish the flame. The limiting concentrations were generally consistent with previous studies but did suggest that geometry had an effect on the limiting conditions. Between the extinction and non-extinction limits, the suppression characteristics depended on the extinguishing agent, flow velocity, and O_2 concentration. The limiting velocity data from the CO_2, He, and N_2 suppressants were well correlated using an effective mixture enthalpy per mole of O_2, indicating that all act via O_2 displacement and cooling mechanisms. In reduced gravity, the agent concentration required to suppress the flames increased as the velocity increased, up to approximately 10 cm/s (the maximum velocity evaluated in this experiment). The effective enthalpy required to extinguish flames at velocities of 10 cm/s is approximately the same as the concentrations in normal gravity. A computational study is underway to further evaluate these findings.

Assessment of CO_2, N_2, and He as Suppressants in Microgravity Environments

Conference-Workshop on

Strategic Research to Enable NASA's exploration Missions

June 22nd -23rd, 2004

Gary A. Ruff - *NASA Glenn Research Center*
Michael C. Hicks - *NASA Glenn Research Center*
Rick Pettegrew - *National Center for Microgravity Research*

Fire Suppression on ISS

Carbon Dioxide is the current suppressant of choice on the ISS. The requirements were developed based on NFPA 12 Regulations that specify that a 50% concentration by volume are required to extinguish smoldering fires (with a 20 minute hold). A concentration of 30% by volume was required to extinguish flaming fires. Carbon dioxide was selected through trade studies that evaluated suppressants based on:

- **Effectiveness on potential spacecraft fires**
- **Reliability**
- **Maintainability**
- **System Weight**
- **Required post-fire clean-up**
- **Compatibility with other spacecraft systems**
- **Toxicity of suppressant and/or post-fire suppression products**

These studies generally conclude that CO_2 and N_2 are close in acceptability with the first choice depending on the weighting of the above criteria. These studies also recommend use of a water-based suppressant should be used for smoldering fires.

Normal-gravity tests were conducted by Sircar *et al.* (1992) that evaluated CO_2, He, N_2, and Halon in a NASA STD 6001 Test 1 configuration (Upward Flame Propagation) with quiescent delivery of the suppressant mixture. Halon was the most effective followed by CO_2. N_2 and He were equally less effective.

ISS Portable Fire Extinguisher
(6 lbs of CO_2 at 850 psi; discharges in 45 sec)

Motivation and Objectives

- Fire response procedure on ISS dictates that ventilation flow is ceased and power removed after annunciation of a fire alarm
- Discharge of a fire extinguisher will induce flow with varying CO_2 concentration
- Effectiveness of these suppressants has never been evaluated in low-velocity convective flows (up to 10-15 cm/s) in microgravity
- Design of next generation, exploration spacecraft will ask the same questions with little new data

➢ Determine the effectiveness of the flow of CO_2, He, and N_2 to suppress fires in microgravity

➢ Conduct tests on the KC-135 on PMMA cylinders for a variety of suppressants and suppressant mixtures

Spacecraft Fire Safety Facility

- **Combustion Chamber**
  - (25.4 cm diam, 51 cm high)
- **Flows up to 17 cm/s**
  - Three mass flow controllers
    - Two 500 slpm
    - 2000 slpm
- **Pressure up to 3 atm**

Test Matrix and Samples

- Chamber Pressure = 1 atm
- Standard Air - 21% O_2, 79% N_2
- Rich Air - 25% O_2, 75% N_2
- Velocity: 1 – 10 cm/s

- 19.1 mm diam x 25.4 mm long PMMA cylinders
- Cartridge heater through center
- Surface and heater t/c

- Hot wire igniter
- Flow from bottom to top

Oxidizer	Suppressant	Concentrations (% vol)
Standard Air	CO_2	12.5%, 25%
	He	12.5%, 25%
	N_2	25%
Rich Air	CO_2	12.5%, 25%
	He	12.5%, 25%
	N_2	25%

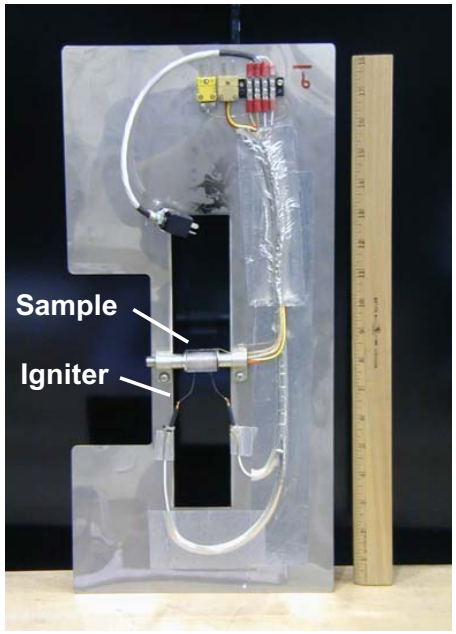

Sample card with sample and cartridge heater

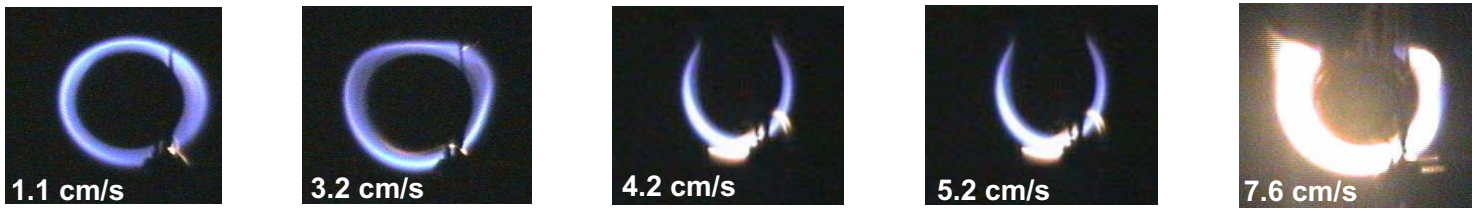

Typical low-g flames for 25% O_2, 75% N_2

Microgravity Results

CO_2, He, N_2 Suppressants

- **Suppressant mole fraction / mole fraction of O_2 as a function of velocity ...**
  - Extinguishment limits in slow flow regime (i.e., less than 10 cm/s) show dependence on velocity
  - Previous studies ...

CO_2 : $X_{CO2} / X_{O2} = 0.62$ (Prasad *et al.*)
$X_{CO2} / X_{O2} = 1.12$ (Takahashi *et al.*.)

He : $X_{He} / X_{O2} = 2.1$ (Takahashi *et al.*)

N_2: $X_{N2}/X_{O2}=2.92$ (Takahashi *et al.*)

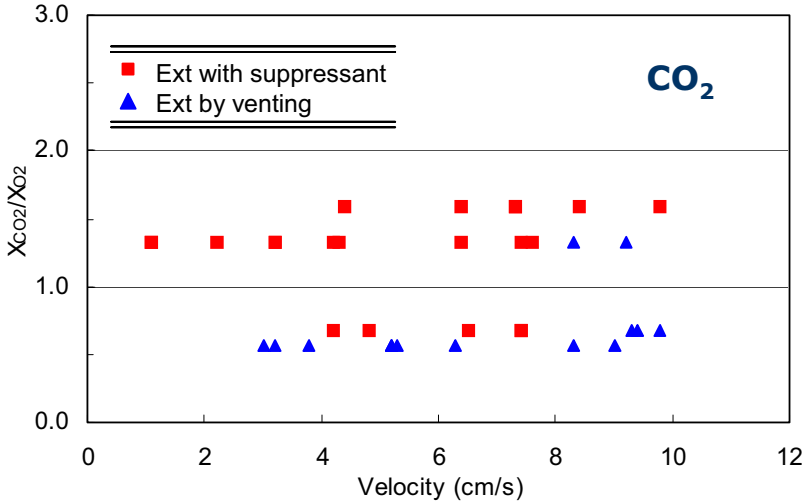

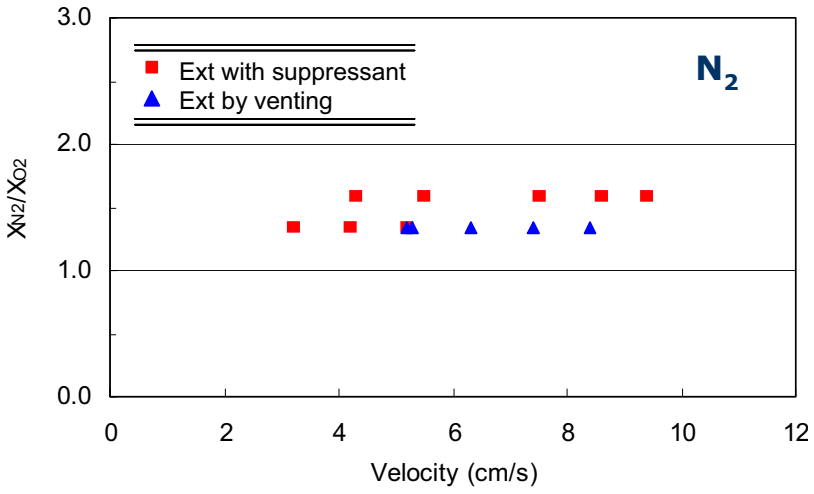

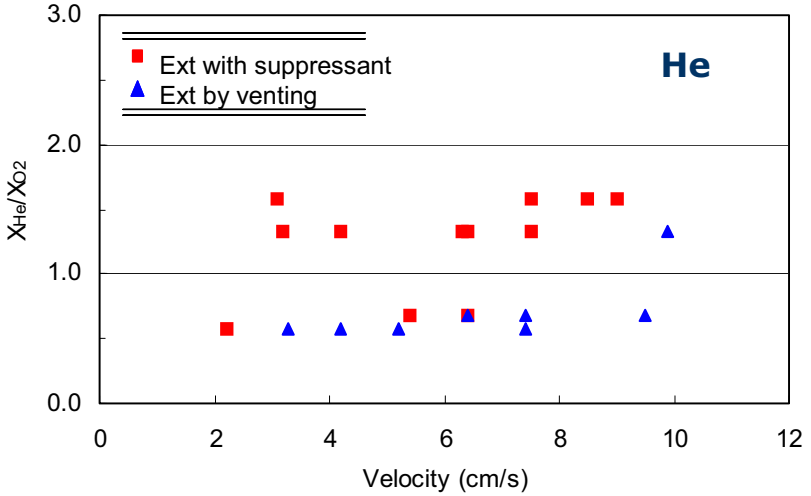

Effective Enthalpy/Mol O_2

- **Huggett (1969, 1973) proposed a "threshold" heat capacity above which organic fuels cease to burn**
  - Showed that at a "mixture" specific heat greater than 40 – 50 cal/C-mol O_2 a flame could not be sustained (at a pressure of 1.0 atm)
  - Determined from strained laminar diffusion flames
- **Sheinson *et al*. (1989) applied this concept to evaluate the physical and chemical performance of various suppressant mixtures**
  - Defined an effective mixture enthalpy as energy required to heat mixture from 298 K to 1600K

$$\Delta H' = \sum_i \frac{X_i}{X_{O2}} \int_{298}^{1600} Cp_i dT$$

- **Calculated the effective enthalpy/mol O_2 for each suppressant mixture**
- **Established a limiting velocity at which there was a transition in suppression characteristics**
  - Averaged bounding velocities
  - Plotted highest velocity tested if no transition was observed

Correlation with Effective Enthalpy

- Helium lies slightly below CO_2 and N_2 presumably because of higher thermal conductivity
- Microgravity flame on PMMA requires less suppressant to extinguish at lower velocities
- Normal gravity suppression is at 63.2 kcal/mol O_2

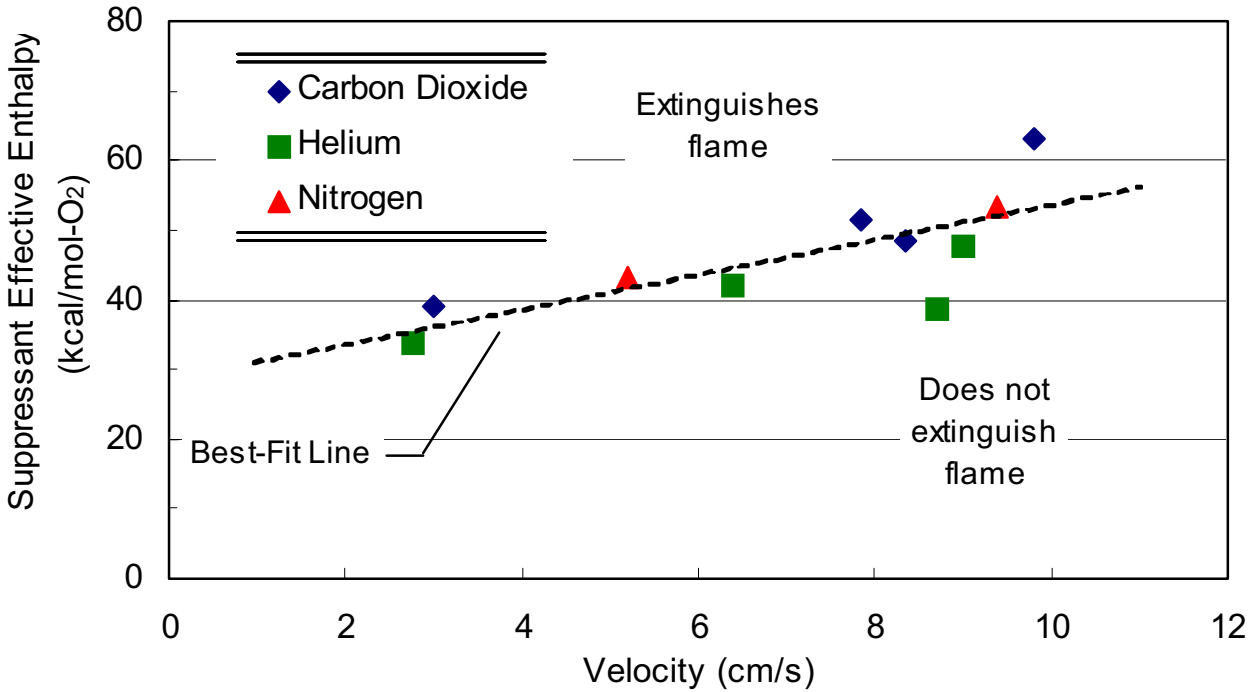

Conclusions

- **Higher suppressant concentrations are required to extinguish flames in microgravity as velocity increases**
  - Up to 10 cm/s investigated in this experiment
  - Effective enthalpy/mol-O_2 correlates limiting velocity fairly well
  - Effective enthalpy at 10 cm/s is nearly normal-gravity value
- **For these conditions, CO_2, N_2, and He all act as passive suppressants**
  - O_2 replacement and cooling
- **Procedures on ISS are reasonable for flaming fires**
  - Specifications for CO_2 concentrations are high enough for smoldering fires but no provision for hold time
  - Use of water-based foam in U.S. modules is not “recommended”

Future Work

- **Continue modeling of the CO_2, He, and N_2 suppression results**
  - Can the suppression and limiting velocity boundaries be duplicated?
- **Complete analysis of partial gravity suppression data**
  - Data obtained for CO_2 at 0.1-g_o, 0.17-g_o(Lunar), 0.38-g_o (Martian), and 0.5-g_o

VISUALIZATION OF ELECTRIC FIELD EFFECTS ON NUCLEATE AND FILM BOILING

Subramanian Sankaran and Jeffrey S. Allen
National Center for Microgravity Research
NASA Glenn Research Center
Cleveland, Ohio

Film boiling is the phenomena whereby a layer of vapor completely covers a heated surface resulting in extreme surface temperatures; a potentially catastrophic condition. Film boiling can easily occur in microgravity and in microscale systems because the characteristic dimension of the vapor bubble is much larger than that of the heater. Electric fields may be employed to provide an effective means to bring liquid into contact with the heater surface thereby maintaining low surface temperatures at high heat fluxes.

Nucleate and film boiling of PF-5060 over a 127 micrometer diameter electrically heated wire are observed. High resolution, high speed imaging show the nature of nucleate and film boiling and the enhancement to heat transfer afforded by the use of electric fields. Preliminary experiments conducted at 12 C and 27 C subcooling levels showed increases in the q_max and q_min heat flux levels by up to 50% when using 2kv across the heater and the screen, compared to the heat fluxes without electric fields. Using electric fields 1) we can enhance the nucleate boiling heat transfer (increase q_max), 2) make the transition, from nucleate boiling to film boiling at the critical heat flux, a slower and controllable process, and 3) destabilize the vapor film earlier and achieve nucleate boiling (increased q_min is a desirable safety/recovery characteristic).

Visualization of Electric Field Effects on Nucleate and Film Boiling

Subramanian Sankaran and **Jeffrey S. Allen**
National Center for Microgravity Research
NASA Glenn Research Center, Brookpark OH

Film boiling is the phenomena whereby a layer of vapor completely covers a heated surface resulting in extreme surface temperatures; a potentially catastrophic condition. Film boiling can easily occur in microgravity and in microscale systems because the characteristic dimension of the vapor bubble is much larger than that of the heater. Electric fields may be employed to provide an effective means to bring liquid into contact with the heater surface thereby maintaining low surface temperatures at high heat fluxes. Nucleate and film boiling of PF-5060 over a 127 micrometer diameter electrically heated wire are observed. High resolution, high speed imaging show the nature of nucleate and film boiling and the enhancement to heat transfer afforded by the use of electric fields.

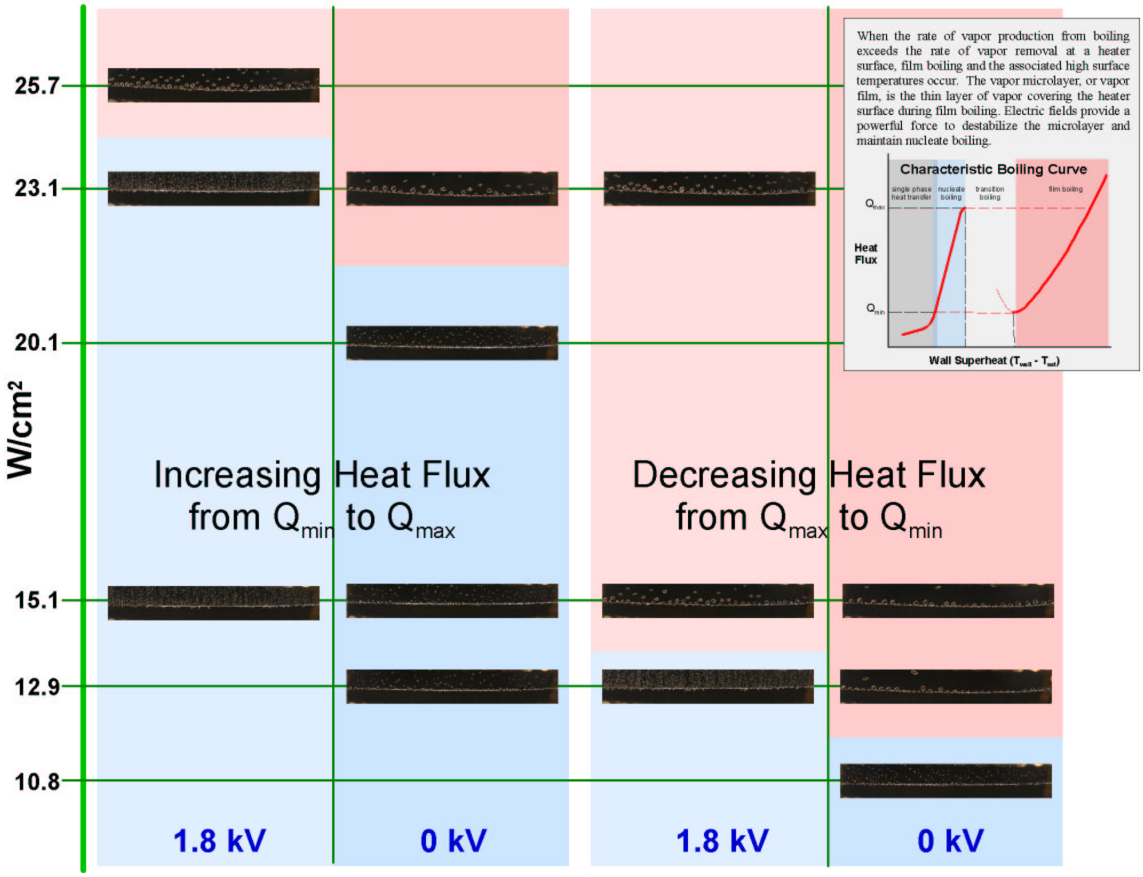

Experiment Setup

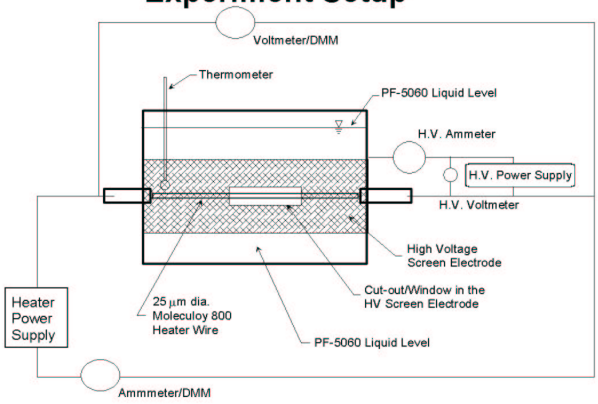

Co-Existence Boiling via 1.8 kV

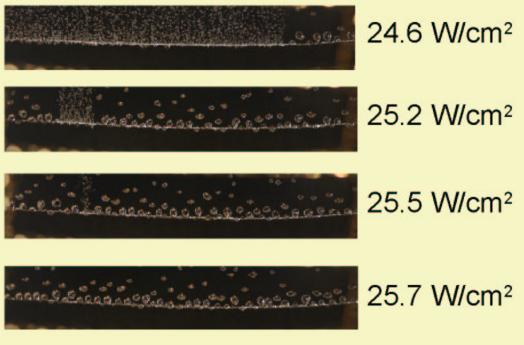

NICKEL-COATED ALUMINUM PARTICLES: A PROMISING FUEL FOR MARS MISSIONS

Evgeny Shafirovich and Arvind Varma
Purdue University, School of Chemical Engineering
480 Stadium Mall Drive, West Lafayette, IN 47907-2100

Combustion of metals in carbon dioxide is a promising source of energy for propulsion on Mars. This approach is based on the ability of some metals (e.g. Mg, Al) to burn in CO_2 atmosphere and suggests use of the Martian carbon dioxide as an oxidizer in jet or rocket engines [1, 2]. Analysis shows that CO_2/metal propulsion will reduce significantly the mass of propellant transported from Earth for long-range mobility on Mars and sample return missions. Recent calculations for the near-term missions indicate that a 200-kg ballistic hopper with CO_2/metal rocket engines and a CO_2 acquisition unit can perform 10-15 flights on Mars with the total range of 10-15 km, i.e. fulfill the exploration program typically assigned for a rover [3].

Magnesium is currently recognized as a candidate fuel for such engines owing to easy ignition and fast burning in CO_2 [1, 2, 4]. Aluminum may be more advantageous if a method for reducing its ignition temperature is found. Coating it by nickel is one such method. It is known that a thin nickel layer of nickel on the surface of aluminum particles can prevent their agglomeration and simultaneously facilitate their ignition, thus increasing the efficiency of aluminized propellants [5, 6].

Combustion of single Ni-coated Al particles in different gas environments (O_2, CO_2, air) was studied using electrodynamic levitation and laser ignition [7]. It was shown that the combustion mechanisms depend on the ambient atmosphere. Combustion in CO_2 (see Fig. 1) is characterized by the smaller size and lower brightness of flame than in O_2, and by phenomena such as micro-flashes and fragment ejection (see image 4). The size and brightness of flame gradually decrease as the particle burns.

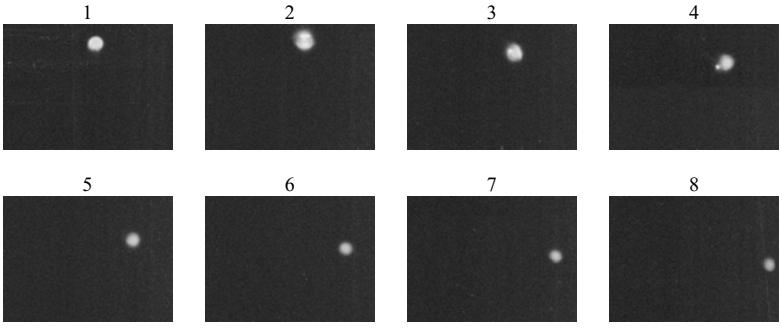

Figure 1: Combustion of Ni-clad Al particle in CO_2.
(0.5 μs between images, viewing area 1236 x 921 μm)

Remarkably, burning of Ni-clad Al particles in air (see Fig. 2) involves two stages, with inverse images of flame (bright core-dark flame and dark core-bright flame). Such images have never been observed in prior experiments with pure Al particles. Thus, we expect that this new phenomenon is caused by the presence of two elements (Al and Ni) in the particles.

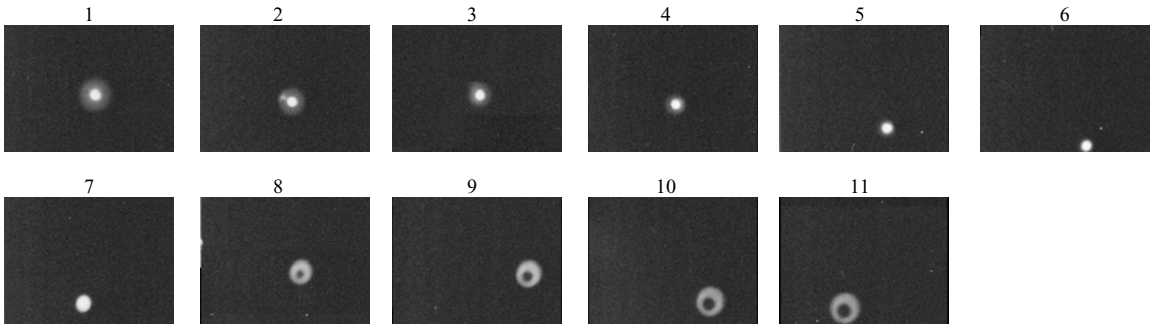

Figure 2: Combustion of Ni-clad Al particle in air.
(1.3 μs between images, viewing area 1236 x 921 μm)

Recent studies [8] show that the Ni coating dramatically decreases both the ignition delay time of laser-heated Al particles and the critical ignition temperature of gas-heated Al particles. Exothermic intermetallic reactions between liquid Al and solid Ni are considered as the main reason for the lowered ignition temperature of Ni-coated Al particles.

The detailed characterization of the process requires spatial and temporal resolutions that can be achieved only with relatively larger particles (1-5 mm). To avoid the natural convection and liquid flow effects, experiments on combustion of such particles will be conducted in microgravity environment using NASA research aircraft. The ignition and combustion will be studied by using high-speed and infra-red video cameras, and product composition analysis. Special attention will be devoted to elucidating the roles of inter-metal reaction and physical processes in surface layers (e.g. cracking of the shell, melt spreading).

This work is supported by NASA (Grant NNC04AA36A).

REFERENCES

1. Yuasa, S., and Isoda, H. (1989) *25th AIAA/ASME/SAE/ASEE Joint Propulsion Conference & Exhibit, July 1989*, AIAA Paper 89-2863.
2. Shafirovich, E.Ya., Shiryaev, A.A., and Goldshleger, U.I. (1993) *Journal of Propulsion and Power*, **9**(2), 197.
3. Shafirovich, E., Salomon, M., and Gökalp, I. (2003) *Proceedings of the Fifth IAA International Conference on Low-Cost Planetary Missions*, *ESTEC, Noordwijk, The Netherlands, 24-26 September 2003,* ESA SP-542, p. 97.
4. Shafirovich, E.Ya., and Goldshleger, U.I. (1997) *Journal of Propulsion and Power*, **13**(3), 395.
5. Breiter, A.L., Mal'tsev, V.M., and Popov E.I. (1988) *Combustion, Explosion, and Shock Waves* **26**, 86.
6. Yagodnikov, D.A., and Voronetskii, A.V. (1997) *Combustion, Explosion, and Shock Waves* **33**, 49.
7. Shafirovich, E., Mukasyan, A., Thiers, L., Varma, A., Legrand, B., Chauveau, C., and Gökalp, I. (2002) *Combustion Science and Technology*, **174**(3), 125.
8. Shafirovich, E., Escot Bocanegra, P., Chauveau, C., Gökalp, I., Goldshleger, U., Rosenband, V., and Gany, A. (2004) To be presented at the *30th International Symposium on Combustion, Chicago, July 25-30, 2004*.

Nickel-Coated Aluminum Particles: A Promising Fuel for Mars Missions

Evgeny Shafirovich and Arvind Varma

Purdue University
School of Chemical Engineering
480 Stadium Mall Drive
West Lafayette IN 47907-2100

PURDUE
UNIVERSITY

Combustion of metals in CO_2 as an alternative approach in Mars in-situ resource utilization

- Typical approach in Mars ISRU: ***To produce rocket propellants from Martian CO_2*** (95% of Mars atmosphere). Problems: high power and chemical processing on Mars are required.
- Alternative approach: ***To use Martian CO_2 directly as an oxidizer in a rocket engine*** [1]. Based on combustibility of metals in CO_2 and easy liquefaction of CO_2 under Martian conditions (pressure 8 mba, typical average temperature 230 K in middle latitudes).

Combustion of Mg and Al particles in CO_2

Al, 50 μm [2]

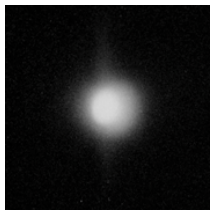

Mg, 50 μm [2]

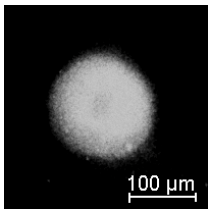

Mg, 2 mm, microgravity [3]

CO_2 Phase Diagram

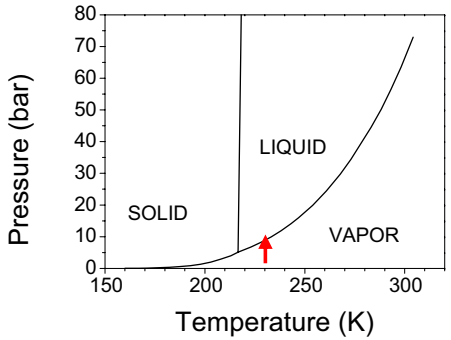

PURDUE UNIVERSITY

Advantages of metal-CO_2 propulsion in Mars missions

- Reduced mass of propellant transported from Earth for ***long-range mobility on Mars***. Several ballistic flights are possible (CO_2 is acquired before every takeoff).
- Only CO_2 acquisition but ***no chemical processing on Mars***.

Missions: hopper, multi-sample return.

Design domain for hopper [4]
Hopper mass = 200 kg, power = 300 W
Propellant: Martian CO_2 and Mg from Earth
Scenario: 10 hops, total range = 10 km, mission duration = 180 Martian days
Conclusion: Mission is possible.

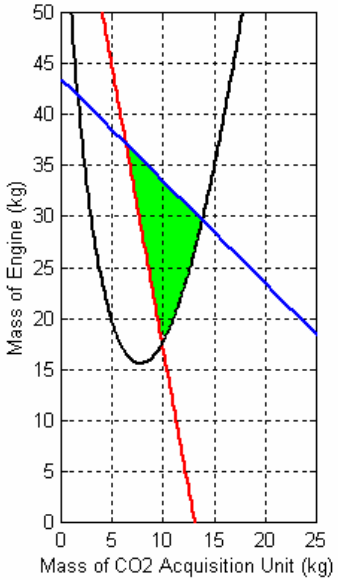

PURDUE UNIVERSITY

Problems in metal-CO_2 propulsion and how to fix them

- ***Low specific impulse*** of Mg-CO_2 rocket, ~200 s
  (though still advantageous because the oxidizer is present on Mars!)

- ***High ignition temperature*** of Al particles in CO_2, >2000 K
  (the ignition temperature of Mg in CO_2 is about 1000 K)

Al will be the best fuel choice if a method is found to reduce the ignition temperature of Al particles. ***Coating by nickel*** is one such method. It is expected that intermetallic reactions of Ni and Al trigger ignition and significantly reduce the ignition temperature [5].

Typical dimensions of Ni-coated Al particles:
Al core diameter: 10 - 100 μm
Ni layer thickness: 0.01 - 1 μm

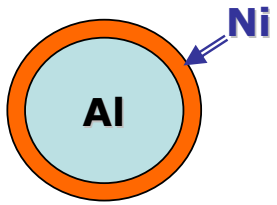

PURDUE UNIVERSITY

Ignition and combustion of single Ni-coated Al particles

Method: electrodynamic levitation

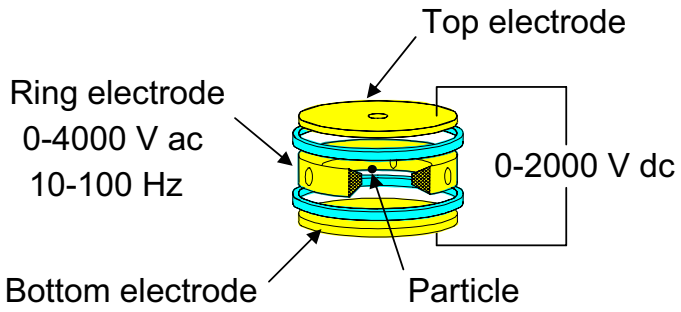

Two-phase burning in air [5]

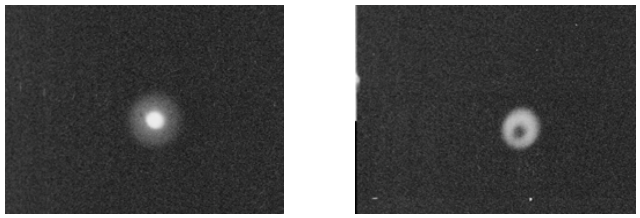

Ignition in air [6]

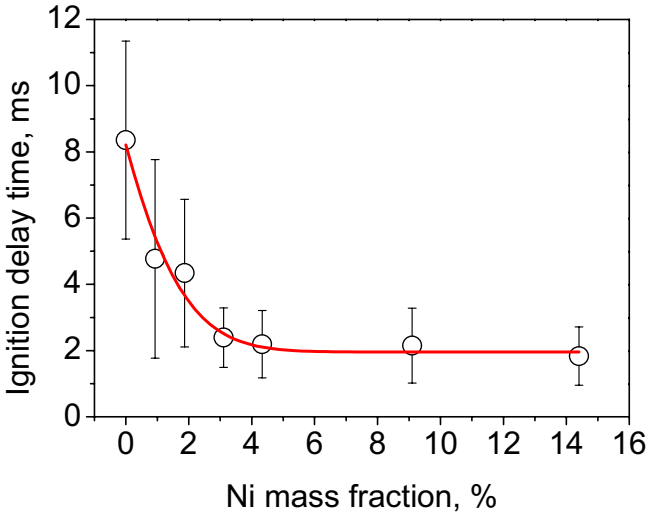

Ni coating dramatically decreases both the ignition delay time and the ignition temperature of Al particles (~1000 K *vs.* >2000 K for non-coated Al)

PURDUE UNIVERSITY

Ignition and combustion of single Ni-coated Al particles (continued)

Combustion in O_2 and CO_2 [5]

Atmosphere: O_2
T_{ad} ~ 4000 K

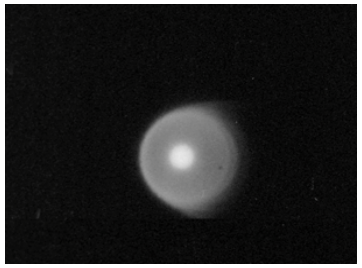

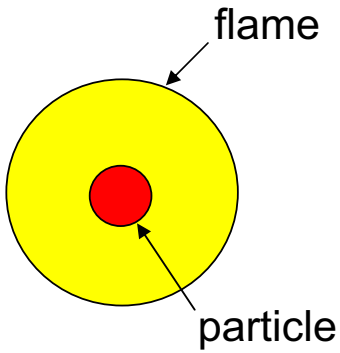

Atmosphere: CO_2
T_{ad} ~ 3200 K

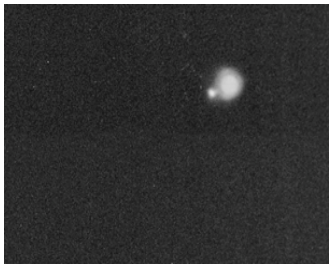

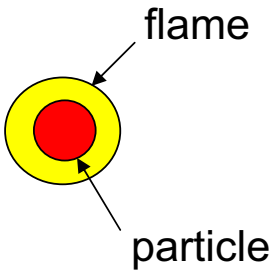

PURDUE UNIVERSITY

Combustion of complex metal particles in microgravity

(NASA Grant NNC04AA36A, started Jan. 1, 2004)

The detailed characterization of the ignition/combustion process requires spatial and temporal resolutions that can be achieved only with particle size 1-5 mm. To avoid the natural convection and liquid flow effects, experiments on combustion of large Ni-coated Al particles will be conducted in microgravity environment using NASA research aircraft. The particles will be installed on thin wires inside a reaction chamber and ignited by a CO_2-laser. Combustion in different gases will be studied.

Schematic diagram of the experimental setup (design in progress)

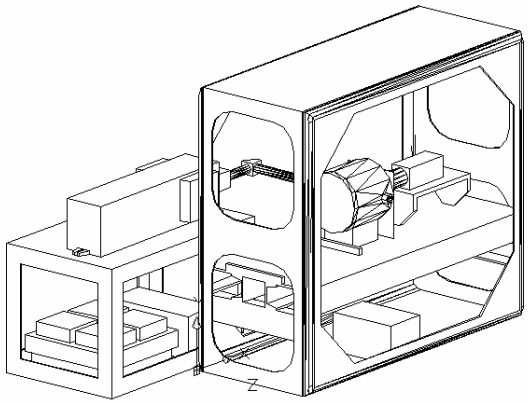

PURDUE UNIVERSITY

What should NASA undertake to make the metal-CO_2 propulsion on Mars a reality?

To organize/support

- Fundamental studies on combustion of metals in CO_2
  Goal: *to identify/develop the best fuel for burning with CO_2 on Mars*
- Development of the liquid CO_2 acquisition system
  Goal: *to develop a reliable and efficient CO_2 acquisition system for operation on Mars*
- Development of the metal/CO_2 engine prototype
  Goal: *to prove that the metal/CO_2 engine can operate smoothly with high performance characteristics*
- Studies of metals recovery from Martian soil or lander used parts
  Goal: *to develop the method for production of metal fuel on Mars with sufficiently low power consumption*

PURDUE UNIVERSITY

References

1. Shafirovich, E.Ya., Shiryaev, A.A., and Goldshleger, U.I., *Journal of Propulsion and Power*, Vol. 9(2), 1993, p. 197.
2. Legrand, B., Marion, M., Chauveau, C., Gökalp, I., and Shafirovich, E., *Combustion Science and Technology*, Vol. 165, 2001, p. 151.
3. Legrand, B., Chauveau, C., Shafirovich, E., Goldshleger, U., Carrea, E., Mounaim-Rousselle, C., Rouan, J.P., and Gökalp, I., *Proceedings of the 6th International Microgravity Combustion Workshop, May 22-24, 2001, Cleveland, OH*, NASA/CP-2001-210826, p. 225.
4. Shafirovich, E., Salomon, M., and Gökalp, I., *Proceedings of the 5th IAA International Conference on Low-Cost Planetary Missions*, *ESTEC, Noordwijk, The Netherlands, 24-26 September 2003,* ESA SP-542, p. 97.
5. Shafirovich, E., Mukasyan, A., Thiers, L., Varma, A., Legrand, B., Chauveau, C., and Gökalp, I., *Combustion Science and Technology*, Vol. 174(3), 2002, p. 125.
6. Shafirovich, E., Escot Bocanegra, P., Chauveau, C., Gökalp, I., Goldshleger, U., Rosenband, V., and Gany, A., to be presented at the *30th International Symposium on Combustion, Chicago, July 25-30, 2004*.

PURDUE
UNIVERSITY

COMPUTER MODELING OF CARDIOVASCULAR RESPONSES TO GRAVITY

M. Keith Sharp
Department of Mechanical Engineering
University of Louisville
Louisville, KY 40292

A recently initiated computer modeling project will investigate a possible contributing factor to postflight orthostatic intolerance (POI) that has to date received little attention. POI compromises crew safety and could have disastrous consequences in emergency situations during landing. A potentially revealing characteristic of POI is that even susceptible astronauts are able to stand postflight for several minutes without symptoms. Many astronauts become dizzy only after 5-10 minutes of standing. Therefore, compensatory reflexes are apparently sufficient to prevent symptoms initially. While many factors, including a well-documented decrease in postflight blood volume, may increase sensitivity, the final cause of POI must have a delayed action consistent with the range of times astronauts are able to tolerate standing. Onset of symptoms during orthostatic stress in nonastronauts is correlated with the gradual rate of loss of blood volume by capillary filtration, which provides a potential explanation for the delayed occurrence of POI. Furthermore, astronauts have increased lower body capillary permeability in space. If permeability remains elevated, then capillary transport may also be responsible for the reduced tolerance of astronauts to upright posture postflight. *Accordingly, it is hypothesized that capillary filtration explains the delayed onset, as well as the increased postflight incidence of dizziness.* The hypothesis will be tested with a computer model of the cardiovascular system that incorporates fundamental biomechanical responses and reflex control. Posture-dependent capillary filtration will be represented with local permeability values and models of local intra- and extra-vascular pressure. A model of cerebral circulation will be included to provide a prediction of dizziness by direct comparison with established thresholds for cerebral flow. Because data is currently unavailable in astronauts, the model will be validated with heart rate, stroke volume and arterial pressure measurements and capillary filtration estimates derived from experiments on nonastronauts. Finally, the plausibility of the hypothesis will be tested by comparing the permeability required in the model to cause dizziness during simulated stand tests to the preliminary inflight values. This modeling effort will elucidate the potential importance of capillary filtration in producing POI and may guide the design of experiments to investigate this mechanism in astronauts.

NASA/CP—2004-213205/VOL2

Biofluid Mechanics Laboratory

Department of Mechanical Engineering

University of Louisville

Computer Modeling of Cardiovascular Response to Gravity

M. Keith Sharp

ABSTRACT

A recently initiated computer modeling project will investigate a possible contributing factor to postflight orthostatic intolerance (POI) that has to date received little attention. POI compromises crew safety and could have disastrous consequences in emergency situations during landing. A potentially revealing characteristic of POI is that even susceptible astronauts are able to stand postflight for several minutes without symptoms. Many astronauts become dizzy only after 5-10 minutes of standing. Therefore, compensatory reflexes are apparently sufficient to prevent symptoms initially. While many factors, including a well-documented decrease in postflight blood volume, may increase sensitivity, the final cause of POI must have a delayed action consistent with the range of times astronauts are able to tolerate standing. Onset of symptoms during orthostatic stress in nonastronauts is correlated with the gradual rate of loss of blood volume by capillary filtration, which provides a potential explanation for the delayed occurrence of POI. Furthermore, astronauts have increased lower body capillary permeability in space. If permeability remains elevated, then capillary transport may also be responsible for the reduced tolerance of astronauts to upright posture postflight. *Accordingly, it is hypothesized that capillary filtration explains the delayed onset, as well as the increased postflight incidence of dizziness.* The hypothesis will be tested with a computer model of the cardiovascular system that incorporates fundamental biomechanical responses and reflex control. Posture-dependent capillary filtration will be represented with local permeability values and models of local intra- and extra-vascular pressure. A model of cerebral circulation will be included to provide a prediction of dizziness by direct comparison with established thresholds for cerebral flow. Because data is currently unavailable in astronauts, the model will be validated with heart rate, stroke volume and arterial pressure measurements and capillary filtration estimates derived from experiments on nonastronauts. Finally, the plausibility of the hypothesis will be tested by comparing the permeability required in the model to cause dizziness during simulated stand tests to the preliminary inflight values. This modeling effort will elucidate the potential importance of capillary filtration in producing POI and may guide the design of experiments to investigate this mechanism in astronauts.

Postflight orthostatic intolerance (POI) is a potentially hazardous condition affecting many astronauts upon reentry.

At least several minutes of standing are required to induce POI

Time to presyncope for nonfinishers of 10-minute stand test. From Buckey, et al. [1996]

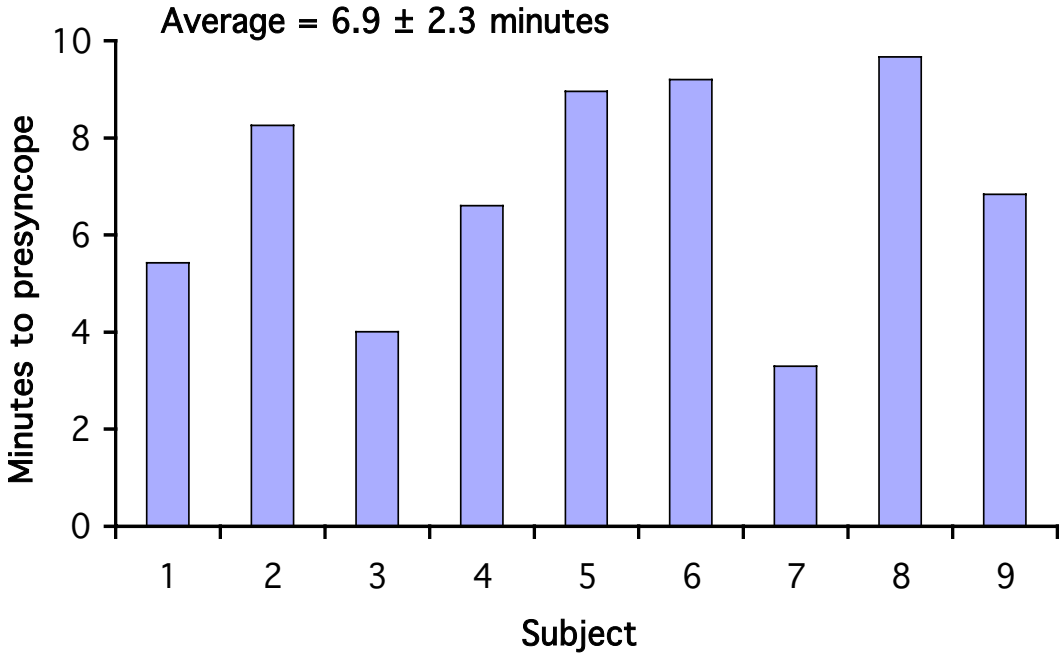

Conclusion: Immediate cardiovascular response is apparently adequate. A stimulus with a longer time constant is necessary to explain POI.

Hydrostatic pressure causes fluid shifts within the vasculature.

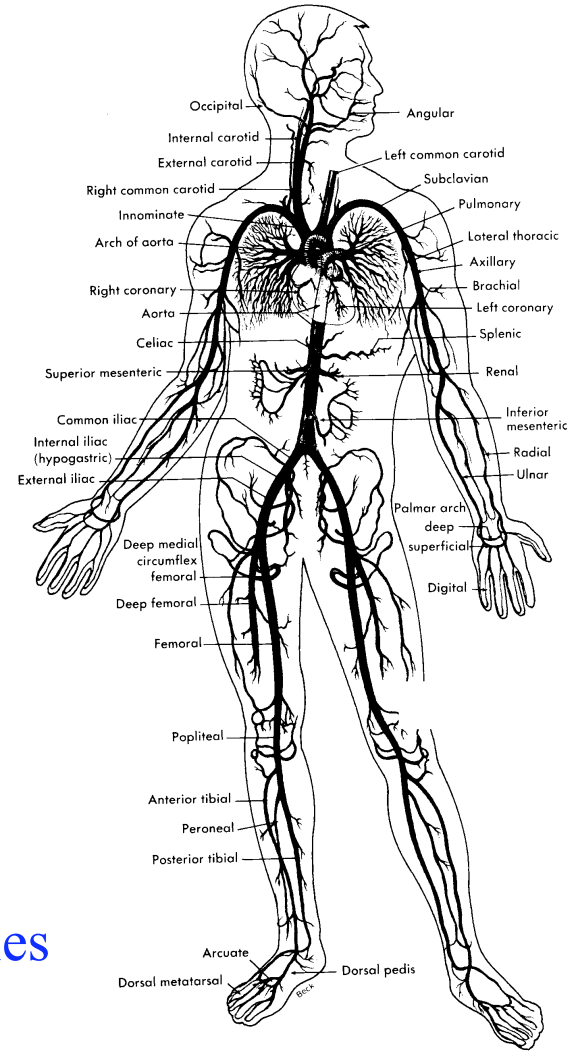

Arteries

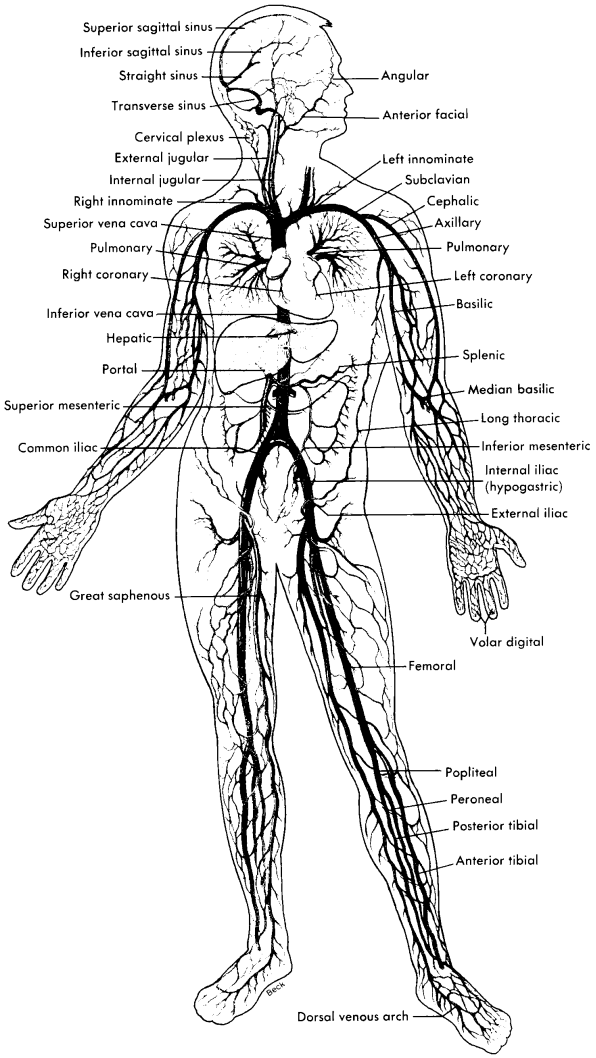

Veins

Two stages of fluid shift:

1. Immediate shift determined by vascular compliance
2. Slower progressive shift by capillary filtration

Decrease in thoracic blood volume (increase in transthoracic impedance Z_0) during 70° head-up tilt in healthy young men. Note unusual changes in two subjects who fainted. (From Ebert, et al. [1986]).

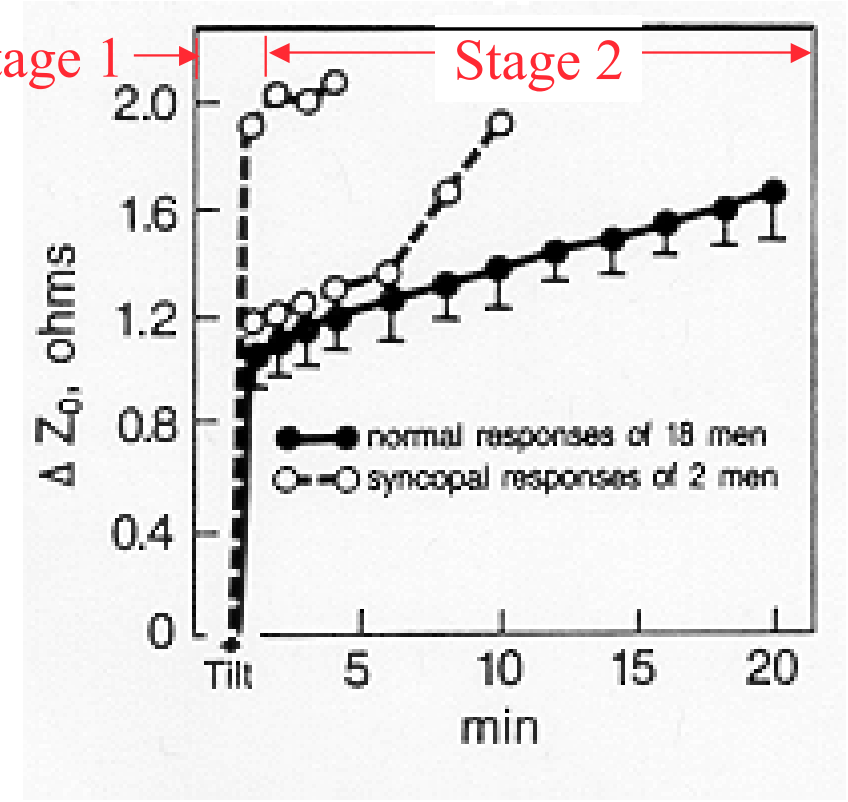

Question: Could increased capillary transport be the ultimate cause of POI?

Increased second stage fluid shifts have been observed in astronauts.

Changes in one subject during stand test before and after 14-day Gemini-7 flight. Solid lines - preflight mean, dashed lines - postflight. From Charles, et al. [1994], after Berry & Catterson [1967].

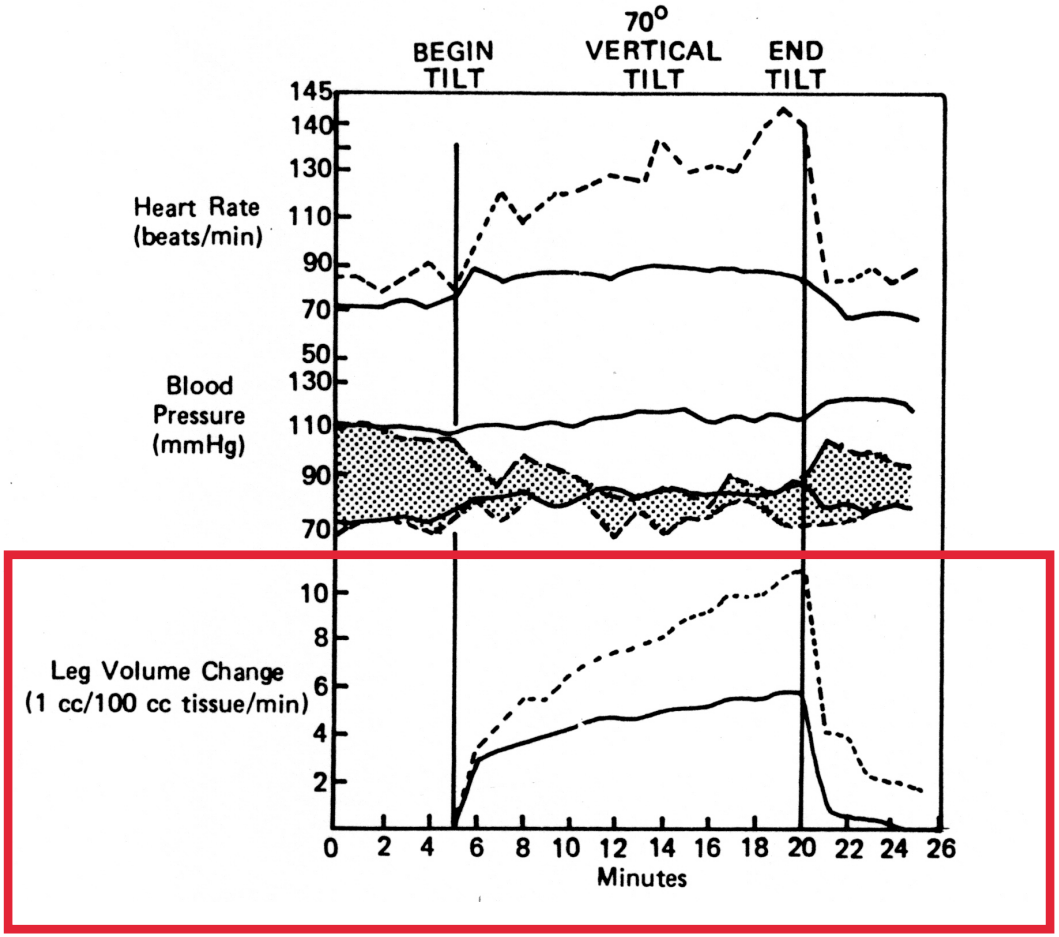

Proposed mechanism: Endothelial cell junctions may adapt in -G to higher hydraulic conductivity, and therefore require time to remodel back to low conductivity in 1-G

Schematic change of occludin in EC junctions:

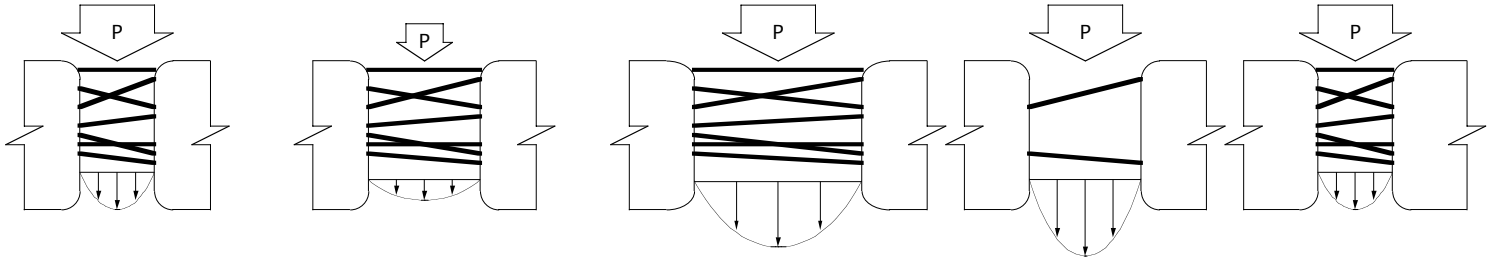

Preflight (High pressure, low conductivity)

Adapted Inflight (Low pressure, high conductivity)

Immediate Postflight (High pressure, high conductivity)

Readapting Postflight (High pressure, even higher conductivity)

Readapted Postflight (High pressure, low conductivity)

Caudal transcapillary pressure difference ~ 75 mmHg standing 1-G, but only ~ 8 mmHg in -G [Aratow, et al. 1993]. Reorganization of occludin takes up to 24 hours [Brey, et al. 2003].

Research Plan:

Evaluate the changes in capillary transport necessary to explain POI with a cardiovascular system model, compare model responses to experimental hemodynamic data.

A, P, V - arterial, peripheral & venous segments,
RV, LV - right & left ventricles,
RA, LA - right & left atria

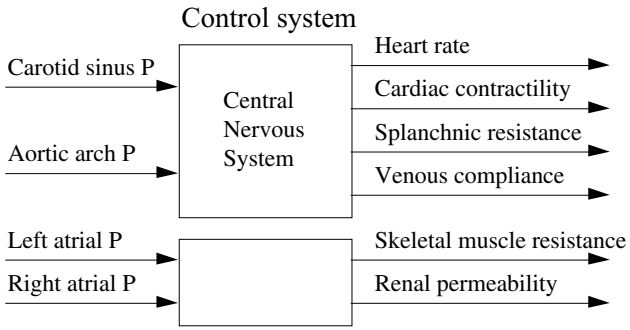

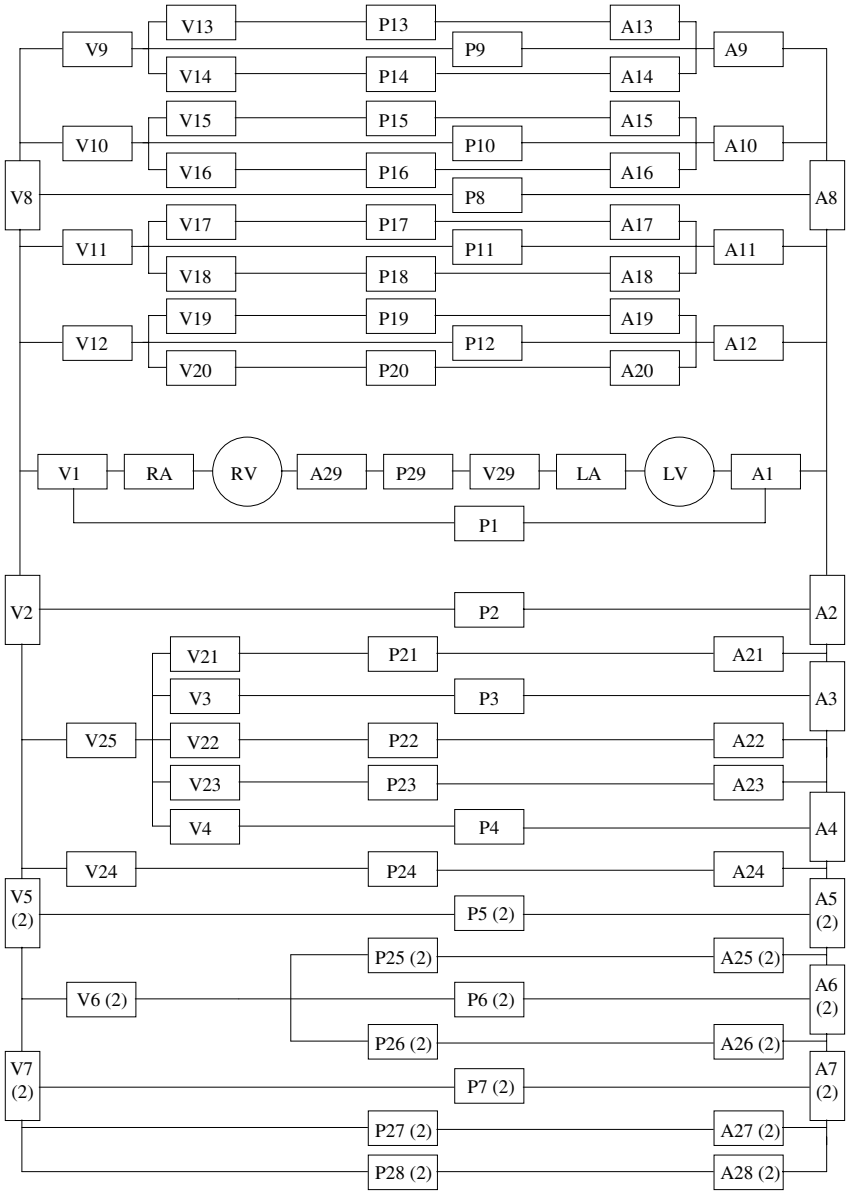

BI-COMPONENT DROPLET COMBUSTION IN REDUCED GRAVITY

Benjamin D. Shaw
Mechanical and Aeronautical Engineering Department
University of California, Davis

ABSTRACT

This research deals with reduced-gravity combustion of bi-component droplets initially in the mm size range or larger. The primary objectives of the research are to study the effects of droplet internal flows, thermal and solutal Marangoni stresses, and species volatility differences on liquid species transport and overall combustion phenomena (e.g., gas-phase unsteadiness, burning rates, sooting, radiation, and extinction). The research program utilizes a reduced-gravity environment so that buoyancy effects are rendered negligible. Use of large droplets also facilitates visualization of droplet internal flows, which is important for this research.

In the experiments, droplets composed of low- and high-volatility species are burned. The low-volatility components are initially present in small amounts. As combustion of a droplet proceeds, the liquid surface mass fraction of the low-volatility component will increase with time, resulting in a sudden and temporary decrease in droplet burning rates as the droplet rapidly heats to temperatures close to the boiling point of the low-volatility component. This decrease in burning rates causes a sudden and temporary contraction of the flame. The decrease in burning rates and the flame contraction can be observed experimentally. Measurements of burning rates as well as the onset time for flame contraction allow effective liquid-phase species diffusivities to be calculated, e.g., using asymptotic theory [1]. It is planned that droplet internal flows will be visualized in flight and ground-based experiments. In this way, effective liquid species diffusivities can be related to droplet internal flow characteristics.

This program is a continuation of extensive ground-based experimental and theoretical research on bi-component droplet combustion that has been ongoing for several years. The focal point of this program is a flight experiment (Bi-Component Droplet Combustion Experiment, BCDCE). This flight experiment is under development. However, supporting ground-based studies have been performed. Some of the most recent ground-based research is summarized below.

Reduced Gravity Experiments

Experiments on combustion of fiber-supported propanol droplets with initial droplet diameters of about 1 mm were conducted in air at standard temperature and with pressures ranging from 0.1 to 1.0 MPa [2]. The experiments were conducted using the 2.2 Second Drop Tower at the NASA John H. Glenn Research Center at Lewis Field in Cleveland, OH. The results indicate significant differences in combustion of propanol droplets at 0.1 MPa relative to higher pressures. The flame at 0.1 MPa is non-sooting with blue coloring during most of the combustion process. For higher pressures, flames exhibited somewhat non-spherical shapes as well as significant amounts of sooting during most of the combustion history. The non-spherical flame shapes were likely a

result of the increased importance of buoyant convection at elevated pressure as inferred from Grashof numbers that were calculated based on flame dimensions. Droplet burning rates were also observed to increase with increasing pressure. Theory indicates that these increases resulted mainly from decreases in liquid densities and enthalpies of vaporization, where these decreases are caused by increases in liquid saturation temperatures.

Analytical Modeling

Simplified analyses of spherically symmetrical combustion of an isolated fuel droplet were developed to account for fuel pyrolysis [3]. Fuel pyrolysis is modeled as a high activation-energy process that occurs within a thin zone between the droplet and the flame. Accounting for fuel pyrolysis changes classical expressions for the transfer number because the flame must supply energy for fuel pyrolysis, which requires the flame to be located closer to the droplet. Sample calculations for combustion of heptane droplets in air at one atm indicate that transfer numbers, burning rates and quasisteady flame standoff ratios can be appreciably reduced when fuel pyrolysis effects are included in the analyses.

Soot shell standoff ratios in reduced-gravity droplet combustion were also investigated analytically [4]. Analysis of energy conservation between the droplet and the flame shows that temperature gradients between the droplet and a flame are influenced by variations in specific heats as well as fuel pyrolysis, which influences thermophoretic soot transport. Analyses show that if endothermic fuel pyrolysis is neglected, soot shells are predicted to be close to the fuel oxidation zone where fuel mass fractions are small. Analyses that account for endothermic fuel pyrolysis indicate that the onset of fuel pyrolysis can be abrupt, leading to local increases in temperature gradients. These temperature gradient changes can be large enough to influence soot transport, causing soot-shell standoff ratios to be smaller than if fuel pyrolysis is neglected. Theoretical predictions of pyrolysis-controlled soot-shell standoff ratios compare favorably with experimental data on reduced-gravity combustion of n-heptane droplets in air at 1 atm

References

1. I. Aharon and B. D. Shaw, Estimates of Liquid Species Diffusivities from Experiments on Reduced-Gravity Combustion of Heptane-Hexadecane Droplets, Combustion and Flame 113, 507 (1998).

2. S. M. Dakka and B. D. Shaw, Combustion of Propanol Droplets in Reduced Gravity, paper 04S-46 presented at the 2004 Spring Meeting of the Western States Section of the Combustion Institute, University of California, Davis, March 29-30.

3. B. D. Shaw, Theory of Spherically Symmetrical Droplet Combustion with Gas-Phase Fuel Pyrolysis, Combustion Science and Technology (submitted).

4. Theory of Influence of Fuel Pyrolysis on Soot-Shell Standoff Ratios in Reduced-Gravity Droplet Combustion, paper 04S-50 presented at the 2004 Spring Meeting of the Western States Section of the Combustion Institute, University of California, Davis, March 29-30.

NASA/CP—2004-213205/VOL2

BI-COMPONENT DROPLET COMBUSTION IN REDUCED GRAVITY

B. D. Shaw
University of California, Davis

BI-COMPONENT FUEL DROPLETS

- Multicomponent liquid fuels are commonly used in practical applications
- Need to understand gasification behaviors of multicomponent droplets
  - Predict rates that particular species gasify from droplets
  - Gas behaviors
    - Determined by species that have gasified
  - Liquid behaviors
    - Determined by species that remain inside droplets

THIS RESEARCH IS COMPRISED OF

- Space-based experiments (future)
  - Up to 4 mm initial diameter
- Ground-based studies (current)
  - Drop tower experiments
    - Up to 1 mm initial diameter
  - Ground experiments at UC Davis
  - Analytical/numerical studies

SOME RECENT EFFORTS FROM THIS RESEARCH PROGRAM

- Numerical Modeling of Droplet Combustion
  - 1-Dimensional
  - 3-Dimensional

- Drop Tower Experiments
  - Propanol droplet combustion
    - Single-component droplets provide baseline data for comparison with bi-component droplets
    - Up to 10 atm in air

- Analytical Modeling
  - Effects of gas-phase fuel pyrolysis
    - Flame standoff ratios
    - Burning rates
    - Soot shell behaviors

ONE-DIMENSIONAL DROPLET COMBUSTION MODELING
Propanol-Glycerol Droplets

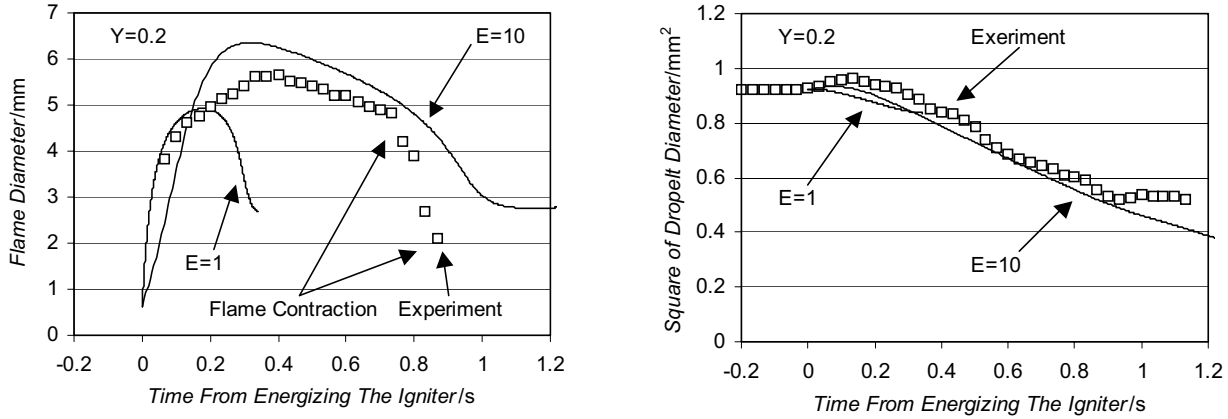

Histories for flame and droplet sizes (initial glycerol mass fraction, Y, of 0.2). The symbols are from experiments and the lines are from the computational model. The variable E is a liquid-phase transport enhancement factor, to account for liquid convectiion effects. Comparison of the computational and experimental results indicates that significant convective mixing was present in the experiments.

One-Dimensional Numerical Model

1. Variable properties with nonideal liquids
2. Spherical symmetry
3. Transient liquid phase
4. Quasisteady gas phase (in agreement with experimental data)
5. Implicit finite-difference formulation with variable gridding

THREE-DIMENSIONAL DROPLET COMBUSTION MODELING (with H. A. Dwyer)

Marangoni flows; gas-phase chemistry; radiation; fiber effects; 3-dim flows; liquid-phase transport; moving gas phase (possible convective effects)

Method of Approach

1. Overset Grid (Chimera) Approach
2. Low-Mach-number reacting Navier-Stokes equations with variable liquid and gas properties
3. Projection solver with ADI preconditioned GMRES
4. Variable surface tension with temperature and concentration dependence
5. Multi-component and non-ideal liquid phase
6. Specified droplet shapes (can be relaxed with effort)
7. 3-Dimensional model
   - Finite-volume formulation
   - Global or detailed chemistry

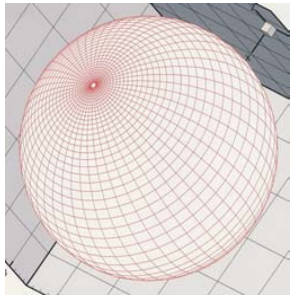

Mesh Schematic

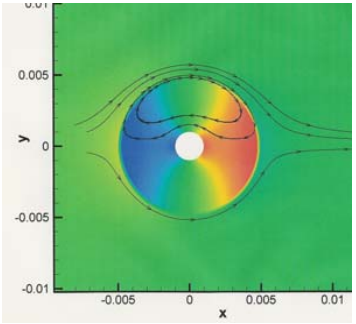

Re=0.1, CH_3OH/Air

REDUCED-GRAVITY COMBUSTION OF PROPANOL DROPLETS

Pressure Effects on Flames

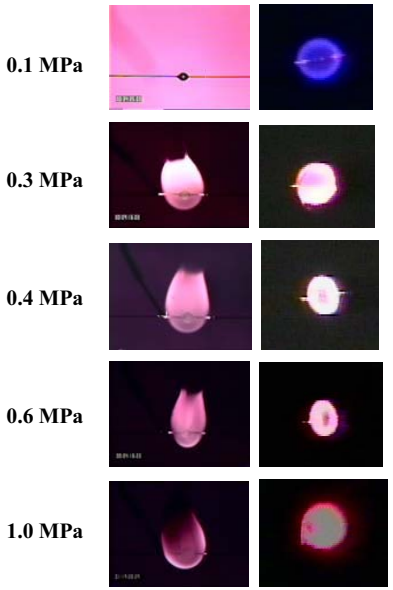

Increasing the pressure increases soot formation and flame distortion

Pressure Effects on Burning Rates

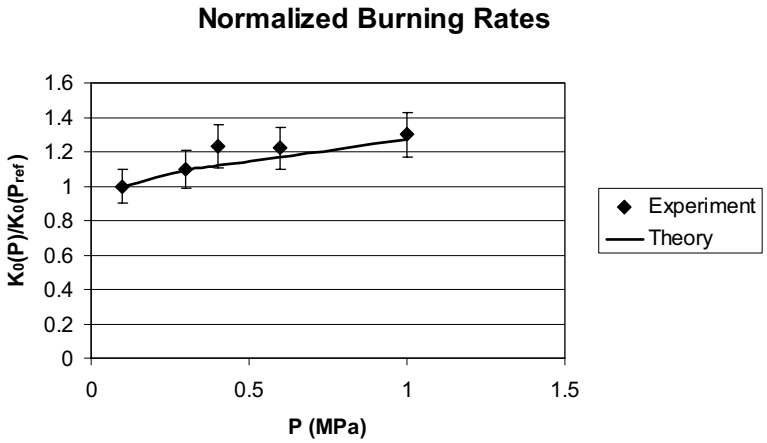

Burning rates increased as the ambient pressure increased

Increases in burning rates can be accounted for by considering influences of pressure on enthalpy of vaporization and liquid density

ANALYTICAL MODELING OF INFLUENCES OF FUEL PYROLYSIS

- Fuel pyrolysis reactions
  - Can be highly temperature sensitive
  - Significantly endothermic
  - Reaction sheet model employed here
- Gas-phase temperature profiles are influenced by fuel pyrolysis
  - Energy required for pyrolysis alters temperature profiles
- Burning rates decrease as a result of fuel pyrolysis
- Flame standoff ratios decrease as a result of fuel pyrolysis
- Soot shell standoff ratios are influenced by fuel pyrolysis

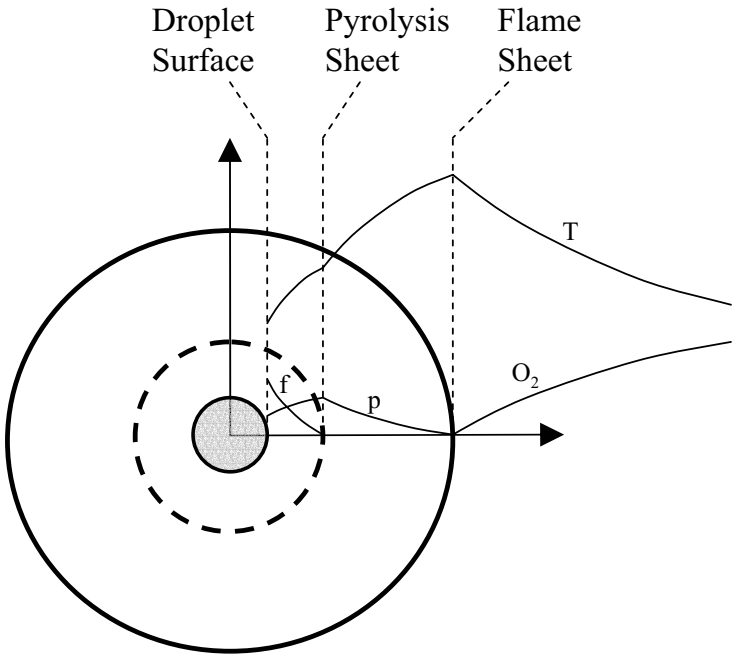

ANALYTICAL MODELING OF INFLUENCES OF FUEL PYROLYSIS

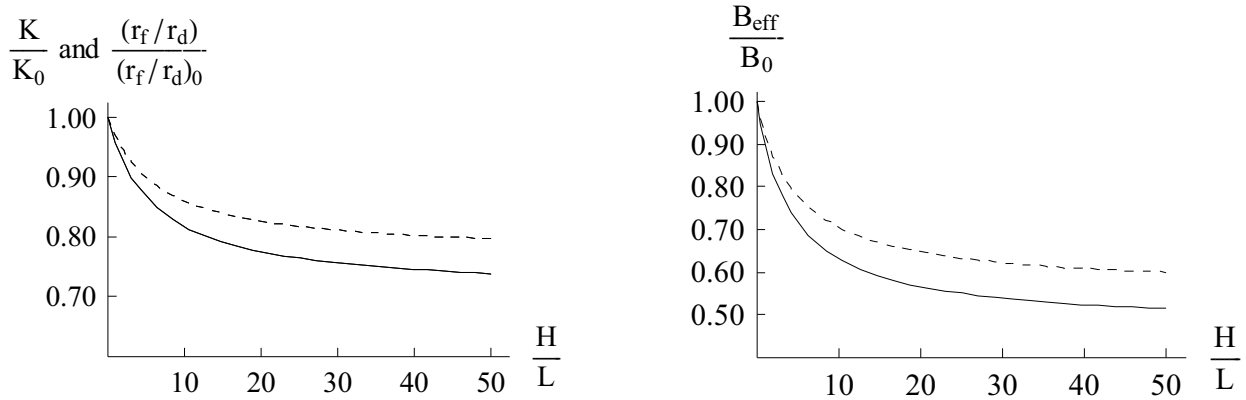

Predicted variations for the normalized burning-rate ratio K/K_0, the normalized flame standoff ratio $(r_f/r_d)/(r_f/r_d)_0$ and the normalized effective transfer number ratio B_{eff}/B_0 as a function of the ratio H/L, where H is the enthalpy change associated with fuel pyrolysis and L is the droplet enthalpy of vporization. The solid line is for a pyrolysis temperature of 900 K ands the dashed line is for a pyrolysis temperature of 1000K. The calculations are for combustion of n-heptane droplets in air at one atm.

ACKNOWLEDGEMENT

- The support provided by NASA is gratefully acknowledged
- Doctor Daniel L. Dietrich provided valuable guidance and assistance

REDUCED GRAVITY STUDIES OF SORET TRANSPORT EFFECTS IN LIQUID FUEL COMBUSTION

Benjamin D. Shaw
Mechanical and Aeronautical Engineering Department
University of California, Davis

Soret transport, which is mass transport driven by thermal gradients, can be important in practical flames as well as laboratory flames by influencing transport of low molecular weight species (e.g., monatomic and diatomic hydrogen). In addition, gas-phase Soret transport of high molecular weight fuel species that are present in practical liquid fuels (e.g., octane or methanol) can be significant in practical flames (Rosner et al., 2000; Dakhlia et al., 2002) and in high-pressure droplet evaporation (Curtis and Farrell, 1992), and it has also been shown that Soret transport effects can be important in determining oxygen diffusion rates in certain classes of microgravity droplet combustion experiments (Aharon and Shaw, 1998). It is thus useful to obtain information on flames under conditions where Soret effects can be clearly observed.

This research is concerned with investigating effects of Soret transport on combustion of liquid fuels, in particular liquid fuel droplets. Reduced-gravity is employed to provide an ideal (spherically-symmetrical) experimental model with which to investigate effects of Soret transport on combustion. The research will involve performing reduced-gravity experiments on combustion of liquid fuel droplets in environments where Soret effects significantly influence transport of fuel and oxygen to flame zones. Experiments will also be performed where Soret effects are not expected to be important. Droplets initially in the 0.5 to 1 mm size range will be burned. Data will be obtained on influences of Soret transport on combustion characteristics (e.g., droplet burning rates, droplet lifetimes, gas-phase extinction, and transient flame behaviors) under simplified geometrical conditions that are most amenable to theoretical modeling (i.e., spherical symmetry). The experiments will be compared with existing theoretical models as well as new models that will be developed. Normal gravity experiments will also be performed.

Experimental research will involve performing reduced-gravity droplet combustion experiments in a NASA Glenn drop tower (the 2.2 s tower). Use will be made of an existing droplet combustion rig. Digital images of the drop rig are shown in Fig. 1. This rig will be used to provide results on Soret effects for droplets initially from about 0.5 mm to 1 mm in diameter. The pressure will range from subatmospheric to as high as about 1.2 MPa (and possibly higher).

The drop rig has a pressure vessel mounted on a NASA-supplied drop frame with associated control electronics and gas and liquid handling systems. Orthogonal views are used with the drop rig; one view is used to image droplets and the other view is used to image flames. The flame view is not backlit, and a Xybion intensified-array CCD camera can be used to image OH emissions in this view (CH emissions can also be imaged).

Theoretical modeling will employ further development of analytical models beyond that described by Aharon and Shaw (1998). Further development of analytical theory will involve accounting for transient effects as well as developing models of Soret effects and multicomponent diffusion effects between droplet and flames. A goal of this modeling will be to develop simplified analytical models that retain the essential physics of Soret transport. In this way, Soret effects can be illustrated in a transparent manner.

Use will also be made of a computer code being developed as part of a NASA-sponsored program to study combustion of bi-component droplets. The numerical modeling involves development of a three-dimensional model for combustion of a droplet on a fiber (as well as a free droplet). The code includes important effects such as gas-phase radiant losses, detailed chemical kinetics, and realistic fiber effects (e.g., a nonslip condition, and fiber radiation in the vicinity of the flame). Soret transport can be turned on or off in the model.

References

Aharon, I., and Shaw, B.D. (1998) Microgravity Science and Technology X/2: 75.
Curtis, E.W., and Farrell, P.V. (1992) Combustion and Flame 90: 85.
Dakhlia, R.B., Giovangigli, V., and Rosner, D.E. (2002) Combustion Theory and Modeling 6: 1.
Rosner, D.E., Israel, R.S., and La Mantia, B. (2000) Combustion and Flame 123: 547.

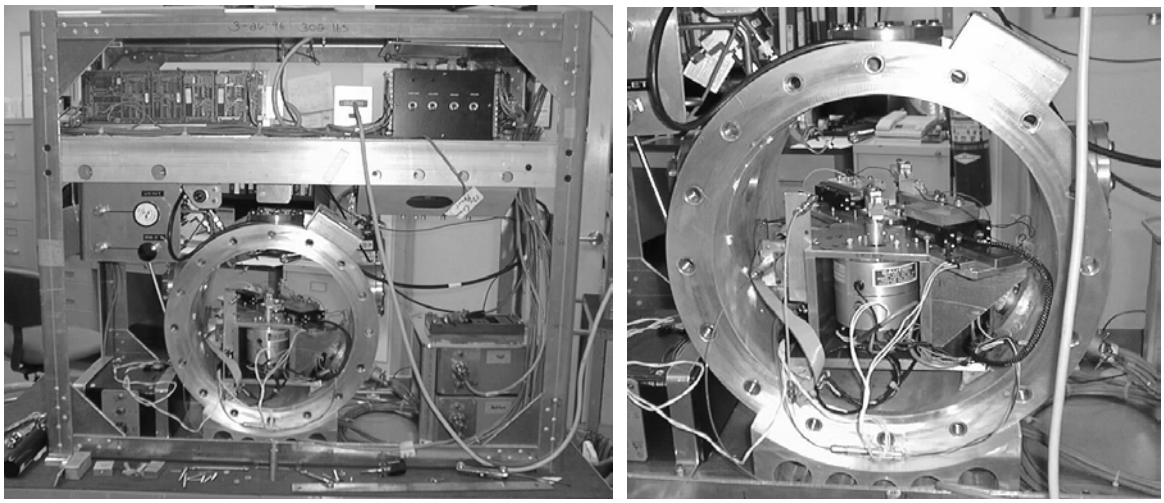

(a) (b)

Figure 1. Digital images of the drop rig: (a) overall rig; and (b) closeup of the pressure chamber interior. The endcaps for the pressure chamber are not shown.

NASA/CP—2004-213205/VOL2

REDUCED GRAVITY STUDIES OF SORET TRANSPORT EFFECTS IN LIQUID FUEL COMBUSTION

B. D. Shaw
University of California, Davis

RESEARCH GOALS

Investigate effects of multicomponent diffusion and thermal (Soret) diffusion

These phenomena can be important when large differences exist between molecular weights of gas species

H or H_2 with other species

Liquid hydrocarbon fuel (e.g., C_8H_{18}) with air
(can be important with diffusion flames)

This research utilizes droplet combustion to gain information on how Soret transport and multicomponent diffusion influence liquid fuel combustion in general

The following topics will be investigated

Transport of O_2 to the flame zone around a droplet
Transport of fuel to the flame zone
Sooting behaviors
Flame unsteadiness
Burning rates

THEORY FOR TRANSPORT OF OXYGEN TO THE FLAME ZONE (Aharon and Shaw, 1998)

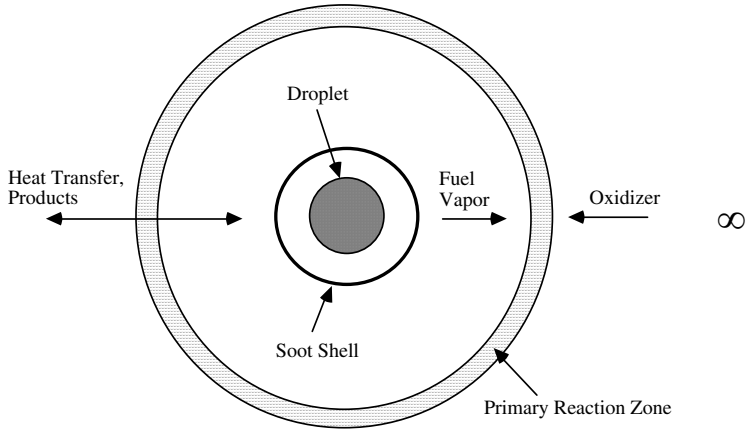

$$\frac{d_f}{d_d} = \frac{r_f}{r_d} \approx \frac{\rho_d K \nu_O}{8 W_F n D_0 x_{O,\infty}}$$ Standoff Ratio

$$D_O = \beta \phi D_{IO}$$ Effective O_2 Diffusivity

$$\beta = 1 - x_{I,\infty} \alpha_{T,O} \, ln\left(T_f / T_\infty\right)$$ Soret Transport

$$\phi = \left[x_{I,\infty} - x_{O,\infty} \sum_{j \neq O} \Gamma_{Oj} \frac{\varepsilon_j}{\varepsilon_O} \right]^{-1}$$ Multicomponent Diffusion

FLAME UNSTEADINESS

$$\tau_d = \frac{4r_{d0}^2}{K}$$ Characteristic Droplet Lifetime

$$\tau_g = \frac{\left(2r_{f0}\right)^2}{D_g}$$ Characteristic Gas-Phase Diffusion Time

D_g = Effective gas-phase species diffusivity.

Quasisteady Flame Behavior is Promoted if τ_g/τ_d Decreases

$$\frac{\tau_g}{\tau_d} = \left(\frac{r_{f0}}{r_0}\right)^2 \frac{K}{D_g} \approx \left(\frac{\rho_d \nu_o}{8 W_F n X}\right)^2 \left(\frac{K}{D_g}\right)^3$$

Reducing D_g should increase flame unsteadiness.

D_g is influenced by inert species in the gas phase by changes in Soret transport and multicomponent diffusion effects.

PREVIOUS EXPERIMENTS (Shaw and Dee, 2003)

Drop-tower experiments
- NASA Glenn 2.2 s Drop Tower
- NASA Glenn drop dig

Test conditions
- Fiber-supported droplets
- Ambients at 1 atm

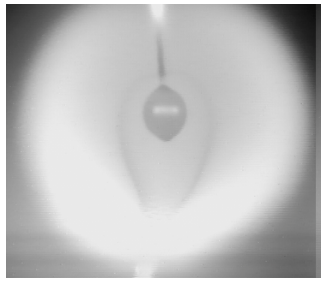

  - O_2/He
  - O_2/N_2
  - O_2/Xe

- O_2 Mole Fraction
  - X = 0.21, 0.5

Heptane-hexadecane droplets
- Initial hexadecane mass fractions
  - Y = 0, 0.05, 0.2

Considered flame unsteadiness, burning rates and sooting

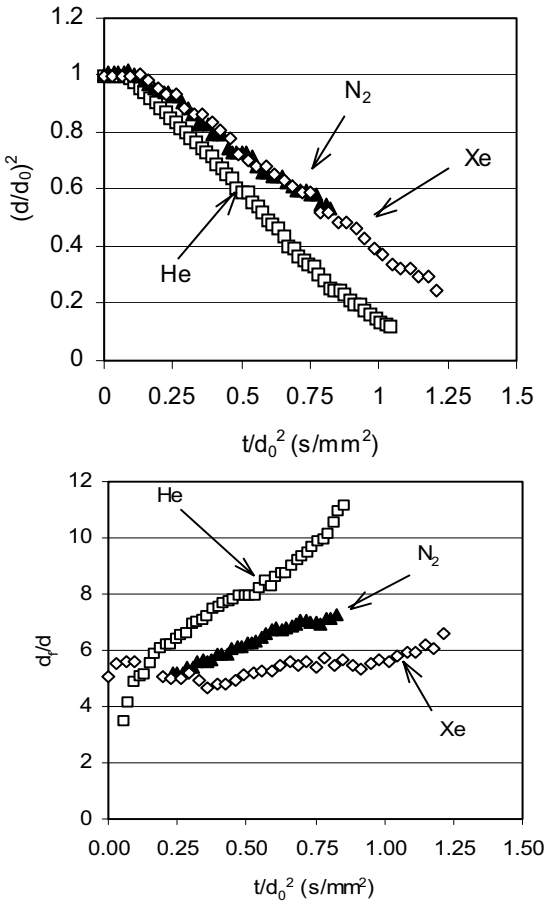

Increasing the inert molecular weight promoted flame unsteadiness

FLAME UNSTEADINESS INTERPRETATION

Inert	D_{IO} (cm^2/s)	ϕ	β	τ_g/τ_d ($D_g = D_{IO}$)	τ_g/τ_d ($D_g = \beta\phi D_{IO}$)
He	10.3	0.65	0.43	0.024	1.2
N_2	3.3	0.94	0.97	0.24	0.37
Xe	2.4	1.03	1.34	0.8	0.32

Multicomponent and Soret transport effects can reverse gas-phase unsteadiness trends with respect to inert species molecular weight

SOOT FORMATION

Inert	Le ($D_g = D_{IO}$)	Le ($D_g = \beta\phi D_{IO}$)
He	1.4	5.0
N_2	1.05	1.15
Xe	0.64	0.46

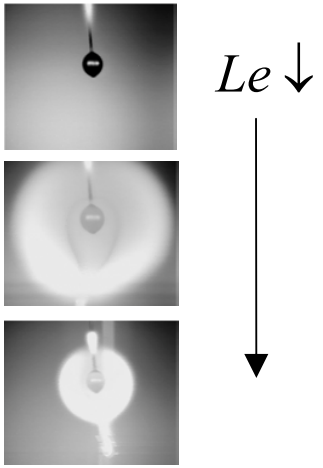

Decreasing the effective O_2 Lewis number promoted sooting in the experiments

Multicomponent and Soret transport effects can change effective Lewis numbers, which influence flame temperatures and sooting

SUMMARY

Soret transport and multicomponent diffusion can influence combustion behaviors

- Oxygen transport to flames
- Flame unsteadiness
- Sooting
- Burning rates
- Fuel transport to flames

Previous experiments have provided a preliminary indication that Soret transport and multicomponent diffusion can significantly influence combustion of liquid fuel droplets

Further research is presently being pursued to provide more information about these effects

This research will investigate Soret transport and multicomponent diffusion effects in significantly greater detail

- Future reduced-gravity experiments with different fuels and gas-phase compositions will be performed
- Analytical and numerical modeling will also be performed

ACKNOWLEDGEMENT

- The support provided by NASA is gratefully acknowledged
- Doctor Daniel L. Dietrich provided valuable guidance and technical assistance

COMPARISON OF CARBON DIOXIDE AND HELIUM AS FIRE EXTINGUISHING AGENTS FOR SPACECRAFT

Youngjin Son and Paul D. Ronney
University of Southern California, USA

Suleyman Gokoglu
NASA Glenn Research Center, USA

The effects of radiation heat transfer in microgravity compared to convection heat transfer in earth gravity for opposed-flow (downward) over thermally-thick fuel using low density foam fuel were investigated. Microgravity experiments on flame spread over thermally-thick fuels were conducted using foam fuels to obtain low density and thermal conductivity, and thus large flame spread rate compared to dense fuels such as PMMA. And thereby valid microgravity results were obtained even in 2.2 second drop-tower experiments not to mention for the longer duration tests in Zero Gravity Facility. Contrast to the conventional understanding, it was found that steady flame spread can occur over thick fuels in quiescent microgravity environments, especially when radiatively-active diluent gases such as CO_2 were employed. This is proposed to result from radiative heat transfer from the flame to the fuel surface, which could lead to steady spread even when the amount of the heat transfer via conduction from the flame to the fuel bed is negligible. Radiative effects are more significant at microgravity conditions because the flame is thicker and thus the volume of radiating combustion products is larger as well.

These results suggested that helium may be a better inert or extinguishment agent on both a mass and a mole bases at microgravity even though CO_2 is much better on a mole bases at earth gravity, and these are relevant to studies of fire safety in manned spacecraft, particularly the International Space Station that uses CO_2 fire extinguishers. CO_2 may not be as effective as an extinguishing agent at μg as it is at earth gravity in some conditions because of the differences in spread mechanisms between the two cases. In particular, the difference between conduction-dominated heat transport to the fuel bed at earth gravity and radiation-dominated heat transport at μg indicates that radiatively-inert diluent such as helium could be preferable in μg applications. Helium may be a superior fire suppression agent at μg on several bases. First, helium is more effective than CO_2 on a mole basis (thus pressure times storage volume basis) at μg, meaning that the size and weight of storage bottles would be smaller for the same fire-fighting capability. Second; helium is much more effective on a mass basis (by about 11 times) at μg. Third; helium has no physiological activity, unlike CO_2 that affects human respiration. Fourth, as compared to N_2 or CO_2, is not very soluble in water and thus has fewer tendencies to cause bloodstream bubble formation following rapid spacecraft cabin depressurization.

Paul D. Ronney
3650 McClintock Ave. OHE430
Los Angeles, CA, 90089
ronney@usc.edu
TEL: 213-740-0490
FAX: 213-740-8071

Comparison of carbon dioxide and helium as fire extinguishing agents for spacecraft

NASA grant NCC3-1056

Youngjin Son, Paul D. Ronney

University of Southern California, USA

Suleyman Gokoglu

NASA Glenn Research Center, USA

Department of Aerospace & Mechanical Engineering

Motivation

- Flame spread over solid fuels; a useful means of understanding more complex two-phase non-premixed flames
- Radiation is substantial, especially at reduced gravity – important in fire modeling in manned spacecraft
- Benefits of this research
  - Spacecraft fire safety - ISS will use CO_2 fire extinguishers, but flames spread *faster* at reduced gravity with CO_2 diluent due to radiative heating of fuel!
  - He has lots of advantages over CO_2 in ISS, at reduced gravity

Flame spread model for opposed flow with radiation

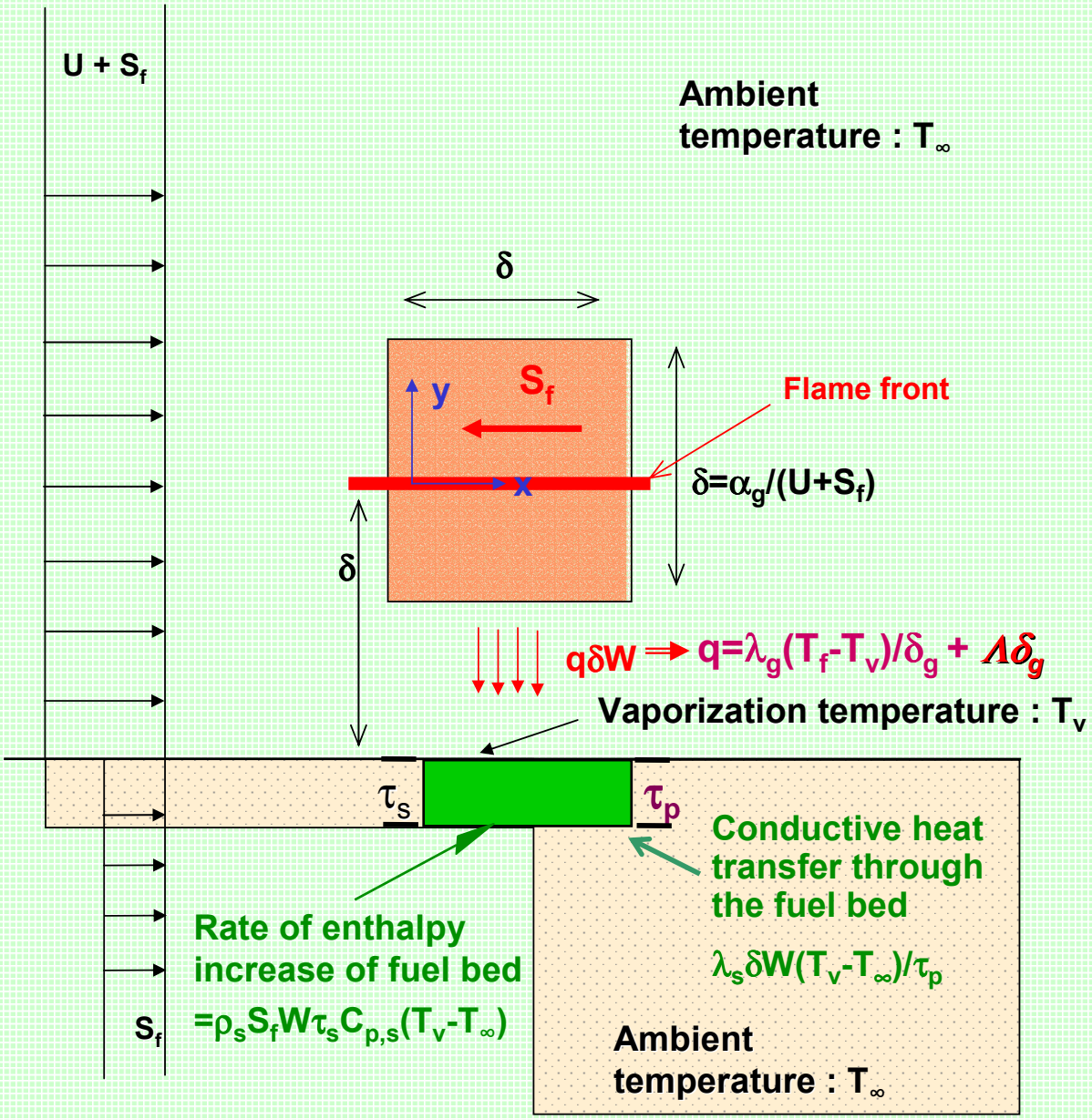

Theoretical background

- Equating heat generation from fuel with heat conduction through the gas q *(= heat transferred to fuel bed per unit area)*
- de Ris (1969): Radiative transfer from external source to fuel bed leads to steady spread over thick fuel bed even if U = 0
- Estimation of radiative flux from the flame to fuel bed leads to combined effects of conduction and radiation because hot gases such as CO_2 and SF_6 radiate by themselves:
- $q = \lambda_g (T_f - T_v)/\delta_g + \Lambda\delta_g$, Λ = radiative emission per unit volume
- $\delta_g = \alpha_g/S_f$ assume U=0
- Substitute into the equation

$$S_f \sim \frac{q^2\delta_g}{\rho_s C_{p,s}\lambda_s (T_v - T_\infty)^2}$$

$$S_f = \left[\frac{\Lambda\alpha_g^2}{\sqrt{\alpha_g\rho_s C_{P,s}\lambda_s}(T_v - T_\infty) - \lambda_g(T_f - T_v)}\right]^{1/2}$$

Experimental setup

- μg experiments; 2.2 second drop tower facility & Zero gravity facility were used
- Fuel
  - Problem with conventional thick fuels
    - Low S_f (e.g. PMMA ~ 0.006cm/sec in air,1atm):
    - Time scale ~ α/S_f^2 too large for drop towers
    - Length scale ~ α/S_f possibly too large even in space
  - Need very low $\rho_s\lambda_s C_{p,s}$ - use foams
  - Also high pressure - ρ_s higher, Q/V higher
- Polyphenolic foam; used in floral arranging, density : 0.029 g/cm^3
- Polyurethane foam; used in packing, density : 0.03 g/cm^3

Diluent gas effect on S_f

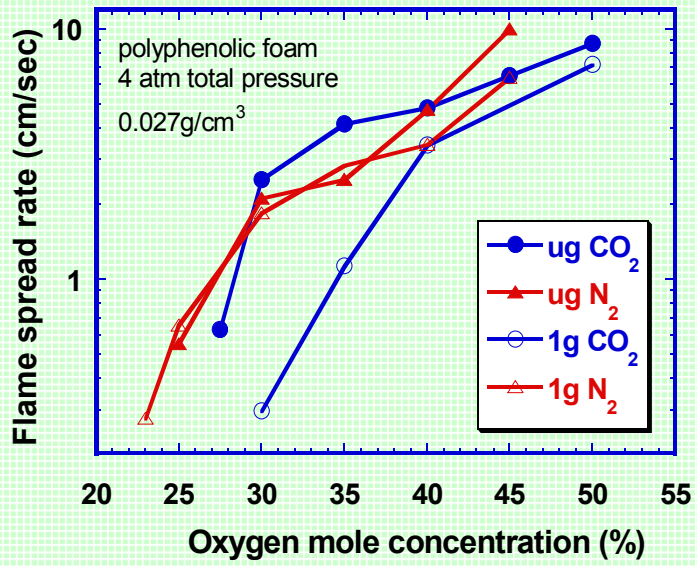

- For CO_2, S_f at μg is higher than at 1g, especially with CO_2 diluent & low O_2 concentrations, whereas for N_2 diluent, similar S_f
- At μg, S_f can be higher in CO_2 than N_2 at the same % O_2

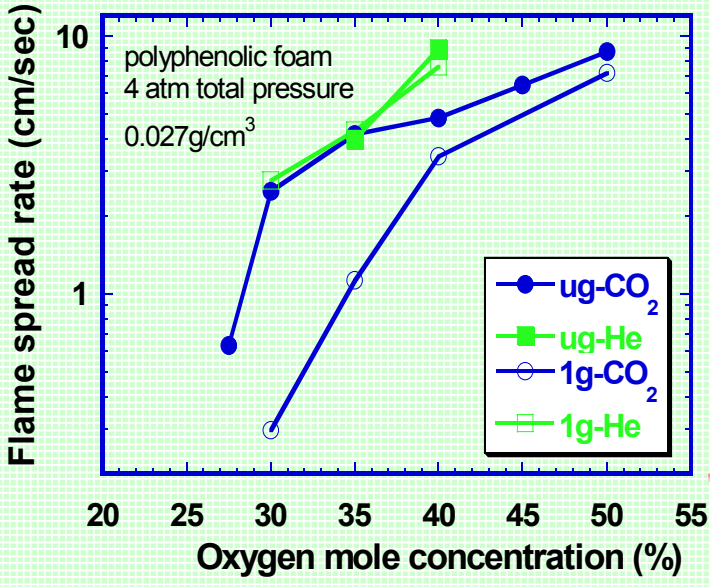

- He and CO_2 diluent shows similar S_f for fixed O_2 mole concentration even though mole based $C_p(CO_2) > C_p(He)$, $\lambda_g(CO_2) < \lambda_g(He)$ - T_f thus S_f is higher in He than CO_2 diluent;
- MOF (min. O_2 fraction) at 1g similar, but He has higher MOF at μg

Department of Aerospace & Mechanical Engineering

Helium and CO_2 comparison, μg

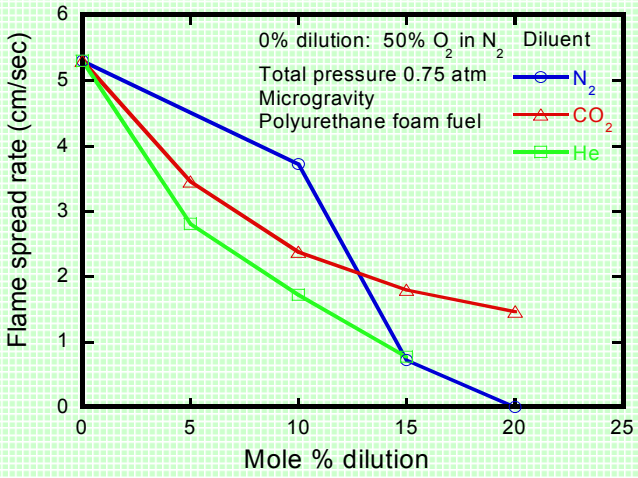

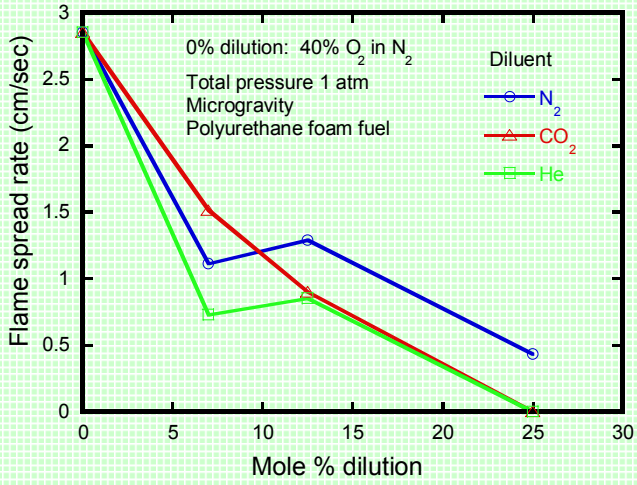

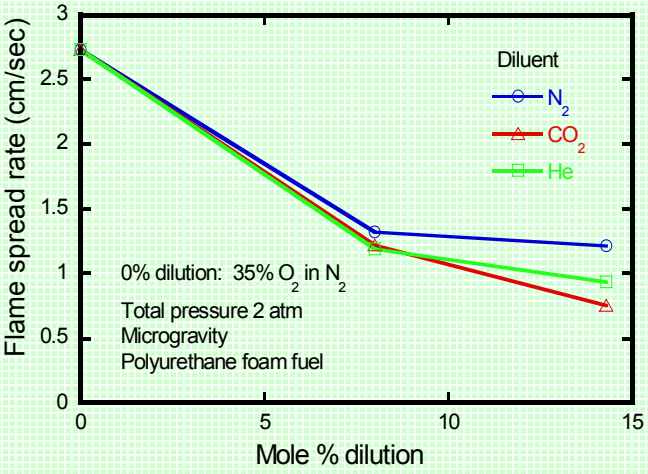

- He shows slower S_f than CO_2 diluted case at 0.75 atm, 50%O_2-N_2 of 0%dilution which is close to the space environment, µg
- The trend between He and CO_2 as an extinguisher or inert agent shows reverse as pressure increases; CO_2 shows higher S_f than He at 0.75 atm but lower S_f at 2 atm

Department of Aerospace & Mechanical Engineering

Helium and CO_2 comparison, 1g

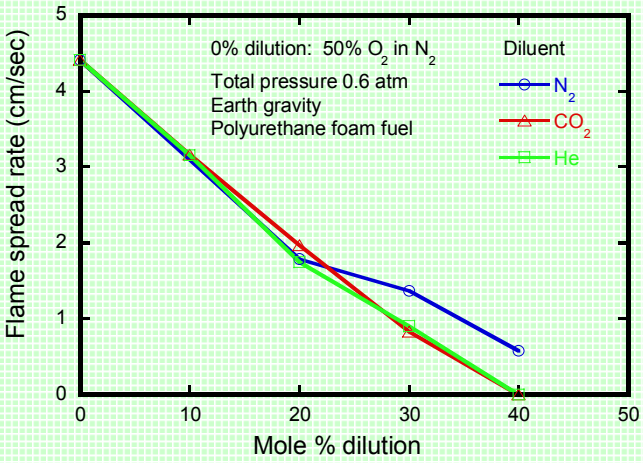

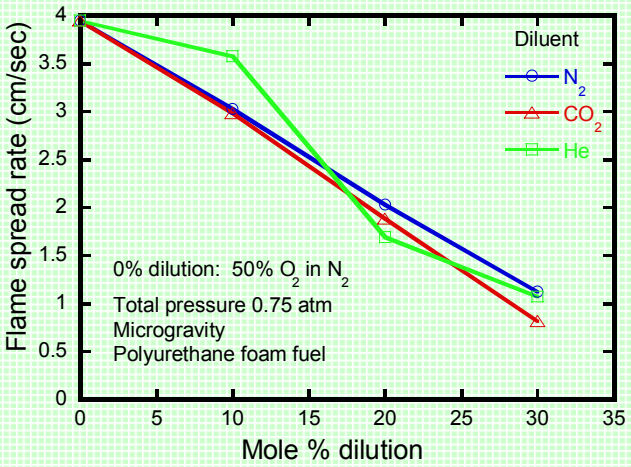

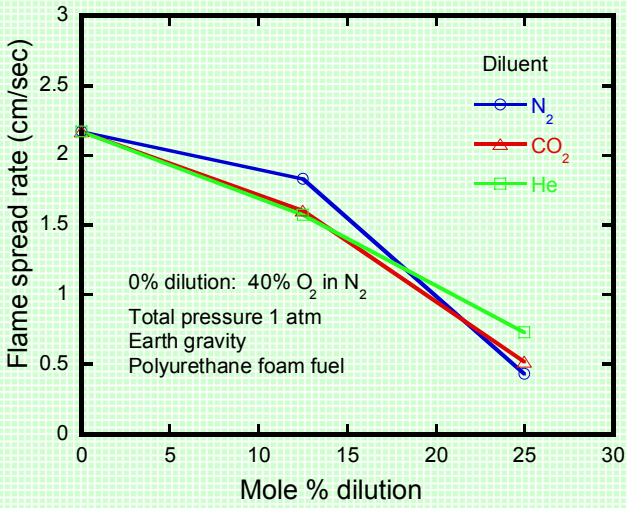

- **At 1g, CO_2 shows lowest S_f or similar**
- **He has more effects at μg**
- **1) Lewis No. effect; high Le → lower T_f → lower S_f (Zhang, *et.al.*, 1992)**
- **2) He; high $\lambda_g \rightarrow \alpha_g$ → thicker flame → more heat loss**
- **3) He; radiatively non-participating**
  - **No re-absorption**
  - **No re-radiation**

Department of Aerospace & Mechanical Engineering

Conclusion

- Drop-tower experiments show
  - S_f at μg in O_2-CO_2 sometimes *faster* than O_2-N_2 or O_2-He with same $\%O_2$
  - At high $\%O_2$ & low pressure, the addition of CO_2 diluent results in faster S_f than He at μg, but not at 1g.
- Results due to
  - Re-absorption and re-radiation of emitted radiation in O_2-CO_2 vs. no re-absorption and no re-radiation in O_2-N_2
  - Thicker flames (more volume ⇒ more radiation) at μg
- Radiative preheating of the fuel bed by the gas is significant and re-absorption effects can prevent massive heat losses (thus extinction) in radiatively-active atmospheres at μg
- ***He may be better extinguishing agent at μg than CO_2***
  - Same efficiency per mole (advantage for storage bottle mass & volume)
  - Much better per unit mass
  - **No physiological impact** (CO_2 affects human respiration)
  - Helium is **not soluble in water thus less tendency to cause bloodstream bubble formation** following cabin depressurization
  - Relevant to fire safety in manned spacecraft, specially ISS which uses CO_2 fire extinguisher

AGGREGATES AND SUPERAGGREGATES OF SOOT WITH FOUR DISTINCT FRACTAL MORPHOLOGIES

C.M. Sorensen, W. Kim, D. Fry, and A. Chakrabarti
Department of Physics
Kansas State University
Manhattan, KS 66506

Soot formed in laminar diffusion flames of heavily sooting fuels evolves through four distinct growth phases which give rise to four distinct aggregate fractal morphologies. These results were inferred from large and small angle static light scattering from the flames, microphotography of the flames, and analysis of soot sampled from the flames. The growth stages occur approximately over five successive orders of magnitude in aggregate size. Computer simulations can reproduce the kinetics observed in aggregation and aerogelation of soot clusters and indicate that these four growth stages involve either diffusion limit aggregation or percolation in either three or two dimensions.

Aggregates and Superaggregates of Soot with Four Distinct Fractal Morphologies

C.M. Sorensen, W. Kim, D. Fry, and **A. Chakrabarti**

Department of Physics
Kansas State University
Manhattan, KS 66506-2601

Abstract

Soot formed in laminar diffusion flames of heavily sooting fuels evolves through four distinct growth stages which give rise to four distinct aggregate fractal morphologies. These results were inferred from large and small angle static light scattering from the flames, microphotography of the flames, and analysis of soot sampled from the flames. The growth stages occur approximately over four successive orders of magnitude in aggregate size. Comparison to computer simulations suggests that these four growth stages involve either diffusion limited cluster aggregation or percolation in either three or two dimensions.

Fig.1 Diagram of the small angle and large angle light scattering apparatus. These apparatii allow us to probe soot morphologies from 70 nm to nearly 60 μm.

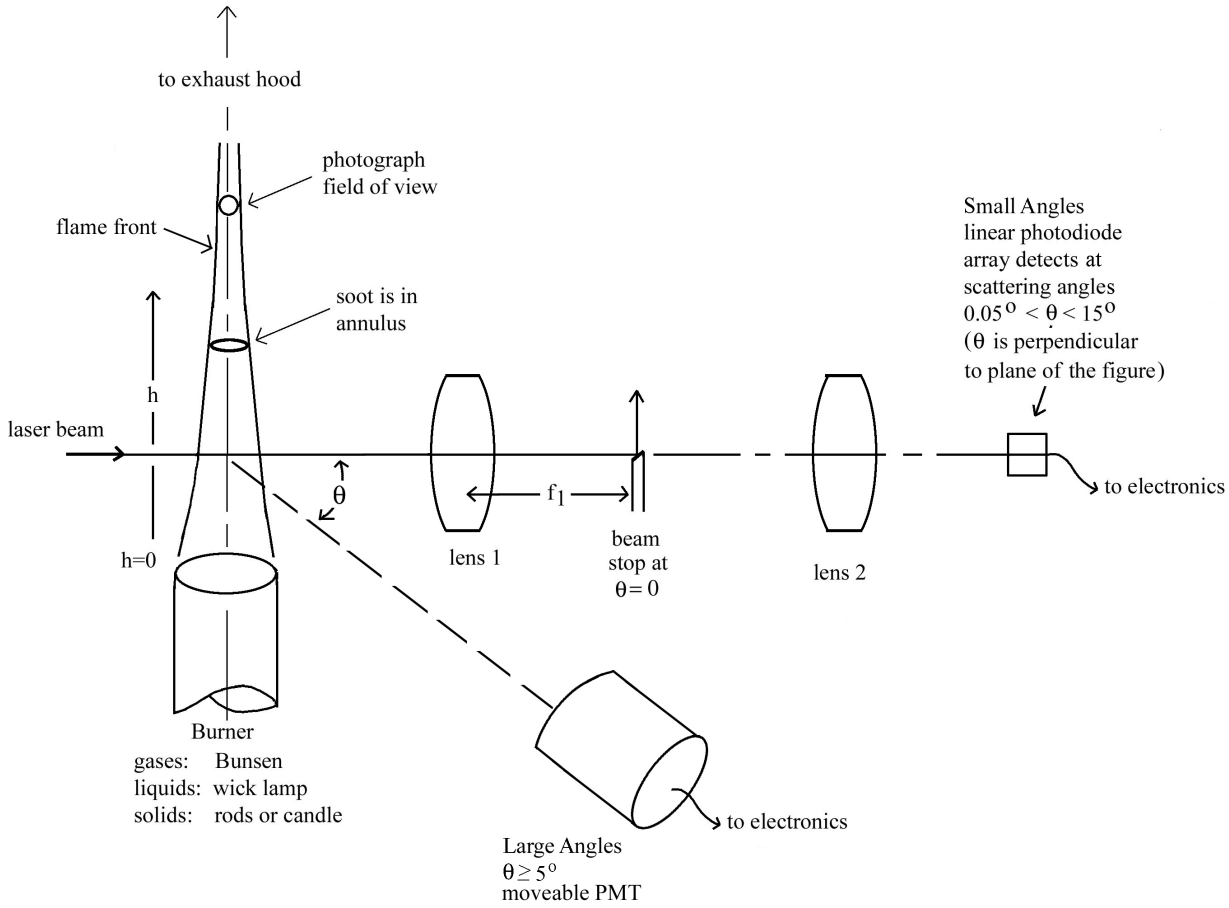

Fig. 2 Scattered Intensity as a function of wavevector, I(q), for an acetylene flame for various heights h above the burner.

Note the presence of: D ≃1.8 aggregates with size ~ 0.3 μm and D ≃2.6 aggregates with size ~ 12 μm at large h.

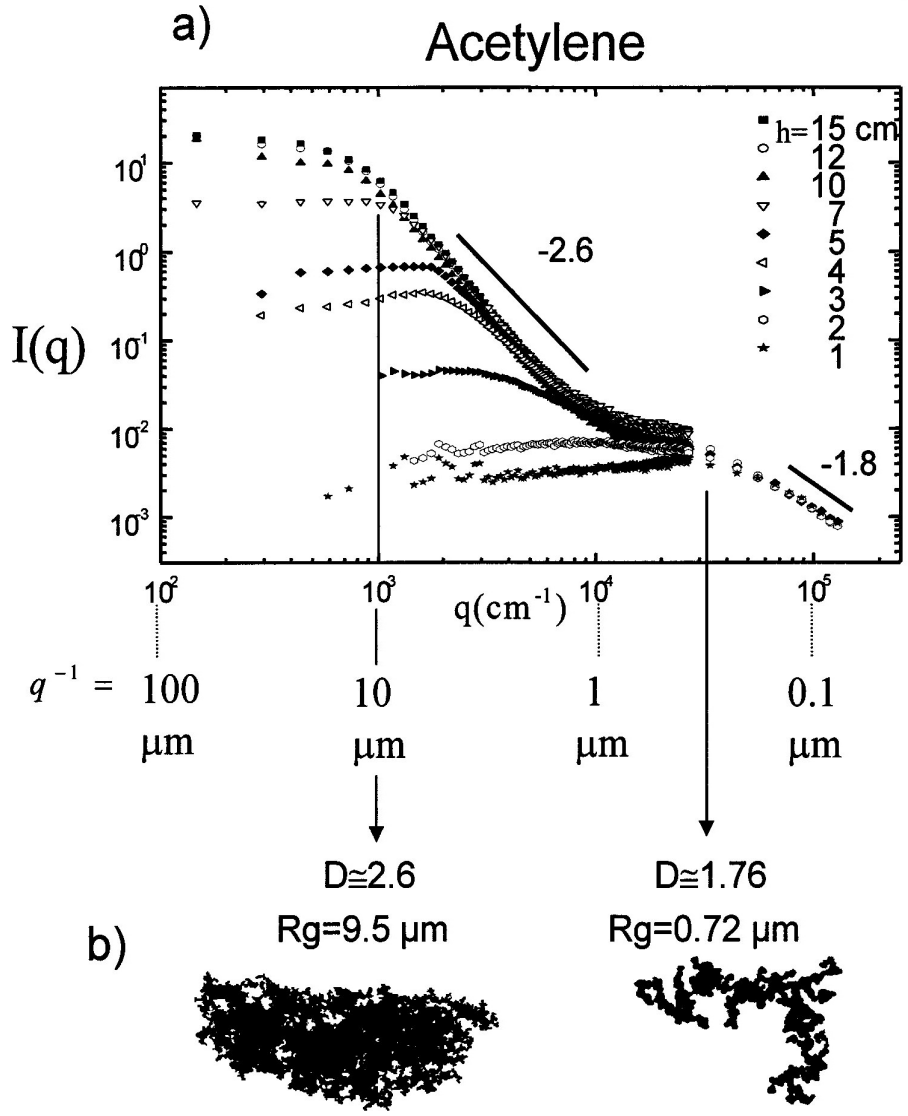

Right side of Fig.2b shows an example of submicrom soot (Stage 1) while left side shows supermicron soot superaggregates (Stage 2).

Similar behavior was observed for Toluene and 1-methylnapthalene.

Fig. 3 Transmission electron micrographs of large soot (supersoot) aggregates.

Next to each image is the perimeter of the aggregate.

Values for the radius of gyration R_g and mass fractal dimension D are given for each cluster. D was determined from the perimeter fractal dimension D_p following Julien, Thouy, and Ehrburger-Dolle (1994).

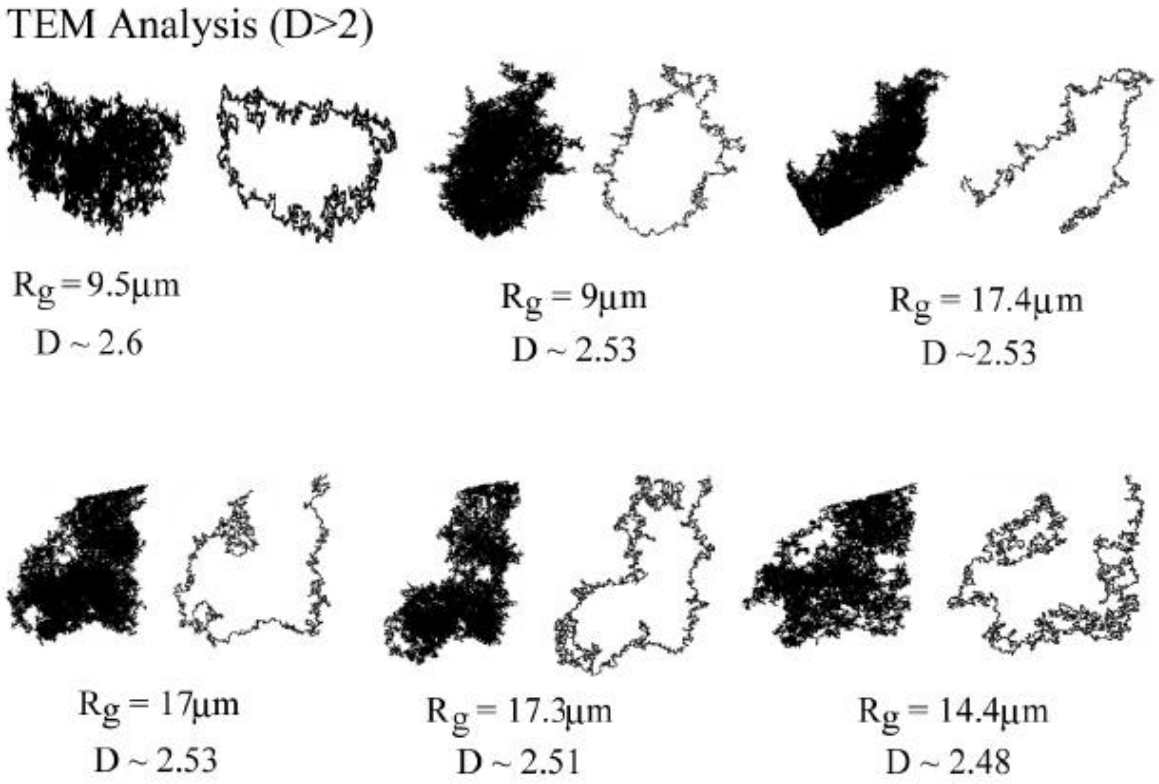

Fig. 4 Structure factor of an off-lattice, DLCA simulation in a cubic box (3d) of side L (measured in primary particle radii a) with N_m primary particles.

The structure factor S(q) is proportional to the light scattered intensity I(q) for a real system.

S(q) evolves with increasing time, as represented by the decreasing number of clusters, N_c, from a system with solely 3d, DLCA, $D \simeq 1.8$ aggregates to a system with percolated superaggregates with $D \simeq 2.6$ composed of the smaller $D \simeq 1.8$ aggregates.

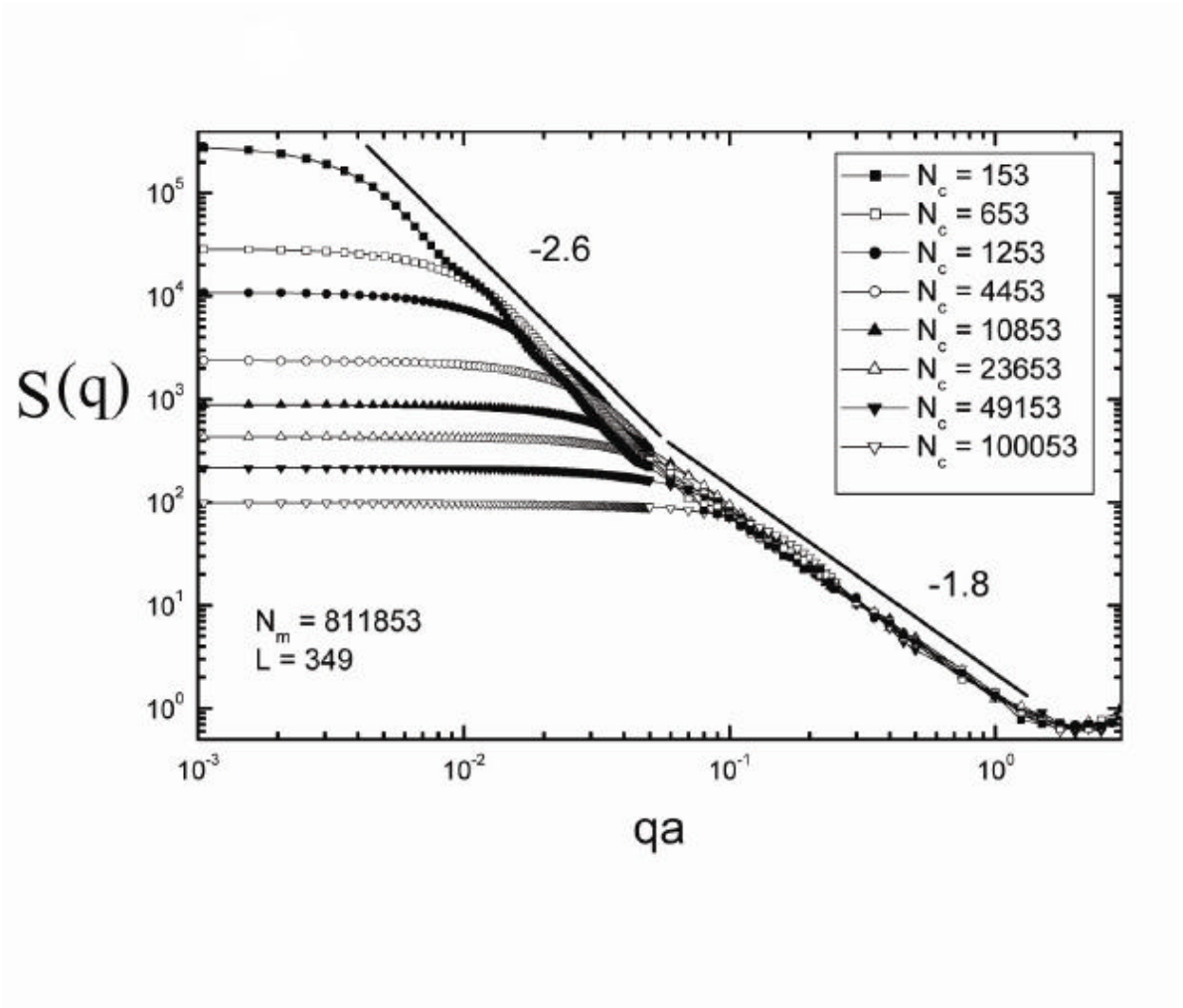

Fig. 5 Diagram of a Superaggregate

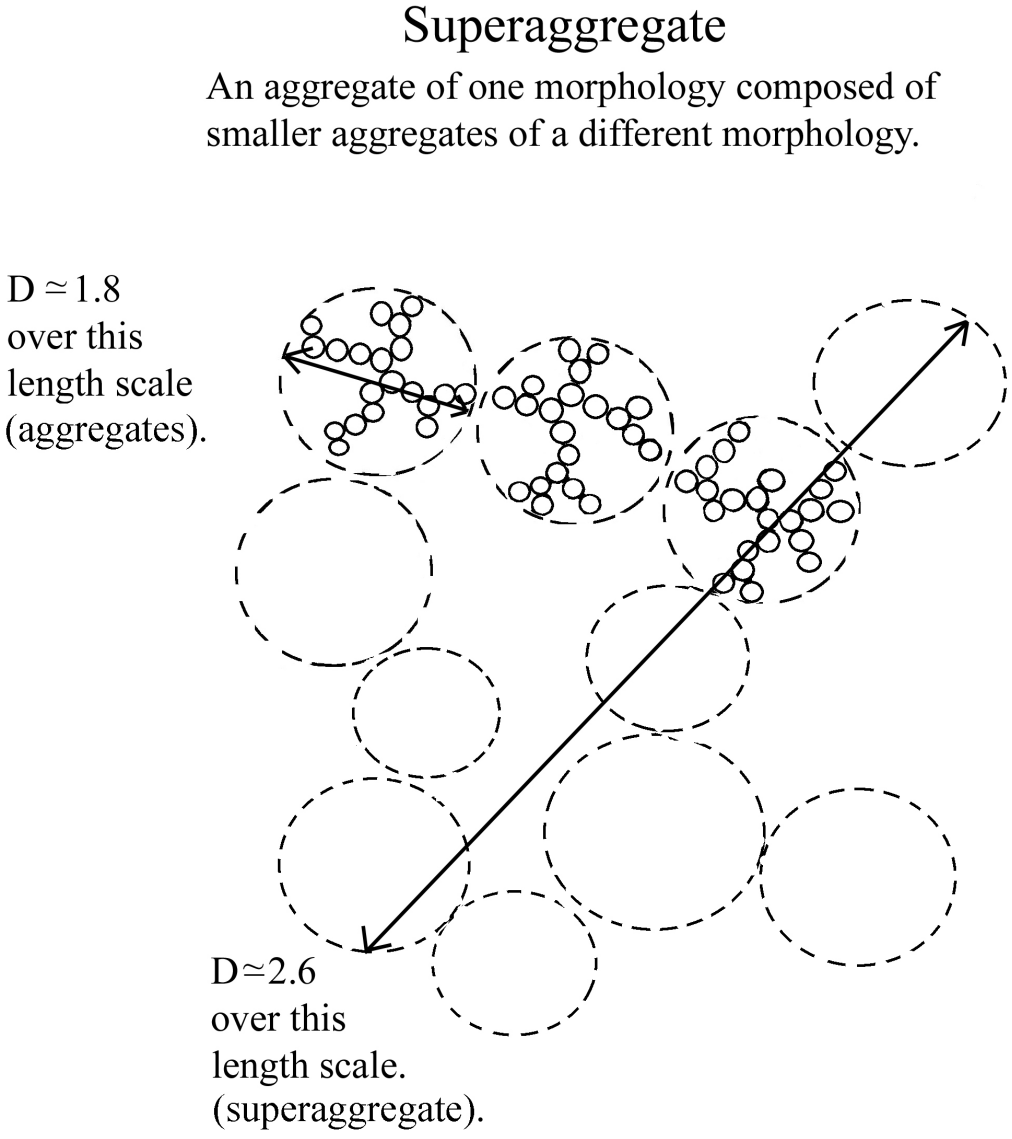

Fig. 6 (a) 7 nsec exposure photograph of soot in an acetylene/air flame at a height above burner of h=10cm. The width of the picture is 1mm.

(b) Binary digitized version of (a).

(c) Number of pixels per aggregate versus radius of gyration for an ensemble of soot clusters including those in (a).

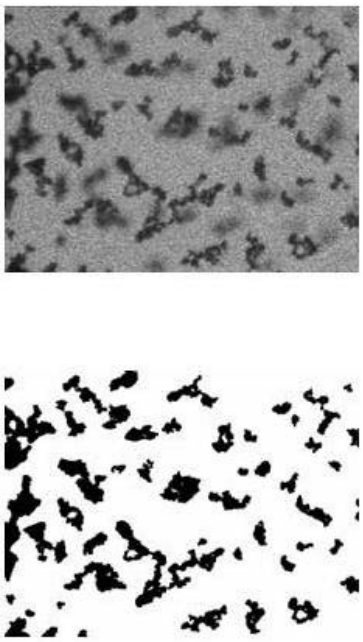

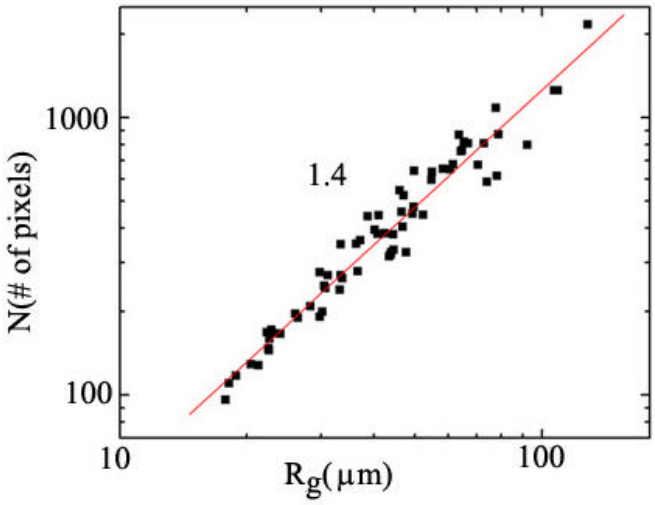

Fig. 7 Fourier transform, hence structure factor S(q), of the digitized image of a flame soot network, lower left corner, in a laminar acetylene/air diffusion flame at a height above burner of h=12cm.

Note the crossover from a slope of ≃ 1.4 to a slope of ≃ 2.1 indicating the formation of a 2d aerogel network.

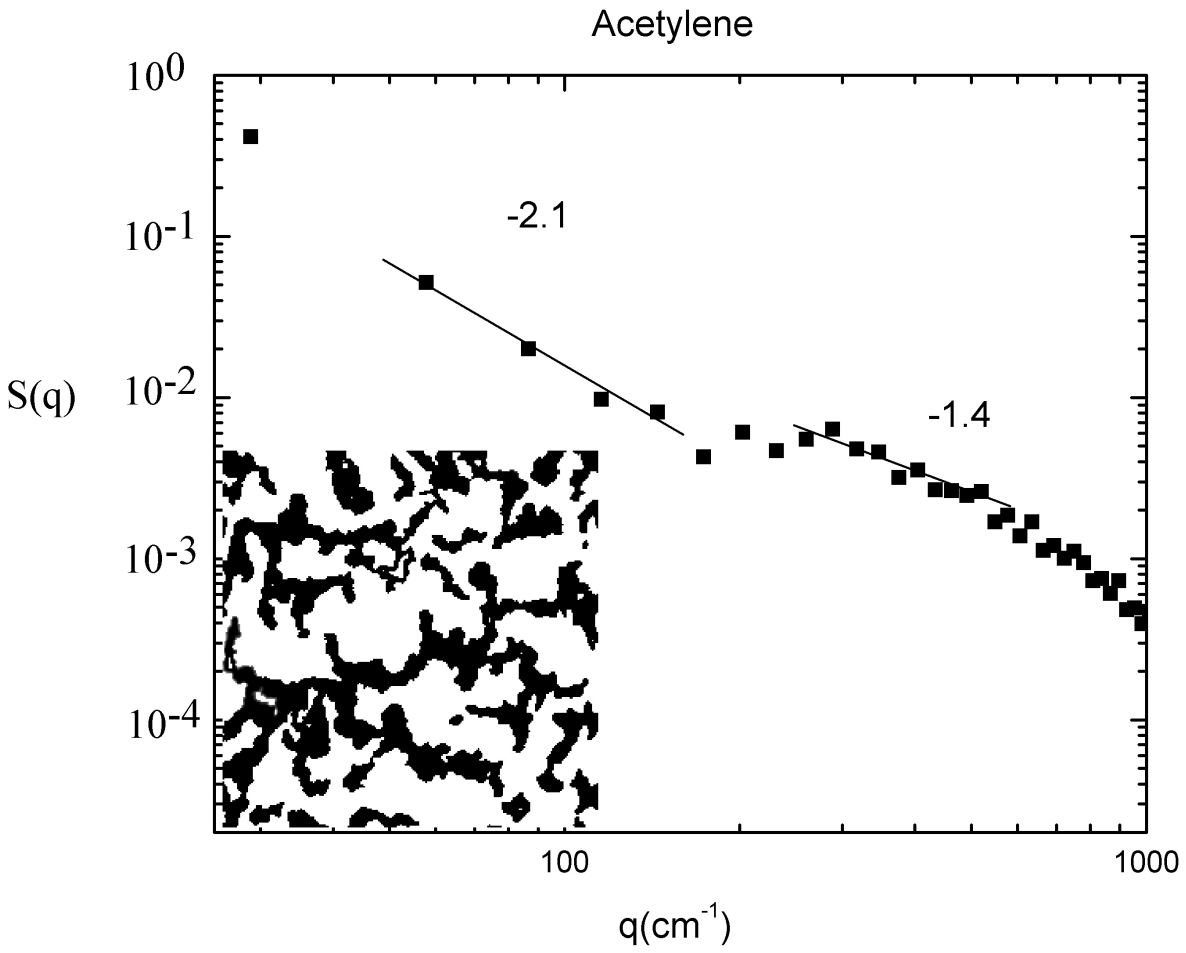

Fig. 8 Structure factor of an off-lattice, DLCA simulation on a square lattice (2d).

The $q^{-3.0}$ regime is the Porod regime of the square box with $q^{-(d+1)}$, d=2 and interference ripples due to the sharp edges of the box.

The $q^{-2.1}$ regime is due to percolated superaggregates with a fractal dimension of 1.9.

The $q^{-1.45}$ regime is due to 2d, DLCA aggregates that make up the superaggregate. The volume fraction of monomers is f_v=0.25.

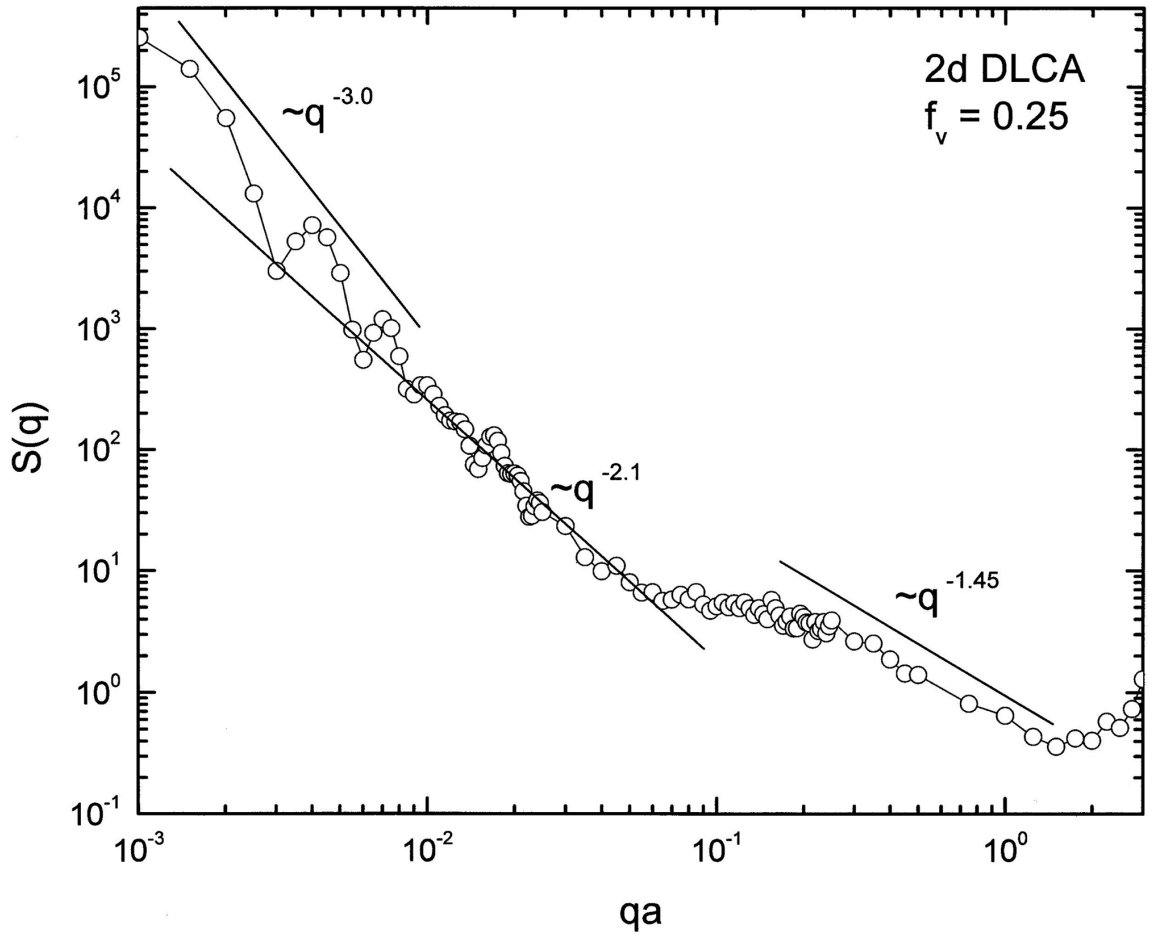

CONCLUSIONS

- **Current work leads to new picture of Soot Morphology in Heavily Sooting Laminar Diffusion Flames.**
- **With increasing Soot aggregate size, a rich phenomenology unfolds.**
- **Four different stages of growth --- each causing a specific morphology in the resulting aggregates.**
- **Summary of Current Work:**

Table I. The Realm of Supersoot

Stage 1	**Stage 2**	**Stage 3**	**Stage 4**
3d DLCA	3d Percolation or Restructuring?	2d DLCA	2d Percolation
$D \simeq 1.8$	$D \simeq 2.6$	$D \simeq 1.4$	$D \simeq 1.9$
aggregates	superaggregates	supersuperaggregates	gel network
$\sim 1 mm$	$\sim 10 mm$		$\sim 100 mm$

Aggregates and Superaggregates of Soot with Four Distinct Fractal Morphologies

C.M. Sorensen, W. Kim, D. Fry, and A. Chakrabarti

Department of Physics
Kansas State University
Manhattan, KS 66506-2601

The current view of soot formation and growth in flames involves a series of steps including fuel thermal decomposition to small radicals (Palmer and Cullis, 1965; Glassman, 1988) that react to form polyaromatic hydrocarbons (D'Anna, D'Alesso and Minutolo, 1994; Dobbins and Subramaniasivam, 1994; Dobbins, Fletcher and Chang, 1998; Frenklach, 2002) that subsequently nucleate, coalesce and dehydrogenate to yield roughly spherical, graphitic, primary particles of soot with diameters in the few tens of nanometer range (Lahaye and Prado, 1981). After this, the physical process of three-dimensional diffusion limited cluster aggregation (DLCA) (Meakin, 1999; Oh and Sorensen, 1997) proceeds to make noncoalesced clusters which have a fractal morphology with a universal fractal dimension of $D \simeq 1.8$ (Samson, Mulholland and Gentry, 1987; Zhang, Sorensen, Ramer, Olivier and Merklin, 1988; Dobbins and Megaridis, 1990; Sorensen, Cai and Lu, 1992; Koylu and Faeth, 1992). Thereafter environmental restructuring might occur, but with this single step of DLCA, the present description of in-flame soot growth ends.

Our work of the past few years has indicated that this picture is seriously incomplete for the soot produced in heavily sooting laminar diffusion flames. This includes the observation of gel-like networks of soot (Sorensen, Hageman, Rush, Huang and Oh, 1998), flat, two-dimensional soot (Sorensen and Hageman, 2001), and soot with a fractal dimension of 2.6 that was found in a variety of different flames (Sorensen, Kim, Fry, Shi and Chakrabarti, 2003; Kim, Sorensen and Chakrabarti, 2004). In this report we show that with increasing soot aggregate size, a rich phenomenology for soot in these flames unfolds. Four different stages of growth occur each causing a specific morphology in the resulting aggregates. These results are displayed in Table I (of main poster, conclusions section), and the evidence for these results will be described below. Our work is relevant to soot formation in common laminar diffusion flames in which the fuel and the oxidizer (e.g., oxygen in air) flow in a parallel manner in adjacent regions and diffuse together at the flame front.

In our experiments static light scattering was used to measure the structure of the soot aggregates in the flames (Sorensen, 2001). These measurements gave the scattered intensity I(q) as a function of q, the scattering wave vector, $q = 4\pi\lambda^{-1}\sin(\theta/2)$ where λ is the optical wavelength and θ is the scattering angle. An argon ion laser operating at $\lambda = 488\text{nm}$ was used as the light source. Both a small angle apparatus (Ferri, 1997), with $150\ \text{cm}^{-1} \le q \le 2.7\times10^{4}\ \text{cm}^{-1}$ (ca. $0.07° \le \theta \le 12°$) and a large angle apparatus, with $10^{4}\ \text{cm}^{-1} \le q \le 1.4\times10^{5}\ \text{cm}^{-1}$ (ca. $5 \le \theta \le 70°$) were used. A diagram of the apparatus is presented in Fig. 1 (of main poster). Since q^{-1} is the length scale of the scattering experiment, these apparatii allow us to probe soot morphologies from 70nm to nearly $60\mu\text{m}$.

Direct observation of the very large soot in the flame and the flame structure was accomplished using a 10 power photomicroscope with an object distance of 15 cm. The flame was backlit by a 7ns pulsed Nd:YAG laser with $\lambda = 532\text{nm}$ shining on a white background behind the flame. The flames were all laminar diffusion flames in ambient air. Gaseous fuels at controllable flow rates emanated from a brass tube 0.9 cm inside diameter. Liquid fuels were burned with a simple wick burner with wick diameter of 0.6 cm. Solid naphthalene was molded into a candle 0.6 cm in diameter. The fuels used are listed in Table 2 below.

Figure 2a of main poster shows the scattered intensity as a function of the wavevector, I(q), for an acetylene flame. Low in the flame, i.e., for heights above burner of h<2cm, the scattering is isotropic for low q but then bends over to a power law with slope ca. -1.8. The bend occurs near $q \simeq 3\times10^{4}\ \text{cm}^{-1}$ to imply an aggregate size of $q^{-1} \simeq 0.3\mu\text{m}$. This corresponds to the often observed and well known phase of submicron, fractal dimension $D \simeq 1.8$ soot which is a result of a 3d DLCA aggregation process (Meakin, 1999; Oh and Sorensen, 1997) (stage 1, Table 1).

Table 2. Fuels, threshold soot indices (TSI), and measured fractal dimensions within the 4 stages of soot growth. Dash means no measurements were attempted although stage 1 is expected for all flames.

Fuel	TSI	Stage 1	Stage 2	Stage 3	Stage 4
Gases					
Methane	~0	1.8	No	No	No
Ethylene	0.7	1.8	No	No	No
Acetylene	11	1.7	2.7	1.44	1.9
Liquids					
Hexadecane	5.8	-	No	No	No
Isooctane	6.4	-	No	No	No
1-Hexadecene	11	-	No	No	No
JP5 Fuel	-	-	Marginal	No	No
Decaline	15	-	Marginal	No	No
Toluene	44	1.7	2.6	1.39	1.9
Styrene	67	-	2.6	-	-
1-Methyl Naphthalene	91	1.8	2.5	(1.4)	1.9
Solid					
Naphthalene	100	-	2.7	1.5	1.9

With increasing height above burner, which corresponds to increasing time for the soot to grow, a very intense, second phase appears at low q. In the region ca. $800 \le q \le 8000\ cm^{-1}$ the slope of the log-log plot indicates a power law $I(q) \sim q^{-2.6}$ for this second phase. Note that the $q^{-1.8}$ regime remains at large q. This scattering behavior may be interpreted to indicate a phase of ca. $12\mu m$ soot with a fractal dimension of $D \simeq 2.6$ for length scales of $1.2\mu m$ to $12\mu m$ (stage 2) and $D \simeq 1.8$ for scales smaller than $0.3\mu m$ down to the primary particle size (ca. 25nm as determined by TEM). Results for the toluene and 1-methylnaphthalene show the same behavior. We have shown (Kim, Sorensen and Chakrabarti, 2004) that this large, $D \simeq 2.6$ phase occurs in laminar diffusion flames of all heavily sooting fuels as quantified by the Thermal Sooting Index (TSI) as defined by Calcote and Manos, 1983 and Olson, Pickens and Gill, 1985, specifically when $TSI \ge 10 \pm 2$ (roughly, the larger the fuel TSI, the sootier the flame). Otherwise, for less sooty flames only the submicron, $D \simeq 1.8$ soot is seen; no $D \simeq 2.6$ phase nor the subsequent phases to be described below (see Table 2).

To corroborate the light scattering measurements soot was sampled from the flame using a well established thermophoretic technique (Dobbins and Megaridis, 1987). Figure 2b (right side) shows an example of submicron soot (stage 1) collected low in the acetylene/air diffusion flame and Fig. 2b (left side) shows an example of supermicron soot superaggregates (stage 2) collected high in the flame. Visual inspection shows the much more compact appearance of the large soot than the small, qualitatively supporting a larger fractal dimension for the larger aggregate. Previous real space analysis of projected images of submicron soot have confirmed the $D \simeq 1.7$ to 1.8 fractal dimension (Dobbins and Megaridis, 1987; Koylu and Faeth, 1992; Cai, Lu and Sorensen, 1993).

For the large soot aggregates we applied an analysis developed by Jullien, Thuoy and Ehrburger-Dolle, 1996 for 2d projected images of 3d fractal aggregates with D>2. Using simulations they found the relation $D = 3 - (D_p - 1)^{2/3}$ between the perimeter fractal dimension D_p and the true 3d mass fractal dimension D. Figure 3 in the main poster gives more examples of these large, relatively dense soot aggregates. We measured 10 large clusters to find $D_p = 1.26 \pm 0.06$. This D_p implies $D = 2.6 \pm 0.06$, in excellent agreement with our light scattering results. Furthermore, the average size we measure for the collected aggregates is $10 \pm 3\mu m$, also in excellent agreement with light scattering.

The mechanism that creates this second phase is still somewhat uncertain. One scenario is that it represents 3d DLCA clusters with initial $D \simeq 1.8$ that have grown to ca. $10\mu m$ or larger and then restructured to a denser $D \simeq 2.6$ (hence smaller) under the shear stress at the flame front. There is evidence for shear restructuring of

DLCA aggregates to larger fractal dimensions in colloids (Martin, Wilcoxon and Schaefer, 1990; Carpeneti, 1990; Jung, Amal and Raper, 1996; Selomulya, Bushell, Amal and Waite, 2002). There is, however, no evidence for ca. $10\mu m$, $D \simeq 1.8$ aggregates in our flames necessary for restructuring. A second scenario, that we consider more likely and have described previously (Sorensen, Kim, Fry, Shi and Chakrabarti, 2003; Kim, Sorensen and Chakrabarti, 2004; Fry, Chakrabarti, Kim and Sorensen, 2003), was inspired by our recent simulations (Fry, Chakrabarti, Kim & Sorensen, 2003) of 3d DLCA that show when the aggregates grow, they eventually fill all space and then jam together. The result is a percolated, $D \simeq 2.6$ *superaggregate* of the smaller $D \simeq 1.8$, DLCA aggregates. Structure factors of our simulations, Fig. 4 is an example, show both the $D \simeq 2.6$ and $D \simeq 1.8$ regimes as seen in our flame data, e.g., Fig. 2a. We have shown that the crossover length scale between the $D \simeq 1.8$ and 2.6 regimes is consistent with soot volume fraction measurements (Sorensen, Kim, Fry and Chakrabarti, 2003; Fry, Chakrabarti, Kim and Sorensen, 2003, Fry, Sintes, Chakrabarti and Sorensen, 2002). Figure 5 shows a diagram of our vision of a superaggregate.

Figures 6a shows 7nsec exposure photographs of submillimeter soot in acetylene. These clusters are flat, quasi-2d (they are seen face on in Figs. 6a) similar to those seen previously in acetylene flames (Sorensen and Hageman, 2001) (stage 3). Following that previous analysis, cluster images were digitized into binary format (Figs. 6b) then were analyzed to determine the number of dark pixels N_p, which is proportional to cluster mass, and R_g, the cluster radius of gyration for each cluster. If the clusters are fractal, then the well known relationship $N_p \sim R_g^D$ will hold. Figures 6c shows a log-log plot of N_p vs. R_g yielding a fractal dimension of $D = 1.44 \pm 0.05$. Thus flames yield flat aggregates with a fractal dimension of ca. 1.45 over length scales of ca. 10 to $100\mu m$. This morphology is stage 3 in Table 1. Similar results were found previously (Sorensen and Hageman, 2001).

In previous work on laminar acetylene/air flames we concluded that this phase of soot occurs because the soot, which is confined to an annular flame front, becomes larger than the thickness of the flame front and thus is confined in an effectively two-dimensional (2d) space (Sorensen and Hageman, 2001) in which to aggregate. Simulations of 2d DLCA yield fractal aggregates with D=1.44 consistent with our measurements (Meakin, 1999). Thus we named this phase "two-dimensional soot." Since this phase of soot is immediately larger than the second phase of soot described above, and since it has a different fractal dimension, 1.45 as opposed to 2.6, we propose that it is a third phase of soot consisting of 2d, DLCA aggregates of the superaggregates of phase two. We call these aggregates of superaggregates "supersuperaggregates." They have three levels of structure, each level having its own fractal dimension, and two crossover length scales, one between each consecutive level, as outlined in Table 1, stages 1, 2, and 3.

Flame spanning networks of soot are seen higher in the flames or at larger fuel flow rates. Example of a digitized image for acetylene flames is given in the lower left hand corner of Fig. 7. Once again we stress that as for the supersuperaggregates these networks are confined to the thin cylindrical annulus of the flame front. In previous work we argued that this network was an aerogel (Sorensen, Hageman, Rush, Huang and Oh, 1998), an argument that we will now support quantitatively. Analysis of this aerogel network structure was accomplished by Fourier transformation of the digitized images obtained with the photomicroscope. Analysis of Fourier transform data at low q is hampered by the finite size of the picture that is 1mm square. The raw data show "interference ripples" due to the hard edges of the picture box. To remove this box effect the uniform box was Fourier transformed, and the raw data were normalized with this to yield a corrected structure factor showing only the structure of the image, not the picture box. The resulting q-space function is a structure factor, S(q) vs. q, is proportional to a light scattering result, I(q), shown in Fig. 7.

In each analysis at large $q\left(>1000cm^{-1}\right)$ a slope of -3 is found (not shown in the figures) We interpret this as Porod scattering, $I(q) \sim q^{-(d+1)}$ for d=2, to imply that the image is uniformly black for lengths $q^{-1} < 10^{-3} = 10\mu m$. This value is consistent with our photographic resolution limit which we estimate to be $5\mu m$, i.e., for length scale less than 5 to $10\mu m$ the image is uniformly black and two dimensional. This is a mild test of our analysis.

For $200 \le q \le 700cm^{-1}$, which corresponds to length scales q^{-1} of 14 to $50\mu m$, the I(q) data roughly follow a power law of $I(q) \sim q^{-1.4}$. This is a poor resolution observation of a remnant of the 2d, $D \simeq 1.45$ supersuperaggregates, stage 3. We propose that it is these supersuperaggregates that come together to form the gel network. For $30 \lesssim q \lesssim 200\ cm^{-1}$, i.e., length scales of 50 to $300\ \mu m$, data for all flames showed a $I(q) \sim q^{-2.1}$ power law. This power law can be understood by comparing to simulations of 2d DLCA aggregation we performed. These simulations were allowed to proceed until the system percolated to form a gel network. Figure 8 shows the

structure factor for a simulation with nearly 4×10^5 monomers allowed to aggregate via Brownian motion in a 2d box until only one large cluster formed. Real space analysis of this large cluster showed it had a fractal dimension of 1.9, consistent with a 2d, percolation cluster (Stauffer and Aharony, 1992). The entire box was Fourier transformed for direct comparison to the flame network data. The results in Fig. 14 are strikingly similar to the flame data including both the $q^{-1.4}$ and $q^{-2.1}$ regimes (and interference ripples due to the finite system size). The power law exponent (2.1) does not equal the fractal dimension, $D\simeq1.9$, in this case because D is almost equal to the spatial dimension d. Note that when D=d, a Porod law with power –(d+1) results, which would be q^{-3} for this 2d situation. Thus the $q^{-2.1}$ power law implies that the fractal dimension of the network, in both the flame soot and the simulation, is less than but very close to the spatial dimension of d=2. This strongly supports the contention that the gel-like network structure in our flames is the result of a 2d percolation of the $D\simeq1.4$, 2d DLCA, supersuperaggregates.

ACKNOWLEDGMENT

This work was supported by NSF grant CTS0080017 and NASA grant NAG3-2360.

REFERENCES

1. Cai, J., Lu, N. & Sorensen, C. M. (1993), *Langmuir, **9**,* 2861-2867.
2. Calcote, H. F. & Manos, D. M. (1983), *Combust. Flame, **49**,* 289-304.
3. Carpineti, M., Ferri, F., & Giglio, M. (1990), *Phys. Rev. A, **42**,* 7347-7354.
4. D'Anna, A., D'Alesso, A. & Minutolo, P. (1994), in H. Bockhorn (Ed), *Soot Formation in Combustion: Mechanisms and Models* (p. 83), Springer-Verlag, Heidelberg.
5. Dobbins R. A. & Megaridis, C. M. (1987), *Langmuir, **3**,* 254-259.
6. Dobbins, R. A. & Megaridis, C. M. (1990), *Combust. Sci. Tech., **71**,* 95-109 .
7. Dobbins R. A. & Subramaniasivam, H. (1994), Soot precursor Particles in Flames, in H. Brockhorn (Ed.), *Soot Formation in Combustion: Mechanisms and Models* (pp. 290-301), Springer-Verlag Berlin, Heidelberg,.
8. Dobbins, R. A., Fletcher, R. A. & Chang, H.-C. (1998), *Comb. & Flame, **115,*** 285-298.
9. Ferri, F. (1997), *Rev. Sci. Instr., **68,*** 2265-2274.
10. Frenklach, M. (2002), *Phys. Chem. Chem. Phys., **4**,* 2028-2037.
11. Fry, D., Sintes, T., Chakrabarti, A. & Sorensen, C. M. (2002), *Phys. Rev. Lett., **89,*** 148301-148301-4.
12. Fry, D., Chakrabarti, A., Kim W. & Sorensen C. M. (2004), *Phys. Rev. E, **69**,* 061401-1-061401-10.
13. Glassman, I. (1988), Soot formation in combustion processes; *Twenty-Second Symposium (International) on Combustion* (pp. 295-311), The Combustion Institute.
14. Jullien, R., Thouy, R. & Ehrburger-Dolle, F. (1994), *Phys. Rev. E, **50,*** 3878-3882.
15. Jung, S. J., Amal, R. & Raper, J. A. (1996), *Powder Tech. **88**,* 51-54.
16. Kim, W., Sorensen, C. M. & Chakrabarti, A. (2004), **20**, 3969-3973.
17. Koylu, U. O. & Faeth, G. M. (1992), *Combust. Flame, **89,*** 140-156.
18. Lahaye J. & Prado, G. (1981), Morphology & internal structure of soot & carbon blacks, in D.C. Siegla, and G.W. Smith (Eds.), *Particulate carbon: Formation during combustion* (pp. 33-51); Plenum Press, New York.
19. Martin, J. E., Wilcoxon, J. P., Schaefer, D. & Odinek, J. (1990), *Phys. Rev. A, **41**,* 4379-4391.
20. Meakin, P. (1999), *J. of Sol-Gel Sci. & Tech., **15**,* 97-117.
21. Oh, C. & Sorensen, C.M. (1997), *J. Aerosol Sci., **28**,* 937-957.
22. Olson, D. B. Pickens, J. C. and Gill, R. J. (1985), *Combust. Flame, **62,*** 43-60.
23. Palmer, H. B. & Cullis H. F. (1965), *The Chemistry and Physics of Carbon*, Vol. 1, 205, Marcel Dekker, New York.
24. Samson, R. J., Mulholland, G. W., & Gentry, J. W. (1987), *Langmuir, **3,*** 272-281.
25. Selomulya, C., Bushell, G., Amal, R. & Waite, T.D. (2002), *Langmuir, **18,*** 1974-1984.
26. Sorensen, C. M., Cai, J. & Lu, N. (1992), *Appl. Optics, **31,*** 6547-6557.
27. Sorensen, C.M., Hagemann, W.B., Rush, T.J., Huang, H. & Oh, C. (1998), *Phys. Rev. Lett., **80,*** 1782-1785.
28. Sorensen, C. M. & Hageman, W.B. (2001), *Langmuir, **17,*** 5431-5434.
29. Sorensen, C. M. (2001), *Aerosol Sci. Tech., **35,*** 648-687.
30. Sorensen, C. M., Kim, W., Fry, D., Shi, D. & Chakrabarti A. (2003), *Langmuir, **19**,* 7560-7563.
31. Stauffer, D. & Aharony, A. (1992), *Introduction to Percolation Theory*, Taylor and Francis, London.
32. Zhang, H. X., Sorensen, C. M., Ramer, E. R., Olivier, B. J. & Merklin, J. F. (1988), *Langmuir, **4**,* 867-871.

DYNAMICS AND STABILITY OF CAPILLARY SURFACES: LIQUID SWITCHES AT SMALL SCALES

Paul H. Steen, Anand Bhandar, and Michael J. Vogel
School of Chemical and Biomolecular Engineering
Cornell University
Ithaca, NY 14850

Amir H. Hirsa
Rensselaer Polytechnic Institute
Troy, NY 12180

The dynamics and stability of systems of interfaces is central to a range of technologies related to the Human Exploration and Development of Space (HEDS). Our premise is that dramatic shape changes can be manipulated to advantage with minimal input, if the system is near instability. The primary objective is to develop the science base to allow novel approaches to liquid management in low-gravity based on this premise. HEDS requires efficient, reliable and lightweight technologies. Our poster will highlight our progress toward this goal using the capillary switch as an example.

A 'capillary surface' is a liquid/liquid or liquid/gas interface whose shape is determined by surface tension. For typical liquids (e.g., water) against gas on earth, capillary surfaces occur on the millimeter-scale and smaller where shape deformation due to gravity is unimportant. In low gravity, they can occur on the centimeter scale. Capillary surfaces can be combined to make a switch – a system with multiple stable states. A capillary switch can generate motion or effect force. To be practical, the energy barriers of such a switch must be tunable, its switching time (kinetics) short and its triggering mechanism reliable. We illustrate these features with a capillary switch that consists of two droplets, coupled by common pressure. As long as contact lines remained pinned, motions are inviscid, even at sub-millimeter scales, with consequent promise of low-power consumption at the device level. Predictions of theory are compared to experiment on i) a soap-film prototype at centimeter scale and ii) a liquid droplet switch at millimeter-scale.

NASA/CP—2004-213205/VOL2

Dynamics and stability of capillary surfaces: low-dissipation liquid switches

P. H. Steen[1], A. S. Bhandar[1], M. J. Vogel[1], A. H. Hirsa[2]

[1]Chemical Engineering, Cornell University

[2]Mechanical Engineering, Rensselaer Polytechnic Institute

NASA NAG3-2713

Will the liquid micro-switch become to ‘micro-fluidics’ as the transistor is to ‘micro-electronics’?

‘Capillary surface’ ~ shape determined by σ

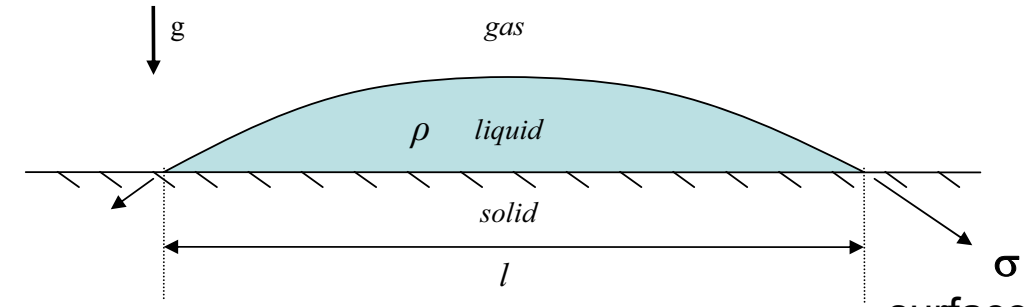

σ
surface tension

λ~ 3 mm
for water

Capillary length

$$\lambda \equiv \left(\frac{\sigma}{\rho g} \right)^{\frac{1}{2}}$$

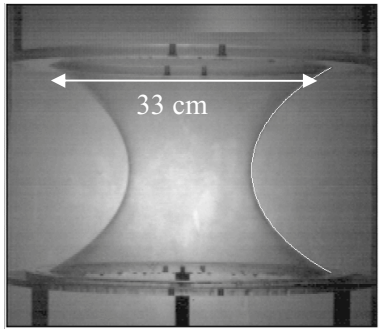

Robinson & phs
JCIS 2001

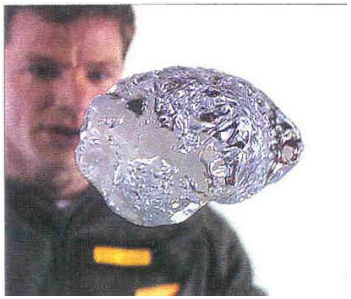

Weislogel & Lichter
Phys. Fluids 1998

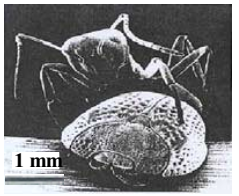

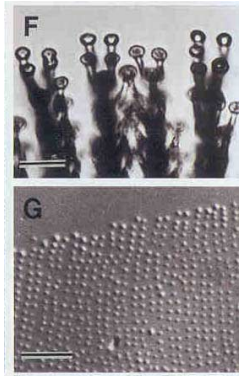

10 μm

50 μm

Eisner & al.
PNAS 2000

Switches

Mechanical Switch

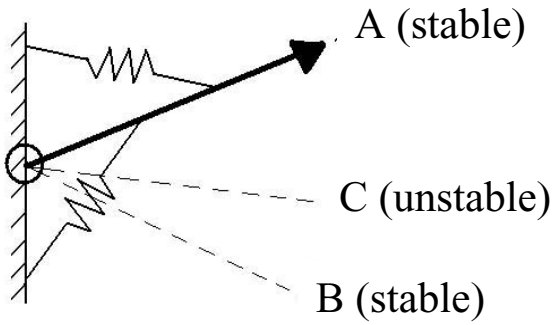

Concept:
Use capillary instability to advantage to produce devices that require low power

Issues:

- bistability (thermostatics)
- toggling (activation physics)
- switching time (kinetics)
- robustness (basins of attraction)

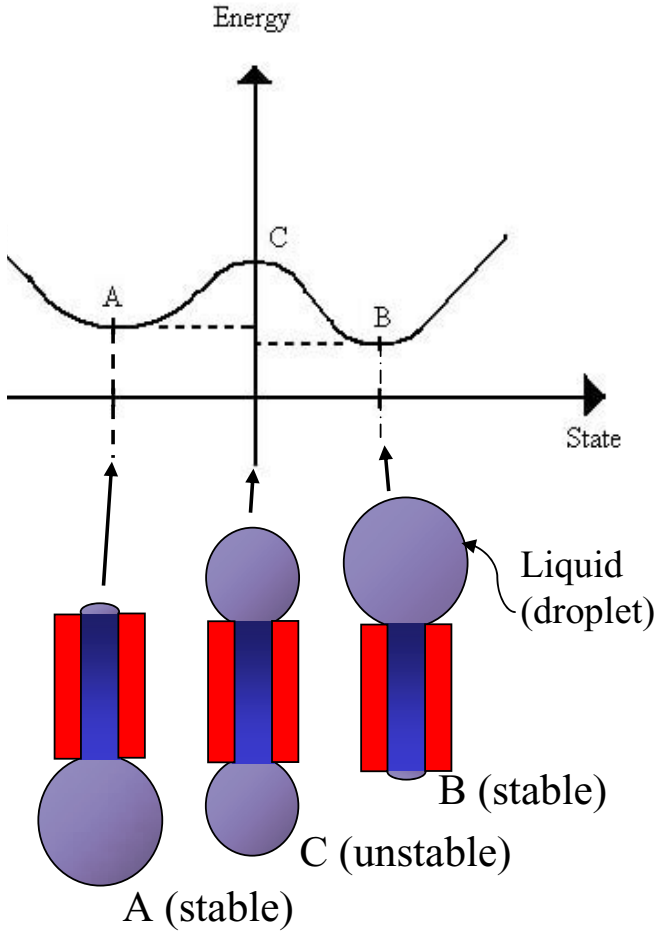

capillary bistability
(axisymmetric)

CV Boys 1890

Response of droplet-droplet system: bistability

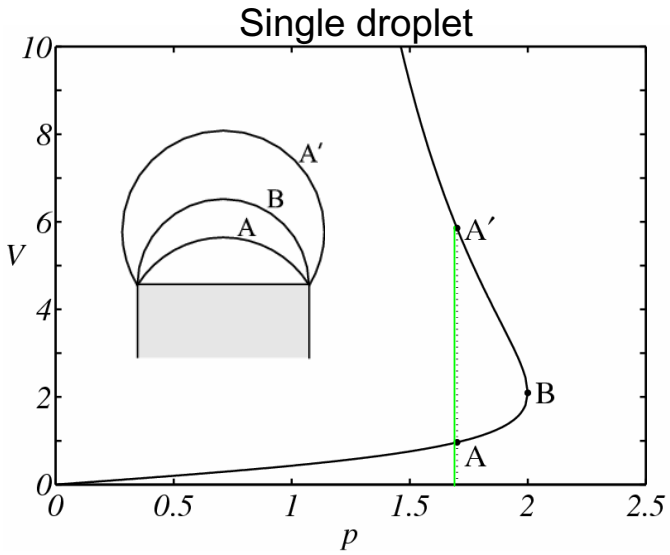

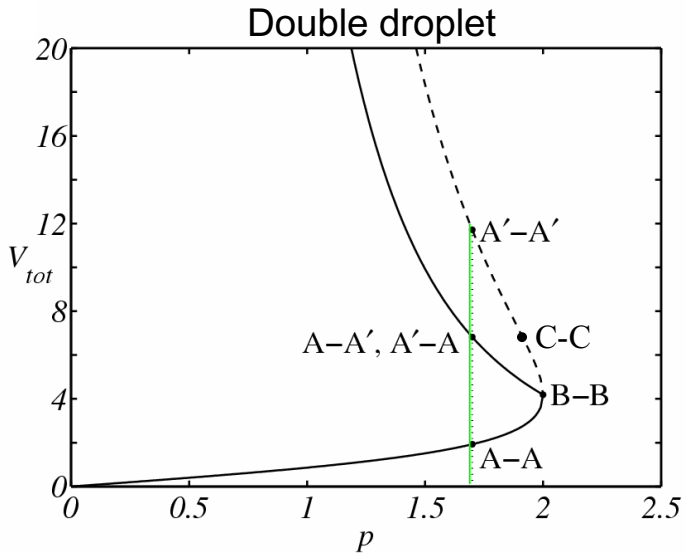

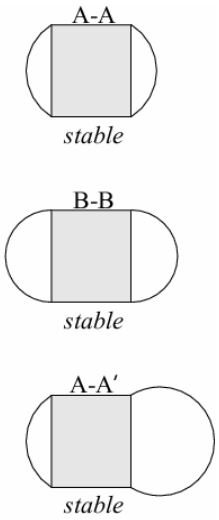

Young-Laplace:
$p=2\sigma/R$

Energy minimization
⬇
spherical surfaces

(Steen et. al. 2002)

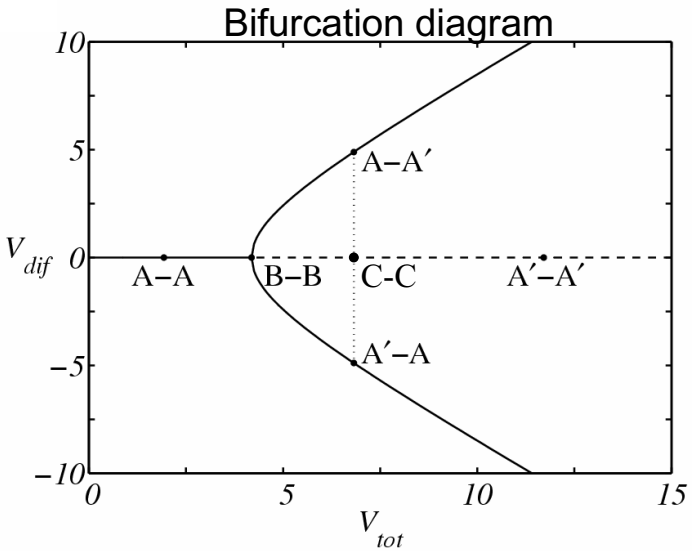

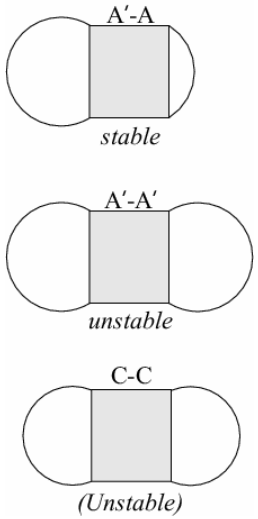

Conceptual applications: towards efficient, reliable and lightweight HEDs technology

Droplet/Particle Mover

(e.g., transport droplets to analysis sites on a 'lab on a chip')

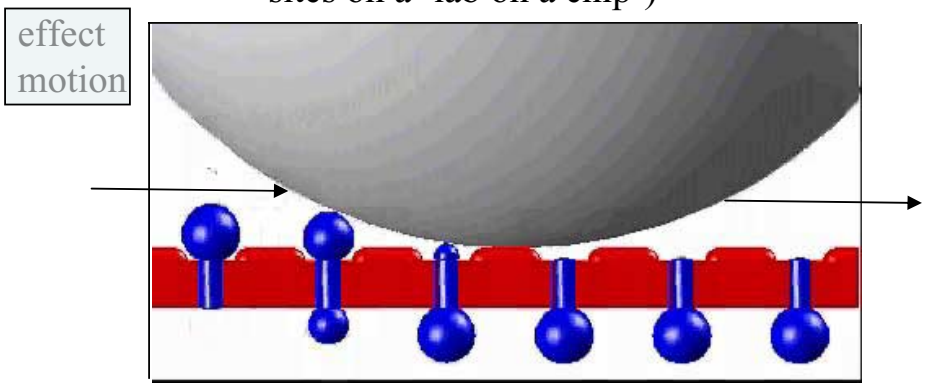

Optical 'Switchboard'

(redirect optical signals, acting as microlens)

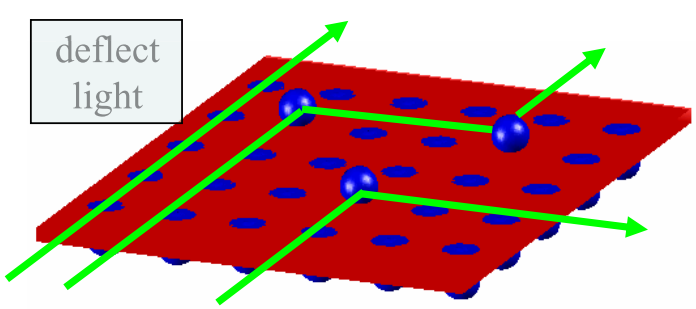

Adhesion Device

(to grip objects, as does palm beetle)

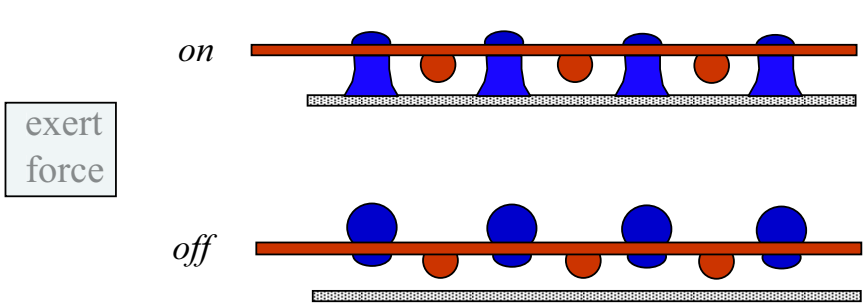

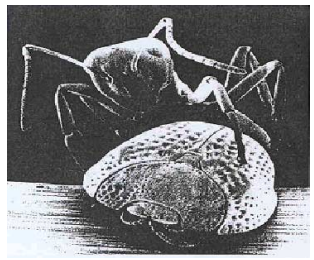

(Eisner & Aneshansley 2000)

Bistable capillary system: coupled bubbles

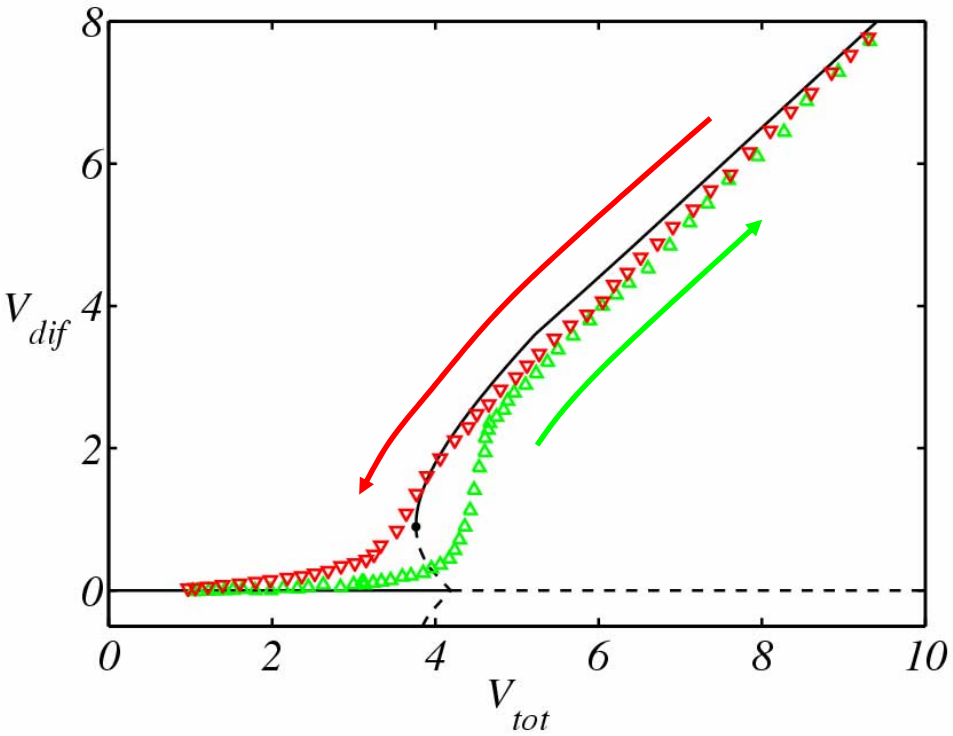

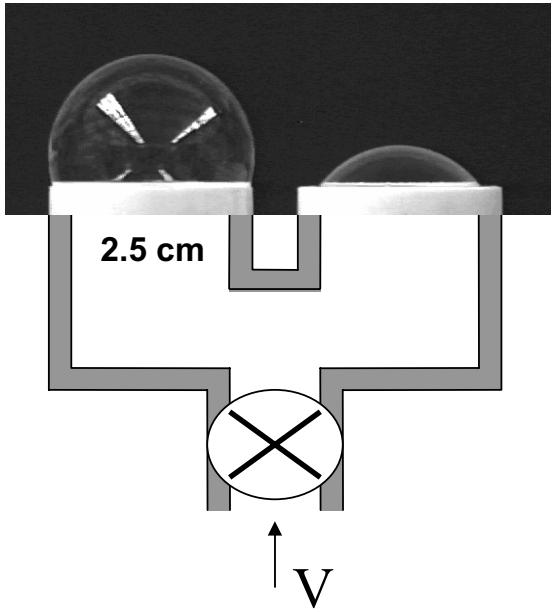

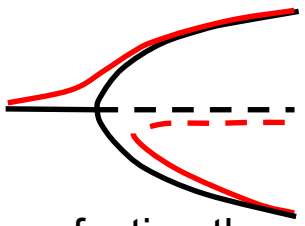

Imperfection theory

Pressure-toggled droplet switch

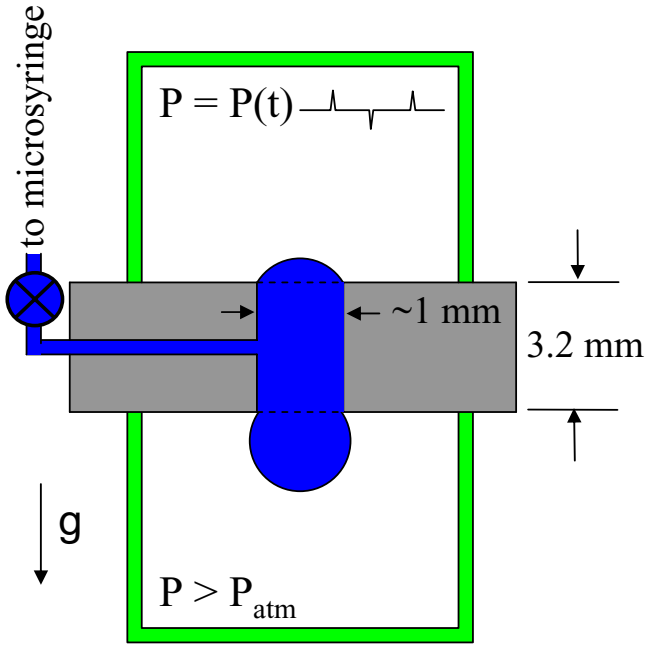

Laytin et. al. 2003

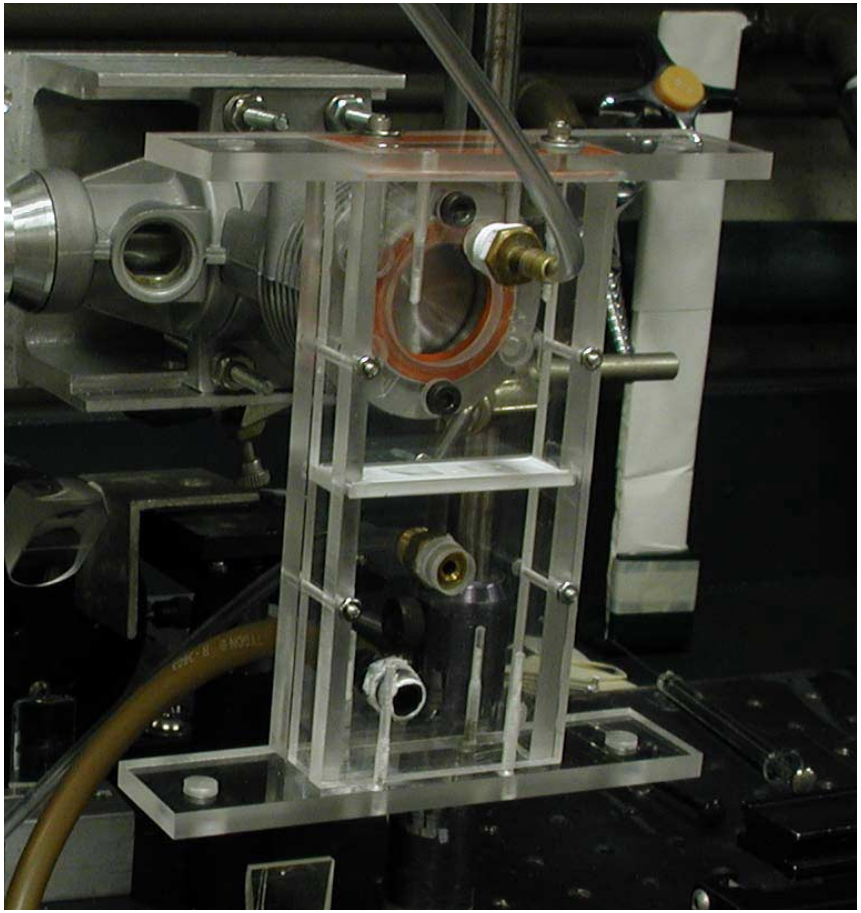

Bifurcation comparison

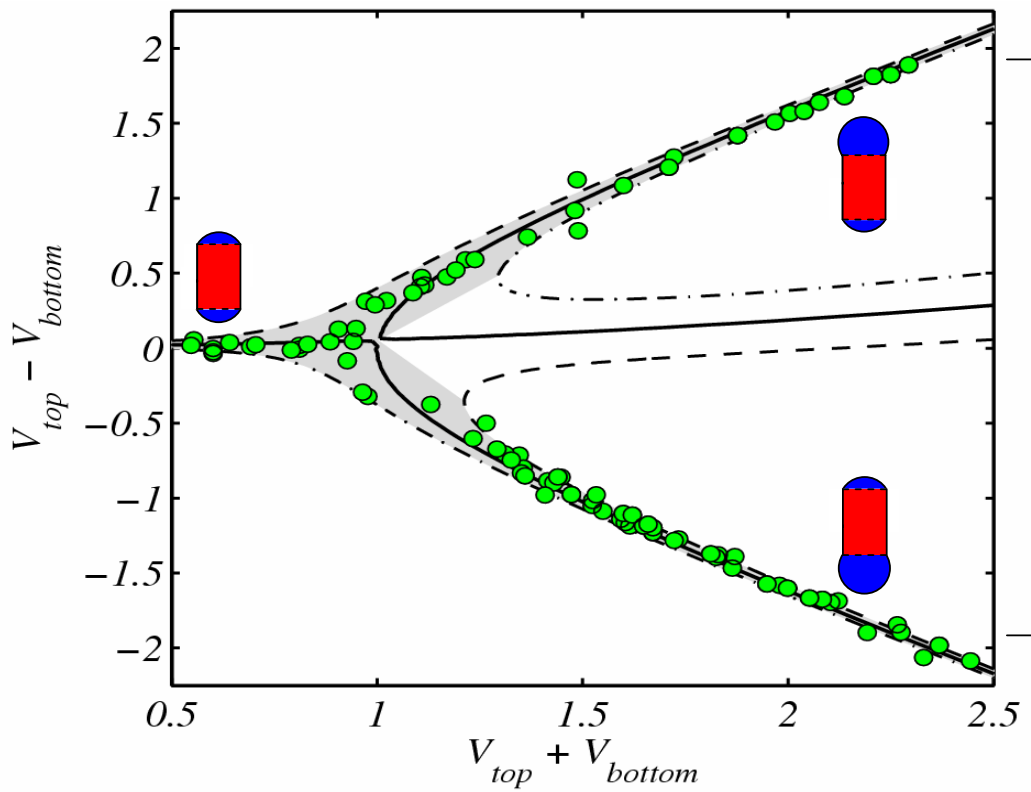

'Up'

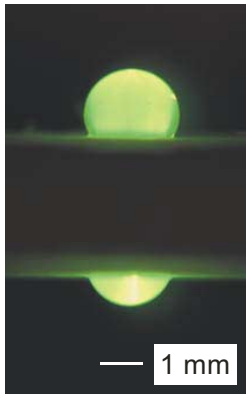

'Down'

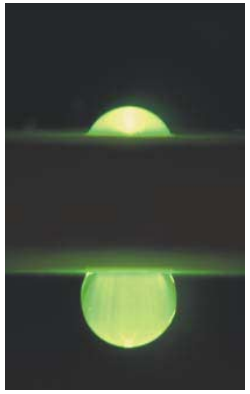

Experiment (symbols)
Theory (solid line)

Hirsa et. al. 2004

- with gravity
- pressure bias perfectly offsets gravity
  (dashed lines and shaded region show +/- 15% error in the pressure bias)
- circular contact-lines

Pressure perturbation for activation

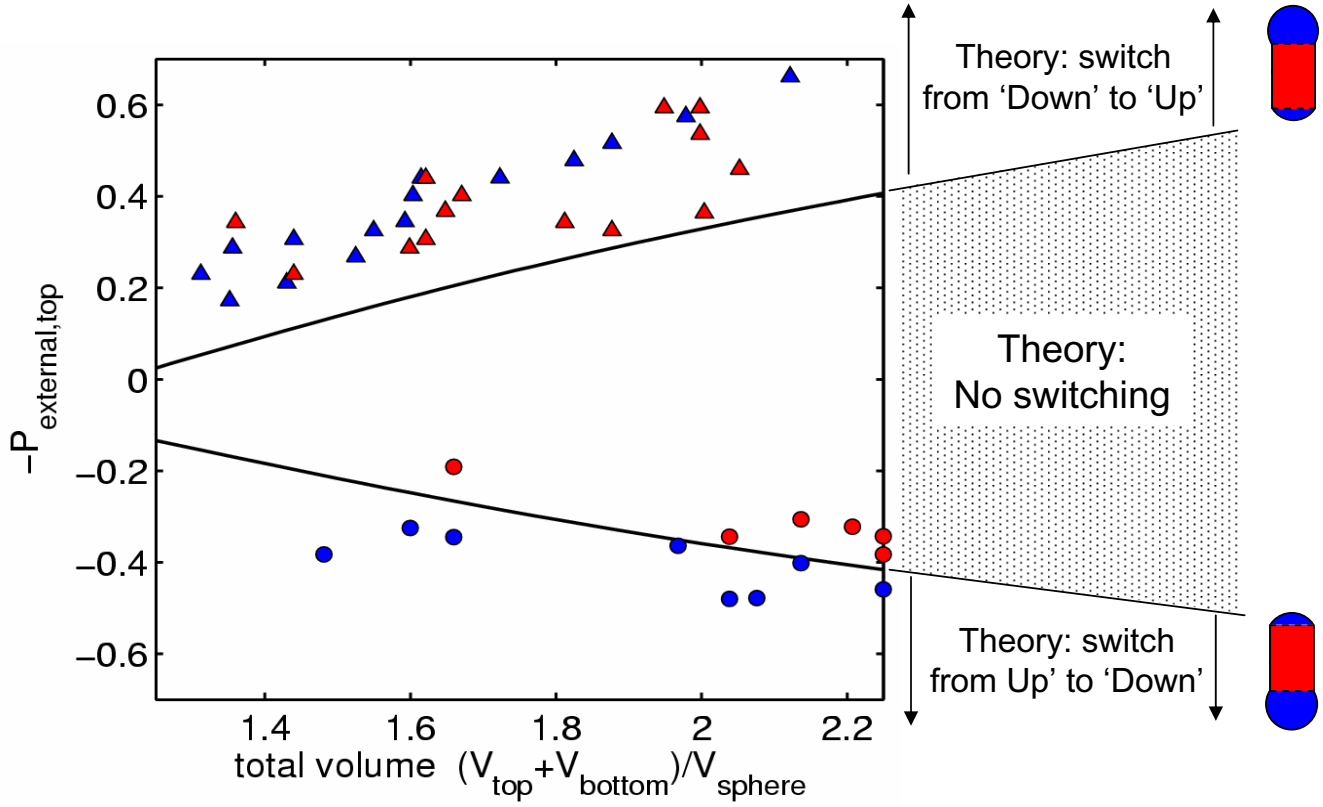

Theory (solid line)
Experiment (symbols)

- triangle = switch from 'Down' to 'Up'
- circle = switch from 'Up' to 'Down

- blue = successful switch
- red = insufficient pressure for switching

Individually addressable droplet switches

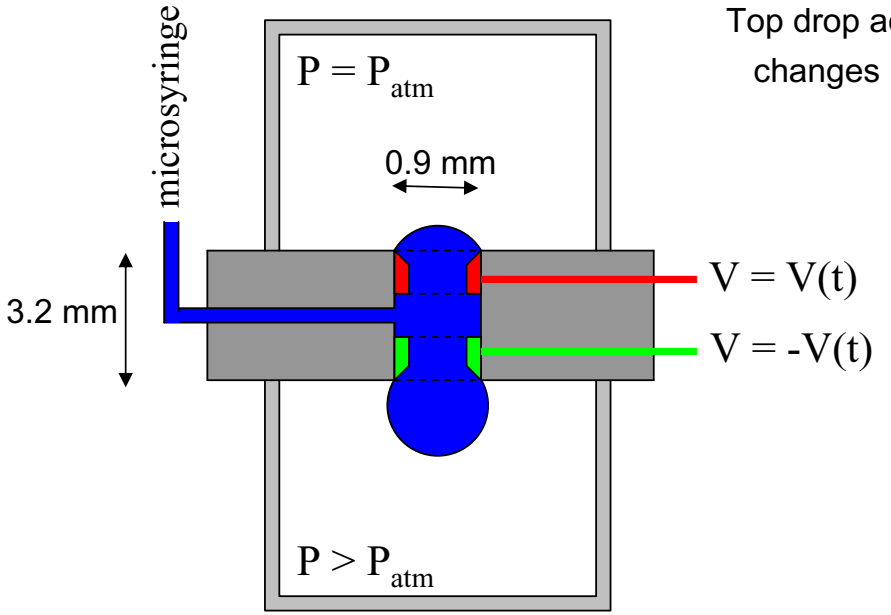

Top drop acts as microlens to laser sheet; change in shape changes focal length, as seen amplified in bottom drop.

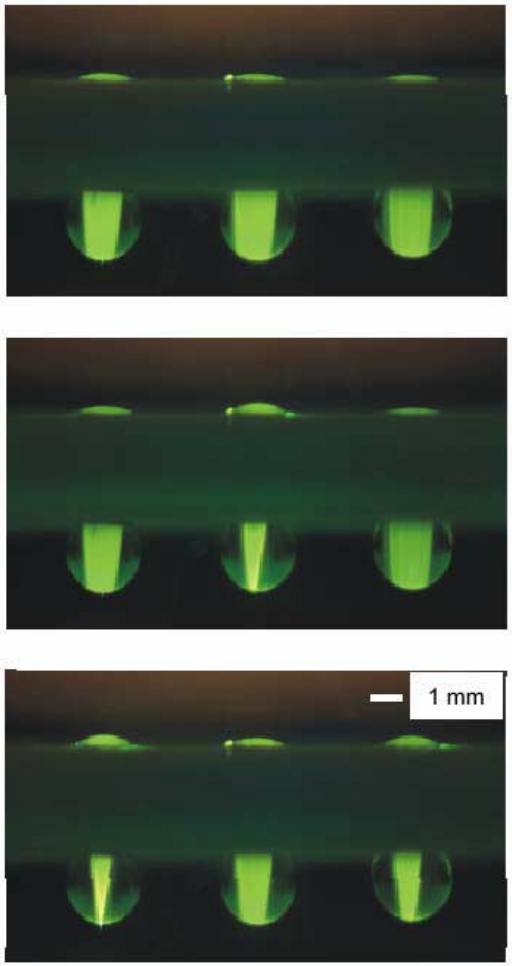

applied voltage

0 0 0

0 + 0

+ 0 +

Hirsa et. al. 2004

FTMA
(Gallardo et. al. 1996)

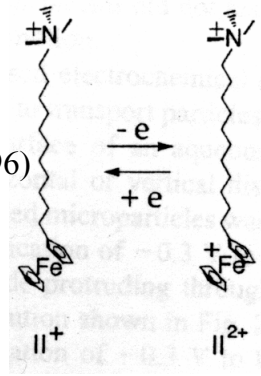

electrochemical shape-change mechanism

Electroosmotic pump as toggling physics

$$\Theta \equiv \frac{V_{total}}{\frac{4}{3}\pi B^3} \quad \text{(constant)}$$

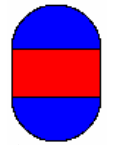

$\Theta = 1$

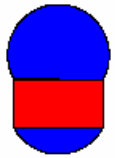

$\Theta = 2$

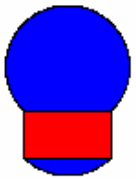

$\Theta = 3$

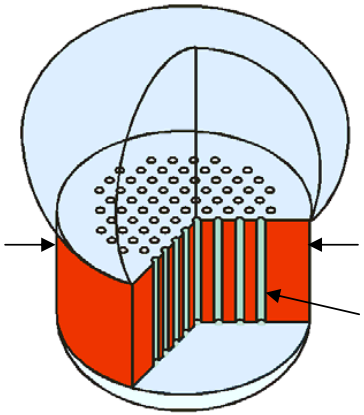

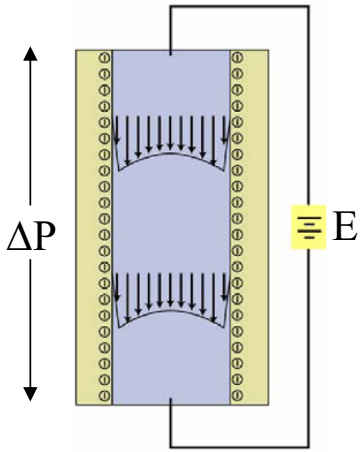

Design/operation parameter space

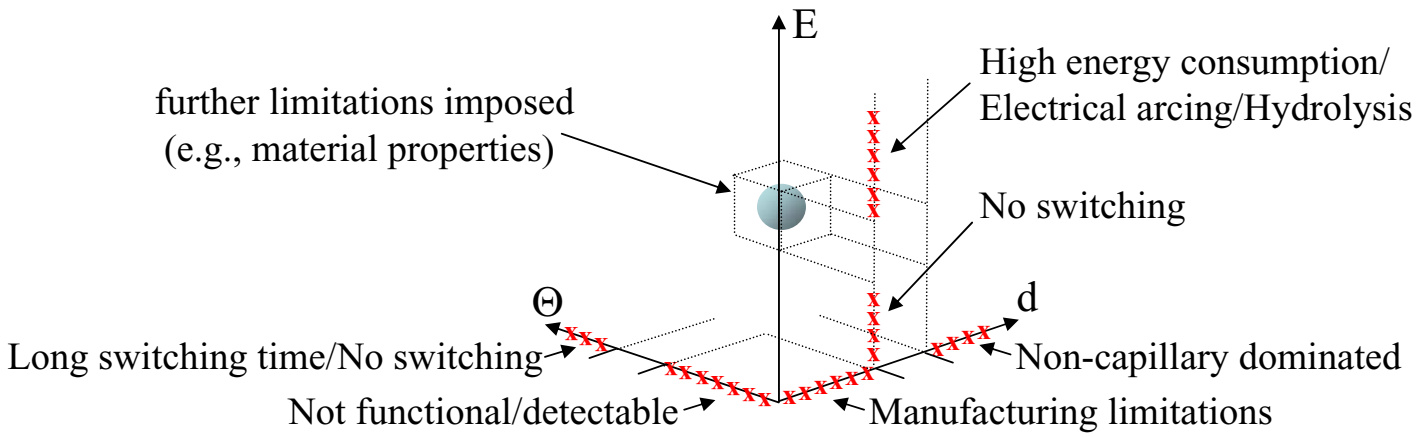

Realization

(April 2004, IKET, FzK)

switching time [sec], *f*(electric field, total volume)

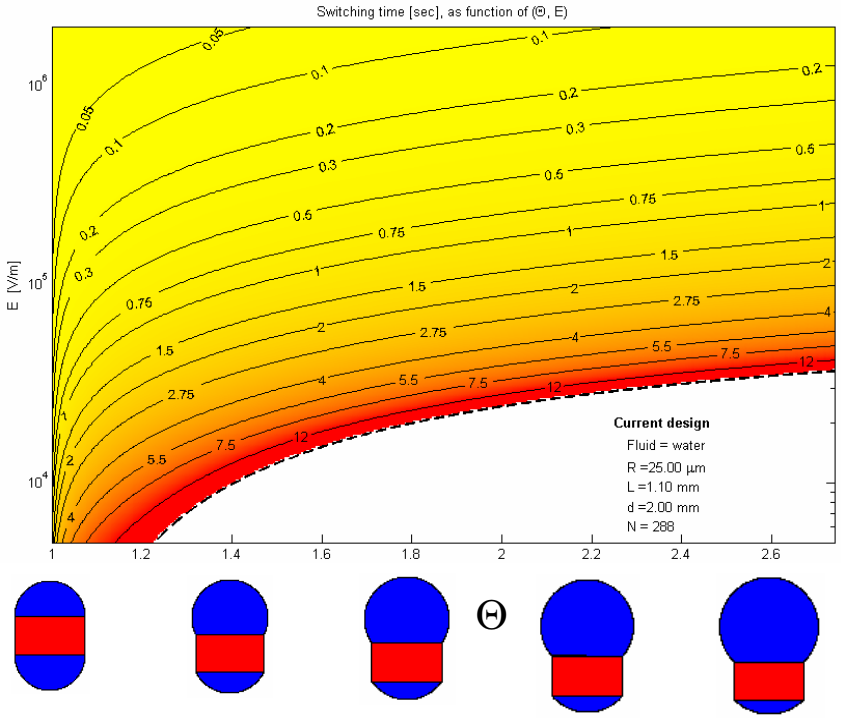

prototype device

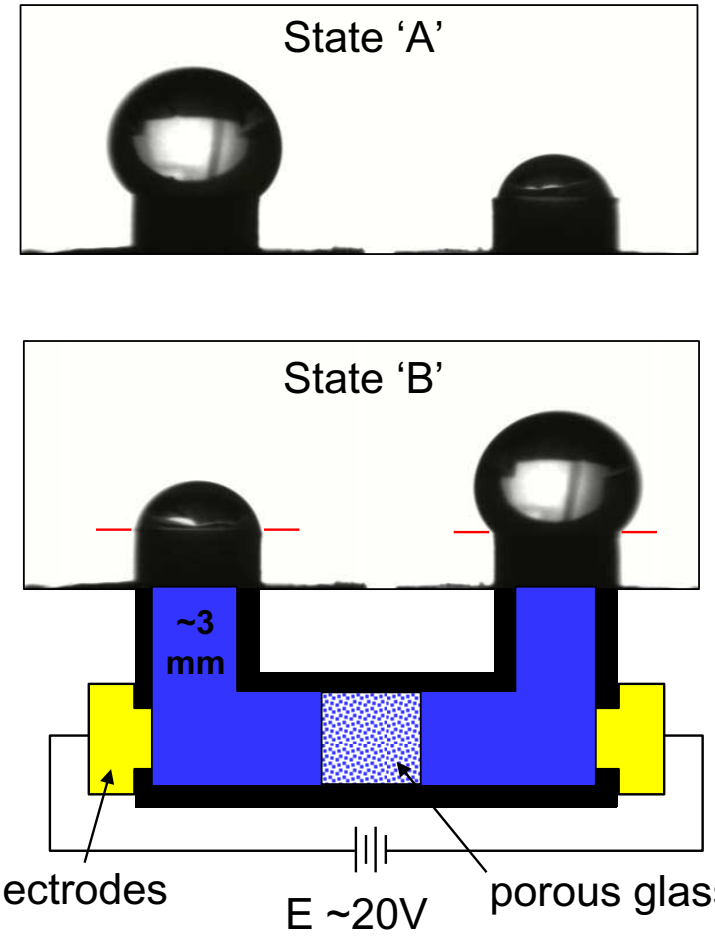

References & Acknowledgements

References

Boys, CV (1890), *Soap bubbles and the forces which mold them*, Society for Promoting Christian Knowledge; New York E.& J.B. Young.

Steen PH, C Matalanis, AH Hirsa, and C Cox (2002) "Capillary micro-switches," *Bulletin of the American Physical Society* **47** (10), 129-130.

Eisner, T and DJ Aneshansley (2000) "Defense by foot adhesion in a beetle," *Proc. Nat. Acad. Sci.* **92**(12), 6568-73.

Laytin, M. CC Lee, A Wirecki, J. Meyerholz, A. Hirsa and PH Steen (2003) "Capillary micro-switch activation", *Bulletin of the American Physical Society* **48** (10), 24.

Hirsa AH, C Lopez, M. Laytin, CC Lee, and PH Steen (2004) "Low-dissipation capillary switches at small scales," (submitted).

Gallardo, B. S., Metcalfe, K. L. & Abbott, N. L. (1996) Ferrocenyl surfactants at the surface of water: Principles for active control of interfacial properties. *Langmuir* **12**, 4116-4124.

Related publications

Atreya, S. and P.H. Steen, "Stability analyses of long liquid bridges in the presence of gravity and flow," Proc. Roy. Soc. A. 458, 2645-2669 (2002).

Robinson, N.D., and P.H. Steen. "Observations of singularity formation during capillary collapse and bubble pinch-off of a soap-film bridge", J. Colloid Int. Sci. 241, 448-458 (2001).

Bhandar, A.S., M.J. Vogel and P.H. Steen (2004) "Energy landscapes and bi-stability to finite-amplitude disturbances for the capillary bridge", to appear, Phys. Fluids.

Nitsche, M. and P.H. Steen (2004) "Numerical simulations of inviscid capillary pinchoff", to appear, J. Comp. Phys.

Acknowledgements:

NASA NAG3-2713, NASA NAG3-2713 (ND Robinson), NASA NAG3-801 (BJ Lowry), NASA NAG3-1854 (YJ Chen)

Dr. Srini Atreya, Dr. Anand Bhandar, Dr. Mike Vogel, Brian; Lowry(PhD), Yi-Ju Chen (PhD), Steven Cryer (PhD), Nate Robinson (PhD); Ivan Gospodinov (MS); John Faria, Matt Rizk, Claude Matalanis, Chris Cox, Agnes Wirecki, Mike Laytin, James Meyerholz, Chen-Chen Lee

FIRE SUPPRESSION IN LOW GRAVITY USING A CUP BURNER

Fumiaki Takahashi
National Center for Microgravity Research on Fluids and Combustion
NASA Glenn Research Center
Cleveland, OH 44135
E-mail: Fumiaki.Takahashi@grc.nasa.gov, Fax: (216) 977-7065, Phone: (216) 433-3778

Gregory T. Linteris
Fire Research Division
National Institute of Standards and Technology
Gaithersburg, MD 20899

Viswanath R. Katta
Innovative Scientific Solutions Inc.
Dayton, OH 45440

Longer duration missions to the moon, to Mars, and on the International Space Station increase the likelihood of accidental fires. The goal of the present investigation is to: (1) understand the physical and chemical processes of fire suppression in various gravity and O_2 levels simulating spacecraft, Mars, and moon missions; (2) provide rigorous testing of numerical models, which include detailed combustion-suppression chemistry and radiation sub-models; and (3) provide basic research results useful for advances in space fire safety technology, including new fire-extinguishing agents and approaches.

The structure and extinguishment of enclosed, laminar, methane-air co-flow diffusion flames formed on a cup burner have been studied experimentally and numerically using various fire-extinguishing agents (CO_2, N_2, He, Ar, CF_3H, and $Fe(CO)_5$). The experiments involve both 1*g* laboratory testing and low-*g* testing (in drop towers and the KC-135 aircraft). The computation uses a direct numerical simulation with detailed chemistry and radiative heat-loss models. An agent was introduced into a low-speed coflowing oxidizing stream until extinguishment occurred under a fixed minimal fuel velocity, and thus, the extinguishing agent concentrations were determined. The extinguishment of cup-burner flames, which resemble real fires, occurred via a blowoff process (in which the flame base drifted downstream) rather than the global extinction phenomenon typical of counterflow diffusion flames. The computation revealed that the peak reactivity spot (the reaction kernel) formed in the flame base was responsible for attachment and blowoff of the trailing diffusion flame. Furthermore, the buoyancy-induced flame flickering in 1g and thermal and transport properties of the agents affected the flame extinguishment limits.

This research was supported by NASA's Office of Biological and Physical Research, Washington, D.C.

Conference-Workshop on Strategic Research to Enable NASA's Exploration Missions Cleveland, Ohio, June 22, 2004

Fire Suppression in Low Gravity Using a Cup Burner

Fumiaki Takahashi
National Center for Microgravity Research, Cleveland, Ohio

Gregory T. Linteris
National Institute of Standards and Technology, Washington, D.C.

Viswanath R. Katta
Innovative Scientific Solutions, Inc., Dayton, Ohio

Background

- Longer duration missions to Mars, the moon, or aboard the International Space Station increases the likelihood of fire events
- NASA's fire safety program of manned space flights is based largely upon controlling the materials flammability and eliminating ignition sources
- This project investigates fire suppression in the reduced-gravity environment

Objectives

- Understand physical/chemical processes of fire suppression in various gravity and O_2 levels simulating spacecraft, Mars, and moon missions
- Provide rigorous testing of analytical models, which include comprehensive combustion and suppression chemistry
- Provide basic research results useful for advances in space fire safety technology, including new fire-extinguishing agents and approaches

Approach

Experiment:

- Using a cup burner, which resembles real fires, measure the critical extinction mole fraction of fire suppression agents for selected fuels
- Determine physical/chemical effects of agents on flame structure/suppression processes

Computation:

- Simulate unsteady fire suppression phenomena in various flames using a 2D code with detailed chemical reaction and radiation models

Cup Burner Flames (1g)

- Simulations with full chemistry predict the experiment in Minimum Extinguishing Concentration, flame shape, flickering frequency (~11 Hz)

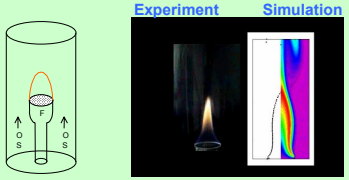

d =2.8 cm, U_{CH4}= 0.92 cm/s, U_{air}= 10.7 cm/s

Drop/KC-135 Rig

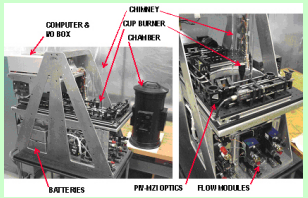

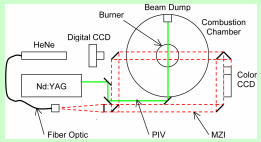

Diagnostics:

Particle image velocimeter (PIV)
Mach-Zehnder interferometer (MZI)

Parameters:

Fuel: Gas: CH_4, C_2H_6, C_3H_8
Liquid: n-C_7H_{16}, CH_3OH
Solid: trioxane (3[CH_2O]), PMMA

Oxidizer: O_2-N_2 mixture
Oxygen mole fraction: 0.21 – 0.3
Velocity: 3 – 20 cm/s

Agent: CO_2, N_2, He, Ar
CF_3H(HFC-23), C_3F_7H (HFC-227ea), CF_3Br
Water Mist, Inert/Water Mist, Microencapsulated Water

Gravity: μg, lunar (1/6 g), Martian (1/3 g), 1g

Pressure: 0.7 – 1 atm

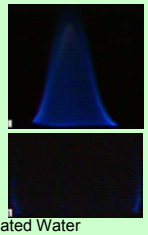

Numerical Simulations (1g)

- Suppression of cup-burner flames occurs via blowoff rather than global extinction typical of counterflow diffusion flames

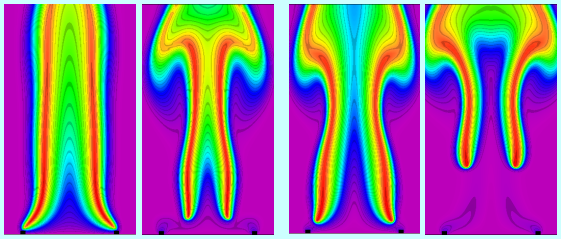

5.0% CO_2 in Air | 14.5% CO_2 in Air | 10.05% CF_3H in Air | 10.1% CF_3H in Air

Numerical Simulations (low-g)

- Flame flicker (~11 Hz) ceases at < 0.5 g
- Heat-release rate decreases with reducing g, while radiative heat loss remained const

0.5g

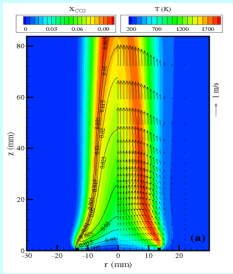

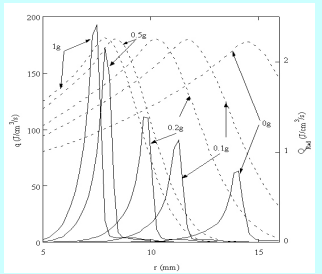

Agent Effectiveness

- The effectiveness of a fire-extinguishing agent depends upon the flame characteristics.

Phosphorus is:

3 x better than CF_3Br in counterflow* flames
17 x " " " " premixed** "
but ½ as good as " " cup burner "

* Macdonald et al. Combust Flame 116:166 (1999) ** Korobeinichev et al. HOTWC 2000 p. 164.

- Performance advantage of chemically active agents over CO_2: variation with flame type.

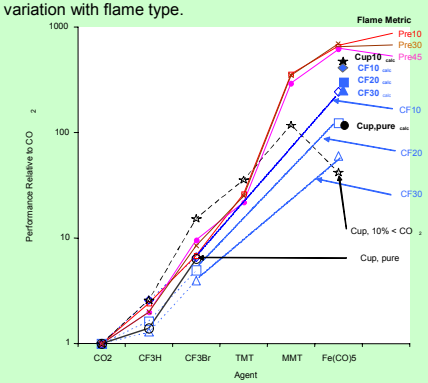

- Catalytic inhibitors are better than CF3Br at low concentrations, but lose their effectiveness at higher conc.

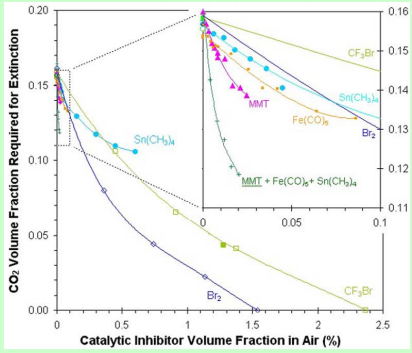

Flame Flicker in 1*g*

- Flame flicker affects suppression processes and the flickering frequency varies with CO2 content and co-flow velocity

Conclusions

- Suppression of cup-burner flames occurs via blowoff rather than global extinction typical of counterflow diffusion flames.
- Performance of agents is highly dependent upon the flame characteristics.
- Chemical agents reduce concentration (and amount) of inert agent required for suppression.
- Flame flicker (~11 Hz) affects suppression processes and ceases at < 0.5 *g*.
- Flame tip opens in low *g* due to radiative heat loss.
- Critical CO_2 concentration in 0*g* is ~32% higher than in 1*g*.

Numerical Simulations (low-*g*)

- Flame tip opens at low *g* due to radiative heat loss
- Critical CO2 concentration at 0*g* is ~32% higher than in 1*g*

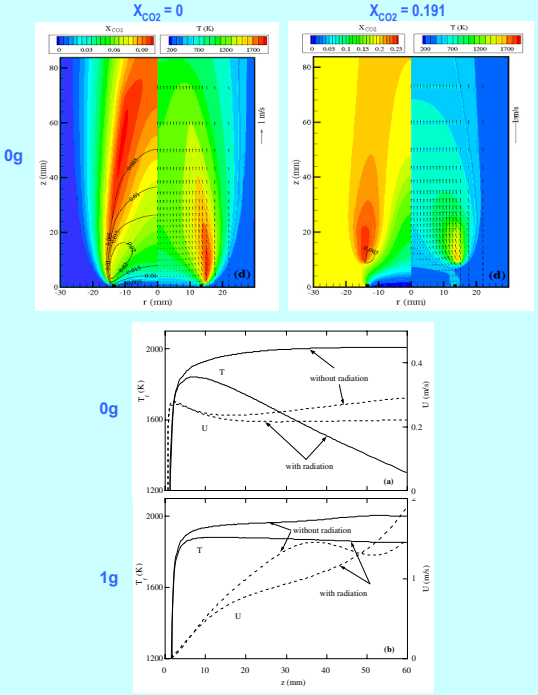

Key findings from numerical work

- Form vorticies in 1g
- Extinguish due to flame base de-stabilization
- Have tips that open in 0-g (due to radiation losses)
- Flicker at ~11 Hz. in 1-g, but as g decreased, flicker decreased (below 0.5 g, don't flicker).
- Require 32% more CO2 to extinguish in 0g than in 1g.

A BIOSENSOR FOR SINGLE-MOLECULE DNA SEQUENCING

Nerayo P. Teclemariam and Susan J. Muller*
Department of Chemical Engineering, University of California, Berkeley, CA 94720-1462
Phone: 510-642-4525, fax: 510-642-4778, e-mail:muller2@socrates.berkeley.edu

Victor A. Beck and Eric S.G. Shaqfeh
Department of Chemical Engineering, Stanford University, Stanford, CA 94305-5025

ABSTRACT

This project is a collaborative effort to develop a biosensor for obtaining sequence information from single DNA molecules. The sensor will allow rapid screening for specific genes which may be indicators of susceptibility to space radiation damage. The basic concept is to use hydrodynamics to fully extend genomic DNA in a microfluidic device. Fluorescent beads with surface-bound, complementary oligonucleotide probe sequences (corresponding to genes or sequences of interest) will be introduced and hybridized to the stretched DNA. Any unhybridized beads will be separated from the DNA-bead complexes. Imaging of the bead positions along the stretched, linear DNA backbone will then provide sequence information since the beads act as position and sequence sensitive markers. Realization of the device will require both detailed experiments and simulations aimed at designing flow geometries to stretch the DNA, optimizing the hybridization and transport of the DNA-bead complexes, and determining the resolution and limits of this sequencing method.

Introduction & Research Plan

In a series of seminal papers, Chu and co-workers used epifluorescence microscopy and fluorescently labeled DNA to directly visualize the effects of simple flows on DNA conformation (Perkins, Smith, and Chu, *Science* 276:2016 (1997), Smith and Chu, *Science* 281: 1335 (1998), Smith, Babcock, and Chu, *Science* 283:1724 (1999)). These studies provided unprecedented insights into the dynamics of single, macromolecular chains in steady shear and planar extensional flows; they also revealed the potential for direct comparisons between experiments and Brownian dynamics simulations of DNA chain trajectories in flow. Such simulations by Shaqfeh and Larson and co-workers have been successful in capturing the DNA dynamics observed in direct visualization experiments (Larson, Hu, Smith, and Chu, *J. Rheol.* 43:267 (1999), Hur, Shaqfeh, Babcock, Smith, and Chu,, *J. Rheol.* 45:421 (2001)). However, to date, very few *complex* flows of DNA have been simulated and compared to experiments. Moreover, it appears that no work has been done on designing flow geometries to produce specific DNA conformation fields.

The use of flow to control macromolecular conformation has wide-ranging potential applications. Here we propose using hydrodynamics to produce stretched, linear DNA for subsequent hybridization to fluorescently labeled beads; subsequent imaging of the beads will provide information about the location of certain genetic markers. Existing experimental and simulation capabilities will be extended to 1) identify the flow geometries that are most effective in stretching DNA in a microfluidic device, 2) determine the bead transport and binding kinetics for formation of the complementary DNA-bead complex, 3) quantify transport of the DNA-bead complex through the microdevice and its relaxation dynamics, 4) identify appropriate geometries

and flow parameters for separation of the unbound beads from the DNA-bead complexes, and 5) determine the resolution and limitations of this technique for sequencing.

Preliminary Results

Initial work has focused on identifying the flow geometries that will be most effective in stretching DNA. Several candidate geometries consisting of high aspect ratio post arrays of varying spatial arrangements, extents, and post densities have been fabricated in silicon at the Berkeley Microlab. Posts, flow channels, and deep trenches for capillary interconnects are defined through a series of lithography and etching steps. The final step is anodic bonding of the silicon device to a glass cover, which seals the flow channel and provides optical access. Optimization of the fabrication processing steps is currently underway. In particular, the deep reactive ion etch used to create the posts is extremely sensitive to operating parameters in the etch chamber; non-optimal conditions can result in undercutting of the posts or "grass" – i.e., large scale roughness on the bottom of the etched channels. To date, a number of fairly dense post arrays have been completed; a scanning electron micrograph of one such array, a 15 row hexagonal array of 2 micron diameter posts in a rectangular flow channel, is shown in figure 1.

Fluorescence microscopy will be used to visualize stretching of λ-DNA immediately upstream and immediately downstream of the arrays. Preliminary results for a 7 row post array are shown in figure 2. Under the flow conditions examined, this 7 row array results in a significant amount of stretching of DNA molecules as evidenced by the shift in the histogram to higher extensions after the post array. The array results in an increase in the mean extension of a DNA molecule of approximately 124%.

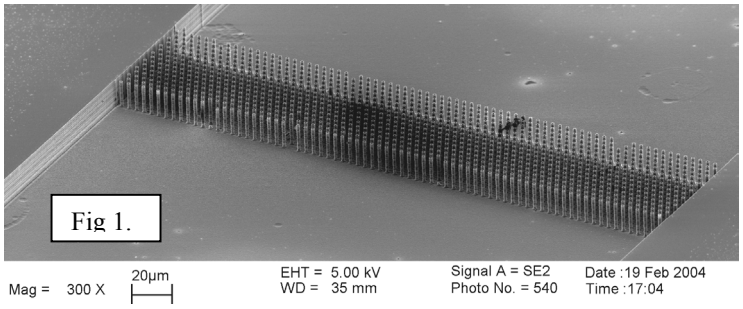

Preliminary Brownian dynamics simulations of DNA interactions with single posts and with extended post arrays are also underway. These simulations indicate that, through appropriate post column and row spacing, up to 42% of the DNA molecules can be extended past 80% of full extension after twenty rows of posts. Thus, fully stretched DNA molecules should be achievable through the use of appropriately designed post arrays, or through a combination of post arrays and contraction flows. A quantitative comparison of experiments to simulations, using the measured initial DNA extension and center of mass position upstream of the post array as inputs for the Brownian dynamics simulations, will be completed in the near future. Successful comparison will validate the simulations in these complex flows and allow us to use simulations to rapidly screen potential stretching geometries. Results will then guide the design and fabrication of the next generation of microfluidic devices.

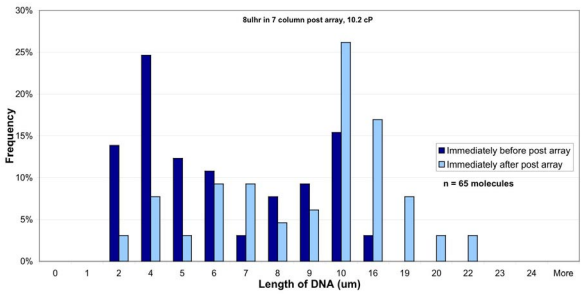

Figure 2. Histogram of λ-DNA extension in a 7 row post array.

SUPPORTED CAPILLARY PIPES

David B. Thiessen and Philip L. Marston
Department of Physics
Washington State University
Pullman, WA 99164-2814

Preliminary experiments have been conducted in a Plateau tank on supported capillary structures, which might have application to chemical separations and other processes in zero gravity including those associated with life support. Countercurrent flow of gas and liquid or of two liquids is ubiquitous in chemical processing. Examples include distillation, absorption, stripping, and extraction. A large amount of surface area is necessary for efficient operation of such processes. On earth, gravity drives the countercurrent flow because of a density difference between the two phases. Various support structures are used to create large amounts of surface area between the two phases such as structured or dumped packings or bubble-cap trays. In zero gravity, free-surface liquid flow can be inertial or driven by capillary forces or applied forces. It is proposed that supported capillary pipes can sustain sufficient pressure gradients to drive flow over significant distances for liquid-gas or liquid-liquid contacting. Liquid tubes of arbitrary length can be supported by parallel wires with the proper wetting characteristics arranged in regular polygonal arrays or by a helical coil of wire. The static stability of these structures has recently been investigated theoretically.

Supported Capillary Pipes

D. B. Thiessen and P. L. Marston
Department of Physics, Washington State University, Pullman, WA 99164-2814, USA
B. J. Lowry
Department of Chemical Engineering, University of New Brunswick, Fredericton, N.B., E3B 5A3, Canada

ABSTRACT

Preliminary experiments have been conducted in a Plateau tank on supported capillary structures which might have application to chemical separations and other processes in zero gravity including those associated with life support. Countercurrent flow of gas and liquid or of two liquids is ubiquitous in chemical processing. Examples include distillation, absorption, stripping and extraction. A large amount of surface area is necessary for efficient operation of such processes. On earth, gravity drives the countercurrent flow because of a density difference between the two phases. Various support structures are used to create large amounts of surface area between the two phases such as structured or dumped packings or bubble-cap trays. In zero gravity, free-surface liquid flow can be inertial or driven by capillary forces or applied forces. It is proposed that supported capillary pipes can sustain sufficient pressure gradients to drive flow over significant distances for liquid-gas or liquid-liquid contacting. Liquid tubes of arbitrary length can be supported by parallel wires with the proper wetting characteristics arranged in regular polygonal arrays or by a helical coil of wire. The static stability of these structures has recently been investigated theoretically.

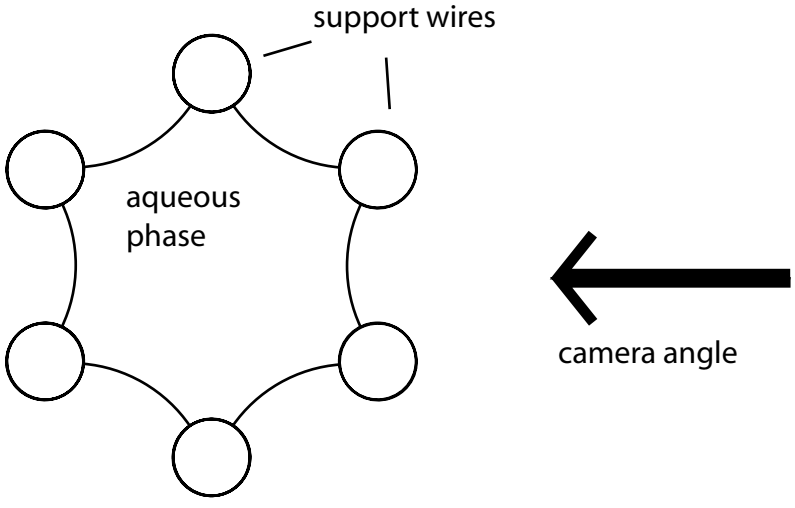

Figure 1: Cross-sectional view of Plateau-tank setup for hexagonal wire array structure.

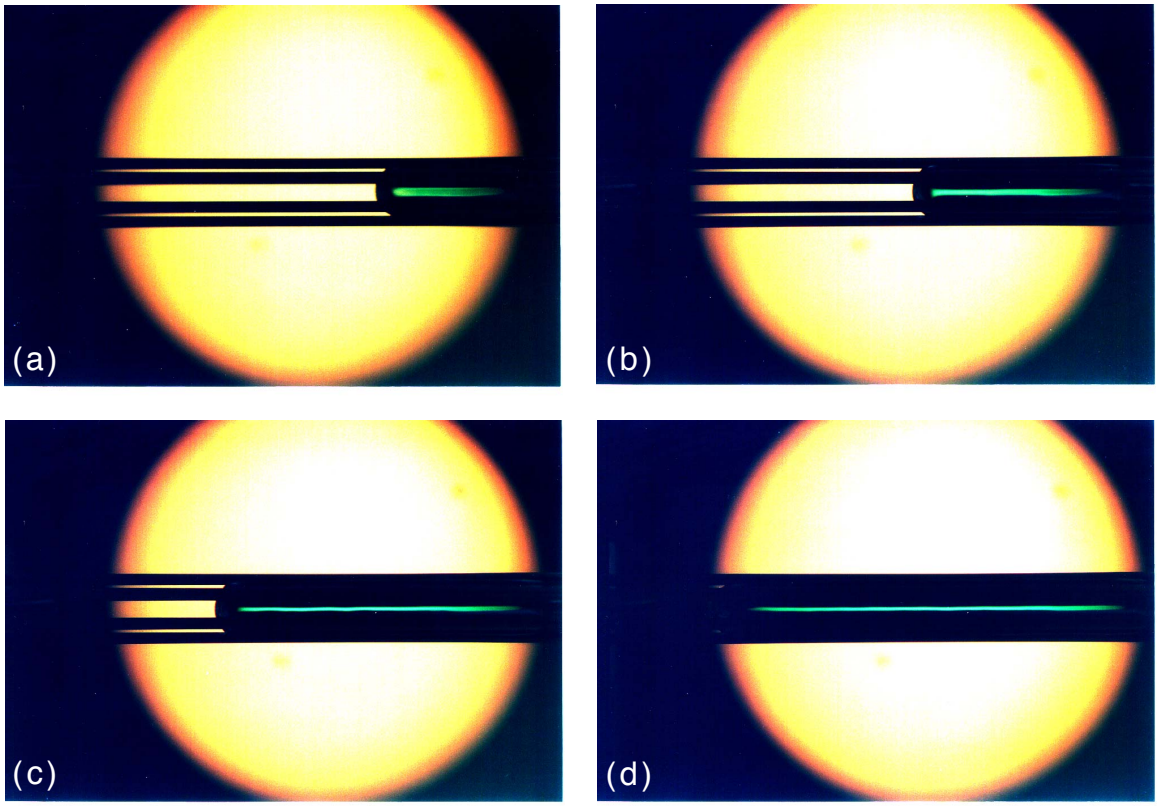

Figure 2: Injection of aqueous phase into hexagonal array support structure made up of 0.05 inch diameter steel rods. The pipe diameter is around 0.25 inches and is over 2 inches long.

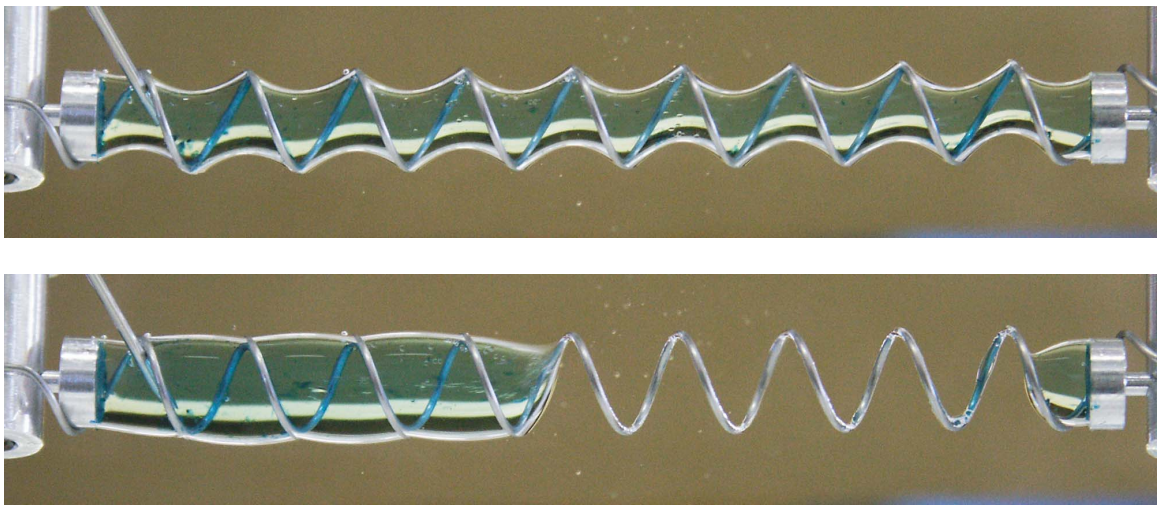

Figure 3: Helix supported capillary structure. The top image is very near the low-volume stability limit for the given helix pitch. In the bottom image a slight reduction in the volume has resulted in breakage and retraction of the liquid.

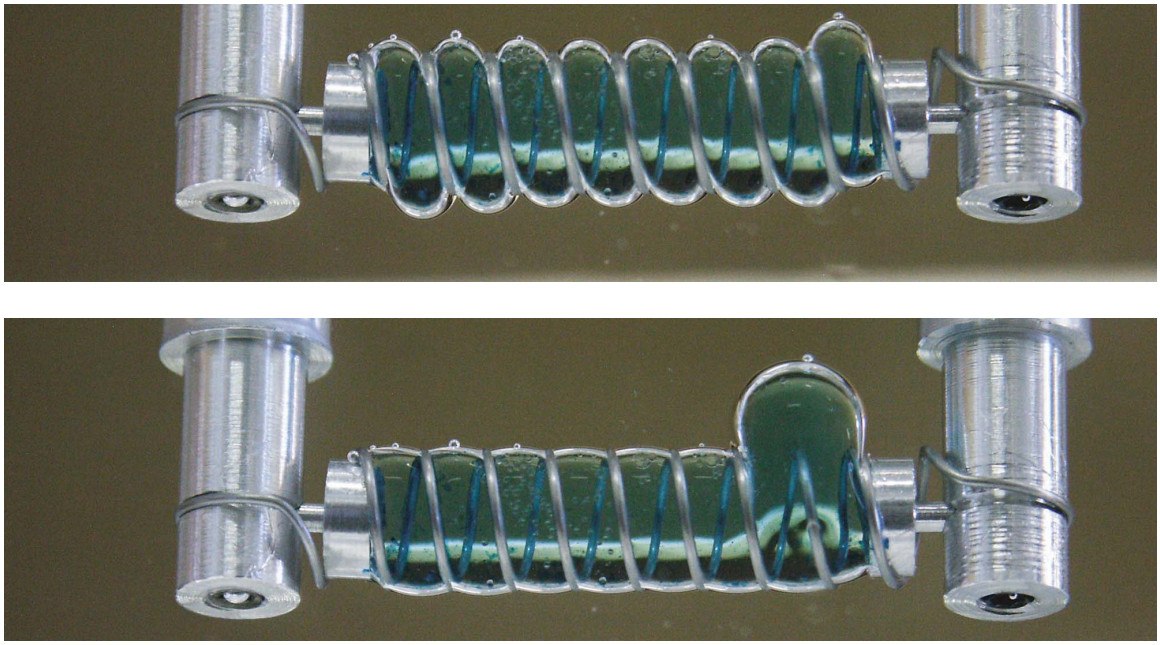

Figure 4: The top image is near the high-volume stability limit. In the bottom image slightly more volume was added causing the liquid to engulf the wire leading to a blowout.

OSCILLATORY FLOWS AS A MEANS OF SEPARATION OF CONTAMINANTS FROM AIR

Aaron Thomas
University of Idaho

Oscillatory flows in tubes can be used as a mechanical means to separate species and enhance mass transport. This work applies the theory of oscillating flows toward the removal of trace organic contaminants and submicron particles from air that can be the result of off gassing, chemical spills, or even a fire that may occur in areas occupied by humans. For long-manned space missions, oscillating flows will reduce the load placed on traditional separation methods such as membranes, molecular sieves, and the like. These separation devices require replacement and/or regeneration of materials, so decreasing the load on these materials will increase their effective life and reduce the amount of material and man-hours needed (at some cost to extra power requirements). The current focus of our work is in a) optimization of the separation process using the tuning of geometric length scales with transport length scales in irregular geometries b) the enhancement of separation by operating the flows under increased concentration gradients and c) extension of this work to heat transfer as well as liquid phase systems.

This research is of use in space-enabling technologies but also has terrestrial applications to a) enhanced heat transport, b) separation of species in the liquid phase for biomedical devices and c) pre concentrators for detection of small concentration species in Homeland Security. Past results on experiments in regular geometries as well as preliminary results on velocity profiles and mass transfer in irregular geometries (wavy-walled tubes) will be presented during this poster session.

Contaminant Removal Using Oscillating Flows in Unique Geometrical Configurations

Aaron Thomas
University of Idaho
Chemical Engineering

R. Narayanan and Jonathan Volk
University of Florida
Chemical Engineering

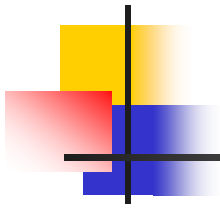

Motivation

- Separation of CO_2 or other contaminants from air is important to the space program
- Periodic flow uses purely mechanical (non-chemical) means to *assist* in the separation
- Gain a better understanding of periodic flow to optimize a system to give a reasonable separation with a high throughput (mass transfer).

General Theory

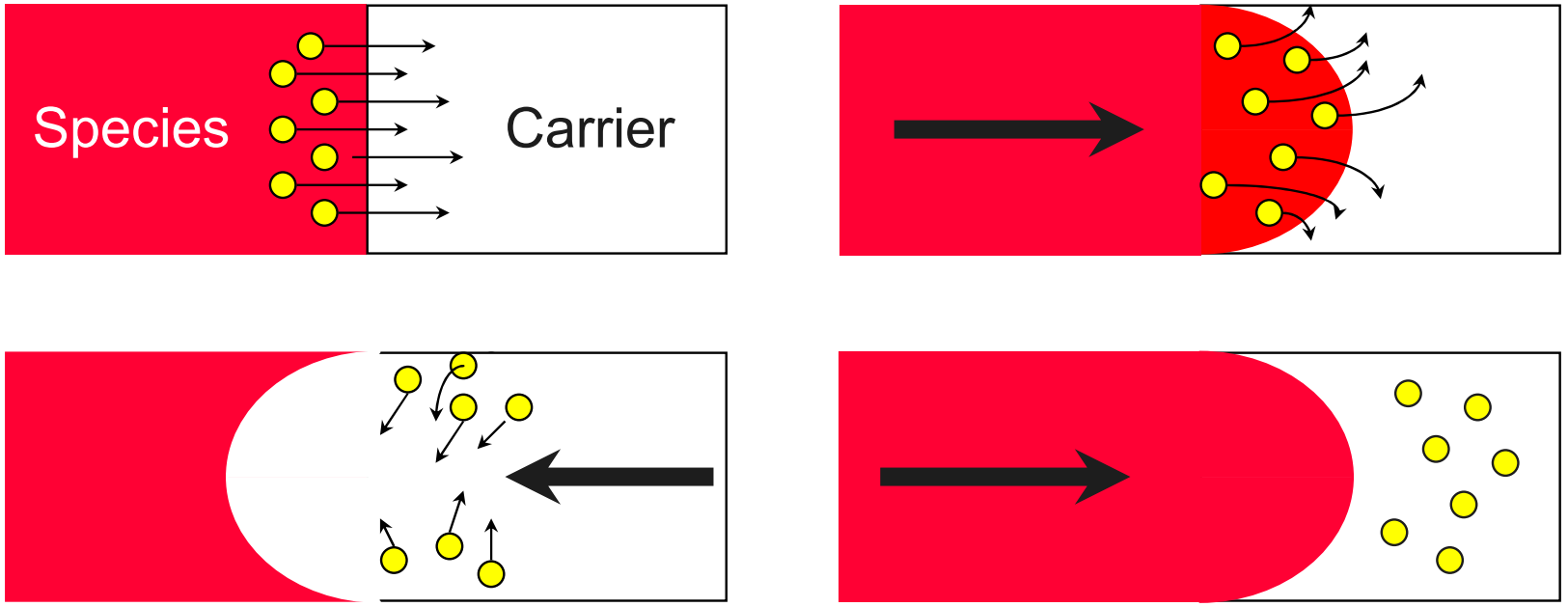

TRANPORT DURING OSCILLATING FLOW

Regeneration Cycle

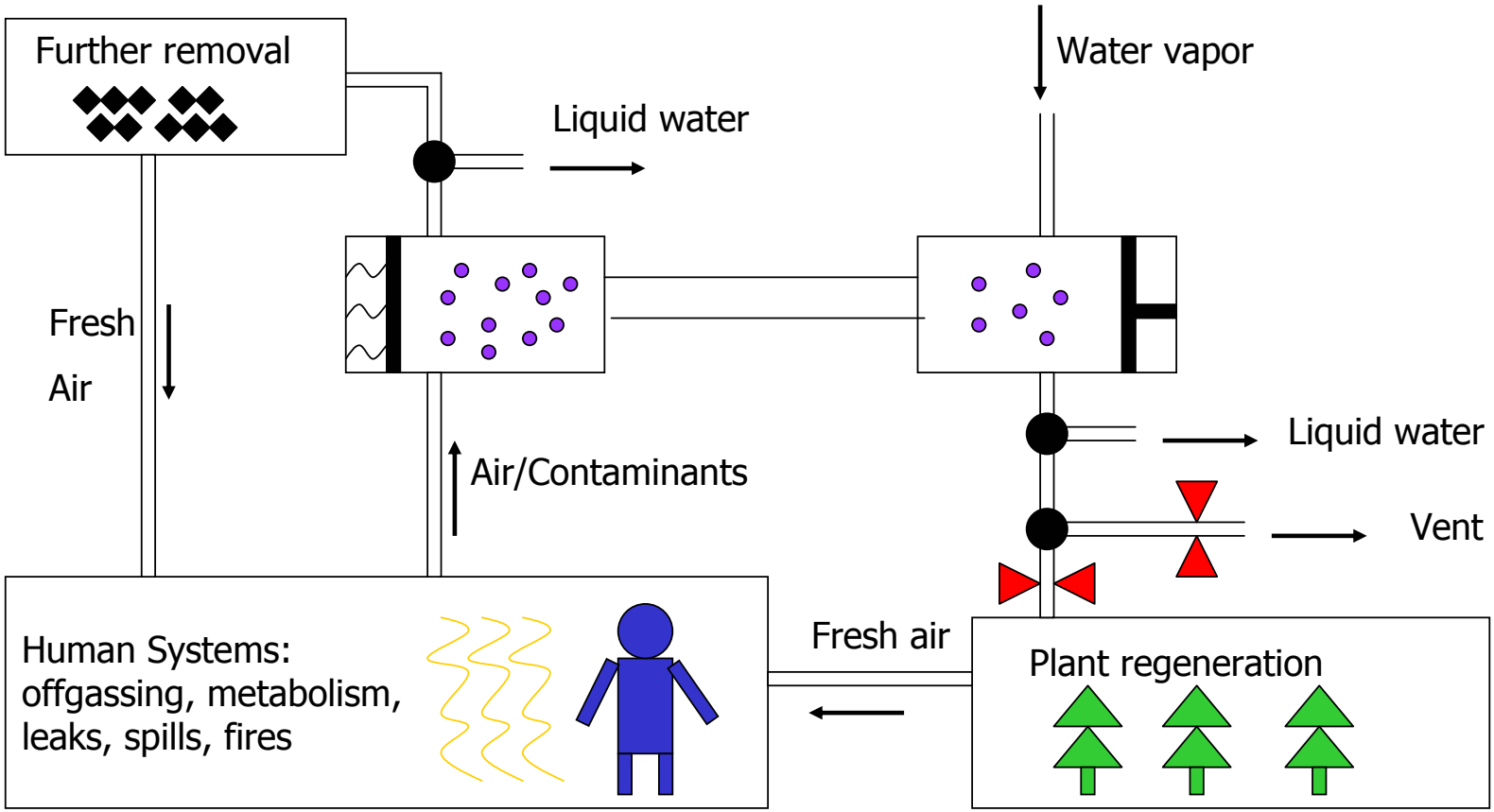

Total Mass Transfer

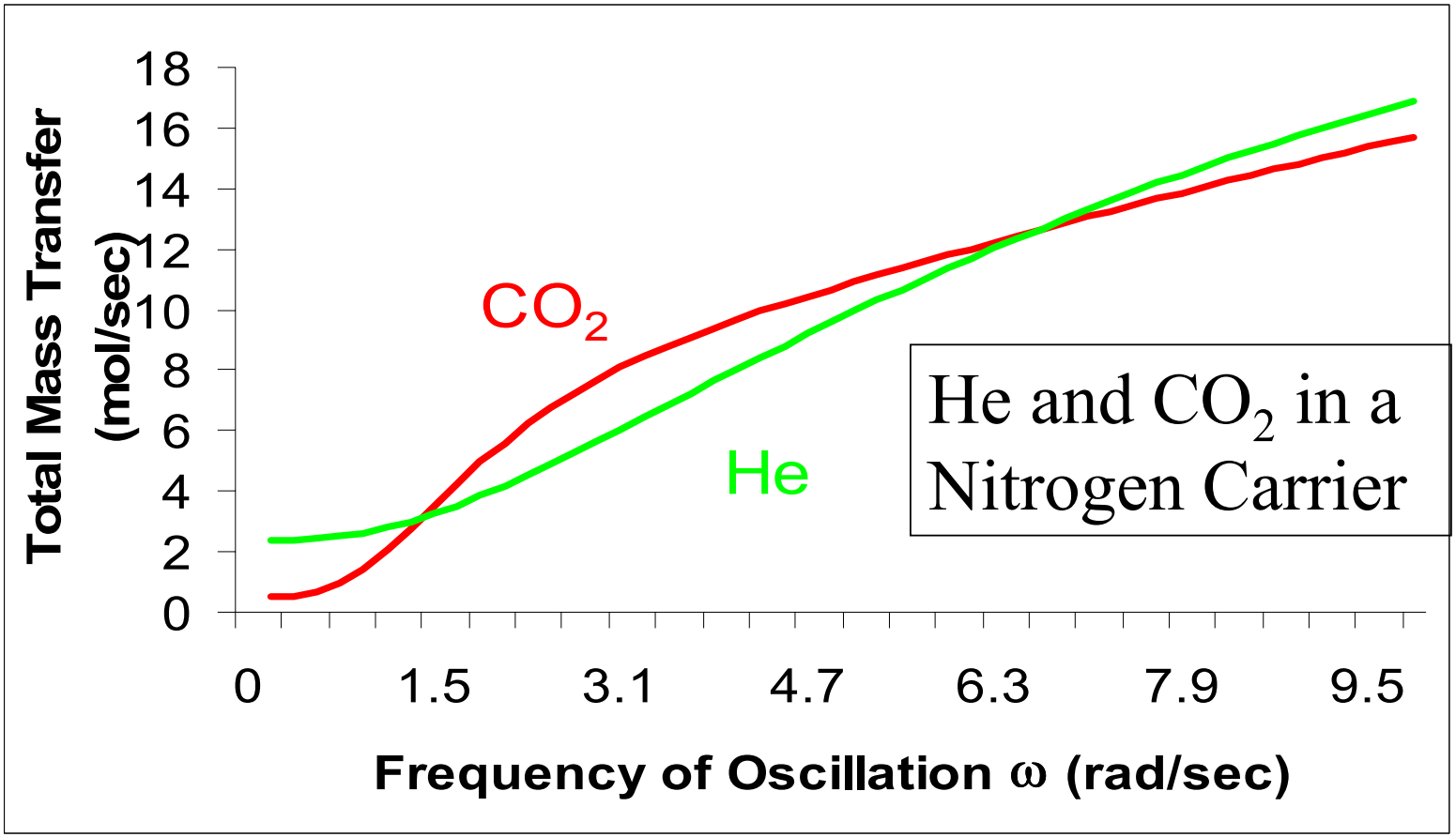

Separation of Species

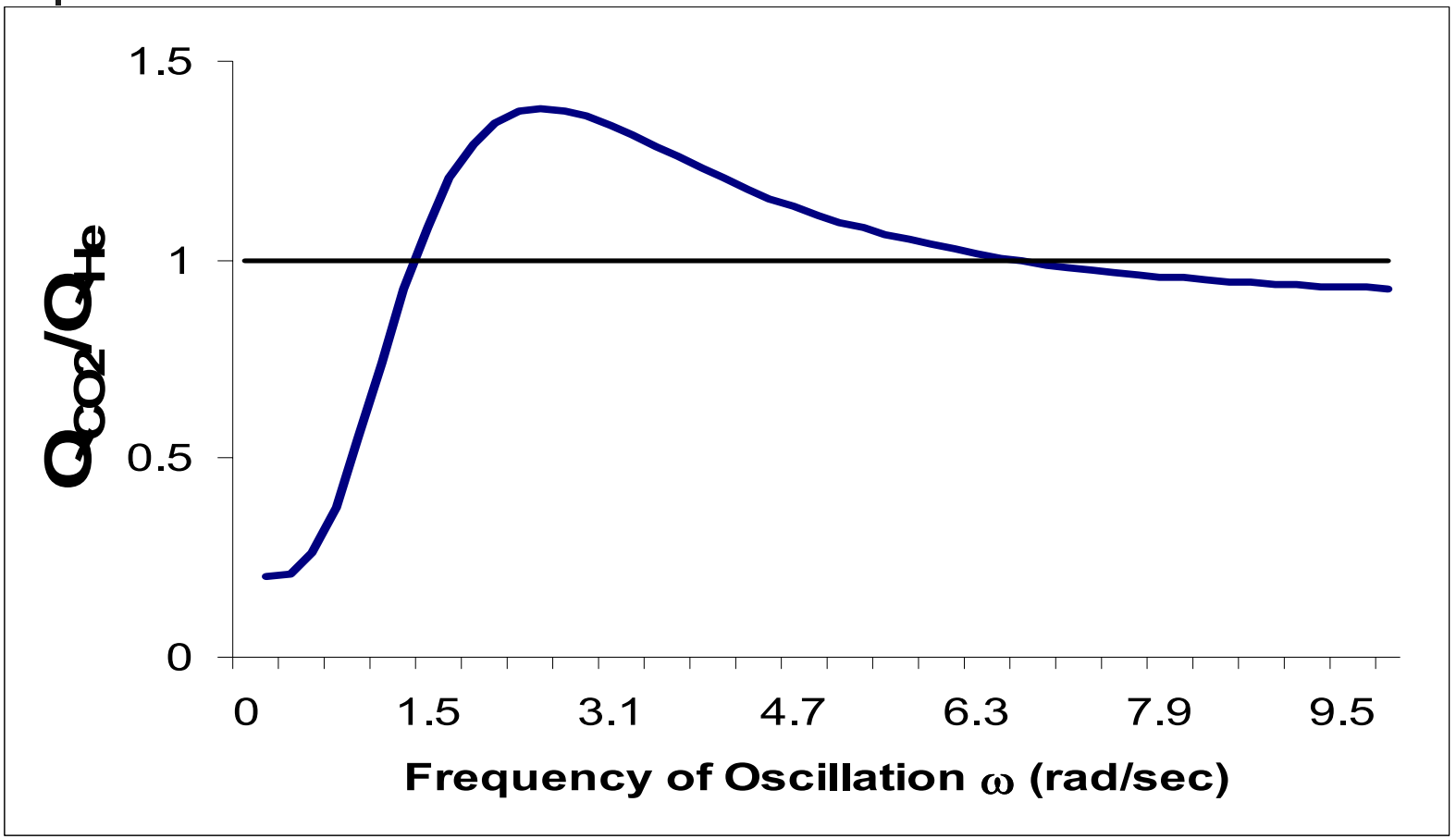

Experimental Setup

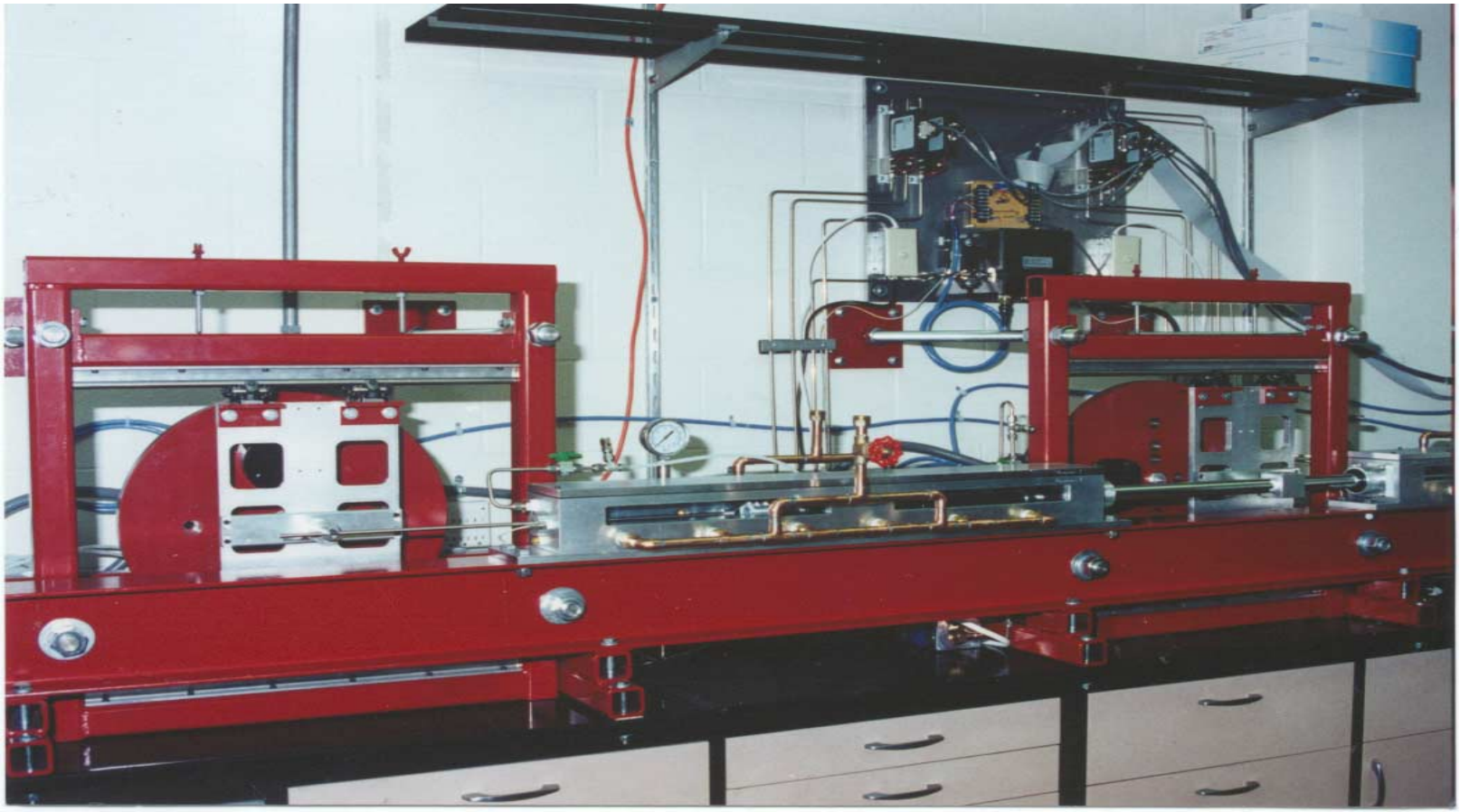

Separation Ratio for CO_2-CH_4 System

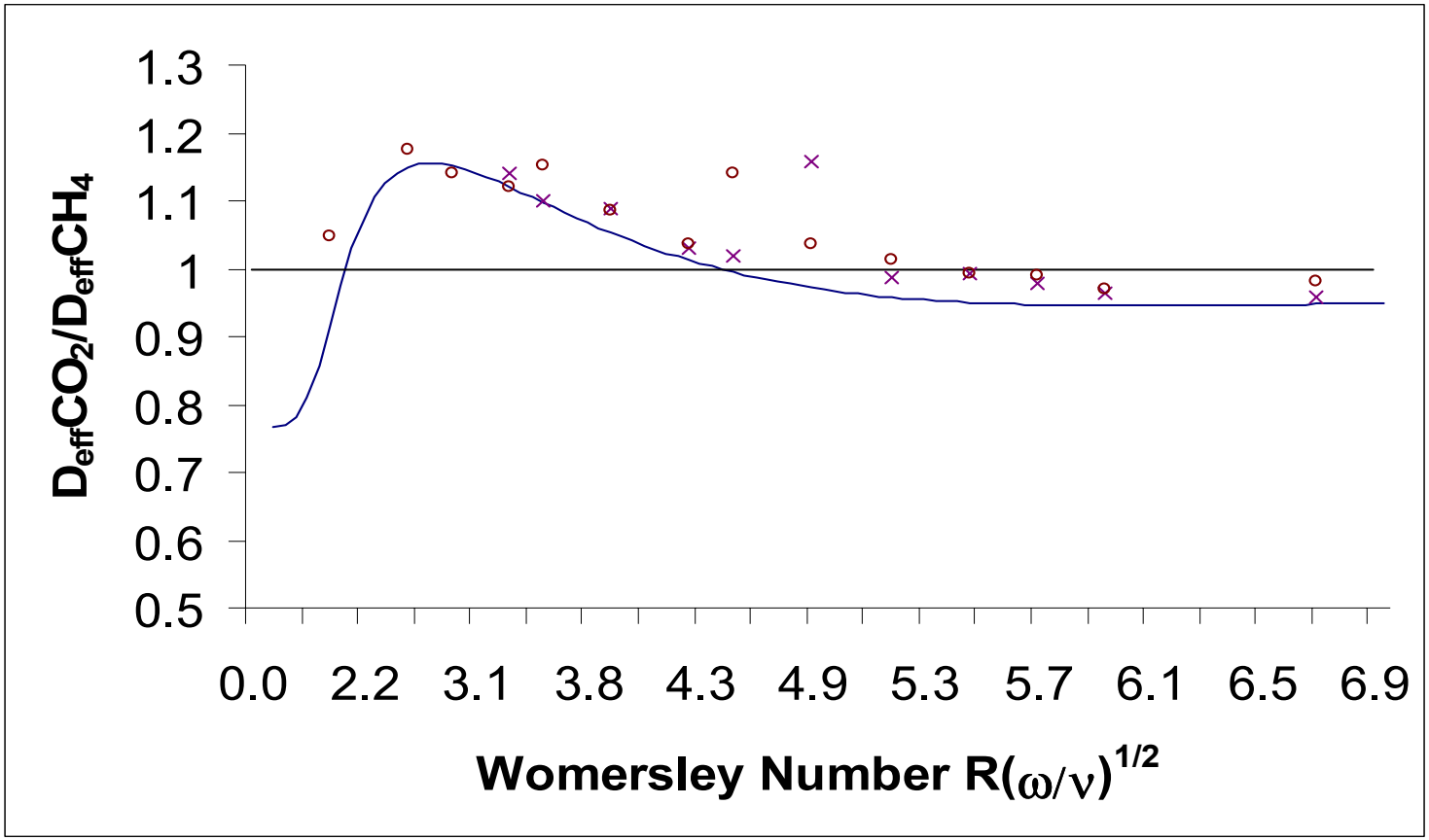

Separation Ratio for CH_4-He System

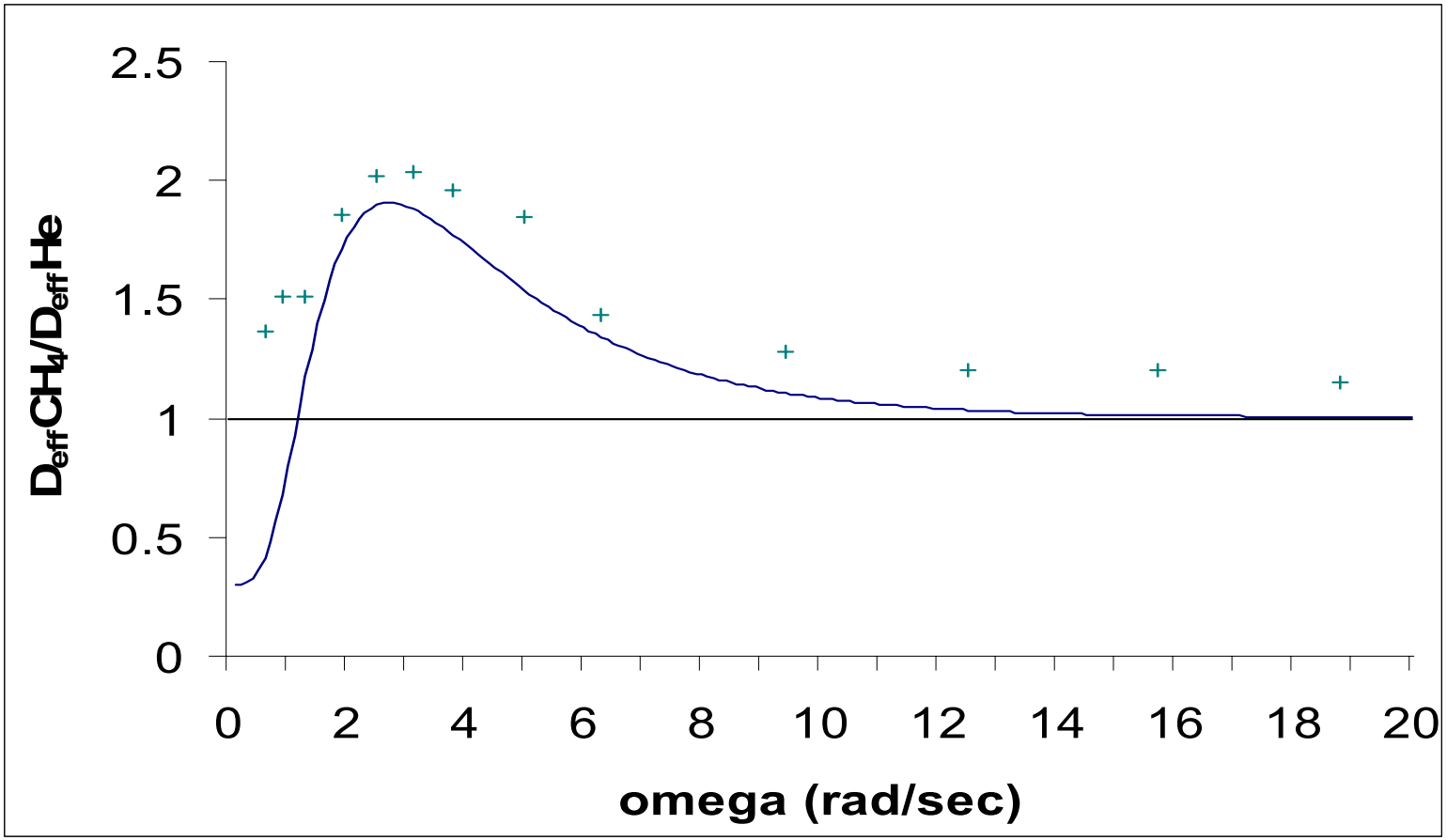

Periodic Recesses (Wavy Wall)

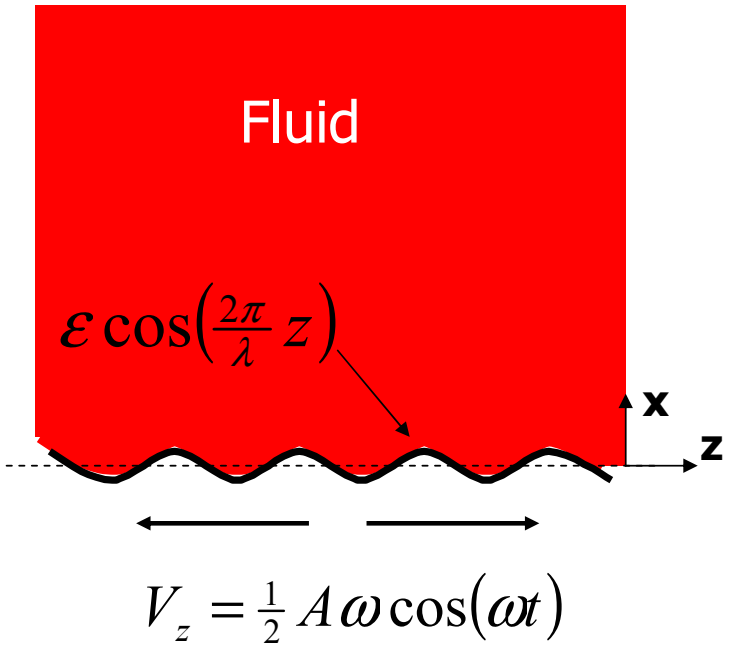

- Oscillating flat plate in a semi-infinite fluid
- Perturbation analysis performed about a small deflection ε
- Velocity, concentration, and mass transfer found to $O(\varepsilon^2)$

Preliminary results

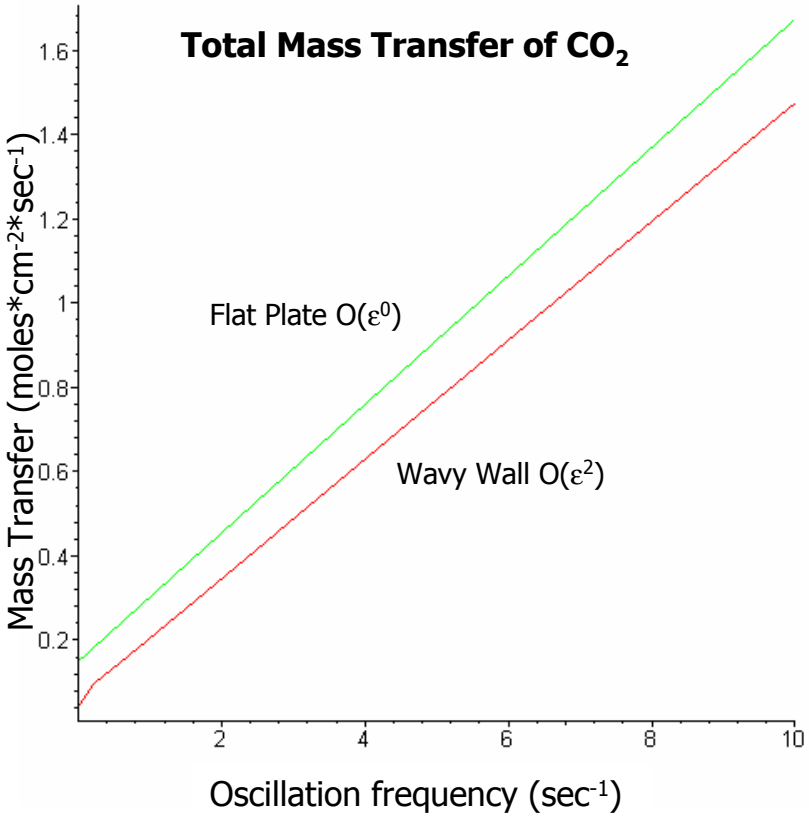

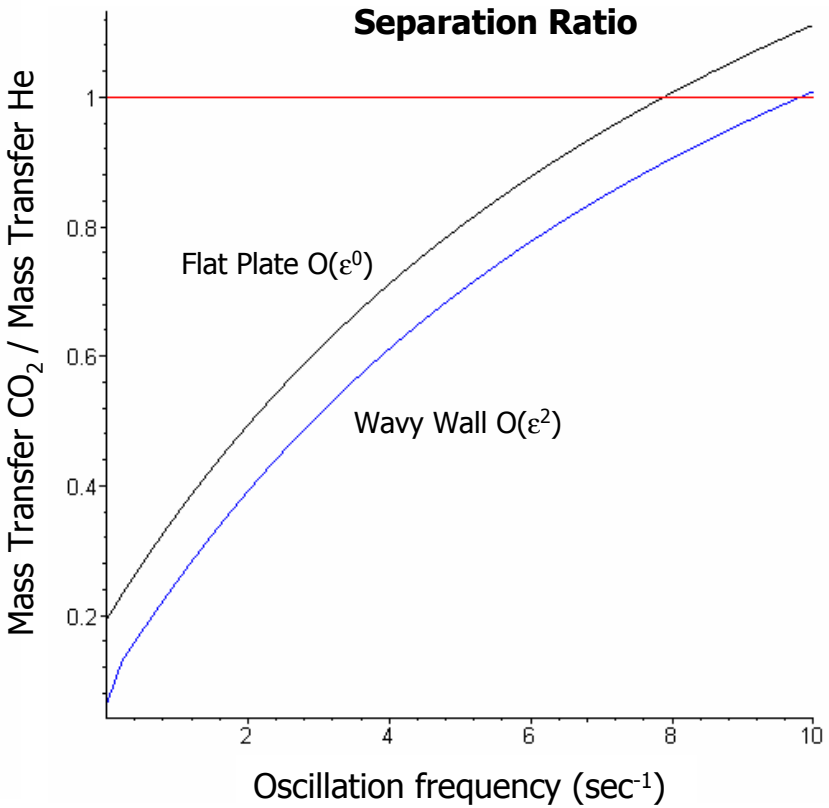

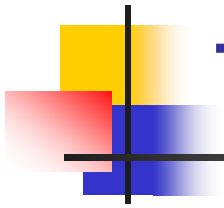

The Future

- Continue analysis of periodic recesses in other geometrical configurations (between two flat plates, in a tube)
- Start experiments on periodic recesses to assess viability as a contaminant removal process for future space missions
- Continue analysis for heat transport, biological separations, and detection of trace toxins

Reducing Fuel Slosh in Spacecraft Propulsion Systems

Erik Tolmachoff and Michael T. Kezirian

Department of Chemical Engineering
University of Southern California

Understanding the sloshing motion of liquid propellants in a partially-filled fuel tank is essential for determining and controlling spacecraft attitude (pointing). This investigation evaluates the importance of incorporating dynamic surface properties into the complete fluid transport model used to determine hydrodynamic flow stability.

Pointing stability requirements necessitate an understanding of the fuel motion and its interaction with the complete spacecraft flexible dynamic model. This investigation relates the fluid fuel motion, which at launch can account for approximately one half of the total spacecraft mass, to the overall attitude control. The numerical model developed for this investigation simulates the motion of a liquid fuel and quantifies the surface waves which appear at the interface and the internal waves in the bulk fluid.

COMPARISON OF THE STABILITY OF AN ELLIPTICAL LIQUID BRIDGE WITH A COMPANION CIRCULAR LIQUID BRIDGE

A. Kerem Uguz and R. Narayanan
Chemical Engineering Department
University of Florida
Gainesville, FL, 32611, USA
auguz@che.ufl.edu/ Fax: +1-352-392-9513

Liquid bridges have applications in microgravity contexts in connection to human health as well as materials processing. The small airways of the lungs are covered with a thin viscous film. The surface tension between the film and the air may induce the formation of a liquid bridge blocking the airflow and which might even damage the airway walls because of the pressure build-up. This disease is mostly seen in newborn premature babies who lack enough surfactant. Another application of the liquid bridges is seen in the float-zone crystal growth, which is a crucible-free technique to grow especially silicone. In this technique, in zero gravity, even if the strong thermocapillary flows are neglected, the melt zone, which can be represented by liquid bridge configuration, collapses at what is known as the Plateau limit. In most of the liquid bridge studies, the end disks are considered to be circular. In this presentation, the effect of distortion of the circular end plates to the nearby elliptical ones is studied wherein the volume of the companion cylindrical bridge is conserved. Also, the end plates are deviated from the companion circular plates by keeping either the area or the perimeter of the circular disks constant. We conclude that elliptical liquid bridge is more stable than its nearby circular bridge. A movie of the break-up of an elliptical liquid bridge is also provided.

ELECTRIC CURRENT ACTIVATED COMBUSTION SYNTHESIS AND CHEMICAL OVENS UNDER TERRESTRIAL AND REDUCED GRAVITY CONDITIONS

Unuvar, C.[1]; Fredrick, D.[1]; Anselmi-Tamburini U. [1]; M.; Manerbino, A.[3]; Guigne, J. Y.[3]; Munir, Z. A.[1]; Shaw, B. D.[2]

[1]Department of Chemical Engineering and Materials Science,
[2]Department of Mechanical and Aeronautical Engineering,
University of California, Davis
[3]Guigne Int. Ltd., 685 St. Thomas Line, Paradise, Newfoundland A1L 1C1, Canada

Combustion synthesis (CS) generally involves mixing reactants together (e.g., metal powders) and igniting the mixture. Typically, a reaction wave will pass through the sample. In field activated combustion synthesis (FACS), the addition of an electric field has a marked effect on the dynamics of wave propagation and on the nature, composition, and homogeneity of the product as well as capillary flow, mass-transport in porous media, and Marangoni flows, which are influenced by gravity. The objective is to understand the role of an electric field in CS reactions under conditions where gravity-related effects are suppressed or altered. The systems being studied are Ti+Al and Ti+3Al. Two different ignition orientations have been used to observe effects of gravity when one of the reactants becomes molten. This consequentially influences the position and concentration of the electric current, which in turn influences the entire process. Experiments have also been performed in microgravity conditions. This process has been named Microgravity Field Activated Combustion Synthesis (MFACS). Effects of gravity have been demonstrated, where the reaction wave temperature and velocity demonstrate considerable differences besides the changes of combustion mechanisms with the different high currents applied. Also the threshold for the formation of a stable reaction wave is increased under zero gravity conditions. Electric current was also utilized with a chemical oven technique, where inserts of aluminum with minute amounts of tungsten and tantalum were used to allow observation of effects of settling of the higher density solid particles in liquid aluminum at the present temperature profile and wave velocity of the reaction.

Conference-Workshop on Strategic Research to Enable NASA's Exploration Missions
June 22 - 23, 2004; Cleveland, Ohio USA

Microgravity Field Activated Combustion Synthesis (MFACS)

Unuvar, C.[1]; Fredrick, D.[1];

Anselmi-Tamburini U. [1]; M.; Manerbino, A.[3]; Guigne, J. Y.[3]; Munir, Z. A.[1]; Shaw, B. D.[2]

[1]Department of Chemical Engineering and Materials Science,

[2]Department of Mechanical and Aeronautical Engineering,

University of California, Davis

[3]Guigne Int. Ltd., 685 St. Thomas Line, Paradise, Newfoundland A1L 1C1, Canada

NASA # NCC3872

FACS Procedure

(Field Activated Combustion Synthesis)

Turbula mixing precursor elements

Cold pressed to give initial shape

Sample held by electrodes is placed in chamber

Reactants

Mixture

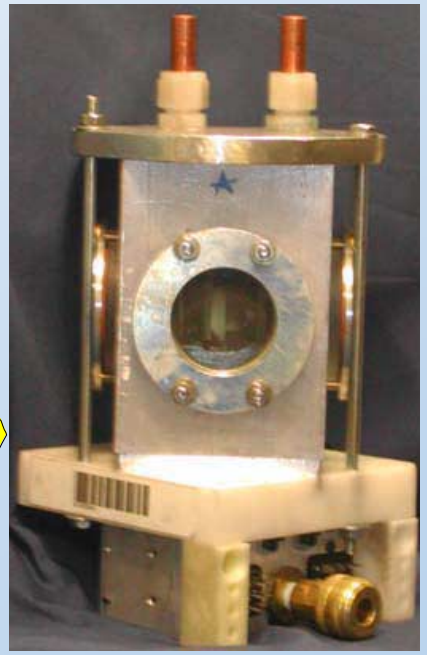

Combustion wave direction

Final product

Combustion

Ignition

Achieved in a few seconds!

Electric current passes perpendicular to the wave direction

Ultra-high purity argon environment

Chambers placed in COSYM (Guigne Int.) apparatus for KC-135 experiments

Two Contributing Fields in CS

Gravitational field induced
- Buoyancy and phase separation
- Convective flows and heat losses

Electric field affected
- Joule heating
- Capillary and Marangoni flows

↓

Temperature and phase distribution

↓

Effective electrical conductivity

↓

Current density distribution

↓

Degree of field activation

- Fundamental aspects of electric field in SHS can be investigated by reducing interactions with gravitationally induced phenomena

Ti+Al Wave Velocities vs. Current

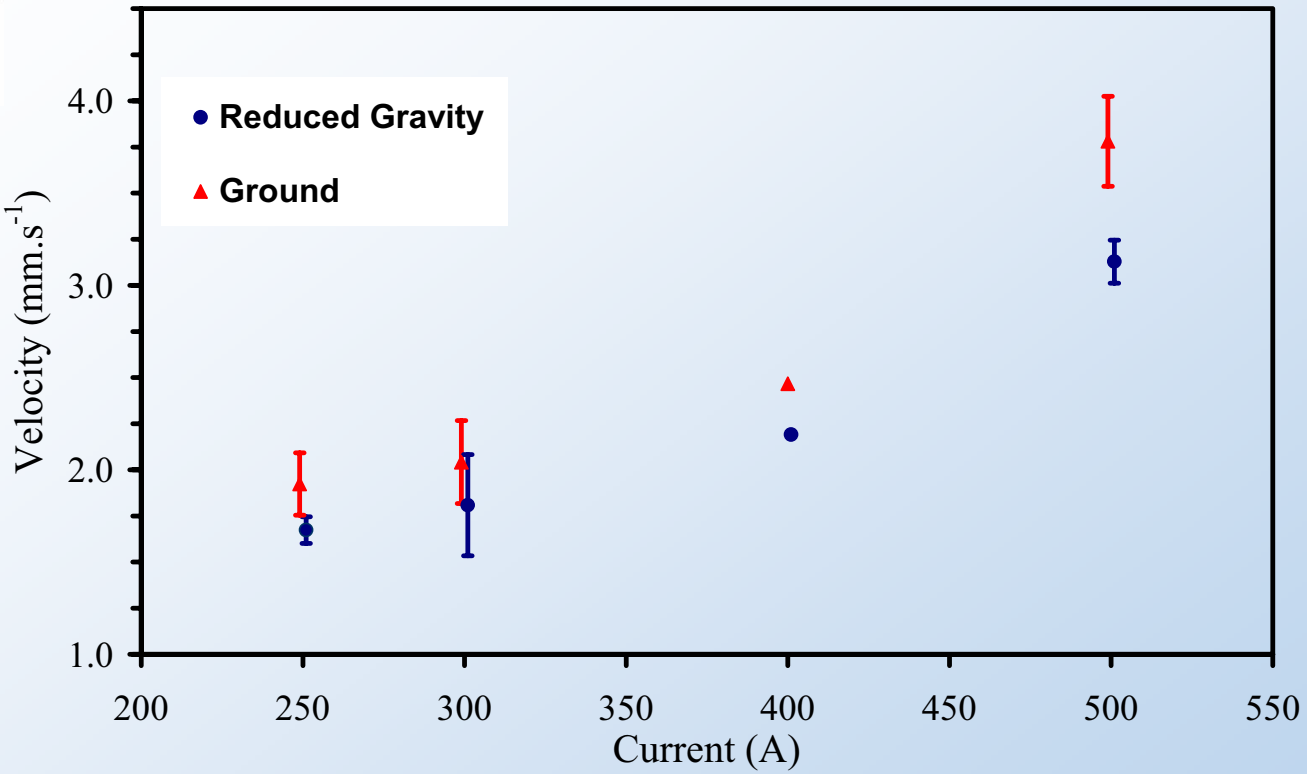

- Below the threshold value 250A, reaction waves are not self propagating
- At 250A higher percentage of waves extinguished in reduced gravity conditions, probably due to reduced convection
- 1-g experiments had higher velocities than the 0-g, with increasing currents.

Ti + Al Temperature vs. Current

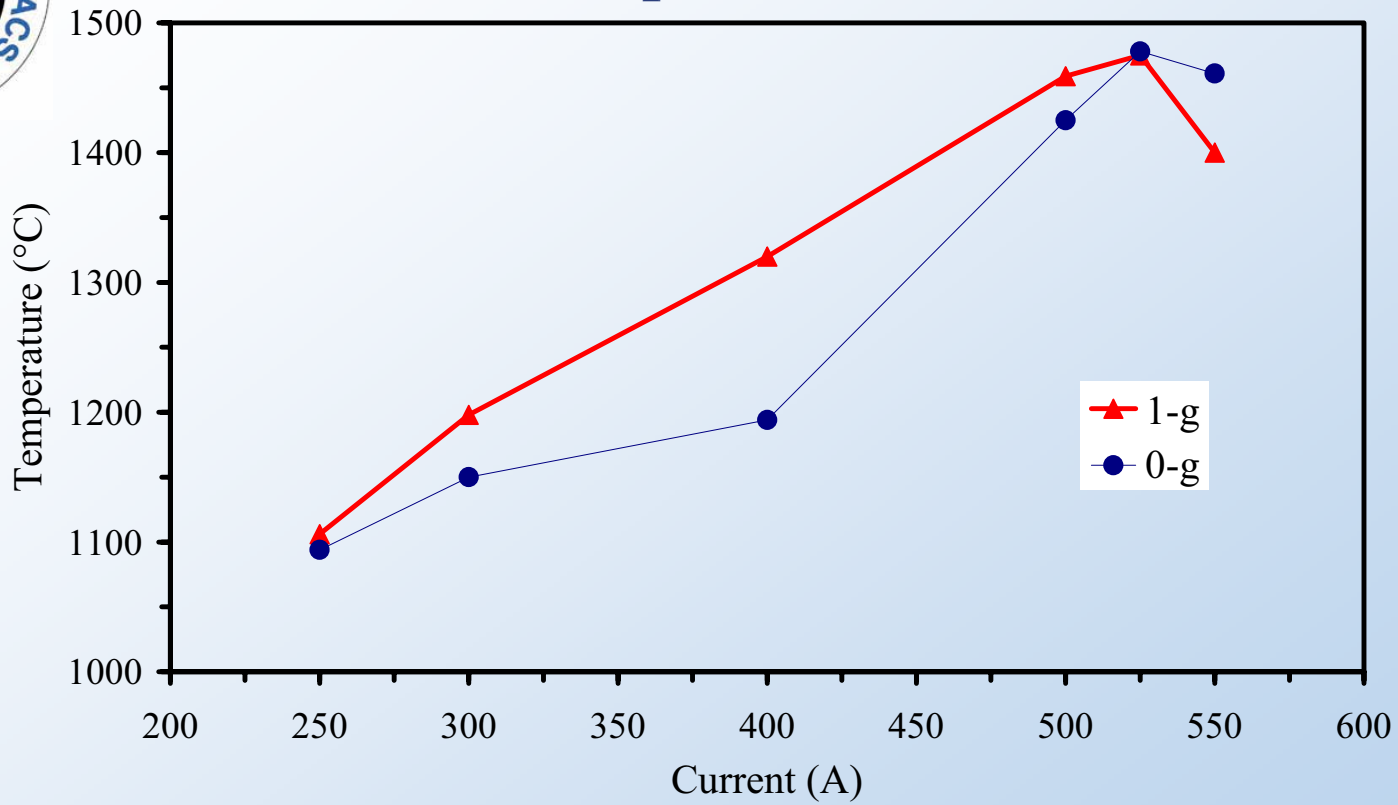

- Experiments in 1-g have higher temperatures for most currents.
- Cavities are created above 500A resulting in possible erroneous temperature measurements
- Temperature and velocity data show comparable trends with increasing current

Ti + 3 Al, Temperature vs. Current

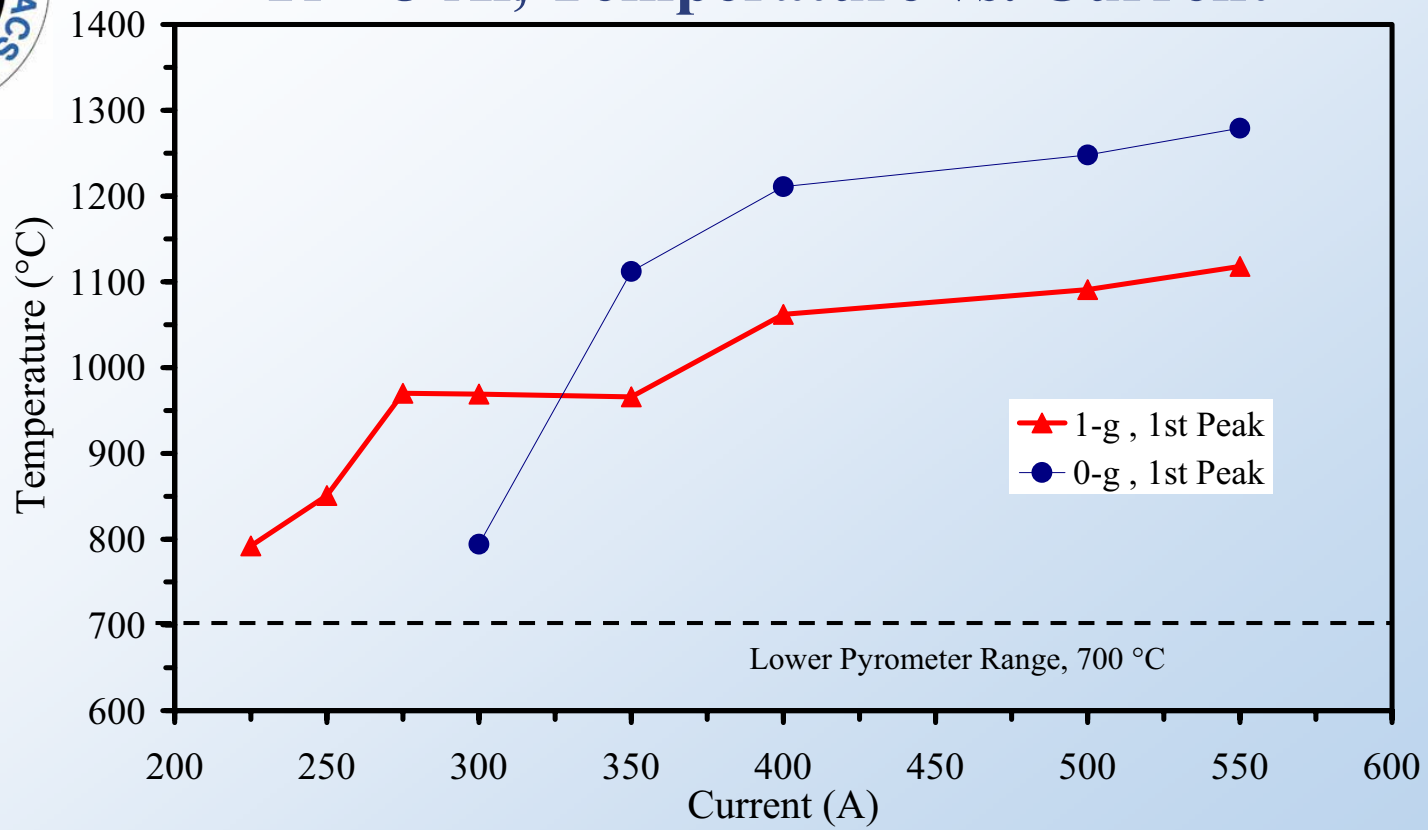

- Presence of increased liquid (3 moles Al) alters the behavior of the system and pronounces the effects of gravity
- 0-g exp. @ 225, 250, 275 A are below 700°C
- Switch in maximum temperatures with increased current occurs sharply above 300A at 0-g.

Chemical Oven (CO) Inserts

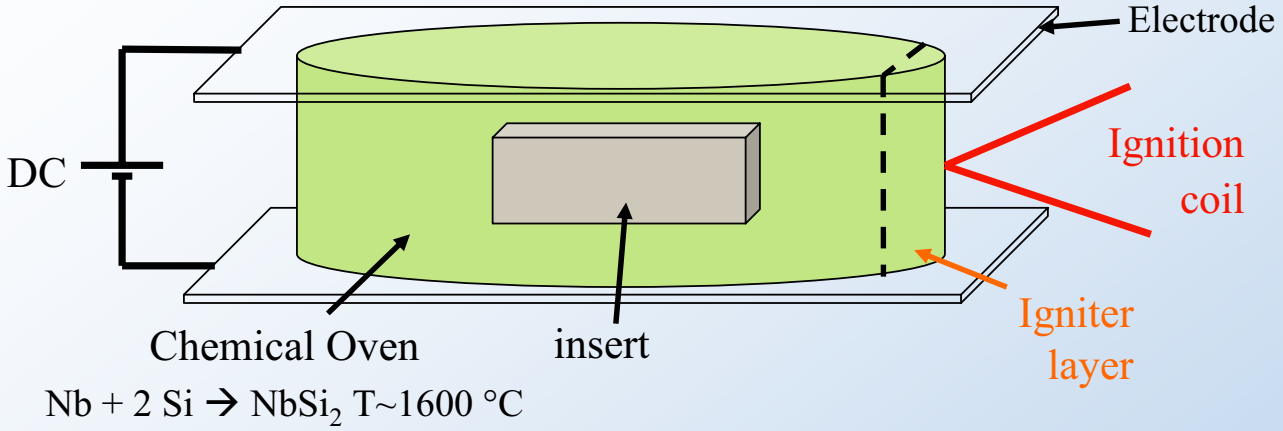

$Nb + 2\ Si \rightarrow NbSi_2$ T~1600 °C

- CO allows for larger amounts of liquid in the insert therefore gravitational effects are accentuated with minimal deformation caused by the presence of liquid
- Shows effects of gravity on *settling* of the denser solid metals in liquid Al

Insert content	Al	W	Ta	WC	TaC
Density (g/cm^3)	2.70	19.35	16.40	15.63	14.30

0.1W+Al insert, NbSi2 CO ignition from the *bottom*

wave direction

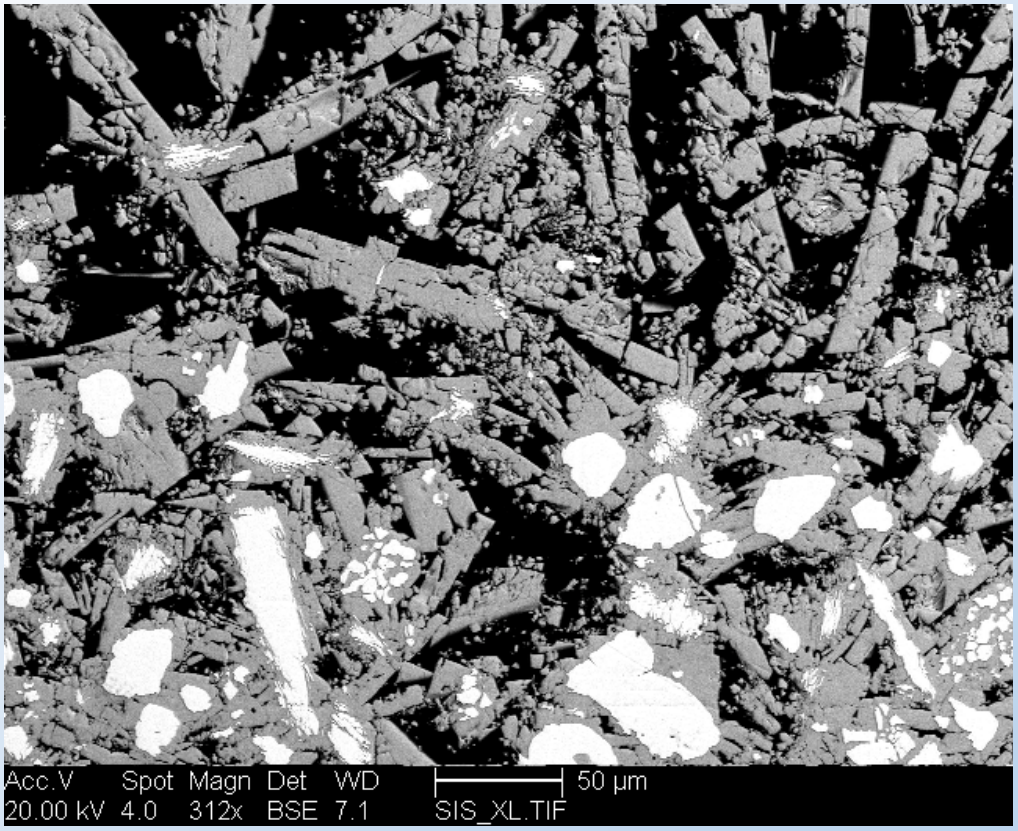

- Settling of W towards bottom
- Large precipitates of intermetallic compound

0.1W+Al insert, NbSi2 CO ignition from the *top*

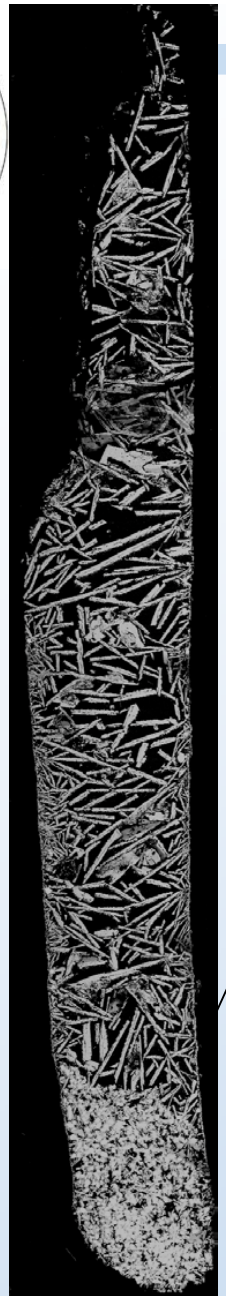

wave direction

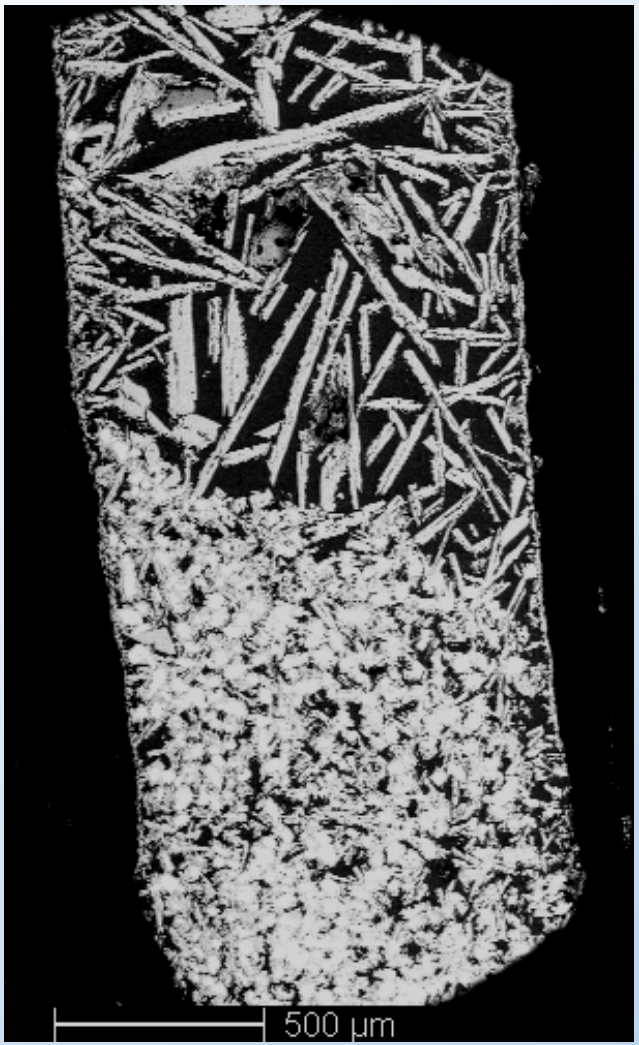

- Settling of W with the direction of *gravity* not the *wave*
- Large ppt's of intermetallic (Composition differences to be analyzed along insert)

Missions to Mars and the Moon

- Products required for extended stays: Structural, Electrical, Aerospace, etc.
  - Transport final products→Expensive!
  - Produce from available raw materials to final shape on site!
- Field Activated Combustion Synthesis (FACS) is an economical and time efficient on-site process
- By understanding the fundamentals behind this process, advanced materials can be created in various gravitational fields

Droplet-Surface Impingement Dynamics for Intelligent Spray Design

Randy L. Vander Wal, John P. Kizito, Gretar Tryggvason,*
Gordon M. Berger, and Steven D. Mozes

The NCMR c/o NASA-Glenn
Cleveland, OH 44135

* Worcester Polytechnic Institute
Worcester, MA 01609

Spray cooling has high potential in thermal management and life support systems by overcoming the deleterious effect of microgravity upon two-phase heat transfer. In particular spray cooling offers several advantages in heat flux removal that include the following:

1. By maintaining a wetted surface, spray droplets impinge upon a thin fluid film rather than a dry solid surface
2. Most heat transfer surfaces will not be smooth but rough. Roughness can enhance conductive cooling, aid liquid removal by flow channeling.
3. Spray momentum can be used to a) substitute for gravity delivering fluid to the surface, b) prevent local dryout and potential thermal runaway and c) facilitate liquid and vapor removal. Yet high momentum results in high We and Re numbers characterizing the individual spray droplets. Beyond an impingement threshold, droplets splash rather than spread. Heat flux declines and spray cooling efficiency can markedly decrease.

Accordingly we are investigating droplet impingement upon a) dry solid surfaces, b) fluid films, c) rough surfaces and determining splashing thresholds and relationships for both dry surfaces and those covered by fluid films. We are presently developing engineering correlations delineating the boundary between splashing and non-splashing regions.

Determining the splash/non-splash boundary is important for many practical applications. Coating and cooling processes would each benefit from near-term empirical relations and subsequent models. Such demarcations can guide theoretical development by providing definitive testing of its predictive capabilities. Thus, empirical relations describing the boundary between splash and non-splash are given for drops impinging upon a dry solid surface and upon a thin fluid film covering a similar surface. Analytical simplification of the power laws describing the boundary between the splash and non-splash regions yields insight into the engineering parameters governing the splash and non-splash outcomes of the fluid droplets.

Figure 1 shows the power law correlation separating the splashing versus non-splashing regions as developed for droplets impinging upon a dry solid surface. Splashing upon a dry surface is reasonably described by $Ca > 0.85$, reflecting the competing roles of surface tension and viscosity. Figure 2 shows the power law correlation separating the splashing versus non-splashing regions as developed for droplets impinging upon a thin fluid film covering the solid surface. Splashing upon a thin fluid film, as described by $v\,(pd/s) > 63$, is governed by fluid density and surface tension, but is rather independent of viscosity. Finally, the data presented here suggests that a more direct dependence upon the surface tension and viscosity, given a better understanding of their interplay, would allow accurate description of the droplet-surface impacts for more complicated situations involving non-Newtonian fluids, specifically those exhibiting viscoelastic behavior.

Acknowledgment
This work was supported by a NASA NRA 01-HEDs-03 Fluid Physics award administered through NASA cooperative agreement NCC3-975 with The National Center for Microgravity Research on Fluids and Combustion (NCMR) at the NASA Glenn Research Center.

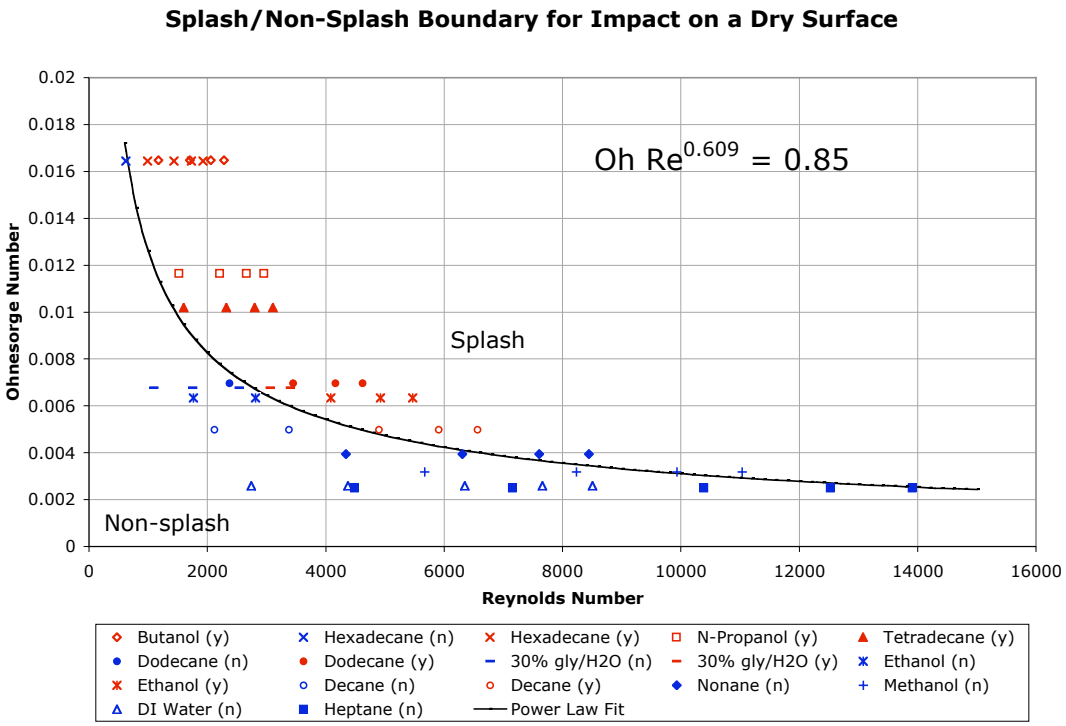

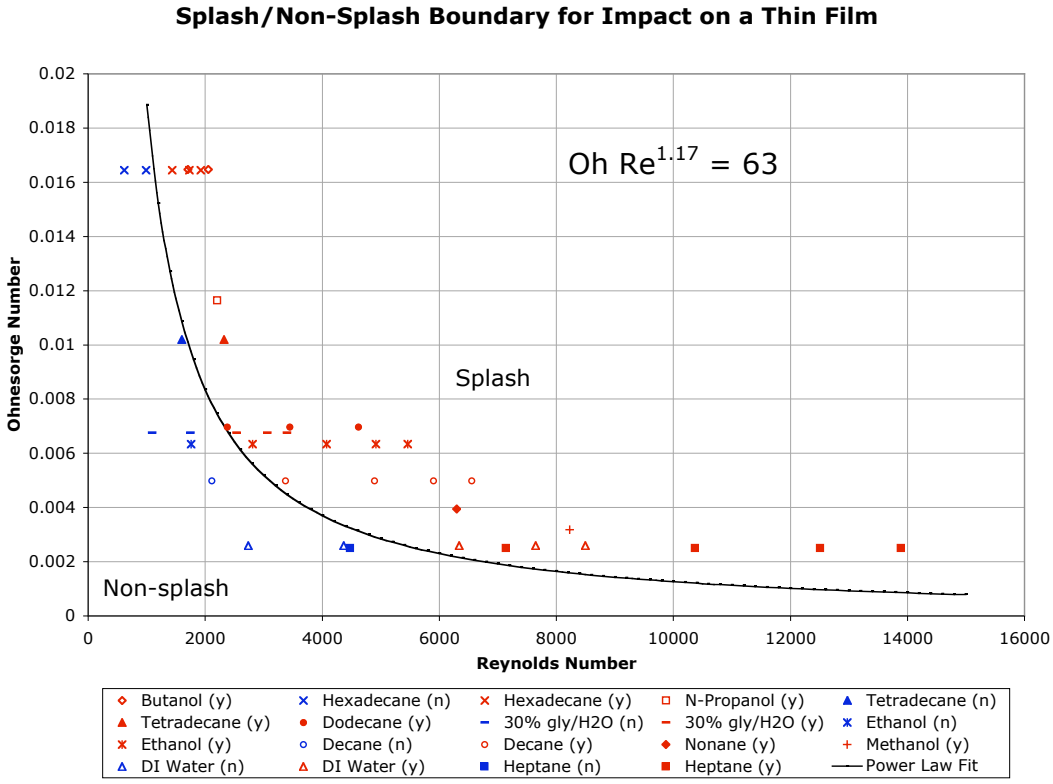

Figures 1&2. Splash behavior on a dry solid surface and on covered by a thin film, respectively, each plotted with respect to Ohnesorge and Reynolds number values. Red plot marks correspond to splashing behavior and blue to non-splash. The equation for the boundary fit line is included on the graph.

CONVECTIVE INSTABILITIES IN LIQUID FOAMS

Igor Veretennikov,
Department of Chemistry and Biochemistry, University of Notre Dame, Notre Dame, IN 46556,
email: ivereten@nd.edu, phone: (574)-631-7601, fax: (574)-631-6652

James A. Glazier,
Department of Physics, Indiana University, Bloomington, IN 47405

ABSTRACT

The main goal of this work is to better understand foam behavior both on the Earth and in microgravity conditions and to determine the relation between a foam's structure and wetness and its rheological properties. Our experiments focused on the effects of the bubble size distribution (BSD) on the foam behavior under gradual or stepwise in the liquid flow rate and on the onset of the convective instability. We were able to show experimentally, that the BSD affects foam rheology very strongly so any theory must take foam texture into account.

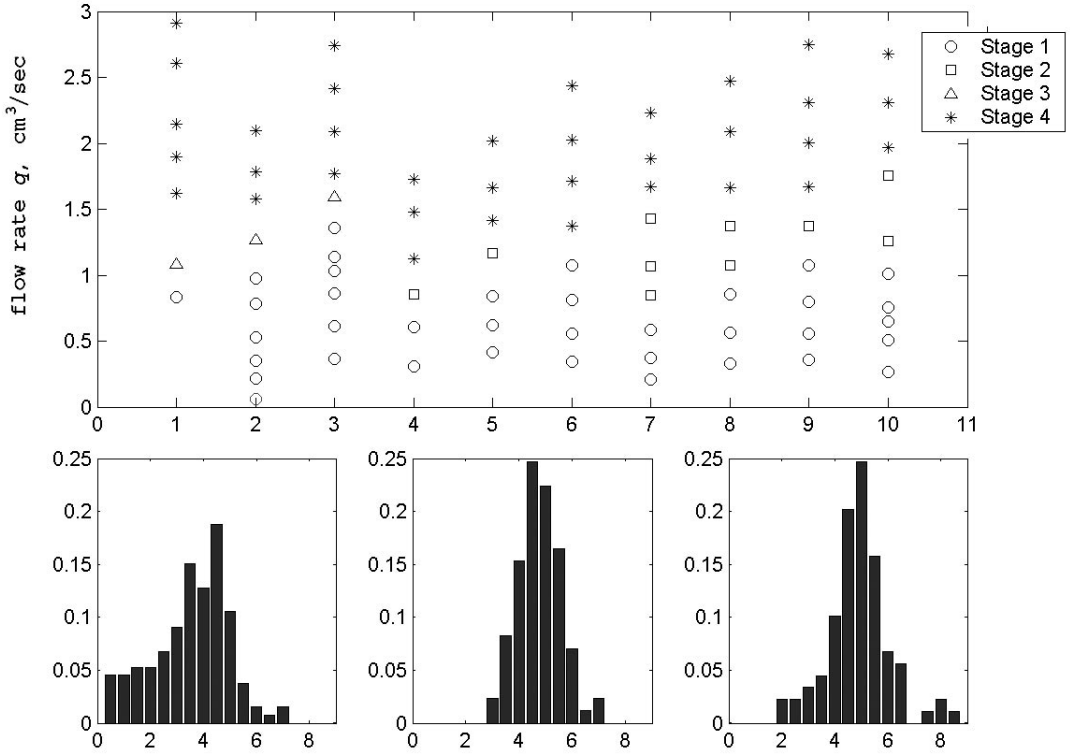

Figure 1: Behavior of stabilized foams as a function of liquid flow rate *q*. The BSD histograms corresponding to data sets 1-3, 4-6 and 7-10 are shown in a lower row.

When we change liquid flow rate by small increments, we detected four different stages of foam evolution. At low flow rates, increase in liquid supply produces only thickening of membranes and borders but does not induces bubbles motion (Stage1). For larger flow rate, but before the onset of global convection, we observed two possible types of foam behavior. One of them includes localized bubbles rearrangements in response to variations in liquid supply, which

stop after few minutes (Stage 2). For almost monodispersed foams (data sets 4-6) this stage presents for the narrow range of liquid flow rates or may be even absent. If the BSD is wide, with appreciable fraction of large bubbles (data sets 7-10), these rearrangements are typical for larger liquid flow rates range. Such "placing right bubbles to the right place" reduces stress in foam lattice and delays the onset of global convection for polydispersed foams. This stage was not observed for foams containing relatively large fraction of small bubbles. Instead, we have seen "scattered motion" (Stage 3): bubble cluster start to move, stops after few seconds or minutes, then similar motion begins at other place at the foam column, and so on. Such flow pattern persists as long as liquid flow rate does not change. Both Stages 2 and 3 for the same foam were never observed. "Scattered" motion always starts from the displacement of the smallest bubbles while the larger ones become involved later. Small bubbles, which may travel along the borders between large ones, may acts as increase effective viscosity of basic fluid, such that the passage of small bubbles between larger ones locally destabilizes the foam. The large-bubble motion stops after structure adjustment, but may start again if another cluster of small bubbles will be provided by incoming liquid flow.

We also examine the development of convective pattern under rapid increase in liquid flow rate from subcritical (Stage 1) to supercritical value (Stage 4). Typically, the melting wave propagates down along one side of the cell while the much slower upward foam flow develops on the other side. During few seconds after the flow rate change, there is no bubble motion while liquid flow through the foam slightly increases. After that, the entire foam downstream of the convective front moves down. Bubbles slightly compresses, but still do not moves relative to each other. When the melting wave passes few centimeters, the upward counterflow begins to develop. If the difference in flow rate is large, bubbles at the front of the wave may be significantly compressed. Behind the front, the borders thicknesses increase and bubbles may rotate while moving down. When the melting front reaches the bottom of the column, steady convective pattern develops. We captured the foam motion by digital video camera and measured the averaged image density. Borders are darker than lamellae, such that the average density provides information about liquid distribution in the foam. During the initial prewetting, the wetness of motionless foam increases uniformly over entire column. For the compression stage, we see the growth of wetness fluctuations and beginning of development of wetness maximum in front of approaching melting wave. The position of moving melting front is clearly seen on the vertical density profile. The wetness difference behind the front and downstream and the front slope are related to the wave speed and, in turn, to jump in liquid flow rates. When the convective roll is fully developed, vertical profiles of relative density again become uniform, while on horizontal profiles typically appear two maxima corresponding to downward and upward foam flows. The amplitude of these intensity maxima is roughly proportional to the foam velocity. The surprising is the overall decrease of the relative density during the compression stage. The physical mechanism behind it is not clear and requires additional study.

NASA/CP—2004-213205/VOL2

Convective Instability in Liquid Foam.

Igor Veretennikov† and James A. Glazier‡

† University of Notre Dame, Notre Dame, IN 46556

‡ Indiana University, Bloomington, IN 47405

Convection in “Stabilized” Foams

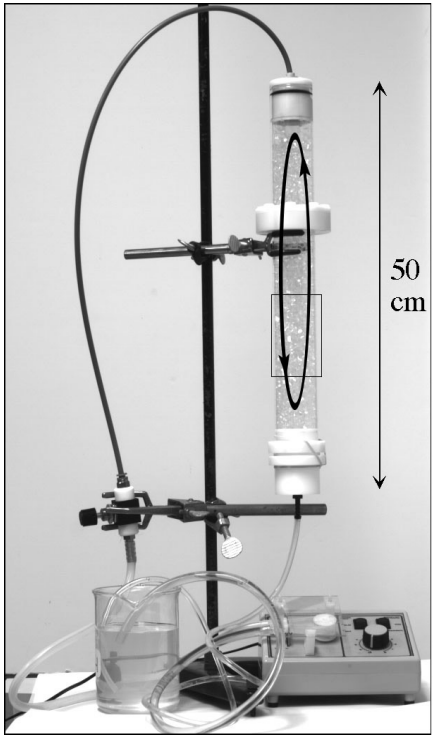

standing foam

convection starts

Stepwise Increase in Liquid Supply

- Compression wave propagates downward, preceding melting wave.
- Fast increase in thickness of Plateau membranes and Plateau borders.
- Second increase in thickness and adjustment of curvatures of the membranes and Plateau borders.
- The degree of compression is roughly proportional to the increase in liquid flow rate.
- Convective roll develops.

Propagation of the Melting Front.

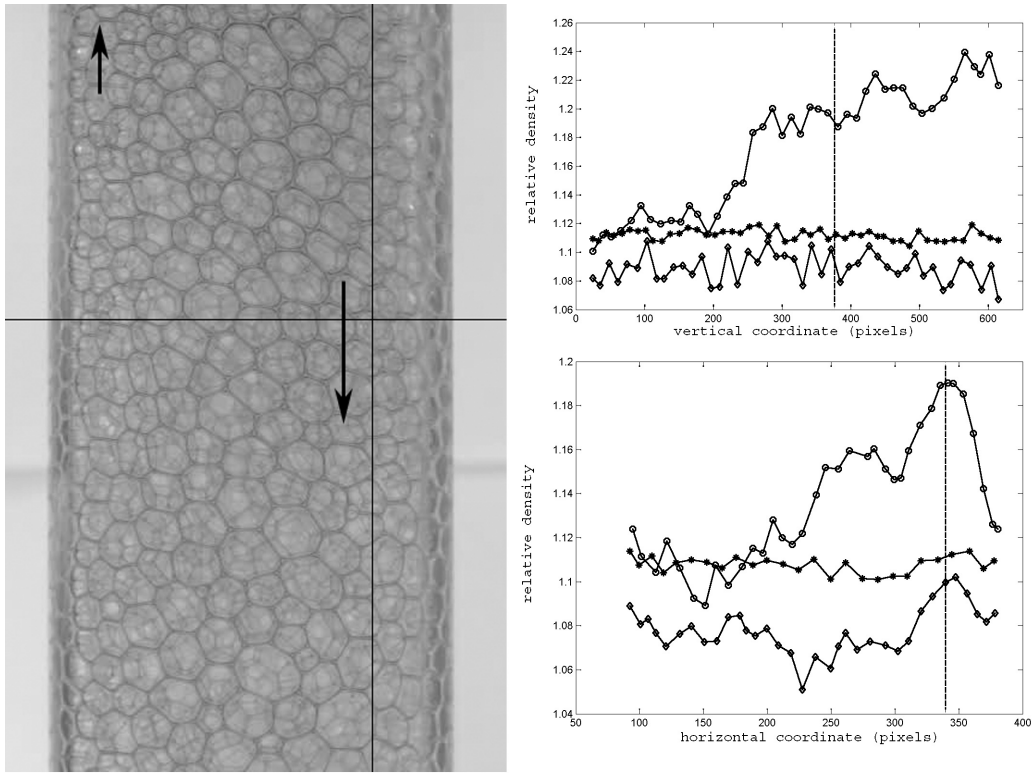

The liquid flow rate increased from 0.375 to 2.03 cm^3/sec. (Right) Vertical and horizontal profiles of relative image density. * – initial prewetting, no motion; ◊ – compression, O – melting front passes.

Critical Flow Rate Measurements

- We increased the flow rate slowly in small increments until the foam began to move. We defined the critical flow rate as the flow rate at which global convection, which affects every bubble, starts.
- We found four stages of foam evolution under the gradual increase in liquid supply:

  1. Membrane thickness increases, no bubble motion.
  2. Localized bubble rearrangements. The motion stops when “right” bubbles are placed into “right” places.
  3. Scattered movement in different areas of foam column.
  4. Global convection.

- Critical flow is measured as a function of viscosity of basic fluid, BSD and fluid fraction for foams in cylindrical and rectangular (6.2 cm $\times$ 4.7 cm $\times$ 25 cm) foam cells.

Effect of Bubble Size Distribution – 1

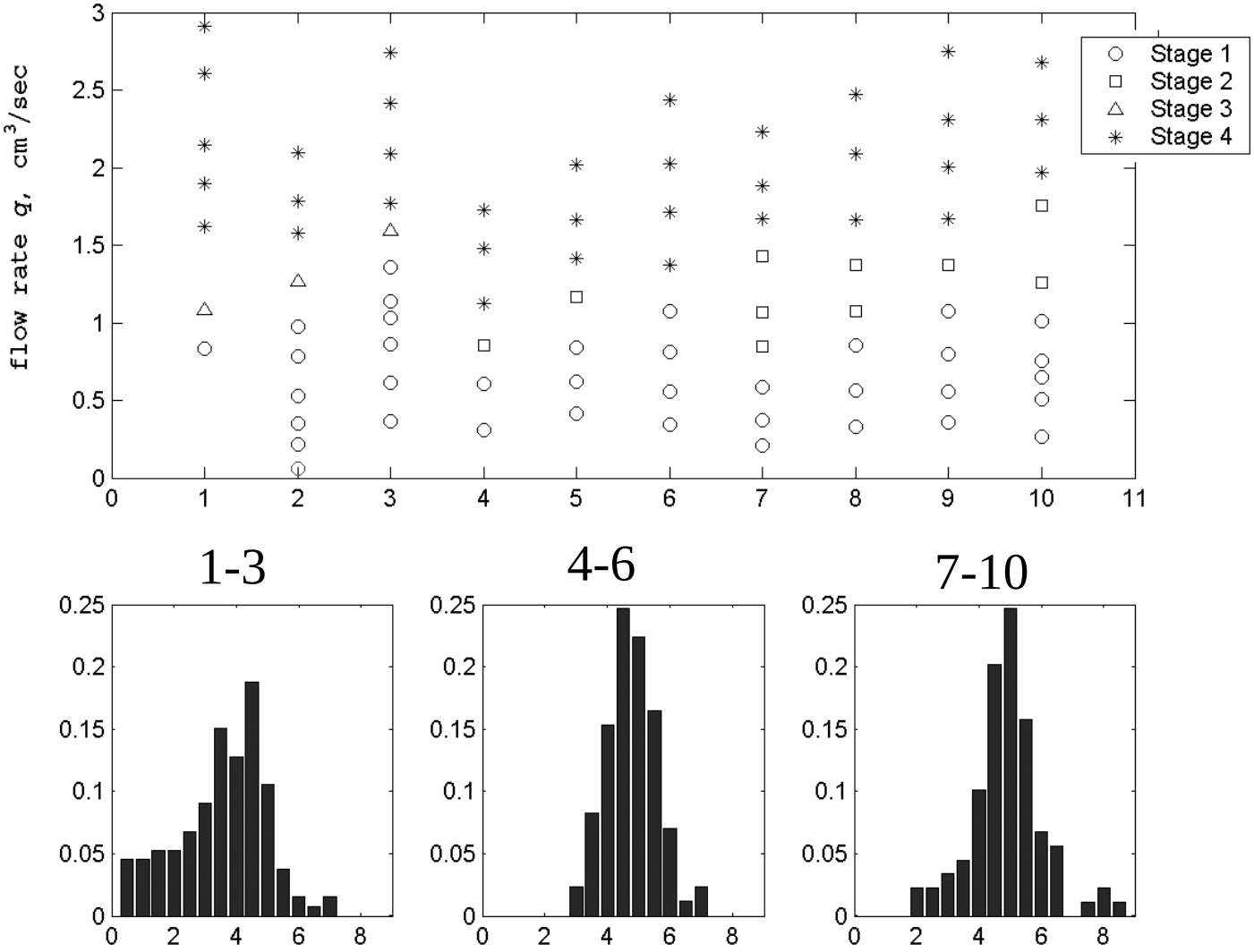

Effect of Bubble Size Distribution – 2

rectangular cell

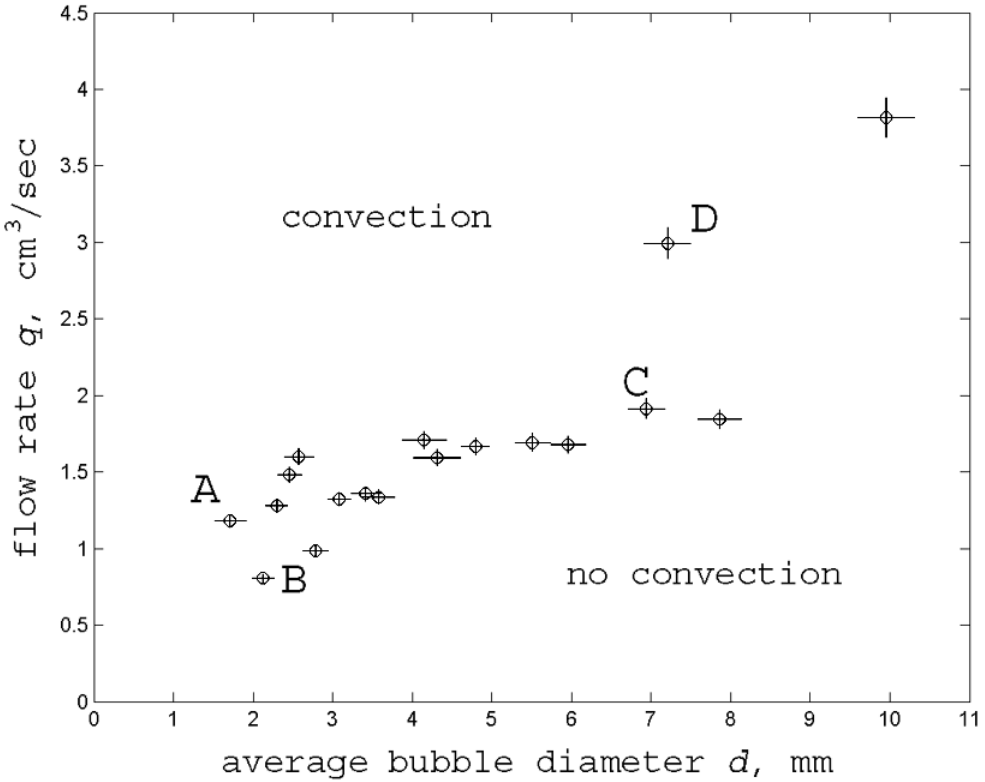

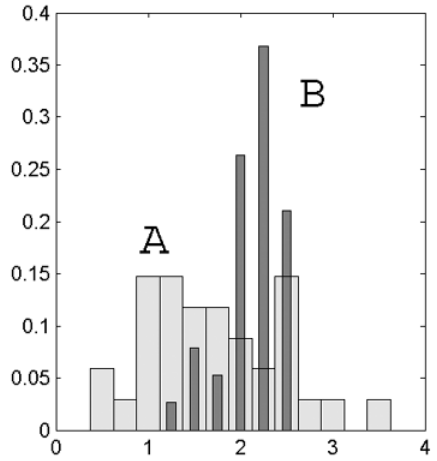

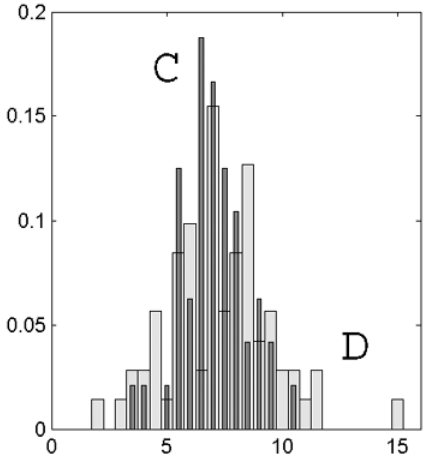

Effect of Bubble Size Distribution – 3

- Foams with smaller average bubble diameter are more UNSTABLE than those with larger average bubble diameter.
- Homogeneous foams are more UNSTABLE to global convection than polydisperse foams with the same average bubble diameter. Additional stress may appear within the foam lattice because uniform bubbles are not able to fill the cell perfectly.
- Foams are very STABLE when average bubble diameter is comparable with cell dimensions.
- The results for small bubbles are hardly reproducible.

Effect of Base Fluid Viscosity

cylindrical cell

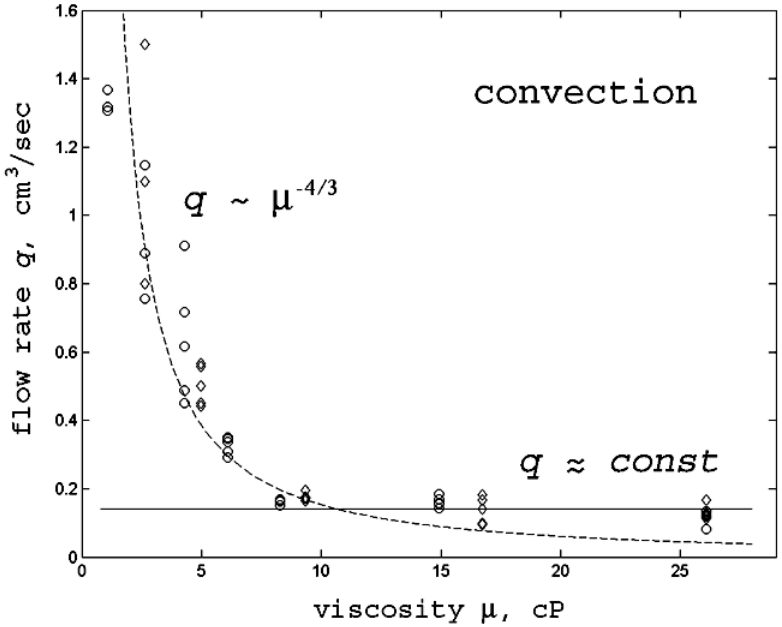

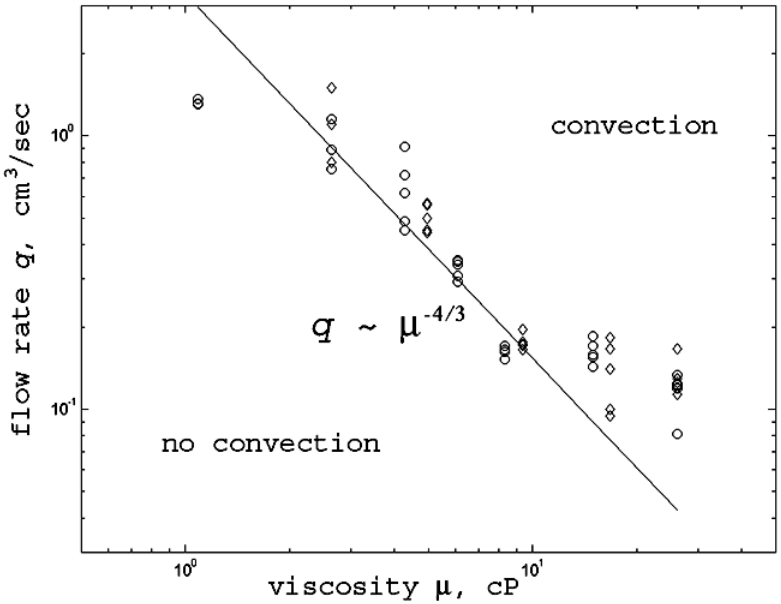

- Data scattering is mostly due to variations in bubble size distribution (BSD). Critical flow rate becomes almost independent of viscosity at $\mu \geq 10$ cp
- Only one convective roll is found in our cylindrical foam cell (diameter ~ 4.5 cm) if the flow rate is high enough.

Critical Liquid Fraction

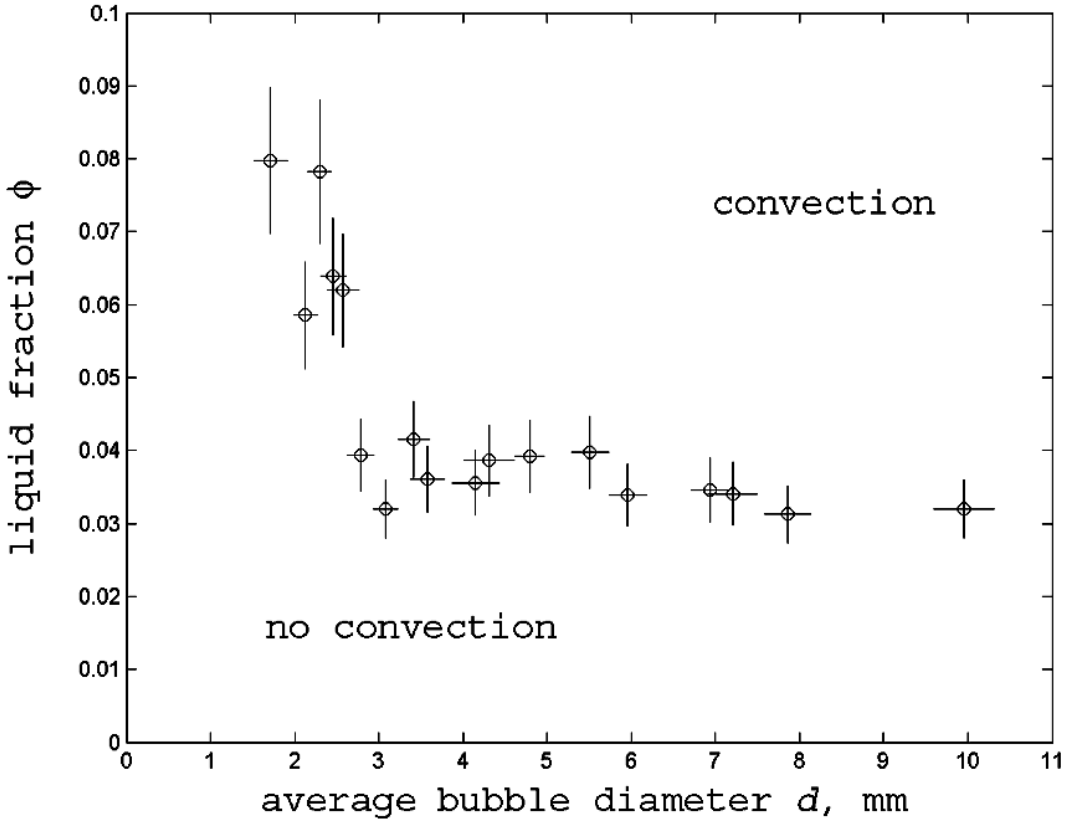

- In the rectangular foam cell (6.2 cm × 4.7 cm), one or two rolls may be formed.
- Presence of cell corners reduces foam stability and increases its sensitivity to nonuniformities in liquid supply.

• In stressed foams, the critical wetness is significantly below the close packing loss transition ($\phi_c \sim 0.36$).

The estimate for average liquid film thickness *h*

For one bubble within foam lattice:

$$\phi = \text{liquid fraction} = \frac{1/2 \text{ volume of liquid}}{\text{bubble volume}} \approx V_{gas}$$

$$\phi = \frac{1/2 \pi d^2 h}{\pi d^3/6} \Rightarrow h = \frac{\phi d}{3}$$

Flow rate ***Q*** per one bubble in the cell cross-section

$$Q = \frac{\text{total flow rate}}{\#\text{ of bubbles across the cell}} \Rightarrow Q = \frac{q \pi d^2}{4A}$$

Scaling

For one draining soap film with parabolic velocity profile inside:

$$Q \approx \pi d \frac{h^3}{12\mu}\left|\frac{dP}{dx}\right| \sim \frac{h^3}{\mu}\frac{d\Delta P}{d} \sim \frac{h^3}{\mu}\frac{\sigma}{r_{\min}}$$

downstream pressure gradient

minimal possible radius of Plateau border curvature

difference in capillary pressure along the film

Global convection starts when border curvatures cannot be adjusted to pass large incoming liquid flow.

Effect of Average Film Thickness

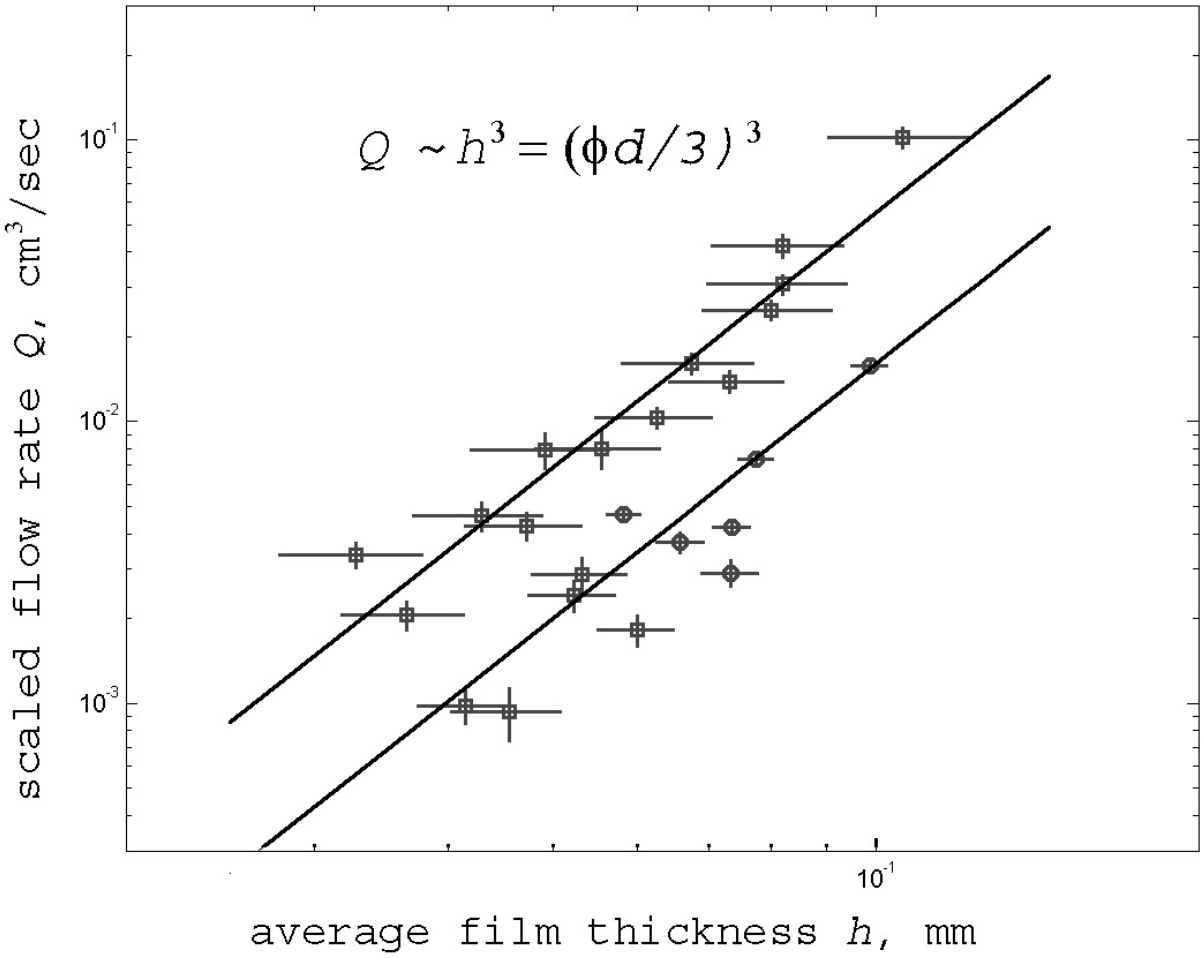

Conclusions

- Stressed foams can undergo melting transition when foam wetness is significantly below the one which corresponds to the close packing loss transition.
- This melting transition may start when the balance between border curvatures (local pressure gradient) and local flow in membranes and boarders breaks down.
- The critical parameters for this transition depend heavily not only on the bubble size distribution but also on the spatial distributions of bubbles.

Acknowledgments

Financial support from NASA is greatly appreciated.
Marius Asipauskas, Karl Fedje, Ivan Silva.

SEPARATION OF CARBON MONOXIDE AND CARBON DIOXIDE FOR MARS ISRU

Krista S. Walton and M. Douglas LeVan
Department of Chemical Engineering, Vanderbilt University
VU Station B #351604, 2301 Vanderbilt Place, Nashville, TN 37235
krista.s.walton@vanderbilt.edu
m.douglas.levan@vanderbilt.edu
Ph: (615) 322-2441 Fax: (615) 343-7951

The atmosphere of Mars has many resources that can be processed to produce things such as oxygen, fuel, buffer gas, and water for support of human exploration missions. Successful manipulation of these resources is crucial for safe, cost-effective, and self-sufficient long-term human exploration of Mars. In our research, we are developing enabling technologies that require fundamental knowledge of adsorptive gas storage and separation processes. In particular, we are designing and constructing an innovative, low mass, low power separation device to recover carbon dioxide and carbon monoxide for Mars ISRU (in-situ resource utilization). The technology has broad implications for gas storage and separations for gas-solid systems that are ideally suited for reduced gravitational environments. This paper describes our separation process design and experimental procedures and reports results for the separation of CO_2 and CO by a four-step adsorption cycle.

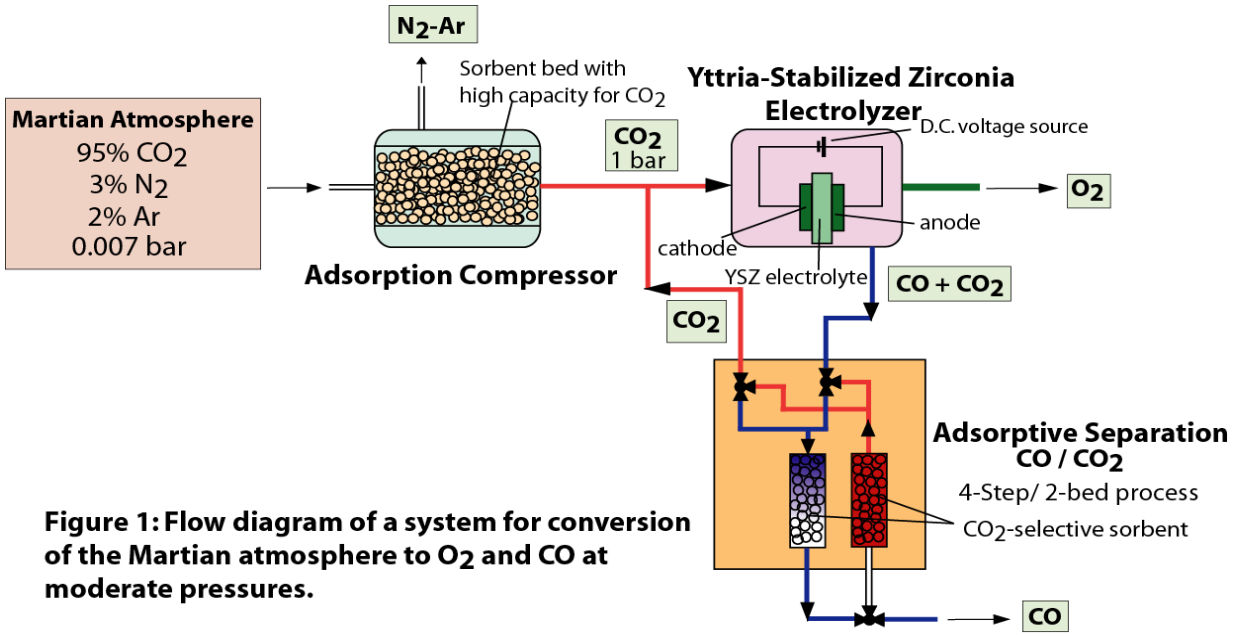

Figure 1: Flow diagram of a system for conversion of the Martian atmosphere to O_2 and CO at moderate pressures.

As illustrated in Figure 1, this work comprises one-third of an overall process for producing O_2 and CO at moderate pressures from the Martian atmosphere. An adsorption compressor, developed by Dr. John E. Finn at NASA Ames Research Center, adsorbs CO_2 from the atmosphere and compresses it to a pressure of 1 bar. The CO_2 is then passed to a solid oxide electrolysis cell developed by K. R. Sridhar at the University of Arizona. This electrolysis cell makes use of yttria-stabilized zirconia to produce oxygen from the compressed planetary CO_2 and will then reject CO and unreacted CO_2 in a separate stream. The efficiency of the oxygen-production process is greatly improved if the unreacted CO_2 is separated and recycled back into the feed stream. The separation will also have a positive impact on the mass of the adsorption compressor because less CO_2 will needed from the atmosphere. Additionally, the CO by-product is a valuable fuel for space exploration and habitation, with applications from fuel cells to production of hydrocarbons and plastics.

Our separation device contains a CO_2-selective sorbent such that when the mixture is fed from the electrolyzer, CO_2 adsorbs and CO passes through the bed with minimal adsorption. The cycle is illustrated by Figure 2. The mixture is fed at a temperature of 273K. When the bed reaches capacity, it is isolated and heated with no flow at 398K to desorb the CO_2. CO_2 at high pressure is then allowed to pass to a storage tank at sufficient pressure to feed the electrolyzer. The bed is then cooled back to 273K prior to returning to the feed step. We envision a two-bed system in which one bed is onstream for the feed step while the other is undergoing regeneration and blowdown of CO_2.

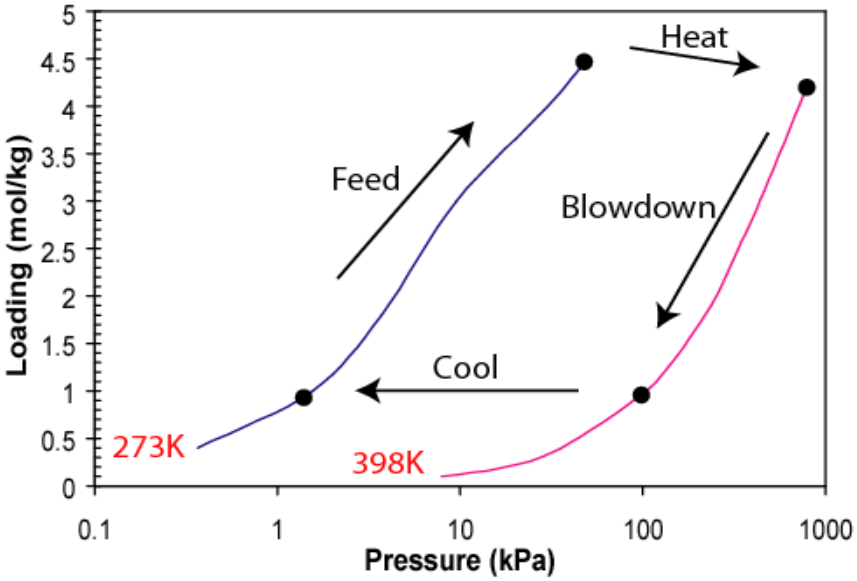

Figure 2: Depiction of four-step adsorption cycle between CO_2 adsorption isotherms on NaY zeolite.

We have a working prototype and have performed the proposed cycle. We have developed process models and are continuing to optimize the separation. All of these results will be discussed.

Separation of Carbon Monoxide and Carbon Dioxide for Mars ISRU

Krista S. Walton and M. Douglas LeVan
Department of Chemical Engineering, Vanderbilt University, Nashville, TN 37235

ABSTRACT

The atmosphere of Mars has many resources that can be processed to produce useful materials like oxygen, fuel, buffer gas, and water for support of human exploration missions. In this research, we are designing and constructing an innovative, low mass, low power separation device to recover carbon dioxide and carbon monoxide for Mars ISRU (in-situ resource utilization). The separation is accomplished by a four-step adsorption process. The technology has broad implications for gas storage and separations for gas-solid systems that are ideally suited for reduced gravitational environments.

Overall Process Description

YSZ Electrolyzer

CO_2 diffuses through the electrode and liberates an oxygen atom through thermal dissociation and electrocatalysis. The oxygen atom acquires two electrons from the cathode to form an oxygen ion. The electric field drives the ion through the electrolyte. The ion transfers its charge to the anode as it reaches the anode-electrolyte interface and combines with another oxygen atom to form O_2 then diffuses out of the anode. CO and unreacted CO_2 will pass to the separation device.

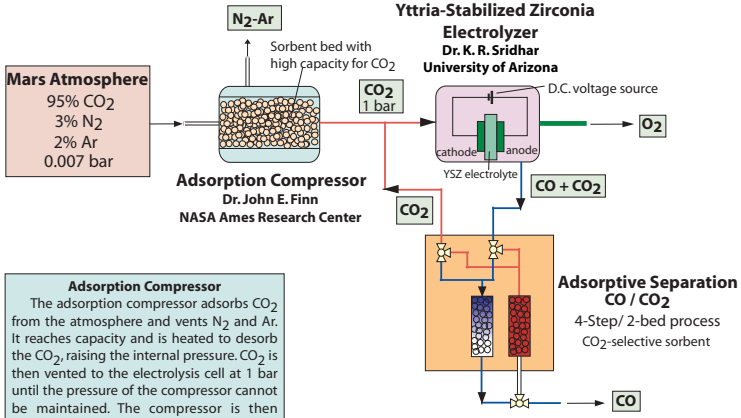

Adsorption Compressor

The adsorption compressor adsorbs CO_2 from the atmosphere and vents N_2 and Ar. It reaches capacity and is heated to desorb the CO_2, raising the internal pressure. CO_2 is then vented to the electrolysis cell at 1 bar until the pressure of the compressor cannot be maintained. The compressor is then cooled until the system pressure is the same as the environment, and a new cycle begins.

Adsorptive Separation

The separation device contains a CO_2-selective sorbent. The CO/CO_2 mixture is fed from the electrolyzer. CO_2 adsorbs and CO passes through the bed with minimal adsorption. When the bed reaches capacity, it is isolated and heated to desorb the CO_2. CO_2 at high pressure is then allowed to pass to a storage tank at sufficient pressure to feed the electrolyzer. The bed is then cooled prior to returning it to the feed step. The two-bed system allows one to be fed the CO/CO_2 mixture while the other is undergoing regeneration and blowdown of CO_2.

Acknowledgements: We are grateful to NASA for providing support for this research.

Adsorption Equilibria: Measurements and Modeling

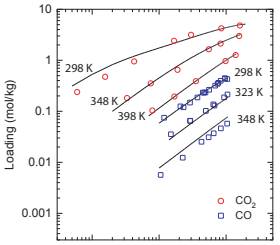

Pure-component adsorption isotherms on NaY zeolite. Lines are multisite Langmuir fits.

We have measured both pure-component and binary adsorption equilibrium data for CO and CO_2 on NaY zeolite molecular sieve. These data and their description are critical for designing an adsorptive separation process. A temperature-dependent multisite Langmuir equation has been used to model successfully all adsorption equilibria data, both pure component and binary, using only one set of parameters. This model can be used easily in non-isothermal fixed-bed simulations.

$$n_i = \frac{m_b b_i P_i}{(1+b_i P_i + b_j P_j)} + \frac{m_d d_i P_i}{(1+d_i P_i + d_j P_j)}$$

$$b_i = b_{i0} \exp\left[\frac{q_{bi}}{R}\left(\frac{1}{T} - \frac{1}{T_{ref}}\right)\right] \qquad d_i = d_{i0} \exp\left[\frac{q_{di}}{R}\left(\frac{1}{T} - \frac{1}{T_{ref}}\right)\right]$$

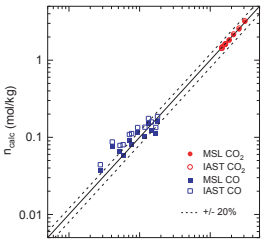

Comparison of binary adsorption data with values calculated from multisite Langmuir and IAST

4-step Adsorption Cycle

Our separation device contains a CO_2-selective sorbent such that when the mixture is fed from the electrolyzer, CO_2 adsorbs and CO passes through the bed with minimal adsorption. The mixture is fed at a temperature of 273 K. When the bed reaches capacity, it is isolated and heated with no flow at 398 K to desorb the CO_2. CO_2 at high pressure is then allowed to pass to a storage tank at sufficient pressure to feed the electrolyzer. The bed is then cooled back to 273 K prior to returning to the feed step. We envision a two-bed system in which one bed is onstream for the feed step while the other is undergoing regeneration and blowdown of CO_2.

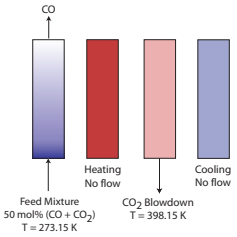

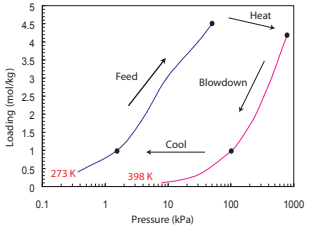

Experimental Apparatus

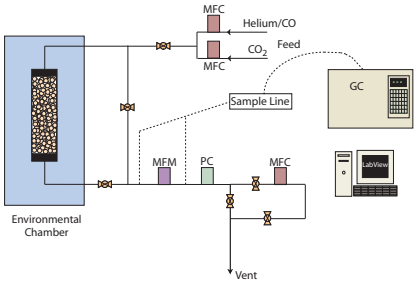

The device is heated or cooled by an environmental chamber. Mass flow controllers allow constant feed of the mixture at prescribed rates. A mass flow meter measures the product flow and a pressure controller maintains downstream pressure at setpoint. An additional mass flow controller is used to control the flow of CO_2 during blowdown. A gas chromatograph allows analysis of the composition of the product stream. The process is automated by National Instrument's LabView software.

CO_2 Breakthrough Curve

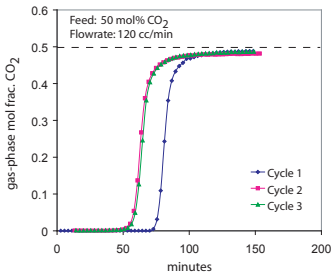

CO_2 begins to breakthrough the bed around 1 hour and 10 minutes after the feed step has begun for the first cycle. For the subsequent 2 cycles, CO_2 begins to breakthrough earlier after a feed duration of approximately 1 hour. Before CO_2 breakthrough, we are producing mostly pure helium with small traces of CO_2. We expect similar behavior for a mixture of CO and CO_2 based on binary adsorption measurements.

ENHANCED DAMPING FOR CAPILLARY BRIDGE OSCILLATION USING VELOCITY FEEDBACK

Wei Wei, David B. Thiessen, and Philip L. Marston
Department of Physics
Washington State University
Pullman, Washington 99164-2814

The stability of cylindrical liquid bridges in reduced gravity is affected by ambient vibrations of the spacecraft. Such vibrations are expected to excite capillary modes of the bridge. The lowest-order unstable mode is particularly susceptible to vibration as the length of the bridge approaches the stability limit. This low-order mode is known as the (2,0) mode and is an axisymmetric varicose mode of one wavelength in the axial direction. In this work, an optical system is used to detect the (2,0)-mode amplitude. The derivative of the error signal produced by this detector is used to produce the appropriate voltages on a pair of ring electrodes which are concentric with the bridge. A mode-coupled Maxwell stress profile is thus generated in proportional to the modal velocity. Depending on the sign of the gain, the damping of the capillary oscillation can be either increased or decreased. This effect has been demonstrated in Plateau-tank experiments. Increasing the damping of the capillary modes on free liquid surfaces in space could be beneficial for containerless processing and other novel technologies. [work supported by NASA]

Enhanced damping for capillary bridge oscillation using velocity feedback

Wei Wei, David B. Thiessen, and Philip L. Marston
Department of Physics, Washington State University, WA 99164-2814

Abstract

The stability of cylindrical liquid bridges in reduced gravity is affected by ambient vibrations of the spacecraft. Such vibrations are expected to excite capillary modes of the bridge. The lowest-order unstable mode is particularly susceptible to vibration as the length of the bridge approaches the stability limit. This low-order mode is known as the (2,0) mode and is an axisymmetric varicose mode of one wavelength in the axial direction. In this work, an optical system is used to detect the (2,0)-mode amplitude. The derivative of the error signal produced by this detector is used to produce the appropriate voltages on a pair of ring electrodes which are concentric with the bridge. A mode-coupled Maxwell stress profile is thus generated in proportion to the modal velocity. Depending on the sign of the gain, the damping of the capillary oscillation can be either increased or decreased. This effect has been demonstrated in Plateau-tank experiments. Increasing the damping of the capillary modes on free liquid surfaces in space could be beneficial for containerless processing and other novel technologies.

1 Introduction

Various capillary modes of liquid bridges are susceptible to vibration in a zero gravity environment. Under zero gravity, in the absence of any stabilization method, the (2,0) mode shown in the graph below is the first mode to become unstable and breaks if the slenderness $S = L/2R$ exceeds π. This is known as Rayleigh-Plateau limit.

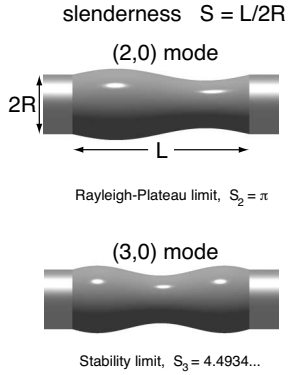

When the vibration frequency of the environment is near the natural frequency of a capillary bridge mode, mode-coupled electrostatic stress in proportion to the modal amplitude can be used to shift the frequency of the mode higher, and at same time the electrostatic stress in proportion to the modal velocity can be used to further enhance the stability of the bridge. This is useful for reducing the effect of g-jitter.

2 Setup

2.1 System configuration

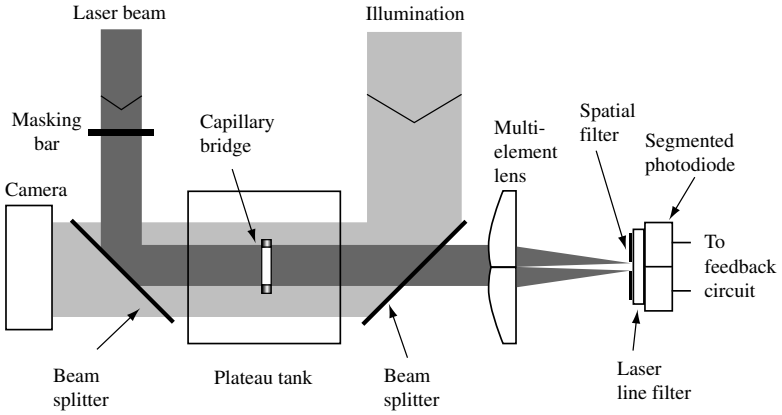

As shown in the above illustration, the laser beam illuminates the bridge which has a composition of 52 wt% CsCl and 48 wt % H_2O. The tank liquid is a 3M product, HFE 7500 which has the same density as the bridge liquid so that a weightless condition is simulated. A multi-element lens is used to focus the laser beam onto the segmented photo diode, which detects the deformation of the bridge and generates a signal to the feedback circuit which will generate the proper voltage (in proportion to the square root of the modal velocity) on the ring.

The bridge is horizontal in the Plateau tank, and this is the top view.

2.2 Bridge profile

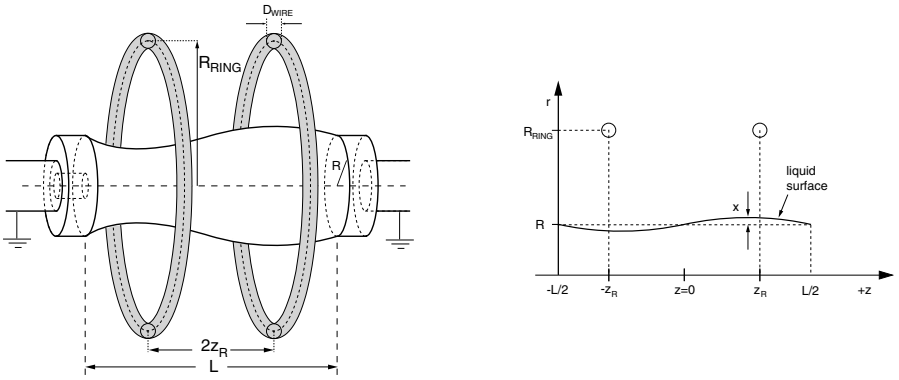

The left figure above shows a grounded bridge with two concentric ring electrodes. In this figure the bridge has a (2,0) mode shape. Since the voltage on the ring is proportional to the square root of the modal velocity, $(dx/dt)^{1/2}$, so is the electric field. Note that the stress is proportional to the square of the electric field, therefore, the generated stress on the surface of the bridge is proportional to the modal velocity dx/dt, which is the derivative of the modal amplitude, shown as x in the above graph.

3 Simple model and model prediction

The bridge is similar to a driven, damped harmonic oscillator. The feedback force can be expressed as: $F_{fb} = -R^2\left[Gx(t-\tau) + G_v\frac{dx}{dt}|_{t-\tau_v}\right]$. where G, G_v are the modal amplitude gain and velocity gain. Therefore the equation of motion is

$$\begin{aligned} m_0\frac{d^2x}{dt^2} = & - k_0x(t) - \gamma_0\frac{dx}{dt} - R^2\left[Gx(t-\tau) + G_v\frac{dx}{dt}|_{t-\tau_v}\right] - \\ & - \alpha\sqrt{2}\int_{-\infty}^{t}\frac{1}{[\pi(t-t')]^{1/2}}\frac{d^2x}{dt'^2}dt', \end{aligned}$$

where $x(t)$ is instantaneous modal amplitude. For the eigenmode solution $x(t) = x_0e^{i\Omega t}$, the characteristic equation is

$$\begin{aligned} (k_0 + R^2G) & - \Omega^2\left(m_0 + \frac{1}{2}R^2G\tau^2 - R^2G_v\tau_v\right) + \alpha i\,(1+i)\,\Omega^{3/2} \\ & + i\Omega\left(\gamma_0 - R^2G\tau + R^2G_v\right) = 0. \end{aligned}$$

This equation can be rewritten as

$$k_e - \Omega^2m_e + \alpha i\,(1+i)\,\Omega^{3/2} + i\Omega\gamma_e = 0$$

where k_e, γ_e are the effective spring constant and damping rate respectively,

$$\begin{aligned} k_e &= k_0 + R^2G, \\ k_0 &\propto \left[(\frac{\pi}{S})^2 - 1\right], \\ \gamma_e &= \gamma_0 - R^2G\tau + R^2G_v, \\ m_e &= m_0 + \frac{1}{2}R^2G\tau^2 - R^2G_v\tau_v. \end{aligned}$$

Inspection of the above equations suggests that:

- When the slenderness of the bridge is larger than π, k_0 becomes negative, thus the bridge is unstable, but by introducing amplitude gain G, k_e can be made positive, the bridge can therefore be stabilized.
- Increasing the velocity gain can increase the damping rate γ_e linearly.

4 Experimental procedure

- Check the density match between bridge liquid and tank liquid,deploy the bridge
- Excite the bridge with a 20 cycle sine wave burst
- Record the P.D signal, fit decay to Duffing equation to get $\Omega = \omega + i\gamma$, where ω is the frequency and γ the damping rate.

$$\frac{d^2x}{dt^2} + (\omega^2 - ax^2)x = -2\gamma\frac{dx}{dt},$$

5 Experiment results

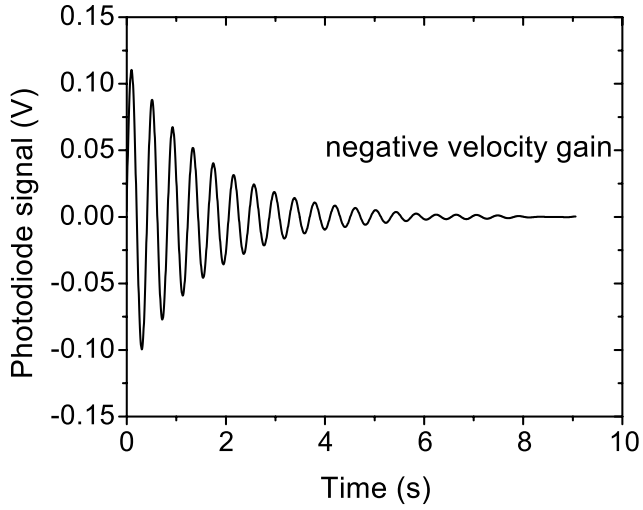

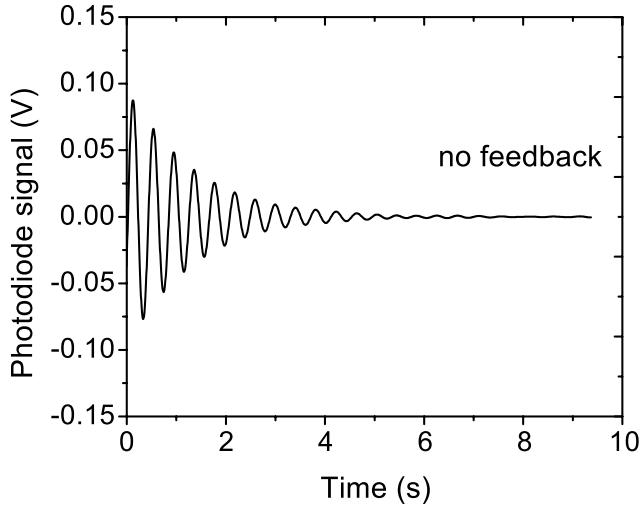

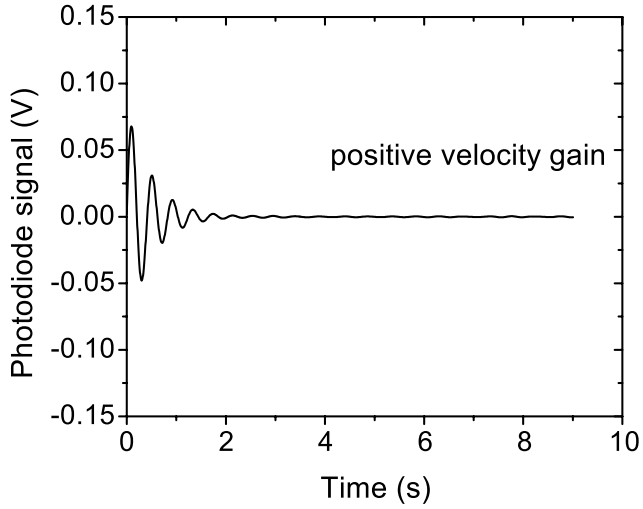

This figure shows the qualitative effect of velocity feedback. One can see that positive velocity gain can enhance the damping while negative velocity gain decreases the damping.

The experimental results also show that

- The velocity gain doesn't affect the frequency a lot.
- Increasing the velocity gain can increase the damping rate.
- Damping increases linearly with the velocity gain, after the gain correction factor (due to non-ideal feedback electronics) is taken into account.
- when the velocity gain becomes sufficiently negative, the quality factor or the damping rate can become negative, this will cause the naturally stable bridge to break up.

6 Conclusions

- Enhanced damping of the axisymmetric (2,0) capillary mode is demonstrated by applying mode-coupled electrostatic Maxwell stress that is proportional to the modal velocity.
- Damping increases linearly with velocity gain as predicted from the model.
- Amplitude feedback shifts the natural frequency higher and has been used for bridge stabilization. Amplitude and velocity feedback can be used together to further enhance the stability.

Acknowledgment

This work is supported by NASA.

References

[1] D. B. Thiessen, M. J. Marr-Lyon, and P. L. Marston, "Active electrostatic stabilization of liquid bridges in low gravity," J. Fluid Mech. **457**, 285 (2002).

[2] M. J. Marr-Lyon, D. B. Thiessen, Florian J.Blonigen and P. L. Marston, "Stabilization of electrically conducting capillary bridges using feedback control of radial electrostatic stress and the shapes of extended bridges," Phys. Fluids, **12**, 986(2000).

THE STUDY OF TOPOLOGICAL STRUCTURE DISTRIBUTIONS IN STRATIFIED SOAP FILM CONVECTIONS

Jie Zhang, Yonggun Jun, and X.L. Wu
Department of Physics
University of Pittsburgh
Pittsburgh, PA 15260

The statistical properties of local topological structures (centers and saddles) are studied using a vertically suspended soap film. The turbulent convection of the film is created by a vertical temperature gradient (ΔT). The quantitative description of local topology is given by $\Lambda(x,y) \equiv \frac{1}{4}(\omega^2 - \sigma^2)$, where ω is the local vorticity and σ is the local strain rate. The PDFs of Λ were measured within a broad range of ΔTs. After normalizing Λ by its Λ_{rms}, one found that the PDFs of Λ were collapsed to two different curves at low and high ΔT regimes. Interestingly, the non-dimensional compressibility $C \equiv \frac{<(\nabla \bullet \vec{v})^2>^{\frac{1}{2}}}{<(\nabla \vec{v})^2>^{\frac{1}{2}}}$ was found to have two different constant values at these low and high ΔT regimes within experimental uncertainties. At low ΔT, C was found 0.32, and at high ΔT was 0.24. We believe the two different behaviors of Λ PDFs and C at low and high ΔTs are closely related and are result of the vertical stratifications of the soap film

REPORT DOCUMENTATION PAGE

Form Approved
OMB No. 0704-0188

1. AGENCY USE ONLY (*Leave blank*)	2. REPORT DATE	3. REPORT TYPE AND DATES COVERED
	August 2004	Conference Publication

4. TITLE AND SUBTITLE
Strategic Research to Enable NASA's Exploration Missions Conference and Workshop
Poster Session

5. FUNDING NUMBERS
WBS–22–101–58–09

6. AUTHOR(S)
Henry Nahra, compiler

7. PERFORMING ORGANIZATION NAME(S) AND ADDRESS(ES)
National Aeronautics and Space Administration
John H. Glenn Research Center at Lewis Field
Cleveland, Ohio 44135–3191

8. PERFORMING ORGANIZATION REPORT NUMBER
E–14713–2

9. SPONSORING/MONITORING AGENCY NAME(S) AND ADDRESS(ES)
National Aeronautics and Space Administration
Washington, DC 20546–0001

10. SPONSORING/MONITORING AGENCY REPORT NUMBER
NASA CP—2004-213205-VOL2

11. SUPPLEMENTARY NOTES
Proceedings of a conference held at and sponsored by the NASA Office of Biological and Physical Research and hosted by NASA Glenn Research Center and the National Center for Microgravity Research on Fluids and Combustion, Cleveland, Ohio, June 22–23, 2004. Responsible person, Henry Nahra, organization code 6712, 216–433–5385.

12a. DISTRIBUTION/AVAILABILITY STATEMENT
Unclassified - Unlimited
Subject Category: 34 Distribution: Nonstandard
Available electronically at http://gltrs.grc.nasa.gov
This publication is available from the NASA Center for AeroSpace Information, 301–621–0390.

12b. DISTRIBUTION CODE

13. ABSTRACT ***(Maximum 200 words)***

The primary focus of the conference on Strategic Research to Enable NASA's Exploration Missions is to inform the research community of the changing direction of the NASA Office of Biological and Physical Research programs to support the future exploration missions. The conference includes invited plenary talks, technical paper presentations, poster presentations, and exhibits in the areas of Human Life Support Technology and Human Health. This CP is a compilation of the abstracts, presentations, and posters presented at the conference.

14. SUBJECT TERMS
Reduced gravity; Advanced life support; Multi-phase flows; Fire prevention; Detection and suppression; Human health; Bio fluids; Bio medical devices; Micro systems and astronaut health

15. NUMBER OF PAGES
522

16. PRICE CODE

17. SECURITY CLASSIFICATION OF REPORT	18. SECURITY CLASSIFICATION OF THIS PAGE	19. SECURITY CLASSIFICATION OF ABSTRACT	20. LIMITATION OF ABSTRACT
Unclassified	Unclassified	Unclassified	